CRANFIELD UNIVERSITY

CARLOS HANNOVER GALINDO-LÓPEZ

OPTIMISATION OF CONVECTIVE HEAT DISSIPATION FROM VENTILATED BRAKE DISCS

SCHOOL OF APPLIED SCIENCES

PhD THESIS

CRANFIELD UNIVERSITY

SCHOOL OF APPLIED SCIENCES

PhD THESIS

CARLOS HANNOVER GALINDO-LÓPEZ

Academic Year 2008-2009

Optimisation of Convective Heat Dissipation from Ventilated Brake Discs

Supervisor: Dr. Marko Tirović

May 2009

Abstract

Fast heat dissipation from brake discs is sought in current vehicles, where high power braking duties demand harmonic combination of strength, (undamped) disc mass and cooling abilities for a wide speed range. This work analyses the convective heat dissipation from ventilated brake discs and proposes means for its optimisation.

The focus of research is the ventilation geometry of a standard brake disc with an outer diameter of 434mm and radial channels of 101mm in length. After analysing in detail data calculated with CFD simulations and from experimental work for various ventilation patterns, a parameter relating the local channel-averaged convective heat transfer coefficient to channel circumferential width, and radial location was derived. This new numerical parameter termed Flow Index, depicts graphically the link between channel geometry (width and position) to the heat transfer coefficient level attained. The FI was not only used as a tool to analyse the convective performance of conventional and new ventilation geometries, but it also allowed clear identification of changes necessary in the channel width in order to improve its convective heat transfer coefficients. New, optimised for convective heat transfer, ventilation geometries designed with the FI were achieved in this Thesis.

Industrial (patenting) and academic applications are foreseen from the results of this Thesis and its future activities. Also, the work developed in this Thesis gives path and supporting frame for future research in the field of brake disc convective heat dissipation.

Aknowledgements

The author and his family are grateful for the invaluable support, guidance and advise from Dr. Marko Tirović during the course of this work.

The author is also grateful to the School of Applied Sciences and School of Engineering of Cranfield University for supporting this research project. Thanks also to Drs. Chris Thompson and Julian Turnbull for their support in CFD matters. Special thanks are also given to ORSAS-UK for partial fees funding and to CONACyT México (grant 192813) for partial bursary funding.

The author and his family also thank to the Cranfield University Community Development and Housing Offices for their kindest and prompt support during our stay in the Campus. A recognition also for those mexicans and friends who never let us down.

Para tí Mercedes.

Para mis padres: Rosalba y Avelino.

Carlos Hannover Galindo-López, May 2009.

Contents

1 Introduction and Research Objectives **1**

1.1 Terminology 4

1.2 Research Objectives 5

2 Literature Review **7**

2.1 Heat Dissipation by Conduction 7

2.2 Heat Dissipation by Radiation 13

2.3 Dissipation by Convection 16

2.3.1 Automotive Brakes 16

2.3.2 Railway Brake Discs 23

2.3.3 Computational Convective Dissipation in Brakes Discs 24

2.3.4 Experimental Flow Studies in Ventilated Brake Disc 27

2.3.5 Flow and Convection in Rotating Channels 31

2.4 Summary 32

3 Research Methodology **34**

3.1 Flow and Heat Transfer Modelling 34

3.1.1 Overview of Fluid Dynamics Equations 35

3.1.2 Turbulence Modelling 39

3.1.3 Computational Approach 44

3.1.4 Convective Heat Transfer Modelling 45

3.1.5 Evaluation of Rotational Effects 70
3.1.6 CFD Model and Grid Definition, BC's and Solution Parameters . . . 75

4 Experimental Approach 80
4.1 Brake Discs 81
4.1.1 Standard CV Brake Disc 81
4.2 New Disc Prototypes 82
4.3 Spin Rig 84
4.4 Disc Heating: Heating Box 85
4.5 Disc Heating: Induction Heater 86
4.6 Temperature Measurement: Thermocouples 87
4.7 Angular Speed and Torque Measurement 89
4.8 Hot Wire Anemometry 89
4.9 The Hot Wire Anemometry Test Set-up 91
4.10 Brake Disc Cooling Tests Set-up 98
4.11 Raw Data and Derived Results 98
4.11.1 Experimental Uncertainty 99
4.11.2 Heat Transfer Coefficients Derivation 100
4.11.3 Uncertainty of Heat Transfer Coefficients 103
4.12 Summary 107

5 Baseline Brake Disc Convective Cooling 109
5.1 Convergence Analysis 110
5.2 Computational Flow and Heat Transfer Modelling 121
5.2.1 Stationary CFD Model 123
5.2.2 Rotating Frame of Reference CFD Model 124
5.2.3 Comparison of Results: Stationary vs RFR Models 125
5.2.4 Characteristics of the Baseline Disc CFD Model 127
5.3 Experimental Convective Cooling Results 130

5.3.1 Tests Conditions . . . 130
5.3.2 Recording of Cooling Temperatures . . . 131
5.3.3 Total and Convective Heat Transfer Coefficients . . . 133
5.4 Validation of CFD Results . . . 135
5.5 Flow Characteristics in Standard Brake Disc Vents . . . 137
5.5.1 Averaged Results and Analysis of Flow Characteristics . . . 147
5.6 Torque Measurement . . . 154
5.7 Hot Wire Anemometry Measurements . . . 156

6 Channels Researched 160
6.1 Cylindrical Channels . . . 161
6.1.1 Geometry . . . 161
6.1.2 CFD Model . . . 162
6.1.3 CFD Results . . . 162
6.2 Trapezoidal Channels . . . 167
6.2.1 Geometry . . . 167
6.2.2 CFD models . . . 169
6.2.3 CFD Results . . . 170
6.3 Small Vane Inside the Channel . . . 177
6.3.1 Geometry . . . 180
6.3.2 CFD Models . . . 181
6.3.3 CFD Results . . . 181
6.4 Pillars . . . 193
6.4.1 Geometry . . . 193
6.4.2 CFD models . . . 196
6.4.3 CFD results . . . 196
6.5 Inlet Guide Vanes . . . 204
6.6 Curved IGV - Geometry . . . 207
6.7 CFD Model - IGV1 . . . 207

6.8 CFD Results - IGV1 208
6.8.1 Swirling Flow 212
6.9 Channels with IGV's and SV1 vane - Geometry 214
6.10 Channels with IGV's and SV1 vane - CFD models 215
6.11 Channels with IGV's and SV1 vane - Results 217
6.12 Summary 222
6.13 Experimental Work 224
6.13.1 Non-ventilated Discs 225
6.13.2 Ventilated Discs 227

7 Railway Wheel Mounted Brake Disc 234
7.1 WMD Configuration and Heat Dissipation 234
7.2 WMD Computational Fluid Dynamics Modelling 238
7.3 WMD Computational Fluid Dynamics Results 239
7.4 Wheel Mounted Brake Disc: Improvements in the Design 248
7.4.1 CFD Results of Modified Designs 249

8 Ventilation System Optimisation 258
8.1 Convection in Duct Entry Regions 258
8.1.1 Flow Development in Rotating Brake Disc Channels 263
8.2 Flow Index and Convection Analysis of Brake Disc Passages 264
8.2.1 Flow Index Definition 264
8.2.2 Channel Geometry Characterisation 266
8.3 Variables for Flow Index 266
8.3.1 Flow Index in Radial Channels 269
8.3.2 Flow Index Analysis of Modified Passages 272
8.4 Synthesis of New Disc Designs 280
8.4.1 Three Curved Vane Designs 281
8.4.2 Two Curved Vane Designs 287

8.4.3 The Effect of Rotational Direction 294
8.5 Experimental Modelling 297
8.5.1 Brake Discs Prototypes 299
8.5.2 Cooling History 301
8.6 Local Convection Analysis of Radial Vents 305
8.6.1 A Correlation for Nu in Trapezoidal Channels 307
8.7 Summary 314

9 Discussion **316**

10 Conclusions and Future Work **320**
10.1 Future Work 322

A Brake Disc Test Program **323**

B Experimental Heat transfer Coefficients **325**

C Vents Researched: Complementary Results **332**

D WMD: Complementary Results **340**

E Glossary **343**

List of Figures

1.1 Typical brake system (Eriksson, 2000). 1

1.2 Braking energy per vehicle and speed. 2

1.3 Heat dissipation from a CV gray iron disc. 3

1.4 Ventilated brake disc - see Table 1.1. 4

2.1 Average pressure contact as per formulas 2.4, 2.5 and 2.9. 11

2.2 Average thermal contact conductance as per formulas 2.6, 2.7 and 2.10. . . . 12

2.3 Average thermal contact conductance as per formulas 2.10 and 2.11, using gray iron ultimate tensile strength (293MPa) as S_y. 12

2.4 Radiation and convection from solid and hollowed bodies. 14

2.5 Cooling tests raw data used to obtain the radiation heat transfer coefficients. 15

2.6 Radiation heat transfer coefficients obtained using data in Figure 2.5 and equation 2.12. 15

2.7 Straight vane rotor diagram, 20 to 40 vanes (Sisson, 1978). 17

2.8 Vent geometries researched by Palmer *et al* (2006). 20

2.9 Dimensions of the brake disc model used by Wallis *et al* (2002). 25

2.10 Channel geometries modelled by Wallis *et al* (2002). 25

2.11 Convective heat transfer coefficients, CV standard brake disc; Voller (2003). 26

2.12 Convective heat transfer coefficients, TGV brake disc; Voller (2003). 27

2.13 Relative velocity vectors at channel midplane, n=684 rpm, Johnson *et al* (2003). 28

2.14 Disc geometry used by Barigozzi *et al* (2003). 29

2.15 Non-dimensional radial velocities at the channels exit, Barigozzi *et al* (2003). 30

2.16 Disc geometry used by Parish & MacManus (2005). 30
2.17 Channel geometry and rotating coordinate system, Dutta *et al* (1996). . . . 31
2.18 Secondary flow patterns in rotating channels, Dutta *et al* (1996). 31
2.19 Flow separation mechanisms in rotating channels, Dutta *et al* (1996). 32
2.20 Nusselt numbers in a long rotating square-duct, $Z = \frac{z}{D_h}$; Yan & Soong (1995). 32

3.1 Turbulent fluctuation of momentum according to Prandtl mixing length theory. 43
3.2 Velocity boundary layer on a flat plate. 46
3.3 Boundary layer thickness on a flat surface, length=0.095m. 52
3.4 Wall shear stress on surface, $U_\infty = 1.5m/s$. 53
3.5 Wall shear stress on surface. 54
3.6 Laminar thermal boundary layer on a flat hot plate. 55
3.7 Local convective heat transfer coefficient (laminar flow), $\Theta_w = 100^oC$, $\Theta_\infty = 20^oC$. 56
3.8 Thermal boundary layer representation in turbulent convective cooling of a flat plate. 57
3.9 Thermal turbulent boundary layer thickness, from equations 3.52 and 3.45. . 63
3.10 Friction velocity on plate wall using equations 3.37 and 3.46. 64
3.11 Y^+ calculated along the plate using $y = \delta_{th}$ in equation 3.38. Plate length=0.095m. 65
3.12 Θ^+ calculated along the plate using y^+ from Figure 3.11, and equations 3.68 and 3.72; Kader (1981) and Kays & Crawford (1980). Plate length=0.095m. 66
3.13 Turbulent heat transfer coefficients calculated along the plate using $\Theta_{nw} = \bar{\Theta}$, and equations 3.68 ($y/\delta = 1$), and 3.72; from Kader (1981) and Kays & Crawford (1980). Plate length=0.095m. 67
3.14 Turbulent heat transfer coefficients calculated along the plate using $\Theta_{nw} = \Theta_\infty$, and equations 3.68 ($y/\delta = 1$), and 3.72; from Kader (1981) and Kays & Crawford (1980). Plate length=0.095m. 68
3.15 Rotational Reynolds number for three typical brake discs. 73
3.16 Full computational domain and the smallest periodic sector. 76
3.17 CFD model bounding dimensions using double periodic sector. 77
3.18 Typical CFD model of a ventilated brake disc, considering two channels. . . 77

4.1 Cast iron standard brake disc. 81
4.2 General dimensions in mm of the ventilated brake disc used for experiments. 82
4.3 Detachable Vane Brake Disc. Left to right: Outboard side disc, vanes, inboard side disc, dowls and bolts. 83
4.4 Brake disc cooling test apparatus (Spin Rig). 84
4.5 Heating equipments. 85
4.6 Brake disc cooling test history using induction heating. 86
4.7 Rubbing K type thermocouple used on brake disc friction surface. 87
4.8 Data loggers. 88
4.9 Hot wire probe types: (a) unplated, (b) plated, and (c), (d) for boundary layer flows. From Bruun (1995). 90
4.10 Hot Wire Anemometry equipment: Mini-CTA, Wire probe, BNC cables, Power cable. 92
4.11 Probe alignment for flow measurement, parallel (left) and perpendicular to channel endwalls. 93
4.12 Single wire in normal direction to main stream. From Bruun (1995). 93
4.13 Wire probe positioned for tests and schematics for location and signal acquisition. 94
4.14 Brake disc cooling test set up, *A, B,...,J* indicate thermocouples. 98
4.15 Selection of temperatures for calculation of heat transfer coefficients. 102
4.16 Typical process for CFD simulations. 108

5.1 Simplified CAD model of the baseline disc. 110
5.2 Mesh and flow alignment. 111
5.3 Schematic of CFD model for convergence analysis, see Table 5.1, $z_c = h/2$. . 112
5.4 Visualization of CFD model used for convergence analysis. 112
5.5 Location of lines for postprocessing of data during convergence analysis. . . . 113
5.6 Computational grid for first model of convergence analysis. Tetrahedral grid, c =4 mm 114
5.7 Computational grid for second model of convergence analysis. Hexahedral grid, c =4 mm 114

5.8 Computational grid for third model of convergence analysis. Grid composed by hexahedrals, four cells near the wall separated c =0.5 mm, elsewhere c =2 mm. 115

5.9 Computational grid for fourth model of convergence analysis. Grid near the wall is refined with 9 cells covering 2.07 mm, with variable width (constant inflation ratio of 1.2), elsewhere c =2 mm 115

5.10 Numerical convergence of $\overline{u_x}$ using grids 1 to 4. 117

5.11 Convergence analysis of $\overline{\Theta}$ using grids 1 to 4. 117

5.12 Convergence error on channel leading side between refined meshes 3 and 4. . 118

5.13 Final convergence error on channel leading wall (vane trailing wall) side for h_c. 119

5.14 Final convergence error on channel trailing wall (vane leading wall) side for h_c. 120

5.15 Secondary flow patterns in rotating channels. 121

5.16 Airflow pattern in a rotating ventilated brake disc. Ideal (left) and CFD predicted (right) patterns. 122

5.17 Stationary channel CFD model (no angular speed). 123

5.18 Periodic CFD model of baseline brake disc in rotating frame of reference (RFR). 124

5.19 Line for airspeed postprocessing (stationary and RFR models). 125

5.20 Radial airspeed results predicted by the stationary CFD model compared with RFR results for baseline brake disc at 100 rpm. 126

5.21 Heat transfer coefficients in the RFR and stationary CFD models, n=100 rpm. 127

5.22 Mesh details in the channel region of the baseline model. 127

5.23 Mesh details in the external surfaces of the baseline model. 128

5.24 Details of the mesh on the cut face (PF) of the baseline model. 129

5.25 Locations of lines for CFD data postprocessing. 129

5.26 Suction effects on air due to brake rotation. 131

5.27 Detachable vane brake disc mounted on Spin Rig. 132

5.28 Experimental cooling history, baseline (30 vanes) standard brake disc. 132

5.29 Logarithmic plots of experimental results using the baseline (30 vanes) standard brake disc. 133

5.30 Convective heat transfer coefficients from cast iron and detachable (Al) vane brake prototypes. 134

5.31 Comparison between experimental and computational (CFD) disc heat transfer coefficients (cast iron disc). 136

5.32 Comparison between experimental and computational (CFD) disc heat transfer coefficients (DVBD). 136

5.33 Streamlines of relative mean speed on the periodic face plane, n=400rpm. . . 138

5.34 Streamlines of absolute mean speed on the periodic face plane, baseline brake disc at n=800rpm. 138

5.35 Streamlines of relative speed within brake disc channel, n=400rpm. 139

5.36 Streamlines of relative speed within brake disc channel, n=800rpm. 140

5.37 Total pressure contours in stationary frame on channel midplane, n=400rpm. 140

5.38 Circumferential relative speed vectors within the channel showing secondary flow patterns, n=400rpm. 141

5.39 Circumferential relative speed vectors within the channel showing secondary flow patterns, n=800rpm. 142

5.40 Air temperature on channel midplane. 142

5.41 Air temperature on the periodic face, n=400rpm. 143

5.42 Convective heat transfer coefficient contours on vane surface. Baseline brake disc rotating at n=400rpm, (about $+z$). 144

5.43 Convective heat transfer coefficient contours on vane surface. Baseline brake disc rotating at n=800rpm, (about $+z$). 144

5.44 Convective heat transfer coefficients on channel endwall; outboard brake side toward $+z$, n=400rpm. 145

5.45 Convective heat transfer coefficients on channel endwall, outboard brake side on $+z$ direction, n=800rpm. 145

5.46 Convective heat transfer coefficients on hub and friction faces. 146

5.47 Convective heat transfer coefficient contours on brake disc outer ring surfaces. 147

5.48 Turbulent kinetic energy on a midplane inside the channels and on the periodic face of the model (channel centre). 148

5.49 Averaged absolute radial air speed through the channels of baseline disc. Comparison against Sisson (1978) and Limpert (1975) formulae. 148

5.50 Air mass flow through the channels of the baseline brake disc as predicted by CFD simulations 149
5.51 Disc Nusselt numbers from CFD and empirical predictions. 151
5.52 Channel averaged Nusselt number from CFD and empirical predictions. . . . 152
5.53 Lines for postprocessing of absolute $\overline{u_r}$ and $\overline{\Theta}$ 2 mm away from vane walls. . 152
5.54 Channel radial absolute airspeed and Reynolds numbers at n=800rpm. . . . 153
5.55 Air temperature near the vane walls and local heat transfer coefficient, n=800rpm. 154
5.56 Torque measurements for rolling resistance, 2 sample/sec. 155
5.57 Averaged torque readings from shaft only. 155
5.58 Averaged torque measurements,baseline brake disc mounted on the Spin Rig. 156
5.59 HWA raw signal and ergodic representation, baseline disc at 200rpm. 157
5.60 Post-process of HWA signal, baseline disc at 200rpm. 158
5.61 Fluctuating component of the signal, baseline disc at 200rpm.. 159
5.62 PSD functions, baseline disc at 200rpm. 159

6.1 Views of a 24 degree sector of a brake disc with cylindrical channels. 161
6.2 CFD model of the brake disc with cylindrical channels. 162
6.3 Cylindrical channels, flow streamlines at n=400rpm. 163
6.4 Cylindrical channels. Secondary flow patterns at n=400rpm. 163
6.5 Cylindrical channels. Air temperature contours, n=400rpm. 164
6.6 Cylindrical channels, heat transfer coefficient distribution, n=400rpm. 165
6.7 Averaged convective heat transfer coefficients, cylindrical channels vs baseline design (data from CFD). 166
6.8 Disc cooling rates comparison, cylindrical versus baseline channel design. . . 167
6.9 Local values of temperature and absolute speed at the stream core. 168
6.10 Local h_c in the channel poles. 169
6.11 Trapezoidal channels, Left: 20 vanes disc sector, right: 45 vanes disc sector. . 169
6.12 Trapezoidal channels, Left: 60 vanes disc sector, right: 90 vanes disc sector. . 170
6.13 Relative speed streamlines, 20 and 45 vane designs, n=400rpm. 171

6.14 Total pressure, channel midplane, 20 and 45 vane designs, n=400rpm. 172
6.15 Air temperature in channel midplane, 20 and 45 vane designs, n=400rpm. . . 172
6.16 Secondary flow activity, discs with 20 and 45 vanes at n=400rpm. 173
6.17 Convective heat transfer coefficients in vanes, 20 and 45 vane discs, n=400rpm.174
6.18 Convective heat transfer coefficients in endwalls, 20 and 45-vane design at n=400rpm. 175
6.19 Streamlines on channel midplane, 60 and 90 vane designs at n=400rpm. . . . 176
6.20 Air temperature on channel midplane, 60 and 90 vane designs at n=400rpm. 177
6.21 Convective heat transfer coefficients in vanes, 60 and 90-vane designs, n=400rpm.178
6.22 Convective heat transfer coefficients in endwalls, 60 and 90-vane designs, n=400rpm. 179
6.23 Averaged heat transfer coefficients versus angular speed. 179
6.24 Comparison of $\frac{A_w}{m_d C_{p_d}}$ for researched brake discs (radial vanes). 180
6.25 Convective cooling rates and aerodynamic torque, discs with radial vanes. . . 181
6.26 Mass flow in brake disc channels with radial vanes, (data from CFD). 182
6.27 Channel flow pattern modification. Left: original pattern, right: modified pattern. 182
6.28 Channel sector characteristics, (a) Baseline channel, and channel with: (b) SV1 at inlet, (c) SV1 at half channel, (d) SV1 at outlet. (e) Location details. 183
6.29 Streamlines of relative speed on channel midplane, discs at n=400rpm. . . . 184
6.30 Air temperature in channel midplanes, discs at n=400rpm. 185
6.31 Convective heat transfer coefficients in vanes, discs with SV1 at n=400rpm. . 186
6.32 Convective heat transfer coefficients on endwalls, disc with SV1 at n=400rpm. 187
6.33 Comparisons of convective heat transfer coefficients, discs with SV1 vane. . . 187
6.34 Convective cooling rates and aerodynamic torque, discs with SV1 vane (data from CFD). 188
6.35 Mass flow from discs with the SV1 vane versus the baseline brake disc, (data from CFD results). 189
6.36 Absolute speed of air near vane wall, per channel side, n=800 rpm. 190
6.37 Air temperature (per channel side) near the vane wall, n=800 rpm. 190

6.38 Local h_c per channel side, discs with SV1, n=800 rpm. 191
6.39 Net gains in heat transfer coefficient per channel side, discs with SV1, n=800 rpm. 192
6.40 Arrays of tubes or cylinders banks for convective heat transfer purposes, (Bejan 2004). 193
6.41 Values of the constant C_n, from (Bejan 2004). 194
6.42 Pillared disc in configuration 1. 195
6.43 Relative speed streamlines in passage midplane, configurations P1 and P2, n=400rpm. 197
6.44 Streamline patterns in two circumferential planes, configuration P3, n=400rpm. 197
6.45 Air temperature patterns in midplanes for pillared configurations, n=400rpm. 198
6.46 Heat transfer coefficient distributions on configurations P1 and P2, n=400rpm. 199
6.47 Heat transfer coefficient distributions on configuration P3, n=400rpm. 199
6.48 Heat transfer coefficient on endwalls for configurations P1 and P2, n=400rpm. 200
6.49 Heat transfer coefficient on endwalls for configuration P3, n=400rpm. 200
6.50 Pillared discs, average convective heat transfer coefficients. 201
6.51 Convective cooling rates, pillared designs versus baseline disc. 202
6.52 Mass flow and aerodynamic torque, pillared versus baseline discs. 203
6.53 Pillars Nu analysis. Zukauskas correlations versus CFD results. 204
6.54 Swirling flow on axial flow through a stationary duct, (Muralidhar 1996). . 205
6.55 Flow behaviour representation at the inlet baseline channels. 205
6.56 Schematic of swirling motion generation in radial channels of brake disc. . . 206
6.57 Geometry sector showing the curved IGV in the inlet of the baseline design. 207
6.58 Details of the surface mesh in the channel with IGV1. 208
6.59 Velocity streamlines on planes across and beneath the IGV1 span, n =400rpm. 209
6.60 Swirl flow from curved IGV, n =400rpm, left looks from channel inlet. 209
6.61 Secondary flow on planes perpendicular to main path direction, n=400rpm. . 210
6.62 Air mean temperature patterns at n=400rpm, across and beneath the IGV span. 211

6.63 Total pressure patterns in plane crossing the IGV at n=400rpm. 211
6.64 Convective heat transfer coefficients, disc with curved IGV, n=400 rpm. . . . 212
6.65 Aerodynamic characteristics for disc with curved IGV1 213
6.66 Lines for calculation of swirl parameter. 213
6.67 Swirl parameter in channel with curved IGV1 214
6.68 Geometry sector showing the channel with IGV2+SV1. 215
6.69 Geometry sector showing the channel with IGV3+SV1. 216
6.70 Mesh details in redesigned channels. 216
6.71 Relative velocity streamlines on midplane, designs with IGV2+SV1 and IGV3+SV1.217
6.72 Relative velocity streamlines, designs with IGV2+SV1 and IGV3+SV1. . . . 218
6.73 Swirl parameter, S was calculated in same lines as in Figure 6.66. 219
6.74 Air temperature patterns in midplanes, designs with IGV2+SV1 and IGV3+SV1.220
6.75 Distribution of h_c in vanes, designs with IGV2+SV1 and IGV3+SV1, n=400rpm.220
6.76 Distribution of h_c in endwalls, IGV2+SV1 and IGV3+SV1, n=400rpm. . . . 221
6.77 Averaged heat transfer coefficients versus rotational speed. 221
6.78 Convective cooling rates and aerodynamic torque, discs with IGVs. 222
6.79 Summary of Nusselt numbers. 223
6.80 Average channel Reynolds and Nusselt numbers calculated from CFD data. . 224
6.81 Brake disc with channels blocked using high temperature resistant tape. . . . 225
6.82 Non-ventilated prototype using the outboard disc. 226
6.83 Average temperatures from non-ventilated brake disc prototypes at n=400rpm.227
6.84 Experimental total and convective heat transfer coefficients, brake disc with blocked channels and outboard side disc plate. 228
6.85 Disc with blocked channels, Nusselt numbers, experiments vs theoretical data. 229
6.86 Outboard side disc, Nusselt numbers, experiments vs theoretical data. 229
6.87 Outboard side disc plate with SV1 vanes at inlet position. 230
6.88 Brake disc prototype with baseline vanes and SV1 vanes at outlet. 231
6.89 Cooling history in brake prototypes with radial and SV1 aluminum vanes, n=400rpm. 232

6.90 Experimental heat transfer coefficients, ventilated prototypes with radial and SV1 vanes. 232

6.91 Assembled prototype with SV1 vane at inlet. Gaps between the vanes and the disc faces are shown. 233

7.1 Schematic view of the assembly of the WMD with the railway wheel. 235

7.2 Railway wheel mounted brake disc CAD model views, baseline model. 235

7.3 Half cross section of the assembly wheel-WMD. 237

7.4 Heat dissipation from a wheel mounted brake disc. 237

7.5 Wheel mounted brake disc CFD model. 239

7.6 Planes and lines of data postprocessing and analysis. 240

7.7 Streamlines in rotating frame over the channels of WMD, n=400 rpm. 241

7.8 Relative velocity vectors on the near wall plane. 242

7.9 Relative velocity vectors on the midplane. 242

7.10 Relative velocity vectors in the gap plane. 243

7.11 Static pressure contours on two postprocessing planes at n=400 rpm. 244

7.12 Air temperature contours near the disc backface. 245

7.13 Air turbulent behaviour near the disc backface, n=400 rpm. 245

7.14 Turbulence in the gap plane between the wheel and the vane tips, n=400 rpm. 246

7.15 Convective heat transfer coefficients on vanes of WMD at n=400 rpm. 246

7.16 Convective heat transfer coefficients on vanes of WMD at n=1000 rpm. . . . 247

7.17 Average convective heat transfer coefficient versus rotational speed 247

7.18 Convective cooling rates versus rotational speed 248

7.19 Average Nusselt numbers versus rotational speed 249

7.20 Railway wheel mounted brake disc new design. 250

7.21 Relative velocity vectors on nearwall plane, WMD Gap 0 at n=400 rpm. . . 251

7.22 Relative velocity vectors in midplane, WMD Gap 0 at 400 rpm. 251

7.23 Absolute speed along channels of WMD and WMD Gap 0 designs, n=400rpm. 252

7.24 Air temperature contours at the near wall plane, WMD Gap 0, n=400 rpm. 253

7.25 Air temperature contours at the midplane, WMD Gap 0, n=400 rpm. 253
7.26 Convection heat transfer coefficient contours, WMD Gap 0 at 400 rpm. . . . 254
7.27 Relative velocity vectors across the channel of the WMD1 design, n=400 rpm. 254
7.28 Air temperature contours across the channel of the WMD1, n=400 rpm. . . 255
7.29 Convective heat transfer coefficients, WMD1 design, n=400 rpm. 256
7.30 Convective heat transfer coefficient contours, WMD1 design, n=1100 rpm. . 256
7.31 Convective heat transfer coefficients and cooling rates. 257

8.1 Passage Flow Index characterisation. 265
8.2 Brake disc ventilation geometry characterisation. 267
8.3 Geometry for x^+ (top) and x^+_{rot} (bottom). 267
8.4 Stations where FI was calculated. 268
8.5 Flow Index for radial vents in ventilated brake discs. 269
8.6 Rate of change of $FI\,h^*_c$ for brake discs with radial channels. 271
8.7 Flow Index for absolute radial velocity in brake discs with radial channels. . 272
8.8 Lines where local h_c was retrieved for $FI\,h_c$. 273
8.9 Flow Index, $FI\,h_c$, for SV1-middle channel design, n=400rpm. 273
8.10 $FI\,h_c$ for SV1-outlet channel design at n=400rpm. 274
8.11 $FI\,h_c$ for SV1-outlet channel design at n=800rpm. 275
8.12 $FI\,h_c$ for IGV2+SV1 passage design at n=800rpm. 275
8.13 Staggered vane design. 277
8.14 Staggered vane design, heat transfer coefficient distributions, n=400rpm. . . 277
8.15 Streamlines of relative flow in the staggered vane design at n=400rpm. . . . 278
8.16 Places where h_c was retrieved for $FI\,h_c$ calculations. 279
8.17 $FI\,h_c$ of the staggered vane design, n=400rpm. 280
8.18 Curved vane vent design D30, passages dimensions (mm). 282
8.19 Curved vane vent design D30, vanes dimensions (mm). 282
8.20 Curved vane design D30 description. 283
8.21 Convective heat transfer coefficients in vanes, n=400rpm. 283

8.22 Convective heat transfer coefficients in endwalls, n=400rpm. 284
8.23 Relative velocity streamlines at n=400rpm. 285
8.24 Channels average convective heat transfer coefficients, D30, D30+IGV3 and baseline designs. 286
8.25 Brake discs pumping torque and air mass flow. 287
8.26 Locations where h_c was retrieved to calculate $FI\,h_c$. 288
8.27 Convection heat transfer coefficient Flow Index for designs D30 and D30+IGV3. 289
8.28 D32 brake channels design. Widths as per Table 8.10. 290
8.29 Convective heat transfer coefficient distributions in vanes, n=400rpm. 291
8.30 Convective heat transfer coefficient distributions in endwalls, n=400rpm. . . 291
8.31 Relative speed streamlines in vent midplane, n=400rpm. 292
8.32 Channel average convective heat transfer coefficients; D32, D32+IGV2 and baseline designs. 293
8.33 Required torque and pumped air mass flow. 294
8.34 Convective cooling rates comparison. 295
8.35 Locations where $FI\,h_c$ was calculated (D32+IGV2 design shown). 295
8.36 Convective heat transfer coefficient Flow Index, designs D32 and D32+IGV2. 296
8.37 D32 design rotating in backward direction, relative speed streamlines at midplane, n=400rpm. 297
8.38 Heat transfer coefficient distribution, D32 at n=400rpm in backward direction. 298
8.39 Channel average heat transfer coefficients and mass flow for different modes of rotation in D32 design. 298
8.40 Convection heat transfer coefficient Flow Index for design D32 rotating in backward direction at n=400rpm. 299
8.41 Experimental prototype of *D32* brake disc design during assembly. 300
8.42 Experimental prototype of the *D32* brake disc design fully assembled. 301
8.43 Porsche 'JP' brake disc prototype and patent source. 302
8.44 Cooling histories from experimental brake disc prototypes, $\delta_\Theta = \pm 0.8^o C$. . . 302
8.45 Experimental total cooling rates from brake disc prototypes. 303

8.46 Experimental (disc) convective heat transfer coefficients for D32 and baseline detachable vane brake disc prototypes. 304

8.47 x^+ versus channel radial length for baseline channel design (30 vanes), using equation 8.6. 305

8.48 Local channel Nusselt numbers calculated from CFD and with equation 8.9. 306

8.49 Average Nusselt numbers calculated using data for $FI\,h_c$ and equation 8.9. . 307

8.50 Nu_x response under changes in constants A, B and C (see equation 8.9). . . 308

8.51 Local channel Nusselt numbers from CFD and with equation 8.24. 310

8.52 Average Nusselt numbers calculated along the channel for the baseline design (30 vanes), using equations 8.24, 2.21 and 8.9 311

8.53 Local and average predictions of channel Nusselt numbers for brake disc with 45 vanes. 313

8.54 Local and average predictions of channel Nusselt numbers for brake disc with 90 vanes. 313

9.1 Ventilated brake disc master chart at 400 rpm. 317

9.2 Ventilated brake disc master chart at 800 rpm. 319

A.1 7220 RS A/D 16 channel single module connection. 324

B.1 Cooling temperatures from natural convection test, DVB, $\delta_\Theta \approx \pm 0.8^o C$. . . 325

C.1 CFD model of brake disc with cylindrical channels. 332

C.2 Cylindrical channels. Contours of total pressure, n=400rpm. 333

C.3 Brake disc with 30 cylindrical channels, n=400rpm. 333

C.4 Mesh details of 20 and 45-vane designs. 333

C.5 Mesh details of 60 and 90-vane designs. 334

C.6 Streamlines, 20 and 45-vane designs at n=400rpm. 334

C.7 Air temperature contours across channels, 20 and 45-vane designs, n=400rpm. 334

C.8 Turbulent kinetic energy, 20 and 45-vane designs, n=400rpm. 335

C.9 Streamlines in channels, 60 and 90-vane designs, n=400rpm. 335

C.10 Air temperature contours across channels, 60 and 90-vane designs, n=400rpm. 336

C.11 Mesh details, designs with the SV1 vane in the channel. 336
C.12 Streamlines, SV1 vane at the inlet (left) and at the middle (right), n=400rpm. 337
C.13 Streamlines, SV1 vane at the outlet, n=400rpm. 337
C.14 Lines chosen for near wall airflow analysis, n=800rpm. 338
C.15 Pillared disc in configuration 3. 338
C.16 Secondary flow vectors: IGV2+SV1 in the left and IGV3+SV1 in the right. . 339
C.17 Air temperature patterns in planes beneath IGVs, IGV2+SV1 (left) and IGV3+SV1 (right), n=400rpm. 339

D.1 Streamlines (velocity) in rotating frame around the WMD rotating at 400 rpm.340
D.2 Streamlines (velocity) in rotating frame around the WMD rotating at 400 rpm.341
D.3 Streamlines (velocity) in rotating frame in the WMD without gap rotating at 400 rpm. 341
D.4 Streamlines in rotating frame in the new design of WMD (gap=4mm) rotating at 400 rpm. 342

List of Tables

1.1 Brake disc terminology used. 4

2.1 Values of C_2 and C_3 in equation 2.14 17
2.2 Vent heat transfer coefficients as per Sisson (1978). 18
2.3 Results from Wallis *et al* (2002) for three discs researched. 21
2.4 Brake disc systems used by Antanaitis and Ricifi (2006). 22

3.1 Constant C_1 values for calculating c_f in transition regions (equation 3.44) . . 51
3.2 Air properties at 60^oC, from Kreith and Bohn (2001). 52
3.3 Data for Rossby number calculation 71
3.4 Rossby numbers using data in 3.3, n=100rpm 72
3.5 Buoyant conditions in brake discs in Table 3.3,Θ_w=100^{o}C, Θ_∞=20^{o}C, ω=10.47rad/s 72
3.6 Buoyant conditions in brake discs, Θ_w=600^{o}C, Θ_∞=20^{o}C, ω=10.47rad/s. . . 73
3.7 Mesh sizes used in the CFD models 77

4.1 Advantages and disadvantages of the DVB disc 84
4.2 Tungsten wire probe type 55P16 characteristics 92
4.3 Evaluation of partial derivatives 4.27 to 4.31, Basic Differential Method. . . . 106

5.1 Baseline standard brake disc characteristics 109
5.2 Models statistics (Convergence analysis) 116
5.3 Models statistics for Grid 5 119

5.4 Velocity conditions at inlet faces of stationary channel CFD model*. 124
5.5 Comparison of average heat transfer coefficients: Stationary vs RFR models 126
5.6 Solution parameters and CPU times, baseline CFD RFR model. 130
5.7 Characteristics of the cast iron brake disc used in the tests. 133
5.8 Characteristics of the DVB (aluminum vanes; bolts mass included as cast iron).134
5.9 Experimental convective heat transfer coefficients versus CFD results, baseline discs. Data in W/m^{2}K. 137
5.10 CFD Averaged heat transfer coefficients. 150

6.1 Averaged heat transfer coefficients and convective cooling rates. CFD with cylindrical channels. 166
6.2 Channel data for brake discs with radial vanes. 170
6.3 Data calculated at half the channels length. 171
6.4 CFD model mesh statistics for discs with cylindrical channels and with 20, 45, 60 and 90 vanes. 177
6.5 Brake discs convection areas (includes top hat) and mass, radial vanes designs. 178
6.6 Characteristics of the channels with the SV1 implemented, see Figure 6.28. . 181
6.7 Convection (wetted) areas and mass of brake discs designs with SV1 vane. . 183
6.8 CFD model mesh statistics for discs with SV1 vane. 183
6.9 Net gain or loss in heat transfer coefficient per vane wall. 192
6.10 Zukauskas's correlations for cross flow heat transfer in *aligned* cylinders. . . . 194
6.11 Zakauskas's correlations for cross flow heat transfer in *staggered* cylinders. . . 195
6.12 Convection (wetted) areas and mass of brake discs designs with 210 pillars. . 196
6.13 Pillar characteristics. 196
6.14 CFD model mesh statistics for pillared discs. 196
6.15 Reynolds numbers and Zukauskas's constants used, $D \rightarrow D_\pi$. 202
6.16 Nusselt number *per pillar row* from CFD, n=100 rpm and 800 rpm. 203
6.17 Convection areas and mass of brake discs designs with IGV's and SV1 vanes. 217
6.18 Average convective heat transfer coefficients for friction faces (W/m^{2}K). . . . 223
6.19 Non-ventilated brake disc prototypes characteristics. 225

6.20 CFD modelling assessment of brake disc with SV1 at inlet, n=600rpm, W/m^{2}K. 231

7.1 Baseline wheel mounted brake disc characteristics 236
7.2 Rotational Reynolds number and hydrodynamic boundary layer thickness. . 238
7.3 Wheel mounted brake discs characteristics 249

8.1 Limiting Nusselt numbers in ducts of rectangular shape, (Kays *et al* 2005). . 259
8.2 Nusselt numbers in the thermal entry length and hydrodynamic developed conditions, circular duct, CST. From (Kays *et al.* 2005). 260
8.3 Nusselt numbers for thermal entry length and hydrodynamic developed conditions, rectangular duct under CST. From (Kays *et al* 2005). 261
8.4 Nusselt numbers for combined thermal and hydrodynamic entry lengths, circular duct under CST and Pr=0.7. From (Kays *et al.* 2005). 261
8.5 Constants for the Nusselt number in the thermal entry length of circular ducts with Constant Surface Temperature. From (Kilic 2004). 263
8.6 Required length in metres for hydrodynamically developed flow (x_l) in brake disc channels as function of angular speed. 264
8.7 Required length in metres for thermally developed flow (x_l^{Θ}) in brake disc channels as function of angular speed. 264
8.8 Taper ratio (TR) of channels in brake discs with radial vanes. 270
8.9 Channel width characteristics for design D30. 281
8.10 Channel width characteristics for design D32. 288
8.11 Convection area and mass of brake disc vent designs. 294
8.12 Experimental brake discs prototypes data. 300
8.13 CFD vs Experiments for h_{d_c} of brake disc design D32. 305
8.14 Prediction errors using the MGL equation for Nu_{ch}, baseline design (30 vanes). 312
8.15 Errors in the approaches to channel Nusselt number, brake disc design with 20 vanes. 312
8.16 Errors in the approaches to channel Nusselt number, brake disc design with 60 vanes. 314

A.1 Testing Summary. 323

A.2 Coefficients for K-thermocouple function behavior 324

B.1 Experimental heat transfer coefficients from tests performed with cast iron brake disc (baseline model). Temperature range: 120^{o}C to 60^{o}C. 326

B.2 Experimental heat transfer coefficients from tests performed with cast iron brake disc (baseline model), disregarding mass from brake disc hub. Temperature range: 120^{o}C to 60^{o}C. 326

B.3 Experimental heat transfer coefficients from tests performed with cast iron brake disc (baseline model). Temperature range:100^{o}C to 60^{o}C. 327

B.4 Experimental heat transfer coefficients from tests performed with cast iron brake disc (baseline model), disregarding mass from brake disc hub. Temperature range:100^{o}C to 60^{o}C. 327

B.5 Experimental heat transfer coefficients from tests performed with detachable vane brake disc (baseline model). Temperature range: 120^{o}C to 60^{o}C. 328

B.6 Experimental heat transfer coefficients from tests performed with detachable vane brake disc (baseline model), disregarding mass from brake disc hub. Temperature range: 120^{o}C to 60^{o}C. 328

B.7 Experimental heat transfer coefficients from tests performed with detachable vane brake disc. Temperature range:100^{o}C to 60^{o}C. 329

B.8 Experimental heat transfer coefficients from tests performed with detachable vane brake disc (baseline model), disregarding mass from brake disc hub. Temperature range:100^{o}C to 60^{o}C. 329

B.9 Uncertainties of raw data. 329

B.10 Uncertainty of heat transfer coefficient (derivatives evaluation). 330

B.11 Calculation of uncertainty on heat transfer coefficient: Squared contributions and final uncertainty of heat transfer coefficient. 330

B.12 Uncertainty of convection heat transfer coefficients using the cast iron brake disc. 331

B.13 Uncertainty of convection heat transfer coefficients using the detachable vane brake disc. 331

Nomenclature

A	Area	m^2
A_1, B_1	Constants	-
A, B	Constants in King's Law, Eq. 4.2	-
A_s	Swept area	m^2
b	Cooling rate	s
BI	Buoyancy Index, Eq. 3.80	-
c_f	Friction coefficient	-
c_i	Thermocouple constant	-
C_n, $C_{1,2,...}$	Constants, (e.g. Tables 6.10, 6.11	-
C_p	Specific heat capacity	$\frac{J}{kgK}$
D	Diameter	m
D_h	Hydraulic diameter	m
D_π	Equivalent diameter, $\frac{P_w}{\pi}$	m
E	Voltage	V
Ek	Ekman number, Eq. 3.85	-
$f_{1,2}$	Functions in Eq. 8.8	-
$f^*_{1,2}$	Functions in new correlation for Nu_{ch}, Eq. 8.24	-
FI	**F**low **I**ndex, h_{ch} optimiser, Chapter 8	-
$FI\, h_c$	FI for h_c	-
$FI\, u_r$	FI for u_r	-
g	Gravity acceleration	$\frac{m}{s^2}$
Gr_{R_o}	Disc Grashof number, Eq. 3.79	
h	Enthalpy	$\frac{J}{kg}$
h_c	Convective heat transfer coefficient	$\frac{W}{m^2K}$
h_{cond}	Thermal conductance	$\frac{W}{m^2K}$
h_{ch}	Channel h_c	$\frac{W}{m^2K}$
h_{c_p}	Pillars h_c	$\frac{W}{m^2K}$
h_{c_t}	Turbulent h_c	$\frac{W}{m^2K}$
h_{d_c}	Disc experimental h_c	$\frac{W}{m^2K}$
h_{d_r}	Disc experimental heat transfer coefficient by radiation	$\frac{W}{m^2K}$
h_{d_t}	Disc experimental total heat transfer coefficient	$\frac{W}{m^2K}$

h_0	Natural convection in Eq. 2.16	$\frac{W}{m^2K}$
$I_(tot)$	Total rothalpy	$\frac{J}{kg}$
ID	Disc inner diameter	mm
k	Thermal conductivity	$\frac{W}{mK}$
$l_{ch,v}$	Channel, vane length	m
m	Mass	kg
n	Revolutions per minute	rpm
N_s	Readings per ensemble	-
Nu_{ch}	Disc Nusselt number, Eq 5.5	-
Nu_d	Channel Nusselt number, Eq 5.4	-
Nu_D	Cylinder Nusselt number, Tables 6.10 and 6.11	-
Nu_m	Mean Nusselt number	-
Nu_p	Pillars Nusselt number, Eq. 6.2	-
Nu_∞	Limiting Nusselt number	-
Nu^*	New Nusselt number correlation, Eq. 8.24	-
OD	Disc outer diameter	mm
p,P_{avg}	Pressure (Static, Average Contact)	MPa
P_{cr}	Channel circumferential width	mm
Pr	Prandtl number, ν/α	-
Pr_k	Turbulent Pr	-
P_w	Pillar perimeter	m
Q	Energy	W
Q_c	Convected energy, Eqs. 4.22, 4.24	J
q_c	Convective heat flux	$\frac{W}{m^2}$
$q_{c_{turb}}$	Turbulent q_c	$\frac{W}{m^2}$
q_{c_t}	Turbulent component in $q_{c_{turb}}$	$\frac{W}{m^2}$
r	Position vector	-
R	Disc radius, Gas constant	m
Ra	Rayleigh number, Eq 3.81	
Re_D	Duct or channel Reynolds number	$\frac{u_r D_h}{\nu}$
$Re_{D_{loc}}$	Local channel Reynolds number	$\frac{u_{r_{loc}} D_{h_{loc}}}{\nu}$
Re_x, Re_l	Plate Reynolds number, Eq 3.30	

Re_ω	Rotational Reynolds number, Eq 3.31	
$\mathbf{R}_o$	Rossby number, Eq 3.84	-
R_i	Radius to inner vane attack edge in Chapter 8	mm
R_m	Mean swept radius	mm
rms	Root Mean Square	-
S	Swirl parameter, Eq 6.3	-
S_E S_M	Energy and Momentum Sources	-
S_y	Tensile strength	MPa
T	Temperature	K
t	Time	s
t_v	Vane thickness	mm
$\mathbf{U}$	Velocity vector	$\frac{m}{s}$
u^*	Friction velocity	$\frac{m}{s}$
u_r, u_θ, u_z	Cylindrical components $\mathbf{U}$	$\frac{m}{s}$
V_v	Vehicle linear velocity	$\frac{m}{s}$
W	Energy from angular torque	W
X_k	Discrete Fourier Transform	-
x^+, x^+_{rot}	Dimensionless variables	-
z_{ff}	Disc thickness	m
α	Thermal diffusivity	$\frac{m^2}{s}$
α_t	Turbulent α	$\frac{m^2}{s}$
β	Air coefficient of thermal expansion (T^{-1})	$1/K$
$\beta(Pr)$	Function in Kader's (1981) model	-
δ_Θ	Temperature uncertainty	^{o}C
$\delta_{u/th}$	Hydrodynamic/Thermal boundary layer	m
δ_ω	Boundary layer on a rotating disc	m
Δ	Difference	
ϵ	Emissivity	-
η_Q	Brake efficiency, Eq. 2.24	-
$\kappa - \epsilon$	Turbulent model	-
λ	Energy partition to pad	-
μ	Air absolute viscosity	$Pa\,s$
ν	Air kinematic viscosity	$\frac{m^2}{s}$
ν_t	Turbulent ν	$\frac{m^2}{s}$
ρ	Density	$\frac{kg}{m^3}$

σ =5.67x10^{-08}	Stefan-Boltzman constant, standard deviation	$\frac{W}{m^2K^4}$
τ	Bolt torque, timescale	Nm
τ_b	Shaft bearing torque	Nm
τ_d	Aerodynamic torque	Nm
τ_s	Disc measured torque	Nm
τ^R	Reynolds stress	MPa
τ_w	Wall shear stress	MPa
Θ	Temperature	^{o}C
ω	Angular speed about z	$\frac{rad}{s}$
Ω	Angular speed vector	$\frac{rad}{s}$
$\chi(t_i)$	Ensemble average	-
Subscripts		
a	Air	
avg	Average	
ch	Channel	
cond	Conduction	
d	Disc	
i	Inner	
i, j, k	Indicial notation	
int	Interface	
loc	Local value	
nw	Near wall	
o	Outer	
p	Pad	
r	Wetted by radiation	
rel	Relative frame	
rel	Relative frame	
st	Stabilisation	
t	Total	
v	Vane	
w	Wall or wet by convection	
∞	Unperturbed value	
Superscripts		
A	Aluminum	
CI	Cast Iron	
$+$	Dimensionless sign	

Chapter 1

Introduction and Research Objectives

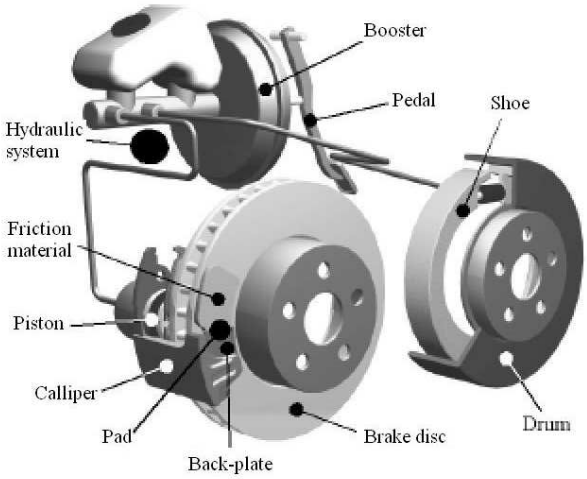

Figure 1.1: Typical brake system (Eriksson, 2000).

This research work deals with the investigation and optimisation of heat dissipation by convection from ventilated brake discs. The *brake disc*, as part of the friction braking systems (Figure 1.1), absorbs most of the vehicle kinetic energy. Other components absorbing braking (kinetic) energy are the brake *pad* and *calliper*. The kinetic energy is dissipated as heat in the disc and from this into the surroundings. The magnitude of energy stored in the disc depends upon its thermal capacity, but invariably the disc must meet the challenges for what is designed. These vary according to the vehicle characteristics. As an example, Figure 1.2 depicts braking energy per disc for three different vehicles: a C-segment car (2 ton), a commercial vehicle (CV, 17 ton) and a Formula 1 car (800kg). The braking energies, in MJ, were calculated as function of the mass and speed of the vehicles. It is noticed that while

the braking duty in the CV is ruled by its mass, the speed is the controlling factor in the F1 car, which despite being the lightest of them achieve a second place in energy input. The energy inputs for the C-segment car brake disc appear to be low, however the disc mass is also small and therefore the bulk temperature rise may be relevant.

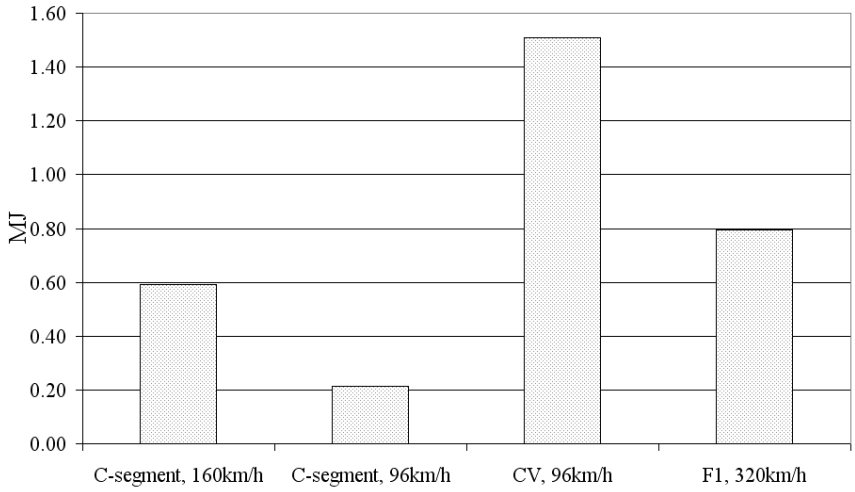

Figure 1.2: Braking energy per vehicle and speed.

Also, the brake discs of a CV must be able to safely absorb and dissipate an energy input equivalent to the vehicle potential energy generated during a 6km-drive on a 6% down-gradient distance at 30km/h (as per the ECE R13 Type II test). Thus, assuming an equal energy distribution amongst the 4 wheels, up to 20808W must be equilibrated per disc. To say that the braking energy input into the disc must be equilibrated is a 4-side process, since the energy equilibrium depends upon the disc thermal mass, and on heat dissipated by convection, radiation and conduction. Heat is mostly dissipated when to some extent a uniform temperature sets in (e.g. repeated or drag braking). During the early stages of braking, thermal gradients occur in the disc and the disc superficial temperature is mainly driven by its thickness, Sheridan *et al* (1988). This scenario is not within this research scope.

Once the temperature has set in, heat dissipation mechanisms activate. Voller's (2003) work with a CV gray iron brake disc at 600^{o}C, demonstrated that convective heat dissipation plays an important role only when substantial rotational speed is available, otherwise heat is mostly dissipated by radiation. Conduction, although sometimes neglected, removes considerable energy if good contact between the disc and its wheel carrier exist. According to Voller (2003), at low speeds 43% of heat dissipates by radiation (assuming an emissivity of 0.55), and 39% dissipates by convection. At moderate to high speeds convection takes 57%, while radiation 25%. In both conditions, conduction removes 18% of the braking energy. Figure 1.3 uses these ratios for a CV brake disc where 20808W are dissipated.

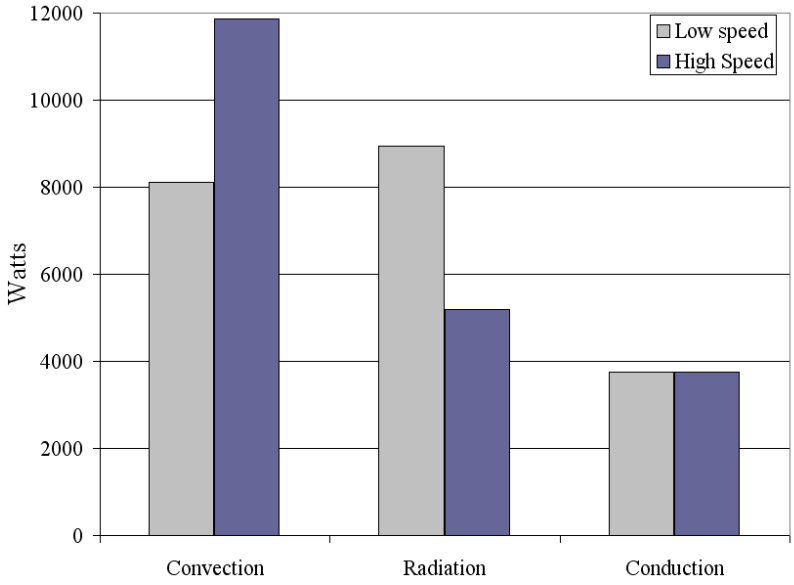

Figure 1.3: Heat dissipation from a CV gray iron disc.

Therefore, investigating ventilation patterns which improve convective heat dissipation has substantial relevance for ventilated brake disc design. However, achieving a good brake disc design is not simple; a disc with an optimal ventilation pattern for convection, must yet be evaluated for issues such as NVH and thermal stress (fatigue).

Brake disc convective cooling depends upon the ventilation geometry design and vehicle speed. In this research CV ventilated brake discs of 434mm outer diameter were used (400 rpm represent approximately 90km/h in these vehicles). The working radius of the ventilation region is 101mm. The size of the disc is also similar to those used in high speed cars. The research considers a range of angular speeds from 100 rpm to 800 rpm in most of the Computational Fluid Dynamics (CFD) simulations whilst experimental work reaches up to 1200 rpm in some cases. Buoyant convection has also been considered.

CFD and experimental work assumed quiescent air for the brake disc which rotated mounted on a shaft, without any other component (e.g. wheel carrier, calliper, etc). CFD simulations were carried out using ANSYS-CFX R10 and experimental work involved an apparatus especially tailored for disc testing (Spin Rig), various brake discs and data acquisition equipment. The discs were heated using a heater box first and an induction heater in the final stages of the work. The results found describe the cooling behaviour of ventilated brake discs as function of number of radial vanes, interaction of large and small radial vanes, inlet guide vanes, pillars and finally the research proposed vane designs following a trend analysis of the cooling behaviour of the vents. The new designs were computationally modelled and one

of them was manufactured and tested. Experimental results demonstrated superior cooling ability of this against the baseline and other discs.

The thesis has been divided into ten Chapters. Chapters 1 to 3 give Introduction, Objectives; Literature Review and theoretical background. Experimental Approach is described in Chapter 4. Convective cooling analysis and results of the baseline ventilated brake disc appear in Chapter 5. The research on new vane patterns is described in Chapter 6. CFD analysis of a railway wheel mounted brake disc heat dissipation has been addressed in Chapter 7. Chapters 8 deals with Ventilation System Optimisation. A short Discussion is offered in Chapter 9 and Chapter 10 finalises the research work with Conclusions and Future Work.

1.1 Terminology

The terminology used in this thesis to refer to a part of a brake disc is summarised here. Figure 1.4 and Table 1.1 give the terms mostly used in this work.

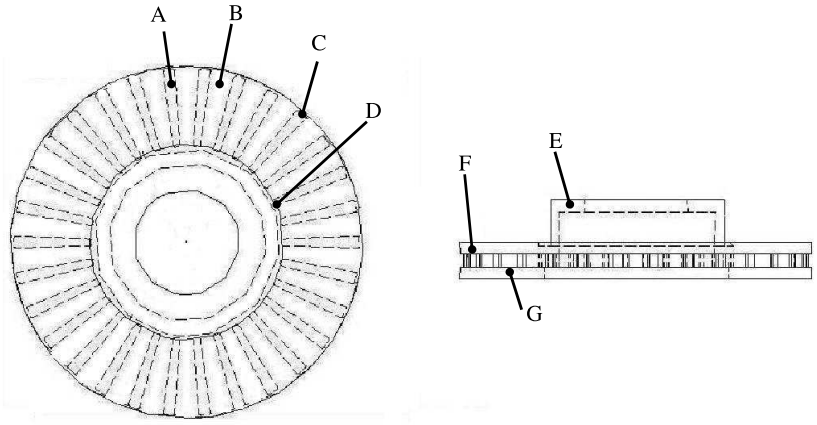

Figure 1.4: Ventilated brake disc - see Table 1.1.

Table 1.1: Brake disc terminology used.

A	Vane	E	Hub
B	Channel	F	Outboard disc
C	Trailing edge	G	Inboard (flying) disc
D	Leading edge		

1.2 Research Objectives

Convective heat dissipation from ventilated brake discs concerns a large field of research activities, including theoretical, computational and experimental analysis. The extent of these largely depend upon financial (hardware) and time resources, while the methods and goals are driven by current technologies and industry needs. Aiming to provide satisfactory closure and useful knowledge in the field of brake disc convective heat dissipation, the following research objectives were considered:

1. Establish a reliable computational methodology using CFD for the analysis of airflow and convective heat transfer coefficients generated in rotating ventilated brake discs in still air.

2. Establish a methodology for the reduction of experimental convective heat transfer coefficients, identify sources of measurement error and evaluate their experimental uncertainties.

3. Propose economically viable test prototypes for experimentally investigating convective heat dissipation from ventilated brake discs highlighting possible sources of discrepancies.

4. Correlate brake disc convective heat transfer coefficients obtained experimentally and numerically (CFD), observe the role of experimental uncertainties and empirical correlations.

5. Perform a research on convective heat dissipation performance of vent geometries developed on an airflow analysis basis. Evaluate also the performance of vane layouts closely related to the baseline.

6. Extend the computational research to convective heat dissipation from railway wheel mounted brake discs.

7. Propose indexes to observe heat transfer coefficients trends within brake disc vents which help in the optimisation of vane or channel geometry.

8. Propose and evaluate brake disc designs with new ventilation geometries optimised for the production of high and stable heat transfer coefficients.

9. Suggest empirical ways for the evaluation of Nusselt numbers in ventilated brake disc with radial channels.

Achieving the above goals will not only provide a more complete understanding of the factors driving heat transfer dissipation by convection from ventilated brake discs but also will result in useful design envelopes and quality indexes connecting the influence of detailed ventilation geometry design on heat transfer coefficient with overall cooling rate capability of the brake disc. This will lead to more competitive ventilated brake discs within early design stages, minimising prototype testing and design turnaround times. Also, the findings of the research provide substantial field for wider scope in the study of convective cooling from brake discs.

Chapter 2

Literature Review

2.1 Brake Disc Heat Dissipation by Conduction

During braking events, heat is generated by friction between the pads and the friction surface of the brake disc. The rise of brake disc temperature begins on the friction surfaces and from there heat is conducted through the disc rings toward the hat section. However, in a single braking event, energy does not distribute evenly in the friction discs and therefore large thermal gradients exist between friction surfaces and other parts of the disc (e.g.: vanes or hat section), generating significant thermal stresses (Abbas *et al* 1969), (Tirović 2005). The degree of temperature distribution will depend upon material properties and area affected by heat flux. Also for a single braking, part of the friction energy is diverted to brake pads, this is known as energy partition Sheridan *et al* (1988) and the energy fraction that is delivered to the brake disc surface follows from equation 2.1. It is clear that pads manufactured of high conductivity materials can absorb relevant amounts of energy. Nevertheless, the largest portion of energy is absorbed in the disc. Equation 2.1 is restricted to a single braking event, since in repeated stops convective cooling and energy storage in the components influence the heat partition.

$$\lambda = \left[1 + \sqrt{\frac{\rho_p C_{p_p} k_p}{\rho_d C_{p_d} k_d}} \frac{A_{s_p}}{A_{s_d}}\right]^{-1} \tag{2.1}$$

Heat conduction plays the most important role during the first seconds of braking, convection and radiation are important after a uniform temperature level has been reached. Therefore, brake thermal diffusivity is relevant for the thermo-structural behavior of the disc. The faster the disc absorbs and spreads the braking energy the smaller temperature gradients exist and

therefore the smaller the risk of thermal shock (Mackin *et al* 2002). The heat conduction problem in brake disc is a multidimensional problem, however separation of variables across the thickness dimension has provided closed forms for friction surface temperature rise and through-thickness transient temperature history. This method reported in Limpert (1999), was used in solid rotors; assuming the brake rotor as a semi-infinite symmetrically loaded slab of metal with constant heat flux over the friction surfaces. Limpert (1975) shows that after the first second of braking a thermal gradient of 33.8 ^{o}C/mm exists in a direction orthogonal to friction surface.

Sisson (1978) used a mixed analytical-numerical method for prediction of rotor, vane, hat and caliper transient temperatures with time dependent heat flux. This work considered a network of resistances and the analytical part was used only for the rotors (the vane was assumed as a nodal resistance). Duhamel's method used in the above work was replaced by Laplace transformation in Newcomb's (1958) research, whose results showed good agreement with measurements. Newcomb's (1958) work was later used by Sheridan *et al* (1988) for single stop braking analysis in rotors, and his work concluded that superficial transient temperature reaches a peak which is function solely of the brake disc material thermal diffusivity, braking time and rotor half-width. The so-called *response parameter*, (Sheridan *et al* 1988), is simply the Fourier number of the brake disc (using as characteristics time and dimension the time to stop and the rotor half-width). Small Fourier numbers (thick rotors) enlarge the peak temperature time at a cost of reaching higher temperatures, whilst bigger Fourier numbers (high thermal diffusivity) shorten the time to reach the peak temperature on the surface.

Numerical approaches to heat conduction equation solving has been also carried out for several authors. The finite differences method was used by Limpert (1975), Sheridan *et al* (1988) and Abbas *et al* (1969) in brake disc temperature analysis. This method was frequently used in the onset of the computational era however it has been currently replaced by dedicated finite element softwares which allow higher degree of complexity in the analysis. The lumped mass model (equation 2.2) described in Sheridan *et al* (1988) assumes a uniform brake disc temperature during braking (power input) or cooling (power dissipation) events. This model predicts the disc bulk temperature as a function of its cooling rate. Equation 2.2 takes into account the braking energy input Q_f, and then its application to many braking cycles must consider different heat transfer coefficients according to the phase of the braking cycle. *Total* heat transfer coefficient values are used. Also, the stabilisation temperature Θ_{st}, is the temperature which the brake mass would reach if no further energy is supplied, then it can be considered as the air temperature Θ_{∞}. If only cooling cycles are considered, then $Q_f = 0$ and the equation 2.2 models mainly convective cooling.

$$\Theta_d - \Theta_{st} = \left[(\Theta_{d_i} - \Theta_{st}) - \frac{Q_f}{h_{d_t} A_w} \right] e^{\frac{h_{d_t} A_w}{m_d C_{p_d}} \Delta t} + \frac{Q_f}{h_{d_t} A_w} \tag{2.2}$$

Once the brake disc temperature is increased up to a uniform semi-stable temperature level as result of braking heat flux and thermal capacity, heat dissipation occurs either by conduction, convection or radiation. The components attached to the brake disc are wheel carrier (or wheel rim) on the outboard side and outer ring of wheel bearing in the inboard side. These offer paths of conductive heat dissipation, due to the temperature difference between the matching surfaces. The characteristic measure of conductive heat transfer through an interface is termed *thermal contact conductance* and it is the ratio of the heat flux through the interface by the temperature drop (equation 2.3), (Kreith & Bohn 2001). The thermal conductance can be understood as the conductive heat transfer coefficient (h_{cond}) of the joint under thermal loading. The inverse of the thermal conductance is the joint thermal contact resistance (TCR). The thermal contact conductance of a bolted joint depends on several independent parameters and therefore its prediction is not simple. However, in analysis of heat dissipation from brakes its value is relevant since it determines the potential amount of heat lost by conduction, predominantly at low rotational speeds, as described in Voller *et al* (2003). Work on thermal contact conductance of brake disc assemblies are reported by Voller (2003), Tirović & Voller (2005) and Voller & Tirović (2007). Generic bolted metallic joints have been widely researched as noticed from papers by Fletcher *et al* (1990), Gmelin *et al* (1990), Wahid & Madhusudana (2003) and Yeh *et al* (2001). The calculation of the conductive heat transfer is usually bounded by an uncertainty range, which fluctuates about ±7.3% (Yeh *et al* 2001), ± 10.8% (Wahid & Madhusudana 2003), ± 20% (Gmelin *et al* 1990), ± 5% (Fletcher *et al* 1990) and ± 10 % (Voller & Tirović 2007).

$$h_{cond} = \frac{Q_{cond}/A_{int}}{\Delta\Theta_{int}} \tag{2.3}$$

The behaviour of the thermal contact conductance is strongly dependent on contact pressure between the plates being joined, and also depends on factors such as: geometry of the joint (surface finish, bolt shank and head diameters, plate thickness, bolts separations), material characteristics (elastic modulus, surface hardness, coefficient of thermal expansion and thermal conductivity) and dynamic factors (force application procedure, loading and unloading factors), as indicated by Voller & Tirović (2007) and Fletcher *et al* (1990). Analytical models for thermal contact conductance have been derived by Yip (1972) for bolted joints in a vacuum with rough surfaces of normal amplitude distribution. His results indicated that nonuniform stress distribution arising from irregularities are not significant in the determination of microcontact resistance. The relevance of surface topography on pressure distributions in bolt-flange junctions was researched by Ito *et al* (1979). The discrimination of the TCR into two scales, a large scale constriction function of the interfacial pressure distribution and a small scale constriction influenced by local values of pressure near the bolt was first proposed by Roca & Mikic (1972). The results showed that large scale constrictions are mainly affected by surface asperities. A similar reasoning was put forward by Fletcher

et al (1990) when the thermal contact conductance was split into a macrocomponent dependent on the bolt characteristics and torque (therefore limited to an area near the bolt head perimeter) and the microscopic component dependent on microgeometry characteristics. Dedicated research by Voller & Tirović (2007) on brake disc assemblies demonstrated that using thermal interface materials, such as thermal pastes and aluminum foil gaskets, increases the thermal conductance by up to 10%. This means that heat dissipation from brakes toward the wheel rim may become important since it is surrounded by air.

Theoretical predictions of the thermal contact conductance as a function of the average pressure between bolts or the applied torque are given by several authors. Equations 2.4 to 2.11 are some of the equations found in the literature for average contact pressure and average thermal contact conductance as a function of torque on bolts or average contact pressure at the interface. The value of P_{avg} in these equations must be in MPa.

Equations 2.4 to 2.8 were obtained as correlations for experimental work carried out by Yeh *et al* (2001) in thin rectangular metallic plates joined by 8 bolts (N_b). Two set of tests were performed (using bolts of ϕ =8, 5 mm de diameter). The torque range applied to bolts in each set of tests fluctuated between 1 and 10 Nm. Therefore it is difficult to compare average pressure contact behaviour between these relations and the one given by Tirović & Voller (2005), since the range of torques used by the tests performed by the former researchers in brake disc assemblies are very different (50 to 300 Nm). This can be seen in Figure 2.1, the only value of torque for which the predictions are similar is near 150 Nm. The above works did not look into lubrication effects.

$$P_{avg} = 1.49 + 0.81\tau^{0.59} \qquad N_b\text{=8, } \phi\text{=5 mm Yeh } et\ al \text{ (2001)} \qquad (2.4)$$

$$P_{avg} = 1.94 + 0.7\tau^{0.59} \qquad N_b\text{=8, } \phi\text{=8 mm Yeh } et\ al \text{ (2001)} \qquad (2.5)$$

$$h_{cond} = 15.1 + 0.35\tau^{2.03} \qquad N_b\text{=8, } \phi\text{=5 mm Yeh } et\ al \text{ (2001)} \qquad (2.6)$$

$$h_{cond} = 12.67 + 0.45\tau^{2.01} \qquad N_b\text{=8, } \phi\text{=8 mm Yeh } et\ al \text{ (2001)} \qquad (2.7)$$

$$h_{cond} = 9.04 + 0.1P_{avg}^{3.79} \qquad N_b\text{=8 Yeh } et\ al \text{ (2001)} \qquad (2.8)$$

$$P_{avg} = 0.107426\tau_s \qquad \text{Tirović \& Voller (2005)} \qquad (2.9)$$

$$h_{cond} = 80P_{avg} + 2300 \qquad \text{Tirović \& Voller (2005)} \qquad (2.10)$$

$$h_{cond} = 10^4 \left(\frac{P_{avg}}{S_y}\right)^{2/3} \qquad \text{Aron \& Colombo (1963)} \qquad (2.11)$$

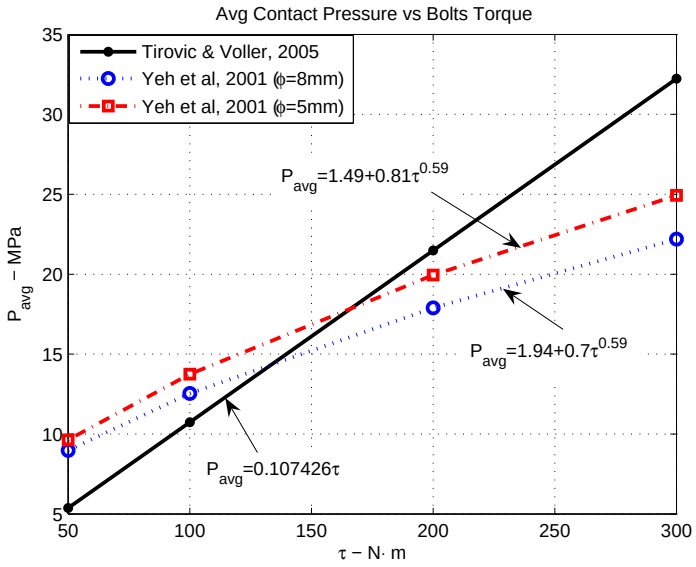

Figure 2.1: Average pressure contact as per formulas 2.4, 2.5 and 2.9.

Figure 2.2 compares thermal contact conductance behaviour from equations 2.6, 2.7 and 2.10 for the same range of torques as in Figure 2.1. As of 100 Nm there exist large differences, being the values predicted by Yeh *et al* (2001) very high. This emphasises that expressions by Yeh *et al* (2001) are restricted to ranges of small torque, therefore they can not be used for applications where relatively high values of torque are used. However, when thermal contact conductance from equations 2.10 and 2.11, (Tirović & Voller 2005) and (Aron & Colombo 1963), are compared for similar torque range, the results are relatively closer (Figure 2.3). Aron & Colombo's (1963) equation, which works only for relations $\frac{P_{avg}}{S_y} < 0.5$, predicts smaller values of h_{cond} when the ultimate tensile strength of gray iron (293 MPa) is chosen as S_y.

In order to get the total energy lost by conduction, the thermal contact conductance value must be multiplied by the temperature drop at that interface and by the area of contact between the disc and the attached surface which is usually small compared with the area considered for convection. According to Voller *et al*'s (2003) work, at low speeds (150 rpm),

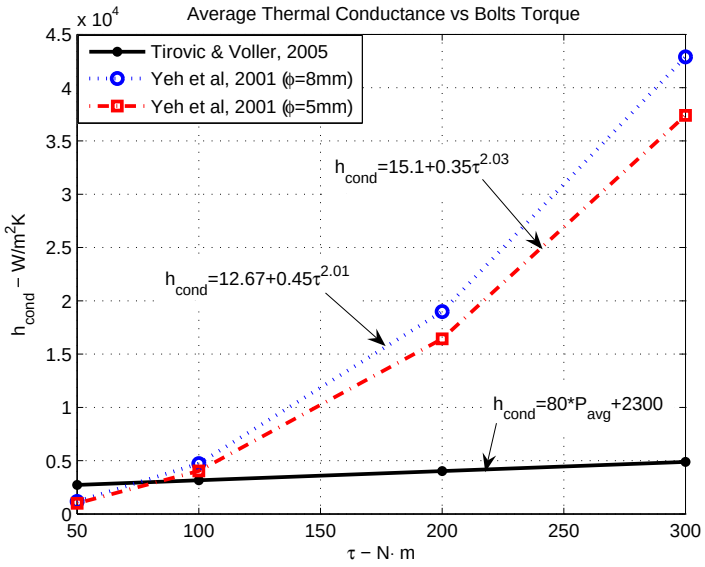

Figure 2.2: Average thermal contact conductance as per formulas 2.6, 2.7 and 2.10.

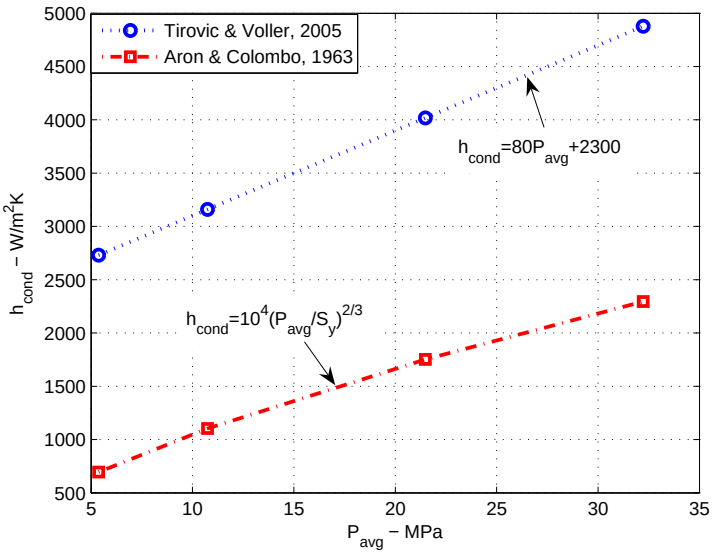

Figure 2.3: Average thermal contact conductance as per formulas 2.10 and 2.11, using gray iron ultimate tensile strength (293MPa) as S_y.

the total percentage of energy lost by conduction reaches 18% of the total energy dissipated (11.5kW in this case) from a gray iron brake disc (mass: 33 kg) heated up to 600 ^{o}C. Provided the conditions of the bolted joint are kept constant during other tests, conductive heat dissipation will remain the same for any speed of rotation of the disc. However, if the temperature level is changed or the joint is dissasembled and assembled repeatedly then the heat flux and average contact pressure will change, and the conductive heat dissipation will be influenced.

2.2 Brake Disc Heat Dissipation by Radiation

Heat dissipation by radiation becomes important whenever the disc surface temperature reaches high levels due to its nonlinear behaviour. However, for its quantification, brake disc emissivity needs to be constantly measured. Eisengräber *et al* (1990) reported that this can change from 0.15 to 0.9 in a test (the latter as result of hot spots). Eisengräber *et al*'s (1990) work also revealed emissivity variations between 0.4 to 0.7 in a drag braking test. The research work done by Noyes & Vickers (1969) assumed a constant emissivity of 0.8. Research work conducted by Voller *et al* (2003) and Voller (2003) demonstrated that emissivity depends upon surface condition. Their work which took into account data logged with rubbing thermocouples and infrared sensors determined ϵ=0.2 for new machined brake disc surface at temperatures between 20 and 200^{o}C, while for corroded brake disc surfaces its value reached 0.9 for a range of temperatures between 20 and 600^{o}C. Corrosion on a brake disc surface is likely removed in each braking application, nevertheless the finding is relevant for cooling research purposes. The characterisation of heat losses by radiation is carried out by using the equation 2.12, (Voller *et al* 2003).

$$h_{d_r} = \sigma\epsilon\frac{T_d^4 - T_\infty^4}{T_d - T_\infty} \tag{2.12}$$

The equation 2.12 results from linearising the typical equation for heat transfer by radiation, forcing it to be equal to a linear relation similar to the one driving the convective heat transfer, (see equation 2.13).

$$Q_r = \sigma\epsilon A_r(T_d^4 - T_\infty^4) = A_r h_{d_r}(T_d - T_\infty) \tag{2.13}$$

However, equation 2.12 should only be used when convective and radiative surfaces (A_r) are mutually exclusive (Incropera & DeWitt 2002), and when no interaction between radiative surfaces may occur. For instance a solid brake disc geometry (or for simplicity, a spherical shape body) can only radiate and convect heat to the surrounding environment. However,

in ventilated brake discs, the channel surface loss heat by convection but the heat lost by radiation is absorbed back into them, therefore, their radiative area should be discarded from the energy balance. This is schematically shown in Figure 2.4, where surfaces at uniform temperature exchange heat by convection and radiation to the surroundings. The circular surface in the left looses heat by radiation and convection from a mutually exclusive boundary, while that in right has an open inner boundary where heat is lost by convection, but radiation beams are absorbed back into the same surface, therefore the radiation surface is smaller than the convection surface.

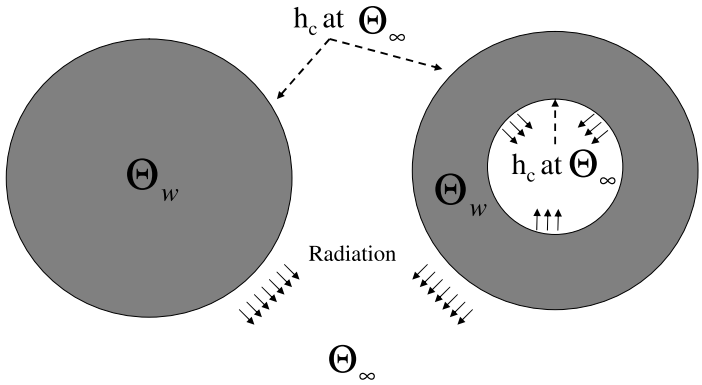

Figure 2.4: Radiation and convection from solid and hollowed bodies.

Using equation 2.12, and data extracted from a cooling test using an anticoning disc, three ranges of values of radiation heat transfer are calculated assuming three different values of emissivity: 0.2, 0.5 and 0.9. The raw data (temperatures read by a rubbing thermocouple on the friction face and air temperature read by another thermocouple far away from radiation effects) is shown in Figure 2.5. Radiation heat transfer coefficients resulting from using these data are shown in Figure 2.6. From the above figures, it can be noticed that radiation heat transfer coefficient highly depends upon temperature difference, surface temperature and emissivity, working as a scaling factor. At a disc surface and air temperatures of $\Theta_d = 185^o$C and $\Theta_\infty = 30^o$C, the radiation heat transfer coefficient varies from 2.5 to 6.7 and to 12 W/m^{2}K, when emissivity takes values of 0.2, 0.5 and 0.9 respectively.

Voller *et al* (2003) determined that at low speeds of rotation (150 rpm), the percentage of heat loss due to radiation from a commercial vehicle brake disc is around 43%, considering an emissivity of 0.55. Although it may be assumed that radiation heat losses occurring among channel inner walls are zeroed due to mutual reflectance, in long channels where cooling air flows, radiation may have an effect upon the convective behavior of flow. The effects of radiation on the dynamics of air within a rotating smooth square channel have been numerically researched by Yan *et al* (1999). Considering radiative properties of air, the

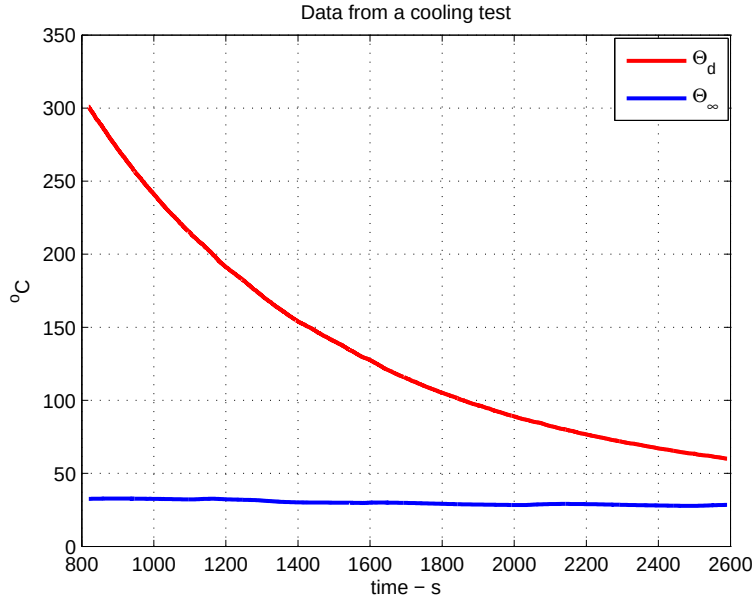

Figure 2.5: Cooling tests raw data used to obtain the radiation heat transfer coefficients.

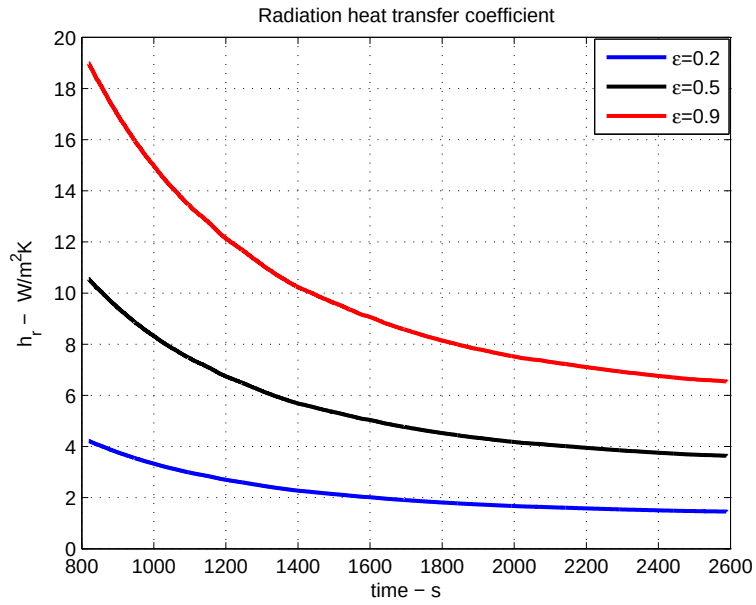

Figure 2.6: Radiation heat transfer coefficients obtained using data in Figure 2.5 and equation 2.12.

results indicated that radiation effects are almost null in the channel inlet, but important later when airflow gets hotter as result of radiative heat flux. The implications of this are a reduction of the friction coefficient towards the regions very near the exit of the channel and a boost of the temperature development profile in the flow, which means that the theoretical thermal entry length is reduced. In this study, the scattering characteristics of the air were also evaluated, and it was reported that there is less radiation absorption by the fluid when scattering is considered than when this is not considered.

2.3 Brake Disc Heat Dissipation by Convection

Out of the three modes of heat dissipation from brake discs, convective heat dissipation attains high importance due to the exposure of the brake to the surrounding air while the vehicle moves or stands. Forced convective cooling has been tagged as the most important brake disc heat dissipation move when the vehicle moves a moderate to high speeds, (Limpert 1975), (Voller 2003) and (Voller *et al* 2003).

Brake discs installed in road vehicles and trains benefit from convection, although the braking duties are different. Trains brake discs can be axle or wheel mounted, and in the latter case the discs are attached to the wheel web (two per wheel), creating asymmetric heat loading on it (see Chapter 7.1). In road vehicles, brake discs are installed in an generic way, by bolting the disc hub to the axle. The wheel carrier and wheel are also assembled to the axle but with the disc in between. In road vehicle brake discs, both friction faces receive energy input by friction.

2.3.1 Automotive Brakes

Limpert (1975) proposed an experimental formula to derive the heat transfer coefficient, linking the heat transfer coefficient of a solid commercial vehicle brake disc to the speed of the vehicle as described in equation 2.14. Imperial units are used in equation 2.14, and the value of the constants depends upon the application as evidenced in Table 2.1.

$$h_{d_c} = 0.92 + \frac{V_v}{C_2} e^{-V_v/C_3} \tag{2.14}$$

In ventilated automotive brake discs, earlier investigations on convective heat dissipation performed by Newcomb & Millner (1965) reported the convective heat transfer coefficient of the ventilation region as a result of a polynomial with a constant component (natural convection) plus a dynamic component powered to an exponent. A similar formula was

Table 2.1: Values of C_2 and C_3 in equation 2.14

Applicability	C_2 $[\frac{hr^oFft^3}{BTUs}]$	C_3 [s/ft]
Solid Rotors	3.0 - 3.5	328
Front drums (CV)	0.7	328
Rear drums (CV)	0.3	328
Front linings	0.15	328
Rear linings	0.06	328

quoted by Sisson (1978) in an experimental research on convective cooling of brake rotors with radial straight vanes with outer diameters ranging from 9 inches to 16 inches and inner diameters from 4 to 7 inches. The rotors were separated by distances ranging from a quarter inch to one inch, and the numbers of vanes varied between 20 and 40 (Figure 2.7). Sisson's (1978) work reported that the massflow driven by the different rotors tested was independent on the number of vanes provided the *flow area* was not substantially changed. Another finding was that the channel radial airspeed depends on outer and inner diameters of rotor and rotational speed. The equation for average radial airspeed through the channel derived by Sisson (1978) is:

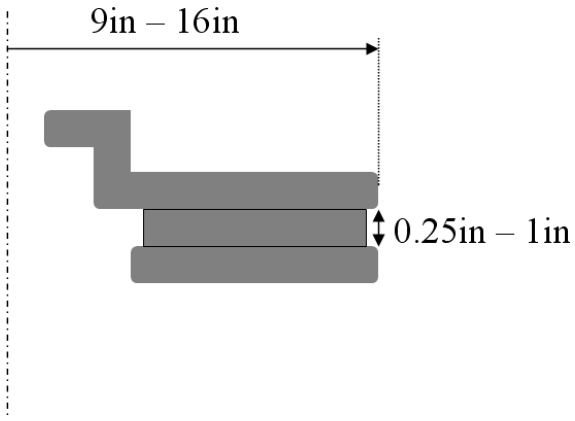

Figure 2.7: Straight vane rotor diagram, 20 to 40 vanes (Sisson, 1978).

$$u_r = 0.01016\pi R_o n\sqrt{-0.0201 + 0.5538R_i - 0.0752R_i^2} \tag{2.15}$$

The equation 2.15 must use feet and revolutions per minute for radii and angular speed

magnitudes. The result is in meter per second due to the factor introduced. The equation for the average heat transfer coefficient through the channels and a list of channel convective heat transfer coefficients for two discs (diameters: disc 1, 266.7 mm and disc 2, 228.6 mm) reported by Sisson's (1978) work are shown in equation 2.16 (where h_0 is the natural convection component), and Table 2.2. Equation 2.16 is of the same form as the one obtained by Newcomb & Millner (1965).

$$h_{ch} = h_0 + C_1 u_r^{0.8} \tag{2.16}$$

Table 2.2: Vent heat transfer coefficients as per Sisson (1978).

n [rpm]	h_{ch}, [W/m^{2}K]	
	Disc 1	Disc 2
50	18.7	22.7
100	28.4	26.1
200	43.2	39.8
400	68.1	56.8
600	94.3	69.8
800	111.3	86.9
1000	132.3	98.2

Limpert's (1975) work also reported an empirical formula, equation 2.17, for the prediction of average radial airspeed at the inlet of channels in ventilated brake discs with radial straigth vanes. The radial air speed at the exit of the channel can therefore be calculated as function of inlet and outlet channel cross sections and the average speed as the arithmetic mean of these speeds.

$$u_{r_i} = 0.0158n(R_o^2 - R_i^2) \tag{2.17}$$

$$u_{r_o} = \frac{A_i}{A_o} u_{r_i} \tag{2.18}$$

$$u_r = \frac{u_{r_i} + u_{r_o}}{2}$$

Both formulas, 2.15 and 2.17, were derived for ventilated brake disc rotors with straigth vanes without specifying the number of vanes, therefore their predictions must be used with

caution. The limitation of equation 2.15 is obviously its application. For a brake disc with constant outer and inner radius, radial airspeed though the channels will be influenced by the number of vanes, inlet conditions and rotational speed. This has been experimentally demonstrated by Johnson *et al* (2003) by means of particle image velocimetry (PIV) methods used in automotive brake discs rotating in still air. From these works can be concluded that inlet size and channel taper influences the ability to uniformly draw air. Qian's (2002) research also points to a strong dependence of the channel mass flow (radial airspeed and geometry) to the number of vanes in brake discs in a research conducted with automotive brake discs rotating at 60 rad/s. The results from this research suggest that the optimum numbers of vanes for maximum mass flow and maximum convective heat transfer production are not the same, with the optimum number of vanes for mass flow about 45 and the optimum number of vanes for heat transfer about 65. The apparent reason of this difference is due to the coupled effect wetted area times average heat transfer coefficient on heat transfer ability, the higher this product the more heat is released. Therefore, what was possibly found by Qian (2002), but not stated explicitly in his work, is that the optimum geometry layout for convective heat transfer of a disc with radial vanes is independent of the aerodynamic characteristics, in the sense that this geometry does not necessarily results in higher mass flow rates. In fact, Qian's (2002) work shows that the number of vanes giving the maximum heat dissipation is within a region where air mass flow falls due to blockage of air as result of narrowness of channels.

A geometrical relation between the circumferential distance available to fill in with vanes and the required channel width was reported by Zhang (1997). The relation is a practical design driven formula dividing the available circumference by the channel-vane circumferential width, see equation 2.19. Therefore, choosing thick or thin vanes will give less or more number of required vanes, as expected. Relations for average heat transfer coefficients in straight channels have been reported by Sheridan *et al* (1988) and Limpert (1975). Sheridan *et al* (1988) reported a relation for the average Nusselt number of the channel as function the average Reynolds number of the channel, see equation 2.20.

$$Vanes = \frac{2\pi R_m}{P_{cr} + t_v} \tag{2.19}$$

$$Nu_{ch} = 0.045 Re_{ch}^{0.8} R_o^{0.2} + 6.6 R_o \tag{2.20}$$

Limpert's (1975) work reported a relation for the average heat transfer coefficient of the channel based on the average hydraulic diameter of the passage. The relation is shown in equation 2.21.

$$h_{ch} = 0.023\left(1 + \frac{D_h}{l_v}\right) Re_D^{0.8} Pr^{0.33} * \frac{k}{D_h} \tag{2.21}$$

The equation 2.21 proposed by Limpert (1975) is a modification of the original Dittus-Boelter equation reported in Kreith & Bohn's (2001) for uniform flow in ducts. Therefore, equation 2.21 scales up Dittus-Boelter equation (2.22), by a factor depending upon the ratio between the mean hydraulic diameter of the channel against its length.

$$Nu_{ch} = 0.023 Re_D^{0.8} Pr^{0.33} \tag{2.22}$$

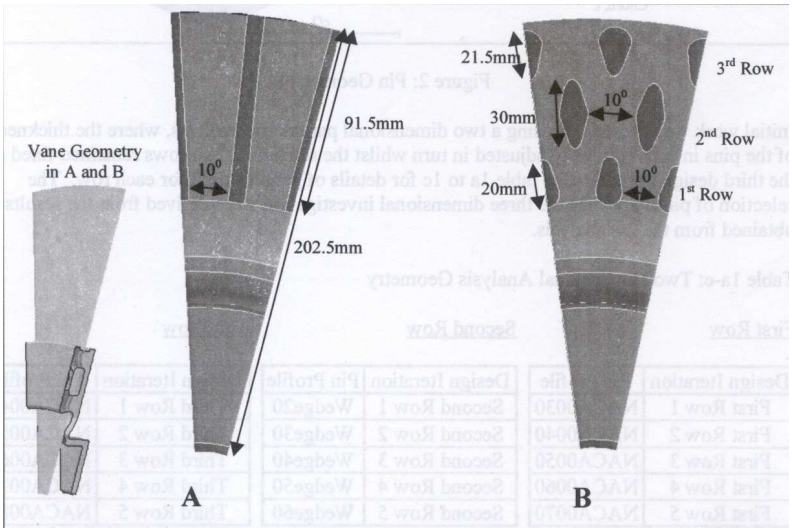

Figure 2.8: Vent geometries researched by Palmer *et al* (2006).

Different geometries for the vents were researched by Palmer *et al* (2006) and Wallis *et al* (2002). Wallis *et al*'s (2002) research compared convective cooling performance of three discs: two with radial vanes of same length with the only difference being a rounded inlet edge (* in Table 2.3), against a cornered inlet edge of the vanes, and a third one with a tear drop-diamond-tear drop (TD-D-TD) pillar arrangement. The discs outer diameter was 290 mm and available channel length 55 mm. Higher mass flow rates were calculated for the brake disc channel with rounded inlet radial vanes; this due to decreased misalignment of the airflow at the channel inlet and because radial vanes provide larger pumping section. Results at 600 rpm show that although the rounded inlet vane disc pumps 10 % more air than the pillared one, the channel average heat transfer coefficient of the former is just 3% less. In other words, the radial vane brake disc does not adequately use the available heat capacity of a larger amount of air passing through, whilst their pillared design advantage lies in its

larger vent wetted area to dissipate heat. Palmer *et al* (2006) found through fluid dynamics simulations that specific pin wedge arrangements can improve convective heat transfer up to 25% at 500 rpm, and that venturi sections at the first row of the ventilation channel increase mass flow and heat transfer rates. The geometries researched by Palmer *et al* (2006) are shown in Figure 2.8.

Table 2.3: Results from Wallis *et al* (2002) for three discs researched.

ω [rad/s]	20		60		100	
Disc	u_r [m/s]	h_{ch} [W/m^{2}K]	u_r [m/s]	h_{ch} [W/m^{2}K]	u_r [m/s]	h_c [W/m^{2}K]
Radial vanes	0.83	18.90	2.29	34.8	3.79	49.3
Radial vanes*	1.04	22.0	3.03	41.6	5.29	58.6
TD-D-TD	0.87	20.0	2.79	40.4	4.76	54.5

The research conducted by Voller *et al* (2003) and Voller (2003) on heat dissipation analysis from commercial vehicle and train brake discs provided significant insight on the relative importance of heat dissipation modes. The tests conducted with a commercial vehicle brake disc rotating in still air with an initial temperature of 600^{o}C showed that at low rotational speeds the contribution of convection is less than the contribution of radiation (39 against 43 %), the remaining is the amount of heat lost by conduction to the axle or wheel carrier. At higher speeds however, convection turns out to be the dominant mode of heat dissipation accounting for 57 % of the total dissipated energy.

Krüseman & Schmidt (1995) researched the optimisation of heat transfer coefficients of a standard brake disc with radial vanes. The vanes geometry remained the same and 'external' modifications that allowed 20% more mass flow through the channels increased the average channel heat transfer coefficient by 15%.

Sensitivity studies of brake cooling due to various factors have been of the interest of brake researchers. Sun (2006) carried out investigations on the convection cooling performance of the brake disc when parameters such as vent geometry, number of vanes, and nearby shield geometry were varied. The research was conducted using CFD and FEA techniques. The results show that a disc with 45 vanes reaches a mass flow rate two thirds larger than a disc with 120 pillars (having the same the outer diameters and vane axial height). Also, the average heat transfer coefficients were 24 % higher in the disc with vanes than in the pillared disc. Out of three number of vanes simulated, 36, 45 and 54; it was noticed that absolute value of average heat transfer coefficient hardly changes. The disc with 45 vanes reached 1 % and 2% larger heat transfer coefficients than discs with 36 and 54 vanes. The rotor size played an important role since the point of view that larger rotors have higher convection area, however it was found that the absolute heat transfer coefficient did not

change significantly from one to another. A modification to the rotor dust shield allowing slots near vents considerably changed the heat transfer coefficient performance (around 17 % more). In general, the research concluded that brake equilibrium temperature rise could be reduced by 44^{o}C, 39^{o}C, 29^{o}C and 70^{o}C if the pillar vents were replaced by vanes, increasing the rotor size from 303 to 323 mm, adding to central slots in the dust shield and replacing the standard steel wheel (16in) by an aluminum wheel.

An extensive experimental research using ventilated brake disc rotors with cross-drilled holes in one specific pattern but with two drill densities was conducted by Antanaitis & Rifici (2006) in test vehicles, from their results only those concerning convective cooling performance are reviewed here. Three set of brake discs were tested as described in Table 2.4.

Table 2.4: Brake disc systems used by Antanaitis and Ricifi (2006).

System	Calipers		Wheels		Discs	
	Front	Rear	F	R	F	R
1	Sliding, aluminum		17”	16”	Radial Vanes	
2	Opposite piston		18”		Curved V.	Pillared
3	Twin piston sliding	Single sliding aluminum	18”	17”	Cross drilled and not drilled	

The research showed that the front brakes from the first system had between 8.8% and 20.1% improvement in convective heat dissipation when a 90-holes pattern was used. In the same set, the rear brakes were drilled with a 64-holes pattern, and this showed only 3.2% and 8.5% improvements in heat dissipation by convection at the lowest and highest test speeds respectively.

Antanaitis & Rifici's (2006) second and third brake sets also showed the same trend, improvement of convective cooling performance in those discs with holes against those without, being the relative difference in equilibrium temperature from one to another case larger at higher vehicle speeds. Antanaitis & Rifici (2006) suggest that the drilled holes may have an influence in the flow pattern and, evidently increase convection area. The paper suggests, however, that in some sense the presence of holes crossing the thickness of the friction faces may be detrimental for the flow stream being dragged into the vents, by inducing a faster drop of radial air speed in the vent due to flow diversion through the holes.

Qian's (2002) work concluded that an optimal vane number exist for maximum air mass flow through discs with radial vanes. The number oscillated between 44 and 52 vanes. For maximum convective heat dissipation, the research showed that the number should be further increased to 64 or 68 vanes. The obviousness of the first statement may reside in the fact that less recirculation flow will exist in narrower channels than in wider channels, increasing

the average radial speed. This however can substantially avoid mixing due to secondary flow effects being less pronounced in these conditions (Greitzer *et al* 2003). The optimum vane numbers for maximum convective heat transfer seems, as said before, to be related more with geometry exposure to air than with enhancement of convective heat transfer characteristics. Others effects such as inlet vane radius were reported to be more important than the location of a smaller vane inside the channel. For this, however, the paper does not provide sufficient information for further analysis. In general, Qian's (2002) research showed a maximum gain of 16% in convective cooling performance (on a heat loss basis –watts–), with 24 vanes being the worst case and 68 vanes the best. As for mass flow through the channels, a similar gain occured when the vanes varied from 24 to 48, and when these varied from 60 to 76, a drop in mass flow of about 35% occurs (with reference in the maximum achieved).

Motorbike brake discs convective cooling have been researched by Aus-der-Wiesche (2002), using a numerical approach for the solution of the energy, momentum and turbulence closure equations. The analysis was performed assuming a constant crossflow over the disc at different rotating speeds. The results indicate that when the ratio of the rotational Reynolds number to crossflow Reynolds number is small, the heat transfer characteristics of the disc can be approached using the flat plate theory for heat transfer (Kreith & Bohn 2001). The correlation numerically found for the Nusselt number as function of the rotational and crossflow Reynolds numbers is shown in equation 2.23.

$$Nu = C_4 + C_5 \log \frac{Re_\omega}{Re_x} \tag{2.23}$$

.

2.3.2 Railway Brake Discs

According to the literature found, the analysis of convective heat dissipation from brake discs for railway vehicles has been investigated with less frequency than in brake discs for automotive industry. The research carried out by Tanvir (1988) addressed the analysis of cooling rates of wheel mounted brake discs, which were mounted in test trains and correlated with laboratory experiments. The procedure followed a drag braking interval in which the disc heated reached 200^{o}C and after, the brakes were released and the train was run at constant speeds up to 130 km/h during 600 seconds, while the temperature and relative speeds were recorded. The results gave an approximate value of the conductive cooling rate between the brake disc and the wheel (b_{cond}=0.45x10$^{-3}s^{-1}$), which allowed that cooling rates for the disc with the vents blocked and open could be calculated. Empirical correlations were derived to approximate the behaviour of the cooling rates experimentally found. From the tests results it was concluded that the proximity of underframe equipment near the boggies may affect significantly the convective cooling performance of ventilated channels

and, when solid discs are used instead of ventilated, then the shielding of the wheel profile brings a reduction in the convective performance of the disc, as noticed when the results were compared with laboratory results using solid disc rotating in still air.

Sakamoto's (2004) research on experimental convective cooling analysis of axle mounted brake discs used as principal design parameter the cooling rate derived by the Newton's law of cooling. The work was conducted using three discs and of which cooling rates were derived for speeds ranging from 22.2 m/s to 35.6 m/s. The maximum temperature registered was also 200^{o}C. The conclusions drawn were that the usage of cooling rates is important in estimating maximum temperatures reached by the discs during service, and it also could be used as a parameter during the design phase of brake disc prototypes.

Both papers, Tanvir's (1988) and Sakamoto's (2004), completely disregard the effects of heat dissipation by radiation from the discs; although not mentioned, the reason could be that heat dissipation by radiation is relatively low.

The research conducted by Voller (2003) on convective cooling and energy consumption from four brake discs (solid, radial vanes, radial-pillar vents and circumferential vents) concluded that the maximal convective heat dissipation is obtained from the brake disc with the radial vanes, followed by the discs with radial-pillar and circumferential vents, and by the solid disc. However, when the ratio of the convected energy to the energy consumed in rotation (pumping energy) is calculated for these disc, the most optimal design is the radial-pillared vent disc whilst the worst ratios are for the radial vane disc. The relation driving the efficiency ratio was derived as a function of temperature difference between the disc and the surrounding ambient temperatures, disc rotational speed and disc average heat transfer coefficient. The empirical formula is of the following type:

$$\eta_Q = \frac{(C_5\omega + C_6)\Delta\Theta}{\omega^{C_7}} \tag{2.24}$$

In general, constants C_i in equation 2.24 should be calculated for each brake disc, however they can be identified as natural convection heat transfer coefficient (C_6), forced convection term ($C_5\omega$) and exponent of the brake torque consumption (C_7).

2.3.3 Computational Convective Dissipation in Brakes Discs

Most of the research on heat dissipation and temperature prediction on brake discs commenced using analytical, empirical and experimental methods, e.g.: Newcomb (1958), Newcomb & Millner (1965), and Morgan & Dennis (1972); brake disc temperature predictions also used numerical methods such as finite differences when computers became more accessible e.g.: Limpert (1975), Sheridan *et al* (1988) and Sisson (1978); however the prediction of

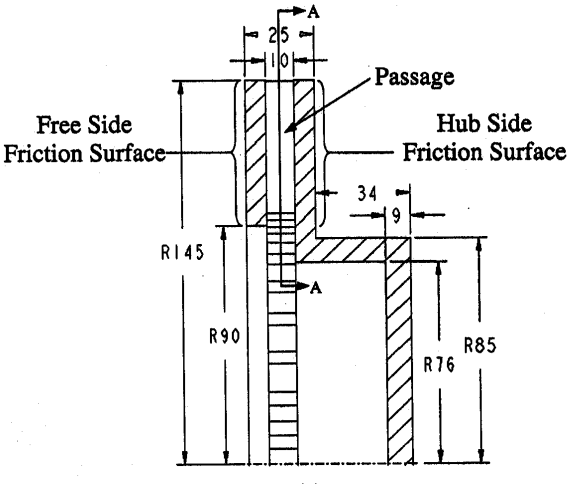

Figure 2.9: Dimensions of the brake disc model used by Wallis *et al* (2002).

the thermal behaviour of air around the brake disc geometry could not be carried out until the volume finite element method was developed for computational fluid dynamics (CFD) softwares.

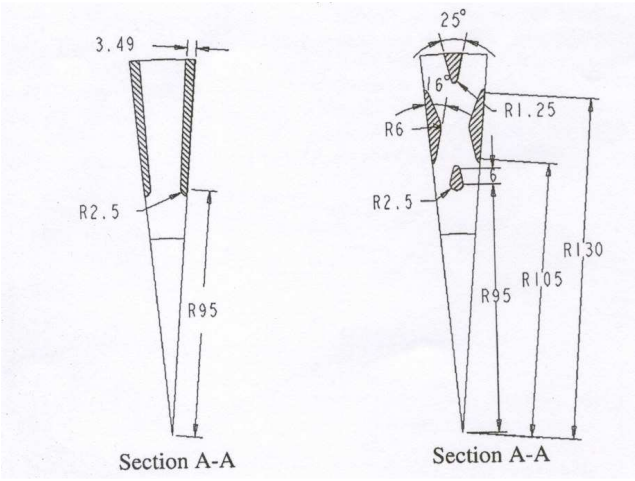

Figure 2.10: Channel geometries modelled by Wallis *et al* (2002).

The potential of CFD in the development and research of automotive components for which air flow variables play a key role was reported by Dhaubhadel (1996). The importance of CFD over traditional experimental methods (e.g. hot wire anemometry) was qualified on the basis of the non-intrusive capability of the former for delivering significant data in spatial regions where otherwise could not be easily known. Not only brake flow behaviour but climate control, in-cilinder flow mixing, engine cooling; airflow in exhaust systems, rotary

machinery and underhood equipment cooling are some of the areas where CFD is usually used nowadays.

Among the first studies of airflow and convective cooling prediction around ventilated brake discs, Krüseman & Schmidt's (1995) work showed that the complex geometry surrounding the brake can be successfully modelled in computer simulation. The computational research considered two frames of references, one for the rotating brake disc and associated geometry and another for the 'linear' displacement of the vehicle. The standard brake disc convective cooling performance was optimised by changing the geometry around the brake disc. Krüseman & Schmidt (1995) reported 20% more massflow through the channels and 15% increment in convective heat transfer coefficients as result of the geometry changes. The model for turbulence closure chosen was $\kappa - \epsilon$.

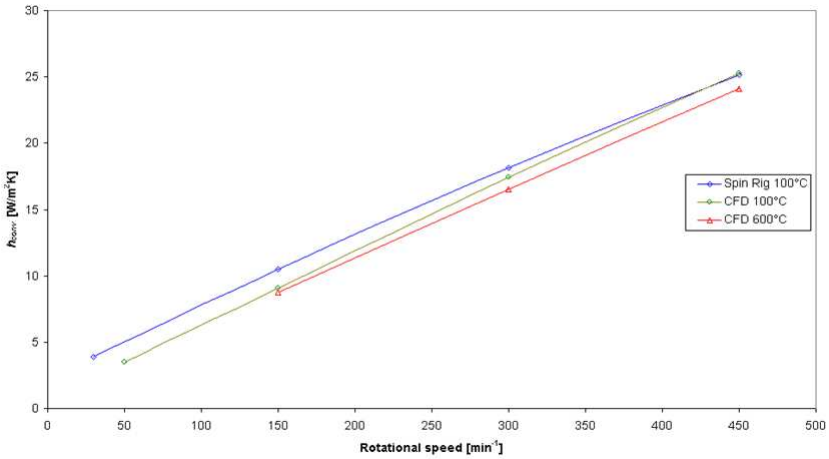

Figure 2.11: Convective heat transfer coefficients, CV standard brake disc; Voller (2003).

The same turbulence model was used by Wallis *et al* (2002) to predict the behaviour of three standard brake discs with different ventilation geometries. Wallis *et al*'s (2002) research validated the numerical approach by comparing the results of the convective heat transfer characteristics of a solid disc modeled in CFD against those predicted by Dorfman (1963) and Cobb & Saunders (1956). The findings of the research on convective performance of the brake discs have been included in Table 2.3. The comparison of the three discs results (Figures 2.9 and 2.10), showed that although the disc with radial rounded edge vanes pumps 10% more air, the average heat transfer coefficient of the former is only 3% larger than that of the TD-D-TD design.

Voller (2003) conducted both numerical (CFD) and experimental research of standard and railway brake discs. Heat transfer coefficients were calculated experimentally and compared against those predicted by CFD (Figures 2.11 and 2.12). The results showed that CFD

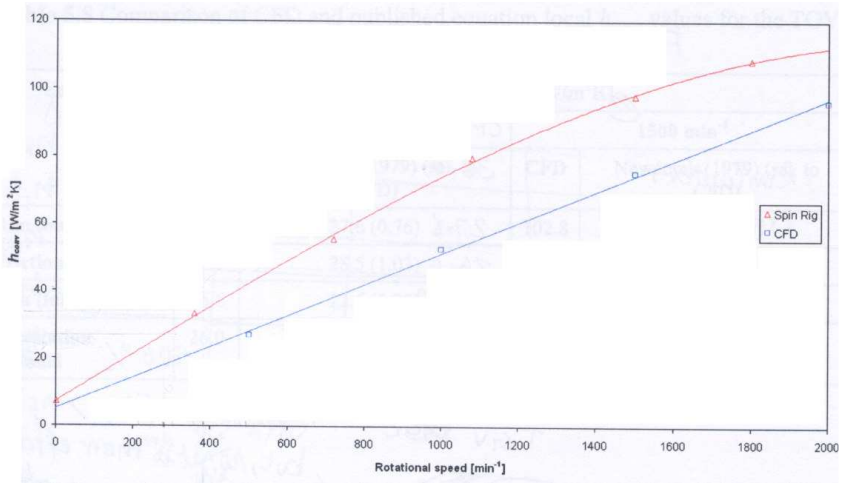

Figure 2.12: Convective heat transfer coefficients, TGV brake disc; Voller (2003).

underpredicted average convective heat transfer coefficients in both cases, with larger discrepancies between experimental and numerical results for the TGV brake disc. Nevertheless, Voller (2003) showed that reasonable agreement is reachable between numerical (CFD) and experimental results. There exist however, the likeliness that in real situations, convective heat transfer coefficients or other flow variables (speed and drag, for instance) will be more difficult to predict . Recent research on convective cooling performance of different vent geometries has been published by Palmer *et al* (2006). CFD modelling was employed for the prediction of air mass flow and convective heat transfer coefficients. The turbulent model model used was also $\kappa - \epsilon$.

Additional research work using CFD for response analysis of convective heat transfer ability of brake discs when changes to disc geometry or associated geometries are performed was also conducted using computational fluid dynamics in the Sun's (2006) work. The works of Qian (2002) and Zhang (1997) also made usage of CFD. The first work dealt with a mixed methodology between CFD and DoE using brake disc geometry as control parameters, while the second work focused on the analysis of the effect of vanes on air mass flow.

2.3.4 Experimental Flow Studies in Ventilated Brake Disc

Although CFD has provided a fast and increasingly accurate solutions for the dynamics of flow behaviour inside the channels of ventilated brake discs, experimental methods have also been used by researchers aiming to have a thorough understanding of the flow characteristics. The results obtained are very valuable, enabling comparison and validation of CFD simulations.

Johnson *et al* (2003) utilised Particle Image Velocimetry (PIV) to determine the characteristics of the airflow around and inside the channels of a cast iron standard ventilated brake disc. The geometry of the brake disc was 282 mm and 152 mm outer and inner diameters respectively, 37 vanes and channel gap of 8 mm. The disc was enclosed within an acrylic box and the field was seeded with particles necessary for the PIV process. Access to flow within the passages was accomplished by removing a section of the inboard disc, instead of which an acrylic plate was inserted.

The results indicate that significant recirculation regions are located near the leading side of the channel as the disc rotates. In these regions, flow separation occurs and semi-stagnant conditions (insignificant radial flow) prevails. Recirculation is an effect of the vane inlet geometry misalignment with the entrant flow (very high incidence angle). Another finding is that a constant ratio of 0.895 exists between the exit velocity and the peripheral speed of the rotor (ωR_o), meaning this a linear relationship between the rotational speed and the volume of airflow through the rotor over the range of speed tested (342, 684 and 1026 rpm). Figure 2.13 shows speed vectors acquired with PIV inside the brake disc channel.

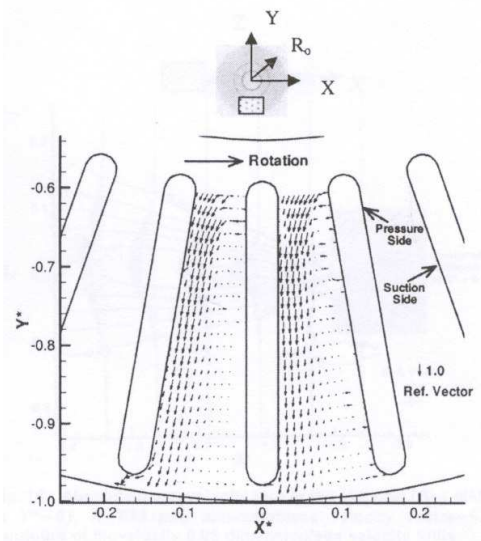

Figure 2.13: Relative velocity vectors at channel midplane, n=684 rpm, Johnson *et al* (2003).

Hot wire anemometry has been used to map the velocity field at the exit of the ventilated brake discs. The work of Barigozzi *et al* (2003) and Parish & MacManus (2005) are examples on the usage of this methodology. A complete theory on the physics of the behaviour of hot wire probes can be found in Bruun (1995). The usage of pressure miniature probes in the measurement of flow fields at the exit of vents in brake discs have been reported by Watkins *et al* (2005) and also by Parish & MacManus (2005).

The disadvantage of using hot wire anemometer methodology is that the brake disc needs

to be free of out of plane vibrations during rotation, since these may introduce significant uncertainties in the results. In all of the above research work the wire probe was sequentially located along several positions and the velocity fields at the outlet of the channel obtained. Figures 2.14 and 2.15 show the disc geometry and the non-dimensional radial velocity field at the exit when the disc spins at 750 rpm.

Barigozzi *et al* (2003) performed flow measurements at the exit disc channels rotating at 750 and 1500 rpm, and at several disc temperatures, ranging from room temperature to 325 ^{o}C. The acquisition system employed consisted of a cold wire thermometer (DANTEC 55P31) and single hot wire anemometer (DANTEC 55P11), both of them connected to a full anemometry system. The results of 'hot disc' tests revealed that the mass flow rate decreases when the temperature increases, showing effects on air density variation due to air heating. The results also showed that typical correlations for the Nusselt channel number (e.g. equation 2.25) underpredict the real behaviour of the channel convective heat transfer coefficient.

$$Nu = A + BRe_D^{0.8} Pr^{0.4} \tag{2.25}$$

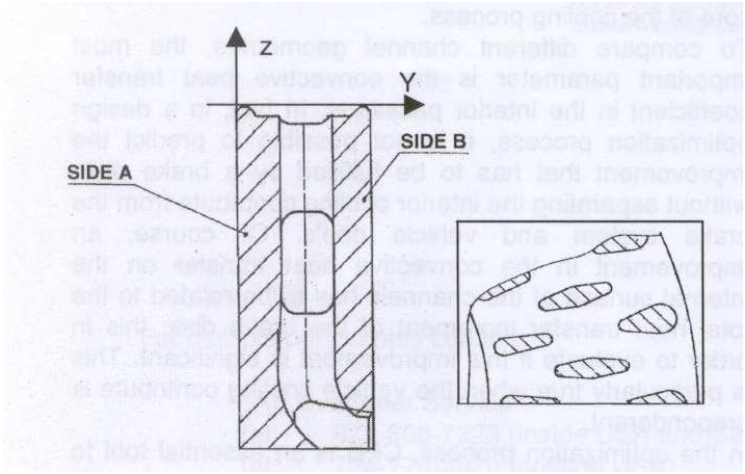

Figure 2.14: Disc geometry used by Barigozzi *et al* (2003).

Four brake disc designs were analysed by Parish & MacManus (2005), three of which had backward curved vanes and one with short vanes and pillars. The instrumentation used were a miniature five-hole pressure probe and a Dantec Streamline 90N10 hot wire anemometry system. The results showed that the reduction in the number of vanes increased the amount of flow mass delivered, and that this was overestimated if the pressure probe was used, since it could not accurately capture the wake regions (on the suction side) at the exit of the channels. A characteristic wake-jet region at the exit of channels was also found. All the tests were performed under room isothermal conditions, and therefore only aerodynamics

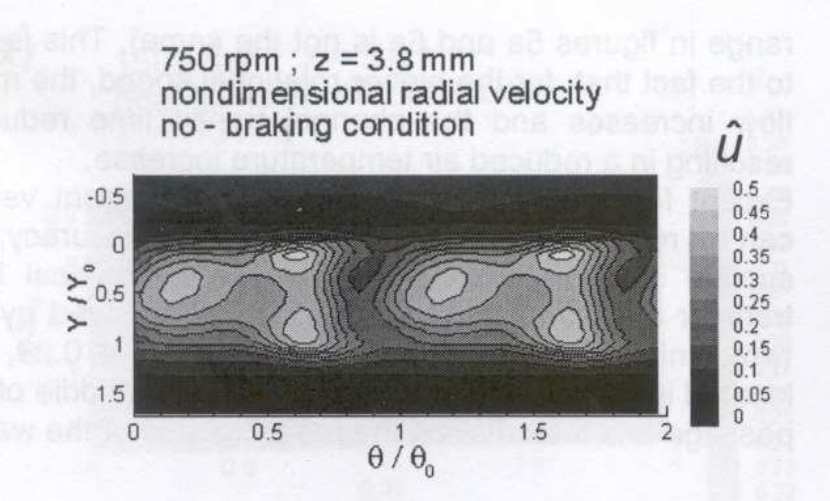

Figure 2.15: Non-dimensional radial velocities at the channels exit, Barigozzi *et al* (2003).

aspects were investigated. The geometry of a curved vane disc geometry is shown in Figure 2.16.

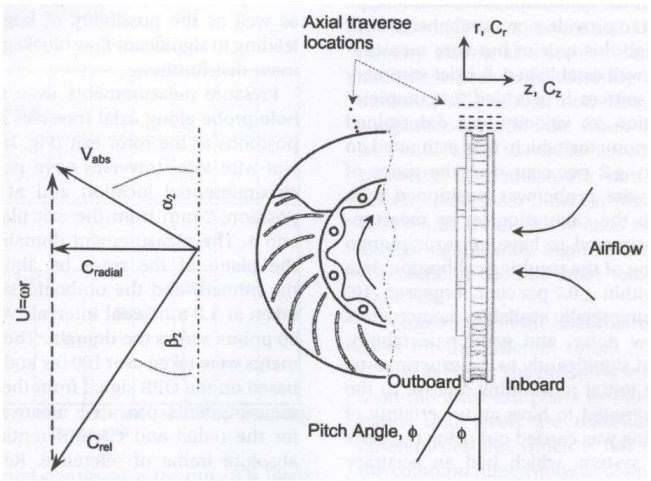

Figure 2.16: Disc geometry used by Parish & MacManus (2005).

In general, work published by Barigozzi *et al* (2003) and Parish & MacManus (2005) concludes that the flow field structure at the exit of the brake disc channels remained independent of the rotational speed (for a specific brake disc design). They also concluded that the flow mass behaviour varies linearly with angular speed. The research carried out by Watkins *et al* (2005) yielded airflow measurements in the exit of channels of discs in three conditions: brake disc rotating in still air, brake disc and wheel assembly rotating in still air and brake disc assembled in a quarter car model within a wind tunnel. The results showed that airflow is significantly reduced during road-driving conditions, compared to still air conditions. The

results also found that air stream entering the wheel cavity appears to reduce the quantity of air flowing through the vented rotor. Watkins *et al* (2005) suggest that the performance of vented rotors would be improved by controlling the amount of air entering the wheel cavity.

2.3.5 Flow and Convection in Rotating Channels

Numerical research of flow in rotating channels has been also attended. Dutta *et al* (1996) analysed the turbulent convective heat transfer in smooth rotating square ducts with uniform temperature and developed flow (Figure 2.17). A rotating frame of reference and the $\kappa - \epsilon$ turbulent model were used. The results showed that local Nusselt numbers is higher at the trailing side than on the leading side of the channel with an increase in downstream direction.

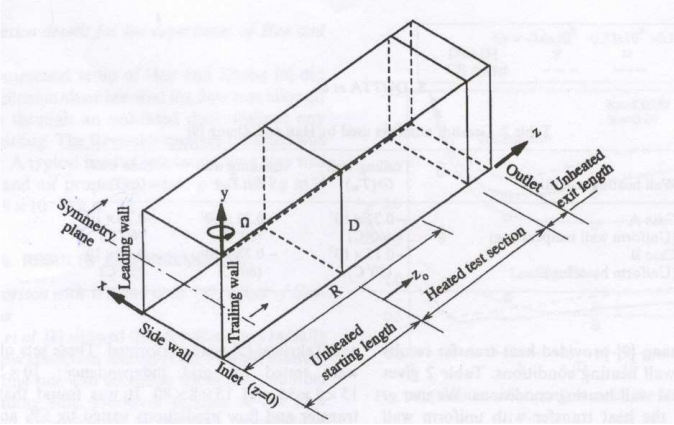

Figure 2.17: Channel geometry and rotating coordinate system, Dutta *et al* (1996).

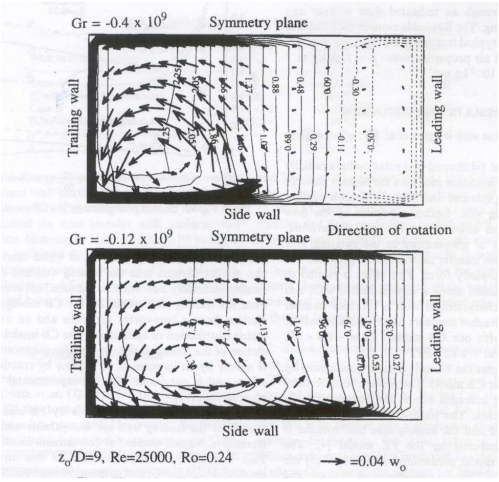

Figure 2.18: Secondary flow patterns in rotating channels, Dutta *et al* (1996).

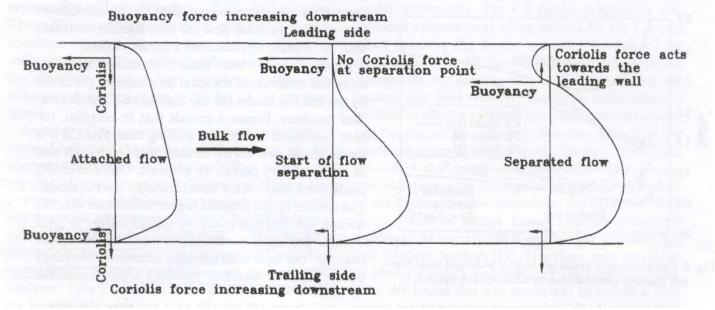

Figure 2.19: Flow separation mechanisms in rotating channels, Dutta *et al* (1996).

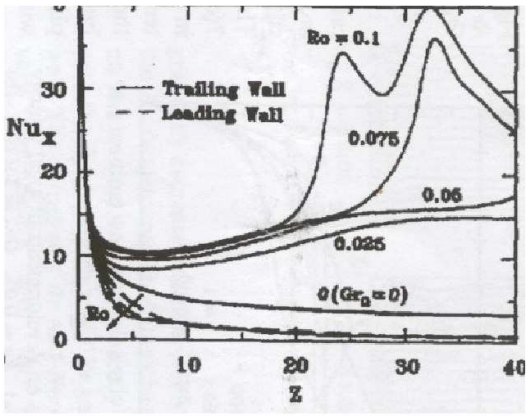

Figure 2.20: Nusselt numbers in a long rotating square-duct, $Z = \frac{z}{D_h}$; Yan & Soong (1995).

Flow separates in the channel leading side where, if the wall is at high temperature, heat flows by buoyant convection. This flow separation induces high speed in the channel trailing side, to meet continuity. Coriolis forces (Figure 2.19) reduce flow separation downstream the channel. Similar results were reported by Yan & Soong (1995) in rectangular ducts, with an initial decay in heat transfer Nusselt number due to entrance effects followed by an increase brought by the onset of secondary flow which promotes flow mixing. Yan & Soong's (1995) results show flow development in the duct, since $Z = \frac{z}{D_h}$ >20, Figure 2.20. In brake disc channels this ratio hardly reaches six. This research found similar convective performance degradation in the channel leading side of trapezoidal channels.

2.4 Summary

The literature on brake disc heat dissipation is wide, and covers nearly 50 years from present, e.g. Newcomb (1958). The methods of analysis have evolved with technology, and concern-

ing the research of convective heat dissipation, CFD has proved to be a valuable tool in indicating the path for better designs. Experimental work however, is still necessary since it gives the validation grounds for computational models. The review of published work on convective heat dissipation from ventilated brake discs has shown the performance of several vent geometries such as number of vanes in Qian (2002), influence of smooth corners in radial vanes versus tear drop pillars in Wallis *et al* (2002), diverse arrangements of drills in rubbing surface, callipers and wheels types in Antanaitis & Rifici (2006), and the performance of standard aerofoil profiles for vents have been researched by Palmer *et al* (2006). Each of the above papers have suggested optimum geometries for brake cooling, however comparing data among these is not simple due to differences in modelling characteristics, e.g.: brake disc outer diameters.

Studies linking the vent geometry and the heat transfer coefficient have not yet been described, since most of the results rely on the evaluation of heat transfer coefficients averaged over vents, channels or full disc surfaces. This may obey the need of having practical numbers which may be used as geometry performance indicators during the early stages of a ventilated brake disc design. Nevertheless, what ultimately drives the average convective performance of the vent is its ability for diverting the airflow path and creating heat transfer rates as result of the wall-air interaction. Then, an understanding of this would give the way to characterise the distribution of heat transfer coefficients or their ranges, and a control of these would definitively bring a new way of designing brake disc vents since not only a single (average) heat transfer coefficient would work as reference for a specific vent pattern, but a established link among vent geometry and convective heat transfer coefficients would be available and this would help in making easier meeting design requirements. Although not mentioned in depth, the mechanical behaviour of the brake disc is of paramount importance and therefore it has deserved numerous studies, some referring to the characterisation of brake disc materials and others to thermo-mechanical effects to which the brake disc is subjected during operating conditions. For example, issues such as crack growth (low cycle fatigue) and thermal stress analysis have been addressed by Yamabe *et al* (2002) and Mackin *et al* (2002), respectively.

Chapter 3

Research Methodology

This chapter describes the methodology used for computational analysis of airflow and convective heat transfer in brake discs. The computational solutions for convective heat transfer and fluid dynamics of the discs were obtained using a general purpose commercial CFD. However, an acquaintance of the equations modelling the air dynamics and convective heat transfer is necessary. Therefore, a brief description of these is given. Then, the construction process of the CFD models is introduced by describing the model and mesh definition, boundary conditions settings, solver selection and solution parameters selected. The post-processing and further analysis are explained in subsequent chapters. A flowchart for a typical CFD solution of the brake disc is also included at the end of the Chapter.

3.1 Flow and Heat Transfer Modelling

Computational fluid dynamics (CFD) has rapidly evolved in the past years and now commercial codes can offer reliable solutions of many engineering problems related to fluid and heat flow. On the other side, computing hardware has also improved and nowadays high performance systems deliver solutions in relatively short times, the timescales have been downsized from weeks to days or even hours to achieve a converged solutions of relatively large models. The use of CFD is important in this work; it allowed fundamental understanding of the physics, leading to the manufacturing of the most promising designs. The analysis of CFD data also lead to optimisation of disc convective heat dissipation.

3.1.1 Overview of Fluid Dynamics Equations

The flow and convective heat transfer behaviour of the brake disc has been modelled assuming that the disc rotates at constant angular speed in irrotational environment (quiescent air) at room temperature. Similar conditions are used for buoyant convection. The disc surface is considered smooth and with uniform temperature.

Once the fluid domain has been meshed, the solver calculates the fluid speed patterns, pressure-forces, temperatures and derived data, using the classical fluid dynamics equations plus turbulence closure models and near wall log-law functions (for speed and temperature) if these are considered. The *conservation* form of the basic equations for three-dimensional, unsteady and compressible flow dynamics and energy are as described in various references such as Versteeg & Malalasekera (1995) and Bejan (2004):

Continuity equation.

$$\frac{\partial \rho}{\partial t} + \nabla \cdot (\rho \mathbf{U}) = 0. \tag{3.1}$$

Momentum (Navier Stokes) equation.

$$\frac{\partial \mathbf{U}}{\partial t} + (\mathbf{U} \cdot \nabla)\mathbf{U} = -\rho^{-1}\nabla p + \nu \nabla^2 \mathbf{U} + S_M. \tag{3.2}$$

Energy equation.

$$\rho \left[\frac{\partial h}{\partial t} + \mathbf{U} \cdot \nabla h \right] - \frac{\partial p}{\partial t} - \mathbf{U} \cdot \nabla p = \nabla \cdot (k \nabla \Theta) + S_E. \tag{3.3}$$

The viscous dissipation term has been disregarded from the energy equation, further details of this are in Bejan (2004). The steady state equations are obtained by dropping all the temporal terms in the above equations.

Continuity equation.

$$\nabla \cdot (\rho \mathbf{U}) = 0 \tag{3.4}$$

Navier-Stokes equation.

$$(\mathbf{U} \cdot \nabla)\mathbf{U} = -\rho^{-1}\nabla p + \nu \nabla^2 \mathbf{U} + S_M. \tag{3.5}$$

Energy equation.

$$\rho \mathbf{U} \cdot \nabla h \; - \; \mathbf{U} \nabla p = \; \nabla \cdot (k \nabla \Theta) \; + \; S_E. \tag{3.6}$$

Although the steady state of the fluid dynamic equations are those shown above, the solution process for steady state simulations considers the full tansient equations, since the steady state solutions are obtained by advancing in a pseudo-time until a time independent flow field is found [1]. The simulations performed in this thesis were all assuming incompressibility. The terms S_M and S_E (equations 3.5 and 3.6) account for source-terms in these equations, which arise if any extra force-term or energy-term is to be considered in the domain of solution.

In the analysis of geometries rotating around a stationary axis, it is convenient to place a coordinate system on the rotating part and observe from it the changes in the flow. This is common practice for analysing flow behaviour around a brake disc rotating at constant speeds, as found in Wallis *et al* (2002) and Palmer *et al* (2006), and it is a widely used technique in turbomachinery analysis (Greitzer *et al* 2003). In this way, the fluid motion being seen is steady, which simplifies the calculations. However, the new coordinate system is not inertial and therefore, the equations must be updated to account for the new effects. Additional terms will appear in equation 3.5 and 3.6. Results referred to the rotating coordinate system are usually termed as *rotating frame results*, and results seen by an external observer in a stationary (non-rotating) coordinate system as *stationary frame results*. Transforming a vector from stationary to relative frames is described in Greitzer *et al* (2003) as:

$$\left(\frac{d\mathbf{F}}{dt}\right)_{stn} = \left(\frac{d\mathbf{F}}{dt}\right)_{rot} + \Omega \times \mathbf{F} \tag{3.7}$$

Equation 3.7 is the general transformation for any vectorial property F of the fluid rotating with an angular speed vector Ω. When applied to brake discs, it is advantageous to consider the axis of rotation as z and therefore only $\omega\mathbf{k}$ plays a role. For example, the *absolute speed* in the stationary system of an air particle inside the ventilation channel, whose position is defined by the vector $\mathbf{r}$, is given as:

$$\left(\frac{d\mathbf{r}}{dt}\right)_{stn} = \left(\frac{d\mathbf{r}}{dt}\right)_{rot} + \omega\mathbf{k} \times \mathbf{r}$$

Then, the magnitude of the airspeed in the rotating frame (*relative speed*) equals to $u_{rel} = u - (\omega)(r)$. The temporal rate of change of *scalar* properties, and the spatial derivatives taken at a fixed time are the same for rotating and stationary systems. Then, *static* thermodynamic properties are independent of the system of reference from which they are analysed. New terms appear in the Navier Stokes equation when this transformation is carried out

[1] The ANSYS-CFX solver uses a fully implicit scheme on time.

(ANSYS-CFX Solver Theory 2005), (Greitzer *et al* 2003); where S_M includes the Coriolis and centrifugal kinematic terms.:

$$(\mathbf{U}_{rel} \cdot \nabla)\mathbf{U}_{rel} \;=\; -\frac{1}{\rho}(\nabla p - \mu\nabla^2\mathbf{U}_{rel} \;-\; S_M) \tag{3.8}$$

$$S_M \;=\; -2\rho\omega\mathbf{k} \times \mathbf{U}_{rel} \;-\; \rho\omega\mathbf{k} \times (\omega\mathbf{k} \times \mathbf{r}) \tag{3.9}$$

Similarly, the energy equation is transformed, and the total enthalpy (h_{tot}) is replaced by the total rothalpy (I_{tot}) in the resulting equation.

$$I_{tot} \;=\; h + \frac{\mathbf{U}_{rel}^2}{2} \;-\; \frac{\omega^2 r^2}{2} \;=\; (h_{tot})_{rel} - \frac{\omega^2 r^2}{2} \tag{3.10}$$

$$\rho\nabla \cdot (\mathbf{U}_{rel} I_{tot}) \;=\; \nabla \cdot (k\nabla\Theta) \tag{3.11}$$

It is noticed from equation 3.10 that only the centrifugal term from equation 3.9 ($\omega \times (\omega \times r)$) adds mechanical energy to the fluid; the Coriolis term does not contribute, (Greitzer *et al* 2003). The continuity equation (3.4) is transformed into rotating coordinates only updating the velocity vector by the relative velocity vector.

$$\nabla \cdot (\rho\mathbf{U}_{rel}) \;=\; 0 \tag{3.12}$$

Equations 3.8, 3.11 and 3.12 are the basic equations used by the software to solve the fluid dynamics in the rotating coordinate system. The treatment of the dependent variables is of instantaneous character (laminar flow). These equations contain seven unknowns (three velocity components, pressure, density, temperature and entalphy), and there exist 5 equations, three from momentum equation (3.8), one from energy equation (3.11) and one from continuity (mass conservation) equation (3.12). The remaining two equations to close the system are the equations of state for ideal gases and the constitutive model for entalphy:

$$p = \rho RT \tag{3.13}$$

$$h = C_p d\Theta \tag{3.14}$$

The behaviour of the flow under the above equations is fully deterministic , that is, the instantaneous value in a certain location can be known to the numerical method degree of accuracy. However, under certain circumstances, the behaviour of the flow field may

seem non-deterministic and random. This condition is given when flow momentum forces disrupt the orderly manner in which viscous equilibrium is maintained inside the flow. When this happens, the flow field is said to be under turbulent conditions. Reynolds was the first who proposed ways to predict turbulence. The turbulent flow field was simplified by assuming that an instantaneous variable (e.g. speed or temperature) can be decomposed into a mean component which is averaged over a long period of time or from a large set of observations from a seemingly similar flow case at a particular time (ensemble average)[2], plus an instantaneous component which eventually determines the final instantaneous behaviour of the variable. In this manner, it may be easy to think of turbulence as a couple of flows flowing with the same purpose (one with a definite mean and another which fluctuates about the mean at a certain rate and amplitude), however this is not the case since the fluid flowing is only one. What the average process pursues is to convert into a deterministic or predictable the random behaviour of turbulence. Another assumption of this process is that the average of the instantaneous fluctuating component is by definition zero.

Then, following Versteeg & Malalasekera (1995) and Bejan (2004), the instantaneous dynamic and thermodynamic properties of a turbulent flow are defined as[3]:

$$\mathbf{U} = \overline{\mathbf{U}} + \mathbf{U}' \tag{3.15}$$

$$p = \overline{p} + p' \tag{3.16}$$

$$\Theta = \overline{\Theta} + \Theta' \tag{3.17}$$

Where the quantities with an over-bar $\overline{(\ )}$ denote temporal or ensemble averages of the property and the quantities with an apostrophe ($'$) are the instantaneous fluctuations of the value. Substituting the above relations in equations 3.8, 3.11 and 3.12, and performing time average on the resulting terms give the turbulent averaged continuity, momentum and energy equations in conservation form.

$$\nabla(\rho\overline{\mathbf{U}_{rel}}) = 0 \tag{3.18}$$

$$\nabla \cdot \overline{\mathbf{U}_{rel}\mathbf{U}_{rel}} = -\frac{1}{\rho}\nabla\overline{p} + \nu\nabla^2\overline{\mathbf{U}_{rel}} - \nabla \cdot \overline{\mathbf{U}'_{rel}\mathbf{U}'_{rel}} - \frac{2}{\rho}\omega\mathbf{k} \times \overline{\mathbf{U}_{rel}} - \frac{1}{\rho}\omega\mathbf{k} \times (\omega\mathbf{k} \times \mathbf{r}) \tag{3.19}$$

$$\rho[C_p\nabla \cdot (\overline{T\mathbf{U}_{rel}} + \overline{T'\mathbf{U}'_{rel}}) + \frac{1}{2}\nabla \cdot (\overline{\mathbf{U}^3_{rel}} + \overline{\mathbf{U}_{rel}\mathbf{U}'^2_{rel}} + \overline{\mathbf{U}'^3_{rel}}) - \frac{1}{2}\nabla \cdot (\overline{\mathbf{U}_{rel}} \times \omega^2 r^2\mathbf{k})] = k\nabla^2\overline{T} \tag{3.20}$$

[2]Others ways of averaging, e.g. space, or mass averages can be found in Davidson (2004)

[3]The arithmetics of averaged quantities can be found in the same references

Equations 3.18 to 3.20 model the behaviour of the averaged variables in a turbulent flow field. Although the first of them is identical to its laminar counterpart, the other two have increased unknowns which resulted from the averaging process (double correlation in the Navier Stokes and double and triple correlations in the Energy equation). The expression 3.19 is better known as Reynold Averaged Navier Stokes (RANS) equation.

The RANS equation may be re-stated as:

$$\rho\nabla\cdot\overline{\mathbf{U}_{rel}\mathbf{U}_{rel}} = -\nabla\overline{p} + \nabla\cdot(\tau + \tau^R) - 2\omega\mathbf{k}\times\overline{\mathbf{U}_{rel}} - \omega\mathbf{k}\times(\omega\mathbf{k}\times\mathbf{r}) \tag{3.21}$$

Where:

$$\tau + \tau^R = \mu\left[\frac{\partial u_i^{rel}}{\partial x_j} + \frac{\partial u_j^{rel}}{\partial x_i}\right] - \rho\overline{u_i'^{rel}u_j'^{rel}}$$

The term τ^R is commonly known as the Reynolds stress term or turbulent momentum flux term, and constitutes the main drawback of turbulence modelling (the term τ is the laminar-like stress in the fluid due to mean speed gradient). It can be seen that τ^R couples the mean flow with the turbulence and although the term stress has been assigned to it, it is not such. The lack of another equation to close the fluid system is what drives to turbulence modelling to obtain accurate and feasible constitutive laws for this term.

3.1.2 Turbulence Modelling

In modelling the Reynolds stress term, one of the most common philosophies of solution aims to have τ^R as end result of the numerical processes of equations derived for that particular purpose. Then, by modelling the associated equations and not the Reynold stress equation itself, closures methods have been proposed. In this and other approaches, the mechanisms of turbulent kinetic energy production and dissipation need to be modelled through specific equations[4].

The two levels of energy in a continuum media are either internal energy and kinetic energy. In cases of incompressible turbulent flow, internal energy can be determined in an independent way, and therefore only kinetic energy remains to be modelled. The equation modelling the turbulent kinetic energy change process in turbulent flows will be given without attending details of its derivation. However, it is important to understand the process by which this is gained in the turbulent stream. What drives changes in kinetic energy levels in a fluid

[4]Other modelling techniques exist which focus to purely model the averaged Navier Stokes equations, these are LES or DNS methods

element is the mechanical work carried out in it by surface (shear) forces. In laminar flow the rate of work that shear stress produces in a fluid element is quantified as (Davidson 2004)[5]:

$$\frac{\partial}{\partial x_j}\left[u_i \tau_{ij}\right]$$

which, on performing the derivation can be decomposed in the rate of work of viscous forces on fluid (changes in mechanical energy given by the term $\frac{\partial \tau_{ij}}{\partial x_j}$ plus changes of internal energy in the fluid given by the deformation work $\frac{\partial u_i}{\partial x_j}$), which finally accounts for the first law of thermodynamics. In laminar flows, the integration of the above expression in a confined fluid volume is zero, then there exist a balance of mechanical energy being dissipated into heat.

In turbulent flow, the rate of work of the Reynolds stress can be thought in a similar manner:

$$\frac{\partial}{\partial x_j}\left[\overline{u_i}\tau_{ij}^R\right]$$

But τ_{ij}^R are fully fictitious stresses, since they arise only from the averaging process, and therefore they can not neither destroy nor create mechanical energy. Then, after performing the derivation the term $\overline{u_i}\frac{\partial \tau_{ij}^R}{\partial x_j}$ can be understood as the rate of loss (change) of kinetic energy from a fluid element in the mean flow as result of the differences in its turbulent stress field. This loss is gained as kinetic energy in the main turbulent stream ($\tau_{ij}^R \frac{\partial \overline{u_i}}{\partial x_j}$) by virtue of deformation work. Then, the Reynolds stress terms do not produce or destroy energy in the turbulent field, but transport energy from the mean flow toward the turbulent core. In the turbulent case, the integration of the above expression does not necessarily conduces to zero, since local balances are difficult to exist, this means that energy removed from one point does not necessarily have to appear as kinetic energy in the same place.

The standard form of the turbulent fluctuating kinetic energy equation is:

$$\frac{D\kappa}{Dt} = \frac{\partial}{\partial x_i}\left[\left(\nu + \frac{\nu_t}{Pr_\kappa}\right)\frac{\partial \kappa}{\partial x_i}\right] + \nu_t\left(\frac{\partial \overline{U}_i}{\partial x_j} + \frac{\partial \overline{U}_j}{\partial x_i}\right)\frac{\partial \overline{U}_i}{\partial x_j} - \epsilon \tag{3.22}$$

Where Pr_κ is a turbulent Prandtl number. The standard form of the turbulent isotropic dissipation rate (ϵ) equation is:

$$\frac{D\epsilon}{Dt} = P_\epsilon^1 + P_\epsilon^2 + P_\epsilon^3 + P_\epsilon^4 + \Pi_\epsilon + T_\epsilon + D_\epsilon - \psi_\epsilon \tag{3.23}$$

[5]The *rel* superscript for rotating frame is dropped in this Section.

Turbulent viscosity is then calculated from turbulent kinetic energy and dissipation rate:

$$\nu_t = C_\mu \frac{\kappa^2}{\epsilon} \tag{3.24}$$

The terms appearing in equation 3.23 and equations for vorticity, Reynolds stress, and enstrophy can be found in Bernard (2002). All these equations are traditionally named RANS equations and the modelling schemes based on them are currently the most used in the industry. However, in most of these the unclosed correlations are approximated by using empirical constants derived from statistical analysis of experiments conducted in so-called canonical flows. Then, the use of these methods may provide good or flawed results and therefore these must be carefully revised.

The RANS models look into providing constitutive approaches to the Reynolds stress transport equation (equation 3.29). The subdivision of these modelling schemes depends upon the degree of mathematical (and phenomenological) links devoted for ν_t predictions. In the *zero equation* models, ν_t is well defined and only depends upon $\overline{\mathbf{U}}$ and upon certain geometrical characteristics such as distance from a boundary. These are the simplest models and are mostly to predict behavior in bidimensional shear flows near boundaries.

Other modelling approaches make ν_t dependent upon turbulent variables such as κ and ϵ. This in order to birng history effects into the determination of ν_t. Then, the dependance of eddy viscosity on mean velocity field is replaced by dependance on turbulent kinetic energy fluctuations which bring better evolutionary processes into ν_t. In order to have differential equations for the behavior of the additional variables, the differential averaged momentum equation is algebraically modified, which results in additional equations for κ and ϵ (for instance), and then a new closed system of equations is obtained. These are the one- or two-equations model which have been widely used up to now. These turbulent models are also known as *eddy viscosity models*.

Despite the apparent strength of the two-equation models in predicting ν_t for equation 3.29, these fail to accurately reproduce anisotropies in the turbulent field, such as flow in rough channels or highly sheared flows in rotating channels. In this cases it is assumed (Bernard 2002) that it is not the calculated value of ν_t which is incorrect, but the constitutive model 3.29 which flaws. Therefore new models not depending or aiming to correlate the behaviour of 3.29 are required. Since in this case is the constitutive model what seems to be incorrect, new modelling techniques look into ways of producing new constitutive laws. One way is by re-shaping the linear behaviour of equation 3.29 and include in it the nonlinear (higher order terms). These models are known as *nonlinear eddy viscosity models*.

The other way to overcome the weakness of the Boussinesq equation is by modelling the Reynold stress terms themselves through their own differential equation. This modelling

technique is known as *second moment closure* (SCM) models. A third way of tackling the problem is by extracting a constitutive model for τ^R out of each SCM term (corresponding to the expansion of $\rho\overline{u_i' u_j'}$). At the end, a set of algebraic equations are obtained which constitute an extended generalisation of the Boussinesq equation. These are known as *algebraic Reynolds stress models*.

The above mentioned methodologies are not necessarily the best nor better than the two-equation models in the all-sense word. Similar limitations as those described for one-, two-equation models can bound them.

The fitness of one model driving its selection depends upon the characteristics sought in the phenomenon. Most of the above methodologies (e.g. the one- or two-equation models) are used to provide engineering accuracy levels in industrially applied flows, where rather than a detailed behaviour prediction is needed, a general trend or response capability is sufficient for suggesting design paths. Besides, simpler one or two-equation models require less computing resources and therefore if an appropriate trade-off is found amongst computing resources required, solution time and reasonably expected behavior prediction, the choice is obvious. However, when the level of inaccuracy is unbearable, then considering more especialised models is the path to follow.

Boussinesq's work (1807), proposed the first model for the Reynolds stress term. The Boussinesq's model suggested that fluid viscosity suffered an increment brought by an additional apparent viscosity resulting from the turbulent mixing. This new viscosity was termed eddy viscosity (ν_t, a temporal state of the fluid and not a fluid property), and the Reynolds stress model for flow in unidimensional direction was re-written as[6]:

$$\tau_{xy} + \tau_{xy}^R = \rho(\nu + \nu_t)\frac{\partial \overline{u}}{\partial y} \tag{3.25}$$

The search of direct mathematical models which predict the behaviour of τ^R had its first approach by means of the kinetic theory of nondense gases, since the velocity fluctuations of a turbulent flow field have some similar characteristics with velocity fluctuations of gases at molecular level. This approach was put forward by Prandtl in his well known Mixing Length model. The mixing length model suggested that the eddy viscosity in one dimensional turbulent flow could be approximated as:

$$\nu_t = l_m V \tag{3.26}$$

Where l_m is the mixing length (that is, the distance that the eddies travel before mixing occurs) and V is a suitable measure for $|\mathbf{U'}|$. Then, for one dimensional shear flow, the

[6]In highly turbulent flows the eddy viscosity is larger than the laminar like kinematic viscosity

mixing length model gives:

$$\tau_{xy}^{R} = -\rho\overline{u'v'} = \rho l_m^2 \left|\frac{\partial \overline{u}}{\partial y}\right| \frac{\partial \overline{u}}{\partial y} \tag{3.27}$$

In this way, after combining with the Boussinesq approximation, the eddy viscosity resulted in:

$$\nu_t = l_m^2 \left|\frac{\partial \overline{u}}{\partial y}\right| \tag{3.28}$$

Although it is not justified that momentum flux is not delivered until a fluid particle has passed a certain distance l_m on arrival to a new fluid layer, the Mixing Length model works well in simple shear flows.

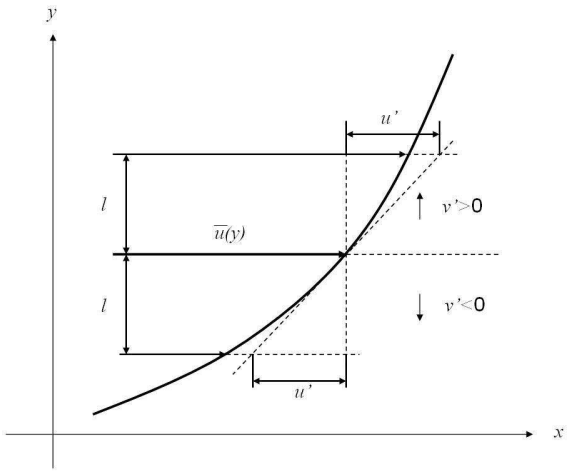

Figure 3.1: Turbulent fluctuation of momentum according to Prandtl mixing length theory.

A physical description of the negative sign in equation 3.27 for turbulent boundary layers is given by considering an air particle in a specific plane within the boundary layer (Figure 3.1), its mean speed $\overline{u}$ can interact with others mean speeds above and beneath the plane due to its $+v'$ or $-v'$ vertical fluctuations. In the first case, the fluctuation $+v'$ causes the original mean speed $\overline{u}$ reaches a plane upwards with bigger $\overline{u}$, the interaction results in a negative fluctuation $(-u')$ on the upper plane's mean speed. Consequently, when the original mean speed fluctuates downwards due to $-v'$, it creates a positive $+u'$ fluctuation in the mean speed of the plane beneath. Therefore, the product $\overline{u'v'}$ yields a negative quantity. Then, the sign of τ_{xy}^{R} is positive, as it is the sign of the laminar-like stress τ_{xy}.

For the purpose of using the eddy viscosity models in more complex flows, a three-dimensional relation for the Reynolds stress found in the literature as the Boussinesq equation is:

$$\tau_{ij}^{R} = -\rho\overline{u_i' u_j'}\left[\frac{\partial \bar{u}_i}{\partial x_j} + \frac{\partial \bar{u}_j}{\partial x_i}\right] - \frac{\rho}{3}\overline{u_k' u_k'}\delta_{ij} \tag{3.29}$$

Note that the second term on the right of equation 3.29 is actually the turbulent kinetic energy of the flow. Equation 3.29 is a first approach to a constitutive model of the Reynolds stress terms, and it is the focus of attention of eddy viscosity models.

Another commonly used turbulence model is the $\kappa - \epsilon$ model which through the usage of equations 3.22, 3.23 model the eddy viscosity (equation 3.24). As mentioned before, this is a two-equation eddy viscosity model and its main numerical modelling challenge is to model the terms in the dissipation rate equation (3.23). This equation depends upon many experimental constant values which have been tuned for isotropic turbulence or homogeneous shear flow conditions. Anisotropy of turbulence is given by direct evaluation of the Boussinesq equation and it is described by the anisitropy tensor as described in Bernard (2002).

The fact of usage of many constants in the ϵ equation has regarded this as an empirically driven equation. The value of these constants are:

$$c_\mu = 0.09, c_{\epsilon_1} = 1.44, c_{\epsilon_2} = 1.92, Pr_k = 1.0, \sigma_\epsilon = 1.3$$

3.1.3 Computational Approach

The above equations are used by the CFD solver to model the behaviour of the flow around the disc and convective heat transfer exchange between the brake disc and the environment. For this purpose, the *fluid domain* is divided into small cells. In order for the equations to be solved within each of these cells, they are transformed in a discrete form by using the Finite Volume Method procedures (see Versteeg & Malalasekera (1995) and ANSYS-CFX Solver Theory (2005)). This reduction of the equations is performed following a fully implicit scheme in the discretisation. The advantage of the implicit scheme is that it yields discrete equations that can be integrated using relatively long time steps without affecting the stability of the solution procedure (this is not possible when explicit schemes are used, since in these the time step can not be greater than that given by the speedwave of the medium through the cell length, Wendt (1995)). The variables are solved in a computational space to which the physical space variables are transformed by means of jacobian matrices.

The finite volumes (cells) that approximate the domain of analysis are defined by linear shape functions similar to those found in Finite Element Method procedures, (ANSYS-CFX Solver Theory 2005). The equations are linked to the geometry of the domain by means of a Cartesian transformation of the derivatives in the cells' local system to the domain global system. The results of the numerical integration are referred to the integration points

of the faces of the cells. The advection schemes that can be implemented in Ansys-CFX are (ANSYS-CFX Solver Theory 2005): First Order Upwind Differencing Scheme, Numerical Advection Correction Scheme and High Resolution Scheme. The Upwind Differencing Scheme is a first order accuracy method which is numerically stable, although is prone to numerical diffusion existing when main flow direction deviates from the cell face normal, as for example in region of high recirculation. Numerical diffusion means that the features of the flow are lost in a certain degree, that is, are *smeared out*.

The Numerical Advection Correction Schemes are anti-diffusive methods in which, by choosing a correction factor, the approximation of the equations can reach second order accuracy. This method downsizes the risk of numerical smearing at a cost of becoming more numerically unstable. The High Resolution Scheme varies dynamically the correction factor and therefore tries to reduce numerical diffusion in regions prone to this.

The numerical solution of the equations in Ansys-CFX proceeds transiently in time for steady state and transient problems. The first is achieved when the dependent variables do not vary significantly with time, that is converges to a solution. The way of knowing that a converged solution has been achieved is by setting a limiting numerical value (convergence error), above which the error difference resulting between two consecutive (in time) solutions is rejected. In this research the maximum root square mean error of the variables equal to 1×10^{-5} has been used .

3.1.4 Convective Heat Transfer Modelling

In a real situation the brake disc, as a part of an assembly, interactively exchanges energy with other components nearby (brake pads, caliper, wheel carrier, wheel, etc.). However, given the relatively large thermal capacity of the disc, most of the friction energy is absorbed into it. Thus, the brake disc is left with the task of dissipating heat to the surrounding environment. This process occurs either by conduction, radiation and convection. Conduction and radiation remove energy independently of the brake disc speed. Convective heat dissipation from a brake disc can occur in two forms, natural convection and forced convection; in both cases the mechanisms of heat removal are similar: temperature difference between the air and the brake disc surface. However, the difference between the two phenomena is given by the relative significance of gravity force in the dynamics of the fluid nearby the brake disc surface. If the fluid speed around the surface is mainly driven due to external sources (e.g.: a fan blowing air, or brake disc rotation), then gravity (body) forces due to changes of air density are not representative and convective dissipation is due to the inertia of the flow; this is termed *forced convection*. If after a braking event, the vehicle remains stationary for long time, *natural convection* sets in inducing buoyant forces on the air near to brake disc surface. Heat flows to air creating regions with lower density near the disc surface, which then move

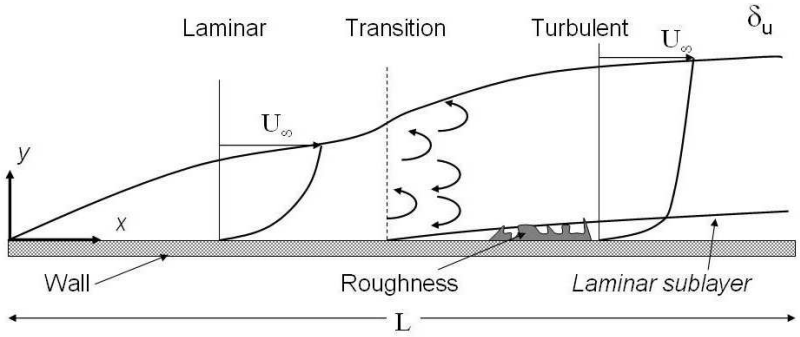

Figure 3.2: Velocity boundary layer on a flat plate.

upwards allowing to heavier (cooler) air to occupy their place and continue the heat removal cycle. Convective heat dissipation can also depend upon the cooling fluid, which in vehicle brakes is air.

Forced Convection Modelling

If a section of the brake disc surface is seen as stationary planar plate immersed within flowing air, the velocity will progressively decrease as it reaches close proximity with the surface, due to increased viscous effects of air. This creates a so-called velocity boundary layer with thickness δ_u, within which inertia forces are weaker than viscous forces. The air velocity (relative speed if the disc rotates or self-generated in natural convection), drops to zero on the surface. The thickness of δ_u is arbitrarily defined as the distance from the surface to the fluid location where 99% of the mainstream speed is reached (outer edge of δ_u), Daily & Harleman (1966) and Kreith & Bohn (2001).

When uniform airflow reaches the plate (Figure 3.2), a regular fluid behavior is set within the layer, and this is known as laminar boundary layer. The velocity gradients inside the layer are linear, and depend upon the shear stresses given the dynamic viscosity of the fluid (velocity follows a parabolic profile). Eventually, after a certain distance from the leading edge of the surface, the inertial forces from the fluid mainstream penetrate into the laminar layer, provoking a vigorous exchange of momentum and energy in the fluid; this exchange of energy feeds what is known as turbulence and an *increased* viscosity effect is felt by the fluid. The chaotic mixing of air in turn gives shape to a velocity profile inside of what is known as turbulent boundary layer. In this latter case, the velocity profile starts as parabolic but immediately develops a quasi linear profile until it reaches the mainstream velocity range. The parabolic profile is very thin and resides only on what is known as viscous sublayer where laminar effects exist.

The conditions controlling the layer behaviour are parameterised by the Reynolds number (equation 3.30). The Reynolds number compares inertial to damping (viscous) effects in a fluid as a function of undisturbed speed, distance from the leading edge (x), and fluid's density and dynamic viscosity (ρ, μ).

$$Re_x = \frac{\rho u x}{\mu} \tag{3.30}$$

Turbulent boundary layer appears when orderly viscous fluid weakens and allow room to disturbances from the main stream; this is the transition region from laminar to turbulent behaviours, which in a fluid flowing uniformly over a flat plate can vary within the range $1.0 \times 10^5 \leq Re_t \leq 3.5 \times 10^5$, (Bejan 2004), (Kreith & Bohn 2001), where Re_t represents the transition Reynolds number. The range seems large and inadequate for establishing a criterion of boundary layer analysis; however, this also indicates that there is no specific Reynolds number value at which transition can be considered as a fact; it rather depends upon other factors such as surface roughness, which is not considered by equation 3.30. Surface roughness can importantly accelerate the transition from laminar to turbulent flow and therefore decrease Re_t.

$$Re_\omega = \frac{\rho \omega R_o^2}{\mu} \tag{3.31}$$

In fluids surrounding rotating circular objects like a brake disc the Reynold number is usually referred to the disc outer radius and to the angular speed (equation 3.31). The behaviour of flows around rotating *solid smooth* discs depends upon the angular speed and on disc surface conditions. Laminar flow exist for rotating discs whose $Re_\omega < 2.4 \times 10^5$ and turbulent flows when $Re_\omega > 2.4 \times 10^5$, Dorfman (1963), Wagner (1948), Cobb & Saunders (1956); it should be noted that these figures are only for solid discs with smooth faces, whose outer radii are much larger than the velocity boundary layer thickness, Dorfman (1963). However, in ventilated brake discs the conditions are different, since the vents soak air from the environment at a rate depending upon the angular speed and the geometry of the vent inlet. The flow conditions inside the ventilation region are affected by Coriolis and centrifugal accelerations, as a result secondary flow appears inside the vents, and therefore laminar flow regime is possibly lost. Additionally, airflow finds geometric discontinuities in its path, which induce shear layers.

The thickness of the laminar boundary layer for uniform flow over a plate was theoretically calculated first by Blasius and after validated by Hansen, (Kreith & Bohn 2001). From their work, the speed gradient on the surface $y = 0$ at any distance within the laminar layer was also derived. The equations to compute them are:

$$\delta_u = \frac{5.0x}{Re_x^{0.5}} \tag{3.32}$$

$$\left(\frac{du}{dy}\right)_{y=0} = 0.332\frac{u_\infty}{x}Re_x^{0.5} \tag{3.33}$$

It can be observed that the laminar boundary layer thickness decreases as the speed rises and that the velocity gradient on the wall gets its maximum in the leading edge of the surface, while it increases with speed. The fluid shear stress on the wall is obtained by evaluating the expression 3.34.

$$\tau_w = \mu\left(\frac{du}{dy}\right)_{y=0} \tag{3.34}$$

After substituting equation 3.33 in equation 3.34, it is evident that the behaviour of the wall shear stress follows that of equation 3.33. The friction coefficient in the laminar boundary layer is defined by dividing equation 3.34 by the flow dynamic pressure:

$$c_{f_l} = \frac{\tau_w}{\rho\frac{u_\infty}{2}} \tag{3.35}$$

Combining equations 3.33, 3.34 and 3.35, an explicit relation for the laminar friction coefficient results in (Daily & Harleman 1966), (Kreith & Bohn 2001):

$$c_{f_l} = \frac{0.664}{\sqrt{Re_x}} \tag{3.36}$$

Similarly, analysis has been performed for the description of turbulent boundary layers. Unlike laminar layers on flat plates, whose behavior is bidimensional; turbulent boundary layers are given with the merging of undamped spots appearing randomly in the fluid field as a result of several causes, (Daily & Harleman 1966). These spots, when merged, form regions of continuously growing disordered flow, which transforms into turbulence. The onset of turbulence is given by interaction of flow boundaries with discontinuities, such as wake-jet flows, flow past object tips, regions of flow with very different velocities lying next each other, boundary layer separation (adverse pressure gradient, backflow), or by surface roughness.

On smooth surfaces, the turbulent boundary layer is formed by 3 regions; the closest to the wall, known as the viscous sublayer (or laminar sublayer), may extend up to few hundred microns out of the surface. The behaviour of the flow in this region is laminar and the velocity fluctuation energy is very low (i.e.: damped by viscosity). Above this region, the buffer zone

is where turbulence mostly sets in, with fluctuating energy of mean speed reaching their peaks. After this sublayer the energy fluctuations start to decrease again down to the main flow turbulence intensity level, this region is simply called the outer region, and it mixes with the core of the fluid. For rough surfaces, the amplitude of micro-peaks on the surface may equalize the thickness of the laminar sublayer, then the buffer region starts earlier (Figure 3.2).

Although the behaviour of a turbulent boundary layer is definitely variable in all directions, its analysis is usually reported with bi-dimensional functions, which only work in the predominant flow direction (x) and for flow past a flat plate or ducts. The profile of its mean velocity, coefficient of friction and thickness are given in terms of different parameters, depending upon the region analysed and on the theory assumed. The literature formulas are mostly experimental and have been drawn under controlled conditions; therefore their application to more complex situations, i.e. in flows with high rotational characteristics, should be taken with caution.

Among the theories for turbulent boundary layer analysis on smooth flat plates with negligible pressure gradient, the most quoted in books are: *law of the wall, velocity-defect law* and the *power law*, e.g. Daily & Harleman (1966), Bejan (2004). Without giving details of derivation, the important expressions are described here. The law of the wall assumes a linear profile for the mean velocity based on wall shear stress, which is kept constant throughout the thickness.

After integration of wall shear stress in equation 3.34, a linear relation for $\bar{u}$ results in:

$$\bar{u} = \frac{\tau_w}{\rho}\frac{y}{\nu}, \qquad u^* = \sqrt{\frac{\tau_w}{\rho}}, \qquad \tau_w = \frac{1}{2}c_f \rho U_\infty^2 \tag{3.37}$$

The term u^* is called the *friction velocity*. Then, re-substituting gives:

$$u^+ = \frac{\bar{u}}{u^*} = \frac{u^* y}{\nu} = y^+ \tag{3.38}$$

The term c_f in equation 3.37 is the turbulent friction coefficient. According to Daily & Harleman (1966), three ranges are defined for y^+:

$$\begin{aligned} 0 < y^+ = \frac{u^* y}{\nu} < 4 \text{ to } 11.6 &\rightarrow \text{Laminar sublayer} \\ 4 < y^+ = \frac{u^* y}{\nu} < 30 \text{ to } 70 &\rightarrow \text{Buffer zone} \\ y^+ = \frac{u^* y}{\nu} > 30 \text{ to } 70 &\rightarrow \text{Outer end} \end{aligned}$$

The transition from the viscous to the buffer layer is usually taken as $y^+ = 11.6$, however, this depends upon the specific application. The modelling of $\bar{u}$ above the laminar sublayer in the law of the wall theory is carried out using the Kármán's logarithmic relation, Daily & Harleman (1966):

$$u^+ = \frac{\bar{u}}{u^*} = 5.6 \cdot \log\left(\frac{u^* y}{\nu}\right) + 4.9 \tag{3.39}$$

Equation 3.39 is valid for $4 < y^+ < 30$. The Kármán's relation may be taken up to near the outer reaches of the buffer zone. A Kármán's expression exists for $y^+ > 30$ as:

$$u^+ = 2.5 \ln\, y^+ + 5.5 \tag{3.40}$$

Other expressions for the prediction of the velocity profile in the turbulent boundary layer are known as the velocity-defect law model and the Rannie's model cited in Bejan (2004). The evaluation of the friction coefficient on the wall in turbulent regions can be performed using relations found in the literature. The expressions and their authors are (Daily & Harleman 1966):

$$c_f = \frac{0.370}{(\log Re_x)^{2.58}} \qquad \text{Schultz-Grunow (1940)} \tag{3.41}$$

$$\frac{1}{\sqrt{c_f}} = 4.15 \cdot \log(Re_x c_f) + 1.7 \qquad \text{Kármán (1934)} \tag{3.42}$$

$$\frac{1}{\sqrt{c_f}} = 4.13 \cdot \log(Re_l c_f), \;\; Re_l = \frac{U_\infty l}{\nu} \qquad \text{Schoenherr (1932)} \tag{3.43}$$

Formulas for c_f in the transition laminar-turbulent region are evidently less available. One proposed by Schultz-Grunow-Prandtl, is a function of the transition Reynolds number (Table 3.1).

$$c_f = \frac{0.427}{(\log Re_l - 0.407)^{2.64}} - \frac{C_1}{Re_l} \tag{3.44}$$

The last theory to be revised for calculation of mean speed across the turbulent boundary layer is the so-called power law for smooth walls. This theory, as well as those above, considers that the pressure gradient is negligible (that is, no substantial curvature exist in the body) and that the Reynolds number calculated on boundary layer thickness basis (Re_δ) is less than 5×10^5.

Table 3.1: Constant C_1 values for calculating c_f in transition regions (equation 3.44)

$Re_t = \frac{U_\infty x_t}{\nu}$	3×10^5	4×10^5	5×10^5	6×10^5	1×10^6
C_1	1060	1400	1740	2080	3340

The advantage of the power law is that it provides useful and explicit relations for the friction coefficient, speed and boundary layer thickness. The relations are based on the assumption that the mean speed is proportional to the square root of the distance from the wall and that the friction coefficient is inversely proportional to the square root of Re_δ. The expressions for the turbulent boundary layer thickness and friction coefficient for $Re_x < 1 \times 10^7$, as reported in (Daily & Harleman 1966), are:

$$\delta_u = \frac{0.38x}{Re_x^{1/5}} \tag{3.45}$$

$$c_f = \frac{0.059}{Re_x^{1/5}} \tag{3.46}$$

$$\bar{c}_f = \frac{0.074}{Re_l^{1/5}} \tag{3.47}$$

The treatment of the mean speed profile for flow past rough plate surfaces is more difficult and usually involves typifying the roughness as shapes with periodic amplitude (uniform sand grain, wire mesh and transverse bars or grooves). The influence of roughness is mostly felt in the laminar sublayer, (Daily & Harleman 1966).

In order to have a better idea of the results that some of the above equations would give for an ideal condition of the flow past a flat surface i.e.: a brake disc vane, examples for two cases are shown. To suit the conditions under which the these equations were established, the vane is assumed isolated and channel effects are disregarded. The interface wall-flow is firstly considered adiabatic. The length of the vane is l_v= 0.095 m and the speeds are U_∞=5m/s, 10m/s. Since the object of the analysis is descriptive, laminar and turbulent relationships are considered. The results show boundary layer thickness under equations 3.32 and 3.45. Friction coefficients are calculated on the surface using equations 3.36 (laminar), 3.41 and 3.46 (turbulent); then, these results are used to get the wall shear stress τ_w in each case, which are later plotted against the length. Air is assumed at 60^oC, and their properties are shown in Table 3.2.

Figure 3.3 shows the development of boundary layers thickness assuming laminar and turbulent flow pattern (using the power law formulation). It is immediately evident that thicker

Table 3.2: Air properties at 60^oC, from Kreith and Bohn (2001).

$\rho \left[\frac{kg}{m^3}\right]$	$C_p \left[\frac{J}{kgK}\right]$	$k \left[\frac{W}{mK}\right]$	$\nu \left[\frac{m^2}{s}\right]$	Pr	$\beta \, [K^{-1}]$
1.065	1009.1	0.0288	$1.78\text{x}10^{-5}$	0.7	$3\text{x}10^{-3}$

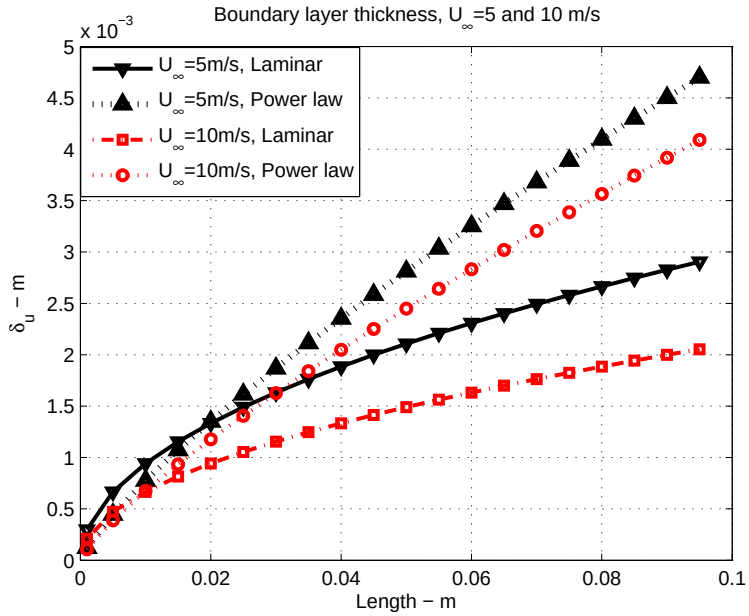

Figure 3.3: Boundary layer thickness on a flat surface, length=0.095m.

boundary layer is generated when the air flows at $5m/s$ than at $10m/s$. This is due to viscous effects on the air layer near the wall dominate more in slow flows than in faster flows. At $5m/s$, the boundary layer thickness for laminar and turbulent regimes follow similar thickness profile during nearly 20% of the initial length. After crossing one third of the total length, the turbulent layer grows faster, and at the end of the vane length, it is 58% thicker.

At $10m/s$, the laminar boundary layer is 30% thinner than the corresponding laminar layer at $5m/s$; while the turbulent layer at $10m/s$ grows 52% more than the laminar one.

Generic understanding of the above leads to the conclusion that turbulent flows promote thicker boundary layers than laminar flows. This could imply that viscous effects are higher in turbulent than in laminar layer, however it is eddy viscosity what drives the growth since viscous effects are damped. As a result, higher aerodynamic resistance is caused by turbulent boundary layers, although these are more stable.

Wall shear stress in the boundary layer was calculated for three air speeds (Figures 3.4, and

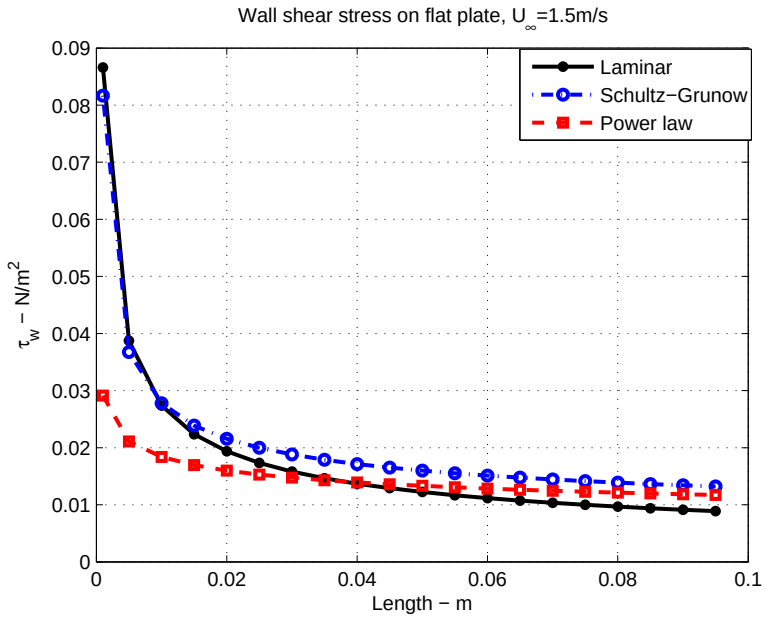

Figure 3.4: Wall shear stress on surface, $U_\infty = 1.5m/s$.

3.5). At 1.5 m/s, laminar and turbulent wall shear stress calculated using friction coefficients from equations 3.36 (laminar), 3.41 (Schultz-Grunow) and 3.46 (Power law) are similar after one third of the length. Nevertheless, unlike the laminar and Schultz-Grunow (turbulent) formulas which predict highly similar values at the leading edge, the Power law predicts lower (-67%) wall shear at the leading edge. It can be concluded from Figure 3.4 that for relatively low mean speed flow, turbulent effects are not representative and momentum transfer is given mainly by laminar behaviour. At higher speeds (U_∞=5m/s, 10m/s), the behavior changes markedly, turbulent prediction shift upwards the wall shear stress profile before reaching 20% of the length. At a position of 0.02 m and 5m/s, the Power law predicts 10% higher shear, while the Schultz-Grunow predicts 20% more than the laminar formula. At 10m/s, the Power law and Schultz-Grunow formulas predict both nearly 34% more whall shear stress at 0.02 m than the laminar case. In both cases, the turbulent behaviour relations make a significant positive difference in wall shear, which is evident in the three last quarters of the length; meaning higher momentum exchange in that region when compared to the laminar side, and therefore larger ability to transfer energy across the boundary layer.

A general view of the above results indicates that the wall shear stress predicted at the leading edge of the surface by the laminar and turbulent relations, is initially very high and then falls rapidly in the first third of the length. This comes as a result of the small thickness of the boundary layer on the leading edges of surfaces. This has a marked effect

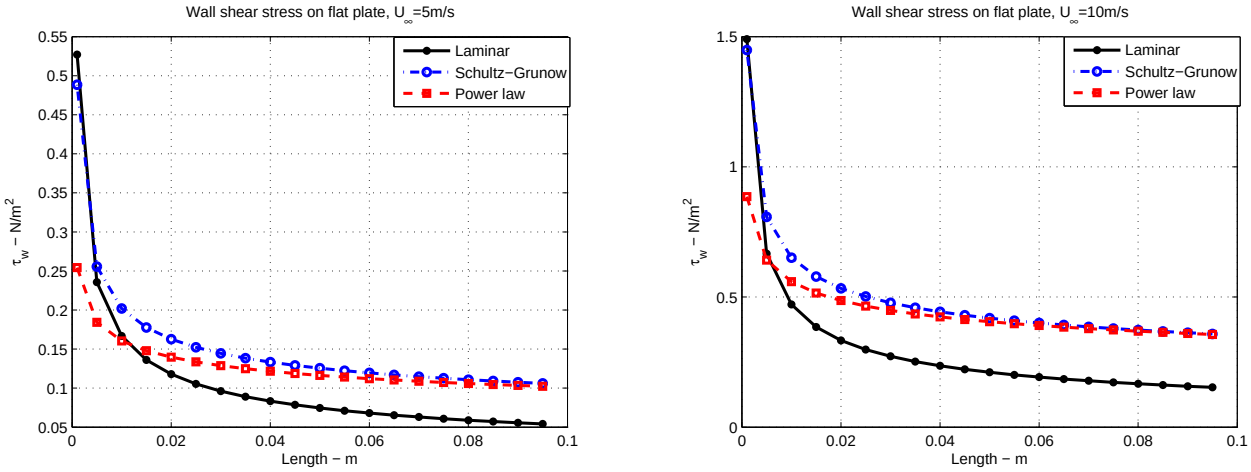

(a) $U_\infty = 5m/s$ (b) $U_\infty = 10m/s$

Figure 3.5: Wall shear stress on surface.

in the convective energy transfer rates usually found in leading portions of moving surfaces.

When the disc temperature rises above air temperature, an exchange of energy toward the air occurs due to the temperature difference. Disregarding radiation, the mechanics of heat transfer by convection to air are analogue to those driving the transport of momentum in the velocity boundary layer. In laminar fluids, heat flows by conduction (molecular difussion) through the laminar boundary layer. After heat conduction bridges the layer, the dissipated energy is carried by the core of the fluid. The energy balance at the interface wall-air requires that conductive heat losses per unit area to the boundary layer are gained as convective energy in the moving air, equation 3.48. The temperature gradient in equation 3.48 is controlled by the ability of the fluid to carry energy out of the wall and transport it to its core; and it falls to zero when subsequent temperatures are equalized at the outer edge of what is termed *thermal boundary layer*, δ_{th}. The width of δ_{th} depends upon the stream characteristics (e.g. whether the flow has laminar or turbulent behaviour).

$$q_c = -k\frac{d\Theta}{dy} = h_c(\Theta_w - \Theta_\infty) \tag{3.48}$$

In Figure 3.6, a convective cooling process in laminar flow is depicted, Θ_w is the disc surface temperature and Θ_∞ is the unperturbed air temperature. The flow direction is from left to right, and heat flows only due to molecular diffusion across the thermal boundary layer.

The typical index to measure the ability of the flow to carry heat out of the surface is called

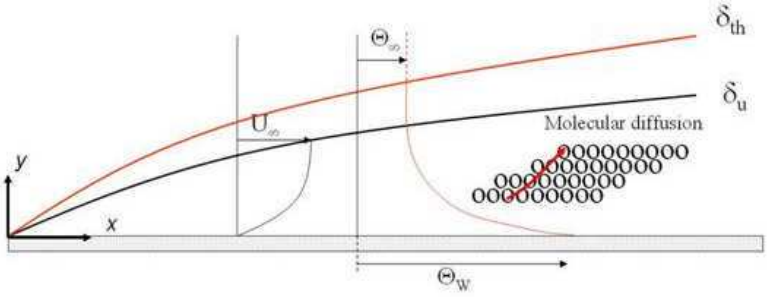

Figure 3.6: Laminar thermal boundary layer on a flat hot plate.

convective heat transfer coefficient, and it arises when equation 3.48 is solved for h_c:

$$h_c = \frac{-k\frac{d\Theta}{dy}}{\Theta_w - \Theta_\infty} \tag{3.49}$$

For flows on flat surfaces with laminar characteristics (based on Re_x) and negligible pressure gradient, the conductive part of equation 3.49 is obtained using the similarities between the energy equation and the momentum equation in the velocity and thermal boundary layers (Kreith & Bohn 2001).

$$u\frac{\partial u}{\partial x} + v\frac{\partial u}{\partial y} = \nu\frac{\partial^2 u}{\partial y^2} \tag{3.50}$$

$$u\frac{\partial \Theta}{\partial x} + v\frac{\partial \Theta}{\partial y} = \alpha\frac{\partial^2 \Theta}{\partial y^2} \tag{3.51}$$

Where α is the fluid thermal diffusivity equal to $k/\rho C_p$. Equations 3.50 and 3.51 have the same solution if their boundary conditions are similar, the wall temperature is uniform and if the ratio $Pr = \nu/\alpha$, the Prandtl number, is equal to one. Using the velocity solution found by Blasius for laminar flow over a flat plate, Pohlhausen solved the energy equation (3.51) in the boundary layer domain for $Pr = 1$. The temperature solution was later empirically modified and allowed to relate the laminar velocity and thermal boundary layers with a range of Prandlt numbers from 0.6 to 50 (Kreith & Bohn 2001) in the following form:

$$\frac{\delta_u}{\delta_{th}} = Pr^{1/3} \tag{3.52}$$

The equation 3.52 shows that for $Pr < 1$, $\delta_{th} > \delta_u$, and vice versa. Likewise, the temperature gradient at the wall surface for laminar boundary layer can be calculated as:

$$\left(\frac{\partial \Theta}{\partial y}\right)_{y=0} = \frac{0.332}{x} Re_x^{1/2} Pr^{1/3} (\Theta_\infty - \Theta_w) \tag{3.53}$$

Then, upon substituting equation 3.53 in equation 3.49, an explicit relation for the local wall heat transfer coefficient in laminar boundary layer on a flat surface is:

$$h_{c_x} = \frac{q_c}{\Theta_w - \Theta_\infty} = \frac{0.332\, k}{x} Re_x^{1/2} Pr^{1/3} \tag{3.54}$$

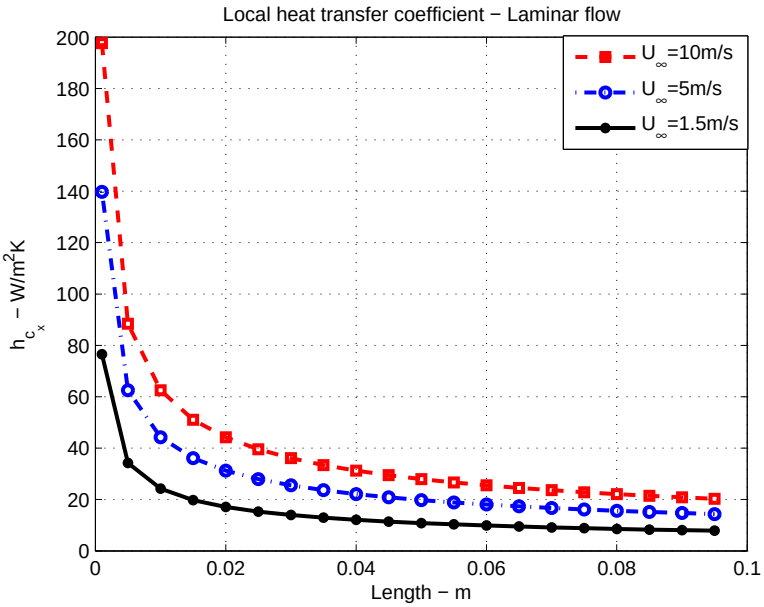

Figure 3.7: Local convective heat transfer coefficient (laminar flow), $\Theta_w = 100^oC$, $\Theta_\infty = 20^oC$.

Equation 3.54 relates local flow properties and dynamics (Re_x), but does not explicitly depend upon temperature difference, although air properties need to be evaluated at midfilm temperature. For temperature ranges in automotive brake discs (up to 600^oC), the Prandtl number varies little, see Kreith & Bohn (2001). This indicates that (restrictive only to forced convection and disregarding centrifugal buoyancy) the convective heat transfer coefficient does not depend upon the temperature difference (wall-air), but only on the dynamics of the flow near the surface; which is also influenced by the surface roughness. This has been experimentally confirmed by Voller (2003).

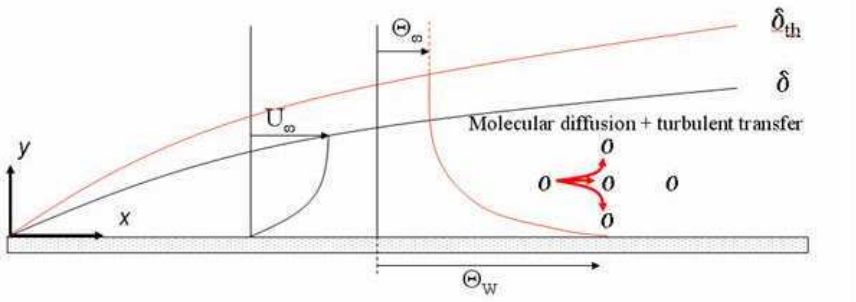

Figure 3.8: Thermal boundary layer representation in turbulent convective cooling of a flat plate.

Local wall heat transfer coefficient values in laminar conditions are shown in Figure 3.7. High values of h_{c_x} are obtained in the leading edge of the plate at all speeds, that is local heat transfer coefficient is proportional to wall shear stress. This is followed by a sharp decrease in h_{c_x}: just in the first 20% of the length, from 197 W/m^{2}K to 44 W/m^{2}K at U_∞ =10m/s; from 140 W/m^{2}K to 31 W/m^{2}K at U_∞ =5m/s; and from 76 W/m^{2}K to 17 W/m^{2}K at U_∞ =1.5m/s. All these reductions represent a drop of heat dissipation performance of around 78% in the first fifth of the total length. In the remaining length an average reduction of 42% is observed. In general, as seen in Figure 3.7, the convective heat transfer coefficient increases with speed. Flows with high speed produce large temperature gradients, while low speeds reduce them. That is, larger amounts of heat are convected for high speed flows (thinner δ_{th}) than for low speed flows. The former is demonstrated by observing the role of the wall temperature gradient in equation 3.49. For equal temperature differences, higher temperature gradients removes more heat, while lower temperature gradients deteriorate the rate of convection.

When the flow over the surface is turbulent, the mechanism of convective energy transfer is enhanced in analogue way to turbulent transfer of momentum. In this case the boundary layer development is more influenced by random fluctuations of particles than by molecular diffusion and the Prandtl number does not play an important role (viscous transport is lower than turbulent transport), and for Pr>0.5 Incropera & DeWitt (2002) suggests that equation 3.45 gives a good approximation to the thickness of the turbulent thermal boundary layer.

The calculation of turbulent heat transfer coefficient implies particular solutions for the convected heat in turbulent behaviour ($q_{c_{turb}}$), by recalculating the temperature gradient as a function of the turbulence model selected. The equation 3.48 needs to account not only for molecular diffusion of heat (laminar-like), but also turbulent heat transfer due to mean

speed fluctuations (see Figure 3.8). The equation 3.48 can be re-written as:

$$q_{c_{turb}} = -k\frac{d\overline{\Theta}}{dy} + q_{c_t} = -\rho\, C_p(\alpha + \alpha_t)\frac{d\overline{\Theta}}{dy} = h_{c_t}(\Theta_w - \Theta_\infty) \tag{3.55}$$

The term α_t accounts for the additional turbulent heat transfer, and it is called *eddy heat transfer diffusivity*. The term q_{c_t} can be written from the formulation of the turbulent energy equation, see Versteeg & Malalasekera (1995), ANSYS-CFX and Bejan (2004).

$$q_{c_t} = \rho\, C_p\overline{v'\Theta'} = -\rho\, C_p\alpha_t\frac{d\overline{\Theta}}{dy} \tag{3.56}$$

Then, the definition of α_t is given only by the selection of the turbulent model for temperature behaviour. Following a similar reasoning for the increment of momentum transfer, and provided the Prandtl mixing length concept is used for the turbulent convective cooling process, an analogue revision can be made for the mean temperature. Assuming that particles of air that travel upwards and downwards due to v' turbulent fluctuations of $\bar{u}$ carry with them their original mean temperature, and that the fluid mean temperature falls as the distance from the wall increases; then, a positive fluctuation v' will cause the particle to arrive to a fluid plane whose mean temperature is lower, giving place to a positive Θ' fluctuation. The opposite happens with $-v'$, which induces a negative $(-\Theta')$ fluctuation. The fluctuations caused in mean temperature are defined, in the same fashion for momentum transfer, by the mixing length. Then $\alpha_t = \overline{v'l}$, (which means that $\alpha_t = \nu_t$), and:

$$q_{c_{turb}} = -\rho\, C_p(\alpha + \overline{v'l})\frac{d\overline{\Theta}}{dy} = h_{c_t}(\Theta_w - \Theta_\infty) \tag{3.57}$$

Equation 3.57 is the simplest representation for the turbulent convective heat exchange according to Prandtl mixing length theory. Since, complex turbulent models (so-called two equation models) do not explicitly work with the Prandtl mixing theory (zero equation models), two additional schemes for the turbulent transfer of convective heat are described next. The first solution scheme (Kader 1981), is currently being used by Ansys-CFX (Release 10) for calculation of temperatures in the boundary layer and extraction of heat transfer coefficients. A second scheme, described by Bejan (2004) is also shown. The 'working' section of equation 3.55 is re-written as:

$$q_{c_{turb}} = -\rho\, C_p(\alpha + \alpha_t)\frac{d\bar{\Theta}}{dy} \tag{3.58}$$

Kader (1981) proposed a solution for equation 3.58 using y^+ (equation 3.38) and the following parameters:

$$\Theta^+ = \frac{\Theta_w - \bar{\Theta}}{\Theta^*} \tag{3.59}$$

$$\Theta^* = \frac{q_{c_{turb}}}{\rho\, C_p\, u^*} \tag{3.60}$$

Equations 3.59 and 3.60 are the dimensionless temperature profile in the turbulent thermal boundary layer (δ_{th}) and the friction temperature, in analogous form to the friction velocity described in equation 3.37. Substitution in equation 3.58 gives the dimensionless temperature gradient in turbulent thermal boundary layer driven by the following boundary conditions.

$$\frac{d\Theta^+}{dy^+} = \frac{1}{\frac{1}{Pr} + \frac{\alpha_t}{\nu}} \tag{3.61}$$

$$y^+ = 0 \;\; \rightarrow \;\; \Theta^+ = 0 \tag{3.62}$$

$$y^+ = y^+(\delta_{th}) \;\; \rightarrow \;\; \Theta^+ = \Theta^+(\delta_{th}) \tag{3.63}$$

Within the turbulent thermal layer there is also a region immediate to the wall where heat is transferred by molecular diffusion (i.e.: conduction). This is termed the conduction sublayer (CSL) and in it the turbulent transfer of heat is negligible as compared to the conduction of heat by viscous effects. Then the term $\frac{\alpha_t}{\nu}$ in equation 3.61 vanishes and the temperature profile in this sublayer is:

$$\Theta^+ = Pr\, y^+ \tag{3.64}$$

The length of the CSL has been suggested to be (Kader 1981):

$$y^+_{CSL} \approx 9/Pr^{1/3} \tag{3.65}$$

For the region above of the CSL, Kader (1981) suggested the following profile:

$$\Theta^+ = \kappa\, \ln y^+ + \beta(Pr) \tag{3.66}$$

Where κ =2.12, and $\beta(Pr) = (3.85Pr^{1/3} - 1.3)^2 + 2.12 \ln Pr$. The equation resembles the Kármán's relation for velocity profile (e.g.: equation 3.40), following a linear logarithmic

style. For the fully turbulent region, Kader (1981) proposed two relations, one for flow on a flat surface and the other for flow inside a duct of radius R (both with smooth surfaces).

$$\Theta^+ = Pr\, y^+ e^{-\Gamma} + \left\{ 2.12 \ln \left[(1+y^+) \frac{1.5(2-y/R)}{1+2(1-y/R)^2} \right] + \beta(Pr) \right\} e^{-1/\Gamma} \qquad y/R \leq 1 \tag{3.67}$$

$$\Theta^+ = Pr\, y^+ e^{-\Gamma} + \left\{ 2.12 \ln \left[(1+y^+) \frac{2.5(2-y/\delta_{th})}{1+4(1-y/\delta_{th})^2} \right] + \beta(Pr) \right\} e^{-1/\Gamma} \qquad y/\delta_{th} \geq 0.1 \tag{3.68}$$

With:

$$\Gamma = \frac{0.01(Pr\, y^+)^4}{1+5Pr^3\, y^+} \tag{3.69}$$

The second solution for equation 3.55 is described by Bejan (2004). In this, the scaling of Θ^+ is as described in 3.59 and the general profile of the dimensionless temperature Θ^+ in equation 3.61 is solved as:

$$\Theta^+ = \int_0^{y^+} \frac{dy^+}{Pr^{-1} + Pr_t^{-1} \left(\frac{\nu_t}{\nu} \right)} \tag{3.70}$$

In equation 3.70 $Pr_t = \nu_t/\alpha_t$, and the ratio of turbulent kinematic viscosity to kinematic viscosity is related to the Kármán constant as $\nu_t/\nu = dy^+/du^+ = \kappa y^+$. Recognising, as before, a conductive sublayer and a fully turbulent layer, Bejan (2004) describes the turbulent temperature profile as:

$$\Theta^+ = \begin{cases} Pr\, y^+ & \rightarrow \quad y^+ < y^+_{CSL} \\ Pr\, y^+_{CSL} + \frac{Pr_t}{\kappa} \ln \frac{y^+}{y^+_{CSL}} & \rightarrow \quad y^+ > y^+_{CSL} \end{cases} \tag{3.71}$$

A particular form of the dimensionless turbulent temperature profile of equation 3.71 ($y^+ > y^+_{CSL}$) is described by Bejan (2004) after Kays *et al* (2005), for fluids having $0.5 < Pr < 5$. This empirical equation results of considering: κ=0.41, $Pr_t \approx$0.9 and y_{CSL}=13.2; and it is expressed as follows:

$$\Theta^+ = 2.195 \ln\, y^+ + 13.2Pr - 5.66 \tag{3.72}$$

Equation 3.72, (Kays *et al* 2005), is the equivalent of equations 3.67 or 3.68, (Kader 1981), and they were obtained through experiments with controlled conditions for turbulent flows

with heat transfer over smooth surfaces. No information on whether the wall was uniformly heated (constant temperature) or the supply of heat flux was constant, is provided in the references. The analysis of turbulent heat transfer over rough surfaces will not be described, but obviously involves higher difficulties in giving predictions for temperature in the boundary layer.

Once Θ^+ has been explicitly calculated by using one of the above equations (3.67, 3.68 or 3.72), the calculation of the turbulent heat transfer from the wall to the fluid $q_{c_{turb}}$ is straightforward; solving equations 3.59 and 3.60 together for $q_{c_{turb}}$. The result can be written as:

$$q_{c_{turb}} = \frac{\Theta_w - \bar{\Theta}}{\Theta^+} \rho C_p u^* = h_{c_t}(\Theta_w - \Theta_\infty) \tag{3.73}$$

From equation 3.73, the value of h_{c_t} can be re-written as:

$$h_{c_t} = \frac{\rho C_p u^*}{\Theta^+} \cdot \frac{\Theta_w - \bar{\Theta}}{\Theta_w - \Theta_{nw}} \tag{3.74}$$

Where the subscript *nw* has replaced the symbol ∞. The reason of doing so is to cast equation 3.74 in terms of what is called *near wall temperature*. Defining the value of local h_{c_t} in this form is a common practice used in computational fluid dynamics solvers.

The understanding of equation 3.74 is as follows: Θ_w is a boundary condition in the system (e.g.: a prescribed temperature or derived from prescribed heat flux source in the wall). Θ^+ and $\bar{\Theta}$ are both evaluated at the same coordinate y, located at a certain distance δ away from the wall, usually somewhere inside the thermal turbulent boundary layer. The definition of the coordinate for evaluating Θ^+ and $\bar{\Theta}$ is of paramount importance, since $\bar{\Theta}$ defines the amount of heat flux being convected, the farther is the coordinate from the wall, the cooler $\bar{\Theta}$ will be, therefore the higher heat flux calculated (see equation 3.73). Besides, due to the derivation of equation 3.73, Θ^+ and $\bar{\Theta}$ can not be evaluated at different coordinates, since both of them result from the gradient term in equation 3.58.

The last term to define is Θ_{nw}. The possible values of Θ_{nw} selected will have an influence on the magnitude of the local h_{c_t} calculated by equation 3.74. Two scenarios are the most important:

$$\Theta_{nw} = \begin{cases} \overline{\Theta} & \rightarrow \quad y = \delta \\ \Theta_\infty & \rightarrow \quad y = \delta_{th} \end{cases} \tag{3.75}$$

The selection of either options will produce different results of h_{c_t} unless $\delta = \delta_{th}$, with which only the second option from equation 3.75 would had been selected. Depending upon the

above selection, two forms of equation 3.74 can be cast:

$$h_{c_t} = \begin{cases} \frac{\rho C_p u^*}{\Theta^+} & \rightarrow \quad y = \delta \\ \frac{\rho C_p u^*}{\Theta^+} \cdot \frac{\Theta_w - \bar{\Theta}}{\Theta_w - \Theta_\infty} & \rightarrow \quad y = \delta_{th} \end{cases} \tag{3.76}$$

Bearing in mind that an specific location δ can be selected for the calculation of Θ^+ and $\bar{\Theta}$, the following can be stated:

A first result from equation 3.76 comes from selecting $\Theta_{nw} = \bar{\Theta}$, which means that a precise distance δ away from the wall has been selected for the computation of the turbulent heat transfer coefficient (both Θ^+ and $\bar{\Theta}$ are calculated at that location). This yields a value of h_{c_t} which is referred to a *local* near wall temperature and not referred to the undisturbed flow temperature Θ_∞ in principle. The mathematical result of this case is just the ratio of the convected heat by the friction velocity divided by the dimensionless temperature Θ^+.

When $\Theta_{nw} = \Theta_\infty$ is selected (second option in equation 3.75), the value of h_{c_t} is lowered, since $\Theta_w - \Theta_\infty$ is larger than $\Theta_w - \bar{\Theta}$, provided δ had been selected below the edge of δ_{th}. This can be easily verified by seeing that $(\Theta_w - \bar{\Theta})/(\Theta_w - \Theta_\infty) < 1$.

In computational fluid dynamics solvers this selection posses a serious task to the modeller, since usually the width of δ_{th} is not known a priory and this changes dynamically over the length of the surfaces (it depends upon the geometry and the flow conditions). Ideally, the values of Θ^+ and $\bar{\Theta}$ would be calculated in the edge of the thermal boundary layer, that is at $y^+ > y^+_{CSL}$ [7], that would give a close fit between $\bar{\Theta}$ and Θ_∞, and therefore the calculated heat transfer coefficient would be very real (i.e.: the quantities $-\rho\, C_p(\alpha + \alpha_t)\frac{d\bar{\Theta}}{dy}$ and $h_{c_t}(\Theta_w - \Theta_\infty)$ in equation 3.55 would be equal). In practice however, CFD solvers like Ansys-CFX define δ for the calculation of Θ_{nw} equal to either the second grid node away from the surface or the undisturbed flow temperature Θ_∞ (an option left to the modeller); and Θ^+ and $\bar{\Theta}$ are calculated following the rule:

$$y^+ = \max(y^+_\delta, 11.06) \tag{3.77}$$

Where y^+_δ is calculated with equation 3.38, substituting $y = \delta$. Then, if δ is left at the second grid node, there is a likelihood that $\bar{\Theta}$ is cooler than Θ_{nw}, since it will be driven by equation 3.77, (therefore, Θ_{nw} will be hotter than Θ_∞) and then, the local h_{c_t} will be predicted only for a local near wall temperature, which can not be used for future analysis based on Θ_∞.

On the other hand, analising equation 3.76, is clear that the value of the turbulent heat transfer coefficient will depend upon the friction velocity u^*, that is, the shear stress on the wall; and upon the value of Θ^+ at the outer regions of the turbulent thermal boundary layer.

[7] y^+_{CSL} is equal to 13.2 according to Kays *et al* (2005), or $y^+_{CSL} \approx 9/Pr^{1/3}$ as per Kader (1981)

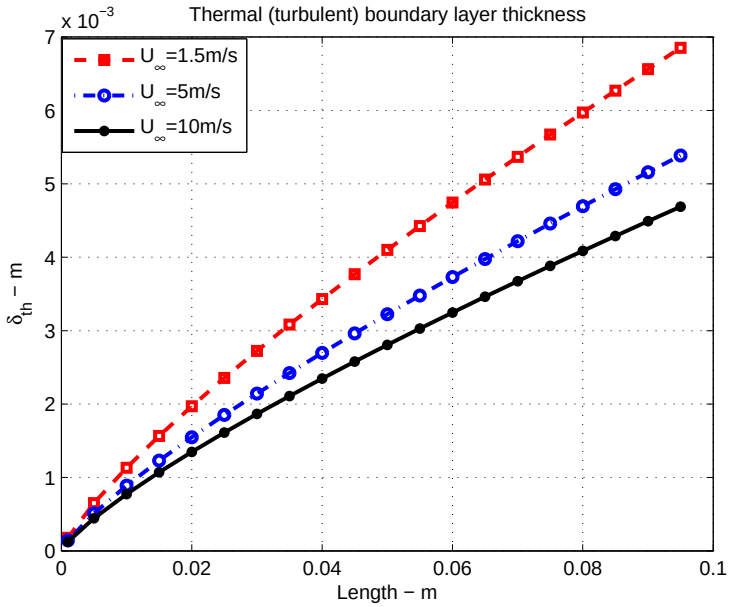

Figure 3.9: Thermal turbulent boundary layer thickness, from equations 3.52 and 3.45.

The effects of speed U_∞, and location of y^+ in Θ^+ and in the resulting turbulent heat transfer coefficient is revised next by performing a set of examples complementing the results shown in Figure 3.7.

The air properties for which the analyses were performed are shown in Table 3.2. The computations use wall shear stresses shown in Figures 3.4 and 3.5. From these, the friction velocity u^* along the plate can be retrieved using equation 3.37. The thickness of the velocity turbulent boundary layer (δ_u) is approximated using equation 3.45, and from equation 3.52, the thickness of the thermal turbulent boundary layer is predicted.

Figure 3.9 shows the profiles of the turbulent layer δ_{th}. The value of δ_{th} at the middle of the length reaches 3.7 mm for U_∞ =1.5m/s; and 2.9mm and 2.5mm for U_∞ =5m/s and 10m/s, respectively.

Friction velocity profiles, calculated as explained before, are shown in Figure 3.10. The highest u^* is produced for an air flowing speed of 10m/s, with an average value of u^*=0.64m/s. The behaviour of u^* falls almost linearly with speed and the averages for air speeds of 5m/s and 1.5m/s are u^*=0.35m/s and u^*=0.12m/s, respectively. The magnitude of u^* can be understood as index of the ability of air to 'rub' the surface and this is proportional to the main stream speed. The drop of u^* also indicates a loss of convective performance with length.

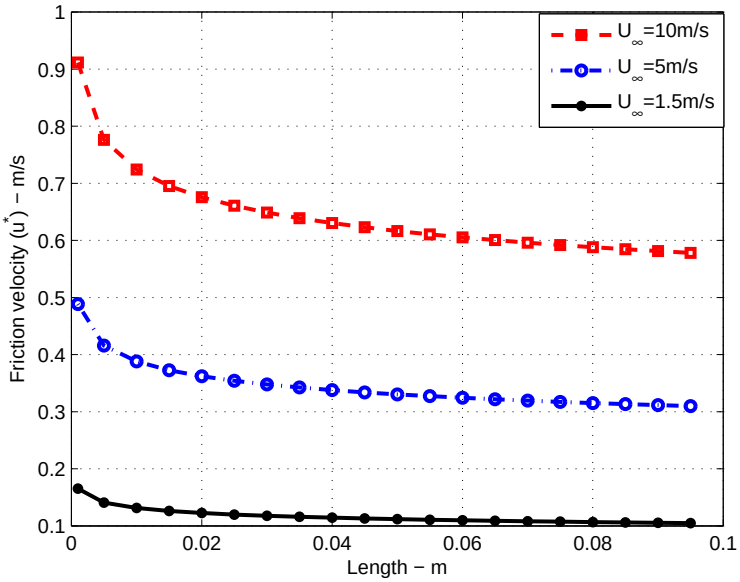

Figure 3.10: Friction velocity on plate wall using equations 3.37 and 3.46.

The profiles of y^+ are calculated using equation 3.38, where y has been substituted by δ_{th} just calculated (Figure 3.9). As displayed in Figure 3.11, the profiles depart from zero at the leading edge of the surface and, at x=0.04 m, reach values of y^+=90, 51 and 22, when the undisturbed speed U_∞ equals 10, 5 and 1.5m/s, respectively. These y^+'s are all above the recommended value of y^+_{CSL} given by Kader (1981), Kays *et al* (2005) and ANSYS-CFX Solver Theory (2005).

The above y^+ computed data and the Prandtl number in Table 3.2 have been used in formulas for prediction of Θ^+ given by Kader (1981), equation 3.68, and Kays *et al* (2005), equation 3.71. Due to the assumption of taking y^+ at the edge of δ_{th}, the ratio y/δ in equation 3.68 should be equal to one. The results are shown in Figure 3.12, where the dimensionless profiles predicted by the two equations are plotted for U_∞=10, 5 and 1.5m/s.

The profiles indicate that equation 3.72 given by Kays *et al* (2005), gives higher predictions than equation 3.68, (Kader 1981), for dimensionless temperature along the edge of the thermal turbulent boundary layer. Obtaining larger values of Θ^+ for similar conditions between the two equations, manifests a conservative estimates of convective heat transfer coefficients, which means low convective heat transfer dissipation. Comparing arithmetic means, at U_∞=10m/s Kays *et al*'s (2005) equation predicts a mean of Θ^+=12.5 while Kader's (1981) equation predicts Θ^+=10.0. At U_∞=5m/s, the former equation predicts an averaged Θ^+=11.4 against Θ^+=8.9 predicted by Kader's (1981) equation. At the lowest speed, 1.5m/s,

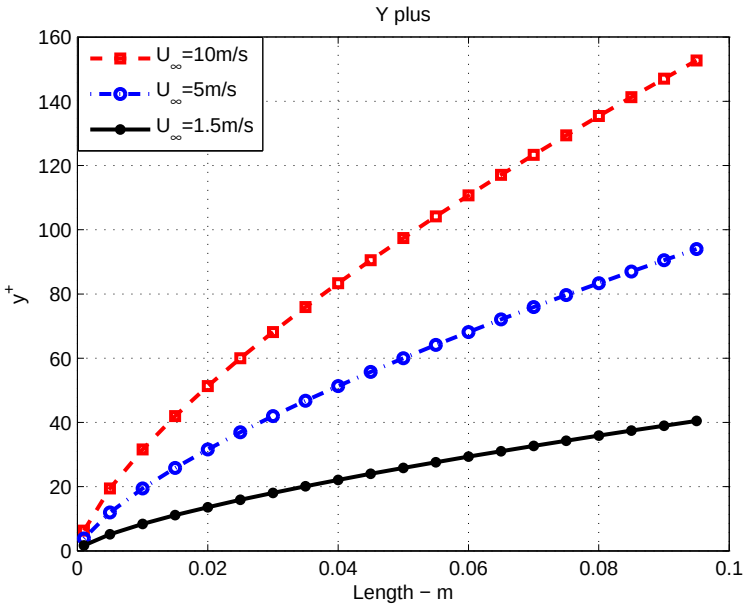

Figure 3.11: Y^+ calculated along the plate using $y = \delta_{th}$ in equation 3.38. Plate length=0.095m.

the mean of the predictions are Θ^+=9.6 (Kays *et al* 2005), versus Θ^+=6.8 from Kader (1981). In general, at high main stream speeds (U_∞=5 and 10m/s), Kays *et al*'s (2005) equation overpredicts by 20% the results from Kader's (1981). At the lowest speed, 1.5m/s, the difference is even larger, 30%.

Having calculated u^*, Θ^+, and considering that those were calculated over the edge of the thermal turbulent boundary layer, the equation 3.74 can be directly used to calculate the local turbulent heat transfer coefficients along the plate length. For this to be taken, the assumption on whether Θ_{nw} equals $\bar{\Theta}$ or Θ_∞ should be done. The two cases are revised here using Θ^+ calculated with Kader's (1981) and Kays *et al*'s (2005) relations.

First, the turbulent convected heat (term in the middle part of equation 3.73) is computed. For this, the thickness δ_{th}, Figure 3.9, calculated previously is used to evaluate the value of $\bar{\Theta}$, since this must be evaluated at the same coordinate as Θ^+. Lacking of means to accurately predict the mean temperature at this coordinate, the laminar temperature gradient given by equation 3.53 is used as follows:

$$\bar{\Theta} \approx [(y = \delta_{th}) - 0]\frac{d\Theta}{dy} + \Theta_w$$

The turbulent heat transfer coefficient are firstly calculated for $\Theta_{nw} = \bar{\Theta}$, followed for those

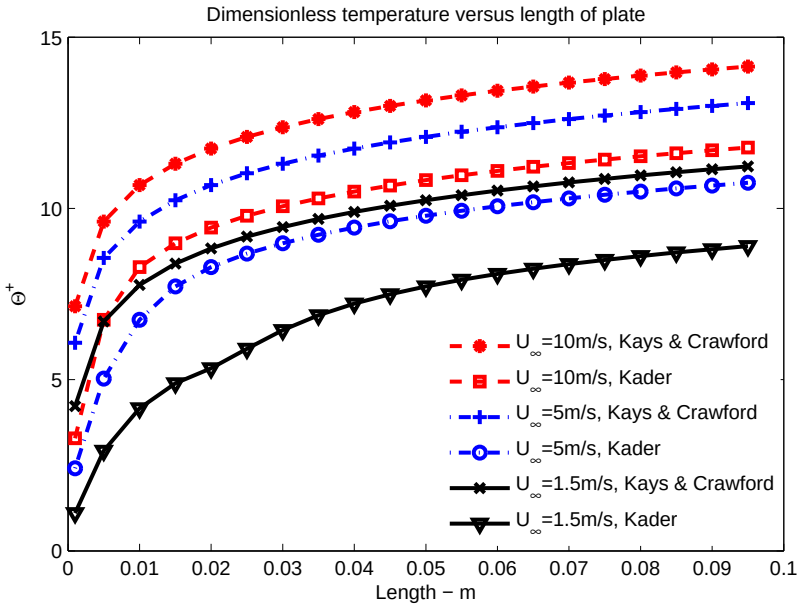

Figure 3.12: Θ^+ calculated along the plate using y^+ from Figure 3.11, and equations 3.68 and 3.72; Kader (1981) and Kays & Crawford (1980). Plate length=0.095m.

corresponding to $\Theta_{nw} = \Theta_\infty$. The results are shown in Figures 3.13 and 3.14. From the first figure, it is evident that using the near wall temperature assumption increases largely the heat transfer coefficients. Comparing means, at U_∞=10m/s Kader's (1981) predicts 78 W/m^{2}K against 58 W/m^{2}K (Kays *et al* 2005). At U_∞=5m/s, the means are 50 W/m^{2}K against 34.5 W/m^{2}K, respectively. And, at U_∞=1.5m/s, the means of the predictions are 26.5 W/m^{2}K against 14.3 W/m^{2}K, Kader (1981) versus Kays *et al* (2005). All of them, in general, predict very high values at the leading edge, falling rapidly in the first 20 % of the lenght towards a semi-stablished value.

When $\Theta_{nw} = \Theta_\infty$ is used as condition, the results are affected by the laminar temperature gradient used to calculate the temperature at the edge of the thermal boundary layer (see Figure 3.14). Obviously, this also affects to the former results, but it is more evident in this case. Since the thermal boundary layer thickness increases along the length, the prediction given by the laminar temperature gradient reduces the temperature as it proceeds on the edge of the boundary layer. This causes that larger convective heat transfer is calculated as x increases. This is more accented for higher speeds, since the temperature gradient is higher for these. Nevertheless, what it is important to notice is that the assumption of taking the near wall temperature as the undisturbed temperature of the air give somewhat smaller and stable heat transfer coefficients. Performing the evaluation of mean of heat

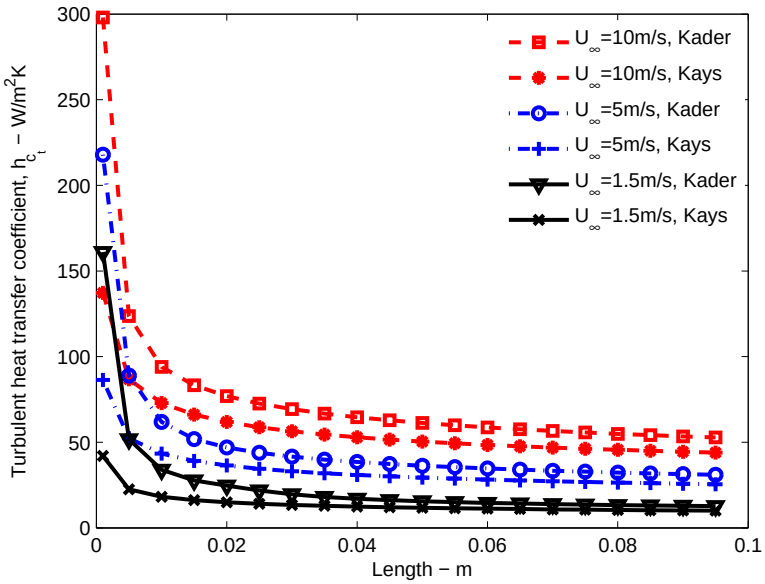

Figure 3.13: Turbulent heat transfer coefficients calculated along the plate using $\Theta_{nw} = \bar{\Theta}$, and equations 3.68 ($y/\delta = 1$), and 3.72; from Kader (1981) and Kays & Crawford (1980). Plate length=0.095m.

transfer coefficients again: At U_∞=10m/s Kader's (1981) predicts 51 W/m^{2}K against 40.5 W/m^{2}K (Kays *et al* 2005). At U_∞=5m/s, the means are 25.7 W/m^{2}K against 19.3 W/m^{2}K, respectively. And, at U_∞=1.5m/s, the means of the predictions are 8.6 W/m^{2}K against 5.4 W/m^{2}K, Kader (1981) versus Kays *et al* (2005).

The corresponding means of the heat transfer coefficient calculated under laminar conditions are: 42.6W/m^{2}K at U_∞=10m/s; 30W/m^{2}K at U_∞=5m/s; and 16.4W/m^{2}K at U_∞=1.5m/s. When comparing these against the above results, it can be seen that Kader's (1981) formula gives much larger mean values of heat transfer coefficient when $\Theta_{nw} = \bar{\Theta}$ than when $\Theta_{nw} = \Theta_\infty$.

Conversely, using Kays *et al*'s (2005) formula with $\Theta_{nw} = \Theta_\infty$ give values much lower than the laminar values at U_∞=1.5m/s and 5m/s, whilst with U_∞=10m/s the turbulent mean value predicted is similar to the corresponding laminar mean. When using $\Theta_{nw} = \bar{\Theta}$, the fit between mean values of laminar and turbulent heat transfer coefficient is closer.

As conclusive remarks, it should be said that the above (turbulent) heat transfer coefficient results should be cautiously considered, since they were calculated using *coarse* assumptions, a more formal behaviour can be obtained by modelling the cases in a dedicated software such as the one that will be used in the research of the thesis. The final judgment on whether Θ_{nw}

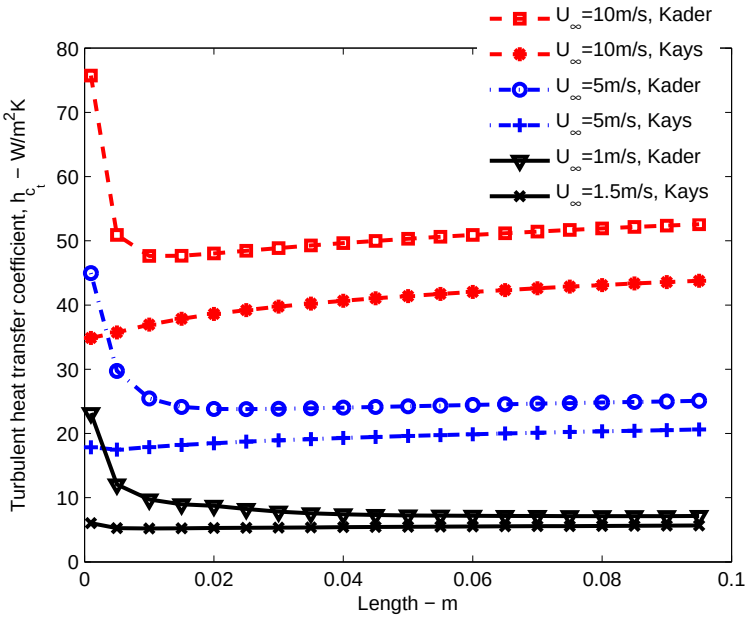

Figure 3.14: Turbulent heat transfer coefficients calculated along the plate using $\Theta_{nw} = \Theta_{\infty}$, and equations 3.68 ($y/\delta = 1$), and 3.72; from Kader (1981) and Kays & Crawford (1980). Plate length=0.095m.

is taken as the undisturbed temperature of air or as a calculated value by the software itself, should be assessed by evaluating numerical results of a particular brake disc case simulation against experimental results obtained from tests replicating the same conditions.

When air around solid rotating discs is considered, the thickness of the velocity and thermal boundary layers over the circular faces need to be redefined. A relation for the thickness of the velocity boundary layer is given by Dorfman (1963), as:

$$\delta_{\omega} = 3.5\sqrt{\frac{\nu}{\omega}} \tag{3.78}$$

The prediction of the thickness of the boundary layers in rotating semi-closed geometries (e.g.: channels), is more difficult. If the channel is sufficiently long, the flow can be assumed as developed and the classical solutions for flows in pipes may give an approximation of the behaviour inside the channel. Nevertheless, the channels of a brake disc have short length compared with their height. As an example, for a commercial vehicle brake disc the relation l_v/h oscillates around 6. Therefore, equation 3.78 can be used for a first guess of the order of the velocity boundary layer thickness over the circular faces. If the absolute radial velocity order within the channels is known before the simulation or a prediction

can be done, then equations 3.32, 3.45, and 3.52 can provide rough approximates to the thickness of the boundary layers inside the channel. Using these results, a first approach to the grid definition near the brake disc surfaces can be done during the construction of the computational model.

Natural Convection Modelling

As explained in page 45, the physics of the convective buoyant flow near a ventilated brake disc is very complex, more perhaps, than that given by the forced convection case (when the disc rotates). The limited size of the brake disc, plus the ventilation region layout may lead to significant variation of heat transfer coefficients over the brake disc surface during natural convection.

A way to estimate the relative importance of the buoyant forces due to temperature variation is by calculating the ratio between two parameters, the Grashof number and the square of the rotation Reynolds number (page 47). The Grashof number is defined as:

$$Gr_{R_o} = \frac{g\beta R_o^3(\Theta_w - \Theta_\infty)}{\nu^2} \tag{3.79}$$

Where β is the air thermal expansion coefficient. The force driving the flow in natural convection is represented by $g\beta R_o^3(\Theta_w - \Theta_\infty)$, and the velocity scale is proportional to $\sqrt{g\beta(\Theta_w - \Theta_\infty)R_o}$. The ratio defining the importance of natural convection is given as:

$$BI = \frac{Gr_{R_o}}{Re_\omega^2} = \frac{g\beta(\Theta_w - \Theta_\infty)}{\omega^2 R_o} \tag{3.80}$$

When the buoyancy index BI is near or above unity, then the effects of buoyant forces are likely to be important in the fluid. When $BI << 1.0$ then inertia forces in the fluid are larger than the forces caused by density changes and buoyancy is not relevant in the analysis.

Unlike forced convection where temperature difference does not represent an important parameter, in buoyant flows temperature difference does play a significant role, since the larger this is the greater are the changes of density in the air near the wall. Initially, buoyant flows are laminar-like, however, large changes in density bring higher activity (kinetic energy) of the flow; and, when this is combined with rough surfaces or geometrical discontinuities, then turbulent buoyant flows may set in.

The strength of natural convection in flows is ranked by the Rayleigh number (Ra), this is defined as:

$$Ra = Gr_{R_o} Pr \tag{3.81}$$

Laminar flow regimes in buoyant flows are given within a range of $Ra < 1 \times 10^8$, and $Ra > 1 \times 10^{10}$ for turbulent buoyant flows, Kreith & Bohn (2001). The gap between these ranges represents transition from laminar turbulent buoyant flows.

The numerical modelling of buoyant flows is performed by adding a momentum source in the Navier Stokes equation (3.5), this source is equal to:

$$S_M = (\rho - \rho_{ref})\, g \tag{3.82}$$

Where ρ_{ref} is an specified reference density for the domain and ρ is calculated following the ideal gas law for air, described in page 37, ANSYS-CFX Solver Theory (2005). When performing buoyancy simulations, the pressure calculated in the momentum equations is related to the absolute pressure in the following form:

$$p_{abs} = p + p_{ref} + \rho_{ref} g(\xi - \xi_{ref}) \tag{3.83}$$

In this way the pressure p excludes the hydrostatic pressure $\rho_{ref} g(\xi - \xi_{ref})$ in the domain. In the above equation p_{ref} is a reference level of pressure for the domain and ξ_{ref} is a reference datum selected against which the hydrostatic pressure is calculated.

3.1.5 Evaluation of Rotational Effects

The rotational Reynolds number equation 3.31 and the buoyancy index equation 3.80 are not the only ways of evaluating at first instance the effects brought by rotation in geometries. An additional way of quantifying those in rotating semi-closed geometries, such as channels of a brake disc, is described by Greitzer *et al* (2003).

Greitzer *et al*'s (2003) analysis of equation 3.8, points to two dimensionless numbers: the Rossby number and the Ekman number. These are defined as:

$$\mathbf{R}_o = \frac{(u_{rel})_{ref}}{\omega R_m} \tag{3.84}$$

$$\mathbf{Ek} = \frac{\nu}{\omega R_m^2} \tag{3.85}$$

Table 3.3: Data for Rossby number calculation

Brake disc	Discs data		
	R_o, $[m]$	R_m, $[m]$	l_{ch}, $[m]$
Commercial vehicle standard disc	0.217	0.165	0.102
Automotive standard disc	0.145	0.118	0.055
Railway wheel mounted disc	0.280	0.230	0.100

The Rossby and Ekman numbers are dimensionless parameters commonly used in the analysis of fluid dynamics of rotating channels. In brake discs, rotational effects like these arise as a consequence of the centrifugal and Coriolis accerelerations inside the ventilation region.

The Rossby number indicates the significance of rotational effects on the fluid, and it is equal to the relative speed scale through the ventilation region (rotating frame) divided by the tangential speed at a point of analysis, (rotating frame inertia to Coriolis forces). A small $\mathbf{R}_o$ indicates important rotational effects in the dynamics of the flow that can not be neglected. Usually for this to happen, $\mathbf{R}_o$ must oscillate around one; much larger values would mean that rotating effects are not relevant. Ekman number gives a measure of the viscous effects in the fluid, particularly when this is enclosed inside rotating walls. If **Ek** is large, then viscous effects are likely to be felt throughout the fluid (that is, everywhere among the walls), while small Ekman number reveals the presence of thin viscous layers in the fluid.

The application of the above expressions for rotating geometries is carried out next using brake disc data. The numerical value of $\mathbf{R}_o$ for brake discs, depends upon the ventilation region design; but it is unlikely that it reaches above 2. The ratio of the average relative radial speed through the channel to the tangential speed of the disc at channel mean length is around 0.12 (that is $\frac{u_{rel}}{\omega}$=0.12m), taking this ratio as a reference, Rossby numbers are calculated using three ventilated brake discs data with different dimensions: the baseline commercial vehicle (CV) brake disc, a smaller automobile standard brake disc Wallis *et al* (2002) and a railway wheel mounted brake disc (WMD), Tirović & Galindo-López[b] (2006). The Table 3.3 shows the relevant dimensions for the analyses.

By varying the ratio $\frac{u_{rel}}{\omega}$ about the reference value (0.12m), it was possible to compute Rossby numbers for 2 more scenarios: One in which the relative radial speed drops by 60% from the reference, and another in which the relative radial speed (u_{rel} is %66 larger). The ratios $\frac{u_{rel}}{\omega}$ and their respective Rossby numbers are shown in Table 3.4.

From Table 3.4, it is clear that as the mean swept radius increases, the rotational effects inside the ventilation channel will be higher (less inertia of the fluid and larger Coriolis effect). The smallest disc, Wallis *et al* (2002), has the lowest rotational effects in the internal flow.

Table 3.4: Rossby numbers using data in 3.3, n=100rpm

Brake disc	Rossby numbers, (equation 3.84)		
	$\frac{u_{rel}}{\omega}$=0.05m	$\frac{u_{rel}}{\omega}$=*0.12*m	$\frac{u_{rel}}{\omega}$=0.20m
Commercial vehicle standard disc	0.30	0.72	1.20
Automotive standard disc	0.42	1.00	1.77
Railway wheel mounted disc	0.22	0.52	0.36

Table 3.5: Buoyant conditions in brake discs in Table 3.3,Θ_w=100^{o}C, Θ_∞=20^{o}C, ω=10.47rad/s

Brake disc	Gr_{R_o}	BI	Ra
Commercial vehicle standard disc	7.6×10^7	9.9×10^{-2}	5.3×10^7
Automotive standard disc	2.3×10^7	1.5×10^{-1}	1.6×10^7
Railway wheel mounted disc	1.6×10^8	7.7×10^{-2}	1.2×10^8

Nevertheless, apart from one case in which $\mathbf{R}_o$=1.77, the remaining Rossby numbers are near or smaller than one. As a conclusion, characteristics of rotating channels such as secondary flow, in planes perpendicular to main flow direction (radial), will exist in the channels of these disc even low speeds (100 rpm). Secondary flows enhance mixing in the main stream, giving path to transition to turbulence.

A similar analysis can be done to investigate whether or not buoyancy is important at low speeds of rotation (e.g: n=100rpm). The discs characteristics are the same as in Table 3.3 and the temperature of the disc and ambient air are assumed to be 100^{o}C and 20^{o}C, respectively. The air thermal expansion coefficient at the mean temperature between the above (60^{o}C), is given in Table 3.2. The gravity acceleration magnitude is 9.81 m/s^2. The Grashof number based on the disc outer radius, the buoyancy index and the Rayleigh number are calculated and shown in Table 3.5. Since the outer radius is considered in the calculations, then it is assumed that the disc remains in vertical position.

Table 3.5 indicates that for n=100rpm the BI's of the brake discs are much smaller than one, which means that buoyancy does not qualitatively influence the convective cooling at this speed. On the other hand, if the data appearing in the fourth column of Table 3.5 is analysed isolated from the rest (that is, if the brake discs are stationary), then it can be noticed that the Rayleigh number of the railway wheel mounted disc is in transition from laminar to turbulence, while natural convection would occur at laminar conditions in the other two discs.

If the disc temperature is considered as high as 600^{o}C (β=0.00175, Pr=0.7 at 300^{o}C),

Table 3.6: Buoyant conditions in brake discs, Θ_w=600^{o}C, Θ_∞=20^{o}C, ω=10.47rad/s.

Brake disc	Gr_{R_o}	BI	Ra
Commercial vehicle standard disc	5.53×10^8	7.17×10^{-1}	3.87×10^8
Automotive standard disc	1.65×10^8	1.07	1.16×10^8
Railway wheel mounted disc	1.19×10^9	5.56×10^{-1}	8.32×10^8

and the ambient and rotating speed remain the same (Table 3.6), then natural convection influences the CV and the automobile brake discs when they rotate at 100 rpm, since their buoyancy indexes are near to one, while the WMD is still within forced convection. If this scenario is considered in static conditions, then the three discs dissipate heat due to natural convection within the transition regime between laminar and turbulent conditions, although the strength of laminar heat dissipation can be still considered for the smallest (automobile) brake disc.

Finally, rotational Reynolds numbers are calculated for the above discs. The Re_ω value is calculated as per equation 3.31, using air properties from Table 3.2. The Re_ω assumes that none of the discs is ventilated and considers only their ability to induce laminar or turbulent flow only due to its outer radius. The disc surfaces are also considered smooth.

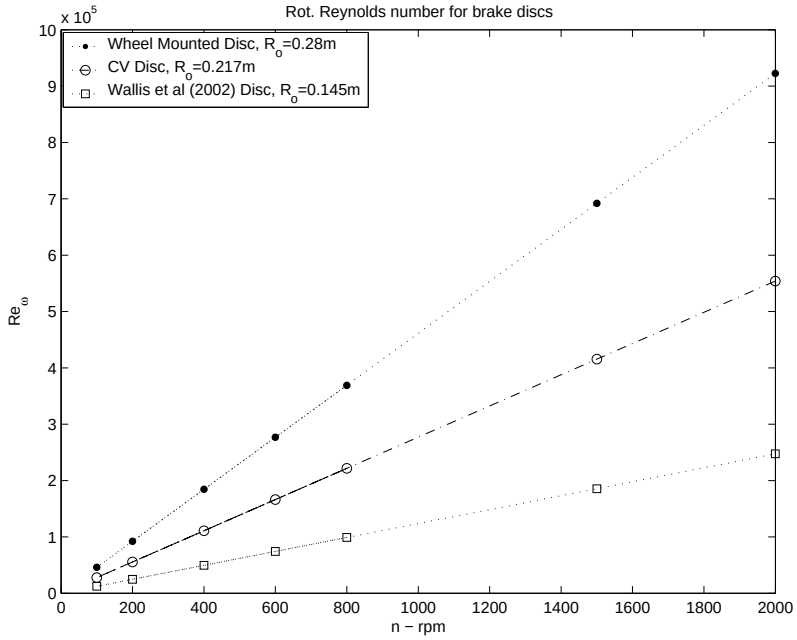

Figure 3.15: Rotational Reynolds number for three typical brake discs.

Figure 3.15 shows huge differences in Re_ω of the discs. Strictly considering that turbulence flow sets in at $Re_\omega > 2.4\times10^5$ for solid (non-vented), smooth discs, then the railway wheel mounted disc induces turbulent flow as of 600 rpm, while the commercial vehicle brake disc gets into turbulence at approximately 800 rpm. The smallest disc (Wallis *et al* 2002), needs to spin up to 2000 rpm in order to induce turbulent flow around its circular faces. Considerations to account for in the planning of a CFD mesh for convective heat dissipation of brake disc result from above analysis:

1. Secondary flows inside the ventilation region as a result of Coriolis forces will appear even at low speeds (see Table 3.4). The circulation of flow in planes perpendicular to main stream direction causes momentum mixing (and possibly turbulence due to shear layers). Also, if the ventilation region is composed by channels whose surface is hotter than the incoming air temperature, a skewed (asymmetric) air temperature pattern will form in those planes.

2. Buoyancy (natural convection) effects at low angular speeds (100rpm), can become important only for discs having small outer radius (e.g.:Wallis *et al*'s (2002) disc, R_o=0.145m). At stationary conditions (zero angular speed), natural convection induced flow near the disc surface can get into transition regime (laminar-turbulent) only for big discs (e.g.: railway wheel mounted disc, R_o=0.280m). High temperature difference between the brake disc surface and the nearby air will also induce transition to turbulence in small discs.

3. If only the outer radius of the disc is considered, or if a particular interest on the flow regime condition around the friction faces exists (disregarded of the effects of channels or disc edge); then turbulence will set off at n >200rpm for discs with R_o=0.560m, at n >800rpm for discs with R_o=0.217m, and at n >2000rpm for discs with R_o=0.145m (Figure 3.15).

4. Care should given to grid definition near the wall (particularly inside the ventilation region) in order to accurately model the temperature gradient necessary for convective heat transfer calculation (e.g.: see pages 56 and 62). Ideally, for turbulent convective heat transfer prediction, a first approximation of the expected boundary layer thickness should be carried out using equations given previously, then, a target y^+ should be selected along the surfaces, and the corresponding y normal coordinate retrieved. Finally, it would be ideal to accurately mesh the region between the surface and the calculated y, so that the near wall temperature assumption can be safely used. This process would need to be repeated for every angular speed.

5. The reference temperature selected for the evaluation of the convective heat transfer coefficients will have an effect on its value. If local near wall temperatures are selected,

convective heat transfer coefficients will be evaluated in a *near wall temperature* basis, which will depend upon the grid quality, the surface irregularities and eventually on the software philosophy. Besides, these heat transfer coefficients could not be used for further analysis (e.g. thermal stress prediction), unless they are referred to their local temperature with which they were calculated. Conversely, if undisturbed air temperature (Θ_∞, outside thermal boundary layer) is chosen, then the convective heat transfer coefficients calculation will be homogeneously referred this temperature; nevertheless, convective heat transferred from the wall will depend upon the grid quality near the wall and in turbulent conditions upon the near wall temperature model.

3.1.6 CFD Model and Grid Definition, BC's and Solution Parameters

The former section gave preliminary recommendations to follow during the planning of a computational fluid dynamics brake disc model solution for the evaluation of convective heat transfer dissipation. This section will complement the guidelines by revising the CFD domain dimensions, setting of boundary conditions, and the definition pseudo-transient time steps. The numerical error assessment and grid independence of results will be shown in Chapter 5.

The brake disc CFD model is constructed departing from a CAD model of the volume surrounding the disc. The CFD domain extends around the brake disc surface following a circular volume. Originally this domain could be converted into a CFD model (see Figure 3.16), however the resulting model would have a large computational size, which would require enormous hardware capabilities, despite using the Rotating Frame technique to simplify the physics of the solution (see page 36). Then, what is done aiming to optimise hardware resources is to construct a CFD brake disc model using only one circumferentially periodical sector of the geometry . This results in an efficient usage of computational hardware resources by having a model with the smallest feasible dimensions. The CFD brake disc model is then bounded by two periodic faces (PF_1 and PF_2) and four bounding faces: one circular at the outermost radius, two more parallel to the friction faces and the last one being the surface of the shaft to which the disc is attached.

The orientation of the CFD model is as follows: the disc and attached geometry rotate about the $+z$ axis (axial direction) with an angular speed ω. The outboard face of the disc hub is aligned with the zero z coordinate, then the body of the disc lies in the negative side of z. The plane of the friction discs faces (and also of the ventilation region) is perpendicular to the axial direction. When rotating, the ventilation region soaks air from the innermost radius and expels it with positive radial direction.

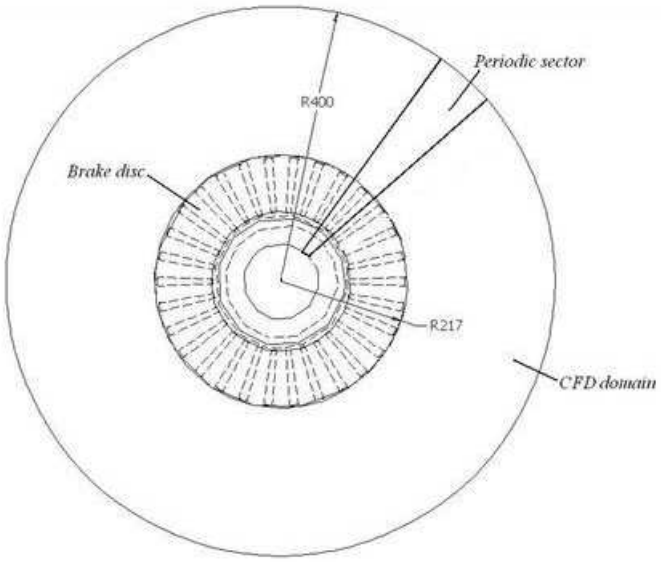

Figure 3.16: Full computational domain and the smallest periodic sector.

The CFD periodic model is mainly composed by the brake disc surfaces, the hub of which is attached to a shaft with length extending along the domain axial length. The air domain radial length (R_d) is 2.1 times bigger than the disc outer radius (R_o), and its axial length (z_d) is 3.5 times that of the axial *height* of the brake disc (z_{disc}) The distribution of the CFD domain and the description of its dimension is shown in Figure 3.17. Note that Figure 3.17 depicts a *double* periodic sector of the brake disc air domain, that is, it covers two channel-vane arrangements instead of only one as shown in Figure 3.16. This philosophy was adopted throughout the research, the reason is that it allows to cross check flow patterns of the 'central' channel with the halves next to the periodic faces.

For the discretisation of the domain into finite cells, the following was taken into account: high *relative* speed and temperature gradients are likely to appear inside the ventilation region, at its inlet and outlet, near the friction surfaces and near the outer and inner disc rings. Therefore, finer mesh size was required in those regions to capture these effects. Besides, further refined mesh was chosen near the brake disc surfaces in order to accurately model speed and temperature gradients near the wall (boundary layer). The final grid spacing near the wall was selected through a convergence analysis carried in the baseline standard brake disc model, (explained in Chapter 5). The mesh sizes adopted in the models researched are shown in Table 3.7. The CFD boundary conditions specified are described in Figure 3.18 and below.

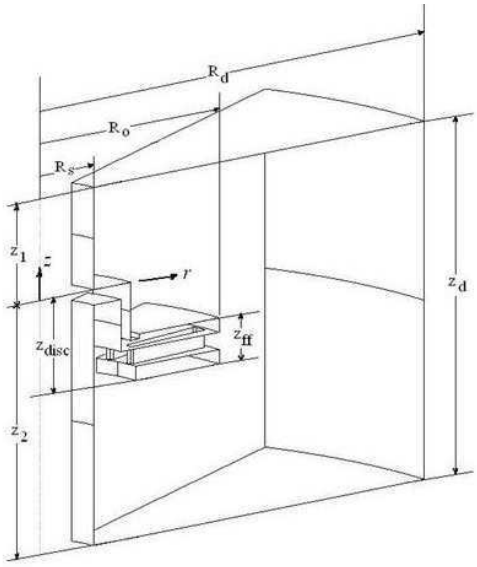

Figure 3.17: CFD model bounding dimensions using double periodic sector.

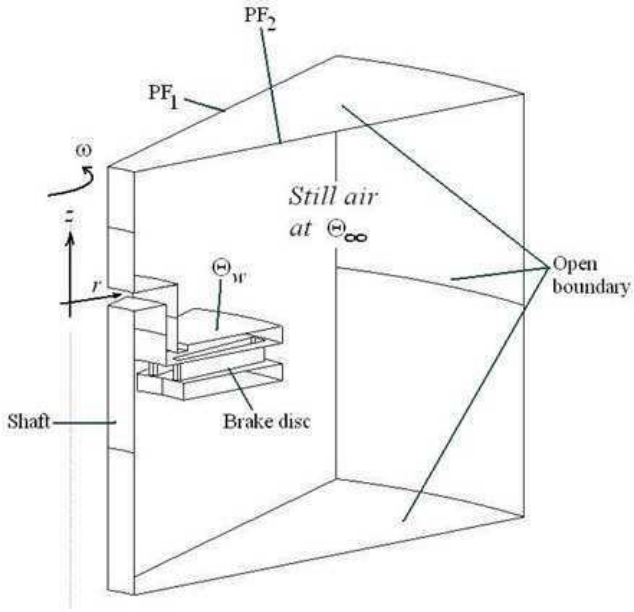

Figure 3.18: Typical CFD model of a ventilated brake disc, considering two channels.

Table 3.7: Mesh sizes used in the CFD models

Inside vents	Up to 30 mm away from walls	Boundary layers	Rest
1.5mm	2.5-3mm	0.1mm @ 1.2 growth ratio	4-8mm

1. Non-slip condition of velocity on all physical walls (shaft and brake disc surfaces), the fluid particle cannot go through the wall, $\mathbf{n} \cdot [\mathbf{U}_w - \mathbf{U}] = 0$, or $\mathbf{U} = \mathbf{U}_w$; where $\mathbf{n}$ is a vector normal to the surface.

2. Uniform temperature on all brake disc surfaces, $\Theta = \Theta_w = 100^o$C at the brake surface.

3. Adiabatic shaft surface, $\frac{\partial \Theta}{\partial \mathbf{n}} = 0$, at the shaft surface.

4. Periodic boundary conditions on periodic faces, $\phi_{PF_1} = \phi_{PF_2}$, where ϕ is any fluid property at the periodic face.

5. *Open* boundaries on the surfaces bounding the domain (other than the brake disc and shaft surfaces). Therefore, there are three surfaces having this kind of boundary, two in the axial ends and one in the radial end. An open boundary allows flow out of and into the domain. Nevertheless, it should be specified if the open boundary moves or not, in this case the open boundary is stationary. In adittion, a relative pressure, static temperature and, in the case of turbulence modelling, turbulence intensity should be specified for the open boundary. These would be the characteristics of the airflow entering the domain if the conditions are met.

Besides the above model boundary conditions, an initial guessed vector field should be supplied at the start of the solution process. The necessity of this is because, despite being a steady state problem, the fluid equations are solved in a pseudo-transient fashion, as described in Wendt (1995). The pseudo-time step used during the solution process is the timescale of the CFD model domain. For the calculation of the timescale ($\Delta\tau$), the length and velocity scales of the domain (Δl and Δu, respectively), should be calculated first. Following ANSYS-CFX Solver Theory (2005), their calculation is as follows:

$$\Delta l = \begin{cases} min(l_{vol}, l_{ext}) & \rightarrow \text{ conservative approach} \\ max(l_{vol}, l_{ext}) & \rightarrow \text{ aggressive approach} \\ l_{spec} & \rightarrow \text{ user defined} \end{cases} \tag{3.86}$$

Where:

$$l_{vol} = \sqrt[3]{V_{domain}}$$

and

$$l_{ext} = max(l_{axial}, l_{radial}, l_\theta)$$

and l_{spec} is a specified dimension. The velocity scale is calculated as:

$$\Delta u = \begin{cases} u_{\Delta p} = \sqrt{\frac{p_{bc_{max}} - p_{bc_{min}}}{\rho}} \\ u_{bc} = max(u_{bc}) \approx R_o \cdot \omega \end{cases} \tag{3.87}$$

Where $u_{\Delta p}$ is meaningful only if there are pressure boundary conditions. Finally, the timescale is calculated as follows:

$$\Delta\tau = min(\Delta\tau_u, \Delta\tau_{u_{\Delta p}}, \Delta\tau_{rot}) \tag{3.88}$$

Where:

$$\Delta\tau_u = 0.3\frac{\Delta l}{u_{bc}}, \qquad \Delta\tau_{u_{\Delta p}} = 0.3\frac{\Delta l}{u_{\Delta p}}, \qquad \Delta\tau_{rot} = \frac{0.1}{\omega} \tag{3.89}$$

If the formula 3.88 is used for the time steps controlling the CFD simulations of the brake discs in Table 3.3, rotating at angular speeds shown in Figure 3.15, it can be proved that the last condition of equation 3.88 is met and the required time steps are easy to calculate (i.e.: $\Delta\tau = \Delta\tau_{rot}$).

Chapter 4

Experimental Approach

Experiments were conducted to validate computational work and to compare heat dissipation performance. In general, the components used in a brake cooling test were a ventilated brake disc, spin rig (Section 4.3), sensors (thermocouples, speed and torque transducer, hot wire anemometer), data logger and digital computer. The tests performed are listed in a Brake Disc Test Program, see Appendix A. Due to the nature of the research, redesigning of the ventilation section of a standard ventilated brake disc was required. As pointed out before (Section 3.1), numerical modelling (CFD) was of significant help in the design and research process, since it enabled appropriate selection of geometries for manufacturing and testing. Nevertheless, since the original brake disc is a cast iron one-piece component, ideally each of the new redesigned geometries would require a brake disc with similar characteristics (cast in one piece). This situation was financially unfeasible for the project and therefore a new cost effective manufacturing method was developed for brake disc prototypes. The tests were conducted for a range of angular speeds, and the raw data sets acquired were:

- Transient (cooling) temperature measurements,
- Torque and angular speed measurements, and
- Air behaviour near the outer radius.

Since measurements from instrumentation used in simulation tests carry intrinsically acquisition errors, it was convenient to estimate the *measurement error* through the uncertainty of data. In this manner, the overall uncertainty resulting from equipment used in the tests was calculated by performing basic uncertainty analysis over each set of data (Moffat 1988).

4.1 Brake Discs

4.1.1 Standard CV Brake Disc

The main element of the experimental research was the brake disc itself. As mentioned before, the baseline brake disc model used was a cast iron commercial vehicle (CV) ventilated brake disc with 30 radial trapezoidal vanes (Figure 4.1). The disc is a one-piece cast component and the roughness of its surfaces, particularly inside the ventilation channels is significant. The total 'height' of the brake disc is 97 mm, 48 mm belong to the friction discs and ventilation region. The thickness of the friction discs is 14 mm and the *height* of the ventilation region is 17 mm. Therefore the height of the hub is 52 mm. The outer (nominal) radius of the disc is 434 mm and the inner radius of the *flying* ring is 232mm. The available ventilation radial length is 101 mm. The vanes are 95mm long and 17mm in height, and they are located 2mm (radially) away of the inner circumference of the flying friction disc, then there is a gap of 4 mm between the trailing edge of the vanes and the disc outer circumference (see Figure 4.2). The vanes are tapered off following an angle of 4^o, while the channel itself has a taper angle of 8^o. There are 30 periodic segments of 12^o each, containing a channel and a vane as above indicated. These characteristics make this disc suitable for experiments, since it channel size (length) allows assessment of effects on heat dissipation due to design changes.

Figure 4.1: Cast iron standard brake disc.

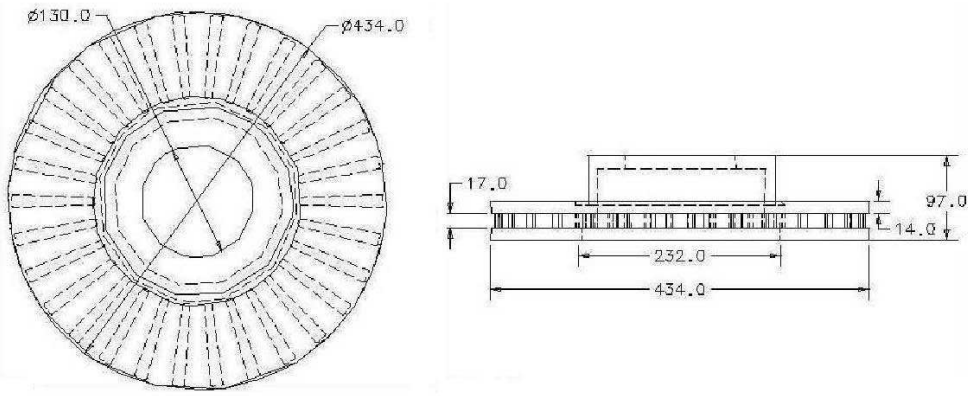

Figure 4.2: General dimensions in mm of the ventilated brake disc used for experiments.

4.2 New Disc Prototypes

New disc prototypes were manufactured following a *detachable vane brake* (DVB) disc philosophy, this allowed production of new designs within budget. The detachable vane brake disc consists of three main parts:

- Upper brake disc section: hat section plus outboard friction ring.
- Lower brake disc section: inboard friction flying ring, and
- Vanes manufactured of aluminum alloy 6082 T651(HE30) to BS1470,1987.

The three parts are bolted together by means of two circular rows of stainless steel M6 DIN7991 countersunk screws, which cross from the friction face of the inboard side ring, through the vanes and up to 6 mm inside the outboard friction ring, see Figure 4.3. Additionally, three dowls were placed through vanes equally spaced in order to center and reinforce the assembly during the tests.

By bolting the parts in that fashion, the outboard friction surface remains intact allowing rubbing thermocouples to be placed in any radius. As for the inboard friction surface, since the bolts have tapered head, the holes drilled through the inboard friction disc had these shape also, then the head of the bolts was aligned with the inboard friction surface. Obviously, thermocouples could not be placed on the circumferential path of the bolts head, but there was available space between the rows of bolts to locate two thermocouple shoes.

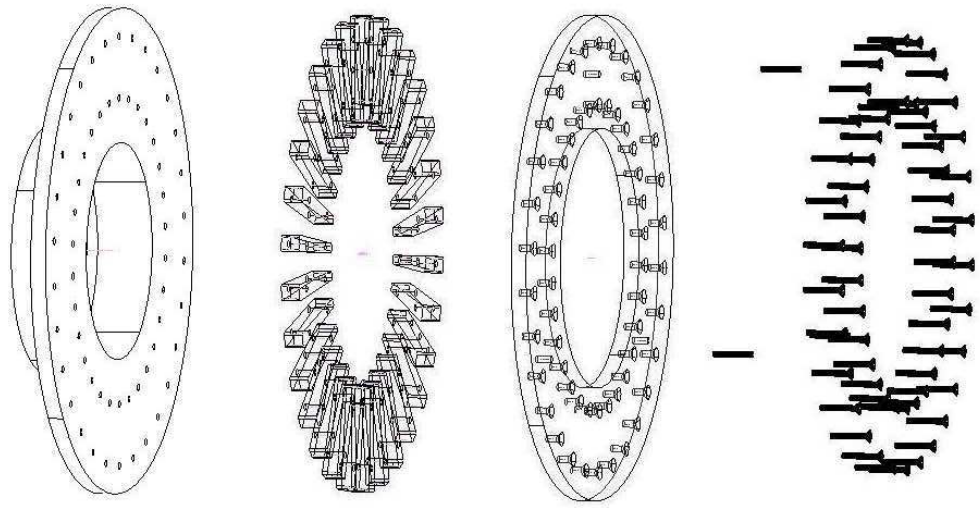

Figure 4.3: Detachable Vane Brake Disc. Left to right: Outboard side disc, vanes, inboard side disc, dowls and bolts.

The steps to manufacture a DVB disc were:

1. Slice a ventilated cast iron brake disc through the middle of the vane height.
2. Remove the remaining material of vanes and skim (flatten) the underlying surface, and
3. Machine aluminum vanes with identical geometrical characteristics to the originals.
4. Create location drills in rings and vanes for bolts or screws for assembly

Several characteristics can be qualitatively compared between a cast (one-piece) brake disc and a DVB disc, as shown in Table 4.1:

From Table 4.1, the best characteristics of the DVB disc are its low cost and versatility, since several configurations and vane shapes can be used with one set of upper and lower friction discs, therefore more than one design can be tested.

Good matching was sought at the vane-disc interface by ensuring appropriate bolt tightening amongst the parts. Also, to help reducing thermal discontinuities, thermal paste was employed. Nevertheless, thermal contact resistance of the matching surfaces is sensible to vane finish (bulk dimensions and surface characteristics) and to vibrations during disc rotation. Small variations in the vane dimensions (mainly height) may cause gaps which affects temperature distribution and induce spurious cooling due to vibration when the disc rotates.

Table 4.1: Advantages and disadvantages of the DVB disc

DVB disc	Cast Iron Disc
Relatively inexpensive	Expensive
Versatile (*many designs in one*)	One disc per design
Internal roughness is lost	Most original features kept
Risk of thermal contact resistance in joints	Not existing problem
Dissimilar materials in one disc	Homogeneous material

4.3 Spin Rig

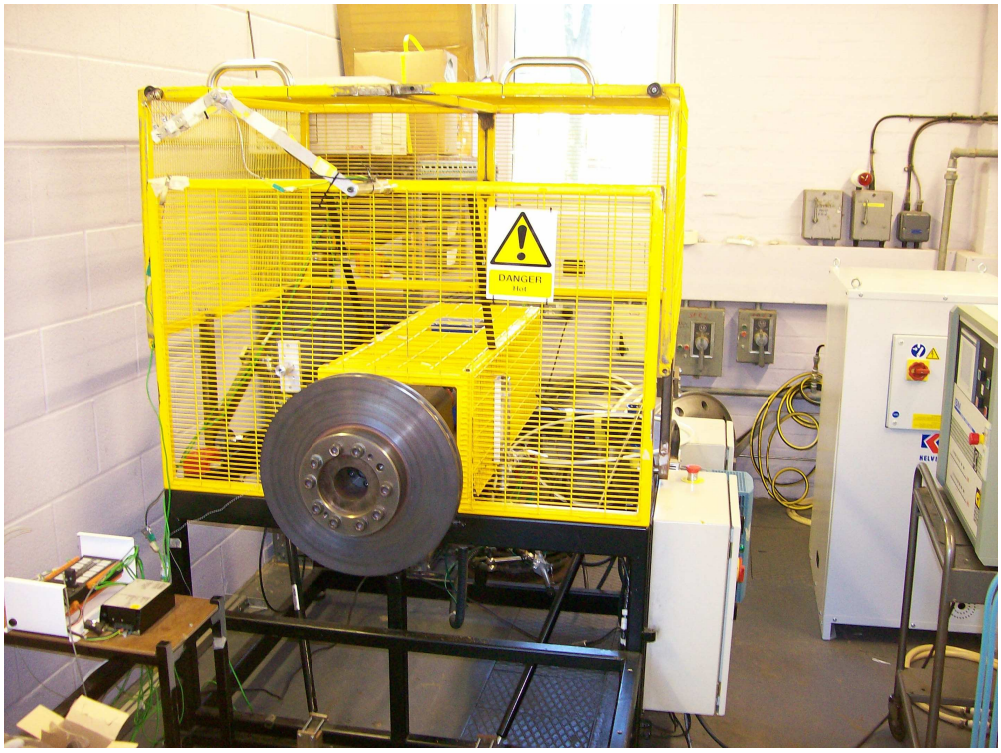

Figure 4.4: Brake disc cooling test apparatus (Spin Rig).

Cooling tests were conducted with a specialised brake disc testing apparatus (Spin Rig, as seen in Figure 4.4). The components of the Spin Rig are a 7.5 kW 3 phase Marelli electric motor which drives a steel shaft up to 2000 rpm. The speed and torque can be recorded by means of a 50Nm IML TRNA/0806 torque and speed sensor, which is located between the electric motor and a 2 bearing housing compartment, supporting the shaft end. A two-piece brake disc adapter is bolted to the shaft end. An insulator (bakelite) plate between

the two adapters avoids having heat conduction losses to the shaft and eventually to the bearing compartment. Increasing the bearing housing temperature would lead to loose of lubrication effectiveness and eventual damage. The angular speed of the motor is controlled by an Eurotherm inverter.

4.4 Disc Heating: Heating Box

In the first stages of the research, two industrial hot air guns (2kW) accommodated in a metallic box, as described in Voller (2003) were used to heat the disc (Figure 4.5(a)). The procedure required removing the rubbing thermocouples from the friction surfaces to close the box containing the disc. The disc rotated at low speed (approx. 30 rpm) and hot air was blown on it. In this way the heating process was carried out only by convection, the hot air discharge of the guns aimed the channel outlets and therefore no substantial radiation helped heating. The disadvantage of this heating method was the long time necessary to bring the disc temperature up and also the relatively low limiting temperatures achieved (no higher than 145^{o}C). Removing the box from the disc and positioning the thermocouples back in place constituted a loss of energy also.

(a) Heating box. (b) Induction Heater.

Figure 4.5: Heating equipments.

4.5 Disc Heating: Induction Heater

In the last stage of the research a 15kW induction heater system was available for heating the discs[1]. The equipment, bought from Cheltenham Induction Heating, has three main components (Figure 4.5(b)): a screen sensible control box, a coil attached to the head for delivering power and a refrigeration unit to cool down the water that prevents overheating coil and head electric components. Additionally, the system has various electronic components. The induction heater system works with a 21kVA input. The working frequency range is 50-150 kHz and it can deliver from 200 to 1000 volts (ISM Range Instruction Manual 2007). The equipment is very user-friendly and allows quick heating of metallic components such a brake disc in very short times.

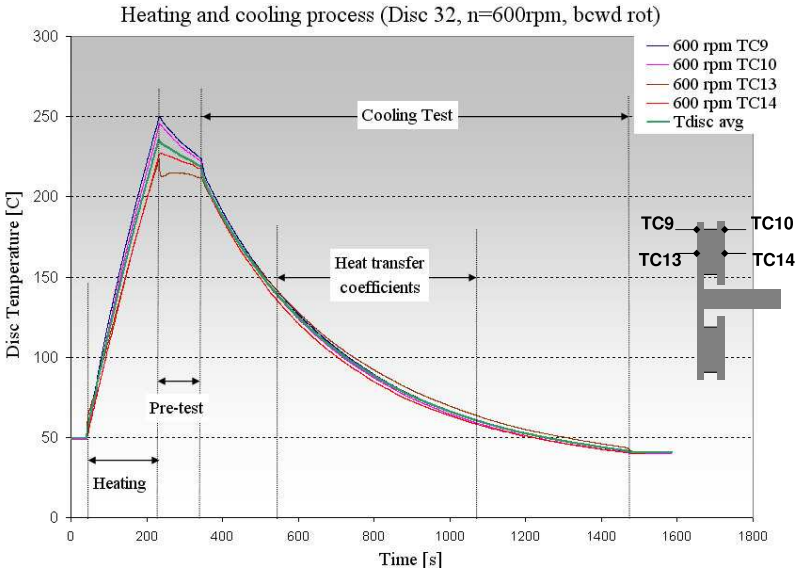

Figure 4.6: Brake disc cooling test history using induction heating.

The heating process of the brake discs with the induction heater is much simpler than that with hot air guns. It basically involved locating the thermocouples in place on the disc friction surfaces, setting up files for logging temperature and speed-torque, positioning the coil around the brake disc and starting the induction heater to heat the disc up to the desired temperature while spinning it at low speed. The great advantage of this system is allowing the user full control on the desired temperature reached by the disc, since by placing the thermocouples before starting the equipment, not only cooling but heating (friction surfaces temperature) could be observed and controlled. The brake disc heating and cooling process

[1]The energy required to rise the disc temperature by 115^{o}C is less than 15kW, this for constant heating during 4 or 5 minutes

involving the induction heater is shown in Figure 4.6, where real test data has been used. The temperatures used to calculate heat transfer coefficients were 150^{o}C to 60^{o}C, this allowed time for temperature setting in the disc.

4.6 Temperature Measurement: Thermocouples

Temperatures were logged using K-type thermocouples, with a working range from -200 ^{o}C to 1370 ^{o}C. The K-type thermocouples joint is made with chromel and alumel and they are commonly used in research and industrial environments due to its good sensitivity. In the range of 0^{o}C <500^{o}C these thermocouples produce a voltage output of 0.0 to 20.644 mV, (NIST Database 1999), and the relation temperature-voltage follows a 9^{th} order polynomial (equation 4.1). With Θ as the thermocouple temperature output (^{o}C), c_i as coefficients of the approximate *inverse* function for K-thermocouple and E is the probe junction voltage output in mV (see Table A.2). The polynomial 4.1 is an approximation to the thermocouple behavior and is hidden as part of the linearisation features of the acquisition system used in the experiments. The linearisation error of equation 4.1 for a temperature range of 0^{o}C < 500^{o}C is $-0.05^oC < \delta_\Theta < 0.04^oC$.

$$\Theta = \sum_{i=0}^{i=9} c_i E^i \tag{4.1}$$

The thermocouples used were *rubbing thermocouples* for brake disc surface temperature and *graphite tip* or *wire tip probe thermocouples* for ambient temperature readings.

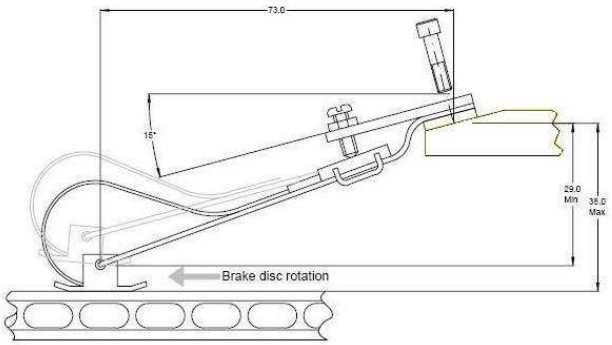

Figure 4.7: Rubbing K type thermocouple used on brake disc friction surface.

Figure 4.7 schematically shows the use of a rubbing thermocouple in a brake discs. The thermocouple sensor is bonded to a stainless steel shoe, whose longitudinal axis should be aligned with the disc tangential velocity direction. Ideally, the thermocouple temperature attained by conduction from the disc is transmitted to the data acquisition system; however, since the thermocouple shoe is kept in contact with the surface due to a normal force against the disc rotating, additional heat is generated due to pressure and relative speed between the thermocouple and the brake disc surface. A way of bridging this is by considering that brake disc cooling tests performed in laboratory are at constant speed, then (disregarding any dependence of the friction coefficient with temperature) the temperature curve will be shifted upwards a certain *constant* value; this means that rates of change observed during the process will remain the same (provided that disturbances e.g. sudden changes in speed or significant cooling by radiation do not occur)[2].In general, the measurement error from the thermocouple probes is considered to be $\delta_{\Theta^{tc}} = \pm 0.2^{o}C$.

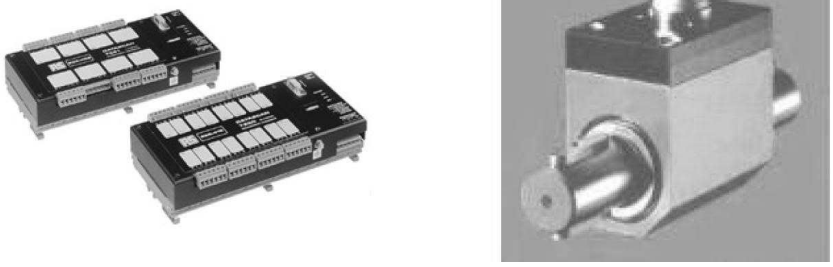

(a) 7220 RS A/D 16 Ch. (b) Torque sensor.

Figure 4.8: Data loggers.

The thermocouples were connected to a *7220-RS 16 channel* A/D data acquisition module (Figure 4.8(a)), which linearised the signal. The 7220-RS A/D converter allows to have either 16 or 14 bits of resolution for data acquisition. The mode used in this research is the 16 bits, in which the module can handle a reading rate of 40Hz with high noise rejection. The signal is then transmitted to the computer using a *RS-232* interface connected to the PC's COMM port and displayed using LabView (see Figure A.1). The 7220-RS module can be used with a wide range of thermocouples and temperatures; in the specific case of K-thermocouples working within a range of $0^{o}\text{C} < 500^{o}\text{C}$ (that is 0 to $20.6mV$) and in the 16 bit mode, the module's accuracy interval is $\delta_E = \pm(0.02\%rdg + 0.01\%range + 5\mu V)$, (RS Data-sheet 1997).

[2]Another way is by doing a set of tests to quantify the increment in temperature read by the acquisition system for particular values of angular speeds

4.7 Angular Speed and Torque Measurement

The acquisition of torque and angular speed readings of a rotating brake disc test was performed using a 50Nm torque transducer (model TRNA/0806 by Industrial Measurement Ltd, see Figure 4.8(b), located between the motor and the bearing housing. The brushless type transducer is fed with 24VDC and outputs $\pm 5V$ for $\pm 50Nm$ of torque and a frequency in-line with angular speed (2kHz=2000rpm). The readings are supplied with less than $\pm 0.05\%$ fs repeatability and less than $\pm 0.1\%$ fs nonlinearity, (IML Data-sheet TRNA/0806).

Whilst the torque transducer signal is fed to a NI PCI-6023E card which then supplies it to the computer, the speed frequency signal is fed to a FYLDE FE-570-FV frequency-voltage converter, where it is converted to an output voltage in the range of 0-10V with the maximum known frequency set to correspond to the maximum output voltage (2kHz→10V). After this, the angular speed signal is processed by the NI PCI-6023E card. The results (torque and speed) are displayed in the computer using an in-built IML software. Both signals, speed and torque, are handled as SRE signals through the multi-purpose NI TBX68 terminal block and NI SH6868 cable before being supplied to the NI PCI-6023E card. The measurement precision of the PCI card is 4.88 mV for a range of ± 10V.

4.8 Hot Wire Anemometry

Airflow characteristics at the exit of the channels were qualitatively investigated using a single wire Constant Temperature Anemometer. The goal of the data acquired focused on analysing the voltage response to air coming out from channels when the disc rotated at an specific angular speed. At the time of tests no specific hardware was available to probe perform calibration tests, and constants to fit in the King's law (Bruun 1995), (Davies 1985), were unavailable for the sensor.

Three types of hot wire anemometers exits, the Constant Current Anemometer (CCA), the Constant Voltage Anemometer (CVA) and the Constant Temperature Anemometer (CTA). All of them work under the same principle, initially the wire is at the working temperature level, as the flow past by its temperature drops and therefore the wire current, voltage or resistance (in the case of CTA) is increased accordingly. The required supply of current or voltage is then proportional to the flow speed and therefore can be correlated. In the case of the CTA, the sensor's resistance is proportional to its temperature, therefore the wire working temperature is attained by adjusting its resistance through a bridge circuit. A servo amplifier adjust the bridge voltage such that the current passing though the wire heats it to the desired temperature value. When the wire is cooled down by the flow, the

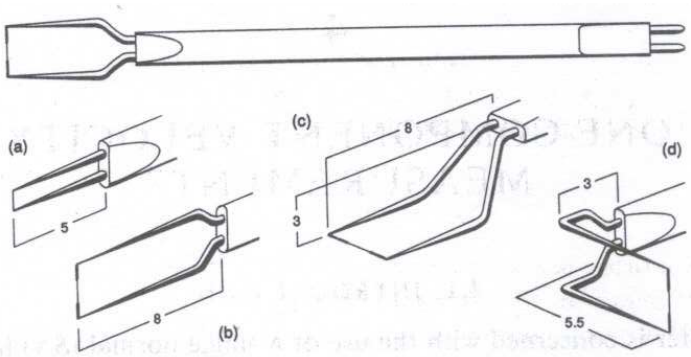

Figure 4.9: Hot wire probe types: (a) unplated, (b) plated, and (c), (d) for boundary layer flows. From Bruun (1995).

bridge voltage is increased so that the wire temperature (resistance) is kept constant. Then a hot wire sensor is better when its temperature coefficient of resistance is high and when its mechanical strength is good. Also, it must offer an electrical resistance that can be heated at practical voltage or current levels.

The CTA probe is a very thin metallic filament, approximately 2 mm long and 5μm in diameter; usually constructed of tungsten, platinum and platinum-iridium alloy. The tungsten made probes are strong with relatively high temperature coefficient of resistance (0.004/^{o}C). However its main disadvantage is the low oxidation resistance (not able to work in high temperature flows). The platinum wire has a similar temperature coefficient of resistance (0.003/^{o}C) but its mechanical strength is low. The platinum iridium wire has higher strength and better thermal oxidation resistance but with lower temperature coefficient of resistance (0.00085/^{o}C).

There exist many types of probes according to the specific application. Figure 4.9 shows some of the existing types. Probes (a) and (b) are for measurements away from wall effects. The main difference between them is the plating technique used in probe (b) to minimise aerodynamic probe perturbance. Probes (c) and (d) are used for measurements in flows near the wall, and the main difference is the bent of the prongs holding the wire at 90 degrees in probe (d) to minimize disturbances associated with them. The probe type used in this thesis is like (a).

$$E^2 = A + BU^{\varphi} \tag{4.2}$$

The King's law governs a hot wire probe behaviour (equation 4.2). King (Bruun 1995)

suggested that φ =0.5, but a better fit was proposed by Collis and Williams in 1959 (Bruun 1995) with φ =0.45 for Reynolds numbers of 0.02 to 44 (based on wire diameter). The above exponent however has been extensively researched and Bruun (1995) suggested that for a typical 5μm diameter wire φ can vary between 0.4 and 0.45. Van der Hegge Zijnen (1956) proposed equation 4.3 for Re ranging from 0.01 to 500000.

$$Nu = 0.35 + 0.5Re_D^{0.5} + 0.001Re_D \tag{4.3}$$

Sidall & Davies's (1971) and Davies's (1985) works improved the King's power law by analysing its dynamic response to speed and concluded that the static behaviour of the wire is better correlated with a three constants equation 4.4. The purpose of the HWA tests aimed initially identifying periodic behaviour in the air. However, a rough analysis of the air fluctuations could be performed by analysing mean and fluctuating parts. The mean would give the signal average strength (hence, related to cooling and flow speed), and the fluctuating component the degree of excitation of air leaving the channel. Low and high frequency fluctuation may both have a noise component, however it was assumed that this has constant mean and that its amplitude is lower than the lowest amplitude registered for the fluctuating signal.

$$E^2 = A + BU^{1/2} + CU \tag{4.4}$$

The following guidelines were taken into for hot wire anemometry testing:

1. The CTA probe must lie as close as possible to the outlet of the channels in order to capture the periodic behaviour of the channels (or vanes)[3].
2. The rate of data acquisition must be at least twice as that of the Vane Passing Frequency (VPF) (Nyquist criterion).
3. After logging the data, statistical and Fourier analysis is carried out. The latter is useful to identify the dominant components of the signal.

4.9 The Hot Wire Anemometry Test Set-up

The equipment used for the a typical anemometry test is composed by :

1. A Dantec Dynamics^{TM} tungsten wire probe type 55P16.

[3]Two locations were evaluated and the results for the best are shown in the followings chapters

Figure 4.10: Hot Wire Anemometry equipment: Mini-CTA, Wire probe, BNC cables, Power cable.

Table 4.2: Tungsten wire probe type 55P16 characteristics

Sensor Resistance [Ω]	Lead resistance [Ω]	TCR [%/^{o}C]
4.01	0.9	0.36

2. A Dantec Dynamics^{TM} Mini-CTA 54T30 bridge resistance anemometer for wire and fiber-film probes in air.

3. A National Instruments SC2040 8-channels acquisition card.

4. A couple of BNC cables and a power supply cable.

5. A tailored LabView interface program and a PC.

Most of the components can be seen in Figure 4.10. The characteristics of the wire probe are shown in Table 4.2. The probe working temperature level can not be greater than 300^{o}C. The Mini-CTA 54T30 anemometer bridge operating resistance can take any value between 4 and 20Ω. The power input for both the anemometer and the wire must be 11-14VDC and the anemometer amplified output is within the range of 0 to 5 volts.

The wire probe is connected to the anemometer box and this with the NI SC2040 through BNC cables. The anemometer box contains the bridge of resistances, the amplifier for the

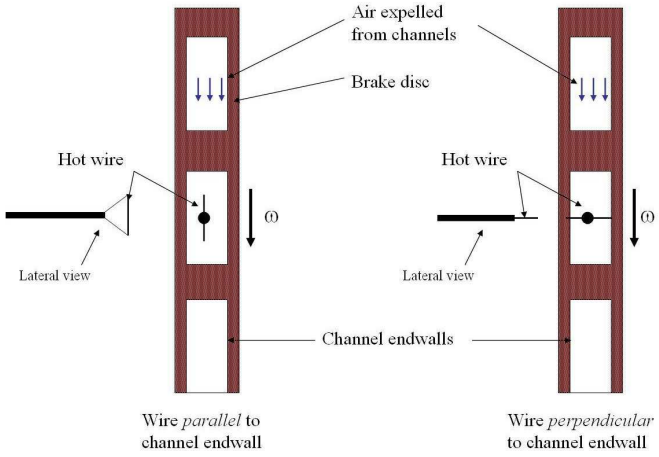

Figure 4.11: Probe alignment for flow measurement, parallel (left) and perpendicular to channel endwalls.

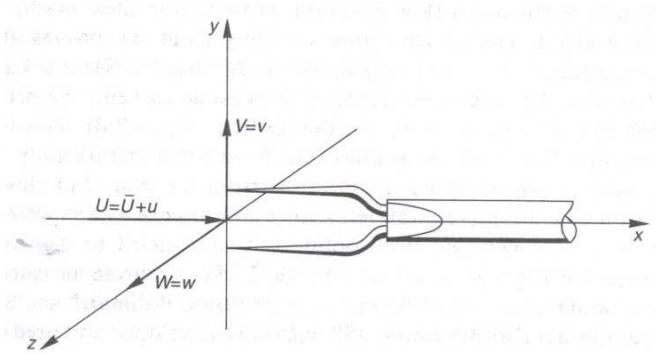

Figure 4.12: Single wire in normal direction to main stream. From Bruun (1995).

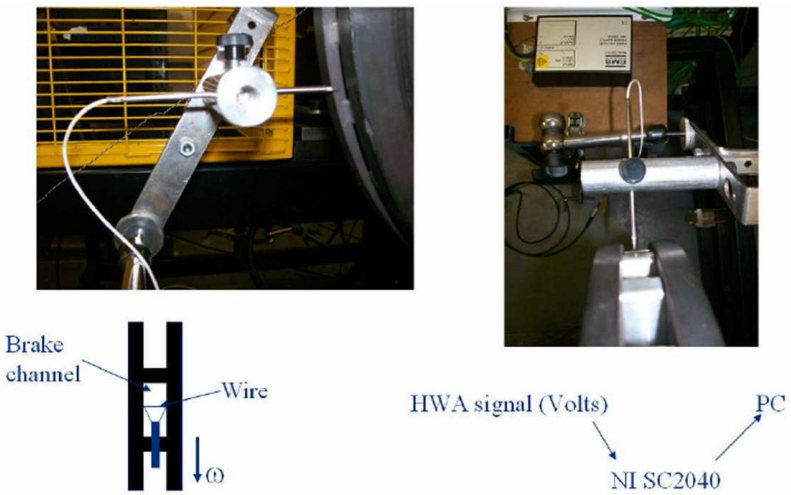

Figure 4.13: Wire probe positioned for tests and schematics for location and signal acquisition.

signal and also is the port for connecting the probe to an external power supply[4]. For this purpose the bridge resistance of the anemometer is altered as function of the desired temperature level. This must be done before connecting the probe with the external power supply, otherwise the wire may burnout.

The probe wire could be aligned in two directions at the exit of the channel (Figure 4.11), however due to its sensitivity along the longitudinal (wire) axis, the most appropriate is when this lies normal to the main flow direction (Figure 4.12), therefore the wire axis must be perpendicular to the channel endwalls. This position is shown in the right side of Figure 4.11 and in Figure 4.13 where the components are pictured along with the disc on the Spin Rig[5]. The acquisition process of the anemometer signal is equivalent to others (e.g. that logged by thermocouples), but due to the nature of the sensor response, the HWA can register high amplitude and frequency phenomena, therefore attention to its logging procedure must be given.

The signal is characterised by its amplitude (strength of changes in the flow stream) and frequency (which determines whether these are slow or fast). To capture this an appropriate sampling frequency f must be set. The number of records logged (N) are determined by the sampling period ($T_s = 1/f$) and the total sampling time (T), then $N = T/T_s$.

[4]The type of connection is NSRE, see (SC 2040 User Manual 1994).

[5]Aligning the wire axis in the other position would have resulted in measurement of the velocity component parallel to the wire rather than measuring that perpendicular to it

The airflow may exhibit relevant phenomena in a wide range of frequencies and the sensor must be able to capture a signal bandwidth covering them, say from 0 to W Hz. Then, the slowest phenomenon to be captured is that occurring at the minimum frequency $f_{min} = 1/T$. If an interesting phenomenon is expected to occur every δ_{t_1} seconds, the sampling frequency required is $f_1 = 1/2 \cdot \delta_{t_1}$. This sampling rate gives independent readings in the time-history record and according to Bruun (1995) represents the optimum sampling criterion for amplitude-domain analysis (Nyquist criterion). In the brake discs, the Vane Passing Frequency (Hz) can be calculated by multiplying the number of vanes in the disc times the revolutions per second. However, the VPF is the lowest frequency required to resolve, more information can be retrieved at higher frequencies.

The behaviour of the air coming out from the vents as the disc rotates is periodic, that is, a somewhat cyclic pattern can be observed. However, within each cycle, the signal behaviour itself is random due to the regions of backflow and through-flow inside the channels which determine the characteristics of the outflow. Unlike a predictable signal behaviour (deterministic), a random behaviour is not able to be explicitly modelled in a timewise form, Dunn (2005).

At constant speed, each revolution of the disc determines a *sample record or event* with a *finite time interval* in which the behaviour can be analysed. The disc angular speed, in revolutions per second, times the total logging time (T) will determine the number of data sets (N_R) making an *ensemble* of samples. The behaviour of the data can be first assessed by calculating the mean at a specific time (t_1)of the event. For this, the instantaneous value of the signal at that time from each sample of the ensemble is summed and its average taken. Repeating this in a discrete manner along the sample gives the mean behaviour of the ensemble (*ensemble average*). The mean at t_1 is calculated as in Bruun (1995):

$$\chi(t_1) = \lim_{N_R \to \infty} \frac{1}{N_R} \sum_{j=1}^{j=N_R} E_j(t_1) \tag{4.5}$$

Where E stands for signal voltage. Therefore equation 4.6 is the vector with the averages of the ensemble, in which the subscript of t is the signal value at consecutive discrete times (determined by the sampling rate used) and the subscript of E represents the event (brake disc revolution) within the ensemble.

$$\chi(t_i) = \lim_{N_R \to \infty} \frac{1}{N_R} \sum_{j=1}^{j=N_R} E_j(t_i) \tag{4.6}$$

$\chi(t_i)$ together with the autocorrelation function (Bendat & Piersol 1993), are used to characterise random processes; which are non-stationary when they vary with t_i. When they

remain constant, then the process is weakly stationary and all possible *moments* are time invariant and the random process is said to be strongly stationary. Further characterisation is performed with a mean and standard deviation calculated *per event* using equations 4.7 and 4.8. Equations 4.7 and 4.8 will yield the same (or closely related) result for each sample record (revolution) of the ensemble if the process being measured is *ergodic*. The time period in which this equation is evaluated corresponds to the time taken by a revolution and N_S is the number of records in each sample of the emsemble (sampling rate divided by the number of revolutions per second). These checks are suggested to verify the overall behaviour of the air and of the sensor itself.

$$\chi = \lim_{T_R \to \infty} \frac{1}{T_R} \int_0^{T_R} E(t)dt = \frac{1}{N_S} \sum_{j=1}^{j=N_S} E_j \tag{4.7}$$

$$\sigma = \sqrt{\frac{1}{N_S - 1} \sum_{j=1}^{j=N_S} (E_j - \chi)^2} \tag{4.8}$$

With the ensemble average, the standard deviation (σ) at a time t_i per sample can be calculated. Both, the ensemble average (or time averaged mean) and the standard deviation of the ensemble are known as statistics of the sample. Formally speaking, (σ) gives the width of the cloud of data around the ensemble average.It also may be understood as a measurement of the spread of data about the average (noise and strength of the flow fluctuations). The expression used to calculate it from the sample is (Dunn 2005):

$$\sigma(t_i) = \sqrt{\frac{1}{N_R - 1} \sum_{j=1}^{j=N_R} (E_j(t_i) - \chi(t_i))^2} \tag{4.9}$$

As mentioned before (page 38), an instantaneous variable of the flowfield can be decomposed into a mean and a fluctuating component. Similar decomposition of the voltage measured by the wire can provide meaningful information regarding the fluctuating potential of the air as it leaves the channels of the brake disc. The fluctuating signal is calculated as:

$$E'_j(t_i) = E_j(t_i) - \chi(t_i) \tag{4.10}$$

Therefore, equation 4.10 yields a collection of data which compose the ensemble of the fluctuating component of the probe signal[6]. The energy contained in the fluctuating signal

[6]The fluctuating component in this way is composed also with noise, which has not been analysed further

can be estimated with the root mean square (rms), calculated as (Versteeg & Malalasekera 1995):

$$rms(t_i) = \sqrt{\overline{E'_j(t_i)^2}} \tag{4.11}$$

The rms of the ensemble is a vector very similar to the standard deviation of the sample and practically the same equation (4.9) can be used to obtain it, replacing the denominator $N_R - 1$ by N_R.

The flow characteristics exiting the channels were investigated with Power Spectral Density (PSD) functions, using the Discrete Fourier Transform (DFT) applied to the original (raw) voltages logged during the test, (Bendat & Piersol 1993)). The area under the PSD diagram contains the energy of the measurements and it remarks significant frequencies of behaviour. The DFT for raw data logged in the time interval $0 \leq t \leq T$ is defined as:

$$X_k(f,T) = \int_0^T E_k(t) e^{j2\pi ft} dt \tag{4.12}$$

With the above calculated, the PSD function is calculated as follows:

$$PSD_k(f,T,k) = \frac{1}{T} X_k^*(f,T) X_k(f,T) \tag{4.13}$$

Where the complex conjugate of the DFT ($X_k^*(f,T)$), must multiply by the left to the original DFT ($X_k(f,T)$). The procedure followed to analyse the probe signal resulting from a hot wire test was:

1. Identify the test parameters: Angular speed (n), sampling frequency (f) and total period of logging (this will determine the number of data to consider in the ensemble).

2. Evaluate ergodicity of the flow (equation 4.7). If this changes largely from sample to sample in the ensemble, then either the probe is damaged, there is excessive vibration of the sensor or the speed of the motor varied too much during the test. Alternatively, this could also imply that the process is fully random-non stationary (not ergodic), see Dunn (2005), Bendat & Piersol (1993), Bruun (1995) for further information on this.

3. Calculate the ensemble based properties: ensemble average, rms (or standard deviation) and fluctuating component vectors. Equations 4.6, 4.9, 4.11 and 4.10.

4. Calculate the PSD function of the raw data (equation 4.13). Identify the frequency components of the signal and their amplitudes.

5. Calculate the PSD function of the fluctuating component to identify the frequency range of these and their amplitudes.

4.10 Brake Disc Cooling Tests Set-up

The set up for a typical brake disc cooling test included the following components: ventilated brake disc, spin rig, gun heater box (or induction heater), k-type thermocouples, torque and speed sensor, data loggers for temperature, and speed and torque (data cards); computer to process the data. The test set up schematic arrangement is as indicated in Figure 4.14.

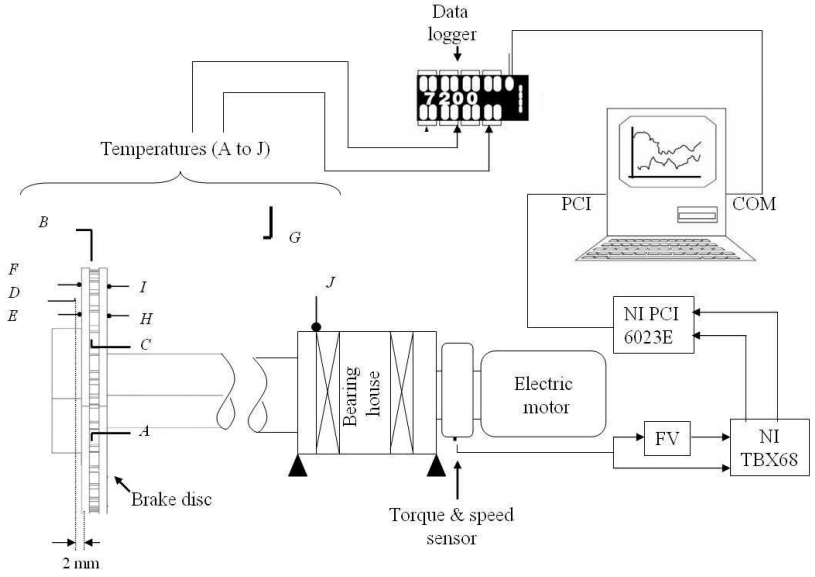

Figure 4.14: Brake disc cooling test set up, *A, B,...,J* indicate thermocouples.

Various thermocouples were used during testing, four for air temperature (A to D), four for brake friction surface temperature (E, F, H, I), one for ambient temperature and one to monitor the bearing housing temperature (to prevent excessive heat penetration into the bearings and potential damage).

4.11 Raw Data and Derived Results

The outputs of the experiments carried out are clear and defined: temperature-*vs*-time readings and torque and angular speed-*vs*-time readings. Another sets of tests data are the

signals recorded from the hot wire anemometer; these, as mentioned earlier were analysed in raw format (as voltages).

4.11.1 Experimental Uncertainty

The technical data of the instrumentation used in the tests provide useful information for measurement uncertainty. While performing the experiments, the sensors and acquisition instruments record measurements of the process being observed, however the true value under which the system is responding (e.g. the brake disc temperature) is unavoidably modified due to measurement errors. Therefore the measurement error can be defined as the difference between the measured and the true values; however, this difference can only be guessed through the uncertainty (Moffat 1988). The measurement uncertainty is then, the limiting range bounding the true value of the process.

Uncertainty of Temperature Measurements

The sources of temperature uncertainty have been identified as follows:

1. Brake disc cooling tests uncertainty sources

   (a) *Instrumentation errors.* These are bounded by the thermocouple probes and data acquisition system accuracies. Fixed temperature acquisition errors are considered in this research as follows:

   - K-thermocouple probe measurement error: $\delta_{\Theta^{tc}}$ and,
   - RS7220 data acquisition system error: $\delta_E = \pm(0.02\%$ rdg + 0.01 % range + 5 μV) for 0^oC-500^oC

   (b) *Sensor interaction.* These type of measurement errors result as a natural response of the thermocouple probe. During the brake disc cooling tests, the probe is in contact with the friction surface and with the surrounding airflow. Then, a quantification of the total error would involve calculating thermocouple heat losses due to 'heat partition' friction surface-probe and due to convective cooling. These errors were disregarded in the current research.

   (c) *System perturbation errors.*

   - Rubbing thermocouple. Since the thermocouple shoe is in contact with the friction surface during tests, a parasitic heat source is added to the system. This is function of the pressure between the thermocouple shoe and the disc, the relative speed (angular speed) and the friction coefficient. The error may

be approximated (assuming even contact of the thermocouple shoe with the friction surface) by conducting a series of tests at several angular speeds with the disc at ambient temperature and calculating the average positive shift of temperature due to sliding. The change of friction coefficient due to drop of temperature in cooling tests could be discarded. Thermal contact resistance issues (such as radiation and convection through micro-gaps are disregarded).

- Wire and graphite probe thermocouple. The kind of system perturbation errors appearing due to presence of these thermocouple probes involves air-probe friction generated heat and radiation surface-probe, ambient-probe. The first error contribution is out of the scope of the present research and the radiation effects are disregarded since temperatures of the disc do not reach above 200^oC.

Therefore, using the maximum voltage in the range of temperatures of interest ($20.6mV$), the voltage uncertainty read by the 7220-RS A/D converter is $\delta_E = \pm 0.0118mV$. Inserting δ_E in equation 4.1 and using the data from Table A.2, the uncertainty in temperature read by the 7220-RS A/D converter is $\delta_{\Theta^{RS}} = \pm 0.295^o$C. Therefore the final uncertainty in temperature measurements is expressed as:

$$\delta_{th} = \delta_{\Theta^{RS}} + \delta_{\Theta^{tc}} = \pm 0.295^oC + \pm 0.5^oC \approx \pm 0.8^oC \tag{4.14}$$

The above uncertainty of the measured temperature should be included in the calculation of derived results using the value of Θ. The introduction of uncertainties in derived results is done by carrying a sequential perturbation analysis as described in Moffat (1985) and Moffat (1988). This analysis will be applied when calculating total and convective heat transfer coefficients.

4.11.2 Heat Transfer Coefficients Derivation

As the disc cools down while rotates at an specific angular speed, three modes of heat dissipation may influence its total rate of cooling b_t: convection, conduction and radiation. The temperatures registered during the cooling process are function of all the heat dissipation modes. Therefore, if heat transfer coefficients or cooling rates are derived from these results the following must be considered:

1. Derived results will represent *averaged total* quantities; i.e.: if the derived quantity is the heat transfer coefficient, then it must be termed *total heat transfer coefficient*. Further analysis should be carried out if, for instance, average convective heat transfer coefficients are calculated.

2. The uncertainty calculated in equation 4.14 must be included by means of a perturbation analysis to obtain the uncertainty of the derived quantities.

The heat transfer coefficients derived from temperature measurements are calculated from an energy balance equation (Kreith & Bohn 2001), (Moffat 1988), applied to the brake disc as follows:

$$Q_{in} \; - \; \left[\overline{h_{d_c}} A_w (\overline{\Theta_d} - \Theta_\infty) \; + \; \sigma \epsilon A_r (\overline{T_d^4} - T_\infty^4) + k \frac{A_c}{l_c} (\overline{\Theta_d} - \Theta_s) \right] \; = \; m_d C_{p_d} \frac{d\overline{\Theta_d}}{dt} \tag{4.15}$$

In the above equation, the product $k\frac{A_c}{l_c}$ can be understood as the conductance across the interface disc-shaft adapter, the rest of the variables are described in the Nomenclature. It must be noted that the brake disc temperature is the average resulting from the rubbing thermocouples E, F, H and I. The tests were conducted using an insulation plate between the disc and the shaft adapter, then conductive heat dissipation has been disregarded from equation 4.15. $Q_{in} = 0$ since during the cooling process no heat is added[7]. Dividing equation 4.15 by $(\overline{\Theta_d} - \Theta_\infty)$, the equation is reduced to:

$$\overline{h_{d_t}} A_w (\overline{\Theta_d} - \Theta_\infty) + m_d C_{p_d} \frac{d\overline{\Theta_d}}{dt} \; = \; 0 \tag{4.16}$$

Where the total heat transfer coefficient h_{d_t} is calculated as the summation of the convective and radiative contributions to the total heat dissipated from the brake disc.

$$\overline{h_{d_t}} A_w \; = \; \overline{h_{d_c}} A_w \; + \; \sigma \epsilon A_r \frac{\overline{T_d^4} - T_\infty^4}{\overline{\Theta_d} - \Theta_\infty} \tag{4.17}$$

Equation 4.16 is recognised as the differential equation ruling the cooling process of a lumped system, (Incropera & DeWitt 2002). It assumes that resistance to conduction inside the brake is very low as compared to the resistance to heat dissipation by convection, that is, temperature gradients inside the brake disc tend to zero during cooling and a uniform temperature is kept. Solving equation 4.16 between two situable times (t_1 and t_2) corresponding to temperatures $\overline{\Theta_1}$ and $\overline{\Theta_2}$ in the cooling test, yields:

$$\frac{1}{\Delta t} \ln \frac{\overline{\Theta_2} - \Theta_\infty}{\overline{\Theta_1} - \Theta_\infty} \; = \; - \frac{\overline{h_{d_t}} A_w}{m_d C_{p_d}} = b_t \tag{4.18}$$

[7]The apparent mixing of units (^{o}C and K) do not pose any inconsistency to the balance

Where $\Delta t = t_2 - t_1$, and $\overline{\Theta_1} > \overline{\Theta_2}$. The ambient temperature used (Θ_∞), should be calculated as the time average ambient temperature read from t_1 to t_2. From equation 4.18 the parameter driving the temperature gradient during cooling is identified as the total cooling rate of the brake disc (b_t). Solving for $\overline{h_{d_t}}$:

$$\overline{h_{d_t}} = -\frac{m_d C_{p_d}}{A_w \Delta t} \ln \frac{\overline{\Theta_2} - \Theta_\infty}{\overline{\Theta_1} - \Theta_\infty} \tag{4.19}$$

When using equation 4.18 to calculate either the total cooling rate or heat transfer coefficient from the disc spinning at a specific angular speed ω, care should be taken to select the lapse of time Δt. The selection of t_2 and t_1 must cover a portion of the experimental cooling curve representative for the nonlinear cooling behaviour, otherwise it may yield erroneous indication. Also, the second limit, t_2 (late phase of cooling tests) should be selected such that effects of thermal gradients coming back from the hub section of the disc do not influence the average temperatures $\overline{\Theta_2}$.

Since the average temperatures at which the cooling tests started were around 150 ^{o}C, it was assumed that leaving a 30^{o}C gap from the start would equalize the temperatures in the disc, and allowing this to cool down to 60^o will avoid influence from the thermal gradient caused by the hub section. These limits are schematically shown in Figure 4.15.

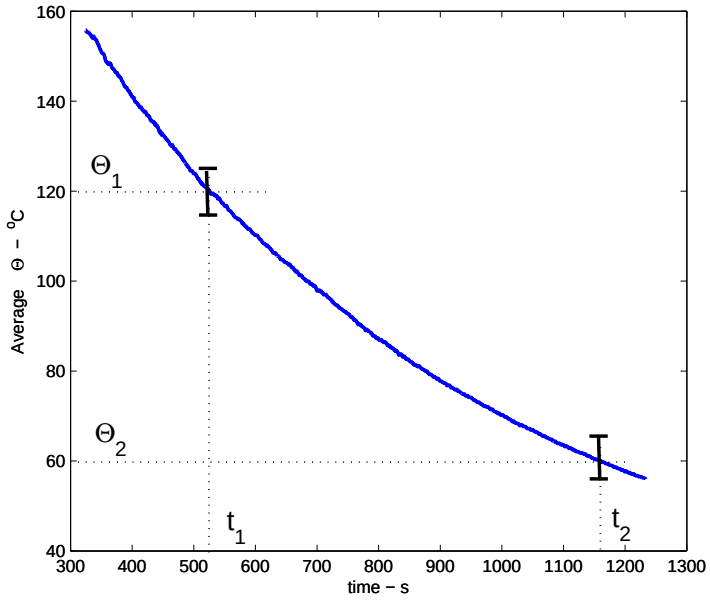

Figure 4.15: Selection of temperatures for calculation of heat transfer coefficients.

Once the total cooling rate and heat transfer coefficient are calculated for a specific condition of speed ω, the average convective heat transfer coefficient $\overline{h_{d_c}}$ of the brake disc is computed subtracting the radiation heat dissipation coefficient from the total:

$$\overline{h_{d_c}} = \overline{h_{d_t}} - \sigma\epsilon\frac{A_r}{A_w}\frac{\overline{T_d^4} - T_\infty^4}{\overline{\Theta_d} - \Theta_\infty} \tag{4.20}$$

Summarizing, the averaged convection heat transfer coefficient can be re-stated as:

$$\overline{h_{d_c}} = \overline{h_{d_t}} - \overline{h_{d_r}} \tag{4.21}$$

The energy convected to air from the disc during the elapsed time Δt can be calculated following Incropera & DeWitt (2002):

$$Q_c = m_d C_{d_p}(\overline{\Theta_2} - \Theta_\infty)\left(1 - e^{\frac{\overline{h_{d_c}} A_w}{m_d C_{p_d}}\Delta t}\right) \tag{4.22}$$

Equation 4.22 could be used to confirm that, provided $\overline{\Theta_1}$ and $\overline{\Theta_2}$ are kept constant for several ω, the energy dissipated by convection is constant and independent of the angular speed.

Calculating heat transfer coefficients for the DVB disc need to take into account both materials (aluminum and gray iron), then equations 4.18, and 4.22 are rewritten as[8]:

$$\ln\frac{\overline{\Theta_2} - \overline{\Theta_\infty}}{\overline{\Theta_1} - \Theta_\infty} = -\overline{h_{d_t}}\left(\frac{A_w}{m_d^A C_p^A + m_d^{CI} C_p^{CI}}\right)\Delta t \tag{4.23}$$

$$Q_c = (m_d^A C_p^A + m_d^{CI} C_p^{CI})(\overline{\Theta_2} - \Theta_\infty)\left[1 - e^{\overline{h_{d_c}}\left(\frac{A_w}{m_d^A C_p^A + m_d^{CI} C_p^{CI}}\right)\Delta t}\right] \tag{4.24}$$

4.11.3 Uncertainty of Heat Transfer Coefficients

Experimental uncertainty of total heat transfer coefficients can be calculated following Moffat (1985) and Moffat (1988).

[8] An equivalent heat capacity can be calculated as $\overline{C_p} = \frac{1}{m_d^A + m_d^{CI}}(m_d^A C_p^A + m_d^{CI} C_p^{CI})$, which when multiplied by the total mass results in the denominator of the term within brackets in equation 4.23

1. The *Sequential Perturbation Method*, (Moffat 1988), yields the total uncertainty of $\overline{h_{d_t}}$ by sequentially perturbing the variables of equation 4.19 with their own uncertainties (Section 4.11.1); perturbed values $\overline{h^a_{d_t}}$, $\overline{h^b_{d_t}}$, etc. are obtained. Then, the differences of perturbed values $\overline{h^a_{d_t}}$, $\overline{h^b_{d_t}}$, etc. minus the original value $\overline{h_{d_t}}$ are independently calculated. The total uncertainty $\delta\overline{h_{d_t}}$ is given as the root mean square summation of the differences. In summary:

   (a) Calculate $\overline{h_{d_t}}$, equation 4.19.

   (b) Calculate:

$$\overline{h^a_{d_t}} = f\left[(\overline{\Theta_1} \pm \delta\Theta)\,,\, \overline{\Theta_2}\,,\, \Theta_\infty\,,\, \Delta t\,,\, \frac{m_d C_{p_d}}{A_w}\right]$$

$$\overline{h^b_{d_t}} = f\left[\overline{\Theta_1}\,,\, (\overline{\Theta_2} \pm \delta\Theta)\,,\, \Theta_\infty\,,\, \Delta t\,,,\, \frac{m_d C_{p_d}}{A_w}\right]$$

$$\vdots$$

   (c) Calculate:

$$\delta\overline{h^{a+}} = \overline{h^{a+}_{d_t}} - \overline{h_{d_t}}, \quad \delta\overline{h^{a-}} = \overline{h^{a-}_{d_t}} - \overline{h_{d_t}}, \quad \delta\overline{h^{b+}} = \overline{h^{b}_{d_t}} - \overline{h_{d_t}}, \cdots$$

   (d) Select the maximum differences [9] and obtain the final uncertainty as:

$$\delta\overline{h_{d_t}} = \pm\sqrt{(\delta\overline{h^a})^2 + (\delta\overline{h^b})^2 + \cdots} \tag{4.25}$$

2. The *Basic Differential Method*, (Moffat 1988), is the source of the Sequential Perturbation Method, and it requires to compute the differentials of the equation 4.19 with respect to each variable. The differentials are explicitly evaluated and each multiplied by its corresponding uncertainty. The total uncertainty is computed from the root-sum-square of the products. The steps to follow are:

   (a) Obtain the differentials:

$$\frac{\partial\overline{h_{d_t}}}{\partial\overline{\Theta_1}}, \quad \frac{\partial\overline{h_{d_t}}}{\partial\overline{\Theta_2}}, \quad \frac{\partial\overline{h_{d_t}}}{\partial\Theta_\infty}, \quad \frac{\partial\overline{h_{d_t}}}{\partial\Delta t}, \quad \frac{\partial\overline{h_{d_t}}}{\partial\varsigma}$$

   Where $\varsigma = \frac{m_d C_{p_d}}{A_w}$.

[9] Moffat (1988) suggests that an average between the partial uncertainties $\delta\overline{h^{a+}}$ and $\delta\overline{h^{a-}}$ can also be used

(b) Evaluate the above and compute the final uncertainty as:

$$\delta\overline{h_{d_t}} = \pm\sqrt{\left(\frac{\partial\overline{h_{d_t}}}{\partial\overline{\Theta_1}}\delta_\Theta\right)^2 + \left(\frac{\partial\overline{h_{d_t}}}{\partial\overline{\Theta_2}}\delta_\Theta\right)^2 + \left(\frac{\partial\overline{h_{d_t}}}{\partial\Theta_\infty}\delta_\Theta\right)^2 + \left(\frac{\partial\overline{h_{d_t}}}{\partial\Delta t}\delta_t\right)^2 + \left(\frac{\partial\overline{h_{d_t}}}{\partial\varsigma}\delta_\varsigma\right)^2} \tag{4.26}$$

The drawback of using the Method of Sequential Perturbation is the number of operations needed, since the method should be periodically repeated at each angular speed ω. Because of this and when possible, the Basic Differential Method is recommended; since it offers a quicker and elegant way of calculating uncertainties. Following this, the derivatives in equation 4.26 calculated from equation 4.19 are:

$$\frac{\partial\overline{h_{d_t}}}{\partial\overline{\Theta_1}} = \frac{\varsigma}{\Delta t}\frac{1}{\overline{\Theta_1} - \Theta_\infty} \tag{4.27}$$

$$\frac{\partial\overline{h_{d_t}}}{\partial\overline{\Theta_2}} = -\frac{\varsigma}{\Delta t}\frac{1}{\overline{\Theta_2} - \Theta_\infty} \tag{4.28}$$

$$\frac{\partial\overline{h_{d_t}}}{\partial\Theta_\infty} = -\frac{\varsigma}{\Delta t}\left(\frac{1}{\overline{\Theta_1} - \Theta_\infty} - \frac{1}{\overline{\Theta_2} - \Theta_\infty}\right) \tag{4.29}$$

$$\frac{\partial\overline{h_{d_t}}}{\partial\Delta t} = -\frac{\varsigma}{\Delta t^2}\ln\frac{\overline{\Theta_2} - \Theta_\infty}{\overline{\Theta_1} - \Theta_\infty} \tag{4.30}$$

$$\frac{\partial\overline{h_{d_t}}}{\partial\varsigma} = -\frac{1}{\Delta t}\ln\frac{\overline{\Theta_2} - \Theta_\infty}{\overline{\Theta_1} - \Theta_\infty} \tag{4.31}$$

Using data from the original cast iron ventilated brake disc (C_{p_d} =445 J/kgK, A_w =0.618m^2, m_d =30.4kg), yields ς =21889.9N/mK; and considering $\overline{\Theta_1} \approx 120^o$C, $\overline{\Theta_2} \approx 60^o$C and $\Theta_\infty \approx 19^o$C as constants, leaves Δt as the variable determining the numerical value of the above derivatives, function only of the angular speed of the brake cooling test, (i.e.: higher ω's yield shorter Δt's). Typically, $\Delta t \in [360s, 1600s]$, for $\omega \in [125.66\frac{rad}{s}, 10.47\frac{rad}{s}]$; which corresponds for n=1200rpm down to n=100rpm. A rough estimate for average Δt is therefore 980s. The numerical evaluation of the partial derivatives 4.27-4.31 with the above data is shown in Table 4.3.

The remaining terms to be known in equation 4.26 are the raw data uncertainties. Temperature uncertainty (Section 4.11.1) is $\delta_\Theta = \pm 0.8^o$C. Uncertainty in time is assumed to be $\delta_t = \pm 0.5$s.

Table 4.3: Evaluation of partial derivatives 4.27 to 4.31, Basic Differential Method.

Derivative	Value	Derivative	Value
$\frac{\partial \overline{h_{d_t}}}{\partial \overline{\Theta_1}}$	0.22 W/m^{2}K^2	$\frac{\partial \overline{h_{d_t}}}{\partial \Theta_\infty}$	0.77 W/m^{2}K^2
$\frac{\partial \overline{h_{d_t}}}{\partial \overline{\Theta_2}}$	-0.54 W/m^{2}K^2	$\frac{\partial \overline{h_{d_t}}}{\partial \Delta t}$	0.020 W/m^{2}Ks
		$\frac{\partial \overline{h_{d_t}}}{\partial \varsigma}$	9.199×10^{-4} 1/s

The uncertainty of the variable ς (enclosing m_d, C_{p_d} and A_w) must be calculated considering only uncertainties of m_d and C_{p_d} (δ_{m_d}, $\delta_{C_{p_d}}$), since an additional differentiation of equation 4.19 against A_w would be needed to evaluate the perturbation of h_{d_t} as A_w varies (differentiating equation 4.19 against A_w, would make A_w^2 appear in the denominator 'boosting' the numerical value of the derivative, since A_w is usually less than one squared metre; however, this would be reduced after multiplication times the convection area uncertainty, δ_{A_w}, which would be of the order of $\pm$ 1.0x10^{-04}m^2). Then, assuming $\delta_{m_d} = \pm 0.10$kg and $\delta_{C_{p_d}} = \pm 10$J/kgK; the uncertainty of ς is $\pm\delta_\varsigma \approx \delta_{m_d} \cdot \delta_{C_{p_d}}$, $\delta_\varsigma \approx \pm 1.0$ N/mK.

After substituting the above values and those in Table 4.3 in equation 4.26, the resulting uncertainty on the total heat transfer coefficient given by equation 4.19 is: $\delta\overline{h_{d_t}} = \pm 0.77$W/m^{2}K. An order of magnitude analysis per variable contributing to uncertainty is meaningful for test planning.

$$\begin{array}{ccccc}
\left(\frac{\partial \overline{h_{d_t}}}{\partial \overline{\Theta_1}}\delta_\Theta\right)^2 & \left(\frac{\partial \overline{h_{d_t}}}{\partial \overline{\Theta_2}}\delta_\Theta\right)^2 & \left(\frac{\partial \overline{h_{d_t}}}{\partial \overline{\Theta_\infty}}\delta_\Theta\right)^2 & \left(\frac{\partial \overline{h_{d_t}}}{\partial \Delta t}\delta_t\right)^2 & \left(\frac{\partial \overline{h_{d_t}}}{\partial \varsigma}\delta_\varsigma\right)^2 \\
\downarrow & \downarrow & \downarrow & \downarrow & \downarrow \\
[(0.22)(0.8)]^2 & [(-0.54)(0.8)]^2 & [(0.77)(0.8)]^2 & [(-0.020)(0.5)]^2 & [(9.19\times10^{-4})(1)]^2 \\
\downarrow & \downarrow & \downarrow & \downarrow & \downarrow \\
< 1 & < 1 & < 1 & << 1 & << 1
\end{array} \tag{4.32}$$

Where $<<$ and $<$ denote values near to zero and one respectively. The scenarios which may end up with high contributions to uncertainty from δ_Θ are those where the differences $(\overline{\Theta_1} - \overline{\Theta_\infty})$ and $(\overline{\Theta_2} - \overline{\Theta_\infty})$ are small or the elapsed time Δt is small (high ω) or the sensitivity of thermocouples is poor (large δ_Θ).

On the other hand, the term involving $\partial\Delta t$ will stay safely small due to its *beneficial* nonlinear nature (t^2 and logarithm of ratio of temperature differences). In the same fashion, the derivative against ς does not represent a significant quantity. These two terms are smoothed by the squaring process.

The above analysis indicates that during brake disc cooling tests it must be ensured that homogeneous friction exists between the thermocouple shoe and the brake disc friction surfaces in order to attenuate to a minimum the *thermocouple probe error*; and, a homogeneous temperature field should be kept in the brake disc during the target interval $(\overline{\Theta_1} - \overline{\Theta_2})$ of the brake cooling test.

Finally, a usual description of the uncertainty of the total heat transfer coefficient is (see Moffat (1985), Moffat (1988)):

$$\overline{h_{d_t}} \pm \delta\overline{h_{d_t}} \qquad (20{:}1) \qquad (4.33)$$

Equation 4.33 means that 19 out of 20 readings can be expected to lie within a range given by $\pm\delta\overline{h_{d_t}}$ for the specific $\overline{h_{d_t}}$ being quoted. The repeatability thus exemplified depends upon several factors such as instrumentation accuracy and easiness of test procedure.

4.12 Summary

Chapters 3 and 4 described the methods used during the research, highlighting weaknesses so that proper attention is paid to them. The supporting theory for the research methodology was described and references were quoted to fulfill possible voids. A typical CFD process flowchart for flow and convective heat transfer simulation around the brake disc is shown in Figure 4.16 as complementing information of these chapters.

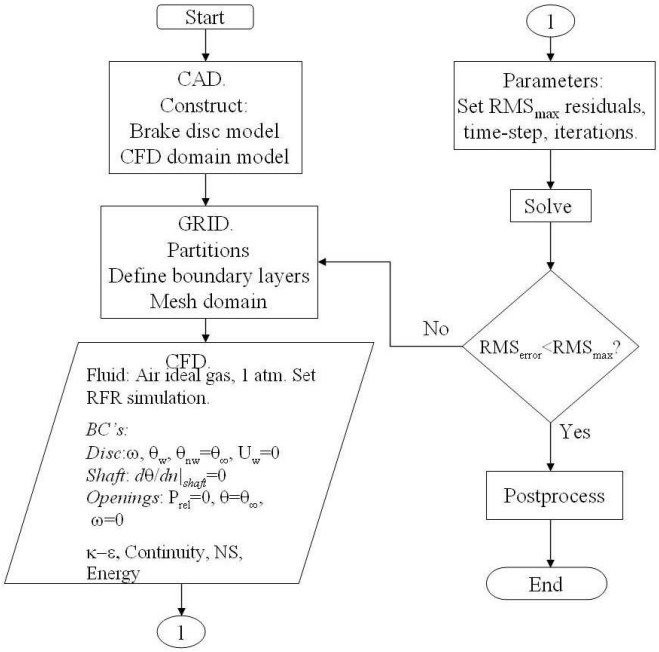

Figure 4.16: Typical process for CFD simulations.

Chapter 5

Baseline Brake Disc Convective Cooling

Computational predictions of airflow and convection heat transfer behaviour and results from experiments performed with the baseline brake disc are described in this Chapter. A convergence analysis is included to evaluate the influence of grid size on results. Once the appropriate grid is selected, two approaches of computational modelling are reviewed. Finally, results of CFD simulations are discussed. Average convective heat transfer coefficients from CFD and experiments were compared and discussed as well.

Table 5.1: Baseline standard brake disc characteristics

Vane number	30		
R_o	0.217 m (OD=434 mm)	D_h**	0.019 m
R_i	0.116 m (ID=232 mm)	l_v	0.095 m
z_{ff}	0.045 m	P_v	0.2097 m
h*	0.017 m	D_v	0.0667 m

*$h_v = h$, ** Mean hydraulic diameter

Complementary information of the brake disc is supplied in Table 5.1, in addition to that given in Section 4.1. Radii of 2.0 mm were set in the vane corners, therefore the available vane wall length is 4.0 mm less than the full vane length (l_v). CAD model simplified views are shown in Figure 5.1.

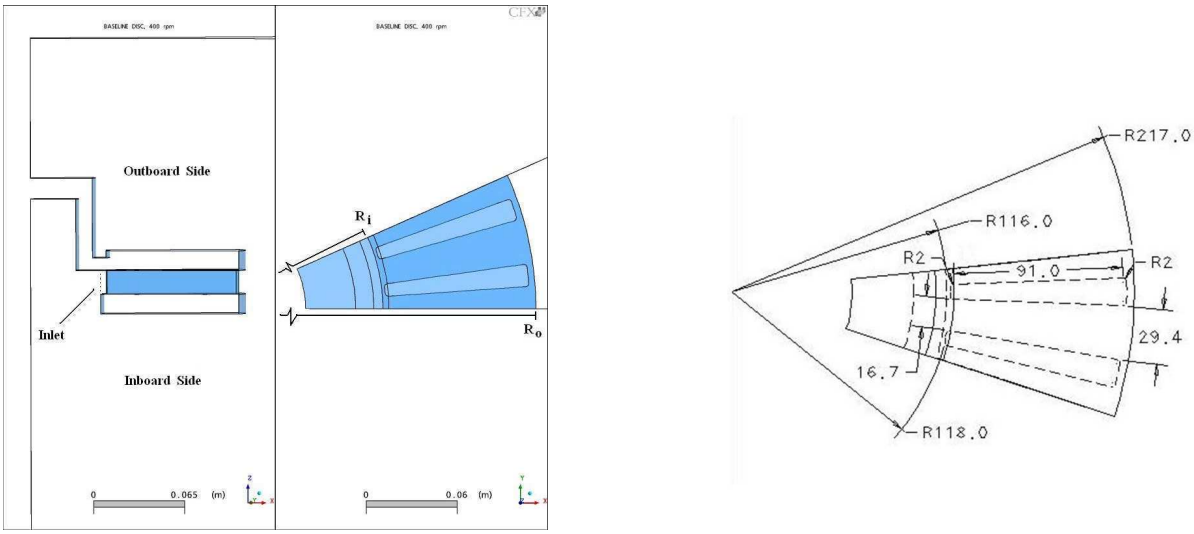

(a) Referencing. (b) Disc sector.

Figure 5.1: Simplified CAD model of the baseline disc.

5.1 Convergence Analysis

This section will explain the effect of the variables influencing the accuracy of the numerical solution. The discretisation of the differential equations modelling the flow dynamics, energy and turbulence carries a numerical error per se. This is the truncation error which results from truncation made to numerical series approximating the equations when the finite volume method is used.

An additional error comes from the differencing scheme used for approximating the convective terms in the Navier Stokes equations. The computational solver used has three schemes: The Upwind Differencing Scheme, the Numerical Advection Correction Scheme and the High Resolution Scheme (UDS, Specified Blend and HRS).

From the three above mentioned, the HRS is the one which provides more accurate solutions. The HRS does not violates boundedness status in the domain and allows dynamic selection of first or second order approaches to the differential equations as required by the physics of the problem. The Specified Blend method allows the user to set whether first, second or 'mixed' approximations are used to solve the equations. This method, as indicated in ANSYS-CFX Solver Theory (2005), should only be used where a definite behaviour of the flow is known beforehand, otherwise it may give non-physical solutions due to numerical dispersion.

The UDS, a first order accuracy method, weights the numerical terms according to the flow conditions in the upstream node; the values assigned to the integration points of the cell (downstream), are controlled by the upstream nodes. The UDS is very robust in the sense that it will not give non-physical solutions (numerically stable), provided the grid is aligned with the flow direction, (ANSYS-CFX Solver Theory 2005).

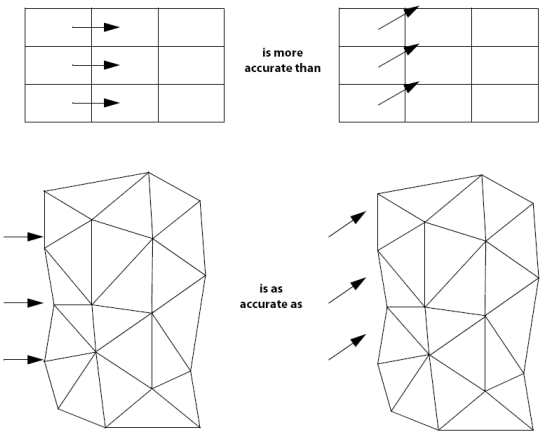

Figure 5.2: Mesh and flow alignment.

The main drawback of the UDS is that it can bring errors in the rate of flow transported quantities when the flow main direction is not aligned with the grid lines, as noted in ANSYS-CFX Solver Theory (2005) and Versteeg & Malalasekera (1995). Figure 5.2 shows four grids, of which only one has preferential direction of flow aligned with the grid direction. The highest accuracy is given for this grid (upper left) when UDS scheme is used. However, if UDS is used for the grid in the upper right of the figure, smearing diffusion errors will appear in the solution. On the other hand, when using tetrahedral meshes, there is not preferential direction to comply with and the error given by the UDS is consistent and uniform throughout the domain. Then, the accuracy level of the grids at the bottom is the same for both flow alignment. This leads to conclude that coarse hexahedral meshes working with UDS will not be able to accurately model recirculation regions in flows.

However, considering the robustness in solutions that UDS may give, the disadvantages above mentioned can be overcome by working toward a grid independent solution (convergence analysis) in those regions where high gradients are expected. This means that if refined hexahedral meshes are located in high gradient or recirculation regions, high stable solutions could be achieved.

The UDS was adopted throughout the simulations of this research, after doing a convergence

analysis of the flow characteristics within the channel of the baseline model brake disc. This convergence analysis is next described.

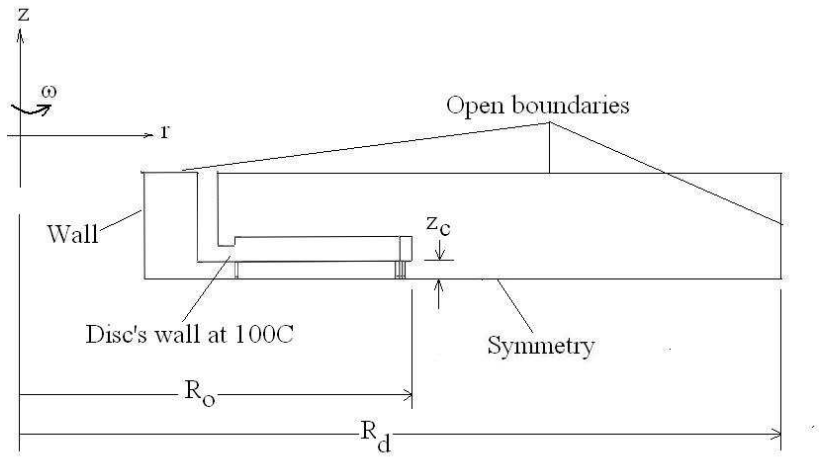

Figure 5.3: Schematic of CFD model for convergence analysis, see Table 5.1, $z_c = h/2$.

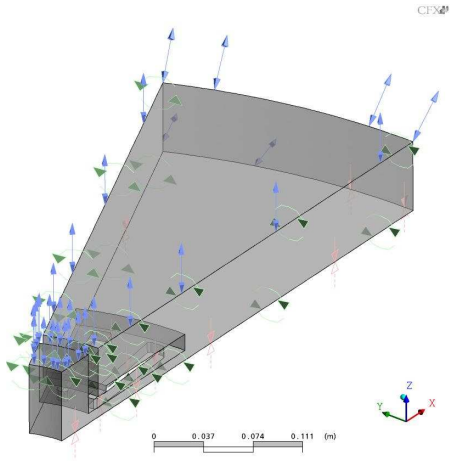

Figure 5.4: Visualization of CFD model used for convergence analysis.

A simplified CFD model of the disc was constructed (Figure 5.3). Only a half of the ventilated disc was modelled using symmetry conditions. The hub of the disc was discarded and instead an open boundary condition was placed avoiding 'starvation' of air at the inlet of the channel. The shaft's wall (adiabatic, smooth) served as inner boundary of the domain and the radial extension of the outermost boundary was located as indicated in Section 3.1.6.

The rotating speed assumed is 600 rpm, an intermediate speed within the angular velocity range of interest, and the turbulent model $\kappa - \epsilon$ was employed. A constant disc wall temperature of 100^{o}C was assumed and the option for heat transfer coefficient calculation was

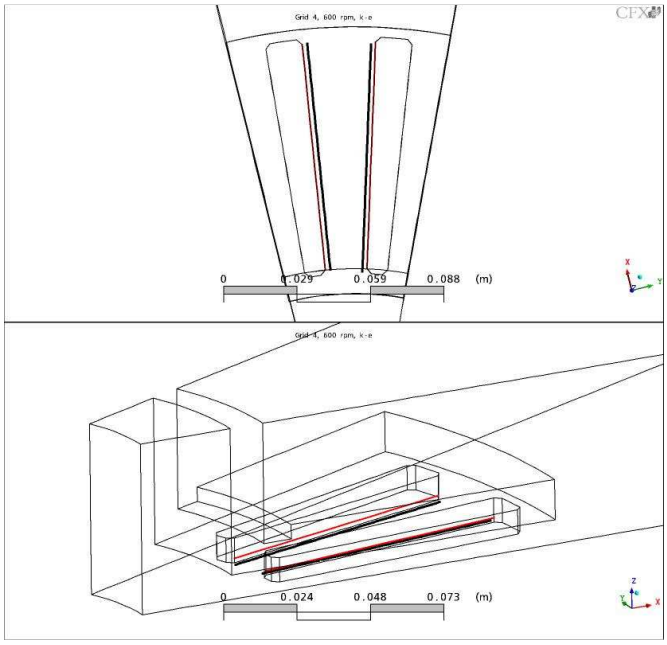

Figure 5.5: Location of lines for postprocessing of data during convergence analysis.

set as $\Theta_{nw} = \Theta_{\infty}$ =20^{o}C, (see page 61 for further details on this). The CFD model used periodic boundary conditions as described in Figure 3.18.

The analysis looked into the consistency of the mean flow characteristics 2 mm away from the vane wall (Figure 5.5). Speed and temperature were retrieved in 50 points distributed along a 91 mm path parallel to vane walls and four models were constructed with different grids

The first model (Figure 5.6) used a tetrahedral mesh with average side length of c =4 mm. No boundary layer was modelled. The second grid model was constructed using hexahedrals having the same average cell side length (Figure 5.7).

The third grid model features fine mesh near the vane walls. In this region four cells (0.5 mm constant width) were used to model the flow near the wall, as seen in Figure 5.8. The fourth model has a finer variable width mesh near the vane surface (constant growth ratio of 1.2), using 9 cells to fill a normal-to-wall length of 2.07 mm. This mesh is shown in Figure 5.9. As noted in these Figures, the line of data retrieval lies in the middle of the near wall cell in models 1 and 2, while for models 3 and 4 it lies at the at the perimeter of the fine mesh.

The models were all run using UDS and the root mean square numerical error was set to RMS=1x10^{-5}. The pseudotime step was chosen as $\Delta\tau_{\omega}$ =1.125x10^{-3}, which is less than that given by expression in page 79. These numerical settings ensure that the convergence error

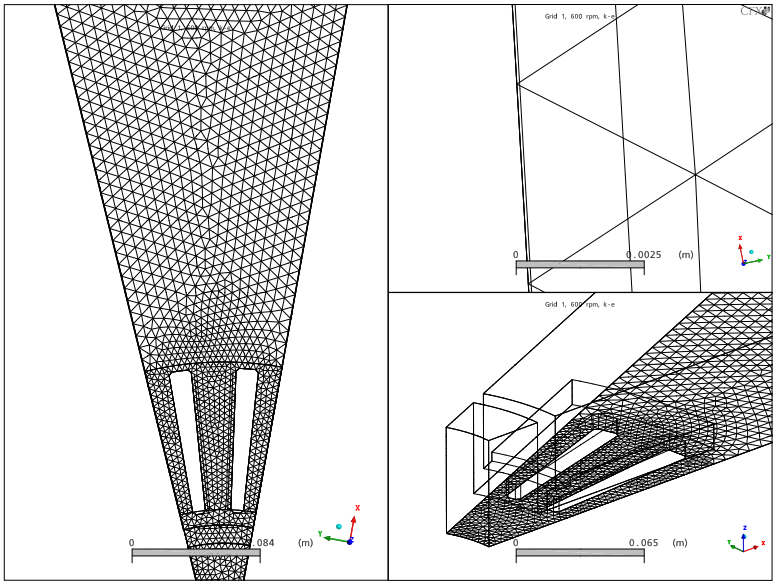

Figure 5.6: Computational grid for first model of convergence analysis. Tetrahedral grid, c =4 mm

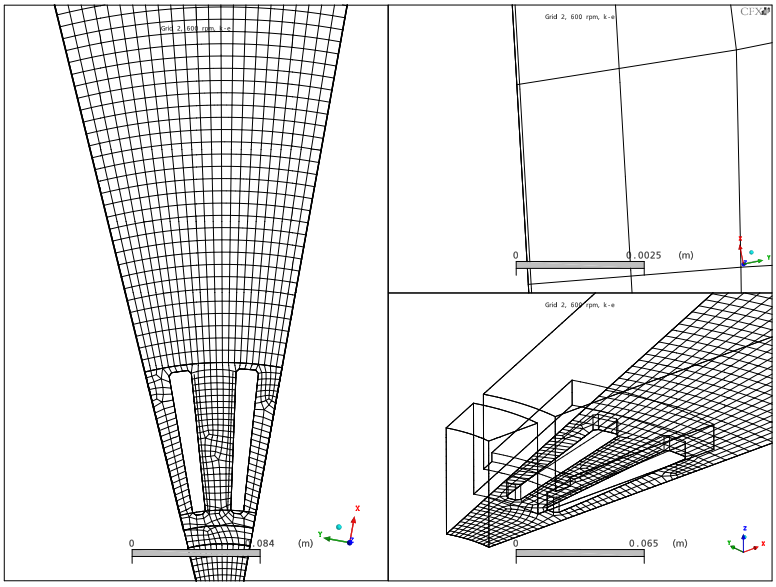

Figure 5.7: Computational grid for second model of convergence analysis. Hexahedral grid, c =4 mm

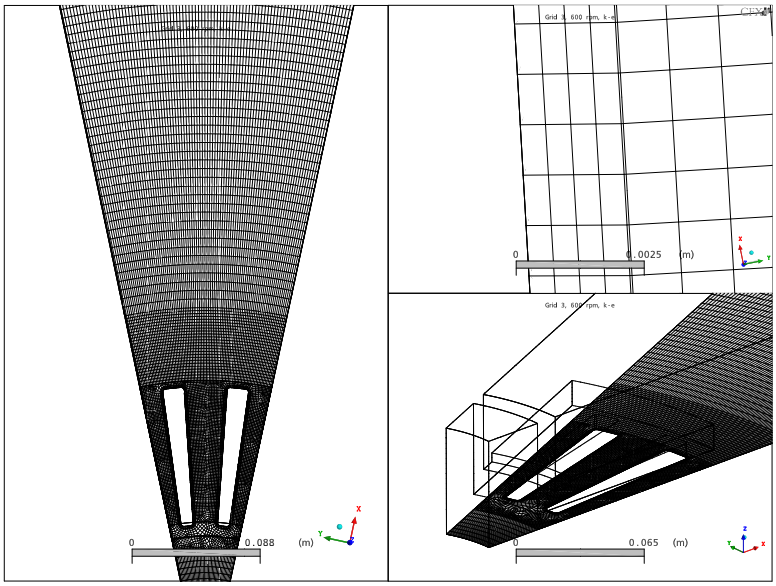

Figure 5.8: Computational grid for third model of convergence analysis. Grid composed by hexahedrals, four cells near the wall separated c =0.5 mm, elsewhere c =2 mm.

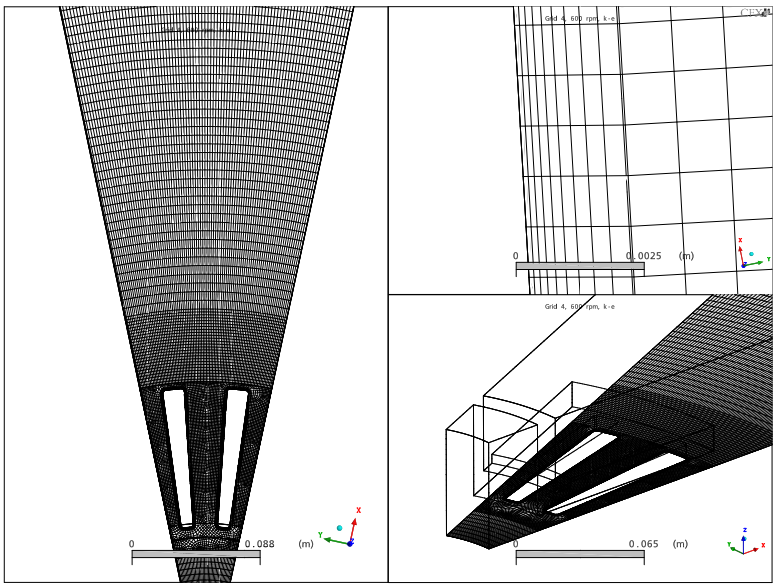

Figure 5.9: Computational grid for fourth model of convergence analysis. Grid near the wall is refined with 9 cells covering 2.07 mm, with variable width (constant inflation ratio of 1.2), elsewhere c =2 mm

Table 5.2: Models statistics (Convergence analysis)

Grid	Grid type	Cells	Nodes	c/h	CPU time [sec]
1	Tetras	76447	16242	0.23	2827
2	Hexas	18123	21612	0.23	1329
3	Hexas	325368	352146	0.03	20290
4	Hexas	395674	425579	$5.8\text{x}10^{-3}$, 0.025*	22170

*Near the vane wall, 2 mm away of it.

(see page 45) is the same for all the grids (same *numerical convergence* quality, but not same accuracy), which implies that the difference between results will be driven by truncation and numerical diffusion (if any) errors solely. The truncation errors depends exclusively upon the mesh size (the smaller this, the less the error), while the diffusion error upon the alignment of the flow with the grid lines, however it is expected that this will be reduced as the mesh is refined in regions of high gradients.

The models were let to run until the target RMS value of the residuals was achieved. The statistics of the four models are shown in Table 5.2, where the ratio of the cells side length at 2 mm away from the vane wall and the CPU time taken to solve are shown [1].

The comparison of convergence analysis data is shown in Figures 5.10 and 5.11. Figure 5.10 shows the variation of absolute (in stationary frame) mean $\overline{u_x}$ along the vane length on the leading and trailing sides of the channel. Speed in the leading side of the channel (Figure 5.10(a)) converges gradually with mesh change and refinement, from 'radially positive' values (without recirculation) to a 'stable' pattern of recirculation given by grids 3 and 4 (backward flow about the inner radius of the disc). This behaviour is the one expected in the leading side of diverging channels as experimentally demonstrated by Johnson *et al* (2003).

The convergence behaviour on the trailing side of the channel (pressure side) shows fluctuating behaviour with mesh change. A downward fluctuation (speed reduction) is observed when the first grid (tetrahedral) changes to mesh 2 (coarse hexahedrons), while finer mesh stabilises the final value nearer to what was predicted with the mesh 1.

Convergence for air temperature (Figure 5.11) shows significant fluctuations with the first two meshes in both sides of the channel. Interestingly, although tetrahedral mesh first predicts high speed in the leading side it also predicts high temperature gain which drastically falls 25^oC when the model mesh changes to coarse hexahedrons (for a lower speed). Finally meshes 3 and 4 predict a closer match. In the trailing side (Figure 5.11(b)), coarse hexahedrons

[1] CPU time is the time used exclusively to solve the problem, unlike wall clock time which is larger

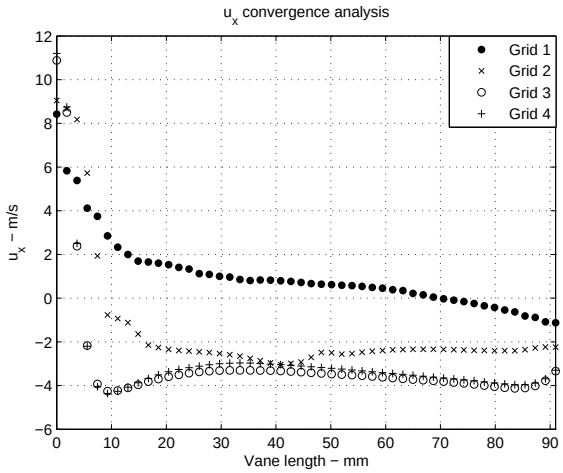

(a) Channel leading side.

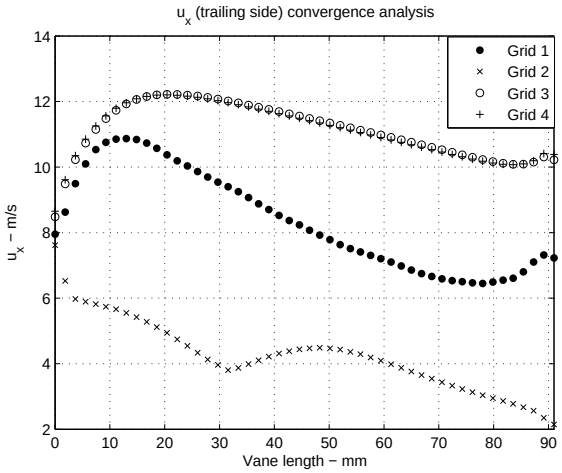

(b) Channel trailing side

Figure 5.10: Numerical convergence of $\overline{u_x}$ using grids 1 to 4.

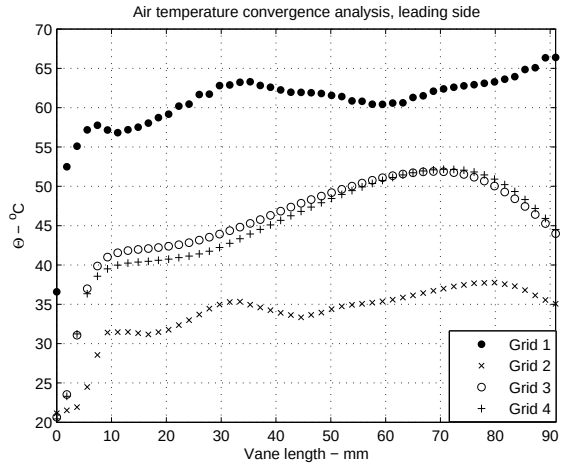

(a) Channel leading side.

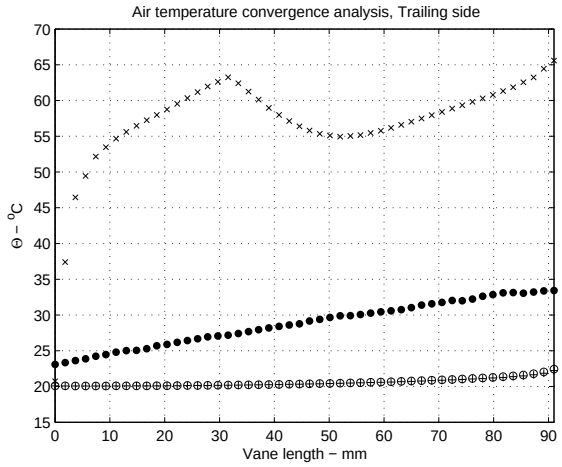

(b) Channel trailing side

Figure 5.11: Convergence analysis of $\overline{\Theta}$ using grids 1 to 4.

results in high temperature due to the badly predicted speeds, while tetrahedral mesh is closer to numerical converged values.

The above variables are primarily calculated by the solver (temperature is proportional to entalphy, which is calculated first). However, convective heat transfer coefficient is a derived quantity which depends upon the above ones and on the wall function used. To review its convergence, a couple of lines were located on the vane walls, in their centre positions (symmetry boundary), and local values of convective heat transfer coefficients were retrieved and compared in the same fashion as carried out with $\overline{u_x}$ and $\overline{\Theta}$.

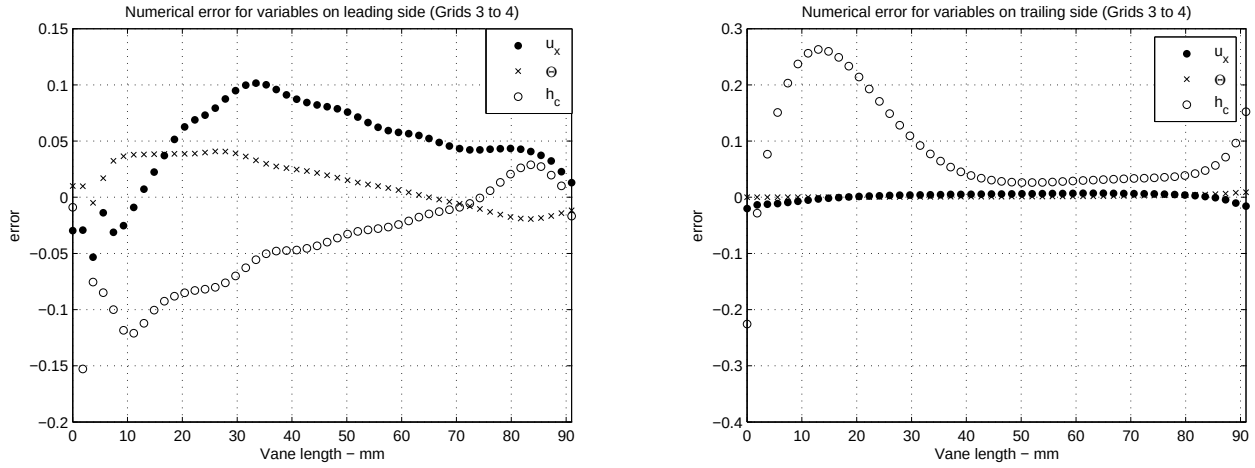

(a) Channel leading side.

(b) Channel trailing side

Figure 5.12: Convergence error on channel leading side between refined meshes 3 and 4.

For the sake of brevity, convergence errors (formula 5.1) for $\overline{u_x}$, $\overline{\Theta}$ and h_c between grids 3 and 4 are shown in Figure 5.12. The largest errors between these grids in the channel leading side are for the local heat transfer coefficient, reaching a maximum of 13% in the first quarter of the vane lenght. This is followed by a peak error of nearly 10% for speed and 4% error for temperature.

$$e_\phi = \frac{\phi^{old} - \phi^{new}}{\phi^{old}} \tag{5.1}$$

In the trailing side of the channel, Figure 5.12(b), $\overline{u_x}$ and $\overline{\Theta}$ show almost perfect convergence between grids 3 and 4 (error drops near to zero). However, this does not occur with the local heat transfer coefficient values, which show a significant error (more than 20%) in the first

half of the vane leading side. Afterwards, the difference in h_c is very close to zero, which means that just one half of the mesh inside the channel gives converged values.

Table 5.3: Models statistics for Grid 5

Grid #	Grid type	Cells	Nodes	c/h	CPU time [sec]
4	Hexas	395674	425579	$5.8\text{x}10^{-3}$; 0.025*	22170
5	Hexas	401680	432544	$5.8\text{x}10^{-3}$; 0.025*	41290

*Near the wall; 2 mm away.

The significant differences in h_c results between grids 3 and 4 only mean that grid 3 is not accurate enough the reproduce the same local heat transfer coefficients when a refinement on the mesh is done. This opens the question as to whether grid 4 is accurate enough to reproduce the same results if a further refinement is performed. The refinement was carried out and a new CFD model was constructed (Grid 5). The only difference with Grid 4 is that the thickness of fine mesh near the wall is increased from 2.07 mm to 3.2 mm, keeping constant the inflation ratio of the grid. The characteristics of the new CFD model are described in Table 5.3.

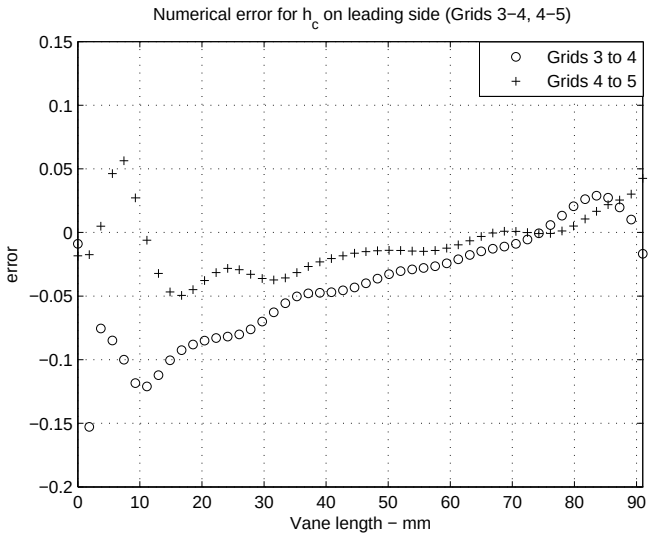

Figure 5.13: Final convergence error on channel leading wall (vane trailing wall) side for h_c.

The new model has 1.63% more nodes than grid 4, however the CPU time has nearly doubled. Convective heat transfer coefficients from grid 5 were retrieved and compared against those

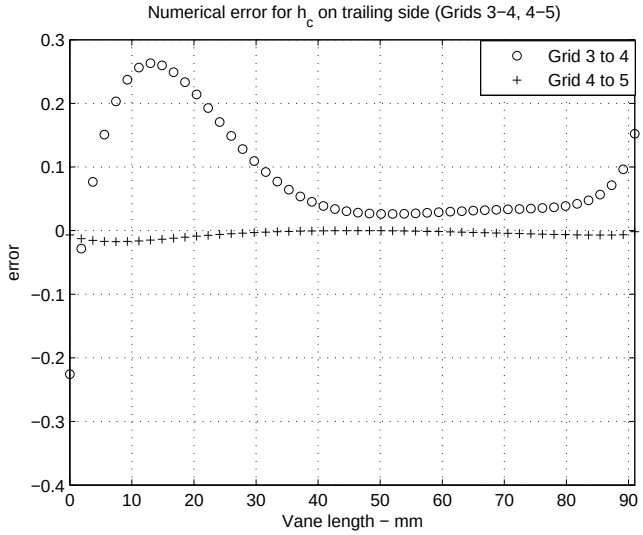

Figure 5.14: Final convergence error on channel trailing wall (vane leading wall) side for h_c.

given by grid 4. The relative error was computed with formula 5.1 and is shown in Figures 5.13 and 5.14.

The results on Figure 5.13 show a reduction in the convergence error between grids 4 and 5 in the leading side of the channel. The maximum difference (nearly 10%) that existed between grids 3 and 4 (circled path), was reduced to 5% maximum in the inlet portion of the leading side of the channel. Afterwards, the convergence error falls close to zero. The behaviour in the trailing side of channel (leading wall of the vane) is better (Figure 5.14). The maximum difference existing between grids 3 and 4 (above 20%) is reduced to nearly zero difference between grids 4 and 5 throughout this side of the vane wall.

The above results indicate that grid 4 is stable and it provides results within the rotating channel which are in a good degree independent of grid refinement (Grid 5). Obviously the most refined mesh, grid 5, is likely to be much more stable, but the accuracy gained is overcome by the tremendous increment in computing time required (see Table 5.3).

Therefore, although a small resilient numerical uncertainty is likely possible on the first quarter of the channel leading side (vane trailing side); the numerical reliability on the trailing side of the channel (vane leading wall) is very good for grid 4. This assures that the highest speeds, gradients, heat transfer coefficients and likeliness of turbulence occurring in this side of the channel will be acceptably predicted by the CFD software. Then, the characteristic grid type selected for the simulations performed in this research is grid 4.

As explained in Table 5.2, grid 4 is a hexahedral based mesh with 9 refined cells near the

channel surfaces. The inflation ratio of this cells is γ=1.2 and the normal (to wall) width of the first cell is c=0.1 mm. Therefore, the subsequent 8 cells have a variable width given by formula 5.2.

$$c_j = c_{j-1} * \gamma \tag{5.2}$$

The above refinement characteristics were employed for those regions near the surfaces of the brake discs, however, regions where the edge of the vane was aligned with the disc ends where difficult to mesh and refinement was sacrificed accordingly.

5.2 Computational Flow and Heat Transfer Modelling

In this Section the procedures developed for computational prediction of brake disc convective heat transfer coefficients and flow characteristics as function of rotational speeds are described. In addition to the modelling strategy described in Section 3.1.6, a simpler approach which aimed to reduce the overall process time is explained. General characteristics of the flow pattern around a brake disc rotating in still air are as follows:

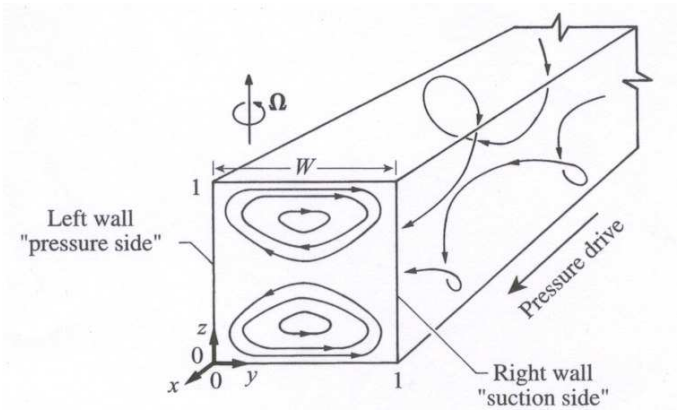

Figure 5.15: Secondary flow patterns in rotating channels.

1. Viscous friction in the air near to surfaces produces flow radially outwards due to the angular velocity of the disc.

2. An axial inward flow is generated to replace the air being expelled by centrifugal effects of the friction faces (mass continuity).

3. Likewise, the suction generated in the channels draws air from the near surroundings toward them.

4. The behaviour of the air inside the rotating channel depends upon the channel design, but in general it can be assumed that an initial acceleration is imposed to it during the first quarter of the channel and after its radial velocity falls due to static pressure build up. The jetflow exiting the channel will have circumferential and radial components (which also exist within the channel), this is known as swirling jets.

5. Flow patterns develop in circumferential direction, these are known as secondary (Coriolis) flows and they may enhance mixing in the channel (see Figures 2.18 and 5.15).

6. In brake discs with radial vanes, a misalignment of these with the entrant flow produces a recirculation flow (suction) region in the channel leading side and a high pressure region in the trailing side of the channel. See also Johnson *et al* (2003).

7. The mass flow, inlet air speed conditions and channel drag (pumping losses) depend upon the rotational speed of the brake disc.

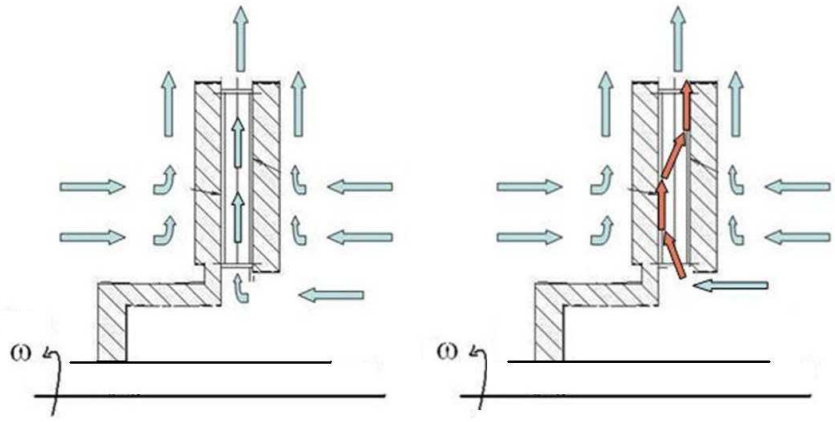

Figure 5.16: Airflow pattern in a rotating ventilated brake disc. Ideal (left) and CFD predicted (right) patterns.

From above explained, a rough simplification of the flow behaviour around the disc and inside the channel is depicted in Figure 5.16, where disregarding swirling and Coriolis effects inside the channel, the flow could be assumed as planar (radial direction). This could lead to try modelling only the channel, disregarding the rest of the geometry and angular speed. Approximate conditions near the inlet would aim to reproduce the rotating channel behaviour at a lower computing cost as is described below.

5.2.1 Stationary CFD Model

In an attempt to reduce computing time and modelling complexity a stationary channel model was created for the baseline disc channel. This disregards the friction surfaces, outer and inner rings, hat section and shaft and its domain (size) was selected from a periodic brake disc sector. The characteristics of the geometry are given by the channel main dimensions (Table 5.1), and the outer radial boundary locates as specified in Section 3.1.6 for CFD modelling.

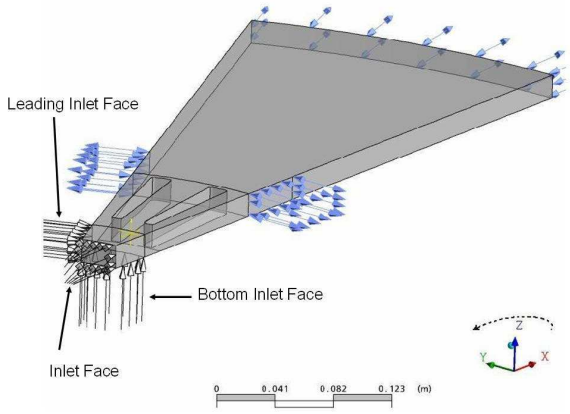

Figure 5.17: Stationary channel CFD model (no angular speed).

Three inlet boundaries have been set in the CFD model of the stationary channel model in order to reproduce as much as possible the real conditions of the rotating channel. These boundaries are depicted in Figure 5.17, and are identified as *Leading, Inlet and Bottom Inlet Faces*. The velocity conditions at those faces were retrieved from the results of a simulation of the standard baseline brake disc using periodic boundary conditions and RFR. The grid characteristics of the model followed those determined by the convergence analysis and the angular speed to model was n=100rpm. The boundary conditions of this model are: non-slip condition at channel walls, inlet normal velocities (u_n) at Leading, Inlet and Bottom faces, and open boundaries with zero relative pressure at the outermost radius of the domain and at two portions of the sides. Uniform temperature (100^oC) was prescribed for the vanes and channel endwalls. The normal velocities used as inlet conditions are shown in Table 5.4. The environment temperature was Θ_∞=20^{o}C, and this was also set as the reference level for wall convection heat transfer coefficients.

The test cases for the stationary channel are described in Table 5.4. Four in total, two of which used one face for u_n and the others considered 'multi-supplies' of air at three inlet faces (extracted from a simulation performed using a full RFR model and $\kappa - \epsilon$ turbulence model). The results from the above mentioned cases were compared against those given by

Table 5.4: Velocity conditions at inlet faces of stationary channel CFD model*.

Case	u_n at inlet boundary faces		
	Inlet Face	Leading Face	Bottom Face
1L	2.15	0.0**	0.0
1T	2.15	0.0	0.0
2L	2.15	0.1	0.24
2T	2.15	0.1	0.24

*Conditions aiming to model 100 rpm

**This condition was replaced with a non-slip wall

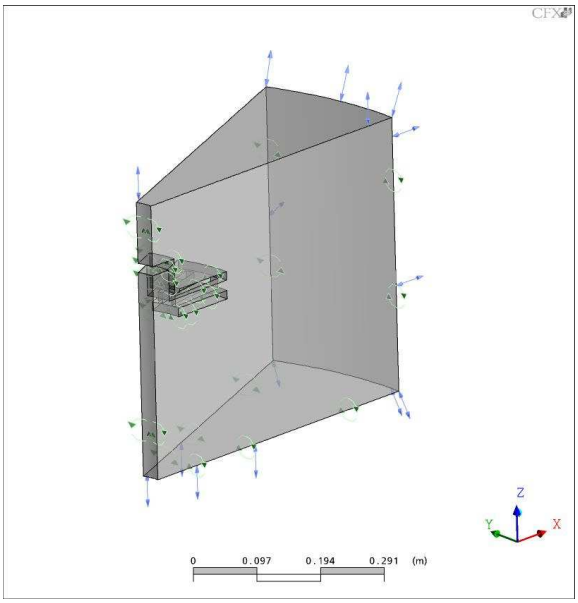

Figure 5.18: Periodic CFD model of baseline brake disc in rotating frame of reference (RFR).

a full RFR CFD model, described next.

5.2.2 Rotating Frame of Reference CFD Model

The second modelling technique chosen is the already described RFR method (Chapter 3). The disc rotates about z axis (as in all the RFR simulations in this work).

The same boundary conditions for angular speed and temperatures were assumed (Θ_∞=20^{o}C was used as reference level for heat transfer coefficient calculation, see equation 3.75); in addition periodic and open boundaries were set as shown in Figure 5.18. The model was run using laminar and turbulent flow models ($\kappa - \epsilon$).

The following Section shows a comparative analysis between the results from the RFR CFD model and the results from the stationary CFD model.

5.2.3 Comparison of Results: Stationary vs RFR Models

The data for comparison was selected as the radial absolute airspeed through the center of the channel and the channel average heat transfer coefficient. The area averaged heat transfer coefficients are calculated by ANSYS-CFX as:

$$\overline{h_{ch}} = \frac{1}{A}\int h dA \tag{5.3}$$

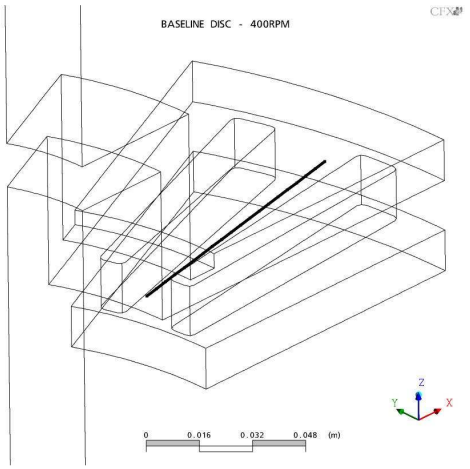

Figure 5.19: Line for airspeed postprocessing (stationary and RFR models).

Airspeed was retrieved over a line across the channel centre (see Figure 5.19). The line spans over 91 mm and speed was read over 20 locations, spaced 4.8 mm. The comparison of radial velocity component at the centre of the channel is shown in Figure 5.20. Assuming the results from RFR simulation as base, it is seen that only on a small portion of the channel inlet is correlated by the case 1L, the rest of the RFR trend and cases show poor correlation. Besides, the drop of velocity in all the stationary channel cases is much less than the one existing in the RFR model. This could imply that there is less friction wall-air in the stationary than in the RFR model. Further implications would be also: as a result of different friction the heat transfer coefficient distribution would also be different between models and, the results obtained from the stationary CFD model (velocity or pressure drop) will not be able to predict the aerodynamic resistance (pumping losses) in a rotating disc. The first of these implications can be seen in Figure 5.21, which shows the convection heat

transfer coefficient distribution for the 1L (stationary channel) case on its right side and the convection heat transfer coefficient for the RFR case in its left hand side.

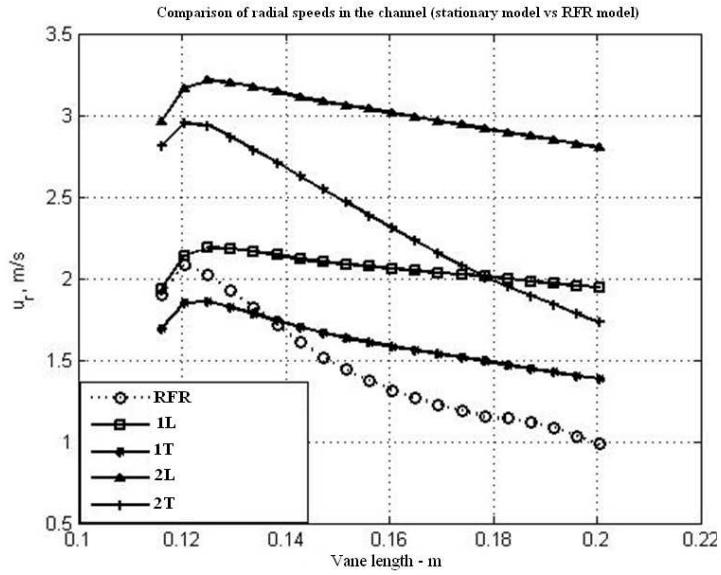

Figure 5.20: Radial airspeed results predicted by the stationary CFD model compared with RFR results for baseline brake disc at 100 rpm.

The main difference is the lack of ability of the stationary model to predict the side-oriented heat transfer coefficient distribution given by the RFR model.

Table 5.5: Comparison of average heat transfer coefficients: Stationary vs RFR models

	RFR (Lam)	RFR ($\kappa - \epsilon$)	1L	1T	2L	2T
W/m^{2}K	13.0	13.5	12.9	9.0	16.4	12.1
Diff.	-	3.8%	-0.8%	-30.7%	+26.1%	-6.9%

The channel average heat transfer coefficients of the simulations performed in the stationary CFD model cases are reported against that given by the turbulent case of the RFR model in Table 5.5 (the laminar flow simulation gave very skewed heat transfer coefficient distribution, with very large values at the inlet of the vane. This was not observed in the turbulent results.

From results in Figures 5.20 and 5.21, it can be concluded that the stationary channel model does not accurately model the behaviour of the rotating channel, not even when multiple supplies of air are used as boundary conditions. This despite that averaged heat transfer

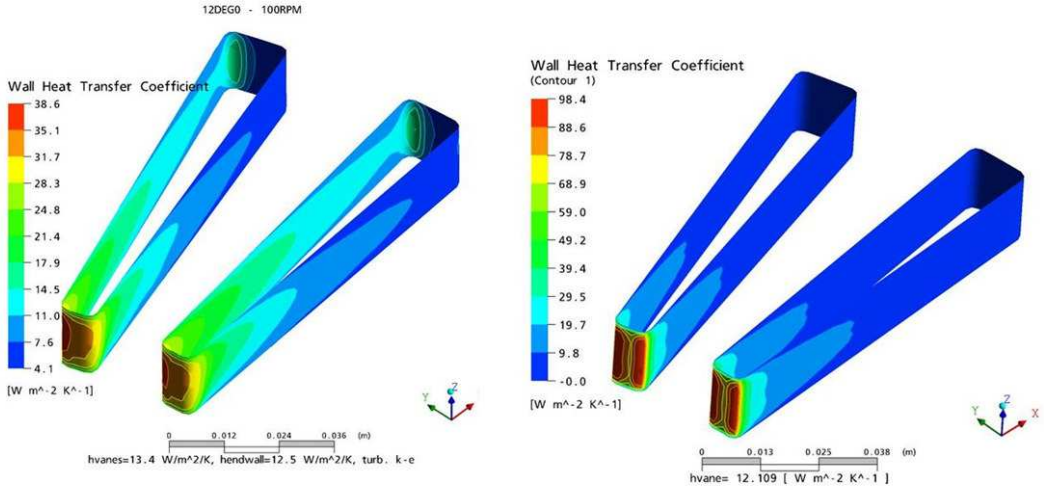

Figure 5.21: Heat transfer coefficients in the RFR and stationary CFD models, n=100 rpm.

coefficients may result in similar values to that given by the RFR model. Also, a drawback of this is that a correlation must be found to guess the velocity field at the inlets as function of angular speed and channel geometry. For these reasons the use of the stationary channel model was discontinued in the research and the CFD models were constructed using Rotating Frames of References.

5.2.4 Characteristics of the Baseline Disc CFD Model

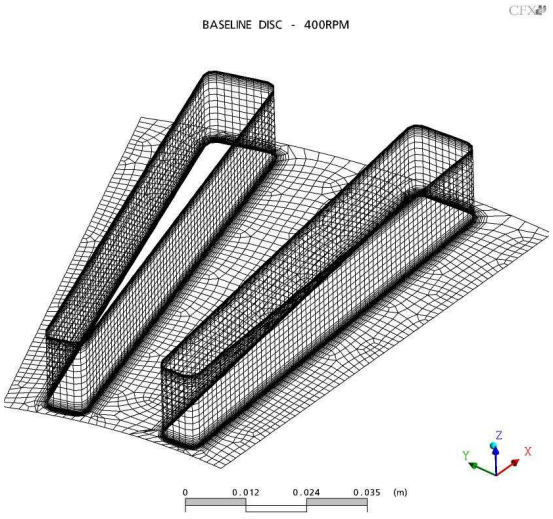

Figure 5.22: Mesh details in the channel region of the baseline model.

Details of the mesh used in the baseline periodic model are shown in Figures 5.22 and 5.23. Near the channel wall, 9 smalls cells were allocated, the first off the wall has a normal to wall length of 0.1 mm and the following 8 develop a length based on an inflation ratio of 1.2. The mesh modelling the flow core inside the channel had an average side length of 1.5 and they were hexahedrals. The model has 775978 cells and 822527 nodes, for which the geometry was first sectioned, boundary mesh set and finally volume mesh implemented (in Gambit).

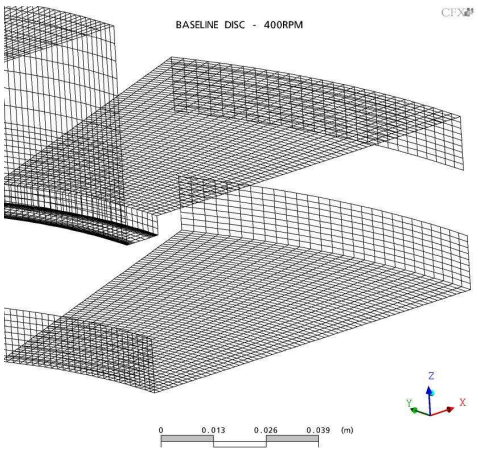

Figure 5.23: Mesh details in the external surfaces of the baseline model.

The mesh used for the rest of the disc surface is shown in Figure 5.23. The grid refinement normal to these walls is as above described (except near the hub). Over the friction faces, the mesh size in circumferential direction was increased from 1.5mm to 2.5mm aiming to save computing time. Finally, Figure 5.24 shows the details of the grid used on the Periodic Face. Fine mesh was used near the disc surfaces and coarse mesh was used elsewhere where the flow gradients are not significant.

The CFD model above described was run for the following angular speeds: 100 rpm, 200 rpm, 400 rpm, 600 rpm and 800 rpm. The remaining boundary conditions are described in page 75. Rotational Reynolds number calculated using disc outer radius have already been shown in Figure 3.15. Re_ω did not change in the research, since the disc outer radius remained constant.

It has been discussed that if the brake disc were not ventilated, angular speeds from 100 to 600 rpm would generate laminar flow fields; nevertheless, flow fields within rotating channels of a ventilated brake disc is likely to experience turbulent behaviour mainly due to the initial misalignment of the vanes with the entrant flow, which constitutes a discontinuity in the flow path. Therefore, the computational fluid dynamics simulations considered turbulent behaviour. The CFD simulations were solved in Ansys-CFX release 10, in serial mode using

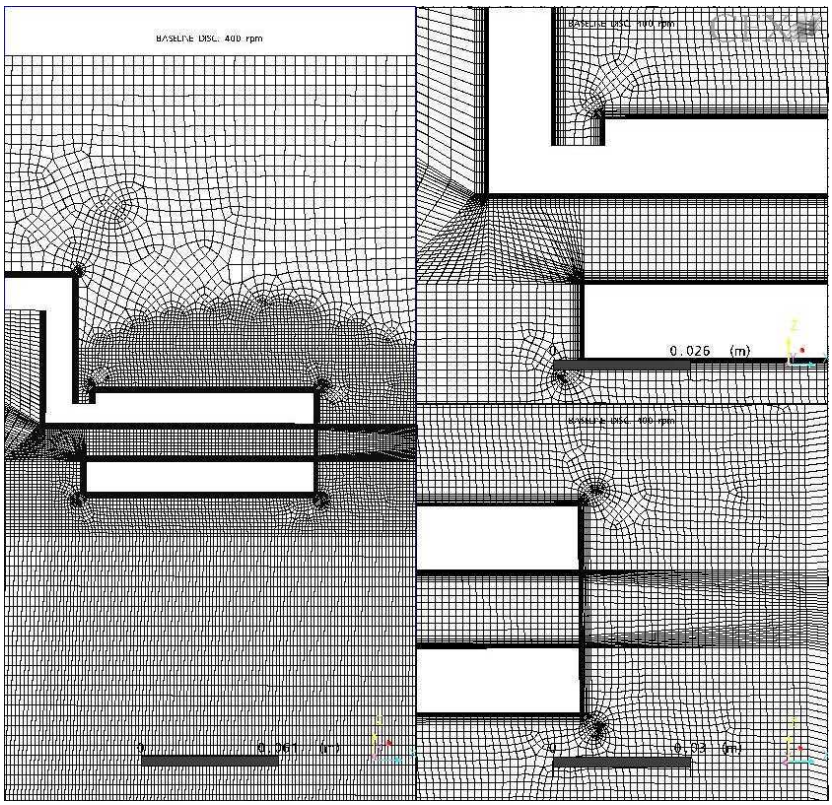

Figure 5.24: Details of the mesh on the cut face (PF) of the baseline model.

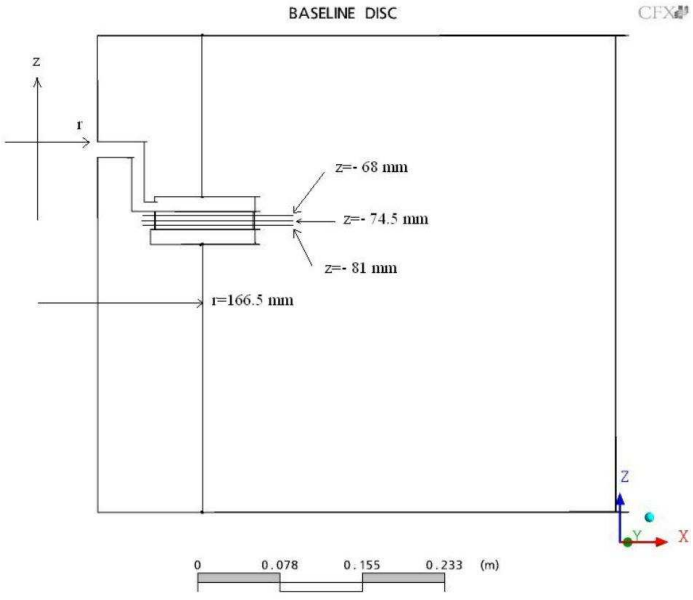

Figure 5.25: Locations of lines for CFD data postprocessing.

the High Performance Computing facilities of Cranfield University. Solution process used results files from lower speeds. The solution process statistics are shown in Table 5.6.

Table 5.6: Solution parameters and CPU times, baseline CFD RFR model.

ω [rad/s]	$\Delta\tau$ [sec]	CPU time [sec]
10.47	0.009	$1.401\text{x}10^{5}$
20.94	0.0045	$1.409\text{x}10^{5}$
41.89	$2.25\text{x}10^{-3}$	$7.736\text{x}10^{4}$
62.83	$1.125\text{x}10^{-3}$	$9.847\text{x}10^{4}$
83.78	$0.5625\text{x}10^{-3}$	$1.305\text{x}10^{5}$

Finally, to asses the size of the domain, Figure 5.26(a) shows the axial (z direction) speed gradients at n=400rpm. The axial ends of the domain (above and beneath the friction faces) are represented by the left vertical axis, and the right hand side of the graph indicates the outboard and inboard side friction faces (see Figure 5.25). Very small axial speed gradients occurs in the left side axis, which means that the CFD domain axial length provides sufficient space for air behaviour during suction. The highest gradients are on the inboard side friction face, since channel inlets are located in this side, making suction larger. The actual values of speed are shown in Figure 5.26(b).

5.3 Experimental Convective Cooling Results

Experimental results of the baseline brake disc prototypes (original and DVB, aluminum vanes) are shown in this Section. Logged (temperature history) and derived results (heat transfer coefficients) are presented with uncertainties considered. Validation of computational against experimental data is also shown.

5.3.1 Tests Conditions

The tests were carried out using a cast iron standard brake disc and the detachable vane brake disc model (see Chapter 4). The discs were heated using a heater box (and induction heating in the latter stages) and spun at different rotational speeds. The test plan is included in Appendix A. The experimental set-up details for the tests have already been described in page 98.

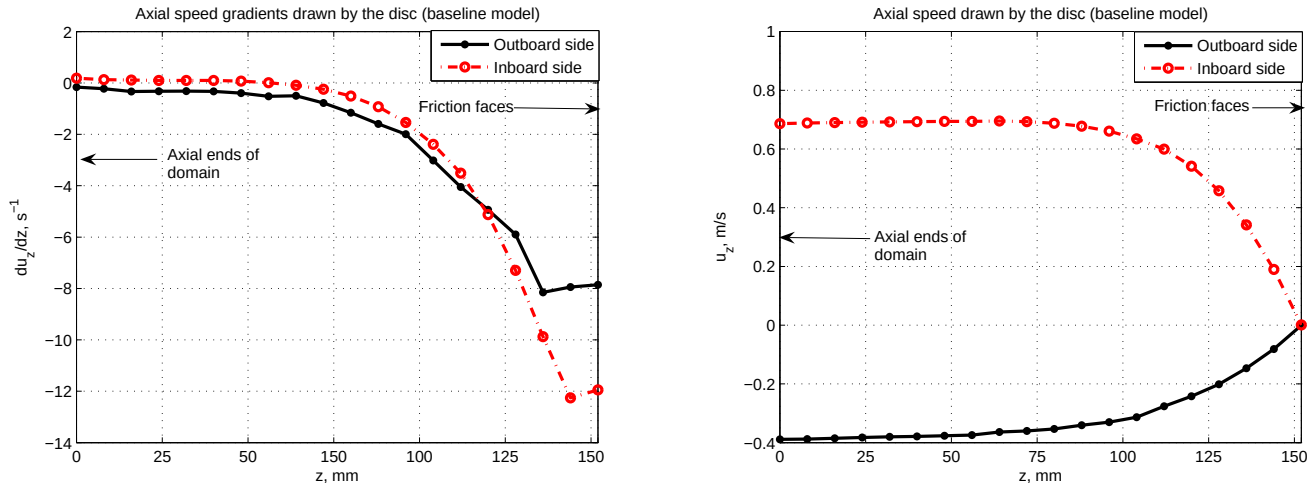

(a) u_z gradient. (b) u_z.

Figure 5.26: Suction effects on air due to brake rotation.

Figures 5.27 shows the brake discs used for testing. As described before, four rubbing thermocouples were located on the brake disc surface, two more were located near the vents inlet and outlet, one more was located away from the disc in order to record ambient temperature during the tests. It was also necessary to monitor the bearing box temperature while tests were run in order to prevent that bearings were damaged by excessive heating caused by prolonged shaft rotation.

The brake discs were heated following the steps described in Section 4. Although the heater box provided a lengthy way of heating the brake disc, it also ensured that uniform temperature levels were reached as consequence of long time exposition to heat source.

5.3.2 Recording of Cooling Temperatures

Temperature logging at 2 samples per second was carried once the disc reached a relevant temperature. Because most of the experiments used the heater box as heating source, reaching testing temperatures above 150^{o}C was difficult since the process of removing the box and positioning the thermocouples implied heat losses due to natural convection. Therefore, an effective *initial* temperature was selected as 120^{o}C in these cases.

The temperatures from the thermocouples on the friction surface of the disc were arithmetically averaged and plotted as in Figure 5.28. The results of the natural convection test are

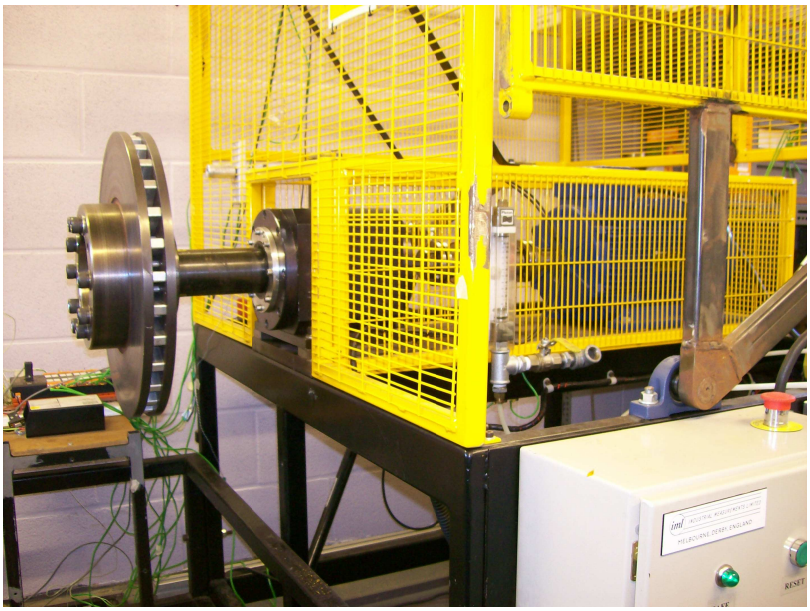

Figure 5.27: Detachable vane brake disc mounted on Spin Rig.

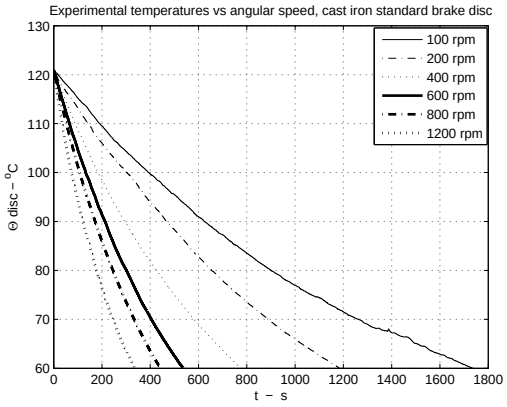

(a) Cooling history, CI disc.

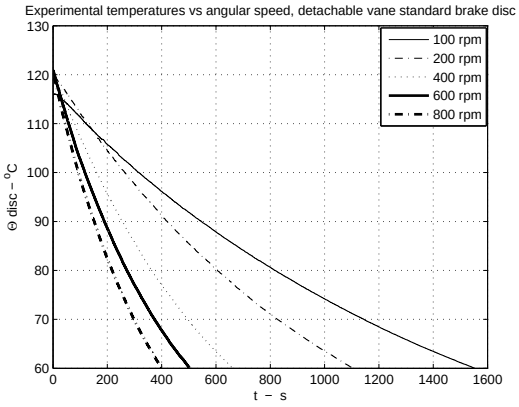

(b) Cooling history, DVB.

Figure 5.28: Experimental cooling history, baseline (30 vanes) standard brake disc.

shown in Figure B.1. The uncertainty of these averaged results is considered to be the same as the thermocouple uncertainty (see page 100). Logarithmic scale plotting of the above results follows a straight line (constant cooling rate) and therefore ensures the feasibility of the procedure for heat transfer coefficients reduction used in the next subsection.

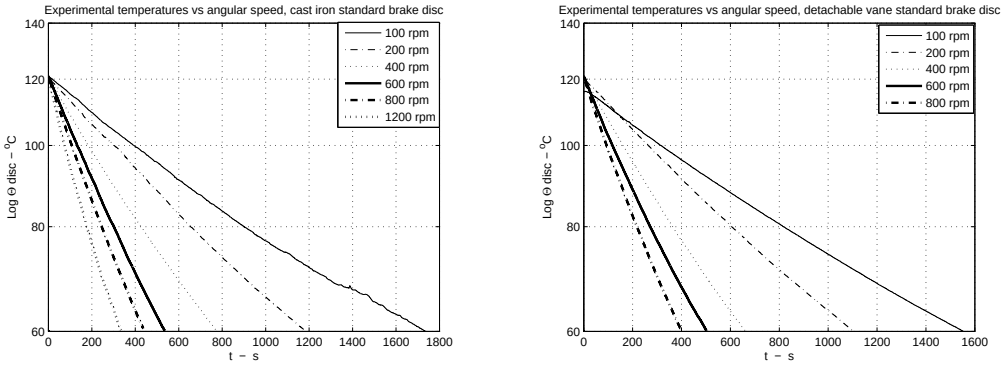

(a) Cooling history, CI disc.

(b) Cooling history, DVB.

Figure 5.29: Logarithmic plots of experimental results using the baseline (30 vanes) standard brake disc.

5.3.3 Total and Convective Heat Transfer Coefficients

Total, radiation and convection heat transfer coefficients are calculated using equation 4.19 for cast iron brake disc, 4.23 for detachable vane brake disc and equation 4.21 in both cases to determine the contribution of radiation and calculate the final average convection heat transfer coefficients. The characteristics of the discs used for testing are shown in Tables 5.7 and 5.8.

Table 5.7: Characteristics of the cast iron brake disc used in the tests.

Mass [kg]			A_w [m^2]			A_r [m^2]
⇑Hub *	⇓ Hub	Vanes	⇑Hub	⇓ Hub	Channels	
30.40	25.69	4.9	0.6181	0.5324	0.2647	0.3179

*⇑: With; ⇓: Without

The first set of raw data and the results is presented in Tables B.1 and B.2 for tests with cast iron brake disc considering a temperature range from 120^{o}C to 60^{o}C. Although the results

Table 5.8: Characteristics of the DVB (aluminum vanes; bolts mass included as cast iron).

Mass ⇑Hub [kg]		Mass ⇓Hub [kg]		A_w [m^2]			A_r [m^2]	
Cast Iron	Al	Cast Iron	Al	⇑Hub	⇓ Hub	Channels	⇑Hub	⇓ Hub
25.92	1.43	21.207	1.43	0.6181	0.5324	0.2647	0.3179	0.2538

*⇑: With; ⇓: Without

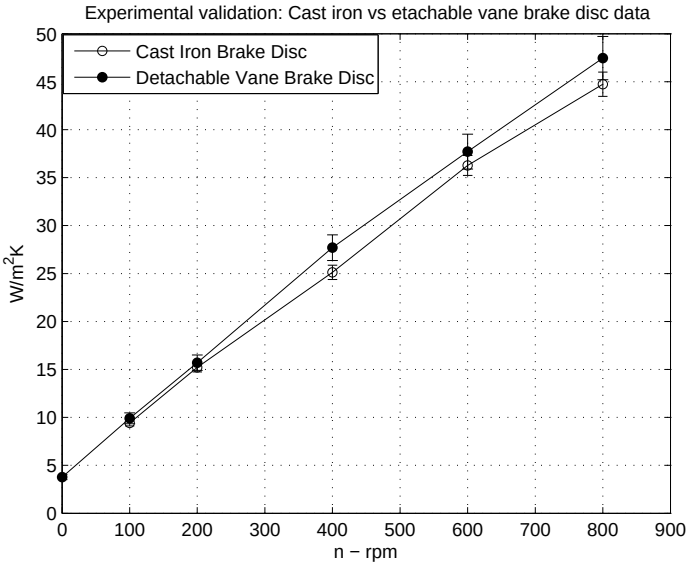

Figure 5.30: Convective heat transfer coefficients from cast iron and detachable (Al) vane brake prototypes.

shown different heat transfer coefficients for brake disc with hub and without hub, these were calculated from the same cooling rate, then the degree of perturbation is minimal. A second set of results from the tests with the cast iron brake disc using a shorter temperature range is shown in Tables B.3 and B.4. The calculation of heat transfer coefficients from tests performed with the detachable vane brake disc follows the same philosophy, the results are shown in Tables B.5 to B.8.

Convective heat transfer coefficients derived from experiments with cast iron and detachable (aluminum) vanes brake discs are shown in Figure 5.30 (from Tables B.1 and B.5) for a range of speed from 100 to 800 rpm and for a temperature range of 120^{o}C to 60^{o}C. The largest disagreement (10%) between these set of results occurs at n=400rpm. This may due to variability of channel airflow characteristics due to vane surface finish, possible vibration in the vane-disc joint or measurement error. Nevertheless, the remaining differences are all

covered by the disc uncertainties. Therefore, except the result at n=400rpm, the agreement is within experimental error. In general, the aluminum vanes disc predicts convective heat transfer coefficients higher than the cast iron disc by 4.5% (disregarding the 10% error at n=400rpm).The heat transfer coeffiecient uncertainty was calculated as per the Basic Differential Method, Section 4.11.3 (see Table B.9 for actual values).

For all cases calculations were done for two temperature ranges, including and excluding disc hub. The numerical evaluation of the derivatives, their squared uncertainty contributions and the final uncertainty as function of angular speed is shown in Tables B.10 and B.11 for the first case only (considering the total mass of the disc). The details for the remaining cases uncertainty are omitted and just the uncertainty values are shown (Tables B.12 and B.13).

The uncertainties derived from the calculations (Tables B.12 and B.13), show that the experimental error lies at a maximum of 3.9% around the value for the cast iron brake disc[2], while for the aluminum vanes disc the experimental error reaches 6% about the reduced value. These maximum uncertainties arise for the shorter range of temperature (100^{o}C to 60^{o}C), which means that the cooling time is shorter and therefore the uncertainty increases, as explained before (see Section 4.11.3). The uncertainties for the wider temperature range oscillates at 3 and 5% respectively. It was seen that the experimental uncertainty varies around half percent when the mass of the hub is disregarded from the calculations. It is also seen that the experimental uncertainty increases when natural convection heat transfer coefficients are calculated.

5.4 Validation of CFD Results

The heat transfer coefficients calculated computationally were averaged using the postprocessor tools and considering the full disc surface (including hat). The expression used for numerical data averaging is equation 5.3. The comparison of experimental versus CFD results is shown in Figures 5.31 and 5.32. Table 5.9 compare the experimental data against CFD averaged values.

The maximum difference between simulations and experiments is for cooling by natural convection (30%). For forced convection, the maximum difference between CFD results and experimental work occurs at n=100rpm in both discs. The differences between CFD and experiments fall with rotational speed.

[2]The relative percentage was obtained by dividing the uncertainty magnitud by the referenced convective heat transfer coefficient.

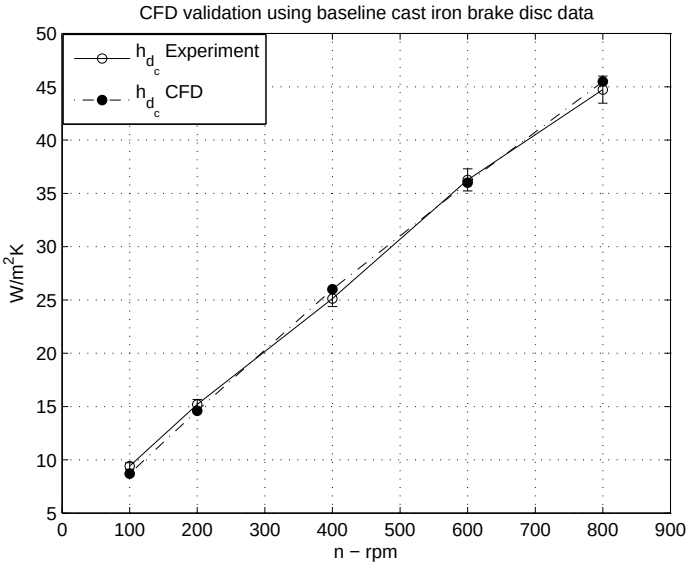

Figure 5.31: Comparison between experimental and computational (CFD) disc heat transfer coefficients (cast iron disc).

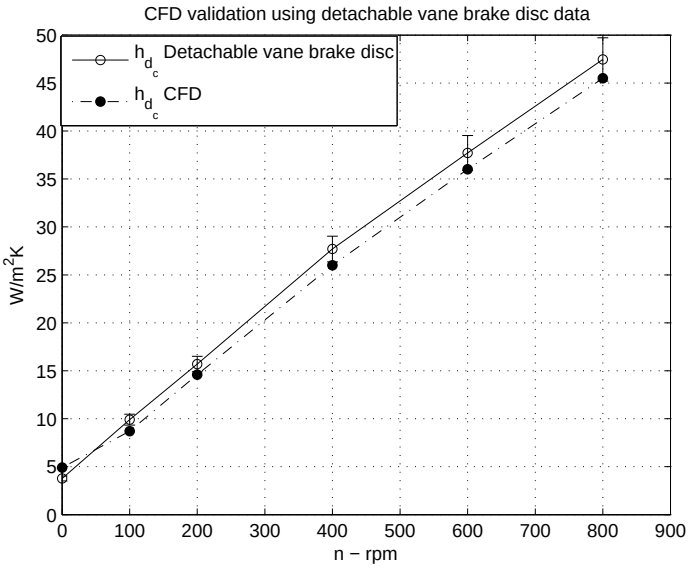

Figure 5.32: Comparison between experimental and computational (CFD) disc heat transfer coefficients (DVBD).

Table 5.9: Experimental convective heat transfer coefficients versus CFD results, baseline discs. Data in W/m^{2}K.

n	CI brake	DVB brake	CFD	CFD vs CI (%)	CFD vs DVB (%)
0	-	3.8	4.9	-	-30.0
100	9.4	9.9	8.7	7.7	12.1
200	15.2	15.7	14.6	4.0	7.0
400	25.1	27.7	26.0	-3.5	6.1
600	36.3	37.7	36.0	0.7	4.5
800	44.7	47.5	45.5	-1.7	4.1

Range 1: 120^{o}C to 60^{o}C

5.5 Flow Characteristics in Standard Brake Disc Vents

CFD results from simulations with the baseline brake disc are shown in this Section. All contoured and streamlines plots show the disc rotating about $+z$ at n=400 or 800 rpm (anticlockwise direction for those on disc circumferential plane). Further postprocessing was carried at locations shown in Figure 5.53.

Airflow inside the channel is strongly drawn by rotation in the first half of the channel, as shown by streamlines in Figure 5.33. The absolute speed up to this region is larger than the disc local tangential speed. Toward the outlet of the channel, airflow speed decays to a magnitude equivalent to disc local tangential speed (therefore relative values show values close to zero). Results for n=800 rpm, Figure 5.34, indicate that relative airspeed increases from 10 to 18 m/s in the channel. A common behaviour in both cases is that airflow bounces first in the upper endwall (z=-68mm on Figure 5.25), a speed drop follows and finally bounces back in the lower endwall. It must be reminded that the actual behavior of air inside the channel is not longitudinal to it as apparent, but highly rotational trying to follow the rotating movement of the disc. This effect is the result of the mechanical work delivered by the vanes.

Although its airspeed drops to 5m/s in the radial end of the domain and points to vortex formation, the accuracy of those being not well predicted have no direct influence on brake disc heat transfer coefficient in the context of the simulation. If the simulation scope included effects of wheel enclosure, then higher degree of accuracy would be needed for farer surroundings of the disc.

Figures 5.35 and 5.36 show streamlines of relative mean velocity on a plane lying in the middle

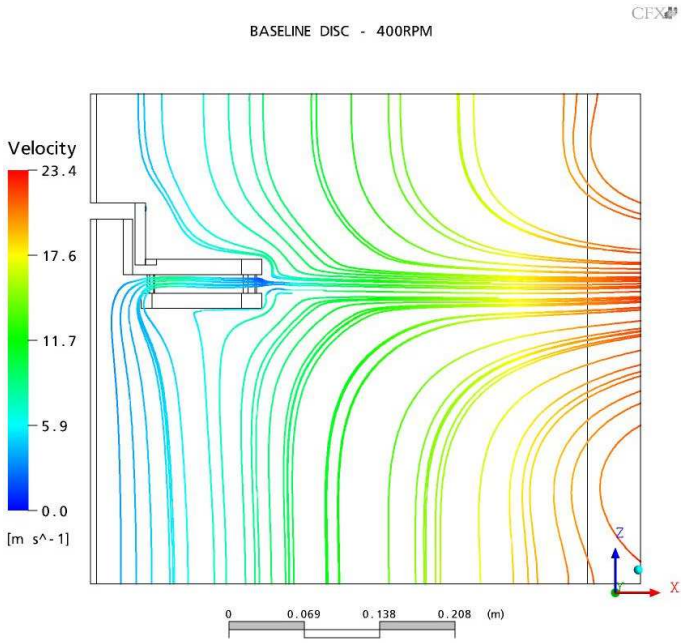

Figure 5.33: Streamlines of relative mean speed on the periodic face plane, n=400rpm.

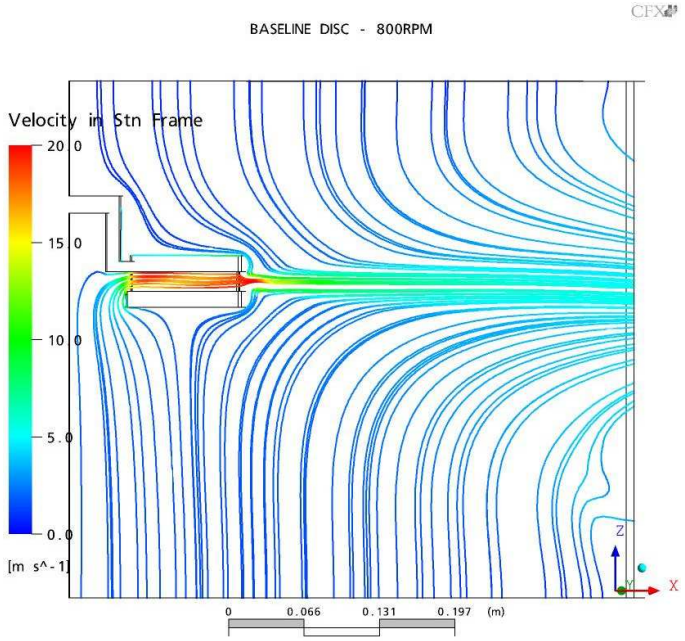

Figure 5.34: Streamlines of absolute mean speed on the periodic face plane, baseline brake disc at n=800rpm.

of the channel (z=-74.5 mm). Because of the misalignment angle between the vane and the air drawn, flow recirculates in a region that extends along the leading side of the channel. The recirculation region widens in radial direction. This conduces to flow separation along the leading side of the channel (no re-attachment). The recirculation region constitutes a virtual barrier which narrows down the effective channel section upstream, then in order to meet continuity requirements, the relative speed in the remaining (trailing) side is increased and therefore remains attached to the wall.

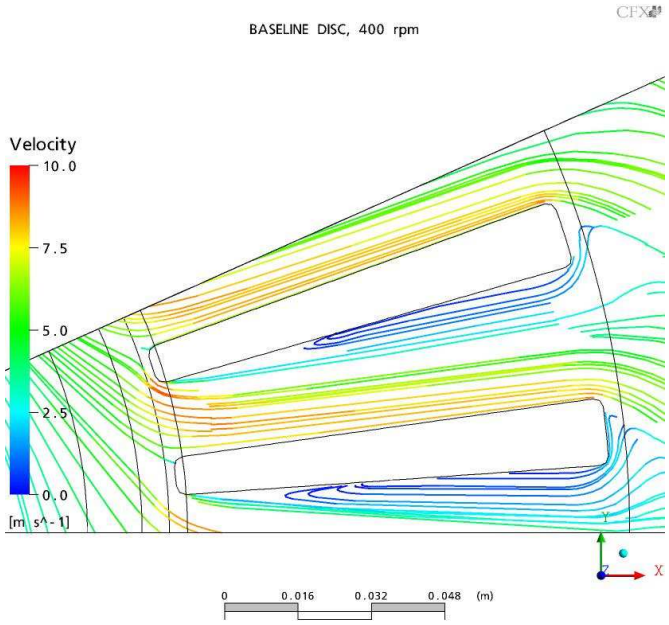

Figure 5.35: Streamlines of relative speed within brake disc channel, n=400rpm.

The flow behaviour near the channel trailing wall gives rise to local vorticity with opposite direction to disc rotation, this condition is regarded as *destabilizing layer*, and its characteristics are enhanced turbulence and therefore better momentum and heat transfer abilities, which gives enough strength to the boundary layer in the channel trailing side as to avoid separation. On the other hand, in the channel leading side, ideally the relative stream speed decays as it reaches the wall (vane trailing wall) and this gives rises to a local vorticity in the same direction as the general rotation of the disc. The above results in a *stabilizing layer*, Greitzer *et al* (2003), where laminar conditions mostly exist and therefore is prone to separation phenomenon given by adverse flow pressure gradients.

Adverse pressure gradients radially develop on the channel leading side as seen in Figure 5.37, changing from suction to positive pressure and triggering flow separation and deflecting and eventually breaking the boundary layer from the wall. On the channel trailing side, the pressure build up is at a lower rate, but with higher values.

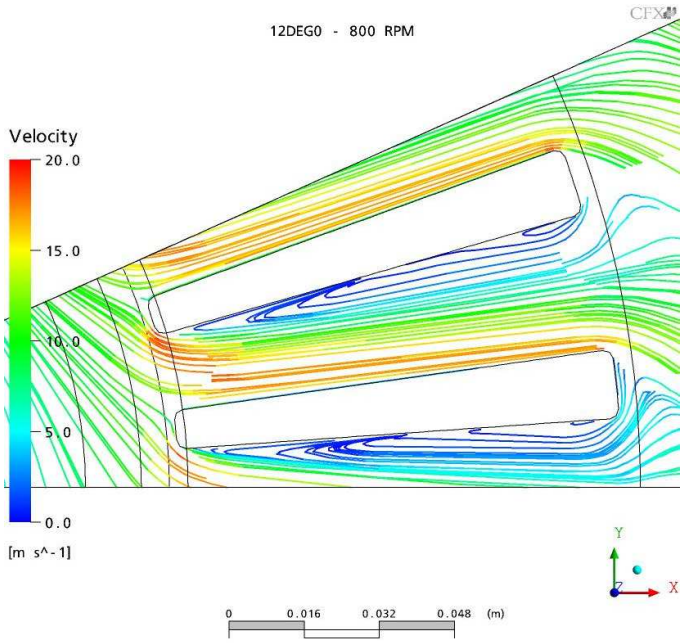

Figure 5.36: Streamlines of relative speed within brake disc channel, n=800rpm.

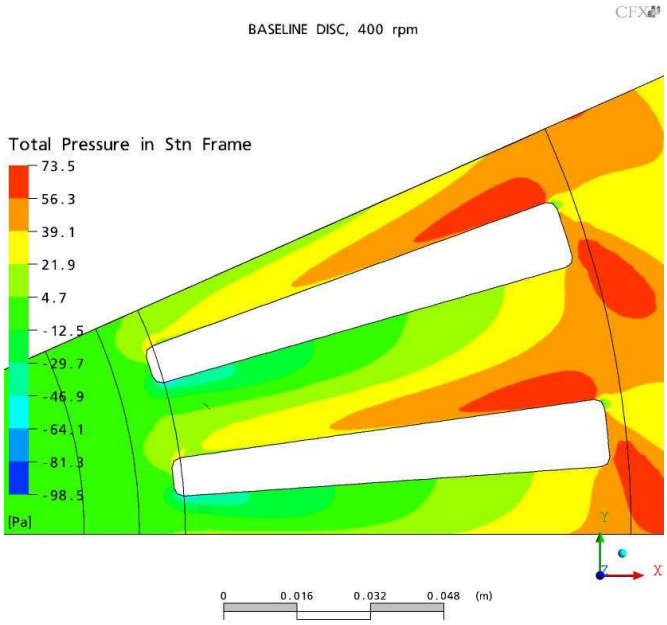

Figure 5.37: Total pressure contours in stationary frame on channel midplane, n=400rpm.

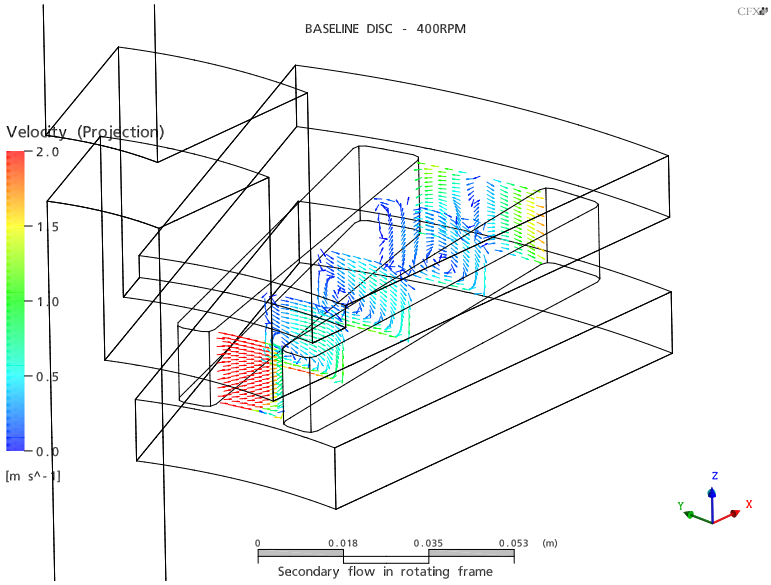

Figure 5.38: Circumferential relative speed vectors within the channel showing secondary flow patterns, n=400rpm.

Another interesting airflow behaviour occurs in planes perpendicular to radial direction. Secondary flows arise due to Coriolis forces (see first term of equation 3.9), which act in perpendicular direction to the plane formed by the angular speed and radial relative speed vectors, (when the radial relative speed component is pointing outward, then the direction of the Coriolis force vector is with the rotational direction and vice-versa). Figure 5.38 shows circumferential relative velocity vectors in five stations along the channel radius, showing secondary flow inside the channel. While planes near the inlet and outlet of the channel show strong influence from circumferential speed, the three planes in between show mainly one cell rotating around a nucleus that shifts location from the leading side to the middle of the channel, and that it is preferentially oriented toward the flying disc face. The secondary flow is mainly driven into the channel trailing wall. A second nucleus seems to form near the channel leading side in the fourth plane (near the outer radius). This additional nucleus is more evident in Figure 5.39. While the brake disc angular speed is doubled between those two figures, the magnitude of the vectors in the secondary flow patterns do not appear to double their value, but to increase at a lower rate.

Air temperature in the channel trailing side is cooler than in the leading side (Figure 5.40(a), (b)), this is due to air speed difference between them. The thermal boundary layer is narrow in the channel trailing side and therefore convective energy transport to fluid core is faster; on the leading side however a boundary layer is uncertain due to air recirculation and low speed. Therefore diffusion of energy dominates and air temperature increases, reducing the

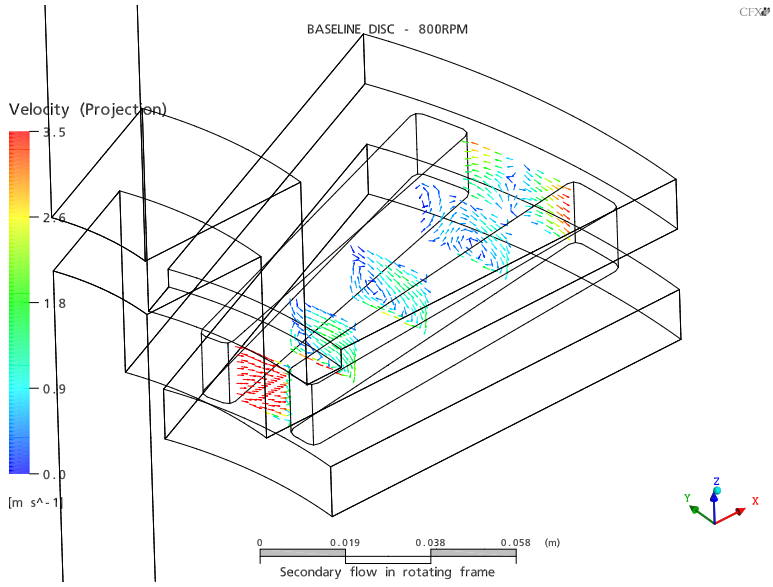

Figure 5.39: Circumferential relative speed vectors within the channel showing secondary flow patterns, n=800rpm.

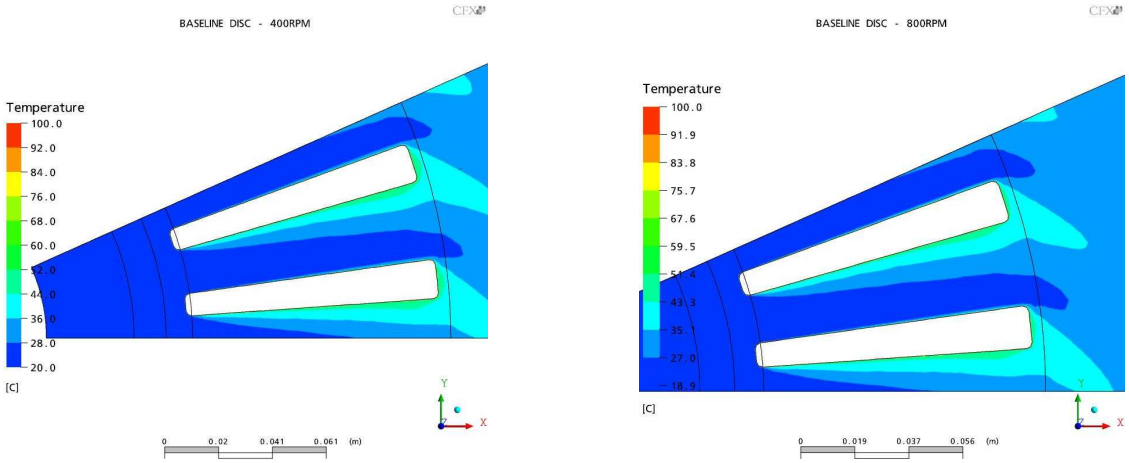

(a) n=400rpm. (b) n=800rpm.

Figure 5.40: Air temperature on channel midplane.

convective ability of this side.

The air temperature contours shown suggest that the thermal layer from one side do not reach the other, therefore airflow is in thermal entry regime. However, on the periodic face, in axial direction, thermal layers meet before reaching the channel outlet, in a point toward the inboard side endwall (see 5.41). The length of the plume leaving the disc is similar to the channel length.

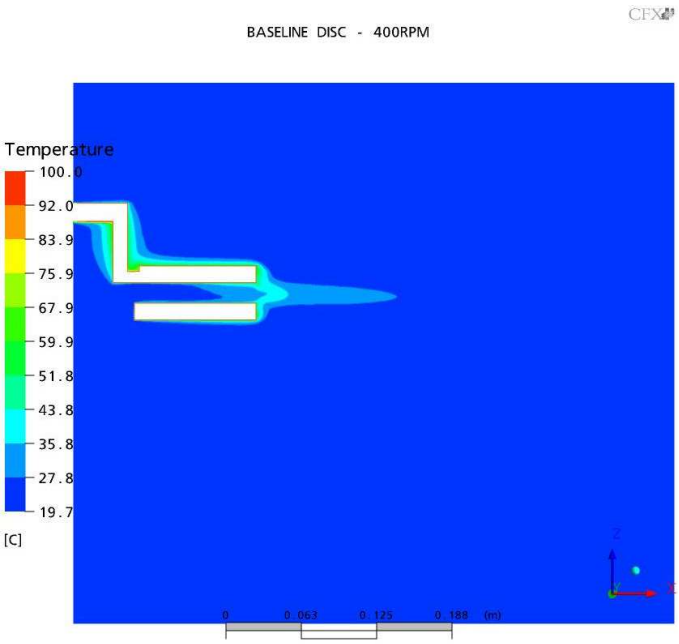

Figure 5.41: Air temperature on the periodic face, n=400rpm.

Heat transfer coefficient contours inside the channel are shown in Figures 5.42 to 5.45 for n=400 and 800 rpm. The lowest heat transfer coefficients locate on the leading sides of the channel, 9.4 W/m^{2}K and 14.1 W/m^{2}K at 400 and 800 rpm respectively. The peak value occurs on the attack edge of the vanes, where air strikes and forms an stagnation region (107.8 and 163.2 W/m^{2}K for 400 and 800 rpm respectively), following this, on the channel leading side, the heat transfer coefficient falls rapidly to 34 W/m^{2}K before reaching half the vane length and the remaining half keeps a value of 24 W/m^{2}K.

On the channel trailing wall the heat transfer coefficient drop is less pronounced and the centre strip of the second half of the vane length preserve 43 W/m^{2}K while the regions close to the endwalls drop to 34 W/m^{2}K (at 400 rpm). At 800 rpm, the same strip of the vane leading side retains a value of 80 W/m^{2}K approximately, which falls to 65 W/m^{2}K on the regions close to channel endwalls.

Also, looking at Figures 5.44 and 5.45, it can be seen that the best of heat transfer ability in

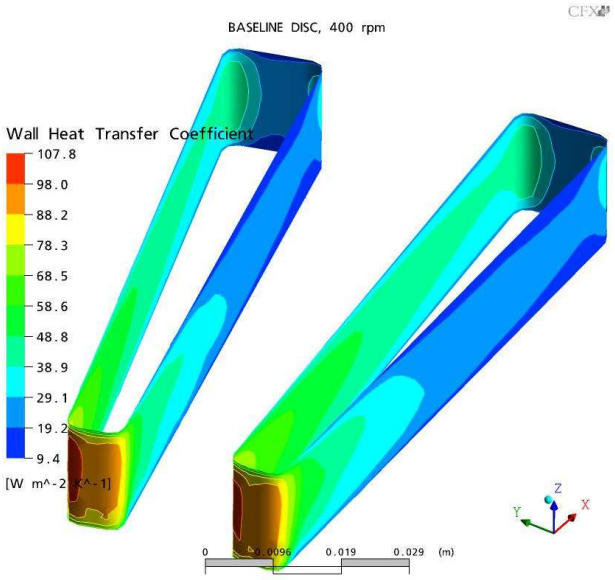

Figure 5.42: Convective heat transfer coefficient contours on vane surface. Baseline brake disc rotating at n=400rpm, (about $+z$).

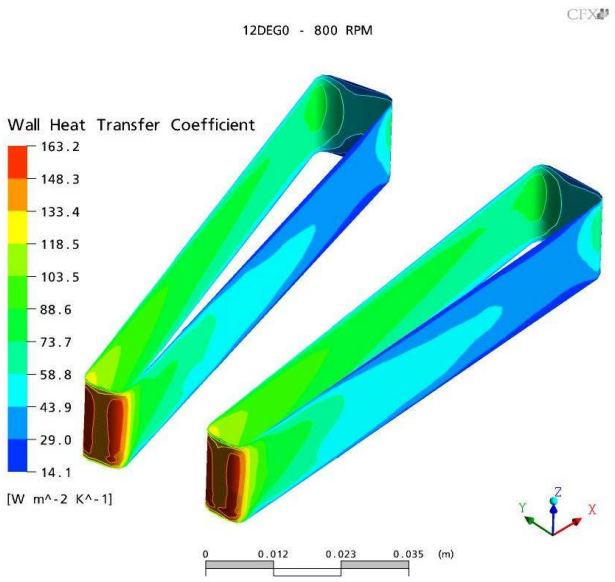

Figure 5.43: Convective heat transfer coefficient contours on vane surface. Baseline brake disc rotating at n=800rpm, (about $+z$).

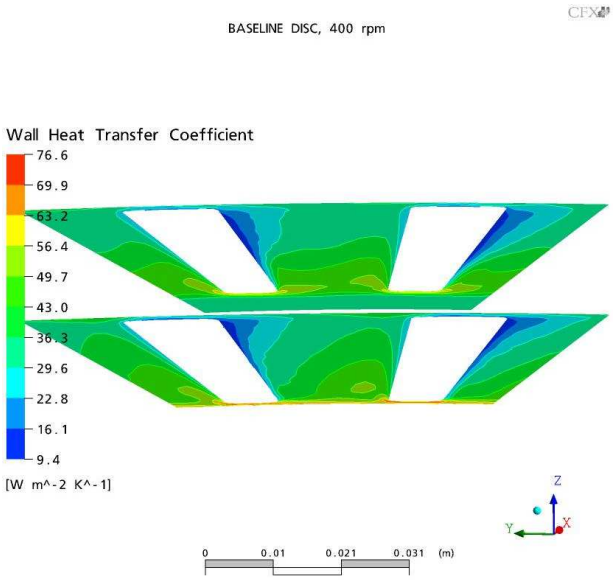

Figure 5.44: Convective heat transfer coefficients on channel endwall; outboard brake side toward $+z$, n=400rpm.

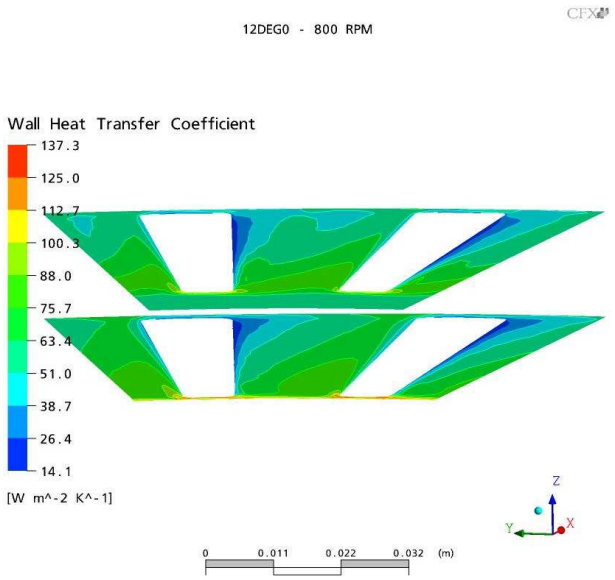

Figure 5.45: Convective heat transfer coefficients on channel endwall, outboard brake side on $+z$ direction, n=800rpm.

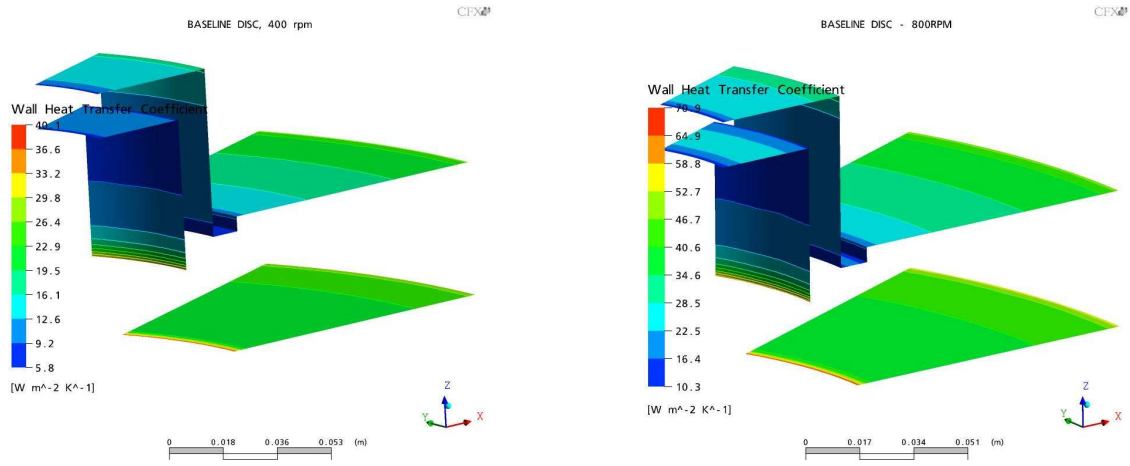

(a) n=400rpm. (b) n=800rpm

Figure 5.46: Convective heat transfer coefficients on hub and friction faces.

the channel locates at the inlet region of channel endwalls. Further down in radial direction, the pattern of heat transfer coefficients follows those predicted by relative speed streamlines and mean air temperature plots shown earlier, high heat transfer coefficients on the trailing side of endwalls and very low heat transfer coefficients on their leading side. Also, in radial direction, the drop of heat transfer coefficient is faster on the outboard side endwall, while in the inboard side endwall the heat transfer coefficient drop is slower. This is due to air bouncing against the endwalls.

Figure 5.46 shows heat transfer coefficients over the friction and hub surfaces of the disc at 400 and 800 rpm respectively. The values shown on the hub are the lowest of the brake disc (about 9.2 and 16.4 W/m^2K for 400 and 800 rpm respectively). On the friction surfaces, higher heat transfer coefficients exist on the inboard side friction surface than in the outboard side friction surface. This correlates with Figure 5.26, where higher speed gradients in the axial direction occur on the inboard side face due to the proximity of channel inlets.

Finally, heat transfer coefficients in the outer ring surface of the brake disc spinning at 400 and 800 rpm are shown in Figure 5.47. A central strip in each of the ring surfaces show heat transfer coefficient of similar order to the lowest reached in the inboard side friction face. High heat transfer coefficients are predicted on the perimeters connecting with the channel exits, although the certainty of this can be questionable due to sharpness of region and therefore, sudden change of geometry in the airflow pattern.

The turbulent characteristics of the flow inside the channel are analysed by observing the

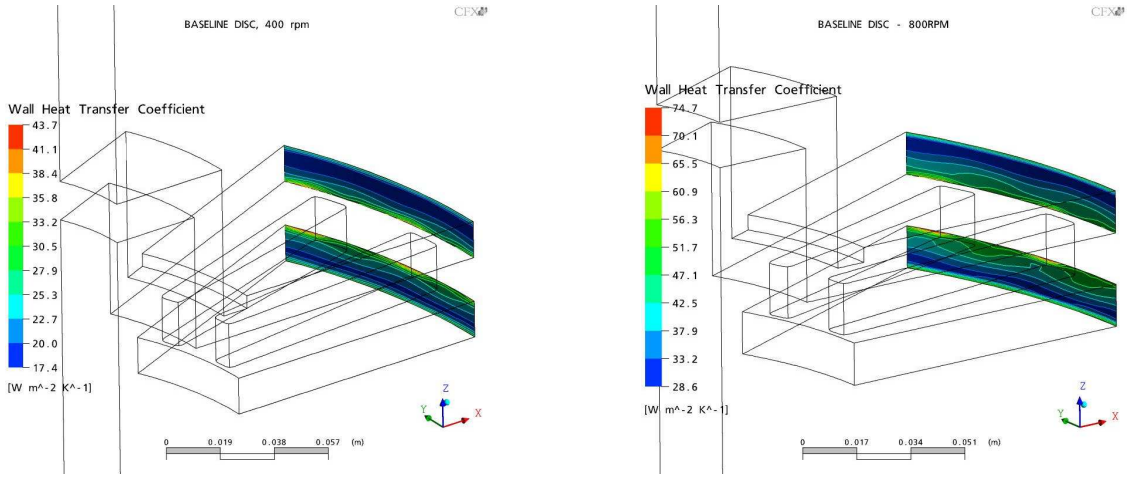

(a) n=400rpm. (b) n=800rpm

Figure 5.47: Convective heat transfer coefficient contours on brake disc outer ring surfaces.

contours of turbulent kinetic energy at the midplane and on the periodic face crossing along the centre of the channel. The highest gain of turbulent kinetic energy across the channel comes from the inlet of the channel, where the mean flow entering the channel is sheared by the vanes (see Figure 5.48). After this, the extraction of kinetic energy from the mean flow along the channel drops, with the lowest values near the vane walls (destruction of turbulence by viscous laminar-like effects). On the periodic face, the turbulent kinetic energy contours show that the jet type flow exiting from the channel delivers higher energy exactly at the outlet of the channel. Minor gains of turbulent kinetic energy are observed inside the channel. Also, it is highly evident the boundary between turbulent flow and potential flow at the exit of the disc.

5.5.1 Averaged Results and Analysis of Flow Characteristics

Averaged discrete values are next shown: heat transfer coefficients per brake disc region, air mass flow, radial speed in the channel centre and torque on the fluid as function of rotational speed. Also, detailed analysis of the flow characteristics near the vane walls is also carried out.

The behaviour of the averaged absolute radial air speed within the channel as function of rotational speed is shown in Figure 5.49. The averages shown were calculated from discrete data retrieved at a line crossing the channel (Figure 5.19). The results were compared with formulae given by Sisson (1978) and Limpert (1975) (pages 17 and 18).

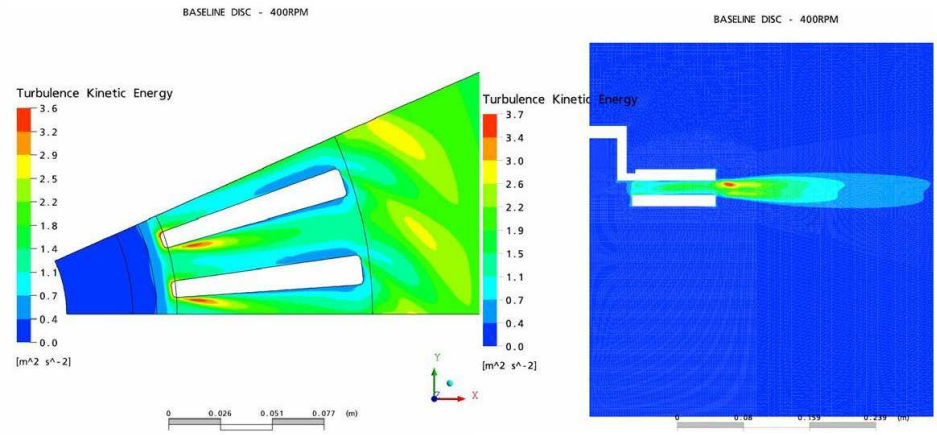

Figure 5.48: Turbulent kinetic energy on a midplane inside the channels and on the periodic face of the model (channel centre).

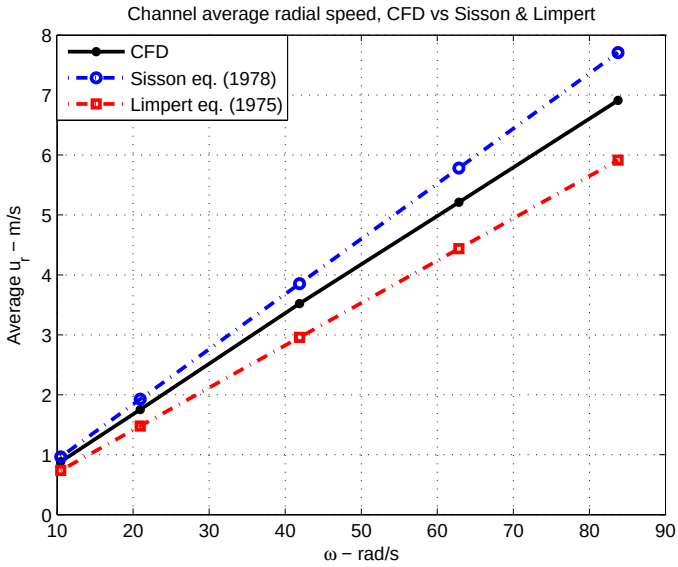

Figure 5.49: Averaged absolute radial air speed through the channels of baseline disc. Comparison against Sisson (1978) and Limpert (1975) formulae.

The behaviour of the average absolute radial air speed is linear with angular speed, therefore the amount of air pumped also increases linearly. The CFD results are overpredicted by Sisson (1978) in nearly 9%. However, Limpert's (1975) formula underpredicts the simulation results by almost 18%. Considering that convective heat transfer in channels increases with average speed (e.g.: see equation 2.21), the above results would point to lower perfomance under Limpert's (1975) predictions whilst the predictions by Sisson (1978) would result in optimistic heat transfer coefficients.

The mass flow was retrieved from a cylindrical surface lying on the edge of the channel inlet, at the inboard disc inner radius, its axial length spanned along the channel height and circumferentially covered the full CFD sector. The results were multiplied by 15 in order to obtain the results on a disc basis (360^o), see Figure 5.50.

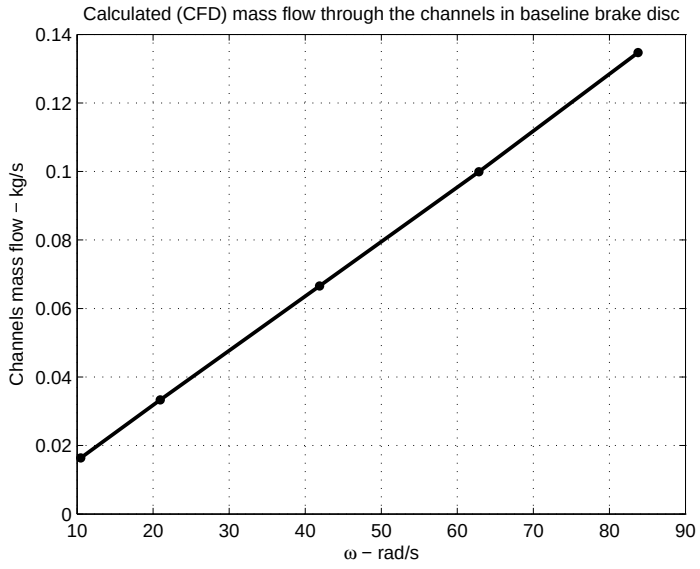

Figure 5.50: Air mass flow through the channels of the baseline brake disc as predicted by CFD simulations

Mass flow also increases linearly with rotational speed. The results indicate that the channels pump 20 grams per second at the lowest angular speed (n=100rpm), which would mean that less than one gram circulates per channel in one second (0.6 g/s approx.). However at n=100rpm, the average radial absolute airspeed through the channels is approximately 0.96 m/s, therefore a particle of air takes around a tenth of a second to cross through the channel (l_v=0.095 m); then, it is realistically inappropriate to consider the time scale of seconds to visualize the convection heat exchange mechanism from channel walls to air whilst the disc rotates. The amount of air soaking heat from a channel at each revolution is minute, therefore redistributing or increasing heat transfer coefficient is key in channel design.

Table 5.10 shows average convection heat transfer coefficients per region as a function of the angular speeds.

Table 5.10: CFD Averaged heat transfer coefficients.

n [rpm]	$\overline{h_v}$ [W/m^{2}K]	$\overline{h_{ew}}$ [W/m^{2}K]	$\overline{h_{ch}}$ [W/m^{2}K]	$\overline{h_{ff}}$ [W/m^{2}K]	$\overline{h_{d_c}}$ [W/m^{2}K]
100	13.4	12.5	13.0	6.2	8.7
200	21.7	19.9	20.8	11.5	14.6
400	39.6	35.5	37.6	20.4	26.0
600	54.2	48.5	51.4	28.7	36.0
800	67.6	60.6	64.1	37.1	45.5

Using average heat transfer coefficients for channel and brake disc reported in Table 5.10 and data in Table 3.2, averaged Nusselt numbers can be calculated (based in the channel hydraulic diameter and outer radius).

$$Nu_d = \frac{h_{d_c} R_o}{k_a} \quad \rightarrow \quad \text{Brake Disc Nusselt} \tag{5.4}$$

$$Nu_{ch} = \frac{h_{ch} D_h}{k_a} \quad \rightarrow \quad \text{Channel (vent) Nusselt} \tag{5.5}$$

Then, using empirical formulas reported in Kreith & Bohn (2001) , Limpert (1975) , Dorfman (1963) and Cobb & Saunders (1956), a comparison is carried out. The equations are 2.22 (Dittus-Boelter) and 2.21 already reported in Chapter 2. The remaining formulae (equations 5.6 to 5.10), are correlations calculated from experiments carried out in solid discs, therefore it can be only compared against Nusselt number based on $\overline{h_{d_c}}$:

$$Nu_d = 0.374 Re_\omega^{0.5} \quad Re_\omega < 2.4x10^5 \quad \text{Dorfman (1963), laminar flow} \tag{5.6}$$

$$Nu_d = 0.0151 Re_\omega^{0.8} \quad Re_\omega > 2.4x10^5 \quad \text{Dorfman (1963), turbulent flow} \tag{5.7}$$

$$Nu_d = 0.345 Re_\omega^{0.5} \quad Re_\omega < 2.4x10^5 \quad \text{Wagner (1948), laminar flow} \tag{5.8}$$

$$Nu_d = 0.36 Re_\omega^{0.5} \quad Re_\omega < 2.4x10^5 \quad \text{Cobb \& Saunders (1956), laminar flow} \tag{5.9}$$

$$Nu_d = 0.015 Re_\omega^{0.8} \quad Re_\omega > 2.4x10^5 \quad \text{Cobb \& Saunders (1956), turbulent flow} \tag{5.10}$$

Figure 5.51 shows the differences that exist between Nusselt numbers calculated using data from CFD results (equation 5.4) and equations 5.6, 5.7, 5.8 and 5.9. Equation 5.10 from

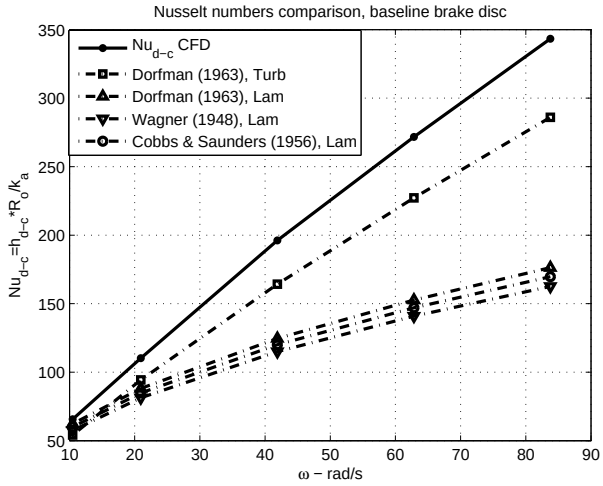

Figure 5.51: Disc Nusselt numbers from CFD and empirical predictions.

Cobb & Saunders (1956) has been disregarded since it is very similar to 5.7. None of the empirical relations correctly correlate the convective heat transfer added by channels in the baseline brake disc, the nearest approximation is given by the turbulent relation given by Dorfman (1963) (eq. 5.7), which underpredicts the convective heat transfer coefficients of the brake disc by 16% in the best case (at ω=20.94rad/s). Laminar predictions are worse. The channel Nusselt is also weakly modelled by the Dittus-Boelter equation (40% average error) and the Limpert's (1975) underpredicts it by an average of 20% (Figure 5.52).

An analysis of airflow behaviour near the vanes was conducted using CFD results at n=800rpm. This looked into links among channel geometry, flow speed, air temperature and convective heat transfer. Data was retrieved in ninety locations on three lines 2 mm away of each vane wall (see Figures 5.25 and 5.53 for reference). The results postprocessed along the above mentioned lines are air radial speed and temperature[3]; temperature data was then averaged per side. A couple of additional lines per channel side, projected on the vane walls at channel mid-heigth was used to retrieve local heat transfer coefficients.

Absolute airspeed near vane walls and Reynolds number based on channel hydraulic diameter is shown in Figure 5.54. On the channel leading side $\overline{u_r}$ drops from 15m/s to 0 m/s in the first two centimetres of vane length, followed by backflow for others 2 cm and finally a weak jump to 1m/s. Boundary layer in this conditions is uncertain, and although in the second half of the vane wall speed slightly increases(flow re-attachment) convection heat removal is likely poor, therefore energy diffusion takes over and air temperature peaks. On the trailing side, radial absolute air speed increases in the first 20 mm of contact with the vane leading

[3]Turbulent mean components

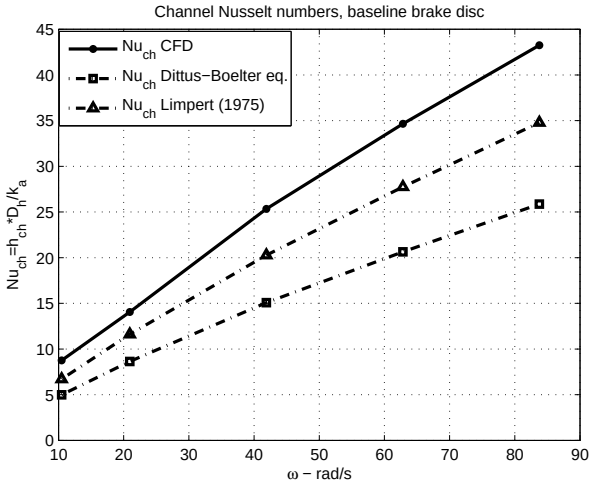

Figure 5.52: Channel averaged Nusselt number from CFD and empirical predictions.

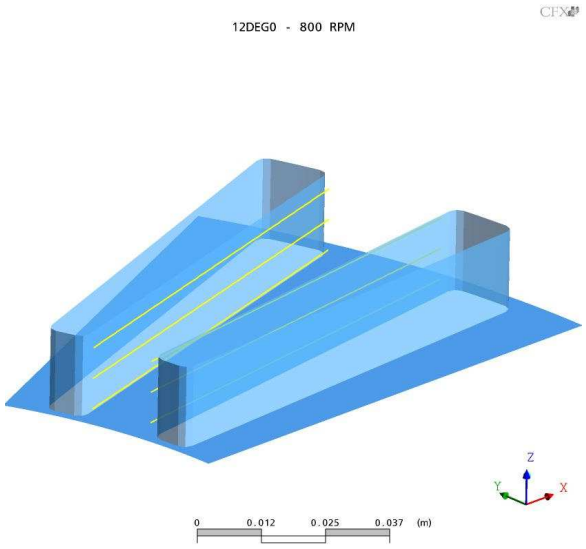

Figure 5.53: Lines for postprocessing of absolute $\overline{u_r}$ and $\overline{\Theta}$ 2 mm away from vane walls.

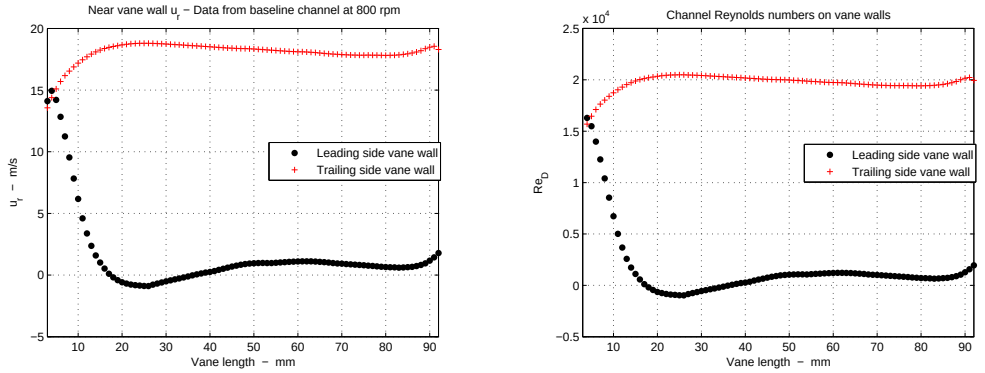

(a) u_r. (b) Re_D

Figure 5.54: Channel radial absolute airspeed and Reynolds numbers at n=800rpm.

wall and then remains almost constant through the channel length. This indicates that much better energy transfer occurs on this side due to continued flow supply at high speed near the vane wall. Depending on the speed values, channel height and on the vane surface characteristics, the boundary layer generated on this side may become turbulent, which in turns improves convection heat transfer.

The characteristics of the momentum and energy transfer abilities of the air near the vane walls can be judged with the Reynolds number (Figure 5.54(b)) using the mean channel hydraulic diameter and data from Table 3.2. The Reynolds number over most of the vane length on the channel trailing side is about 2.0x10^4 which points to a turbulent boundary layer along this vane wall. On the other side, the Reynolds number of the channel leading side, is very low and hardly reaches 2000. Therefore poor momentum and energy transfer abilities characterise the flow on this side.

Figure 5.55 shows average values of air temperature at 2 mm away from the vanes walls and variation of heat transfer coefficient per vane side. Air temperature increases rapidly on the leading side first half (by 20^{o}C), followed by a late increment of 10^{o}C and a sudden decrease of temperature in the exit, probably due to air entering in the disc outer diameter. On the trailing side, air temperature increases only by 5^{o}C along the vane length. This could point to thin boundary layer and improved energy transport ability due to high speed. The heat transfer coefficient, Figure 5.55(b) shows the effect of temperature and speed patterns already seen. On the channel trailing side the values are 30 W/m^{2}K higher than those on the leading side. Although both of them falls along the vane length, the drop of convective heat transfer coefficient is higher on the channel leading side than in the channel trailing side (-40 W/m^{2}K for the former and -30 W/m^{2}K in the latter, considering the length interval

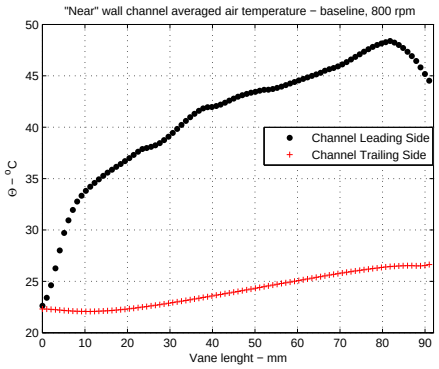

(a) Θ.

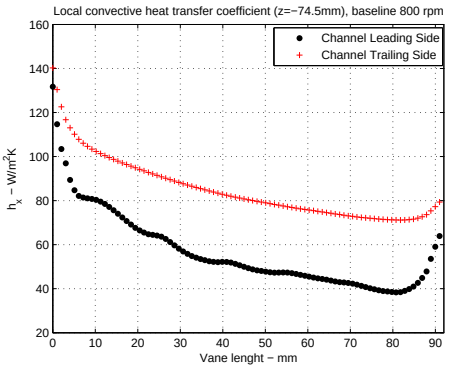

(b) h_c

Figure 5.55: Air temperature near the vane walls and local heat transfer coefficient, n=800rpm.

between 10 mm and 80 mm).

5.6 Torque Measurement

The torque measured from the baseline brake disc was the only way to measure its aerodynamic drag. However, other factors can influence the reliability of the measurements, since the torque sensor installed in the Spin Rig (Figure 4.14) takes also the rolling resistance from the bearings.

Therefore, the final torque reading (τ_s) shown by the acquisition system in the computer is the summation of the bearing rolling resistance (τ_b) plus the brake disc aerodynamic drag torque (τ_d).

$$\tau_s = \tau_b + \tau_d \tag{5.11}$$

The rolling resistance drops with grease temperature increment, therefore is not simple to establish its value due to rheology effects. An attempt to measure this was done by performing tests with the brake disc and supporting flange removed. The shaft was rotated until the bearing box thermocouple (J in Figure 4.14) indicated a semi-stable temperature (about 55^{o}C)[4]. Torque was read after while the angular speed was increased in steps.

[4]This not only depends upon viscous heating in the bearing grease but also on thermal resistance of the casing

Figure 5.56 shows that getting a stable value of torque for an specific speed is difficult. Low speeds measurements show more scatter than the others. Decaying slopes are observed for high speeds while low speeds torque seems to reach a stable value by reducing the initial slope.

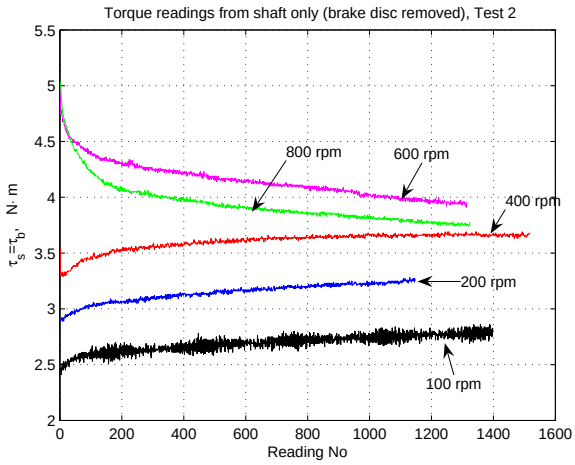

Figure 5.56: Torque measurements for rolling resistance, 2 sample/sec.

Averaged torque results from two tests performed are shown in Figure 5.57. Results show a reduction of shaft torque from 400 rpm to 800 rpm, this can be due to changes in viscosity of the grease with temperature (shear thinning). In this case equation 5.11 reduces to $\tau_s = \tau_b$.

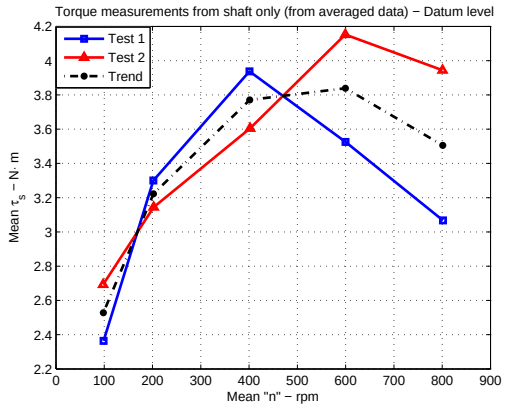

Figure 5.57: Averaged torque readings from shaft only.

After these set of tests, the baseline brake disc was mounted and it was rotated until the bearing box thermocouple gave a similar temperature as in the tests without the brake disc.

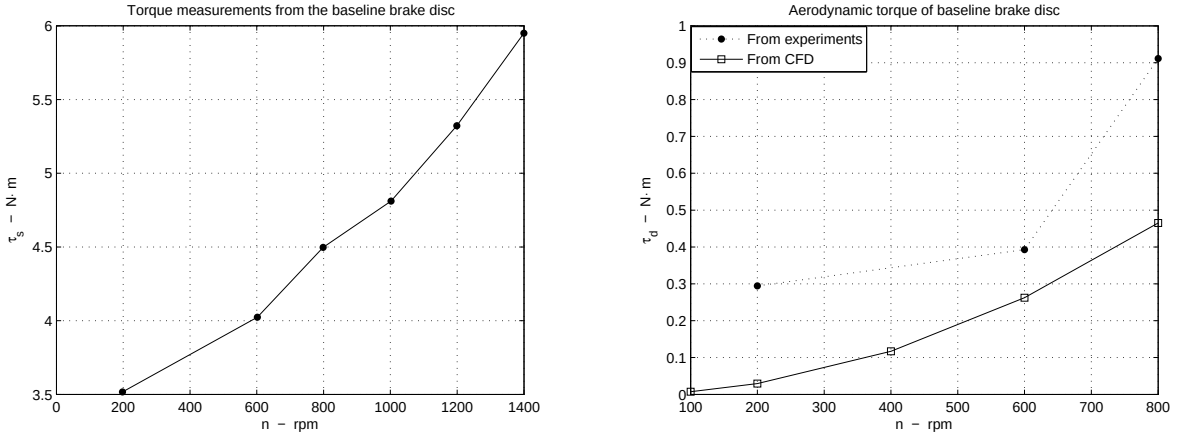

(a) τ_s vs n

(b) τ_d vs n

Figure 5.58: Averaged torque measurements,baseline brake disc mounted on the Spin Rig.

Then, torque was read with ascending angular speed. The averaged results for τ_s from these tests are shown in Figure 5.58. Figure 5.58(a) shows torque generated by the bearing rolling resistance and brake disc rotation (pumping, aerodynamic resistance). Therefore, to obtain the brake disc aerodynamic torque, the trend line in Figure 5.57 is subtracted from that in Figure 5.58(a). This leaves τ_d as function of τ_s and τ_b and provides an approximated value of the brake aerodynamic torque, since torques generated by the bearing rolling resistance with and without the brake disc may differ. The above difference is shown in Figure 5.58(b) where experimental and CFD predicted aerodynamic torques are compared. CFD values represent torque resulting from shearing stresses on the brake disc surfaces plus torque required to pump air through the channels only, that is, aerodynamic torque. The experimental torques are significantly larger these. A cause to this may be increased rolling resistance in the bearings.

5.7 Hot Wire Anemometry Measurements

Hot Wire Anemometry (HWA) tests were done using a Dantec Dynamics^{TM} 55P16-type tungsten probe. The wire was located at the exit of the channels, perpendicular to their endwalls (Figures 4.13 and 4.11). The data was acquired at a rate of 600 samples per second. The angular speed at which the disc rotated was 200 rpm and therefore the Vane Passing Frequency is 100Hz. The amplitude of the raw signal shown in Figure 5.59(a) is about 0.75V and gives the first indication of periodicity and strength of air stream expelled from channels.

The data shown is for an interval of 0.5 seconds.

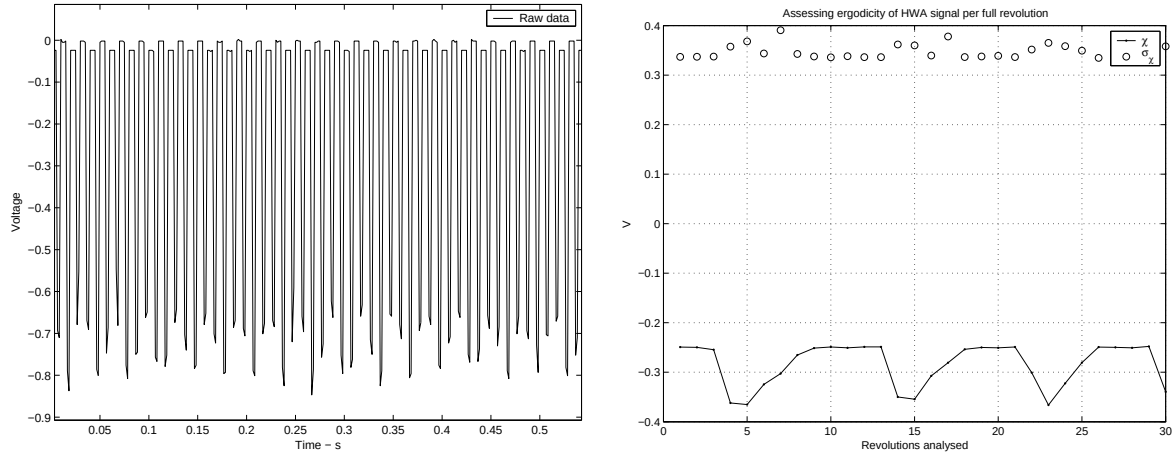

(a) Raw signal (b) Ergodic representation

Figure 5.59: HWA raw signal and ergodic representation, baseline disc at 200rpm.

The average voltage per revolution is approximately 0.3V and the behaviour per revolution seems ergodic (centred about an average), roughly stationary as depicted in Figure 5.59(b). A pulse per channel (or vane) is observed at the mean of the ensemble. The amplitude of the signal, Figure 5.60(a), is reduced to 0.5V due to the averaging process in time, as per equation 4.6. The mean of the ensemble has an amplitude of 0.5V and a pulse per vane (or channel) is observed. An estimation of the energy contained in the signal (equation 4.11), shows that this is about 60% of the raw amplitude, 5.60(b). This result is a rough indication of the kinetic activity in the flow leaving the channels and could be an indicator of the mixing ability in the flow.

The fluctuating component of the signal was obtained using equation 4.10. This signal is balanced about zero volts. The set of fluctuating signals for five revolutions of the disc presented in Figure 5.61 have been displaced by +0.5 volts for ease of reading. The signals wave is similar through the set of data, resembling also periodic behaviour.

The PSD function was calculated from the raw data, part of which is shown in Figure 5.59(a), and from the fluctuating signal. The fundamental frequency (vane related, 100Hz) and the second harmonic at 200hz are visible in the spectra of raw data, Figure 5.62(a). The frequency of the fluctuating signal, Figure 5.62(b), is in phase with the former. The amplitudes are similar also. The harmonic at 100Hz in the fluctuating signal indicates the contact of the air with the vane at its trailing edge. The second harmonics (200Hz) is of lower amplitude and could represent a shearing effect on the air occurring at twice the speed

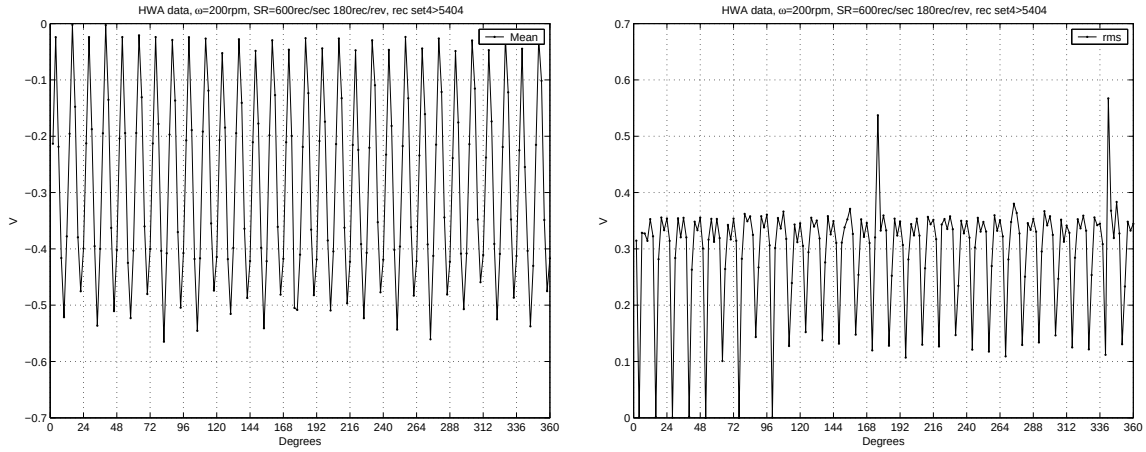

(a) Ensemble Mean

(b) Ensemble *rms*

Figure 5.60: Post-process of HWA signal, baseline disc at 200rpm.

of the vane passing frequency.

Experimentally, power spectra of the raw HWA signal and mean per revolution analysis are useful to confirm cyclic symmetry in the behaviour of the air expelled by the disc channels. Higher sampling frequency would be needed to investigate further the fluctuating signal during the channel travel; the PSD of the fluctuating signal cannot reveal detailed behaviour in this region. Numerical validation of the experimental fluctuating signal would require fully transient CFD modelling and the time step selected in the simulation would determine the frequency range to analyse computationally.

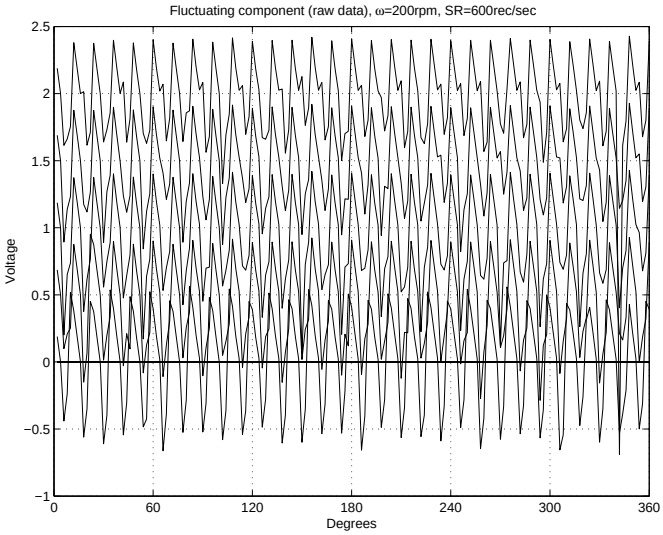

Figure 5.61: Fluctuating component of the signal, baseline disc at 200rpm..

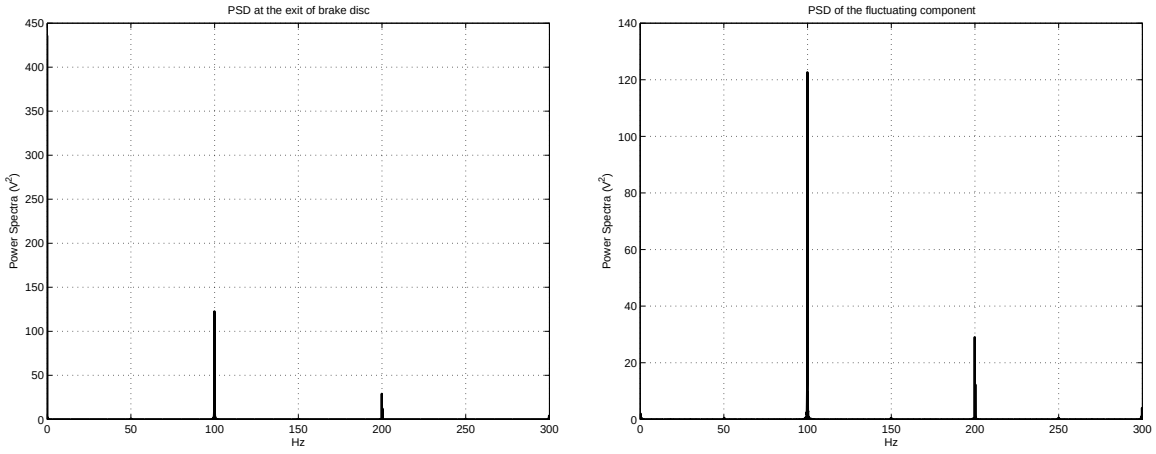

(a) PSD - Raw signal

(b) PSD - Fluctuating signal

Figure 5.62: PSD functions, baseline disc at 200rpm.

Chapter 6

Channel Modifications and Improvements

Knowing that non-handed designs are more affordable to build for future testing, these ventilation geometries were mostly researched in this Chapter using CFD[1]. Variants of vane number, pillared and cylindrical ventilation patterns were revised; and, following that already understood previously, flow management was sought inside the trapezoidal channel by implementing geometry changes. Therefore, the Chapter looks into generic and 'tailored' designs, aiming to identify changes or improvements in channel convective heat transfer coefficients. Dimensions such as vane height (h_v) and available radial length for ventilation purposes remained the same as in the baseline design (see Table 5.1).The geometries were drawn using I-DEAS CAD package. The CFD domain volume surrounds the brake disc solid model without including it. This domain was meshed using GAMBIT, the setting of the CFD model parameters and its solution were obtained using the multipurpose CFD software ANSYS-CFX R10. In order to maintain numerical homogeneity during the comparison of results, the CFD models were constructed following the guidelines given in Chapter 3. This allowed to have CFD models with a common preprocessing, solution and even post-processing philosophy.

The Chapter has been structured into a number of sections equal to the number of channel patterns researched, and within each of these the main characteristics of the geometry are highlighted and a postprocess of results shown including graphs for averaged behaviours versus angular speed (convective heat transfer coefficients, mass flow, cooling rates, and aerodynamic torque). Finally, the boundary conditions set for each model were those described in page 75. The angular speeds used for the simulations were 100, 200, 400, 600 and 800 rpm, all about $+z$. For all the simulations the $\kappa - \epsilon$ model was employed. The simula-

[1]Handed designs were investigated in Chapter 8

tions also considered an ambient temperature of Θ_∞=20^{o}C, which was also used as reference temperature for convective heat transfer coefficient calculations (see Equation 3.75).

6.1 Cylindrical Channels

6.1.1 Geometry

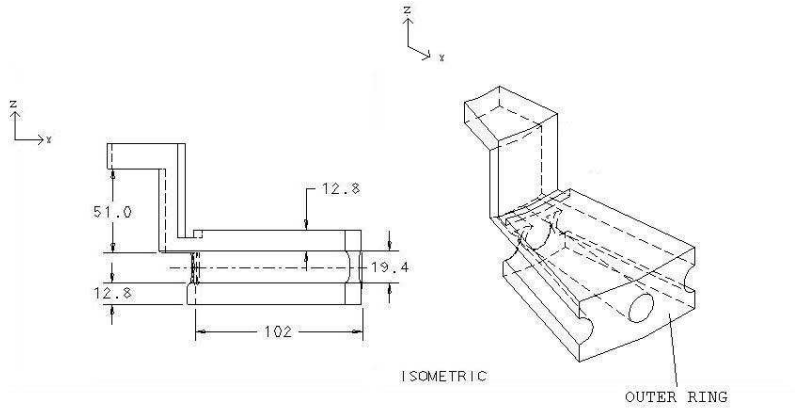

Figure 6.1: Views of a 24 degree sector of a brake disc with cylindrical channels.

The first geometry selected for evaluation is an immediate variant of the original design. From the original geometry with trapezoidal channels, a mean hydraulic diameter was calculated (at the middle of the channel radial length) (Table 5.1). Then, keeping the remaining dimensions constant (except the separation between circular plates), a set of thirty cylindrical channels were drawn in place of the original trapezoidal channels. The diameter of the cylindrical channels was set to 19.4 mm and the axial position of their axis of revolution was coincident with the longitudinal centre of the trapezoidal channels. This meant that the *height* of the channel (that is h in Table 5.1) rose from 17 mm to 19.4 mm, and since the overall thickness of the brake disc (z_{ff}) remained constant, the minimum thickness of each disc plate was reduced from 14 mm to 12.8 mm. However, this did not represented a reduction in weight, since as it is explained below, it increased. Figure 6.1 shows the drawing of the 24 degree sector used to construct the CFD domain volume.

The wetted areas and mass of the brake disc with cylindrical channels are shown in Table 6.5, at the end of Section 6.2. Vanes can not be considered since the channels are cylindrical and reach the outer radius. This differentiates it from the baseline design in the sense that the outer ring of this brake disc has an increased convection surface. However, the channel area is less than the baseline and therefore the final wetted area is less than the baseline disc

by 11.9%. Also, since the channels are radially straight, they take less volume of material out from the brake disc, therefore the mass is 7.7% bigger than the baseline. Finally, cylindrical channels are a selected disc ventilation geometry when machining is employed to manufacture them from solid disc, such as carbon ventilated disc used in F1 racing cars.

6.1.2 CFD Model

The CFD model was constructed with the brake disc sector shown in Figure 6.1. Due to the sharp encounter at the channels inlets/outlets, tetrahedral cells were used in these portions of the model. However in most of the channel duct, hexahedrals cells of appropriate size were used. Figures 6.2 and C.1 (Appendix C) show the CFD model and details of the grid constructed using GAMBIT. As it is evident, the CFD model is composed of an unstructured mesh with hexahedra and tetrahedron cells in the domain. The statistics of the CFD model are shown in Table 6.4.

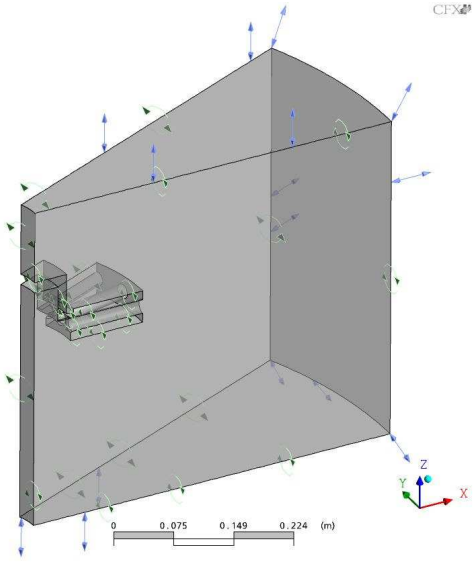

Figure 6.2: CFD model of the brake disc with cylindrical channels.

6.1.3 CFD Results

Absolute speed streamlines show that airflow through the channels do not have the same behaviour as in the baseline model, since the bouncing against the walls disappeared (Figure 6.3(a)), however the fluid orients its highest speed slightly toward the inboard side of the channel. Results on channel midplane show that air develops the standard behavior, see Figure 6.3(b), recirculation appears in the channel leading side. The re-attachment of the

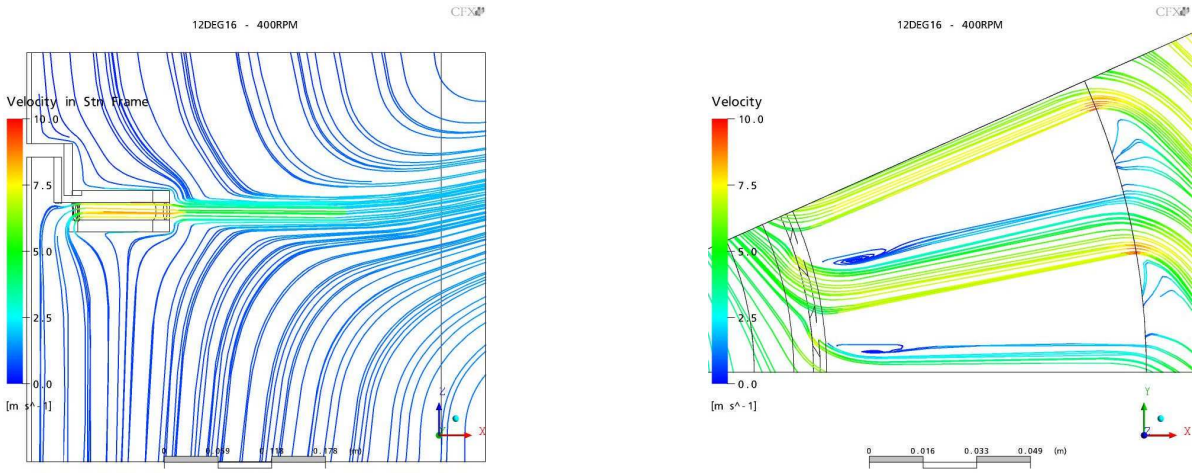

(a) Stationary Frame (b) Rotating Frame

Figure 6.3: Cylindrical channels, flow streamlines at n=400rpm.

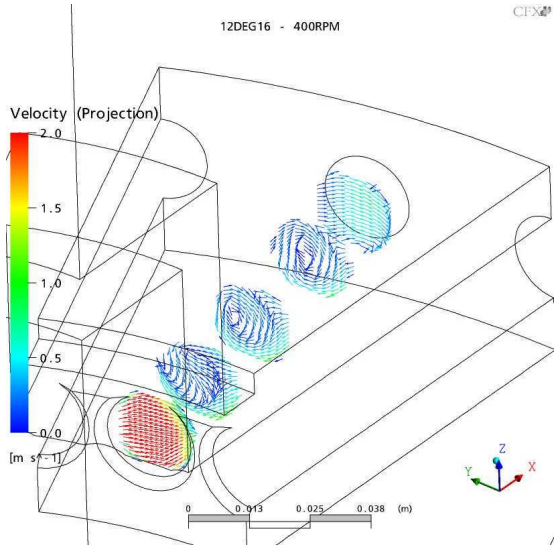

Figure 6.4: Cylindrical channels. Secondary flow patterns at n=400rpm.

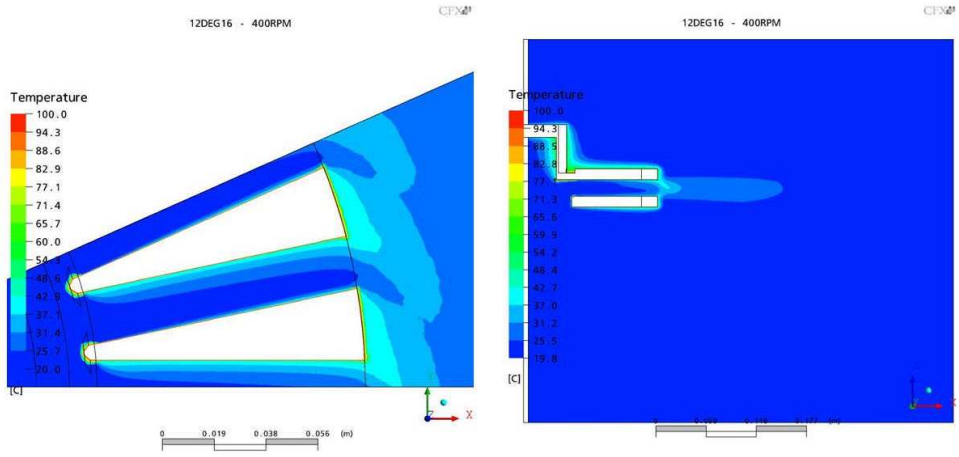

Figure 6.5: Cylindrical channels. Air temperature contours, n=400rpm.

airflow on the leading side is difficult to visualise due to the circular nature of the channel. In comparison with the baseline channel model (Figure 5.35), the relative speed in the cylindrical channels does not reach 7.5 m/s, while in the baseline model values well above of this are observed in a large portion. Then, it is expected that poorer convection heat transfer takes place in cylindrical channels. A complementary plot of the streamlines of relative speed is shown in Figure C.3, where it is seen that the wall region with higher speed in its proximity locates in the trailing upper quarter of the cylindrical wall (toward the outboard side of the brake disc). The contours of total pressure in stationary frame shown in Figure C.2 indicate a similar pattern of pressure on the fluid as in the baseline case. However, the lobule of total pressure at the outlet of the cylindrical channel (on the trailing side) is higher than in the baseline channel by 16% (85.5Pa against 73.5Pa). At this region relative speeds in cylindrical channels are lower than in the baseline channels, it is deduced that the only variable making the total pressure larger is the static pressure, however the airflow about the outer ring is less affected by pressure in cylindrical channels than in trapezoidal. On the other hand, the entrance type of cylindrical channels produces lower suction than the baseline channel, even though they have wider inlet. Secondary flow patterns in Figure 6.4 reveals a single cell of revolving fluid formed toward the second half of the length of the channel. Inlet and outlet cells are dominated by circumferential stream.

Mean temperature patterns seen in Figure 6.5 demonstrate similar behaviour to that of the baseline model, with a clearly marked thick layer on the leading side and a thin layer on the trailing side, and in between core cold flow where entry effects dominate. However, in the PF plane thermal layers seem to meet before the air leaves the channel (cool air towards the inboard side). The temperature patterns discontinuity in the attack edge of the channels is due to the change of grid in that region

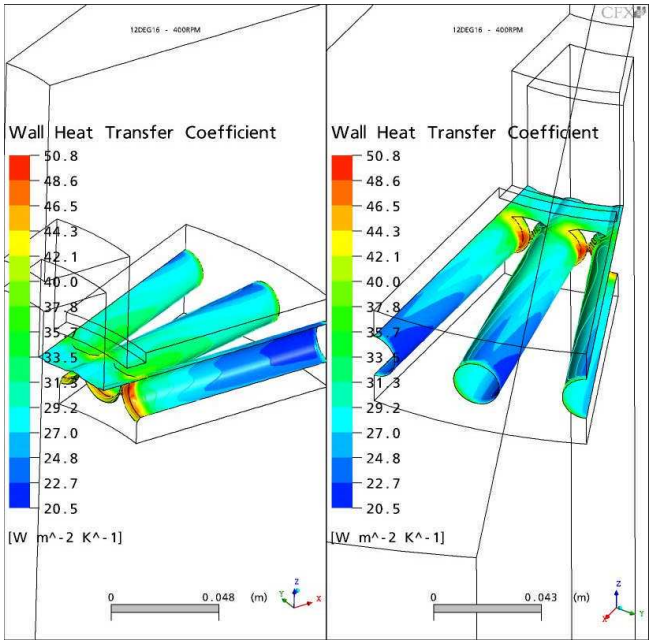

Figure 6.6: Cylindrical channels, heat transfer coefficient distribution, n=400rpm.

The distribution of convective heat transfer coefficients in cylindrical channels are shown in Figure 6.6. The lowest heat transfer coefficient (20.5 W/m^{2}K) is more than twice the lowest heat transfer coefficient in the baseline channel, which means that a more uniform heat transfer rate can be expected from the cylindrical channels than from trapezoidal channels. The heat transfer coefficient distribution concentrates the highest coefficients on the inlet portion of the trailing side of the cylindrical channels, the lowest are located in the outlet portion of the leading side and in between, the coefficients follow a waved distribution about the channel perimeter.

The average heat transfer coefficients and cooling rates calculated using CFD data are given in Table 6.1. These are compared against data from the baseline design in Figures 6.7 and 6.8. Heat transfer coefficient of cylindrical channels represent in average 80% of that produced by trapezoidal channels, while the disc average heat transfer coefficient reaches 86% of the corresponding baseline. In average, convective cooling rates of the brake disc with cylindrical channels represent 74% of the baseline disc cooling rate .

Absolute speed and temperature were retrieved at 21 locations on the channel center line and local heat transfer was read on the four poles of the channel perimeter, at n=400 and 800 rpm. Figure 6.9 shows the speed and air temperature profiles along the channel centre. While radial airspeed increases linearly with angular speed, the core flow temperature drops by 2 to 3%, this indicates that convective dissipation affects predominantly near wall flow, the temperature potential with the core flow remains. The behaviour of the local heat transfer

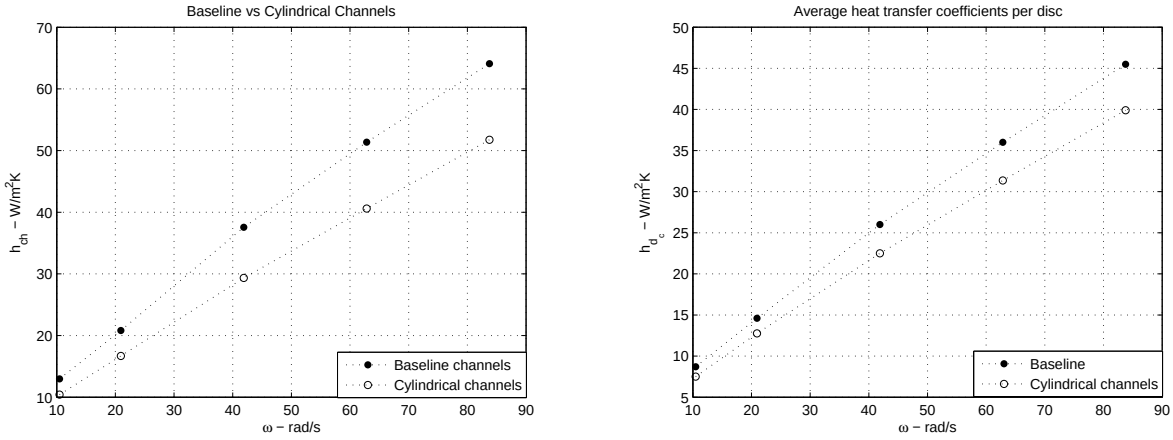

(a) h_{ch} vs ω (b) $\overline{h_{d_c}}$ vs ω

Figure 6.7: Averaged convective heat transfer coefficients, cylindrical channels vs baseline design (data from CFD).

Table 6.1: Averaged heat transfer coefficients and convective cooling rates. CFD with cylindrical channels.

n [rpm]	$\overline{h_{ch}}$ [W/m^{2}K]	$\overline{h_{ff}}$ [W/m^{2}K]	$\overline{h_{d_c}}$ [W/m^{2}K]	b [s^{-1}]
100	10.42	6.22	7.50	3.046x10^{-4}
200	16.69	11.45	12.76	5.183x10^{-4}
400	29.35	20.44	22.50	9.139x10^{-4}
600	40.60	28.56	31.36	1.274x10^{-3}
800	51.75	36.12	39.90	1.621x10^{-3}

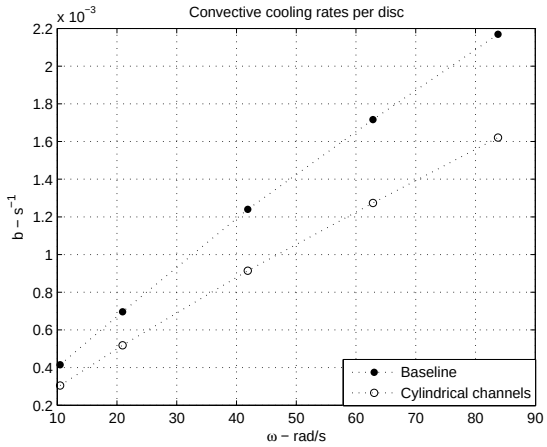

Figure 6.8: Disc cooling rates comparison, cylindrical versus baseline channel design.

coefficient along the leading and trailing sides, Figure 6.10(a), indicates poorer convective heat dissipation from the channel leading side. The trailing side has 20% higher heat transfer coefficient 20 mm after the inlet and the difference widens to 36% after 80 mm, this for both speeds. The sudden peak at the outlet is likely due to the influence of circumferential speed on the outer radius of the brake disc. At n=400rpm, the outboard and inboard poles of the channels have similar distributions of convective heat transfer, however at 800rpm there is a difference, while the inboard side shows constant h_c (50 W/m^{2}K), the outboard side changes from an inlet value of 60 W/m^{2}K to 40 W/m^{2}K at the outlet. In general, it can be concluded that convective cooling of radial cylindrical channels do not perform better than the baseline trapezoidal channels. This due to the lower channel heat transfer coefficients and increased disc mass. If the channels were made wider, it is unlikely that a substantial increment of convective heat transfer coefficient occur, although the wetted area would be augmented and the mass reduced.

6.2 Trapezoidal Channels

6.2.1 Geometry

Trapezoidal channels are one of the most non-handed common shapes in ventilated brake discs. In this work, the mid-channel circumferential width of the baseline design was varied by a factor of 2, 0.5 and 0.25. Designs with 20, 45, 60 and 90 vanes were created. Note that the 45 and 60-vane designs have similar channel width, the difference being the vane thickness, which increases the vane wetted area in the 60-vane design. Designs with 20 and

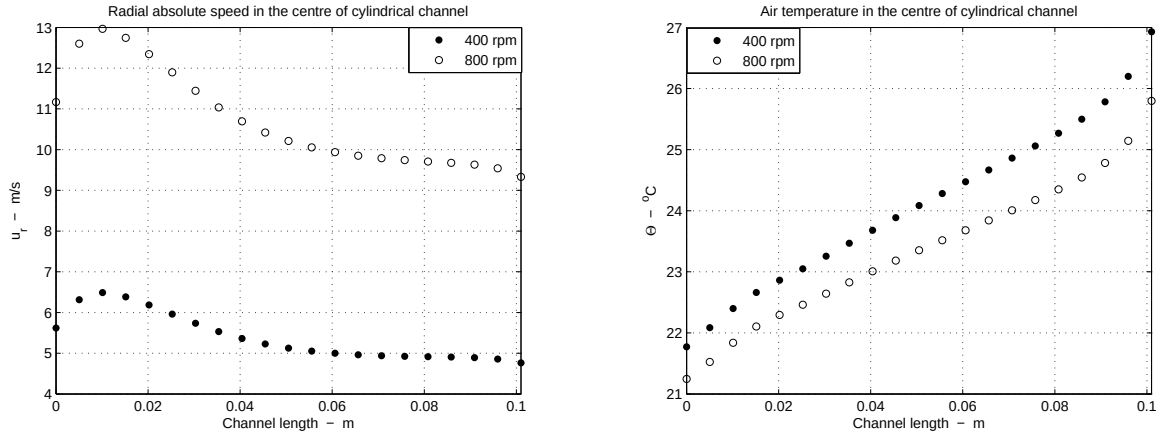

(a) u_r (b) Θ

Figure 6.9: Local values of temperature and absolute speed at the stream core.

45 vanes (Figure 6.11) used the same vane design as in the baseline disc, however vanes were spaced by 14 degrees in the 20-vane design and by 4 degrees in the 45-vane design. The periodic sectors for these were 18 and 8 degrees (the baseline periodic sector has 12 degrees, 30-vane design). Discs with 60 and 90 channels have a redesigned vane (narrower). The thickness of the vane is 6 mm (constant), see Figure 6.12.

The goal was to study the influence of the vane number on the local and average convective heat transfer coefficient. Another idea behind was to inspect the behaviour of the airflow in rotating channels by changing their narrowness.

It must be noticed that by varying the number of vanes, characteristics such as weight and wetted areas for convection change (i.e.: by using a brake disc with 20 vanes, the area for convection heat transfer of the vanes reduces but the areas of the channel endwalls increases). The mass and the wetted areas of the discs with varying number of radial vanes are shown in Table 6.5, page 178. The brake discs were analysed using periodic boundary conditions. Due to the vanes layout the width of the characteristic sectors used varied from case to case. A sector of 36 degrees was used in the case of 20 vanes, 16 degrees for 45 vanes, and 12 degrees for 60 and 90 vanes respectively. The characteristics of the channel for each disc is shown in Tables 6.2 and 6.3

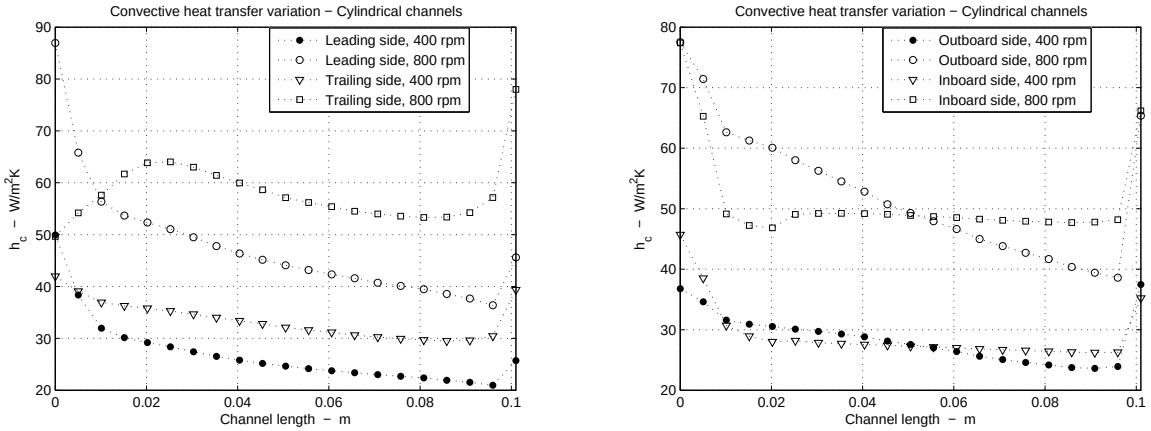

(a) Leading, Trailing poles

(b) Outboard, Inboard poles

Figure 6.10: Local h_c in the channel poles.

6.2.2 CFD models

The mesh followed the guidelines explained before (page 110) in most of the situations, and the boundary conditions are as described at the beginning of this Chapter. The statistics of the CFD models for all the brake discs considered in this Section are shown in Table 6.4. Details of the surface mesh for the vanes, inboard side endwalls and friction face, and inner and outer ring are shown in Figures C.4 and C.5 (see Appendix C).

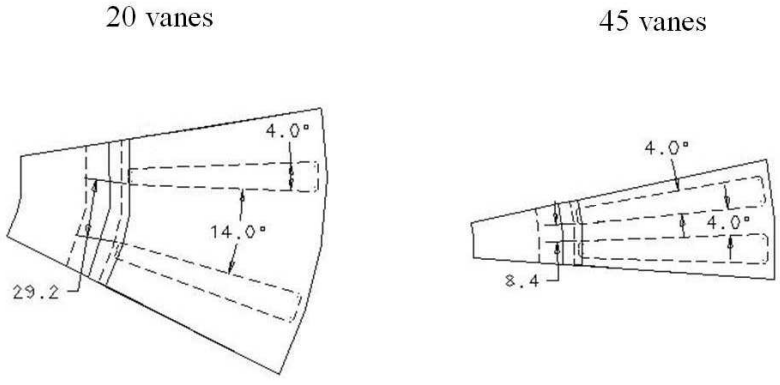

Figure 6.11: Trapezoidal channels, Left: 20 vanes disc sector, right: 45 vanes disc sector.

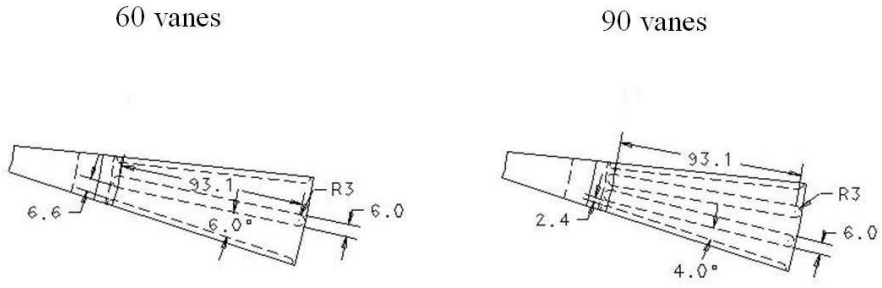

Figure 6.12: Trapezoidal channels, Left: 60 vanes disc sector, right: 90 vanes disc sector.

Table 6.2: Channel data for brake discs with radial vanes.

Disc	Channel data				
	l_v	P_{cr} @ inlet	P_{cr} @ outlet	P^*_{cr}	h
	[m]	[m]	[m]	[m]	[m]
Baseline 30 vanes	0.095	0.016	0.029	0.0225	0.017
20 vanes	0.095	0.029	0.052	0.0405	0.017
45 vanes	0.095	0.008	0.015	0.0115	0.017
60 vanes	0.099	0.0066	0.016	0.0113	0.017
90 vanes	0.099	0.0024	0.009	0.0057	0.017

*Passage width at half channel radial length.

6.2.3 CFD Results

Figure 6.13 shows the streamlines of relative speed for discs with 20 and 45 vanes. The difference in flow behaviors through the channels is evident, with the brake disc with 20 vanes promoting recirculation in large part of the leading side of the passage. Opposite to this, the narrow channel (4 degrees) in the 45-vane design, soaks and pumps air with little or no recirculation at all. In this sense, the narrow channel seems better in controlling flow recirculation. Nevertheless, in the wide channel design the area where air is pumped is significant, airflow maintains 7.5m/s for larger length in the channel trailing side; which does not occur in the narrow channel where air speed rises to 8.5 m/s only in the trailing side of the inlet, but it falls before reaching half channel. This will have an effect on the local distribution of heat transfer coefficients. Complementary information is shown in Figure C.6.

The contours of total pressure (Figure 6.14) reveals a lobule of higher pressure on the channel

Table 6.3: Data calculated at half the channels length.

Disc	A	P_w	D_h	P_{cr}/h
	[m^2]	[m]	[m]	
Baseline 30 vanes	3.83E-04	0.079	0.0194	1.32
20 vanes	6.89E-04	0.115	0.0239	2.38
45 vanes	1.96E-04	0.057	0.0137	0.68
60 vanes	1.92E-04	0.057	0.0136	0.66
90 vanes	9.69E-05	0.045	0.0085	0.34

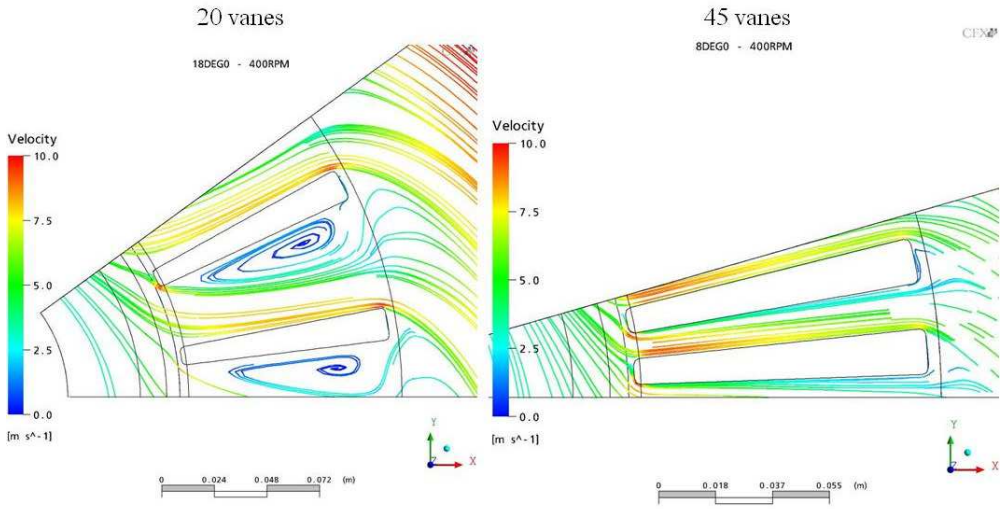

Figure 6.13: Relative speed streamlines, 20 and 45 vane designs, n=400rpm.

trailing side of the 20 vanes disc. This is 83 Pa against 64.1 Pa given by the disc with 45 vanes. This difference points to a higher mass flow pumped by the wider channel with more energy than in the narrow channel. The wider channel brake disc then requires higher force to keep the angular speed (or momentum) than the narrower channel brake disc. Air temperature on channel midplane show particular behaviour for each brake disc. In the brake disc with 20 vanes (left of Figure 6.15), there exist a large region on the leading side where temperature raises. This region corresponds to the low speed recirculating flow. While in the trailing side, due to the high speed, air does not heat up providing with a good sink for heat dissipation from the vane. Also, although there is a wide thermal layer on the leading side, this does not meet the other on the trailing side; however, in the brake disc with 45 vanes, the channel is narrower and this promotes a point of thermal development toward the end of the channel. Air temperature patterns on periodic faces, at channel centre (Figure

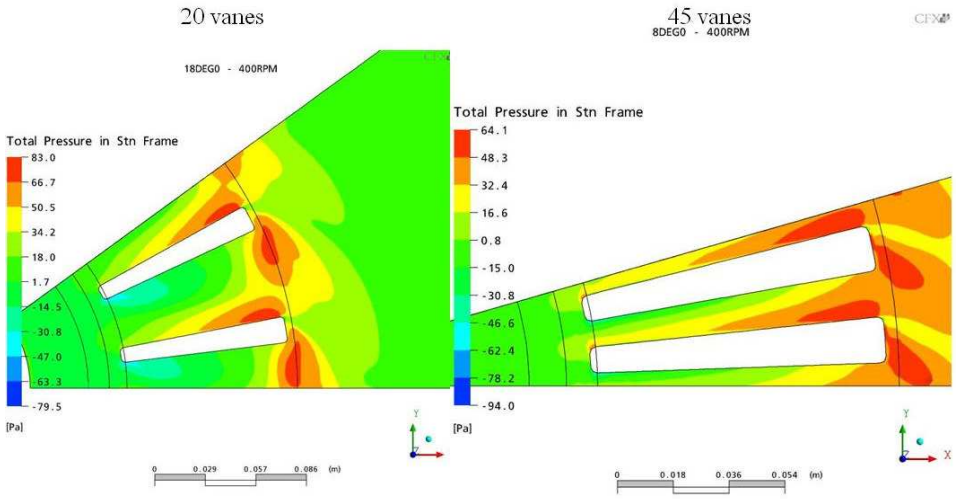

Figure 6.14: Total pressure, channel midplane, 20 and 45 vane designs, n=400rpm.

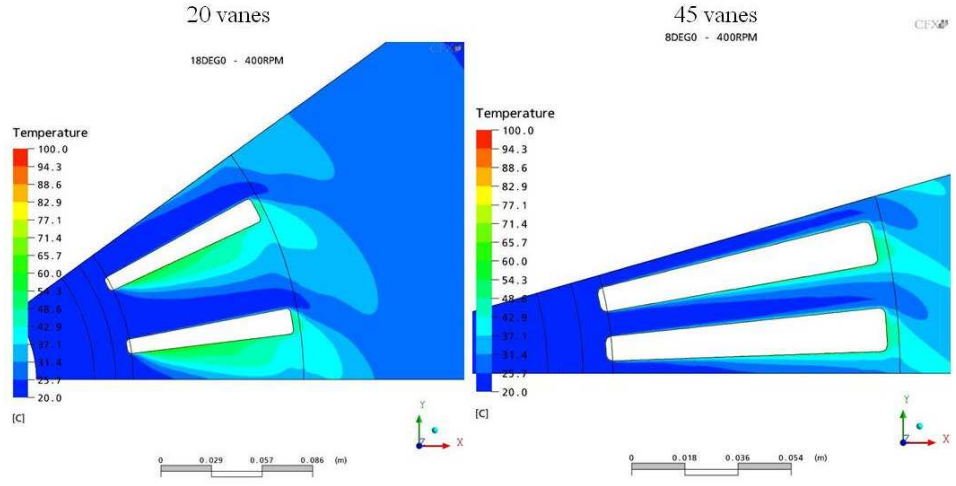

Figure 6.15: Air temperature in channel midplane, 20 and 45 vane designs, n=400rpm.

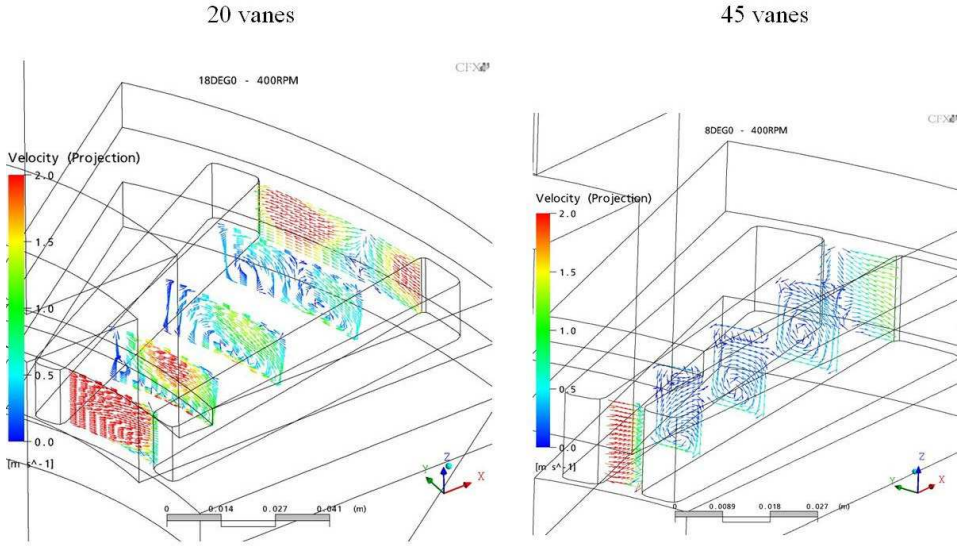

Figure 6.16: Secondary flow activity, discs with 20 and 45 vanes at n=400rpm.

C.7) shows that the influence on air temperature is higher in axial direction for the disc with wider channels.

Secondary flow (Figure 6.16) shows more activity in the disc with wide channels. An initial cell at 2 m/s forms toward the outboard side of the channel, which then dissipates into two cells at lower speed near the outlet of the channel. The activity of secondary flow in the narrower channel is more modest (less than 0.5 m/s), and a cell forms in the inboard side of the channel which then moves toward the centre as the flow proceeds. More uniform heat transfer coefficient distribution is shown in the 45-vane design than in the 20-vane design (Figure 6.17). In the latter, low values (between 7 and 14.1 W/m^{2}K) exist on the vane wall in channel leading side, while on the opposite side 52.7 W/m^{2}K is reached as result of high speed. The semi-symmetric distribution on the 45-vane design could mean that theoretical solutions for convection heat transfer within stationary rectangular ducts would possibly approximate the rotating behaviour. On the endwalls (Figure 6.18), a skewed heat transfer coefficient distribution results for the 20-vane design varying from 7 to 45 W/m^{2}K. Endwalls of the 45-vane design show better (less skewed) distribution with higher average heat transfer coefficients. In general, the 45-vane offers better h_{ch} than the 20-vane design. Kinetic energy levels are higher in the wider channel design than in the narrow design, (Figure C.8), this as result of vane misalignment and larger channel expansion, the higher levels at the channel exit are likely due to encounter between wake (recirculating) and jet streams.

Relative speed streamlines on channel midplanes of 60 and 90 vane designs show that although the channel continues to be trapezoidal, flow recirculation is almost removed as seen

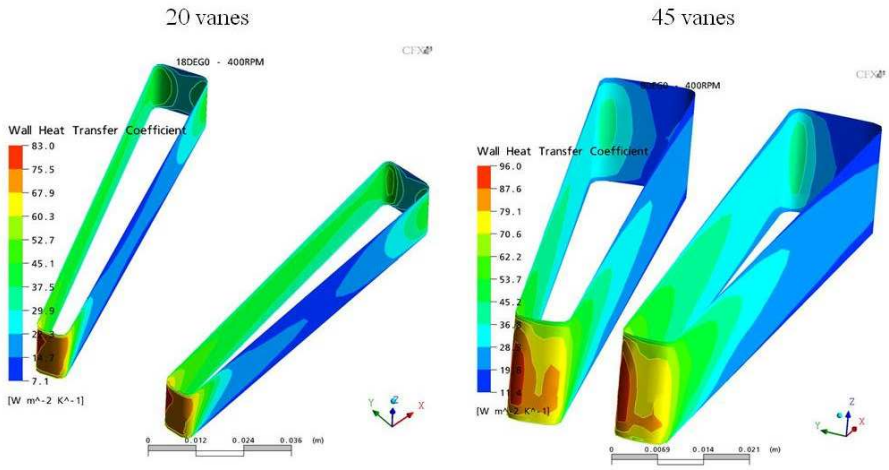

Figure 6.17: Convective heat transfer coefficients in vanes, 20 and 45 vane discs, n=400rpm.

in Figure 6.19). 7.5 m/s are reached on the channel trailing side of the 60-vane design, while the lowest value (2.5 m/s) occur at the leading side outlet. Insignificant flow recirculation exists in the 90-vane design, high speed above 7.5 m/s localises in the channel throttle (inlet), but this falls rapidly to below 5 m/s along the channel. Complementary information is given in Figure C.9. Secondary flow activity less significant and therefore not reported. Flow thermal development is shown by the air temperature patterns, Figure 6.20, in the 60-vane design thermal layers meet after 80% of the channel radial length, while this decreases to 25% for the 90-vane design. Therefore, heat transfer coefficients would reach their lowest values about these lengths. The same effect is observed on the periodic faces (Figure C.10), with the thermal layers meeting at similar distances from the inlet. The quick increment of air temperature in the channel is detrimental to convection and also influences the length of the plume leaving the channel, which in these cases are larger than that given in the baseline brake disc (see Figure 5.41).

On channel trailing sides, convective heat transfer coefficients vary from 85.2 W/m^{2}K (60-vane) and 91.8 W/m^{2}K (90-vane) at the inlet to 38.1 W/m^{2}K and 30.5 W/m^{2}K at the outlet (Figure 6.21). On channel leading sides, the lowest values of heat transfer coefficients are 28.7 W/m^{2}K and 20.3 W/m^{2}K, respectively. Noticeably, the distribution in the 90-vane design is much more symmetric despite disc rotation, this is in line with the temperature pattern observed in Figure 6.20. On the endwalls (Figure 6.22), the heat transfer coefficient distribution of the 90-vane disc is poorer than that of the 60-vane disc. Most of the endwalls second half in the 90-vane design have 10 to 22.7 W/m^{2}K, while in the 60-vane disc they are between 21 and 33.5 W/m^{2}K.

The overall performance of convective heat dissipation was plotted against angular speed. Figure 6.23(a) shows h_{ch} for all the radial vane configurations. Comparing against the

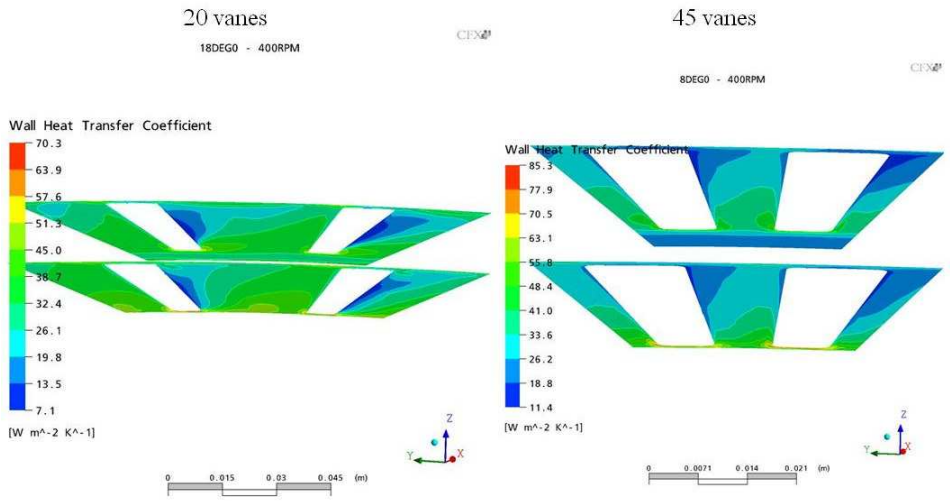

Figure 6.18: Convective heat transfer coefficients in endwalls, 20 and 45-vane design at n=400rpm.

baseline, the poorest channel heat transfer coefficient occurs in the 90-vane design (reduction of 25%), 20 and 45-vane channels are near each other with 13% and 9.4% lower than the baseline, while h_{ch} in the 60-vane channel is just 2.4% lower than the baseline. Heat transfer coefficients averaged per brake disc are shown in Figure 6.23(b). The graph shows that the disc with 60 vanes is the best performer, as is 5.6% above the baseline curve. The results of the brake discs with 20, 45 and 90 vanes are all around 6% below the baseline curve.

From the above results it is foreseen that discs convective cooling rate will be mostly ruled by their wetted area and mass weight, since the specific heat capacity is constant. Cooling rates are calculated using the disc average heat transfer coefficient (from CFD) and substituting in equation 4.18 (in place of h_{d_t}). Therefore if the product $\frac{A_w}{m_d C_{p_d}}$ is calculated for each brake disc and compared, this will give a figure of the brake cooling ability based solely on material and geometry properties. This is shown in Figure 6.24, where the baseline brake disc is the datum (0.0% level) and the relative differences are shown in percentage. It is seen that brake discs with 60 and 90 have better heat exchanger ability than the others, and this is independent of the heat transfer coefficient. The percentage shown is the factor by which their average heat transfer coefficient is boosted during the cooling process. The discs convective cooling rates are shown in Figure 6.25(a) together with the brake disc torque required for rotation (b). Since the brake disc with 60 vanes resulted with 5.6% larger heat transfer coefficients than the baseline, its cooling rate is further increased to 21% over the speed range. The brake disc with 90 vanes is also benefited and overcomes its low fluid based performance by laying with 9% better cooling rates than the baseline brake disc. The worst

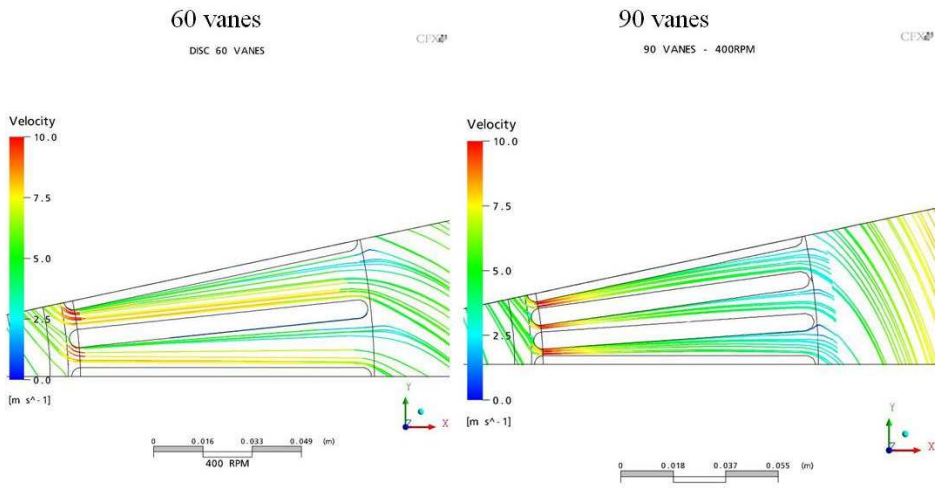

Figure 6.19: Streamlines on channel midplane, 60 and 90 vane designs at n=400rpm.

cooling rates are for the disc with 45 vanes and 20 vanes (-7.7% and -5% lower than the baseline, respectively). The torque graph shows that the disc with 60 vanes would require 6% more than the baseline design, while the discs with 45 and 90 vanes require 15% and 30% less than the baseline. The disc with 20 vanes have similar requirements of energy for rotation as the baseline brake disc.

The required torque for rotation is proportional to the mass flow and to the angular impulse given to it while passing through the channel[2]. From Figure 6.26 it is seen that the 20-vane design is the less efficient (aerodynamically) since it pumps less air (6%) than the baseline with similar torque requirements. The brake discs with 45 and 90 vanes pumps even less mass flow (18.6% and 40%) than the baseline, but with lower torque requirements. The 60-vane design pumps a similar amount of air mass but requires 5% more torque than the baseline. However, this could be considered the most efficient arrangement of radial vanes, due to its high convective cooling rates. The designs analysed up to here are straightforward variations of the original design. Their results have shown that:

1. Brake discs with cylindrical channels with the same hydraulic diameter as the baseline give 14% less disc heat transfer coefficients along the speed range, and due to its increased mass and reduced wetted area, their cooling rates are 26% (in average) lower than those of the baseline disc.

2. Varying the number of radial vanes in the brake disc has pointed to an optimum number of vanes for maximum convective cooling. This is 60 vanes, which along with

[2]Other sources of torque are given by the drag of the friction surfaces

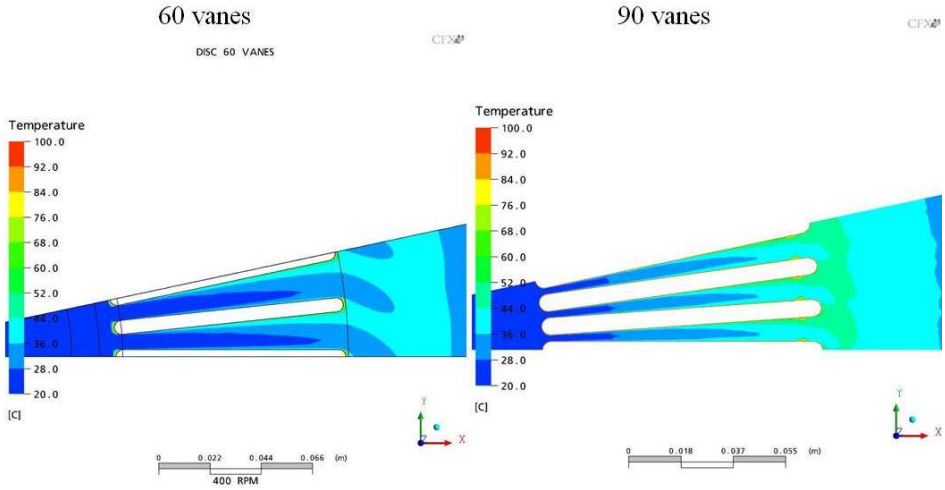

Figure 6.20: Air temperature on channel midplane, 60 and 90 vane designs at n=400rpm.

90 vanes gives higher convective cooling rates than the baseline; however the results of these configuration is highly driven by disc wetted area and material properties (Figure 6.24), rather than by fluid behaviour. This is confirmed by results shown in Figure 6.23, which yield to worst average heat transfer coefficients for discs with 90 and 20 vanes.

Table 6.4: CFD model mesh statistics for discs with cylindrical channels and with 20, 45, 60 and 90 vanes.

Disc	Hexas	Tetras	Prisms	Pyramids	Cells	Nodes
Cyl	805452	131079	45838	6659	989028	891348
20 Vanes	1061608	24980	15130	1931	1103649	1117981
45 Vanes	593230	18699	6020	2409	620358	638119
60 Vanes	663578	8854	7866	822	681120	705432
90 Vanes	362218	54449	16998	4147	437812	413259

6.3 Small Vane Inside the Channel

This design results from analysing the information in Figures 5.35, 5.36, 5.42 and 5.45) and data in Figures 5.54 and 5.55. A characteristic behaviour occurs in radial diverging channels,

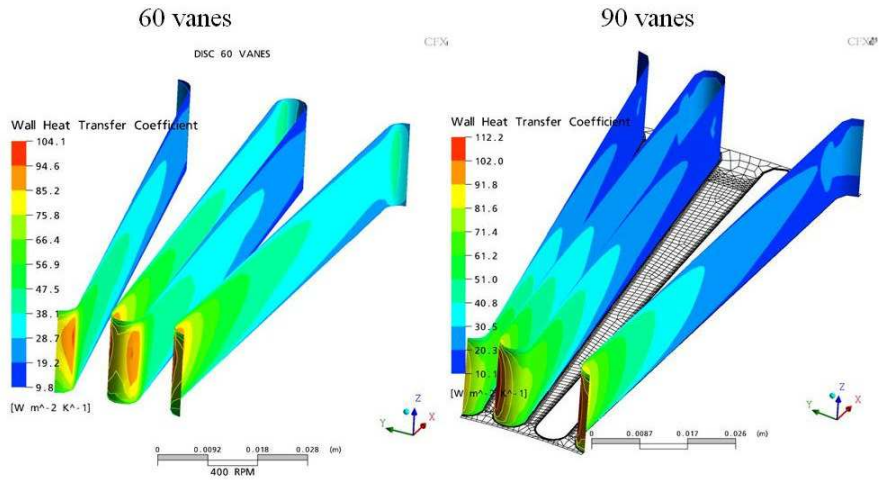

Figure 6.21: Convective heat transfer coefficients in vanes, 60 and 90-vane designs, n=400rpm.

Table 6.5: Brake discs convection areas (includes top hat) and mass, radial vanes designs.

Brake disc	Channels area, m^2		Disc area without channels, $[m^2]$	Disc area $[m^2]$	m_d [kg]
	Vanes	Endwalls			
Cyl Channels	0.1943		0.3978	0.5920	32.8
20 vanes	0.0713	0.1797	0.3802	0.6311	29.1
Baseline (30 vanes)	0.1069	0.1578	0.3802	0.6449	30.4
45 vanes	0.1604	0.1249	0.3802	0.6655	32.4
60 vanes	0.2089	0.1564	0.3802	0.7454	30.7
90 vanes	0.3133	0.1179	0.3802	0.8114	32.8

which disregarding the number of vanes do not change radically[3]: Vane (or channel) inlet misalignment causes low (recirculating) speed flow in channel leading side which lowers the convective heat transfer ability of the nearby vane wall, i.e.: airflow temperature increases without transporting effectively heat to flow core. On the trailing side, high speed provide a significant heat sink (at high speed) for convective dissipation. Also, it was noticed that heat transfer coefficients along vane wall of channel leading side drop in radial direction (toward the outlet), giving uneven distributions not only between sides of the channel but along the vane wall itself.

[3]Only the 90-vane design gave quasi-symmetric patterns of air speed, temperature and heat transfer coefficients through channels, however differences were still evident between low and high speed regions.

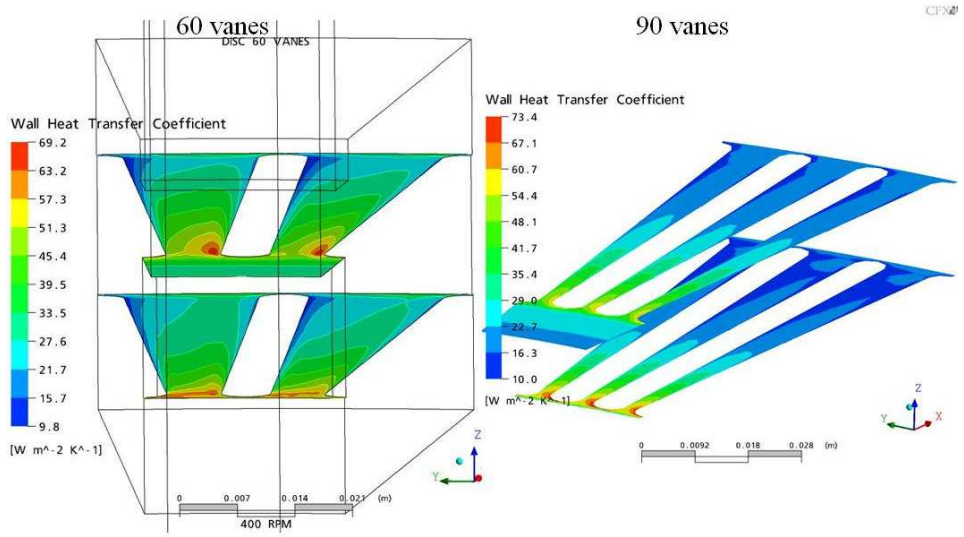

Figure 6.22: Convective heat transfer coefficients in endwalls, 60 and 90-vane designs, n=400rpm.

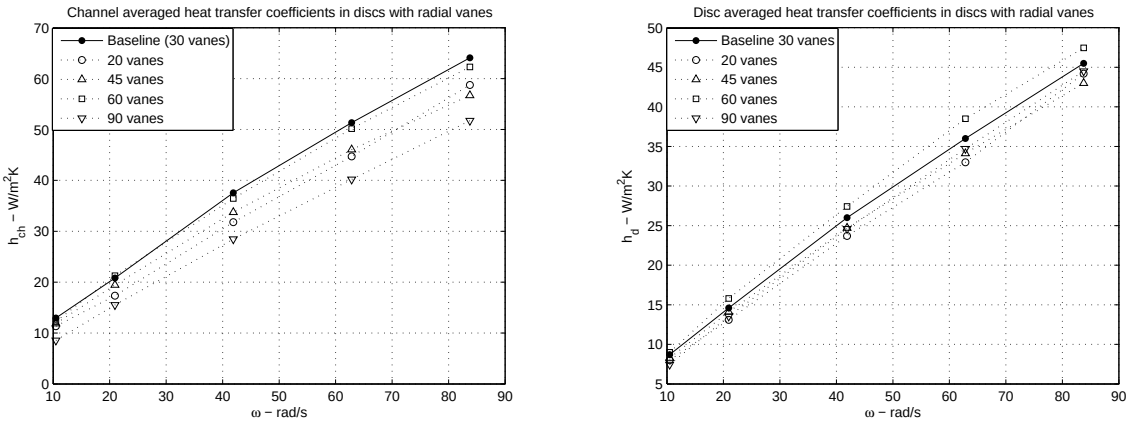

(a) h_{ch} vs ω (b) $\overline{h_{d_c}}$ vs ω

Figure 6.23: Averaged heat transfer coefficients versus angular speed.

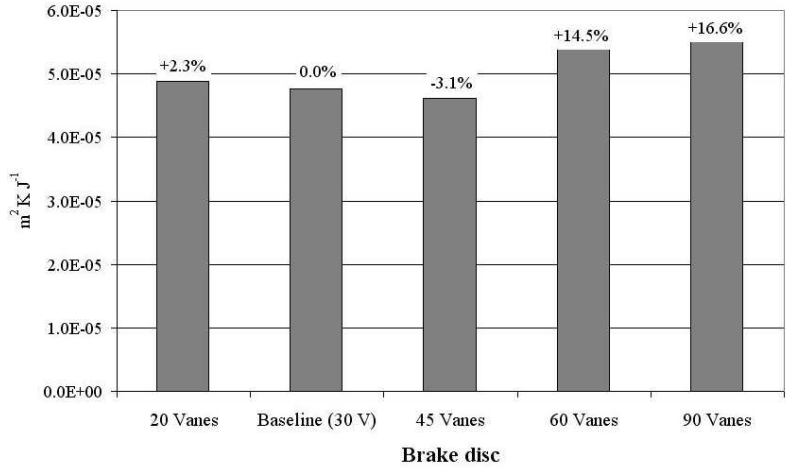

Figure 6.24: Comparison of $\frac{A_w}{m_d C_{p_d}}$ for researched brake discs (radial vanes).

Aiming to redistributing heat transfer coefficient on channel leading side and increasing its value, a local narrowing of the channel was implemented by including a radial straight smaller vane in the channel. This is shown schematically in Figure 6.27. By narrowing channel cross section it is expected that local speed increases due to channel mass flow continuity ($\rho A u_n$ =const). The increase in local speed would augment the speed gradient normal to the vane walls and therefore, increases local heat transfer coefficient. The perimeter of the smaller vane has been chosen as half of the larger vane and its width is 9 mm. The shape followed a filleted rectangle of 51x9mm. The circumferential symmetry does not change and therefore the behaviour is independent of the rotation direction.

6.3.1 Geometry

A smaller straight radial vane (SV1) was located inside the channel. Although the purpose of the SV1 vane was to narrow the channel downstream, three radial locations were investigated, as shown Figure 6.28. Table 6.6 shows geometric characteristics of SV1 and channel.

The length and perimeter of SV1 are 53.7% and 53.5% of the baseline vane. The SV1 vane serves not only as channel constrictor but gives additional convection area and it also brings and an indexed brake disc mass increase, as observed in Table 6.7. The increment in wetted area is balanced by that in brake disc mass, in such a way that the product $\frac{A_w}{m_d C_{p_d}}$ of the brake discs with SV1 included is about 0.4% below that of the baseline brake disc. Therefore their convective cooling rate differences will be driven only by the fluid based performance.

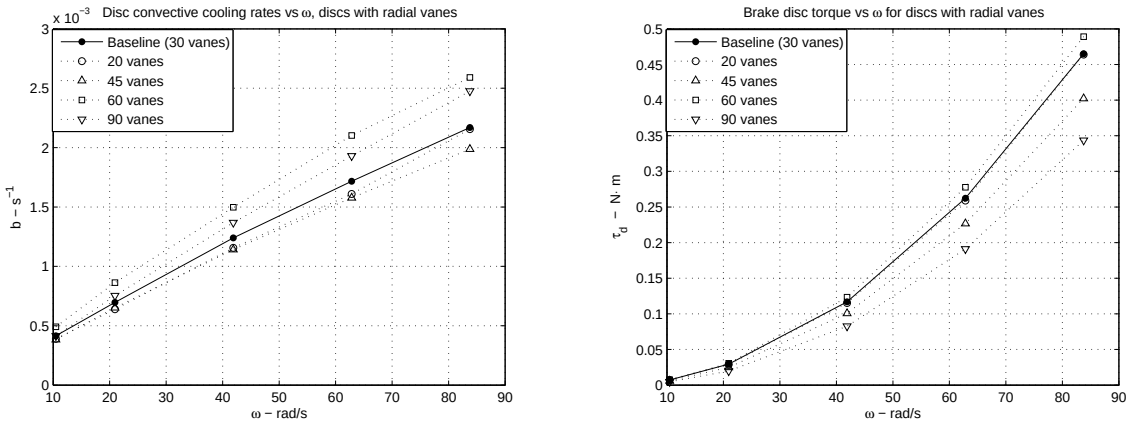

(a) b vs ω (b) τ_d vs ω

Figure 6.25: Convective cooling rates and aerodynamic torque, discs with radial vanes.

Table 6.6: Characteristics of the channels with the SV1 implemented, see Figure 6.28.

Channel design	SV1 inlet (b)	SV1 middle (c)	SV1 outlet (d)
S1, [mm]	0	22	48
S2, [mm]	44	22	-4
$\frac{A_2}{A_{in}}$	A_{in}=68 mm^2 (per side)	0.34	0.44
$\frac{A_2}{A_3}$	0.57	0.66	0.71
SV1 Length, [mm]		51.0	
SV1 Perimeter, [mm]		112.3	

6.3.2 CFD Models

Three independent CFD models were constructed following the recommendations given in Sections 5.1. The boundary conditions were also the same as those described in the beginning of this Chapter. The surface grid details in the region of the vanes is shown in Figure C.11, in Appendix C. The statistics of the CFD models is shown in Table 6.8.

6.3.3 CFD Results

Results are provided for 400 rpm in contour plots and as mentioned earlier disc rotates about z in anticlockwise direction. The analysis is complemented with graphs of discrete

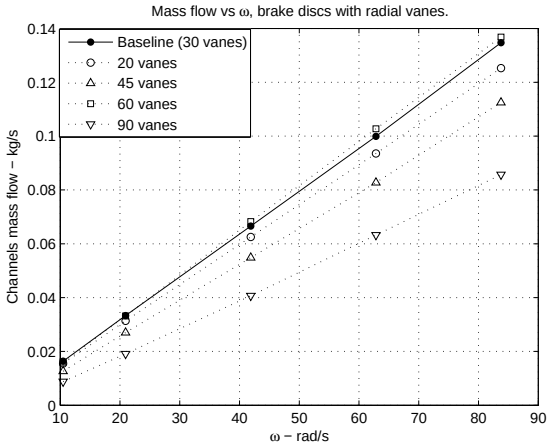

Figure 6.26: Mass flow in brake disc channels with radial vanes. (data from CFD).

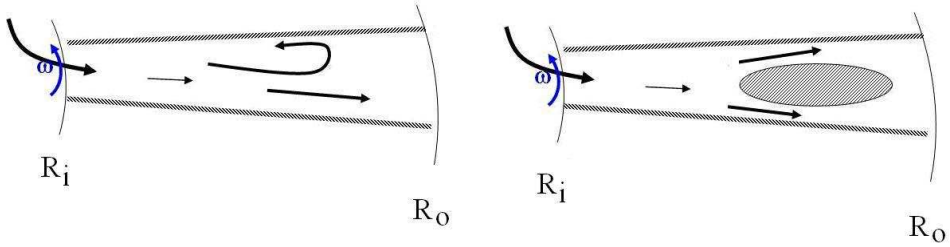

Figure 6.27: Channel flow pattern modification. Left: original pattern, right: modified pattern.

data. Streamlines of relative velocity on channel midplane are shown in Figure 6.29, where as usual, the velocity scale was adjusted between 0 and 10.0 m/s. Evidently the worst flow condition (lowest speed) is given for the channel with SV1 at the inlet, where air stream gets a maximum relative speed below 7.5 m/s in the sides of SV1. Further down, the flow goes into a sudden channel expansion and therefore its speed drops to almost zero in the leading side and 5 m/s in the trailing side.

In the design with SV1 at the middle the initial misalignment gives room to small recirculation in the channel leading side. Near the cross section reduction and on channel trailing side, the local relative speed increases from 6.3 m/s at the inlet to 10.0 m/s while in the leading side constriction the inlet speed is slightly reduced. Despite not having the expected increment in speed, is important to see that SV1 turns the recirculation region into streamlined flow near the vane wall in the channel leading side, this would eventually benefit the convection heat transfer coefficient distribution. Finally, on the trailing side constriction,

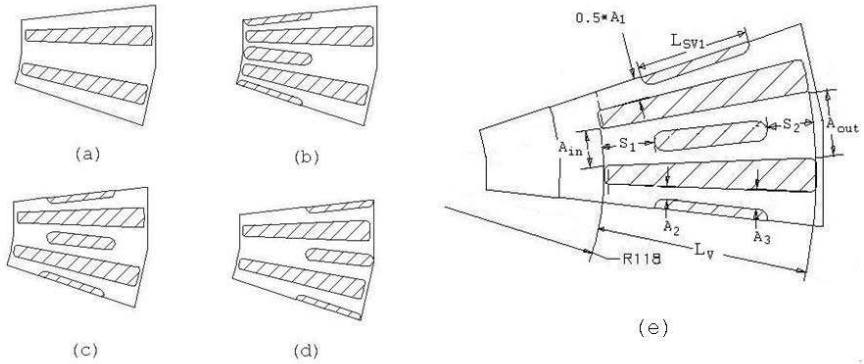

Figure 6.28: Channel sector characteristics, (a) Baseline channel, and channel with: (b) SV1 at inlet, (c) SV1 at half channel, (d) SV1 at outlet. (e) Location details.

Table 6.7: Convection (wetted) areas and mass of brake discs designs with SV1 vane.

Brake Disc	Area channels, m^2		Area disc without channels, [m^2]	Area disc [m^2]	m_d [kg]
	Vanes	Endwalls			
Discs with SV1	0.1642	0.1313	0.3802	0.6756	31.9

flow keeps high speed almost until the outer end of the channel, while the sudden expansion affects more to the air coming out from the leading side constriction. The channel with SV1 at the outlet allows larger recirculation region in the leading side, but this is removed before reaching the SV1 attack edge. The flow relative speed in the leading side constriction increases to values between 2.5 and 5.0 m/s, while in the trailing side constriction the relative speed increases to values near 8.0 m/s. These both speed changes will also benefit the heat transfer coefficient distribution in the outer ends of the vane walls. Flow behaviour visualization is complemented with streamlines shown in Figures C.12 and C.13.

The air temperature profiles in the midplane of the channels (Figure 6.30) show the effect

Table 6.8: CFD model mesh statistics for discs with SV1 vane.

Disc	Hexas	Tetras	Prisms	Pyramids	Cells	Nodes
SV1 inlet	916377	27247	21210	1836	966670	978295
SV1 mid	1076425	16918	9554	1560	1104457	1134045
SV1 outlet	766200	124630	-	4259	895089	836535

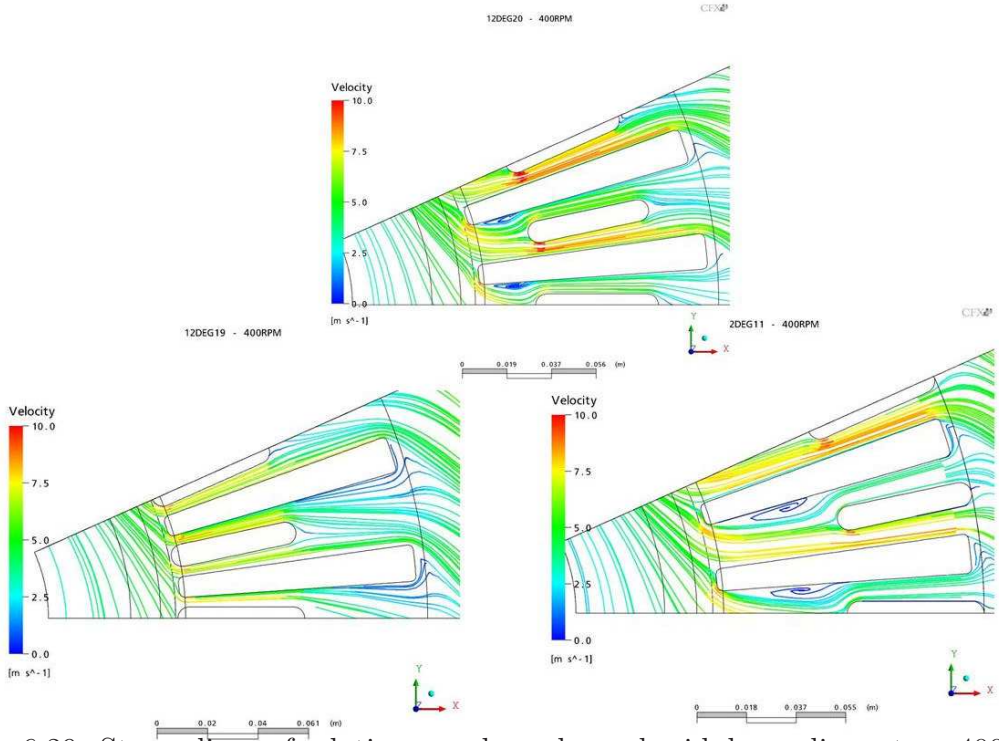

Figure 6.29: Streamlines of relative speed on channel midplane, discs at n=400rpm.

of relative speed. When SV1 is at the channel inlet, low temperature streams flow on its sides, but the speed drop at the channel expansion deteriorates the convective transport of heat and diffusion gains place in the leading side of the outlet region; this promotes thermal development. The channels with SV1 at the middle and the outlet show the best air temperature distributions for convection heat transfer since cooler air reaches radially farther locations on trailing sides, retarding flow thermal development. In the channel leading sides, thermal development occurs at the constriction inlet when SV1 is at the middle, and when this locates at the outlet, the flow in the leading side constriction is thermally developed from the start (which could yield to quasi-symmetric heat transfer coefficient distributions in this channel side).

The heat transfer coefficients of the discs are shown in Figures 6.31 and 6.32. Heat transfer coefficients on the vane walls are better distributed when SV1 is located at the outlet of the channel, since high values (65.7 W/m^{2}K) appear in the leading side channel wall, in the channel constriction zone (the corresponding wall of the baseline channel shows heat transfer coefficients of about 29.1 W/m^{2}K, Figure 5.42). In the trailing side constricted region, another local peak is given also. With the SV1 at the middle, the distribution in the channel leading side (on the vane) is more modest than the above mentioned and the heat transfer coefficient drops afterward. In the trailing side wall, the SV1 at the middle also improves the heat transfer coefficient distribution inlet portion of the trailing side wall, but

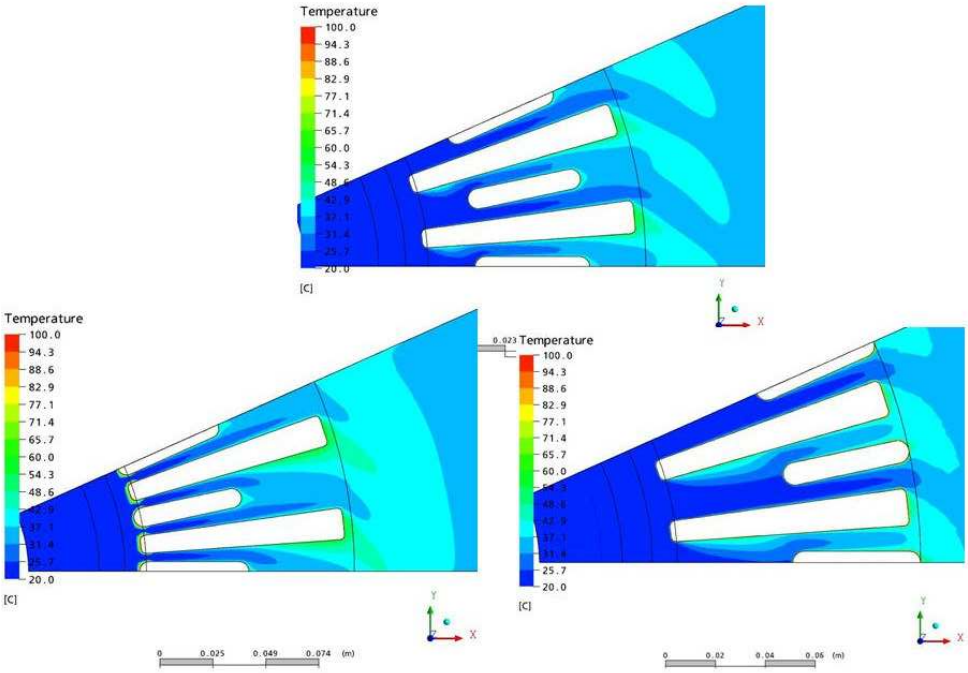

Figure 6.30: Air temperature in channel midplanes, discs at n=400rpm.

this improvement falls along radial direction. When the SV1 locates at the innermost radius low convective heat transfer coefficients are given in the vanes, the highest are at the inlet, but they are still below the other two designs. Also, low values (5.9 W/m^{2}K) occur in the outlet part of the vane wall in the channel leading side.

The distributions in channel endwalls (Figure 6.32) point to the configuration with the SV1 at the outlet as the best of the three. This configuration keeps a semi-constant (45.4 W/m^{2}K) value of heat transfer coefficient along the trailing constricted side channel, while a symmetric low distribution (23 W/m^{2}K) exists in the constriction of the leading side. The endwalls with SV1 at the middle also develop good distribution in the trailing constricted side (46.5 W/m^{2}K), but this drops to quickly to 28.3 W/m^{2}K as it reaches the radial end, in the leading side the heat transfer coefficient drops more to reach values of 10 W/m^{2}K. Finally, the distribution of heat transfer coefficients with SV1 at the inlet, is the less favourable since the maximum value oscillates about 34.9 W/m^{2}K which then falls to 20.4 W/m^{2}K and 5.9 W/m^{2}K in the trailing and leading sides of the channel respectively.

Averaged results as function of the angular speed of the brake discs are shown next in Figures 6.33, 6.34 and 6.35. Figure 6.33 indicates that heat transfer coefficients of the channels with the SV1 at the outlet and at the middle are around 3.5% higher than the baseline for speeds above 600 rpm, while below that speed the difference is minimal. Those with SV1 at the inlet are in average 13% below the baseline brake disc, with poorest performance for angular

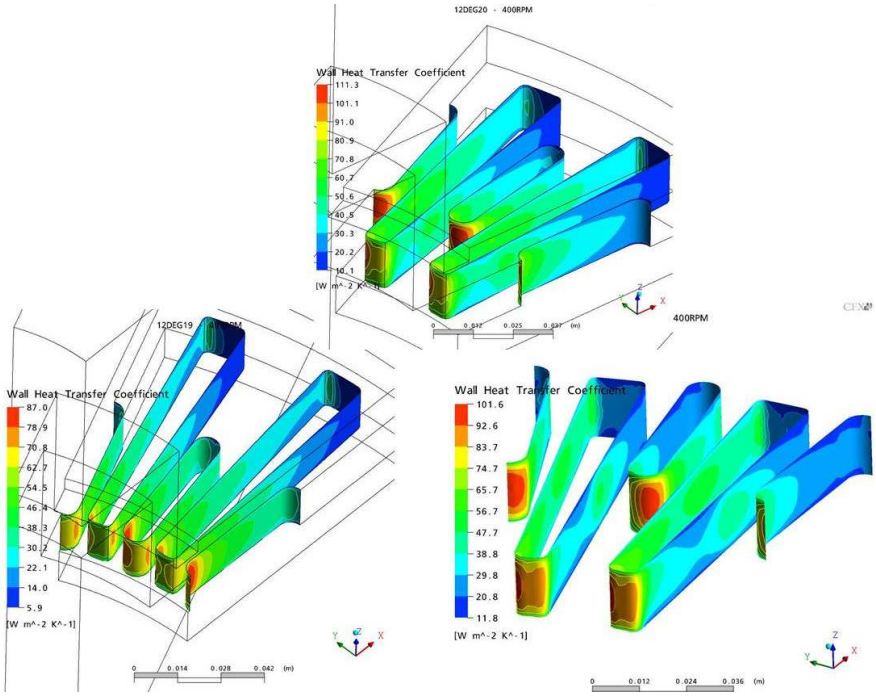

Figure 6.31: Convective heat transfer coefficients in vanes, discs with SV1 at n=400rpm.

speeds between 600 and 800 rpm. The behaviour of the heat transfer coefficients averaged per disc points to the brake disc with SV1 at the outlet as the best with 3% more than the baseline brake disc, while the brake disc with SV1 at the middle equals the baseline. The poorest result is for the brake disc with the SV1 vane at the inlet, which shows a trend 11% below the baseline curve.

As said before, the brake disc cooling rates follow similar behaviour (Figure 6.34), and the percentage differences are as above mentioned. The required torque are all below that of the baseline brake disc, 9% for the SV1 at the outlet, and 16% and 34% lower for the brake discs with the SV1 at the middle and at the inlet. This is mainly due to the lower air pumped (the SV1 vanes reduce air admission), Figure 6.35. The mass flows pumped are 14%, 20% and 40% lower than the baseline for the brake disc with the SV1 vane at the outlet, middle and at the inlet, respectively. While the above averaged results could mean modest improvement in the cooling capabilities using SV1 to narrow the channel, the major achievement of this design modification is the change in heat transfer coefficient distribution within the channels. This is mostly reflected by the gain achieved in the leading sides of the channel. For the cases (c) and (d) of Figure 6.28, the vane wall in the channel leading side develops new heat transfer coefficient coefficient distributions which tend to more homogeneous convective heat rejection from both sides of the channel. This effect also cascades onto the channel endwalls, which behave in a similar manner.

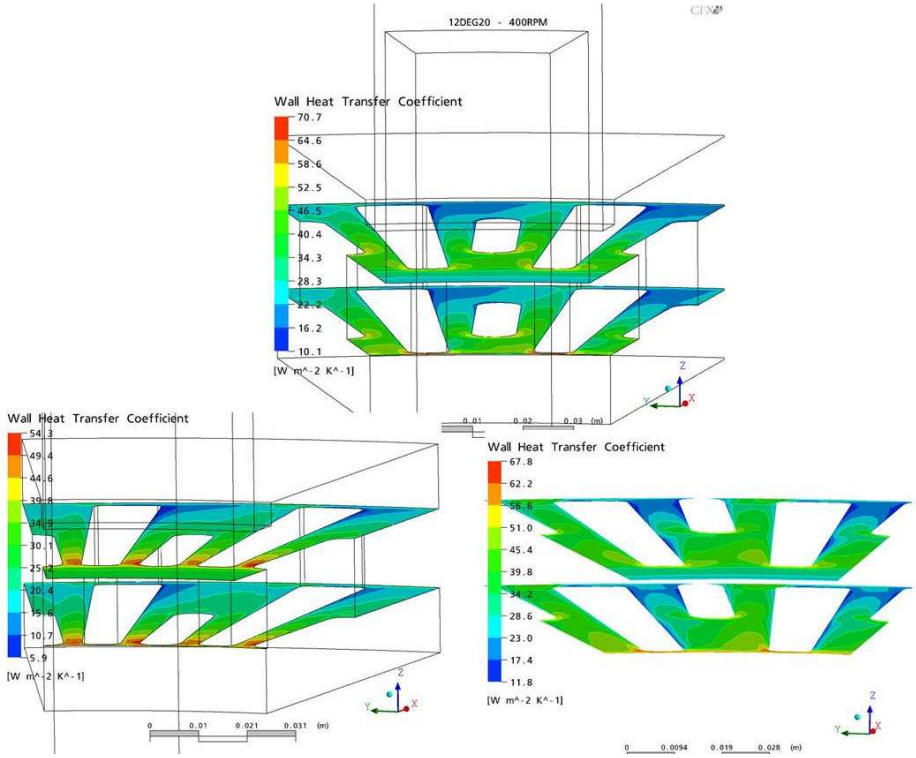

Figure 6.32: Convective heat transfer coefficients on endwalls, disc with SV1 at n=400rpm.

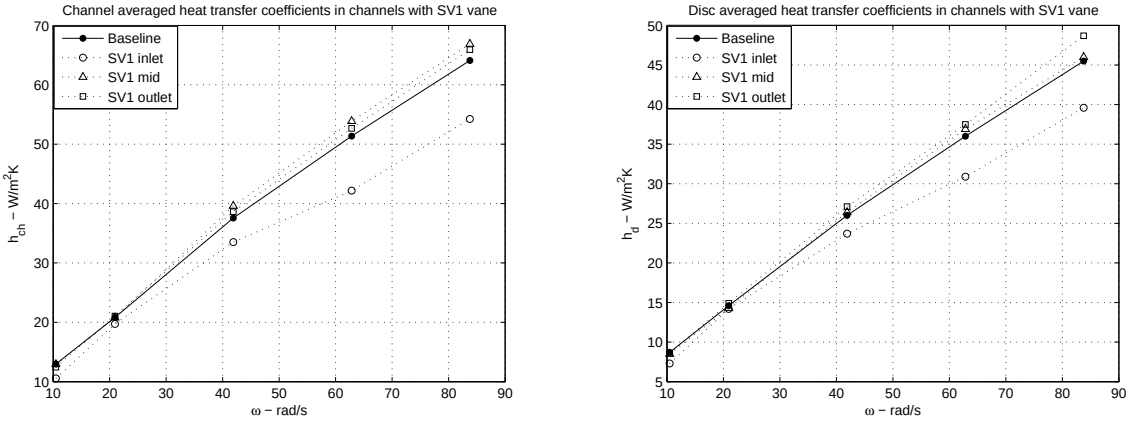

(a) h_{ch} vs ω (b) h_d vs ω

Figure 6.33: Comparisons of convective heat transfer coefficients, discs with SV1 vane.

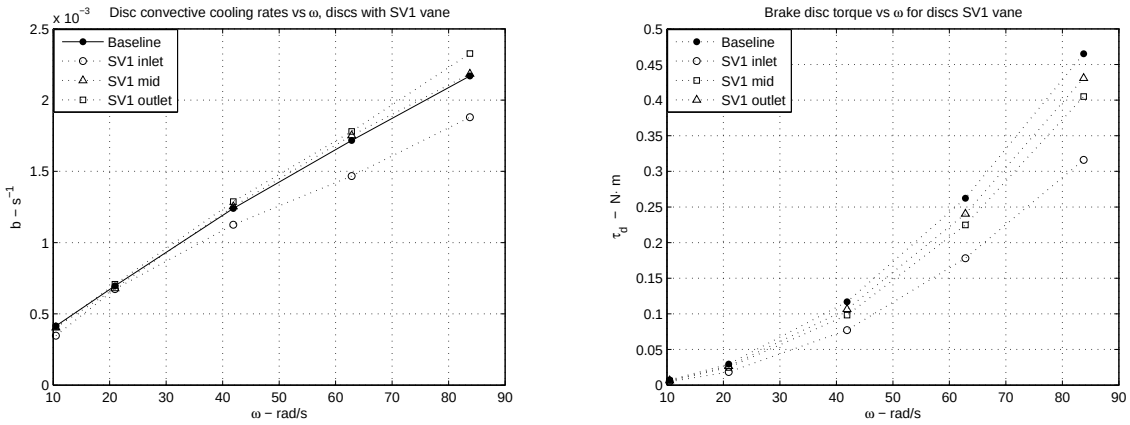

(a) b vs ω (b) τ vs ω

Figure 6.34: Convective cooling rates and aerodynamic torque, discs with SV1 vane (data from CFD).

Unlike the baseline channel, the designs with SV1 indicate a possibility of airflow management in vents of brake discs. This is analysed plotting discrete values of air absolute radial speed, temperature and heat transfer coefficients in zones close to the vane walls, these then were compared against those from the baseline channel. Temperature data was retrieved in three lines which lay parallel to the vane walls 2 mm away, and the results averaged per vane wall (see Figure C.14). Absolute speed, retrieved in the lines on the midplane only, was calculated parallel to vane walls. Heat transfer coefficients were retrieved from the projection of the centre lines on the vane wall, and therefore only one set of data was obtained per vane wall. The results are plotted versus the vane length, with its attack edge in the left end of the graphs. The black, red, magenta and blue colored lines correspond to the baseline, SV1 at inlet, SV1 at the middle and SV1 at the outlet designs respectively. CFD data from simulations at n=800rpm were used.

Radial absolute speed near the vane wall on the leading side shows that all the configurations of SV1 improves locally the velocity of the flow (see left of Figure 6.36). SV1 at the inlet breaks the backflow region existing in the inlet of the baseline channel, but it gives stagnant flow in the last 40 mm of this vane wall side. SV1 at the outlet still gives backflow in about 20 mm after the first 20 mm but then, the air speed substantially increases from zero to 8.0 m/s in a very short length. The configuration with the SV1 at the middle gives the best results for speed in this side, since it breaks recirculation flow and provides a larger and continued increase of speed afterward.

Results for radial absolute speed near vane wall on the channel trailing side (Figure 6.36(b))

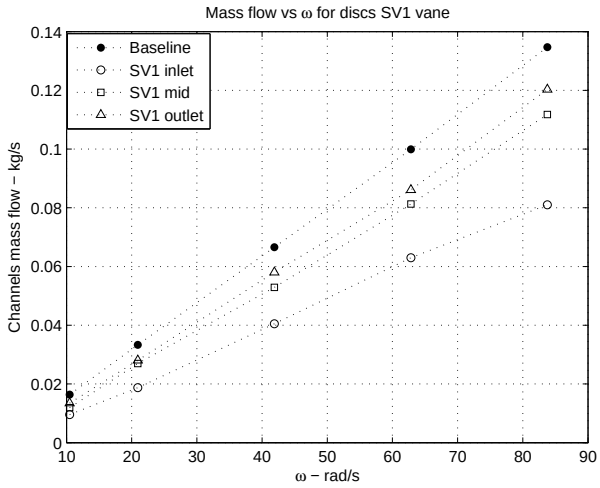

Figure 6.35: Mass flow from discs with the SV1 vane versus the baseline brake disc, (data from CFD results).

shows large negative gradients when SV1 locates in the inlet (8 m/s drop, 6 m/s below the baseline), while u_r increases locally when SV1 is located at the middle and at the outlet. These increments span for about 50 mm from the position of the SV1 attack edge. The maximum increment occurs for SV1 at the middle. On the leading side airspeed changes in all conditions, however SV1 at the inlet increases only at the inlet and immediately drops after. Positions at the middle and outlet significantly change the airspeed behaviour in the channel leading side, virtually breaking the recirculation effects.

Air temperature near the walls of the vanes determines the potential of heat dissipated by convection, and it is also influenced by the air speed. Low air velocity will reduce the convective rate of energy transport (left hand side of equation 3.51), and therefore transport by diffusion will dominate. However, the diffusion ability of air (conduction) is not good (as in metals), and because of low speed any energy gained is not transported, promoting air temperature build up. This results in low heat dissipation from the wall. However, when air speed is high, then heat dissipation is dominated by the convection which is proportional to speed. Averaged air temperature profiles 2 mm away from the vane wall show cooler air in the channel leading side when SV1 locates at the middle and outlet, both cool temperatures are promoted by air speed increment in that side. Air temperature for SV1 at the inlet shows the opposite behaviour, first is cooler and then gains temperature. The behaviour in the trailing side indicates that SV1 at the inlet heats up the air more, while the other two configurations give air temperature slightly bigger than the baseline data.

Figure 6.38 shows the local variation of convective heat transfer coefficients in the vane

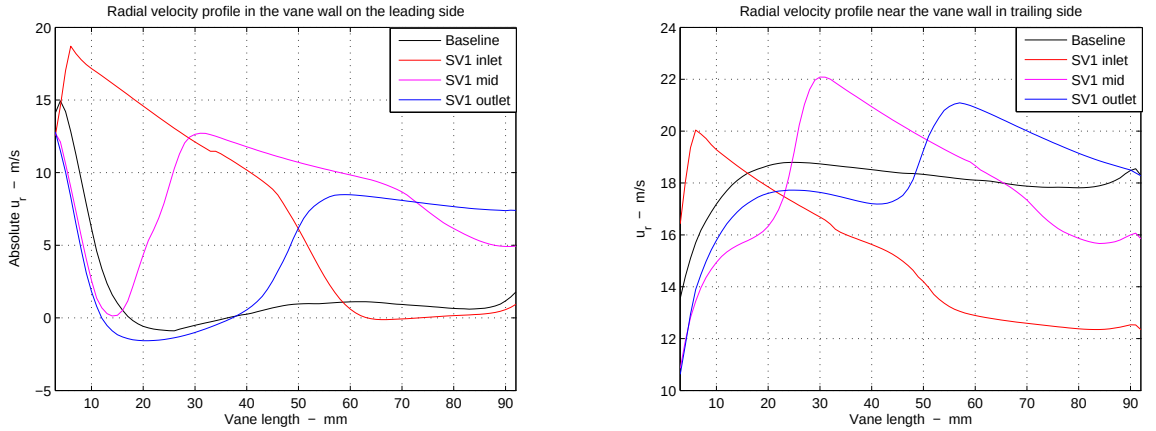

(a) Leading side (b) Trailing side

Figure 6.36: Absolute speed of air near vane wall, per channel side, n=800 rpm.

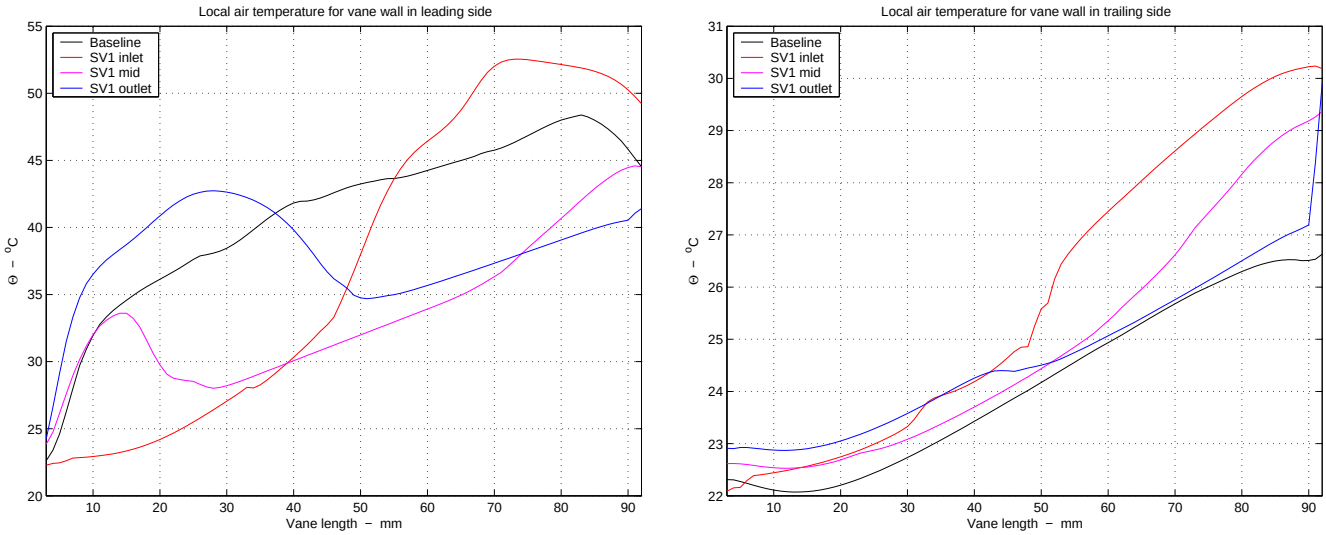

(a) Leading side (b) Trailing side

Figure 6.37: Air temperature (per channel side) near the vane wall, n=800 rpm.

walls on the leading and trailing sides of the channels. On trailing side (b) only the curve corresponding to the design with the SV1 at the outlet shows a significant improvement after the second half of the vane length, while the magenta curve (SV1 at the middle) indicates sequentially lower-higher-lower heat transfer coefficients. The SV1 at the inlet (red curve) worsen the behaviour of h_c on this vane wall. The results in the vane wall on the channel leading side (graph on the left) shows better h_c profiles for the channels with the SV1 at the outlet and at the middle (blue and magenta lines), while h_c with SV1 at the inlet gives similar behaviour to the baseline on the first half of the channel, but then drops.

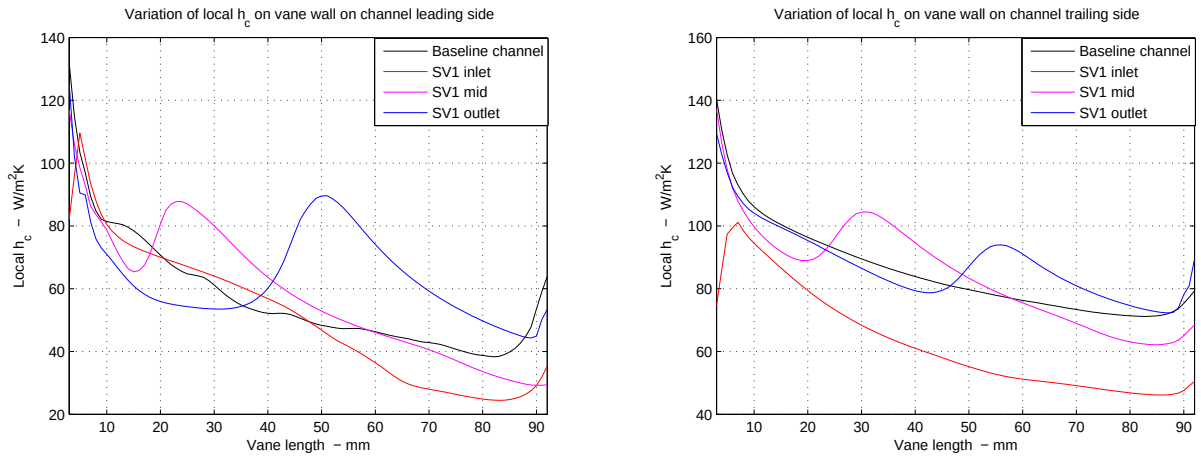

(a) Leading side

(b) Trailing side

Figure 6.38: Local h_c per channel side, discs with SV1, n=800 rpm.

Figure 6.39 shows net gains on h_c values. The zero reference is indicated by the black horizontal line, above which values represent a gain in heat transfer coefficient with respect to the baseline geometry. In order to easily evaluate these differences, an integration of them for each case is performed in the following manner:

$$\int [h_c^{SV1} - h_c^{Base}] dl_v$$

The above integral represents the net area under the curves in Figure 6.39 (with units W/mK), and the values that takes are shown in Table 6.9. The results of the integrals gives the channel configuration with the SV1 at the outlet as the best from the three revised in this Section, since heat transfer coefficient redistributes and gain in absolute terms. The configuration with SV1 at the middle gives a modest gain in heat transfer coefficient distribution, while the worst configuration is the channel with the SV1 at the inlet, since it results in a loss of convective heat transfer coefficient in the vane walls.

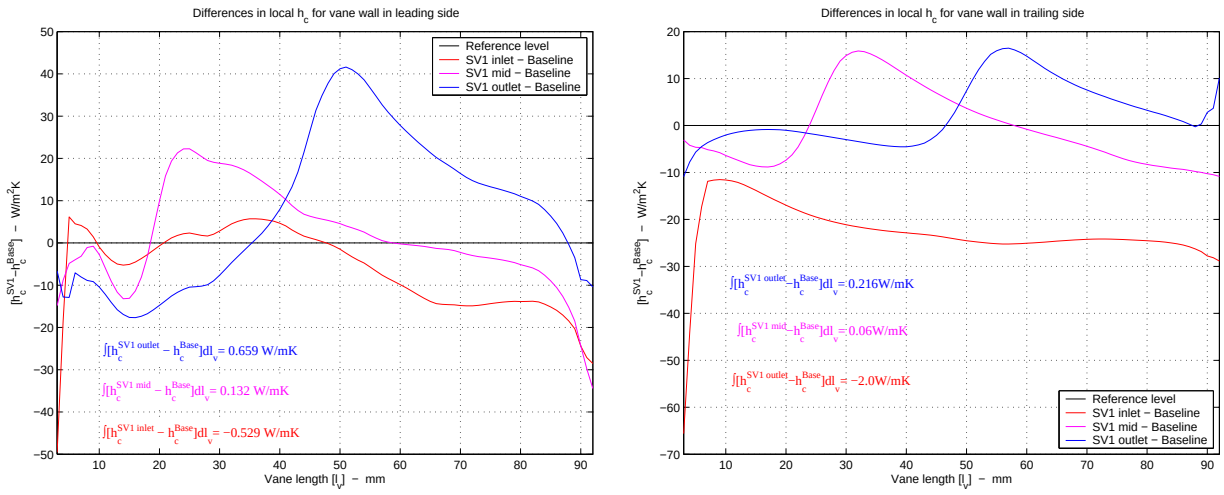

(a) Leading side (b) Trailing side

Figure 6.39: Net gains in heat transfer coefficient per channel side, discs with SV1, n=800 rpm.

Table 6.9: Net gain or loss in heat transfer coefficient per vane wall.

Net area=$\int [h_c^{SV1} - h_c^{Base}]dl_v$, W/mK			
Channel design	Leading Wall	Trailing Wall	Total
SV1 inlet	-0.5286	-2.0	-2.53
SV1 mid	0.1320	0.06	0.19
SV1 outlet	0.6597	0.216	0.86

It could be said that the optimal shape of a constrictor vane is linked to its location in the channel (that is, where the constriction is sought). If the SV1 vane is to be located at the inlet, then it must be thin and therefore, would work as a guide inlet vane (see Sections 6.5 and related). If the constriction is aimed at the mid-radius, then a trade-off between local speed rise (heat transfer coefficient improvement) and kinetic energy drop must be considered. Also, sudden expansion should be also taken into account.

6.4 Pillars

6.4.1 Geometry

A different variant of brake disc vents analysed in this research were pillars distributed periodically along the circumference of the brake disc rings. Regularly spaced cylinders are used in some ventilated disc designs, and they are also typical in industrial heat exchangers where, working under cross flow, is usual that a hot fluid stream past around the cylinders in one specific direction while a cold fluid stream runs inside them, therefore the cold fluid absorbs energy from the hot stream. The cylinders array geometry is characterised by the cylinder diameter (D) and the longitudinal and transverse pitch between their centres (X_l, X_t).

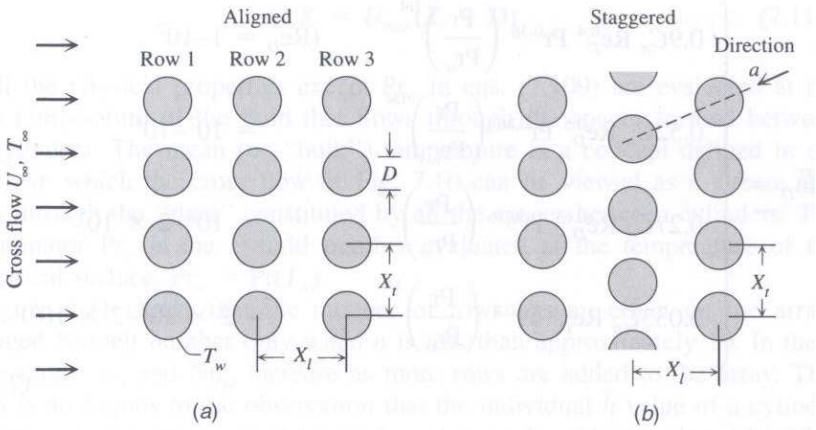

Figure 6.40: Arrays of tubes or cylinders banks for convective heat transfer purposes, (Bejan 2004).

According to Bejan (2004) the downstream cylinder rows usually dissipate more energy than the front rows, this because they are benefited from eddies formed behind the first or second rows, therefore increasing the degree of turbulence in front of the second and subsequent rows of cylinders. Correlations exist for heat transfer prediction from an array of cylinders as function of the number of cylinder rows and Reynolds number based in the diameter of the cylinders and in the maximum (external) flow speed in the main direction (this is calculated in the narrowest section formed between them, in the first row). The correlations are also dependent upon the array itself, that is to say, in whether the cylinders are *aligned* or are *staggered*, see Figure 6.40. The work of Zukauskas, Bejan (2004), gives correlations for array's averaged Nusselt numbers, covering both layouts of arrays. These, given in Tables 6.10 and 6.11, are function of the cylinders Reynolds number (see equation 6.1), a constant C_n (which is itself a weighting factor for the Nusselt number depending also on the Reynolds

number and numbers of rows, (Figure 6.41) and on Prandtl numbers, one evaluated at the midfilm temperature of the wetting stream and the other evaluated at cylinder's temperature (Pr_w).

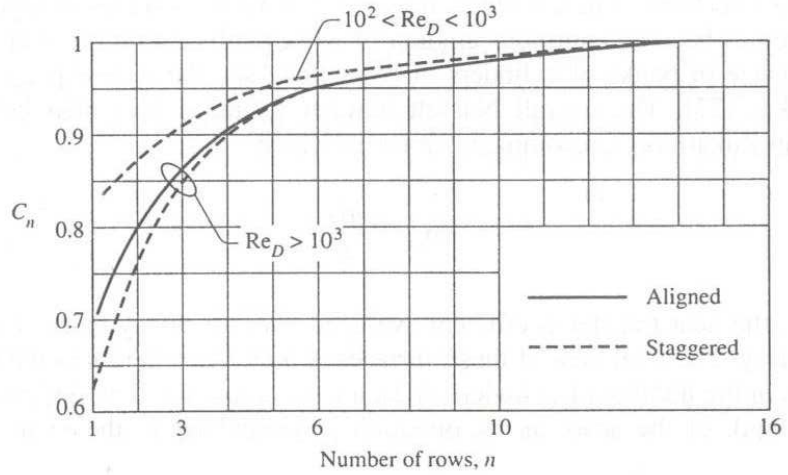

Figure 6.41: Values of the constant C_n, from (Bejan 2004).

Table 6.10: Zukauskas's correlations for cross flow heat transfer in *aligned* cylinders.

Re_D	Nu_D
1 - 1x10^2	$0.9 C_n Re_D^{0.4} Pr^{0.36} \left(\frac{Pr}{Pr_w}\right)^{1/4}$
1x10^2 - 1x10^3	$0.52 C_n Re_D^{0.5} Pr^{0.36} \left(\frac{Pr}{Pr_w}\right)^{1/4}$
1x10^3 - 2x10^5	$0.27 C_n Re_D^{0.63} Pr^{0.36} \left(\frac{Pr}{Pr_w}\right)^{1/4}$
2x10^5 - 2x10^6	$0.033 C_n Re_D^{0.8} Pr^{0.4} \left(\frac{Pr}{Pr_w}\right)^{1/4}$

Observing C_n in the above equations, it is evident that the averaged Nusselt number of the array will increase with the number of rows and with the Reynolds number.

$$Re_D = \frac{u_{max} D}{\nu} \tag{6.1}$$

In this Section arrays of semicircular pillars (instead of cylinders) are used in the brake disc ventilation geometry. Therefore the cylinder diameter (D) in the Reynolds number is redefined as equivalent diameter (D_π), equal to the the ratio between the perimeter of the pillars and π. Three configurations were studied, two using banks of 210 pillars per disc distributed in four rows and the third with 180 pillars plus straight vanes at the inlet. The

Table 6.11: Zakauskas's correlations for cross flow heat transfer in *staggered* cylinders.

Re_D	Nu_D
1 - 500	$1.04 C_n Re_D^{0.4} Pr^{0.36} \left(\frac{Pr}{Pr_w}\right)^{1/4}$
500 - 1x10^3	$0.71 C_n Re_D^{0.5} Pr^{0.36} \left(\frac{Pr}{Pr_w}\right)^{1/4}$
1x10^3 - 2x10^5	$0.35 C_n Re_D^{0.6} Pr^{0.36} \left(\frac{Pr}{Pr_w}\right)^{1/4} \frac{X_t}{X_l}$
2x10^5 - 2x10^6	$0.031 C_n Re_D^{0.8} Pr^{0.4} \left(\frac{Pr}{Pr_w}\right)^{1/4} \left(\frac{X_t}{X_l}\right)^{0.2}$

first configuration (P1), shown in Figure 6.42, has radially aligned pillars (which means that the circumferential spacing widens with radius). The innermost row has 30 pillars giving circumferential a flow inlet port of 16.4 mm. The second, third and fourth rows have 60 pillars each. The radial pitch between pillar rows is 9 mm while the circumferential pitch among pillars is variable: the second row of pillars are separated 6 mm at their inlet, the third row 8.8 mm and the fourth row 11.6 mm.

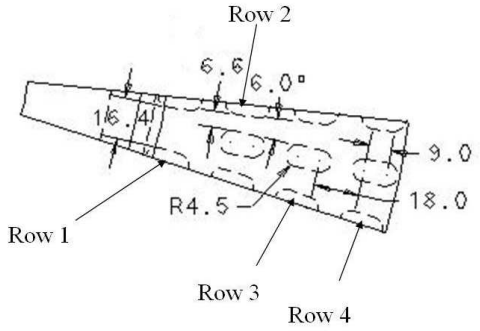

Figure 6.42: Pillared disc in configuration 1.

The second configuration (P2) is a variant of the above in which the second and fourth rows of pillars are rotated 6 degrees about the center of the disc, therefore this is a staggered array of pillars overlaid on a circular geometry. In the third configuration (P3), the first row of pillars from P1 are removed and a set of small straight vanes were placed, see Figure C.15 in Appendix C.

The characteristics of brake disc configurations P1 and P2 are in Table 6.12. The pillars are 18 mm long and 9 mm width with rounded shape. The height of them was the same as the height of the vanes (17 mm). The characteristics of the pillars are provided in Table 6.13.

Table 6.12: Convection (wetted) areas and mass of brake discs designs with 210 pillars.

Brake Discs	Vents area, m^2		Area disc without vents, [m^2]	Area disc [m^2]	m_d [kg]
	Pillars	Endwalls			
P1 & P2	0.1660	0.1623	0.3802	0.7085	30.1
P3	0.2296	0.1574	0.3802	0.7672	30.6

Table 6.13: Pillar characteristics.

P_w	D_π	A_w
[m]	[m]	[m^2]
0.046	0.0147	0.00079

6.4.2 CFD models

CFD models were constructed independently for each configuration using 12 degrees geometry sectors. The grid and boundary conditions were set as usual in this research (see the beginning of this Chapter). The characteristics of the CFD models are shown in Table 6.14.

Table 6.14: CFD model mesh statistics for pillared discs.

Disc	Hexas	Tetras	Prisms	Pyramids	Cells	Nodes
P1	464421	-	-	-	464421	488985
P2	225090	77673	18550	3506	324819	272906
P3	303536	200521	14300	4888	523245	376787

6.4.3 CFD results

The results of the simulations are shown for n =400 rpm, while averaged results are analysed throughout the angular speed range. Streamlines of relative speed on passage midplane show slightly better flow pattern (less disrupted) in configuration P2 than in P1 (Figure 6.43). However in both configurations, there is stall regions behind the first row of pillars and characteristic stagnant or recirculation flow regions in the trailing edge of each pillar. In the third configuration (Figure 6.44), the only visible change is flow direction up to the third row of pillars (it progresses radially rather than circumferentially as in the others), this as a result of the implementation of straight vanes in the inlet.

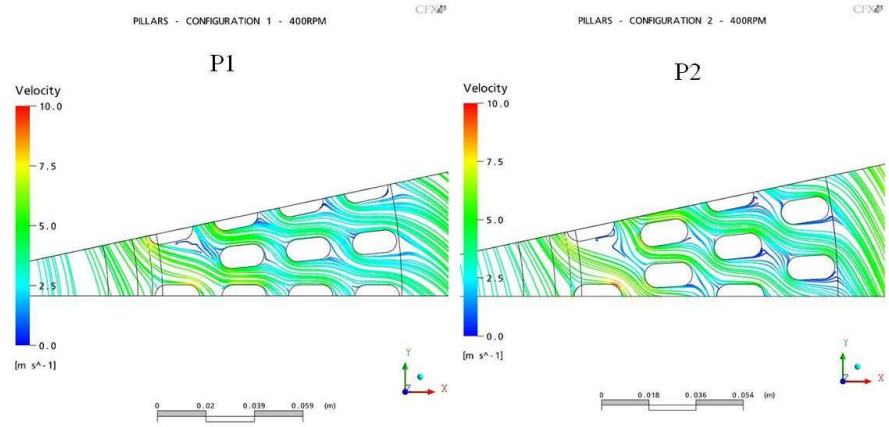

Figure 6.43: Relative speed streamlines in passage midplane, configurations P1 and P2, n=400rpm.

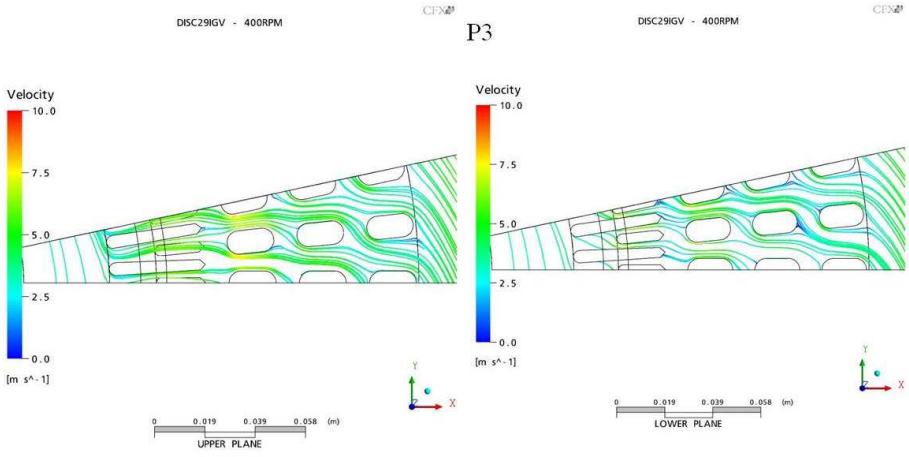

Figure 6.44: Streamline patterns in two circumferential planes, configuration P3, n=400rpm.

Air temperature contours in the midplane of the vents display similar patterns in P1 and P2, with P2 reaching larger radius with cooler air (see Figure 6.45). In configuration P3 pillars, thermal development occurs between the straight vanes, before the first row of pillars, and therefore their convection rate is likely to be lower than in P1 and P2. Total pressure patterns show that in configurations P1 and P2 only rows 3 and 4 build pressure up in the flowfield, therefore any pumped flow gets its maximum impulse in these stages (which is obvious due to larger angular momentum). In configuration P3, the pattern is also similar, but with higher peaks of pressure build up.

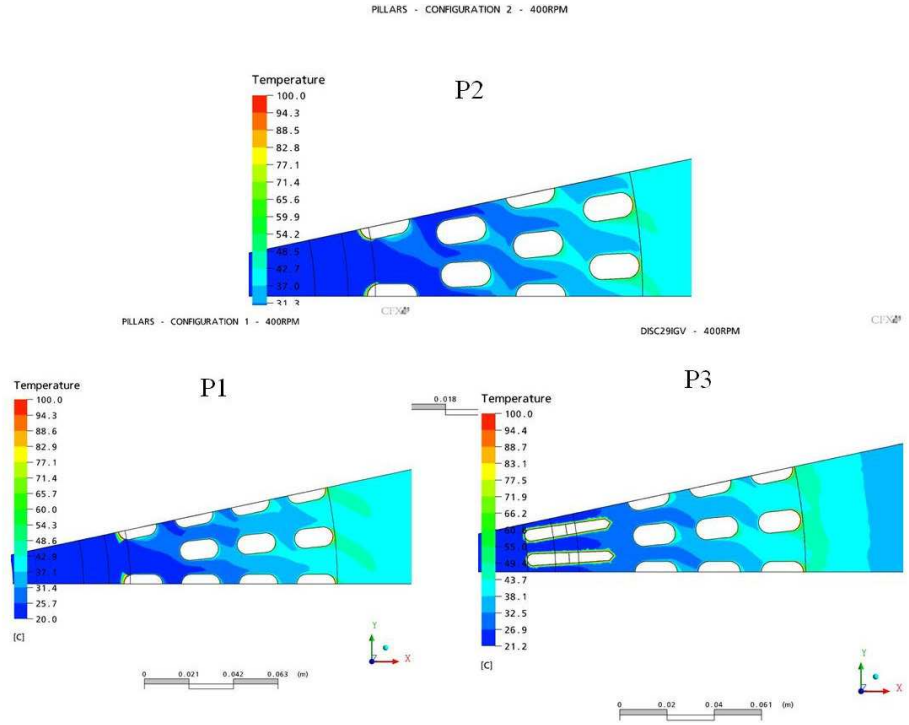

Figure 6.45: Air temperature patterns in midplanes for pillared configurations, n=400rpm.

The distribution of heat transfer coefficients in the pillars exhibits similarities between configurations P1 and P2 (Figure 6.46), with good local distribution in rows 1 and 2 and decaying toward rows 3 and 4. However values for aligned pillars (P1) are 12% higher than staggered pillars (P2). In configuration P3 (Figure 6.47), heat transfer coefficients are better distributed but the peak values are 34% below that of P1.

The heat transfer coefficient distributions in the endwalls follow with the same ranges, the highest for P1, the lowest for P3 and in between P2 (see Figures 6.48 and 6.49. Endwalls in P1 give symmetric distributions after the third row, while in P2 and P3, the outboard endwall gets better distribution than the inboard side.

The trend of the passage averaged heat transfer coefficient (Figure 6.50(a)) is below that of

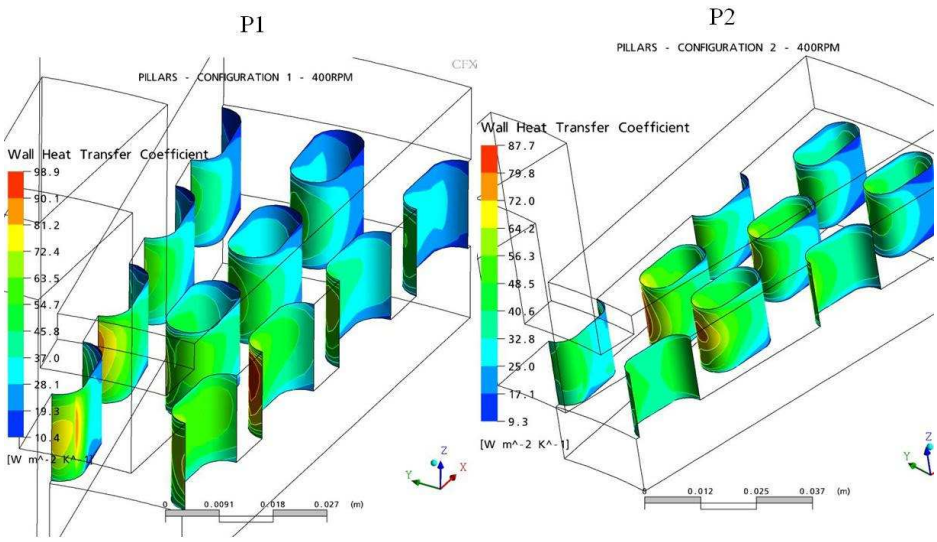

Figure 6.46: Heat transfer coefficient distributions on configurations P1 and P2, n=400rpm.

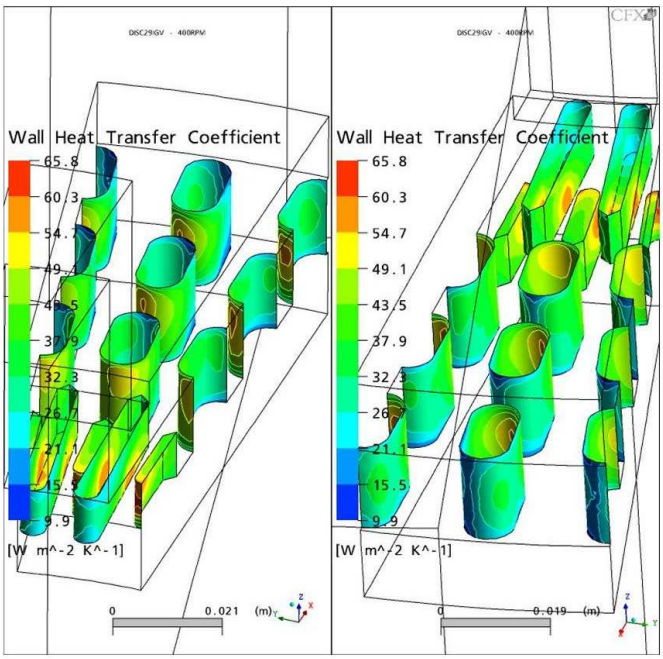

Figure 6.47: Heat transfer coefficient distributions on configuration P3, n=400rpm.

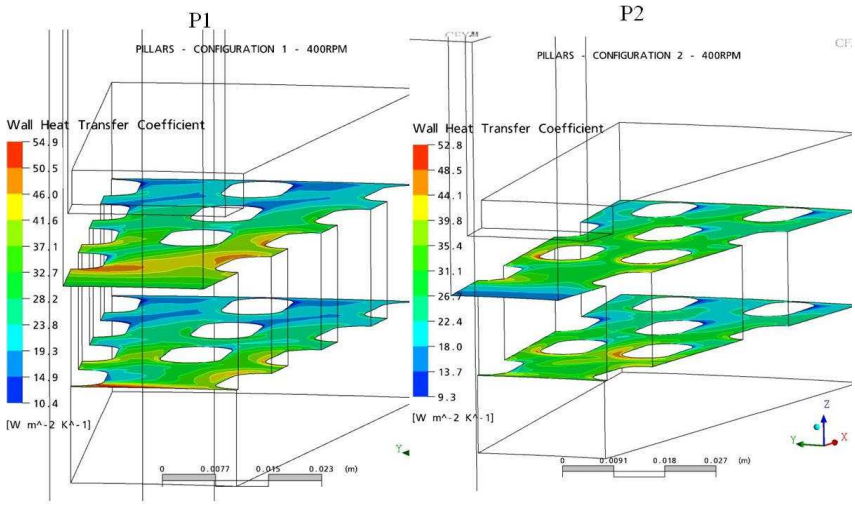

Figure 6.48: Heat transfer coefficient on endwalls for configurations P1 and P2, n=400rpm.

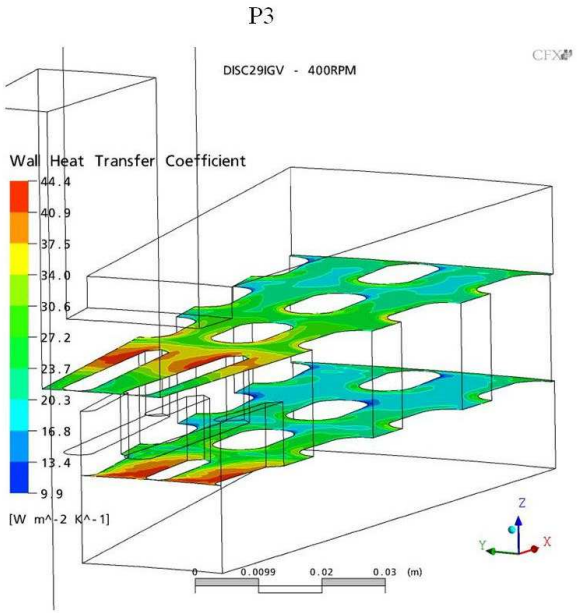

Figure 6.49: Heat transfer coefficient on endwalls for configuration P3, n=400rpm.

the baseline brake disc for all the pillared designs. This is due to low pumping ability (lower airspeed in the passages). The larger difference occurs between the configuration P3 and the baseline. Configuration P2's h_{ch} is 11% less than the baseline disc. The pillared discs averaged heat transfer coefficient is also below the trend of the baseline (Figure 6.50(b)), however the difference is small (around 6%) and for low angular speeds 100 and 200 rpm the difference is even smaller than that. Therefore, the convective performance of the pillared designs is as good as that of the baseline (30 vanes) disc for low rotational speeds ($n \leq 400$ rpm).

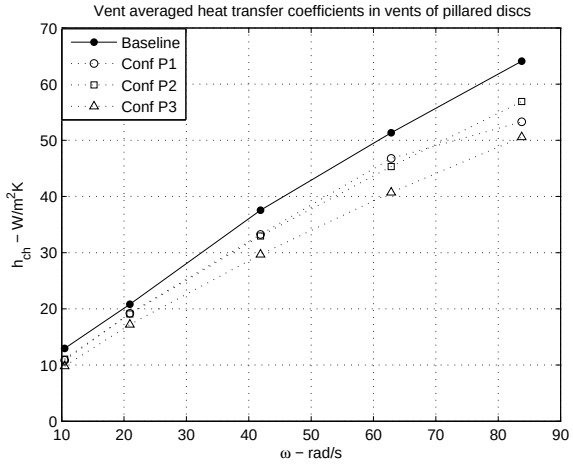

(a) h_{ch} vs ω.

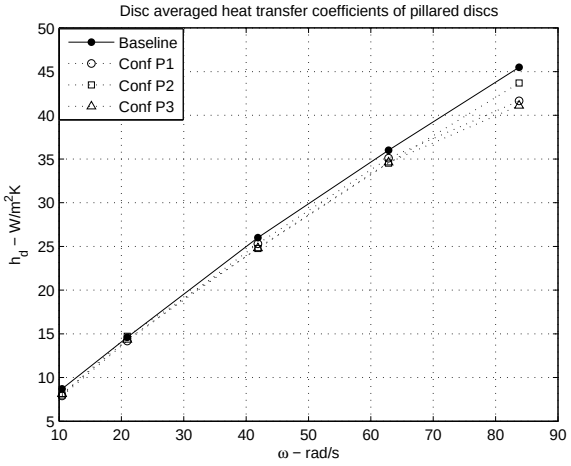

(b) h_{d_c} vs ω.

Figure 6.50: Pillared discs, average convective heat transfer coefficients.

Nevertheless, the convective cooling rates are better in pillared discs than in the baseline design, this is due to the larger convection area in pillared designs while keeping the same mass as the baseline disc(Tables 6.5 and 6.12). The product $\frac{A_w}{m_d C_{p_d}}$ for pillared designs P1 and P2, and for P3 is 10.8% and 18.2% respectively larger than in the baseline. Convective cooling rates (Figure 6.51) for configuration P3 are 12% larger than the baseline, while those for configurations P1 and P2 are 5% and 6% above the baseline design respectively.

As in other designs, mass flow is linear with angular speed, however configurations P2 and P3 pump between 45% and 26% less than the baseline vanes, with configuration P1 within this range. The guide vanes attached to the inner radius in design P3 are blocking rather than enhancing airstream. Required torque for rotation is also very different in respect to baseline design, configurations P2 and P1 require 45% and 35% less torque than the baseline, with torque required for P3 above P1 (Figure 6.52).

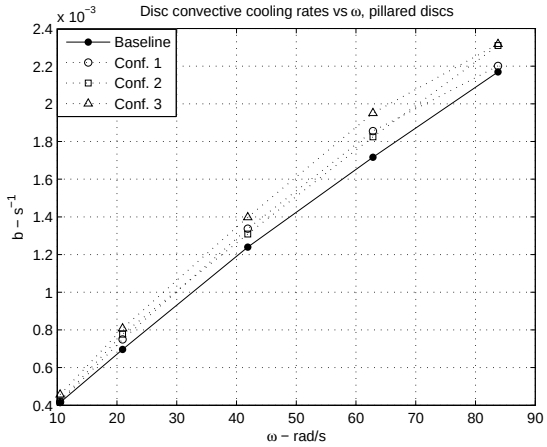

Figure 6.51: Convective cooling rates, pillared designs versus baseline disc.

A heat transfer coefficient analysis is performed using the average value of pillars (four rows in configurations P1, P2 and three in P3) for each angular speed, and calculating their average Nusselt number as follows:

$$Nu_p = \frac{h_{c_p} D_\pi}{k} \tag{6.2}$$

Then, these are compared against those predicted by the appropriate Zukauskas's correlations. The Reynolds number, calculated using CFD data, and the values of C_n are in Table 6.15. Since the Prandtl number of air at 100^{o}C (pillars surface temperature used) and at 60^{o}C are very similar, the ratio Pr/Pr_w is taken as 1. Figure 6.53 shows the outcome.

Table 6.15: Reynolds numbers and Zukauskas's constants used, $D \rightarrow D_\pi$.

n, rpm	Conf P1		Conf P2		Conf P3	
	Re_{D_π}	C_n	Re_{D_π}	C_n	Re_{D_π}	C_n
100	482	0.90	705	0.90	993	0.92
200	1010	0.90	1446	0.90	2043	0.85
400	2085	0.90	2686	0.90	4172	0.85
600	3132	0.90	4009	0.90	6301	0.85
800	4343	0.90	5350	0.90	8432	0.85

Zukauskas' correlations overpredict the Nusselt numbers calculated from CFD by 25% for configuration P1, 60% for configuration P2 and 220% for configuration P3. Then, their

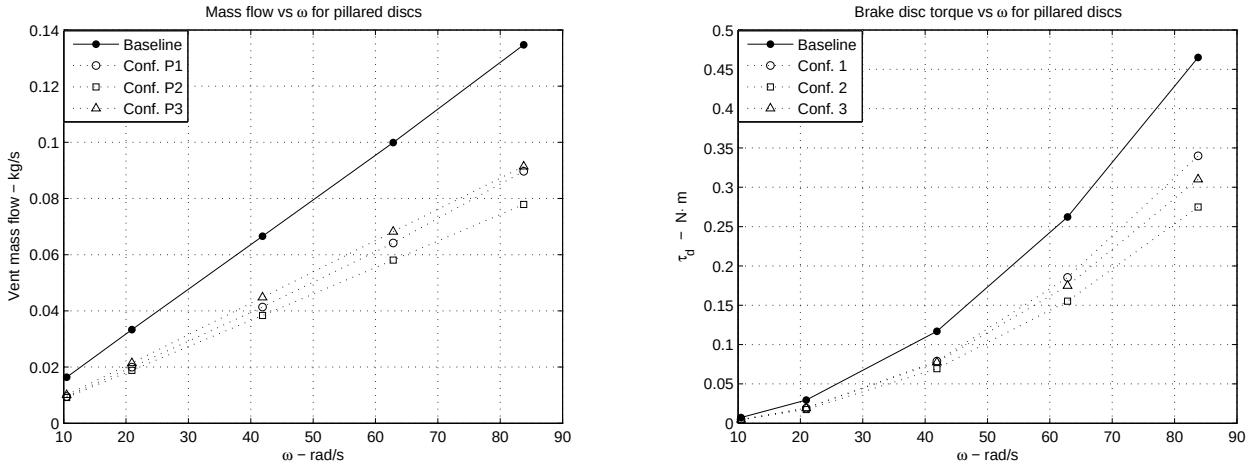

(a) Mass flow.

(b) Torque.

Figure 6.52: Mass flow and aerodynamic torque, pillared versus baseline discs.

usage for design purposes in pillared brake discs is not adequate since would give misleading conclusions. Pillars arrays as those shown in rotating geometries, with air self-fed seem to have lower heat transfer performance than those stationary with externally supplied air flow. An analysis of the Nussel number per pillar row (see Table 6.16) shows interesting findings: At low angular speeds Nu for downstreams rows are lower than those preceding them. At high rotational speeds, a temporal increase in Nu of the second row is observed (16% and 28% increment for P1 and P2), followed by drop of about 33% with respect to the value of the second row.

Table 6.16: Nusselt number *per pillar row* from CFD, n=100 rpm and 800 rpm.

Row #	Conf P1		Conf P2		Conf P3	
	100 rpm	800 rpm	100 rpm	800 rpm	100 rpm	800 rpm
1	8.4	31.5	7.2	30.7	NA	NA
2	8.0	36.5	8.4	39.5	6.6	30.5
3	5.7	31.2	5.9	33.4	5.4	28.1
4	4.4	26.5	4.6	30.0	4.5	28.1

In summary, convective heat dissipation from pillared arrays in rotating brake discs do not follow the same trend as in stationary pillars arrays (aligned or staggered). Reasons for this are: 1)air flow pattern around pillars given by rotation and self-fed: deficient pumping

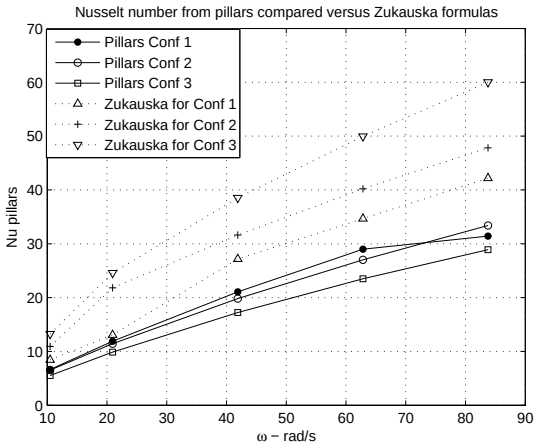

Figure 6.53: Pillars Nu analysis. Zukauskas correlations versus CFD results.

during rotation lowers potential turbulence to be formed by the wake behind pillars (besides air moves circumferentially from row to row and may lead to waste of any turbulence into flow core); this does not occur with wakes behind stationary cylinders and therefore their influence in heat dissipation is larger; and 2) circumferential distance between pillar augmented with radius, (pillars on the outer rows were circumferentially more spaced than those in the inner rows).

6.5 Inlet Guide Vanes

It has been emphasised from baseline design that low heat transfer coefficient is linked to recirculating flows near the channel leading side, which gives way to heat dissipation to air by conduction rather than by convection[4]. A way to overcome was assessed through induction of swirl. Streams with spiraling motion about the flow direction have been targeted for better mixing of fuel constituents in burners and also plays a definite role in ducting of turbomachinery, (Greitzer *et al* 2003). Swirl (swirling) flow is characterised by a swirl parameter defined as the ratio of the tangential velocity to the radial velocity, both relative to the channel; and it is is achieved by generating tangential speed components in perfectly axial flows. For this effect, diametrically opposed sub-inlets are designed on-purpose in ducts where swirling flow motion is to exist (Figure 6.54), or by inserting deflectors in the inlet, like in fuel injectors.

[4]Although recirculating flow may lead to separation/reattachment phenomena which ideally benefits convective dissipation (Ventsislav^a 2004) and (Ventsislav^b 2004), if the relative speed of the separated flow is low, diffusion process dominates convection and therefore low h_c.

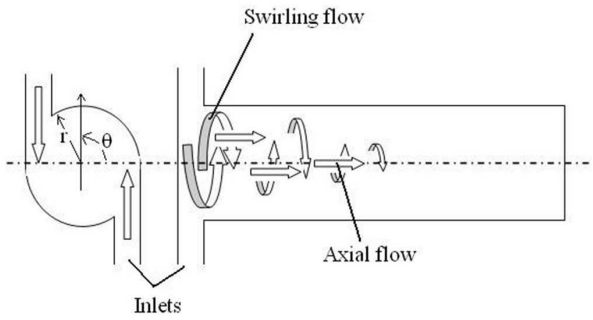

Figure 6.54: Swirling flow on axial flow through a stationary duct, (Muralidhar 1996).

It is feasible to expect higher convective dissipation if swirl is implemented within brake disc vents. However, the conditions to generate swirl in brake disc vents are more difficult, since the flow does not enter to the channel by means of an upstream force with a preferential direction which later could be altered, but air is self-fed due to the rotational centrifugal force. Implementing double-sided inlets is not suitable in brake disc channels and an alternative way of modifying the flow at the inlet into swirling avoiding inlet blocking was designed for the baseline model.

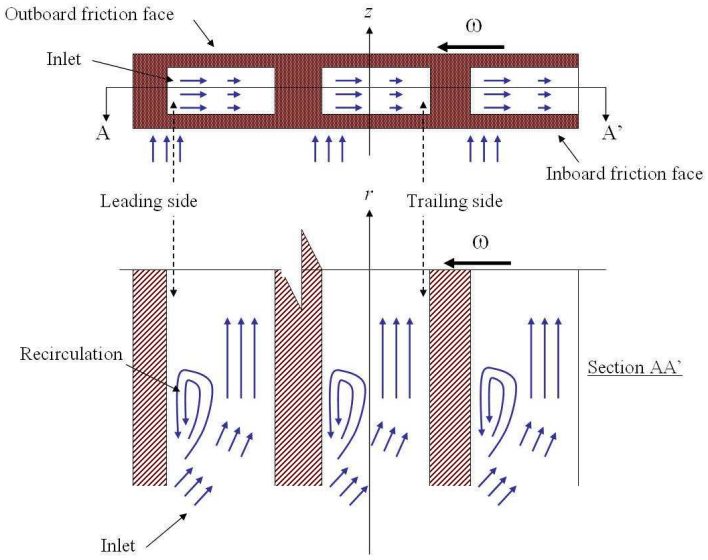

Figure 6.55: Flow behaviour representation at the inlet baseline channels.

The underlying idea of the brake disc swirl generator is to impart an early tangential velocity component and help in initial flow direction without blocking channel inlet. Figure 6.55 schematically shows the classic inlet ports of radial channels (top). These move at a certain constant rotational speed ω about z. Since air can only be drawn from the inboard side, it approaches to the channel inlets first axially and after circumferentially, as shown by sets of

three arrows depicting relative air motion. Because of the misalignment between the vanes –hatched rectangles in Section AA'– (bottom) and the air, recirculation generates near the channel leading side deflecting the flow core to the trailing side. The drawbacks of this design are separated circulating low speed flow in the leading side and streamlined flowon the trailing side, with characteristic heat transfer coefficient distributions already discussed in Chapter 5. No swirl exists.

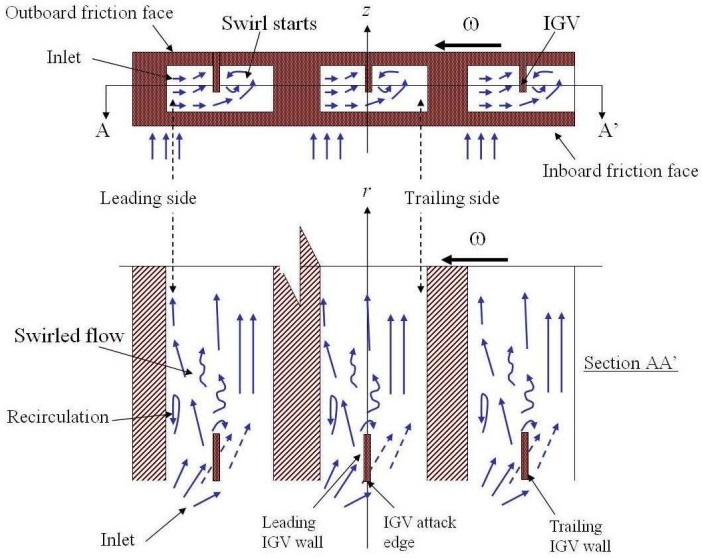

Figure 6.56: Schematic of swirling motion generation in radial channels of brake disc.

The creation of *swirled* and *redirected* air patterns in the inlet and through the channel is recommended in this research by attaching an *Inlet Guide Vane* to the inlet port. It is foreseen that the geometry, location and orientation of the IGV will be influence the quality of the swirl. The IGV is schematically represented in the top drawing of Figure 6.56 as rectangular extensions prolonging from the outboard side endwall towards the inboard side, spanning approximately 50% of the channel axial height. The outboard side endwall was chosen as its support surface because this extends more radially inwards than the inboard side endwall, allowing not only air preswirl but pushing more air into the channel. Having an IGV shorter than the disc vanes follows avoids inlet port division and sequential air blocking to trailing side. In this way, the IGV conceptual design suggested is expected to push and preswirl air in the form shown by the arrows in the inlet ports (Figure 6.56, top): on the leading wall of the IGV (left side of IGV) air will be deflected, while flow past by the IGV attack edge will fall into low pressure and will start swirling motion towards the trailing side of the channel. The deflection of air is expected to break or shrink the low speed recirculation region in the channel leading side by injecting energetic flow in this side (Section AA' of Figure 6.56, bottom). Additionally the air leaving by IGV trailing *edge* will be further swirled by geometry discontinuity found in its path. However, space between the

IGV tip and the inboard side channel endwall will allow air entry toward channel trailing side (dotted arrows), with less swirl than that of the air directly affected by the IGV.

6.6 Curved IGV - Geometry

The IGV design, orientation and location will influence the swirl strength in the flow and ultimately the heat transfer ability of the channel. The first IGV design implemented was curved, circumferentially located approximately at the middle of the channel inlet and with chordal length of 30.7 mm, extending from the inner edge of the outboard side endwall to 13.1 mm *inside* the channel. The incidence angle between the IGV attack edge and a radial line was 15.8 degrees, as observed in Figure 6.57. This IGV is identified as IGV1. The rest of the channel geometry was unchanged.

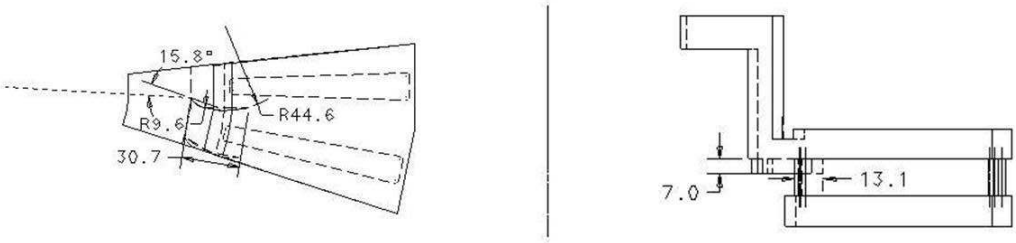

Figure 6.57: Geometry sector showing the curved IGV in the inlet of the baseline design.

6.7 CFD Model - IGV1

The CFD model mesh was built with the geometry shown in Figure 6.57 and with guidelines already discussed. Figure 6.58 shows details of the mesh in the channel section (one vane is not shown to allow seeing the mesh in the curved IGV). The IGV is considered as continuous part of the brake disc and its surface has the same disc temperatureg. For boundary condition see beginning of this Chapter.

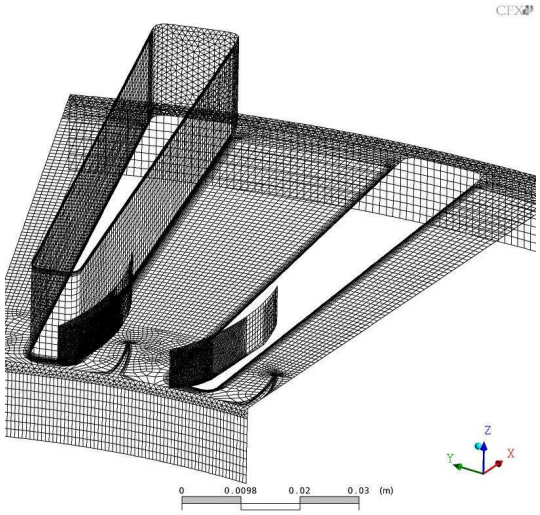

Figure 6.58: Details of the surface mesh in the channel with IGV1.

6.8 CFD Results - IGV1

Two planes were set to visualize the airflow, one across the IGV and another beneath it (see Figure 6.59). Relative velocity streamlines in the plane across the IGV indicate an immediate difference against the airflow behaviour in the baseline channel (Figure 5.35): recirculation region in the leading side has been replaced by radial flow directed by the IGV at significant relative velocities (5 m/s near the wall). On the trailing side of the channel the airflow still reaches the main vane wall. Entry velocity magnitude and direction is increased and changed respectively due to the IGV. In the plane beneath the IGV, streamlines indicate that the IGV does not block the inlet. Streamlined flow near the vane wall in the channel leading side show that recirculation has been removed on this plane.

The existence of swirling motion in the channel inlet due to IGV is shown in Figure 6.60. The streamlines plot in the left shows the airflow behaviour seen over the inlet port, which resembles that schematically shown in Figure 6.56 (top). Because of the postprocess technique it is not possible to determine where the incoming airflow gets the tangential diversion, since the streamline plot in the left shows an *ongoing* swirled flow. Twisted airflow leaving the IGV is also shown, however core flow swirl is attenuated downstream at a distance equal to one IGV chord. This is likely due to the channel cross section opening provoking a drop in velocity. Scant recirculating flow forms near the inboard side endwall in the channel leading side. However, along the outboard side channel endwall, no recirculation exists.

Secondary flow vectors reveal significant behaviour of the swirl pattern (Figure 6.61). Swirl starts immediately in the first cell on the IGV suction. Swirl continues in the second plane toward the outboard side endwall (i.e. compare against Figure 5.38), interestingly a second

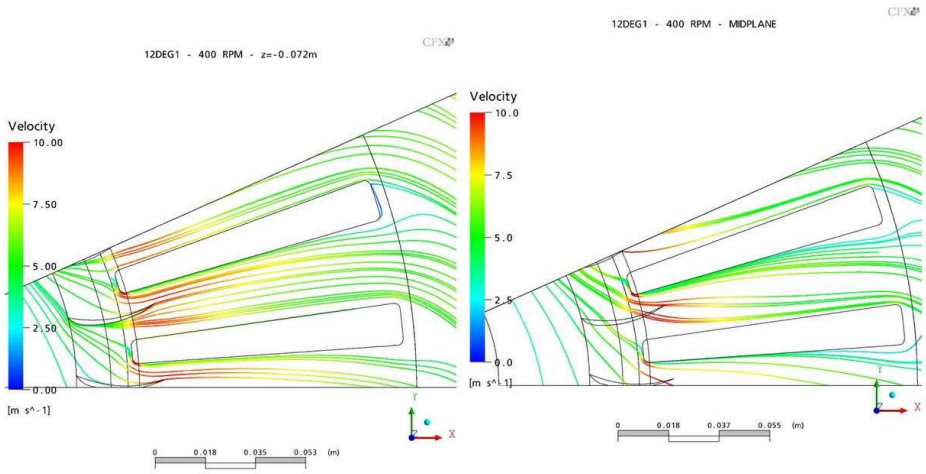

Figure 6.59: Velocity streamlines on planes across and beneath the IGV1 span, n =400rpm.

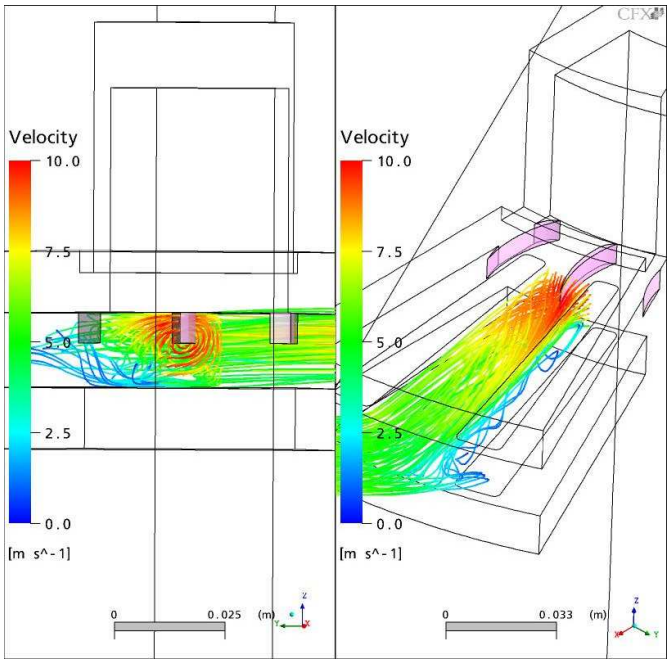

Figure 6.60: Swirl flow from curved IGV, n =400rpm, left looks from channel inlet.

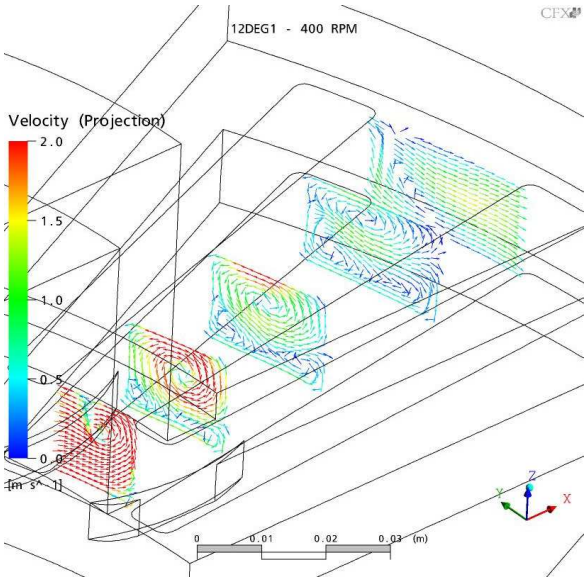

Figure 6.61: Secondary flow on planes perpendicular to main path direction, n=400rpm.

'thin' cell forms near the inboard side endwall. In the third and fourth planes, the double cell secondary flow formation is evident. A thinner hot air layer is now observed in the channel leading side (Figure 6.62) as compared with the baseline channel results. However, because air leaving the IGV has higher temperature, thermal development occurs inside the channel (air temperature increases by 12^{o}C after leaving the IGV. Theoretically this is detrimental for convective dissipation since temperature gap wall-air decreases. However, due to increased inlet speed propelled by the IGV, air temperature does not increases further along the channel (only near the channel leading side wall, in the second half). The temperature contours in the plane beneath the IGV shows a thicker hot air layer near the vane wall in the leading side. In the channel trailing side air remains significantly cooler very near the wall.

Total pressure contours in a plane across the IGV span, Figure 6.63, show maximum pressure levels of 58.9Pa, which is smaller than that given in the baseline channel (73.5Pa). This may be due to lower capacity of the vanes to add work on swirled flow through the channel. Convective heat transfer coefficient distribution in the channel shows a peak of 122.7 W/m^{2}K for the IGV tip, while in the vanes this varies from 78.8 to 45.9 W/m^{2}K between the attack edge of the vane wall and its half, after it falls from 45.9 to 23.9 W/m^{2}K (Figure 6.64). The distribution is now almost symmetric in the leading and trailing sides. This enhances the heat dissipation in the channel leading side but deteriorates it in the other. Heat transfer coefficients in the outboard side endwall are higher than in the inboard side endwall, mostly in the inlet portion of the channel. This agrees with what is observed in the secondary flow plots, where swirled flow is seen skewed toward the outboard side endwall.

Aerodynamic characteristics, mass flow and torque, of the current design are compared

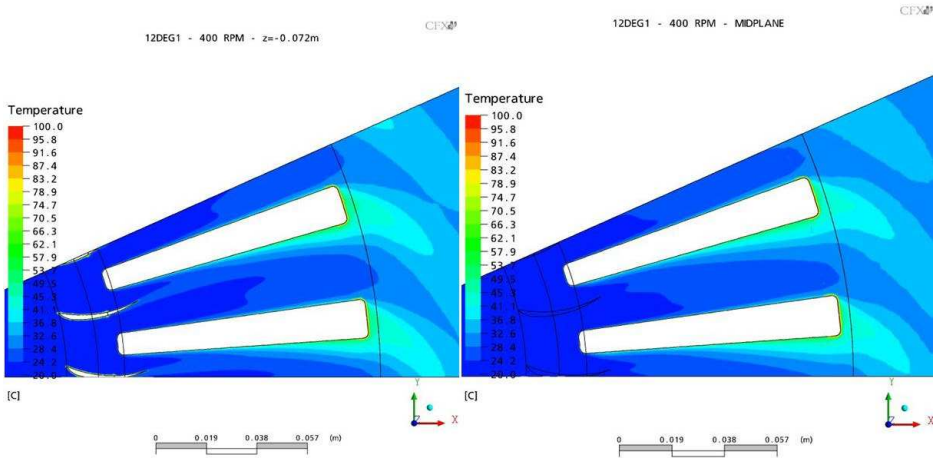

Figure 6.62: Air mean temperature patterns at n=400rpm, across and beneath the IGV span.

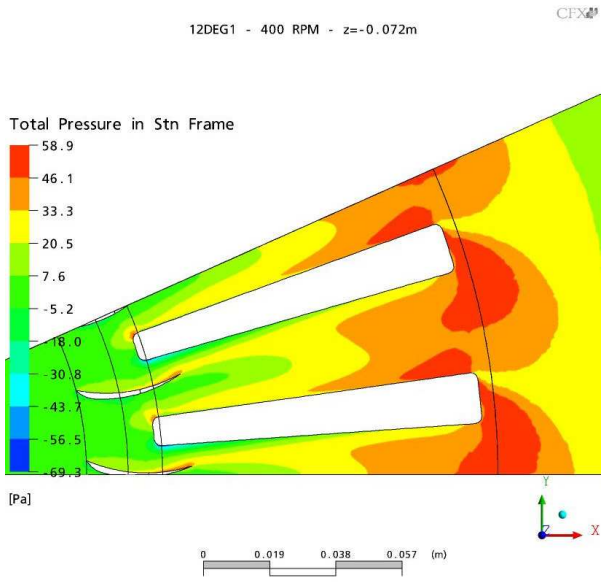

Figure 6.63: Total pressure patterns in plane crossing the IGV at n=400rpm.

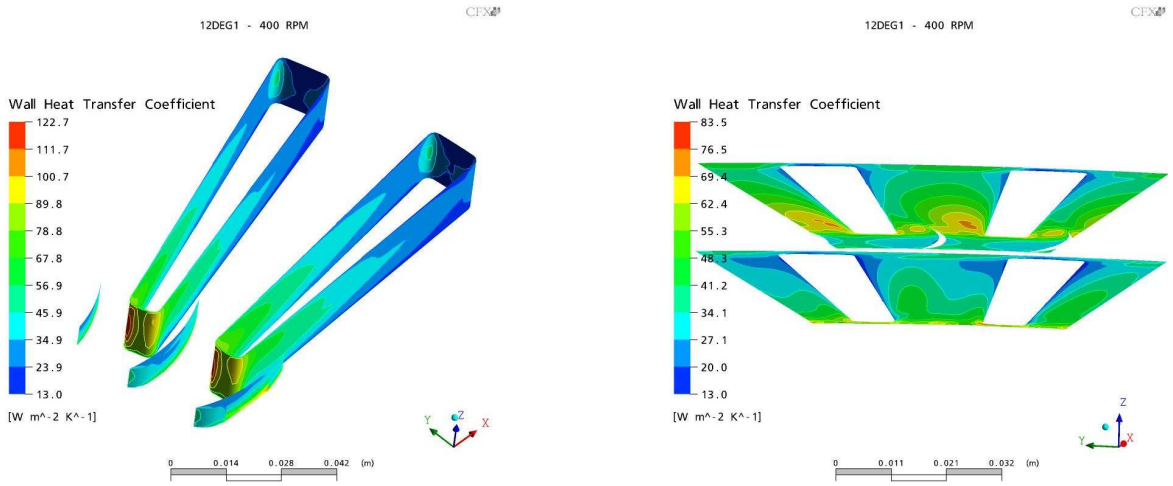

(a) Vanes. (b) Endwalls.

Figure 6.64: Convective heat transfer coefficients, disc with curved IGV, n=400 rpm.

against the baseline model in Figure 6.65. The brake disc with the curved IGV1 pumps 8.5% more air between 100 and 200 rpm, and above these pumping increases to 10.5% more than the baseline (Figure 6.57(a)). As a result, the work required to move the air by the disc with the IGV1 is about 10% larger between 100 and 400 rpm, and 15% larger for angular speeds between 600 and 800 rpm. The above results could have been expected since the interest of the IGV in front of the channel inlet is pushing air into it, and therefore increasing the mass of air being propelled. Torque is increased, since it is directly proportional to mass flow.

6.8.1 Swirling Flow

The evaluation of the swirl strength is carried out calculating the ratio of the tangential to radial velocities in the channel (Swirl parameter, S, Greitzer *et al* (2003)). Since swirling effects occur relative to the channel, velocity in rotating frame (relative) must be used. Velocities were retrieved in 95 positions from four lines parallel to vane walls, these are located in the four quadrants of the channel cross section (Figure 6.66). The velocities components parallel and perpendicular to these lines were calculated and these were considered to approximate the radial (u_r) and tangential (u_θ) components of the relative flow. Then the swirl parameter was calculated (equation 6.3). The analysis of swirl was done on endwalls basis rather than using channel leading and trailing sides. In this way swirl evaluation near the outboard endwall uses data from the lines close to this endwall (from the leading and

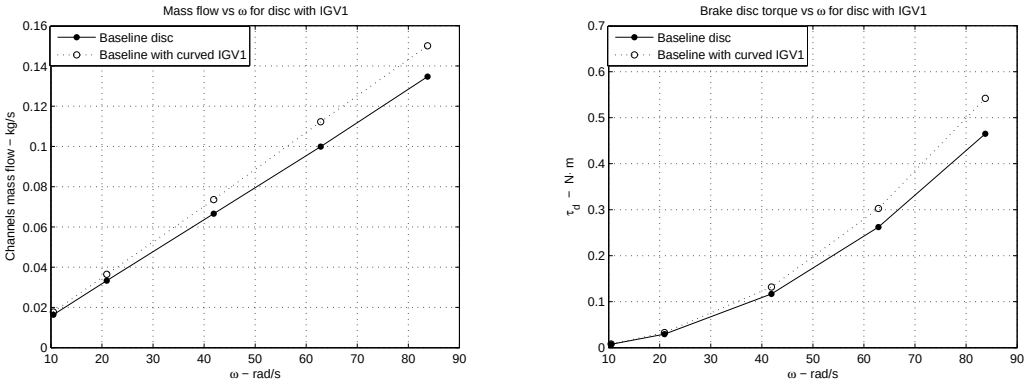

(a) Mass flow. (b) Torque.

Figure 6.65: Aerodynamic characteristics for disc with curved IGV1

trailing sides), while swirl evaluation near the inboard wall uses data from the remaining lines (see Figure 6.66).

$$S = \left(\frac{u_\theta}{u_r}\right)_{rel} \tag{6.3}$$

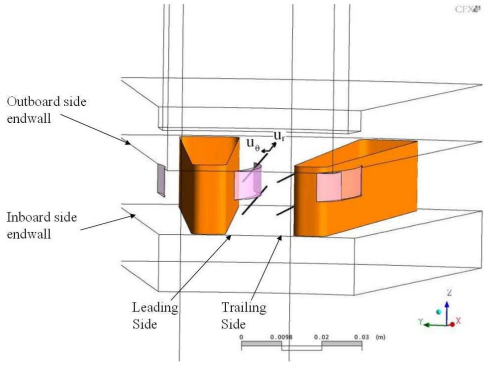

Figure 6.66: Lines for calculation of swirl parameter.

The results in Figure 6.67 were computed for n=400rpm. The solid lines represent S in channels with the curved IGV1 and the dotted lines that for the baseline channel (no IGV). The curve for S in the top leading side of the modified channel starts with S=0.24 and raises to 0.58 in the first 10 mm. This means that the flow is already pre-swirled at the inlet near the IGV1, and then attains its maximum swirl near the trailing edge of the IGV1, after

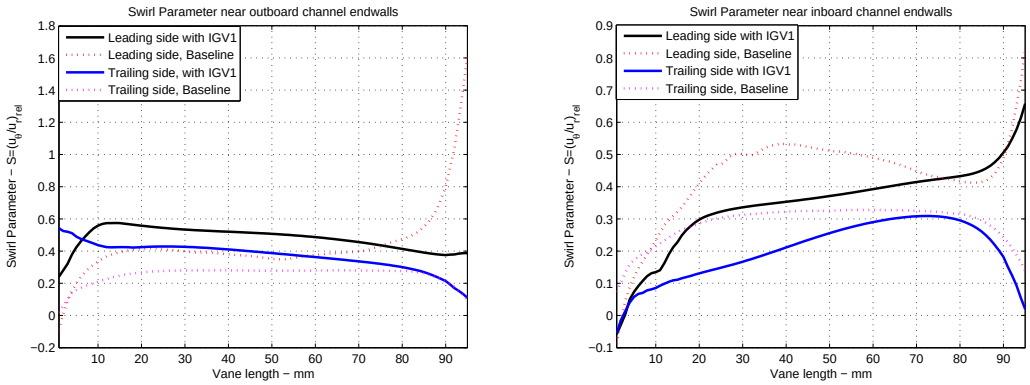

(a) S outboard. (b) S inboard.

Figure 6.67: Swirl parameter in channel with curved IGV1

which follows an steady decay until the outer end where S=0.4 (still above the inlet value). In the baseline channel S starts with -0.1, possibly due to vane attack edge deflecting air in anticlockwise direction (opposite to disc rotation). Then it raises from zero to 0.4 in the first 10 mm (31% less than that with the IGV1), and it remains almost constant and later increases suddenly due to low radial velocity rather than higher tangential velocity. S in the channel trailing side with IGV (Figure 6.67(a)) starts with the highest value, near to 0.6, then falls to 0.4 and keeps that value for most of the length before falling to 0.1 at the end; the corresponding S for the baseline channel has an interesting behaviour since starts with zero swirl, then S raises to 0.25 (60% of that given by the IGV), and remains constant for most of the length, before dropping in the same fashion as the one with the IGV. This constant swirl indicates steadyness of the flowstream in this side, as mentioned before in Section 5.5. In general, near the outboard side endwall, the relative flow is more swirled with the IGV than without it. The effects near the inboard side endwall are poor, since S falls in both sides of the channel when it has the IGV. The reduction is approximately 45% in the extreme cases, however, in the trailing side, S for the channel with the IGV increases steadily, while that of the baseline remains almost constant. At the outer ends S reaches similar figures.

6.9 Channels with IGV's and SV1 vane - Geometry

In order to use as much as possible the momentum and swirl from the IGV, a combined design was implemented by using the SV1 vane and the IGV together. Two shapes of IGV

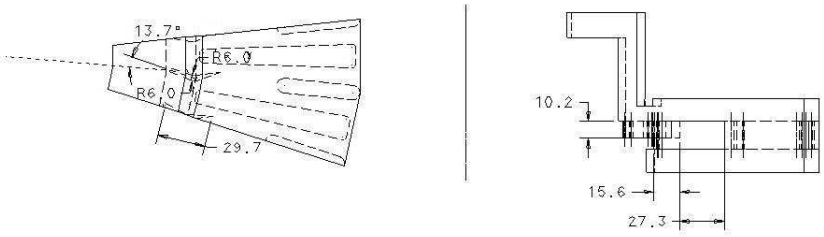

Figure 6.68: Geometry sector showing the channel with IGV2+SV1.

were tested, one curved and another straight drop shaped. The geometry characteristics of the new brake discs sectors with the above modifications are shown in Figures 6.68 and 6.69. In the first case, the original curved IGV1 was slightly modified in its incidence angle and shape, but its span had the most important change: from 7 mm to 10.2 mm, that is, from being 41% of the channel height, it was increased to 60%, aiming to overcome poor results for S near the inboard side endwall given by IGV1. The radial position of the vane was moved outwards, this brought it more inward the channel, in such a way that the length between the main vane edge attack and the trailing edge of the new curved IGV (IGV2) varied from 13.1 to 15.6 mm. The third IGV model was implemented aiming to vanish one drawback of the last two: the preferential direction of disc rotation. Curved IGV models 1 and 2 have to rotate as *forward curved vanes* to have their best performance. The third IGV model (IGV3) was designed as a straight drop-shape IGV allocated in radial direction in the middle of the baseline channel. The attack edge of the IGV3 was positioned at the same radius as IGV2. The characteristics of the brake discs having the IGV are described in Table 6.17. With data therein, the product $\frac{A_w}{m_d C_{p_d}}$ can be calculated, this results 2% larger in average than the baseline brake model. Therefore, since they are very similar, any differences in convective cooling rates will be driven mainly by aerothermal behaviour of the channels.

6.10 Channels with IGV's and SV1 vane - CFD models

The CFD models were constructed with following the guidelines already discussed. The boundary conditions are outlined in the beginning of the Chapter. The details of the surface mesh shown in Figure 6.70 where a main vane is removed to appreciate better the IGVs surface mesh.

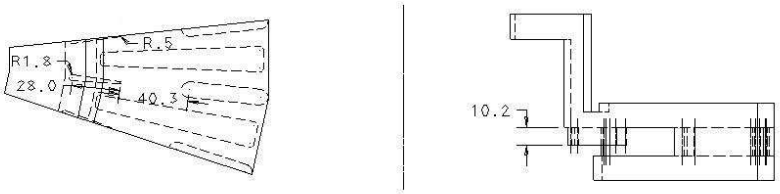

Figure 6.69: Geometry sector showing the channel with IGV3+SV1.

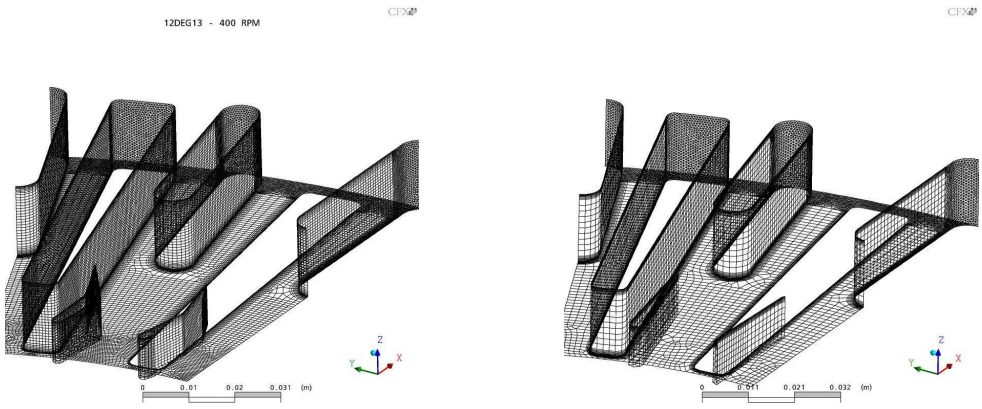

(a) IGV2+SV1. (b) IGV3+SV1.

Figure 6.70: Mesh details in redesigned channels.

Table 6.17: Convection areas and mass of brake discs designs with IGV's and SV1 vanes.

Brake Disc	Area channels, m^2		Area disc without channels, $[m^2]$	Area disc $[m^2]$	m_d [kg]
	Vanes (plus IGV)	Endwalls			
With IGV1 only	0.1213	0.1566	0.3802	0.6581	30.4
IGV2 plus SV1	0.1843	0.1290	0.3802	0.6935	32.1
IGV3 plus SV1	0.1853	0.1292	0.3802	0.6947	32.1

6.11 Channels with IGV's and SV1 vane - Results

Airflow and contour plots of heat transfer coefficients are revised for n=400rpm only, while a compilation of heat transfer results for the three discs with IGV's is carried out for all the angular speed range and compared against the baseline model.

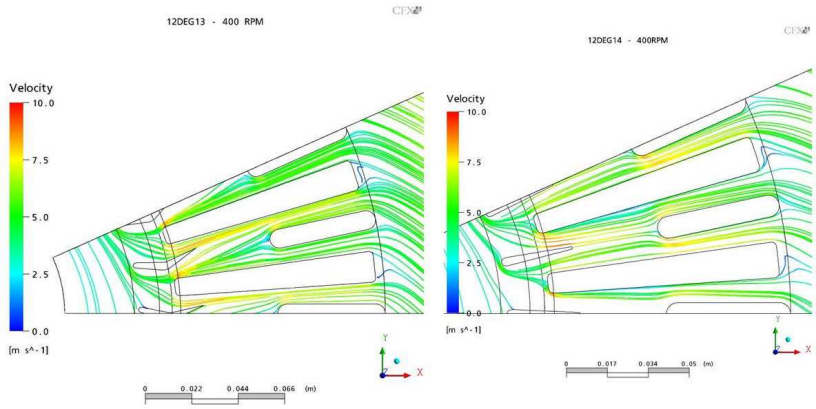

Figure 6.71: Relative velocity streamlines on midplane, designs with IGV2+SV1 and IGV3+SV1.

Streamlines of relative flow shown on channel midplane (Figure 6.71) show significant differences for each IGV shape. At the inlet, air being deflected by the curved IGV2 reaches higher speed near the leading side than that deflected by the IGV3. However, better airspeed distribution is given by IGV3 than by IGV2. Figure 6.72 register higher swirl by the curved IGV2 than by the straight IGV3 at the inlet of the channels. Also, due to the curved shape of the first one and to the division of the channel downstream by the SV1, swirled flow is directed preferentially into the sub-channel in the leading side, in which it reaches a maximum relative speed of 10 m/s, while in the trailing side maximum relative speeds of 7.5

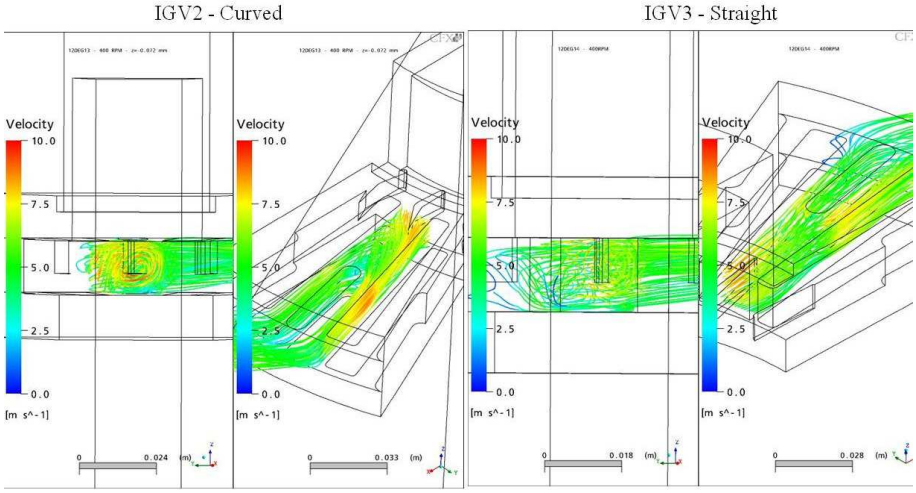

Figure 6.72: Relative velocity streamlines, designs with IGV2+SV1 and IGV3+SV1.

m/s are observed. This is a significant difference in characteristic behaviour brake discs with radial trapezoidal channels, since usually the highest relative velocity is linked to the trailing side. The flow behaviour given by IGV3 is different:the initial swirl is low and absorbed quickly by the main stream. Maximum relative speeds of 7.5 m/s occur in the trailing side sub-channel while in the leading side it hardly reaches 7 m/s. In both designs, conditions of higher relative speed are given nearer to channel outboard endwall than inboard, where swirl effects are not relevant.

Swirl parameters were calculated for both discs at 400rpm and the results are shown per endwall side. Results in Figure 6.73 are self-describing. In the region near the outboard endwall, swirl in the leading side benefits significantly for the IGV2-SV1 layout, with values near 0.65 in the first half and a sudden increment to 0.8 in the throat of the channel, then it decays to 0.52 along the constricted channel. The behaviour for the leading side in the IGV3-SV1 arrangement is scaled down approximately 30% respect to the former. It also presents a sudden increment in the constriction of the channel; however, the difference with the baseline swirl (dotted line) is not significant other than in the channel throat. In the trailing sides near the outboard endwall, swirl parameter starts with high values (0.6 and 0.8 for IGV2 and IGV3 respectively), but they are followed by a steady decay down to 0.4 before the throating occurs, then because of the constriction radial speed increases and a sudden decay occur in both designs, (this brings them below baseline levels). After, S stays steady along the constricted channel in the trailing side, with a value near 0.4.

In the inboard side endwall, results for the leading side gives S for the IGV3+SV1 configuration very similar to the baseline channel, but with a significant improvement in the constriction, while S for the IGV2+SV1 layout is smaller in most of the line length. In

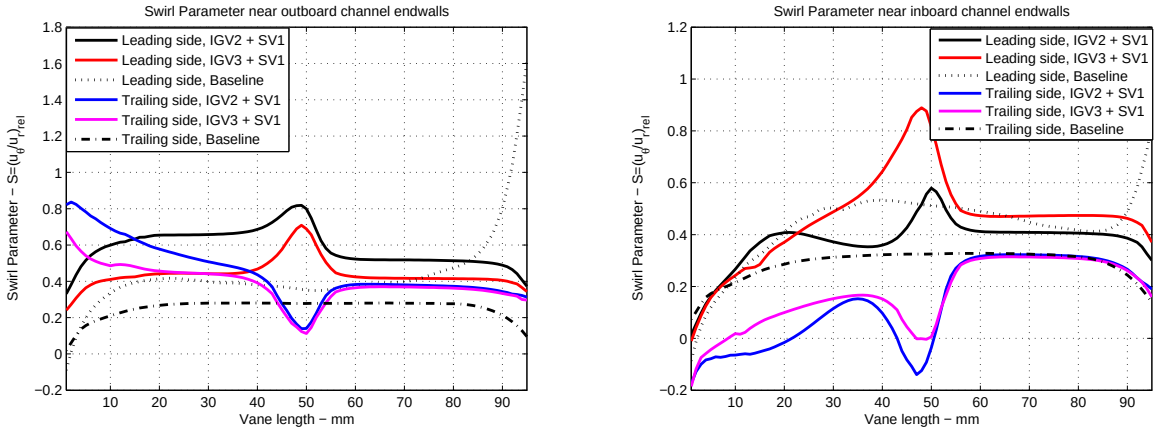

(a) S outboard.

(b) S inboard.

Figure 6.73: Swirl parameter, S was calculated in same lines as in Figure 6.66.

the trailing side near the inboard endwall, poor swirl is given for both configurations, and only after the constriction S reach the baseline trend, which is indeed low. Secondary flow behaviour in both designs is shown in Figure C.16.

The contours of air temperature in circumferential planes across the IGV's show that air temperature increases after the trailing edges of the IGV's (Figure 6.74). However, both patterns have significantly lower temperature in the leading side of the channel as compared when this has only SV1 at the outlet (Figure 6.30). In a plane beneath, air temperature (Figure C.17) increases in the trailing side of the channel with IGV2 before reaching SV1 attack edge, while the leading side still is without the characteristic temperature increment shown in Figure 6.30; this is atypical for trapezoidal channels. For the same plane in channel with IGV3+SV1 air temperature increases in the channel leading side reproducing typical characteristics of trapezoidal channels.

Convective heat transfer coefficients from vanes are shown in Figure 6.75. The IGV2+SV1 layout changes the classic distribution, since now the channel leading side has better distribution than the trailing side. The peak heat transfer coefficient occurs in the tip of the IGV2, but this is due to non existing boundary layer in that region. Therefore, the distribution is asymmetric toward the vane wall in the channel leading side. When the IGV3+SV1 layout is used, an almost symmetric distribution is reached in the main and SV1 vanes.

In the endwalls (Figure 6.76), the heat transfer coefficient distribution is slightly asymmetric when the IGV2+SV1 are used, and more symmetric when the IGV3+SV1 layout is used. Higher values are obtained in the inlet portion of the channel endwalls, however, the heat

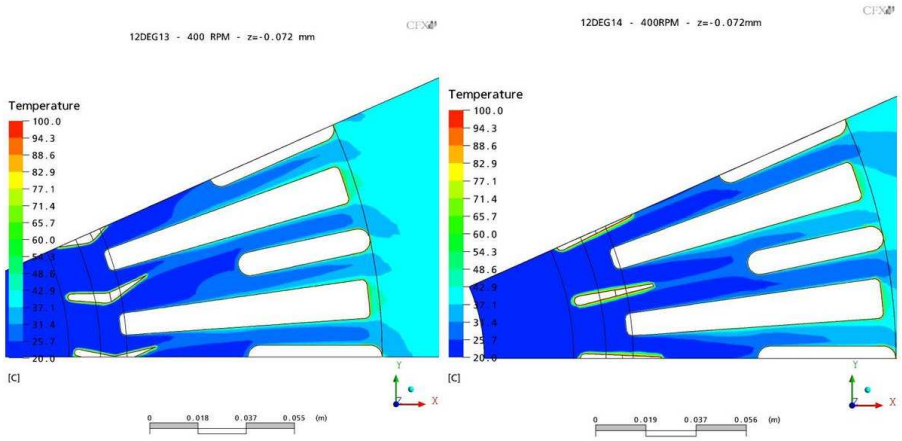

Figure 6.74: Air temperature patterns in midplanes, designs with IGV2+SV1 and IGV3+SV1.

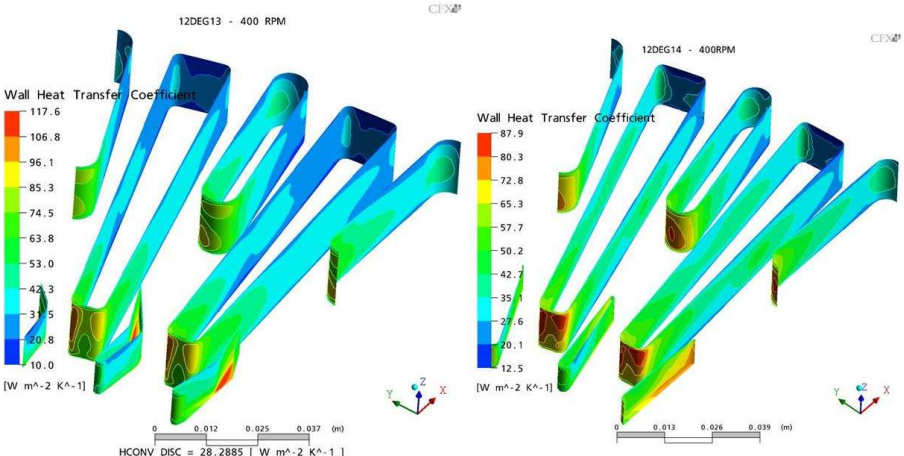

Figure 6.75: Distribution of h_c in vanes, designs with IGV2+SV1 and IGV3+SV1, n=400rpm.

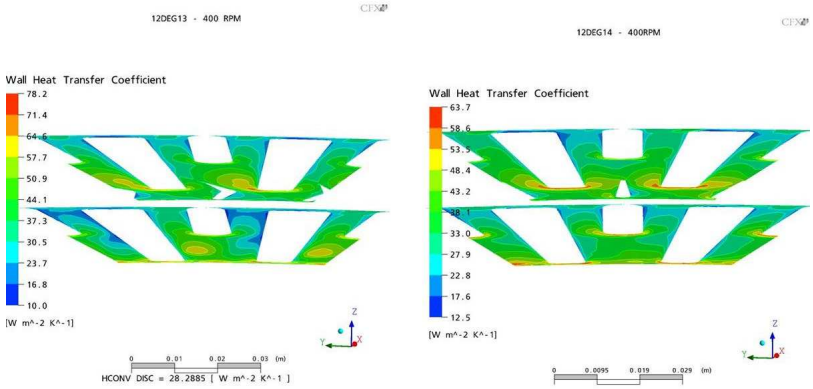

Figure 6.76: Distribution of h_c in endwalls, IGV2+SV1 and IGV3+SV1, n=400rpm.

transfer values in the endwalls drop toward the rear of the constricted channel, e.g.: h_c drops to 23 W/m^{2}K in the inboard side endwalls of both designs, after reaching nearly 50 W/m^{2}K in the inlet part of these.

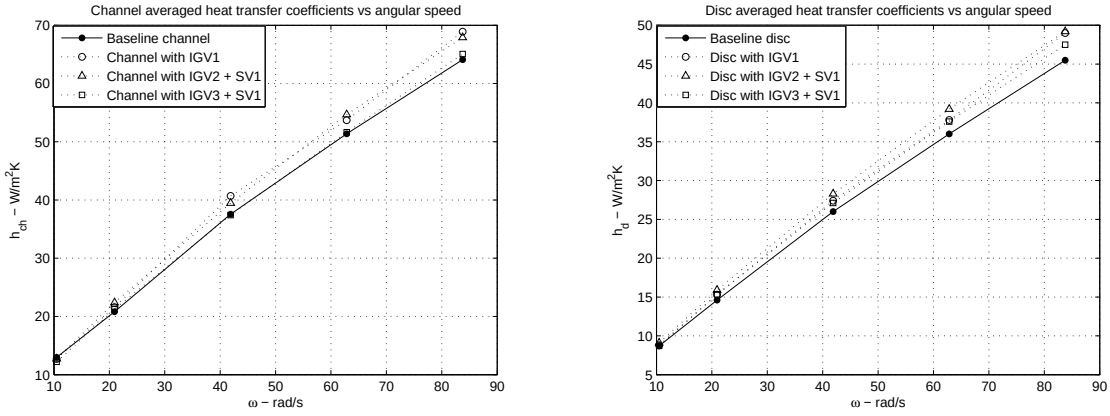

(a) h_{ch} vs ω (b) h_d vs ω

Figure 6.77: Averaged heat transfer coefficients versus rotational speed.

Heat transfer coefficients averaged per channel (Figure 6.77(a)) show that only designs with IGV1 and IGV2+SV1 are above the baseline trend by 5% (8% at 800 rpm). Results shown on a disc basis however (b), demonstrate superiority of the IGV's designs against the baseline, the IGV2+SV1 channel layout gives the highest difference (8%) while the others are 4% above the baseline. Convective performance is driven by cooling rates, which for the IGV2+SV1 design are 10% higher than the baseline, followed by the IGV1 in channel (6%), while the IGV3+SV1 design behaves similar to the baseline. Finally, if torque requirements are plotted for the discs just reviewed (IGV2+SV1 and IGV3+SV1), they both require 11%

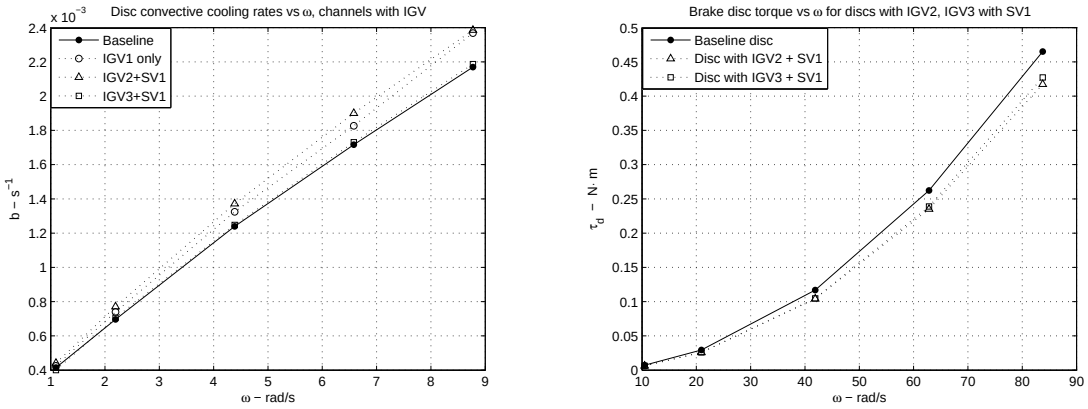

(a) b vs ω (b) τ_d vs ω

Figure 6.78: Convective cooling rates and aerodynamic torque, discs with IGVs.

lower torque in average than the baseline, which means that the amount of air passing through the channels is smaller than that from the baseline channel in the same proportion approximately. This is shown in Figure 6.78.

Relevant findings in aerothermal behaviour of designs with IGVs and SVs are: a)channel with IGV1 gives an increment of 6% in cooling rates but requires 10% to 15% more torque to pump the air; b)IGV2+SV1 layout is the most aerothermally efficient of all since it gives the highest cooling rates with lesser air mass flow. The disadvantage of this is its mass: 5.5% more than the baseline disc.

6.12 Summary

Additional results of brake discs and a summary of relevant Nusselt numbers are reviewed here. The behaviour of the heat transfer coefficients from the friction faces should be similar for all brake disc designs shown since the heat transfer ability of the friction faces is independent of the vent design (unless slots or drills had been used). This is confirmed for discs from Section 6.2 in Table 6.18. The results demonstrate very good agreement despite the CFD models were fully independent from each other.

Taking the mean value per angular speed from Table 6.18, using the face mean swept radius (see Table 5.1) and air properties (Table 3.2), a mean Nusselt number for friction faces is computed with equation 5.4. This can then be compared against that predicted by theoretical equations given by Dorfman (1963) in page 150. The comparison (Figure 6.79(a)), indicates

Table 6.18: Average convective heat transfer coefficients for friction faces (W/m^{2}K).

n [rpm]	Baseline	20 Vanes	45 Vanes	60 Vanes	90 Vanes
100	6.20	6.20	6.00	6.23	5.99
200	11.50	11.40	11.00	11.40	11.15
400	20.42	20.40	20.10	20.40	20.10
600	28.70	28.60	28.29	29.70	28.48
800	37.10	38.30	36.80	36.30	36.14

that close correlation exist between the turbulent formula 5.7 and CFD for lower angular speeds, while above 400 rpm this underpredicts by 11%. Laminar flow equation 5.6 gives higher value at n=100 rpm and lower at 600 and 800 rpm, while the agreement at 200 and 400 rpm is closer (3 and 9%).

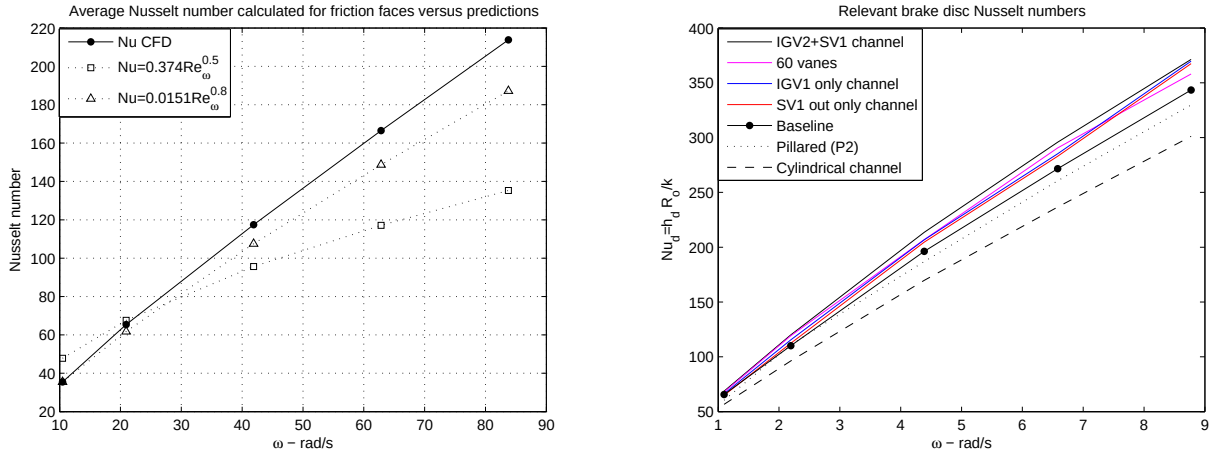

(a) Nu Friction faces

(b) Nu Discs

Figure 6.79: Summary of Nusselt numbers.

Brake disc Nusselt numbers (from CFD) for only those designs showing significant variations from the baseline were calculated using equation 5.4 with disc outer radius as characteristic dimension. Results (Figure 6.79(b)) show that the highest Nu is for the IGV2+SV1 configuration with 9% more than the baseline (solid line with dots) for angular speeds above 200 rpm. Brake disc designs with 60 vanes, IGV1 only and SV1 only give also higher Nu than the baseline. The two worse Nusselt trends are for pillared design (configuration P2) and brake disc with cylindrical channels with 5% and 13% less than the baseline.

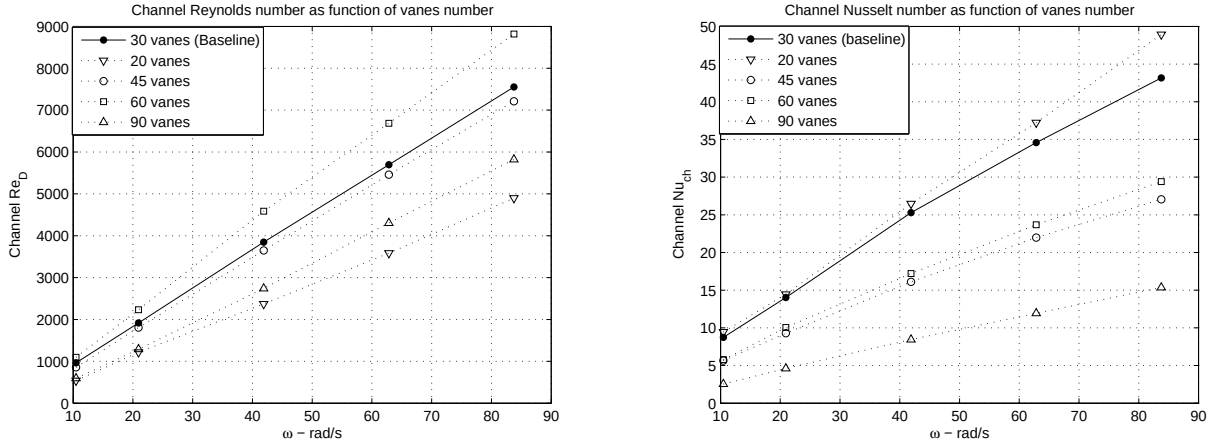

(a) Re_D vs ω (b) Nu_{ch} vs ω

Figure 6.80: Average channel Reynolds and Nusselt numbers calculated from CFD data.

The characteristics of trapezoidal channels are further revised by retrieving their average absolute velocities and calculating the Reynolds number based on the channel hydraulic diameter (Figure 6.80). Using data from Figure 6.23, Tables 6.3, 3.2 and equation 5.5, channel Nusselt numbers were calculated. It is found that the 60-vane design has the largest Reynolds number, despite having lower hydraulic diameter than the baseline, 20-vane and 45-vane discs. This means that the average absolute channel speed is maximum when an array of 60 vanes is used. Channel Nusselt numbers give the largest trend for 20-vane design followed by the others in an order similar to their hydraulic diameter differences.

6.13 Experimental Work

Experimental tests were conducted with a brake disc with blocked channels, an outboard brake disc plate, and two ventilated brake discs with radial vanes and SV1 vanes at outlet and inlet positions. The purpose of the two firstly mentioned prototypes was to have *non-ventilated designs* results of which could be cross linked with empirical correlations, e.g. (Dorfman 1963).

6.13.1 Non-ventilated Discs

Non-ventilated designs were tested using the detachable vane brake disc with channels blocked, using a high temperature resistant tape (Figure 6.81) which allowed a smooth finish, and also using the *outboard side* disc plate from this disc alone (Figure 6.82). However, the outboard disc plate is an assembly component, therefore it has 60 blind drills on the *channel side* face, used for attaching vanes and inboard side disc. These drills were left bare in contact with the surrounding air during the tests.

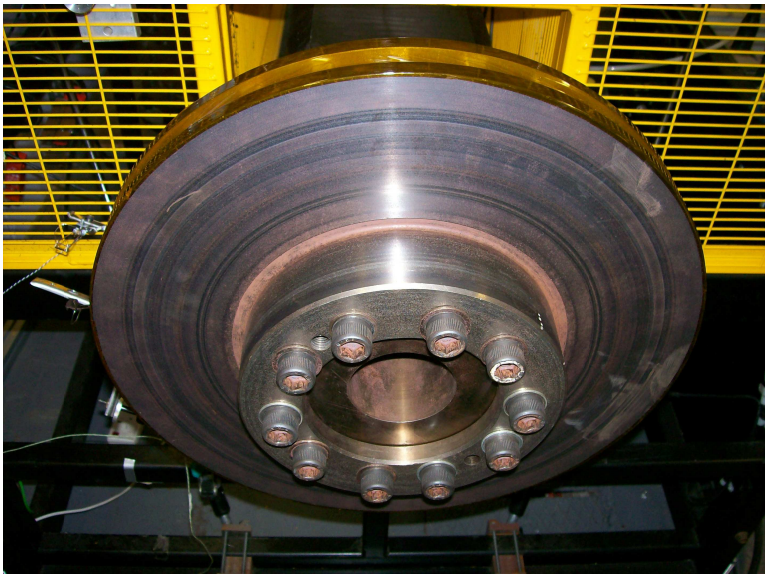

Figure 6.81: Brake disc with channels blocked using high temperature resistant tape.

Table 6.19: Non-ventilated brake disc prototypes characteristics.

Disc	Mass [kg]	A_w [m^2]		A_r [m^2]	
	⇑Hub	⇑Hub	⇓ Hub	⇑Hub	⇓ Hub
Blocked channels	27.35	0.3534	0.2677	0.3179	0.2375
Outboard disc	16	0.3362	0.2505	0.3179	0.2375

*⇑: With; ⇓: Without Hub mass: 4.7 kg.

The characteristics of the above brake discs are shown in Table 6.19. The disc were heated with the induction heater and then spun at constant speeds of 200, 400, 600 and 800 rpm. Typical cooling histories for n=400rpm are shown in Figure 6.83, where averaged temperatures per side are shown. It is seen that when the detachable vane disc is used (channels blocked), the inboard side disc plate cools quicker than the outboard side disc plate, while

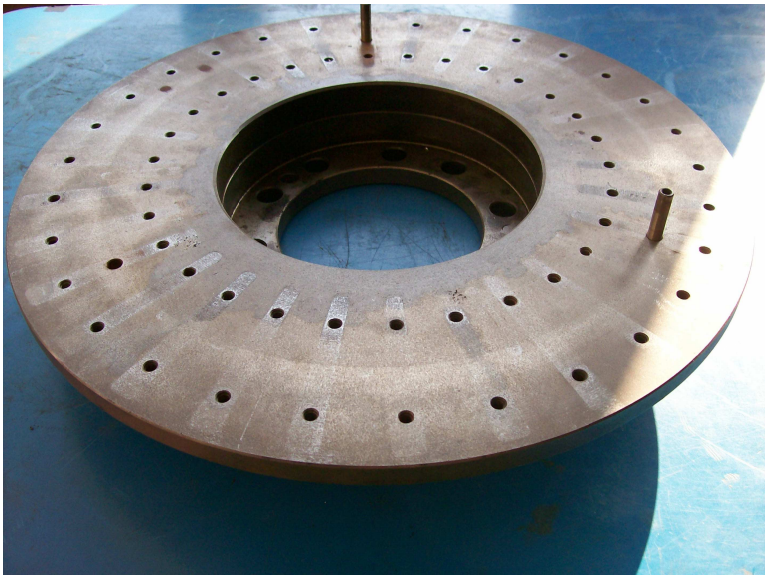

Figure 6.82: Non-ventilated prototype using the outboard disc.

when only the outboard side disc is used, the cooling trends are very similar. The influence of different thermal capacities is also clear, since the outboard side disc plate (41.5% less heavier, 6.83(a)) cools down in about haf the time of the blocked channels disc. Heat transfer coefficients were calculated using equations 4.19 and 4.20 with data from Table 6.19. The total and convective heat transfer coefficients are plotted in Figure 6.84.

Both heat transfer coefficients from the outboard side disc plate are higher than those from the brake disc with blocked channels. The average difference for convective heat transfer coefficients is about 10% for all the speeds except at n=400rpm, where the difference raises to 24% (even higher than that of ventilated cast iron brake disc, Figure 5.31). In order to investigate this phenomenon further, disc Nusselt numbers were calculated using experimental convective heat transfer coefficients and equation 5.4. The results for both disc were calculated and compared against those predicted by Dorfman (1963), equations 5.6 and 5.7. These are plotted in Figures 6.85 and 6.86.

Results show that the theoretical equation for rotating disc in laminar flow underpredicts the convective Nusselt number from the brake disc with blocked channels by 13% at n=200rpm and by an average of 33% for the rest of the speeds. It also underpredicts the Nusselt number of the outboard side disc by 18% and 42%, respectively. Equation 5.7 for a solid disc rotating in turbulent flow correlates better. In this case, the maximum error between experiments and theory for blocked channel disc Nusselt number is 7%, that is, a very good fit exist between the theory and the experiment. However, for the outboard side disc the turbulent relation still underpredicts by 11% roughly (with a maximum underprediction of

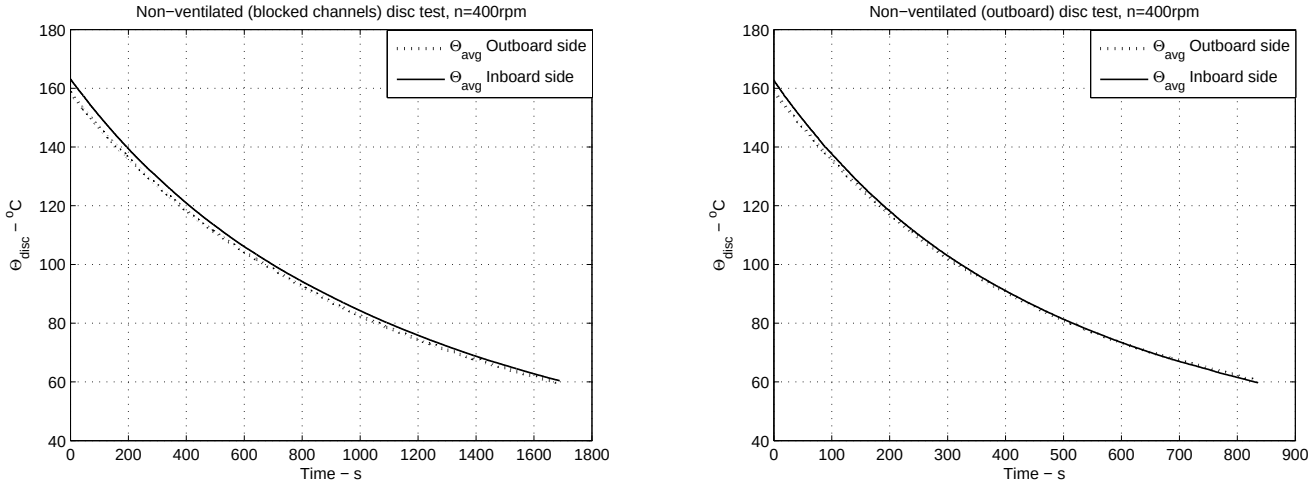

(a) Blocked channels.

(b) Outboard side disc.

Figure 6.83: Average temperatures from non-ventilated brake disc prototypes at n=400rpm.

23% at n=400rpm).

From the above, it may be suggested that the convective dissipation from the brake disc with blocked channels show characteristics more linked to a rotating disc in turbulent flow. In regards to the outboard side disc, the experimental Nusselt number is higher than that predicted by laminar and turbulent theoretical relations. Issues affecting this result are likely to be the presence of drills in one of the faces of the disc which are likely to influence the boundary layer in the inboard side face of the disc. Another issue that may become important for the behaviour of experimental Nusselt number is the presence of the rubbing thermocouple itself since it must influence the behaviour of the boundary layer on the disc.

6.13.2 Ventilated Discs

Designs with radial and SV1 vanes were experimentally tested. The SV1 vane was positioned at two locations (inlet and outlet) and therefore two prototypes were created. The prototypes were manufactured using the philosophy of the detachable vane brake design: the SV1 vane was made of the same aluminum alloy as the main vanes. The SV1 vane was drilled through its height and two M4 socket cap screws were used to attach it to the inboard side disc plate. The inner (channel side) face of this disc was drilled in order to accommodate at least 5 mm of screw length. Therefore, the inboard side brake disc had in total 180 drills, 60 fully crossing the thickness (used to hold 30 main vanes with M6 size bolts/screws) and the 120

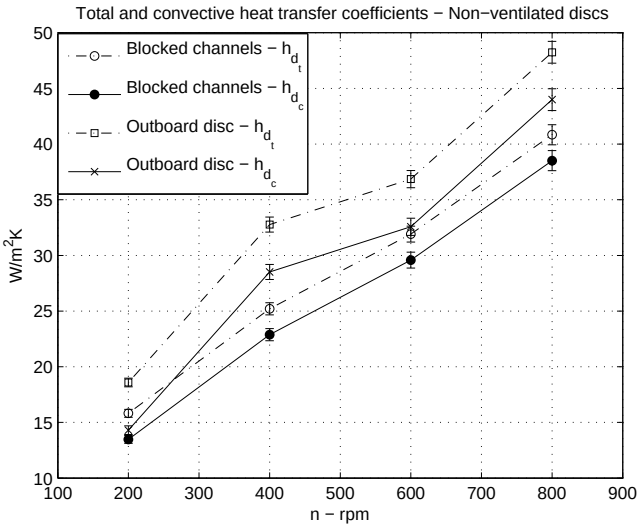

Figure 6.84: Experimental total and convective heat transfer coefficients, brake disc with blocked channels and outboard side disc plate.

remaining were drilled only on the inner face of the outboard side disc (to hold 30 SV1 vanes in two different positions, M4 size).

All the holes had been drilled before any test was conducted. This meant that when the vane SV1 located at inlet, 60 holes remained free toward the channel outlet in the inboard side endwall (Figure 6.87). The alternative position (SV1 at outlet) left free bare holes in the inlet of the channel. Figure 6.88 shows the final version of the brake disc prototype with radial (baseline) vanes and SV1 vanes at the outlet. Cooling histories from the above disc prototypes (SV1 inlet and SV1 outlet designs) are shown in Figure 6.89. The experimental data shown are averaged per disc rubbing face.

Results for the SV1 outlet configuration indicate a almost constant temperature difference between the faces, the outboard side friction surface is 8→9^{o}C hotter than the inboard side. The same occurs for the SV1 at inlet case with a lower temperature difference (3→4^{o}C). Although they display similar cooling times, their cooling rates and heat transfer coefficients are not the same, since they depended upon test ambient temperature [5].

Brake discs total and convective heat transfer coefficients were calculated in the range of $\overline{\Theta_{disc}}$=120^{o}C→60^{o}C. Uncertaintities were calculated as described before. The results reveal similar behaviour in the range of n=100rpm to n=200rpm (Figure 6.90), where total heat transfer coefficients vary between 11 and 18 W/m^{2}K. However, as of n=400rpm the total

[5]A large difference with ambient temperature in these cases yields poorer b and h_{d_c}

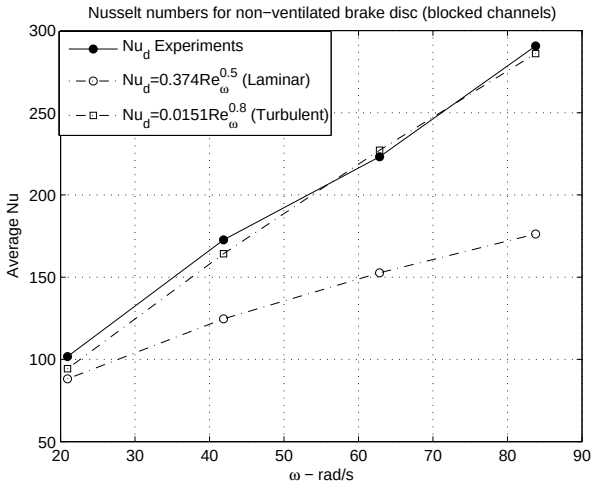

Figure 6.85: Disc with blocked channels, Nusselt numbers, experiments vs theoretical data.

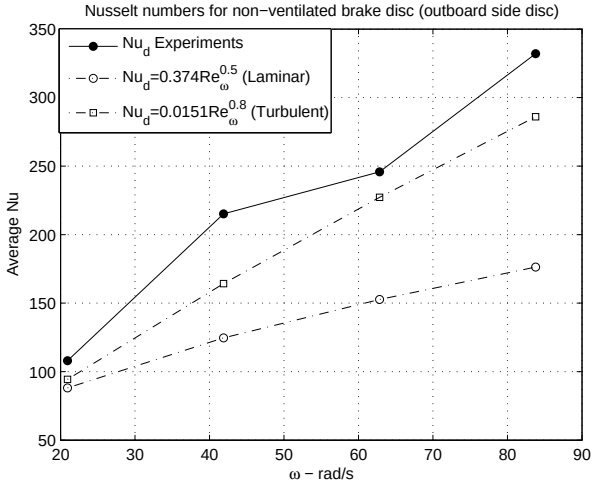

Figure 6.86: Outboard side disc, Nusselt numbers, experiments vs theoretical data.

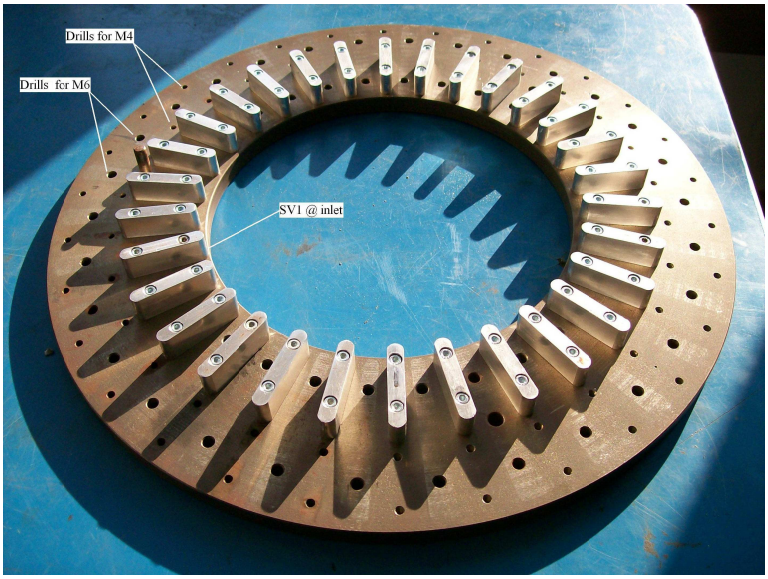

Figure 6.87: Outboard side disc plate with SV1 vanes at inlet position.

heat transfer coefficients of the brake disc with SV1 vanes at inlet are higher than those with SV1 at outlet by 8% at 400rpm, to 20% at 800rpm. The same occurs for convective heat transfer coefficients where the difference is pronounced at 600 and 800 rpm (Figure 6.90(b)).

Experiments and CFD results match well for the prototype with SV1 at outlet, with differences of 5% between CFD and experiments, however this does not occur for the disc with SV1 at inlet. To assess whether experimental data for disc with radial and SV1 at inlet vanes followed a monotonic trend, two more tests were performed (data at n=1000rpm and n=1200rpm in Figure 6.90(b)). It was experimentally proved that h_{d_c} followed a monotonic (increasing), continuous and somewhat smooth behaviour for the brake prototype with radial and SV1 at inlet vanes. The question was then assessing where (a) a flawed behaviour of the CFD solution existed or, (b) what factors (test inconsistencies) could be increasing the cooling rate of the prototypes with SV1 at inlet. The CFD model re-run twice more using different settings for n=600 rpm[6]: the first trial used the $\kappa - \epsilon$ model and High Resolution Solver and the second used tje $\kappa - \omega$ model ANSYS-CFX Solver Theory (2005). In both cases the limiting accuracy of the residuals was reduced from 10^{-5} to 10^{-6}, although accurate solutions with the latest settings only reached rms residuals of about $10^{-4} \rightarrow 10^{-5}$. Average convective heat transfer coefficients for two regions of the brake disc plus the disc averaged magnitude are shown in Table 6.20.

The results indicate that the HRS solution gives higher values mostly for the channel when the $\kappa - \epsilon$ model is used (16% more), which makes the disc averaged value 11% higher than

[6]The first significant difference between experimental prototypes occurred at this angular speed

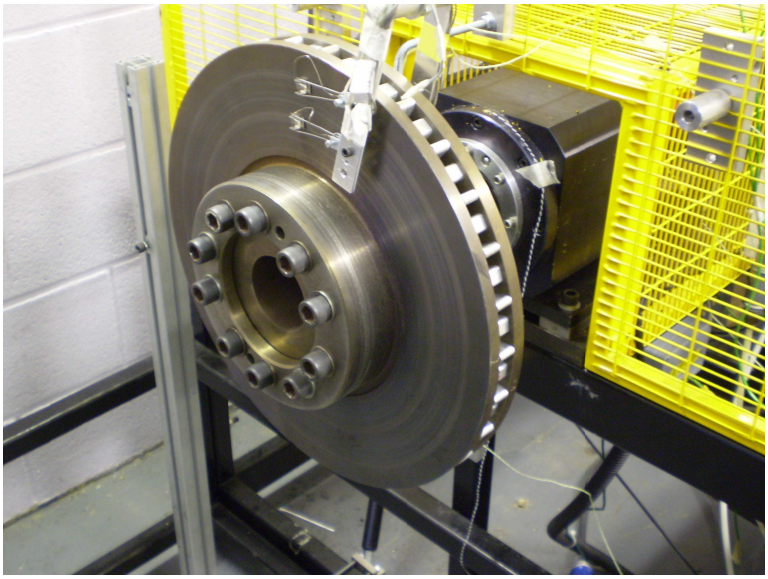

Figure 6.88: Brake disc prototype with baseline vanes and SV1 vanes at outlet.

Table 6.20: CFD modelling assessment of brake disc with SV1 at inlet, n=600rpm, W/m^{2}K.

Modelling	$\overline{h_{ch}}$	$\overline{h_{ff}}$	$\overline{h_{d_c}}$
$\kappa-\epsilon$, Upwind, $rms=10^{-5}$	42.2	27.7	31
$\kappa-\epsilon$, HRS, $rms=10^{-6}$	49	29.2	34.5
$\kappa-\omega$, HRS, $rms=10^{-5}$	52.6	38.3	40.9
Experiment	N/A	N/A	46.6±2.2

that given by the Upwind scheme. The $\kappa-\omega$ HRS compared to the Upwind Scheme, predicts averages substantially higher, e.g.: 38% higher for the friction faces (where it was expected a lower result), and 32% higher disc average heat transfer coefficient. However the large difference in friction face results may indicate a model failure for this solver, and the good correlation with experiments of the first model (Section 5.4) makes the first two approaches more reliable. Nevertheless, none of the above numerical trials predicted such a high experimental value (12% larger than that from $\kappa-\omega$ HRS). Therefore attention was turned to the test side. Careful revision of the brake disc prototypes revealed that when the SV1 vanes located at the inlet, a lack of proper fit existed for some SV1 vanes with the inner faces (endwalls) and therefore a number of main vanes were held loose between the disc plates, that is small gaps vane-disc face remained (Figure 6.91).

It is feasible that during brake disc testing, loose vanes (SV1 and main) could have vibrated. These would have influenced the heat transfer ability of the assembly by enhancing the

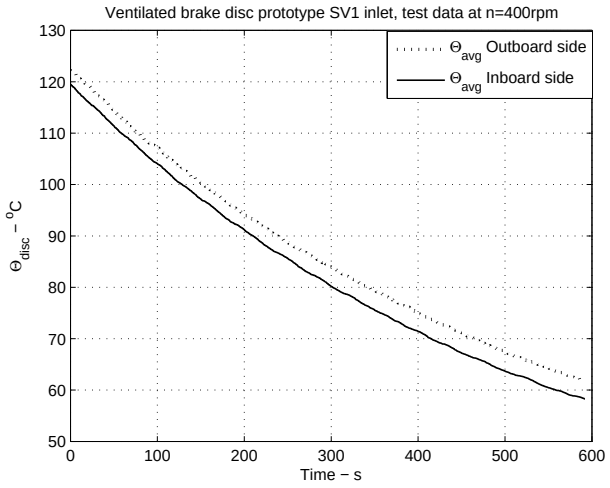

(a) SV1 @ inlet.

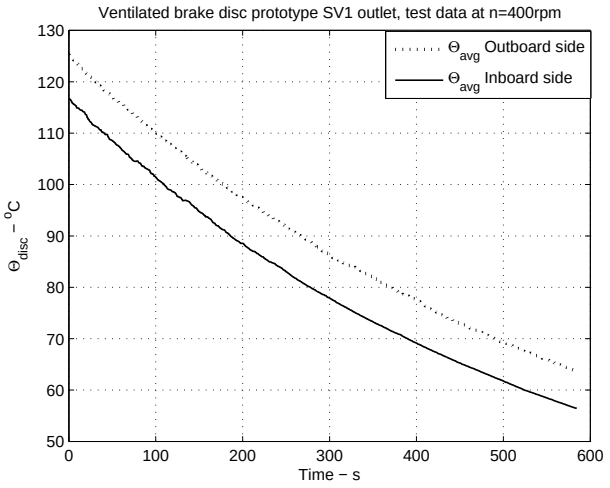

(b) SV1 @ outlet.

Figure 6.89: Cooling history in brake prototypes with radial and SV1 aluminum vanes, n=400rpm.

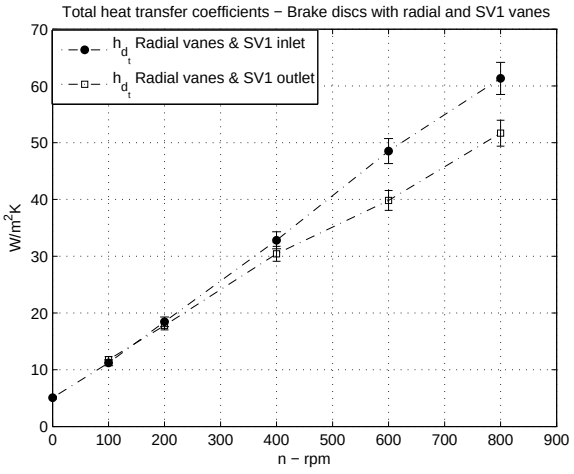

(a) h_{d_t} vs ω

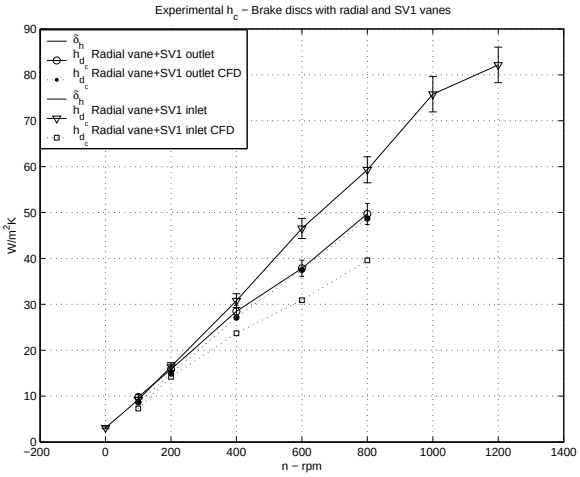

(b) h_{d_c} vs ω

Figure 6.90: Experimental heat transfer coefficients, ventilated prototypes with radial and SV1 vanes.

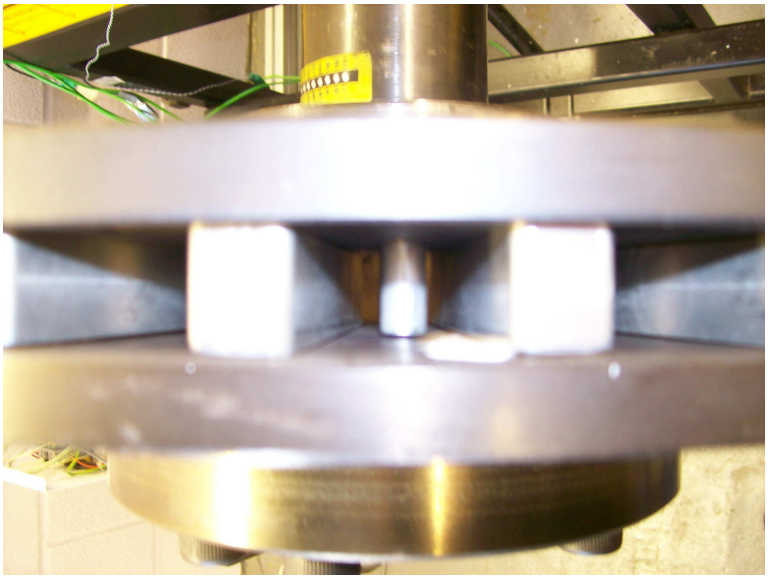

Figure 6.91: Assembled prototype with SV1 vane at inlet. Gaps between the vanes and the disc faces are shown.

convective heat removal. *Acoustic Streaming* is how this phenomenon is termed and it is mainly used for cooling of micro-electronics where minutes gaps do not allow common convection to develop Nicoletti (1996), Wan & Kuznetsov (2003). The mechanics of the acoustic streaming derives from vibratory motion in the near wall fluid layer which promotes steady vortices near the wall, disregarding the bulk flow stream behaviour. This finally increases momentum and energy transfer, although it may create more drag. It is therefore assumed that phenomena such as vibration induced flow motion possibly affected the cooling behaviour of the brake prototype with radial and SV1 at inlet vanes.

Chapter 7

Railway Wheel Mounted Brake Disc

This Chapter concentrates the computational research on convective heat dissipation from railway wheel mounted brake discs (WMD). The Chapter begins with a description of the WMD, follows with the analysis of CFD modelling of a baseline model and two new configurations.

7.1 WMD Configuration and Heat Dissipation

The configuration of a WMD in service is usually in pairs per wheel, one per side, see Figure 7.1. The WMD can be attached to the wheel rim, web or hub, using bolts or an independent carrier, (Tirović & Galindo-López[a] 2006). The discs can be in two sections (180^o each), or as a single component. Friction braking load is asymmetric, one side of the disc, and this limits its usage to low braking duties due to structural issues such as coning (Tirović 1998), (Tirović & Ali 2001). The research considers the Car Carrier WMD (Tirović & Ali 2001), (Tirović & Galindo-López[a] 2006) as starting or baseline model. This WMD design has 72 vanes in total, of which 12 are structural links the friction disc and the hub section (see Figure 7.2). Sets of five thinner vanes are located between the 12 thick vanes and their layout makes the disc design *non-handed* for rotation. The disc material is steel with characteristics similar to steel 15CDV 06. The WMD outer diameter is limited by the wheel size which in this case is 640mm. Geometric characteristics of the WMD are provided in Table 7.1. The disc hub is bolted to the wheel hub by means of 12 M12 bolts, and once it is assembled there exist a *line* contact between a raised lump of the thick vane backface and the wheel hub (Figure 7.3).

Heat dissipation from the WMD can occur virtually in all modes, however, conduction heat losses are restricted due to design configuration: the line contact between the thick vane

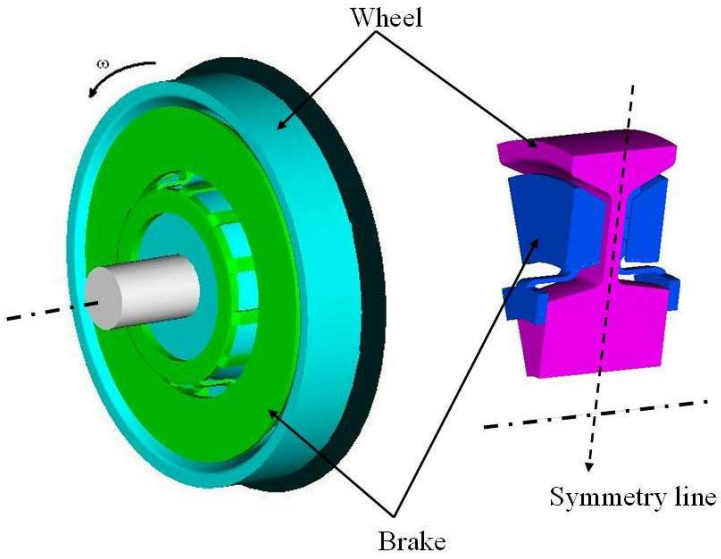

Figure 7.1: Schematic view of the assembly of the WMD with the railway wheel.

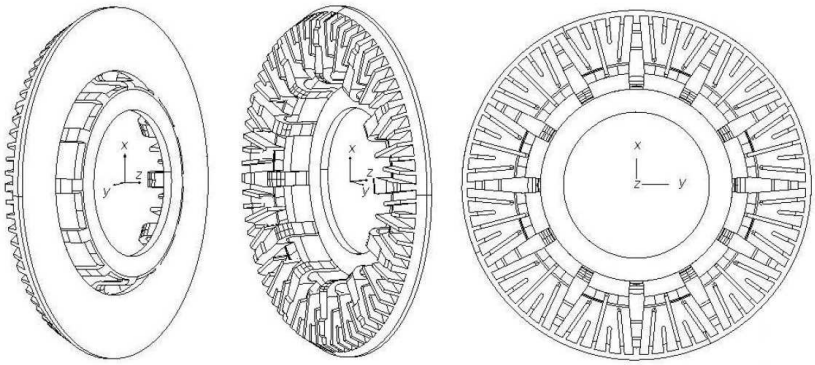

Figure 7.2: Railway wheel mounted brake disc CAD model views, baseline model.

Table 7.1: Baseline wheel mounted brake disc characteristics

Disc OD	560 mm
Friction disc ID	360 mm
Mass (per disc)	35 mm
Friction disc thickness	23 mm
Thick vanes	12
Thin vanes*	60
Height of vanes	22 mm
Convection area (total)	0.65 m^2

*Long and short

and the wheel web provides a negligible path for conduction to the wheel[1] and the slender-long section of the thick vane toward the mounting flange creates a geometric resistance to conduction. Therefore conductive heat dissipation may be neglected. Radiation is important at high temperatures, since the friction surface *looks* to the surrounding air and therefore, depending on its surface characteristics, it could radiate significant amounts of heat, however on the vaned side of the disc, radiation losses are reflected back from the wheel web. This work has neglected radiation in the analysis.

Convection heat dissipation, on the other side is very difficult to foresee. The geometry configuration of the WMD and wheel has a reduced periodic inlet area (near to the friction disc inner radius), which expands suddenly into the vents space between the vanes and the wheel (see Figure 7.4). Air trapped within this vents is centrifugally pushed toward the outer radius which causes air is soaked from the surroundings to replace the one pumped (continuity balance). Additional effects such as Coriolis accelerations and flow recirculation due to adverse pressure gradients (opposite to flow direction) due to vane attack angles will also occur. Besides this, the existence of a 8 mm gap between the tip of the vanes and the wheel web necessarily complicates more the rotational fluid behaviour, since now air can swap between channels in the proximity of the gap (see Detail A in Figure 7.3). As result, convective heat transfer rates will depend very much on the flow dynamics, which in turn depends upon the disc geometry. Distribution of convective heat transfer coefficients is difficult to predict, and only trailing side walls in the channels with aligned flow are likely to have enhanced heat transfer by convection.

[1]Heat loss to wheel web must, in fact, be avoided due to disc design specification

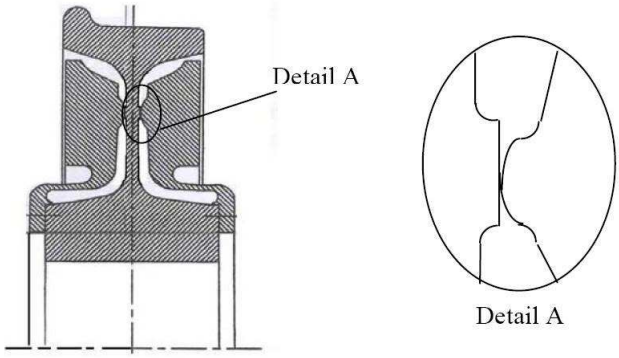

Figure 7.3: Half cross section of the assembly wheel-WMD.

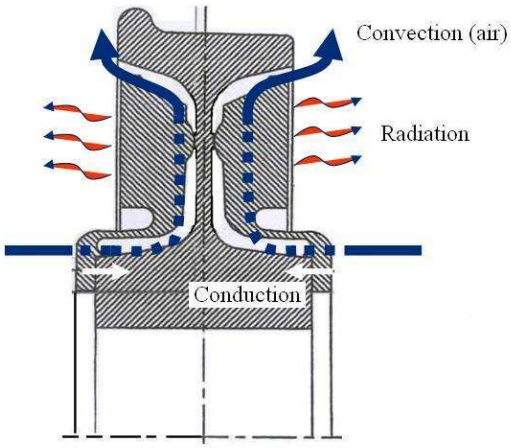

Figure 7.4: Heat dissipation from a wheel mounted brake disc.

7.2 WMD Computational Fluid Dynamics Modelling

A 30^o sector was taken from the CAD drawing to create the CFD model. The pie model selected only accounts for one WMD, that is the model was sliced through the wheel web symmetry line, see Figure 7.1. The CFD domain therefore had the wheel and disc surfaces as walls boundaries. The CFD model was constructed using an unstructured mesh due to complexity of geometry and keeping, where possible, a fine mesh near the surfaces. The grid contained 1,886,971 cells (45.8% tetrahedrons, 48.7% hexahedrons, 3.9% prisms and 1.6% pyramids). The disc angular speeds modelled are those shown in Table 7.2 where the train linear speed is also included, assuming a wheel diameter of 640mm. The order of braking energy to be dissipated at these speeds range from 0.12MJ to 3.8MJ (24km/h to 133 km/h, respectively), for a vehicle mass of 44427kg approximately [2].

The rotational Reynolds number based on the disc outer radius and a first approximation of the velocity boundary layer thickness over the friction face (opposite to wheel web) following the formula 7.1, Dorfman (1963) and assuming laminar conditions are also shown in Table 7.2.

$$\delta_\omega = 3.71\sqrt{\frac{\nu}{\omega}} \tag{7.1}$$

Table 7.2: Rotational Reynolds number and hydrodynamic boundary layer thickness.

Train speed	n	ω	Re_ω	δ_w
[km/h]	[rpm]	[rad/s]	[-]	[mm]
24	200	20.9	$9.25\text{x}10^4$	3.79
48.2	400	41.9	$1.85\text{x}10^5$	2.68
66.4	550	57.6	$2.54\text{x}10^5$	2.28
133	1100	115.2	$5.1\text{x}10^5$	1.61

According to Table 7.2, the two lowest speeds would generate laminar conditions in airflow around the WMD if this was solid. However since the confined space between the wheel web and the disc has vanes and air gap, significant shear layers and speed gradients may occur leading to turbulent behaviour. Figure 7.5 shows the CFD model used for the simulations. The boundary conditions are as follows: Periodic conditions on the angular sides of the domain ($\phi_{PF_1} = \phi_{PF_2}$, where ϕ is any fluid property or variable at the periodic face). Adiabatic conditions at the wheel surface. Smooth surfaces are considered (both wheel and WMD), on which non-slip conditions for velocity exist. The WMD surfaces are modelled at 150^oC,

[2] Each train carriage has eight WMD's

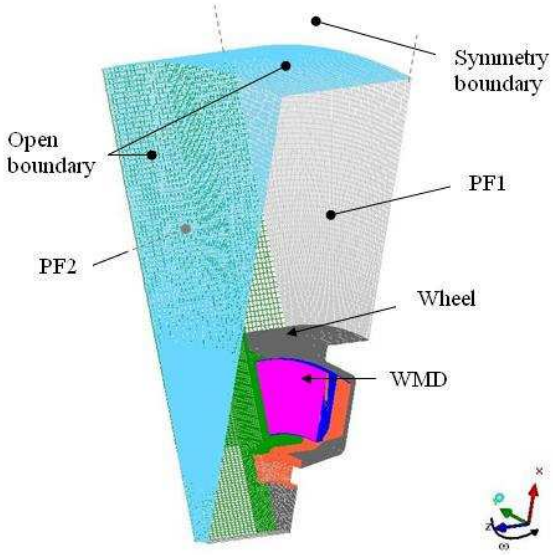

Figure 7.5: Wheel mounted brake disc CFD model.

and only convection is modelled, disregarding radiation heat transfer. The convection heat transfer coefficients are calculated using a reference temperature of 20^{o}C. The turbulence model is $\kappa - \epsilon$. A symmetry plane was located across the wheel web, although this is not likely to have a particular influence on the convection heat transfer behavior of the disc itself (that is, it could be modelled with a smooth wall). The CFD model assumes that the disc and the wheel are to be rotating in still air conditions and no influence of the ground or nearby underframe equipment is considered. Therefore, the disc is modelled in ideal conditions. Each CFD solution took in average 33 hours to reach a prescribed convergence error of RMS=1x10^{-5} in the flow variables (velocity, energy and turbulent quantities). Time-steps were calculated as described in Section 3.1.6. Unless otherwise stated, the disc and wheel rotate in clockwise direction (about $+z$).

7.3 WMD Computational Fluid Dynamics Results

The details of the flow pattern have been retrieved at three axial positions inside the ventilated region of the brake disc. The first plane of postprocessing is located 2 mm away from the disc backface, the second plane is located at the middle of the vanes height (11 mm above of the disc backface) and the third plane locates between the vanes tip and the wheel web surface (4 mm away of the wheel web surface). These are identified as *near wall*,

mid and *gap* planes respectively. Also, the values of flow mean speed [3] were retrieved at ten discrete locations along six lines which cross the channel longitudinally at the middle height of the vanes. The channels have been labeled for easiness of identification. The location of the planes and lines for postprocess is shown in Figure 7.6.

The relative air speed is shown in Figure 7.7, at n=400rpm. Two recirculation regions appear *behind* the two largest vanes (inlet of Trail 1 and Lead 1 channels). Recirculating regions develop on the depressed inlet in front of the vanes and they are due to sudden change of geometry found in the flow path. The air is rapidly slowed down and the recirculating flow serves as a flow barrier at the intake region (see for instance Eck (1973) for a similar explanation on centrifugal fans), that is, it is detrimental on the cooling performance. Some streamlines show that air *leaks* from one side of the disc toward other channels through the gap existing between the wheel and the tip of the vanes. This may be beneficial for cooling since the layer of air in the gap is necessarily cooler than that near the disc surface and therefore it may work as heat sink.

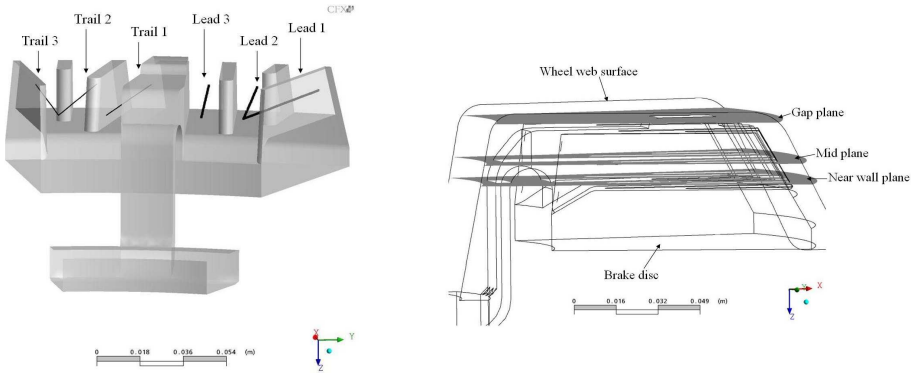

(a) Postprocessing lines. (b) Postprocessing planes.

Figure 7.6: Planes and lines of data postprocessing and analysis.

Figure 7.8 depicts the relative flow pattern in the near wall plane at 400 and 1100 rpm. The recirculation regions appearing behind the two larger vanes have a significant effect on the flow speed downstream. At this plane, channels Trail 1, 2 and 3 are blocked by the recirculation region developing in the entrance; the channel at the trailing side of the thick vane has the lowest airspeed near its backface. Channels Lead 1 and 2 are also blocked due to the recirculation of flow at their inlets. The channel on the leading side of the thick vane (Lead 3) is the channel with better flow behaviour in the sense that it draws air through all its entrance and no apparent recirculation exist. Except the channel in the trailing side of

[3] Mean refers to turbulent averages.

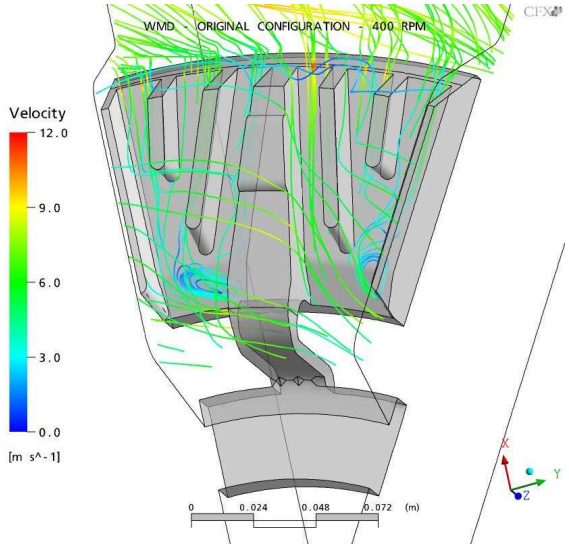

Figure 7.7: Streamlines in rotating frame over the channels of WMD, n=400 rpm.

the thick vane (Trail 1), the relative flow at the exit region of the channels is accelerated. This is due to the proximity with the curvature of the wheel, where the space between the brake disc and the wheel narrows down. This increases the speed in the leaving flow.

The vectors of relative speed in the midplane shows that recirculation regions disappear almost completely, see Figure 7.9. Enhanced flow speed appears at this level of the vanes mostly in channel Lead 3 where a continuous acceleration of air occurs. On the contrary, in the channel of the trailing side of this vane, slow motion air is given. The relative air speed in the remaining four channels is similar (near 5 m/s and 15 m/s for 400 and 1100 rpm respectively). The above indicates that Coriolis force acting tangent to circumferential direction increases with distance from the disc backface to vane tips. This effect benefits heat transfer above the root of the vanes.

At the gap, between the tip of the vanes and the wheel web, air is sheared mainly by the wheel web surface. The most significant constriction of cross section occurs between the tip of the thick vane and the wheel web, therefore and increment of relative speed is observed in this region (Figure 7.10). The vectors shown are as seen by an observed standing on the wheel web or vanes. A better understanding of the flow behaviour inside the vents is acquainted by looking at Figures D.1 and D.2 (Appendix D). The first of these clearly shows two recirculation regions developing at the entrance of the channels. It can be seen that air stream flowing in the gap between the vanes and the wheel web actually serves as a reflecting barrier for the air inside the channels. For instance, air stream deriving from the recirculation region in the trailing side of the thick vane does not follow the channel path, but it is rather drawn out of the channel and it re-enters two channels later. The best intake

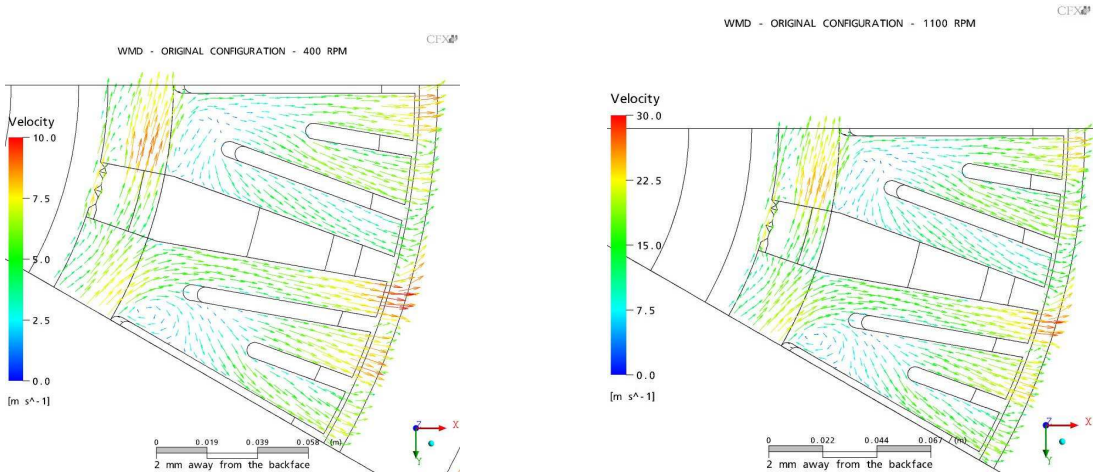

(a) n=400 rpm. (b) n=1100 rpm.

Figure 7.8: Relative velocity vectors on the near wall plane.

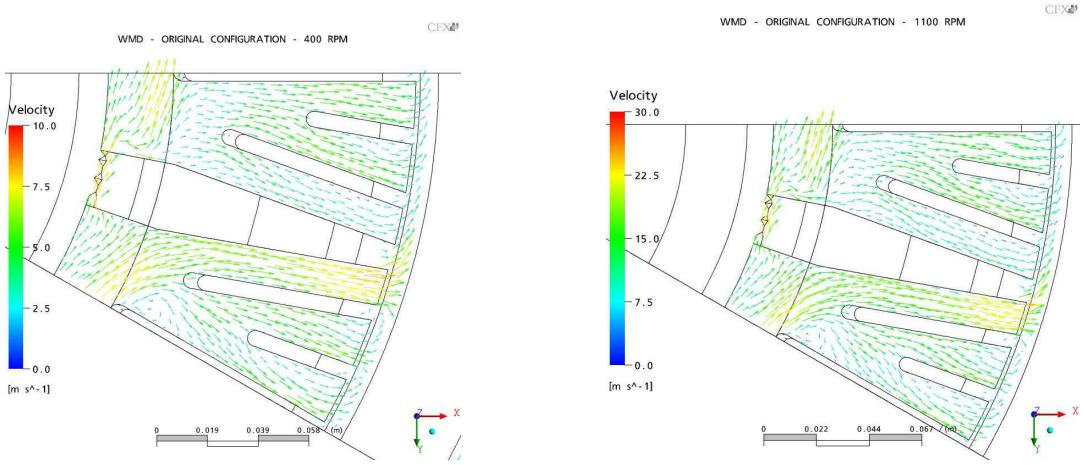

(a) n=400 rpm. (b) n=1100 rpm.

Figure 7.9: Relative velocity vectors on the midplane.

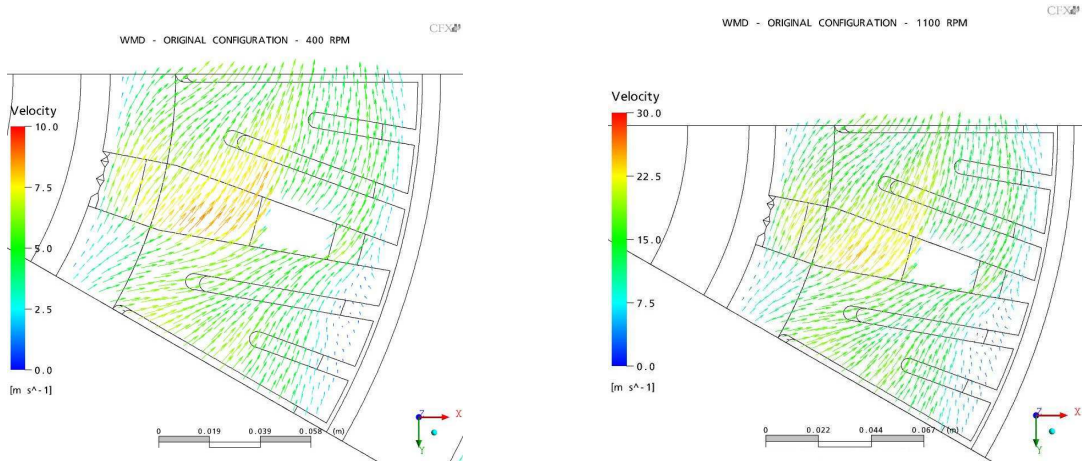

(a) n=400 rpm. (b) n=1100 rpm.

Figure 7.10: Relative velocity vectors in the gap plane.

of air is given in the channel on the leading side of the thick vane, as can be seen in the top of Figure D.2. It is also evident that the recirculation region size is larger on the trailing side of the thick vane. Air behaviour at discharge from channels is also shown in Figure D.2. The channel with starved supply of air is the one located on the trailing side of the thick vane.

Static pressure contours are shown in Figures 7.11 for n=400rpm. Near the wall these show either the forces on the fluid given by the vanes, mainly toward the rear of the leading side of the vanes (pressure recovery due to vane pumping); or suction regions associated with sudden changes of geometries and flow recirculation. Stagnation regions form on the attack edges of the thick and smallest vanes mainly. Contours plots of static pressure have been also retrieved at the gap plane between the wheel web and vanes tip. At this level, only the suction region near the middle radial vane has influence. The fall in flow static pressure over the thick vane is mainly due to high speed flow on that region. Recovery pressure is observed towards the outer radius of the disc, this mainly due to the pumping effect of the disc and wheel.

Temperature contours on the near wall plane are shown in Figure 7.12 for 400 and 1100 rpm. At 400 rpm, channel Trail 1 has the highest air temperature increment from 36.2^{o}C to 58.1^{o}C. On the opposite side of thick vane (channel Lead 3) air increases temperature at a low rate (20^{o}C along the channel). The air temperature in the channel on the leading side of this vane also increases but at a lower rate (36.2^{o}C to 47.2^{o}C). The rest of the channels show lower air heating (36.2^{o}C to 41.2^{o}C), which is good for heat transfer coefficient. At 1000 rpm the behaviour is significantly different, with cooler air near the wall. Air temperature

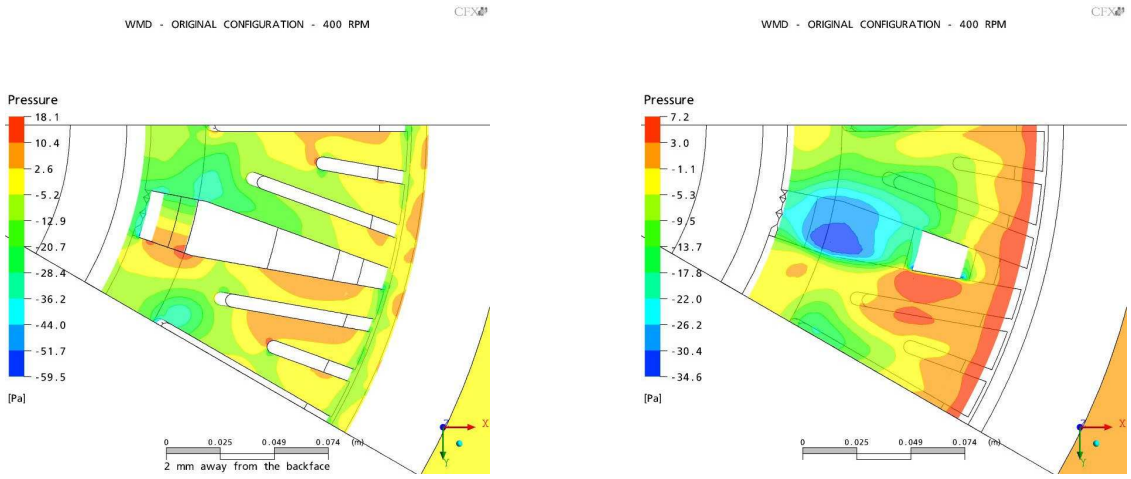

(a) Near wall plane. (b) Gap plane.

Figure 7.11: Static pressure contours on two postprocessing planes at n=400 rpm.

in channel Trail 1 increases from 36.8 to 50.2^{o}C, 8^{o}C less. The rest of the air near the backface remains from 30.2 to 36.8^{o}C. Regions of coolest air temperature near the backface are correlated to high relative air speed, except two isolated cool regions near the shorter channels which do not follow this assumption.

Eddy viscosity and turbulent kinetic energy in the near wall plane are shown in Figure 7.13 for n=400rpm. The first represents the increase in momentum transfer due to turbulence, while the turbulent kinetic energy gives an indication of the mean fluctuation of velocity, therefore they are linked since velocity fluctuations give way to artificial increment in viscosity (eddy or turbulent viscosity) and momentum. It is evident that the highest activity are near to geometry discontinuities found in the flow path. Eddy viscosity and turbulent kinetic energy decrease where the fluid does not have direct interaction with the geometry. This happens in the gap existing between the tip of the vanes and the wheel web surface. In this region only the finger extension and the raised section of the thick vanes have a direct influence on turbulence, see Figure 7.14. Most of the high eddy viscosity regions are linked to high convection heat transfer coefficients rates as it is evident in Figures 7.15 and 7.16. Another region of high heat transfer coefficient is the thick vane surface and its connecting neck to the flange . Low heat transfer coefficients are observed in the channel Trail1 (*behind* the thick vane) and on the sides of the second longest vane, one of these coinciding with a recirculation zone. However, the recirculation behind the thick vane coincides with high eddy viscosity, turbulent kinetic energy and significant heat transfer coefficient.

Average convective heat transfer and cooling rates follow a linear relationship with angular

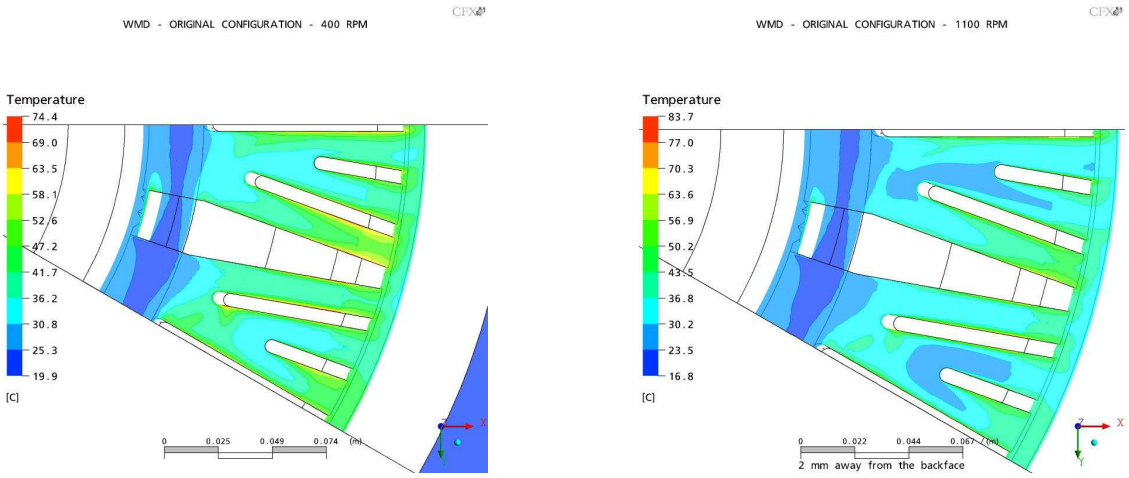

(a) n=400 rpm. (b) n=1100 rpm.

Figure 7.12: Air temperature contours near the disc backface.

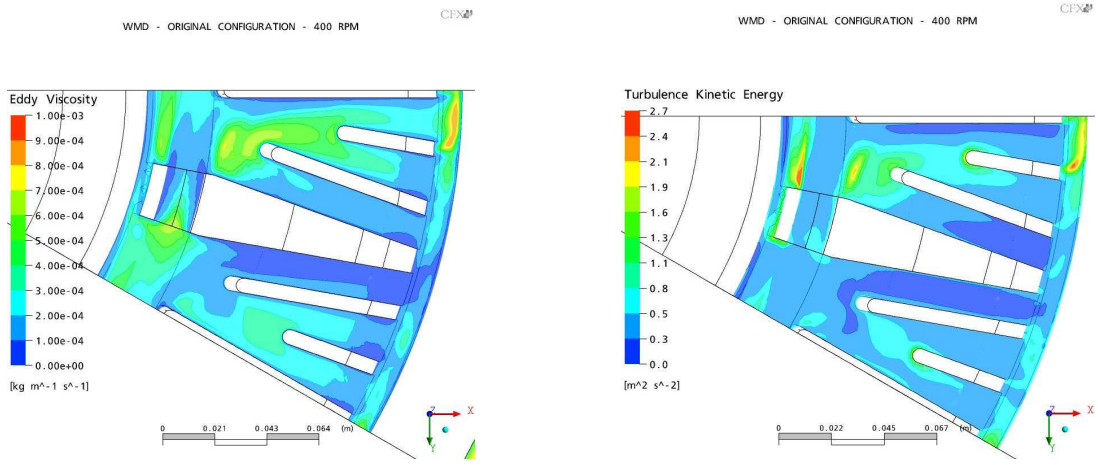

(a) Eddy viscosity. (b) Turbulent kinetic energy.

Figure 7.13: Air turbulent behaviour near the disc backface, n=400 rpm.

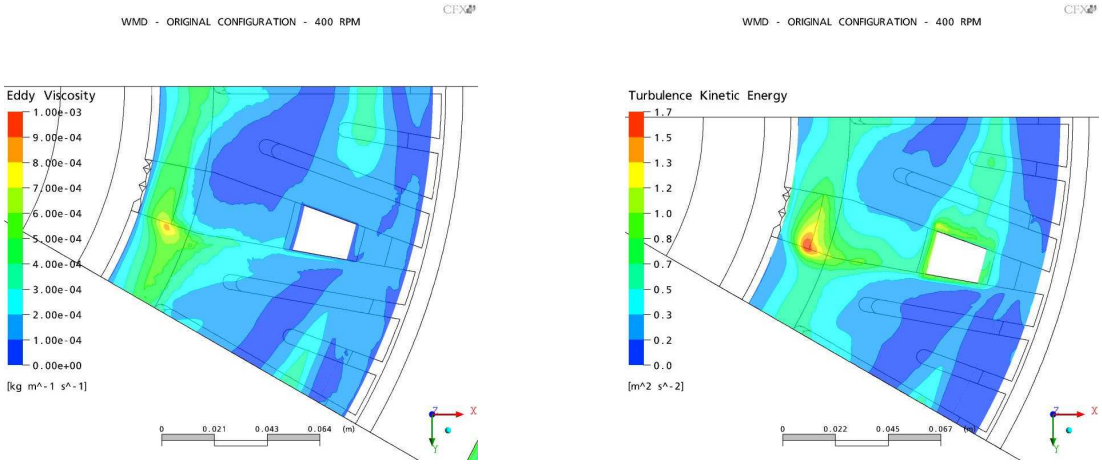

(a) Eddy viscosity. (b) Turbulent kinetic energy.

Figure 7.14: Turbulence in the gap plane between the wheel and the vane tips, n=400 rpm.

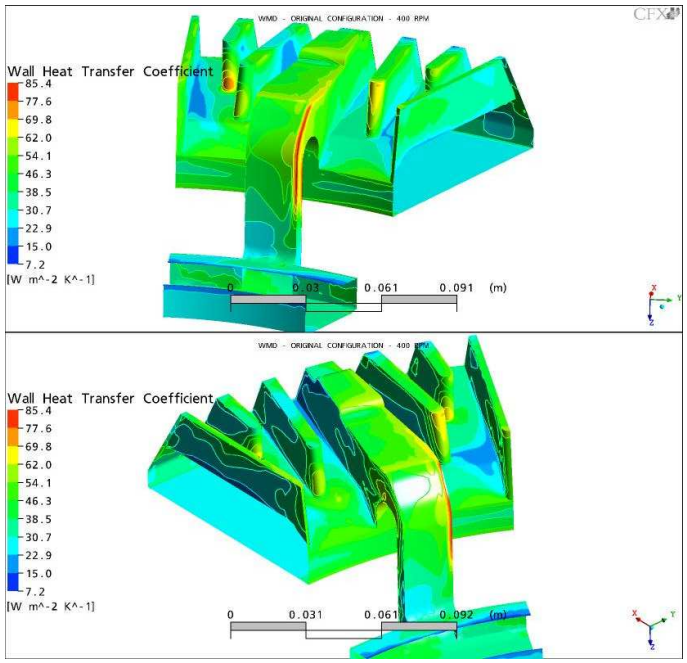

Figure 7.15: Convective heat transfer coefficients on vanes of WMD at n=400 rpm.

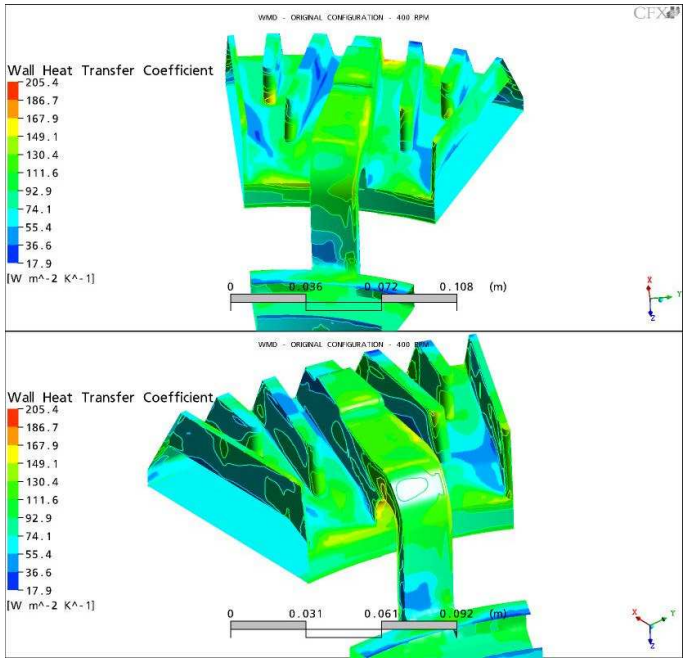

Figure 7.16: Convective heat transfer coefficients on vanes of WMD at n=1000 rpm.

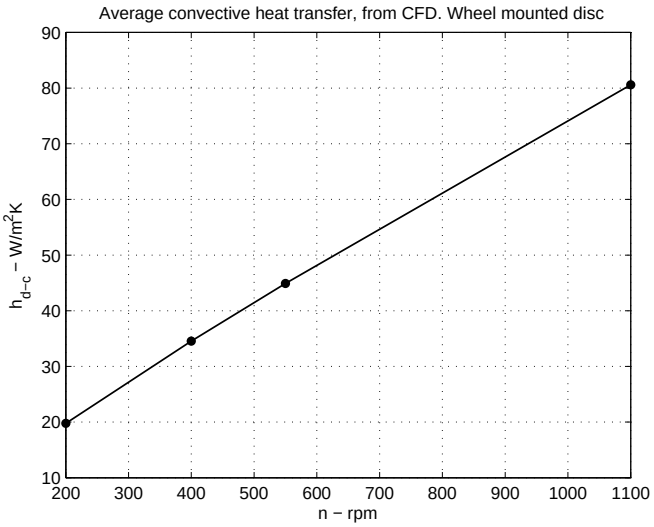

Figure 7.17: Average convective heat transfer coefficient versus rotational speed

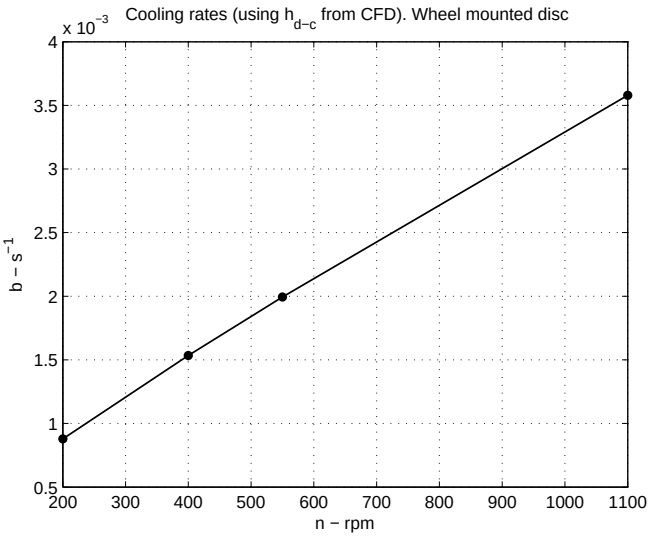

Figure 7.18: Convective cooling rates versus rotational speed

speed for this brake disc (Figures 7.17 and 7.18). Average Nusselt numbers were calculated and compared against those predicted for a rotating disc in turbulent flow, equation 5.7. Dorfman's (1963) equation underpredicts the Nusselt number by 25% and 37% at 200 and 1100 rpm. This difference is due to the influence of the vanes. The correlation that fits the Nusselt number behavior is obtained by modifying the exponent in the equation from 0.8 to 0.822 as described in equation 7.2.

$$Nu_d = 0.0151 Re_{\omega}^{0.822} \tag{7.2}$$

7.4 Wheel Mounted Brake Disc: Improvements in the Design

In this Section an investigation on the response of the convective heat transfer performance is carried out by performing two changes in the original design (referenced as WMD): First, the effect of the gap is analysed by completely closing this. In this case, rather than extending the vanes height up to the wheel web surface, this was brought in contact with their tips (design WMD Gap 0). Although this changes the design statement in regards to conduction area between the wheel and WMD, this will be disregarded and focus was be given only to effects in convection heat transfer and flow pattern. The second design (referenced as WMD1) had a vane layout and number re-design: Keeping the two largest vanes unchanged,

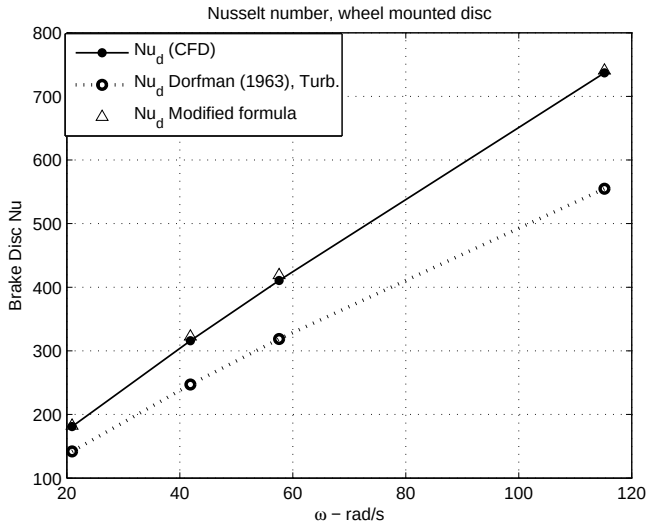

Figure 7.19: Average Nusselt numbers versus rotational speed

three smaller vanes were accommodated between these two vanes and the gap was decreased from the 8 mm to 4 mm. The resulting new disc has larger convection area and it is expected to provide higher interaction with the air in those wide areas existing before. The schematic views of WMD1 is shown in Figure 7.20. The characteristics of the two new discs compared against the original design are summarised in Table 7.3.

Table 7.3: Wheel mounted brake discs characteristics

	WMD	WMD Gap 0	WMD1
A_w [m^2]	0.653	0.619	0.752
m_d [kg]	35	35	36.4
Vanes	72	72	96

7.4.1 CFD Results of Modified Designs

Relative velocity vectors on the near wall plane (WMD Gap 0) are shown in Figure 7.21, two regions of recirculating flow are clearly defined, one appears in the second channel after the trailing side of the thick vane, and the other one on the trailing side of second largest vane. The tridimensional behaviour of these recirculation regions are also shown. These do not occur in circumferential plane only, but the recirculation direction is tilted off the nearwall plane, and there exist a small rate of air mixing as result (vectors shown are all normalised in

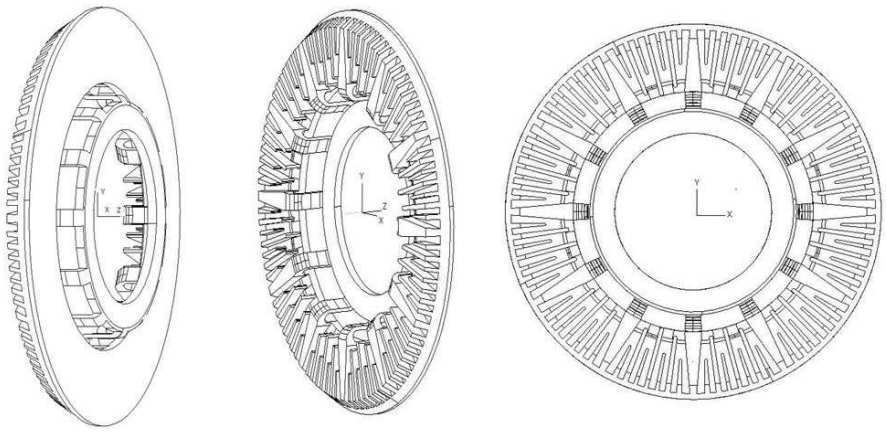

Figure 7.20: Railway wheel mounted brake disc new design.

size). The behaviour of relative velocity on the midplane is observed in Figure 7.22, where it is seen that only one recirculating region remains and it is shifted in downstream direction. On the other side, Figures 7.21 and 7.22 show that the channel on the leading side of the thick vane and trailing side of the second largest vane are those with the largest airspeed. Comparing behaviours from Figures 7.8, 7.21 and 7.22 is noticed that by closing the gap the recirculation regions are decreased in size and moved downstream, and air stream appear to have higher velocities, which can benefit the heat transfer rate from the disc backface. These differences are brought by the reduction in cross section of the channels, since 8 mm have been eliminated from vents cross section.

Another way of qualitatively comparing the effect of the gap in airspeed is by plotting the mean absolute speed values at ten equally distant points over lines shown in Figure 7.6. These lines longitudinally cross the channels at their mid-height and therefore the absolute speed at these lines gives a good idea of their pumping ability. Figure 7.23 shows that the average absolute speed increases in all the channels on the leading side (channels Lead1 to Lead3) when the gap is closed. The most significant increment is in the channel Lead2 (L2 in graph), where absolute speed changes from averages of 2m/s to 5 m/s approximately. On the trailing channels, speed falls in two channels (Trail1 and Trail2, T1 and T2 in the graph), only channel Trail3 is benefited from the gap closing. Therefore, three out of six channels show improvement in airspeed due to gap closing. Air temperature on the near wall plane of the WMD Gap 0 design (Figure 7.24), shows that regions with low relative velocity attain significant temperature, as those appearing in the channel after the trailing side of the thick vane (in the range of 46.9^{o}C to 60.3^{o}C). This is detrimental to heat transfer since low

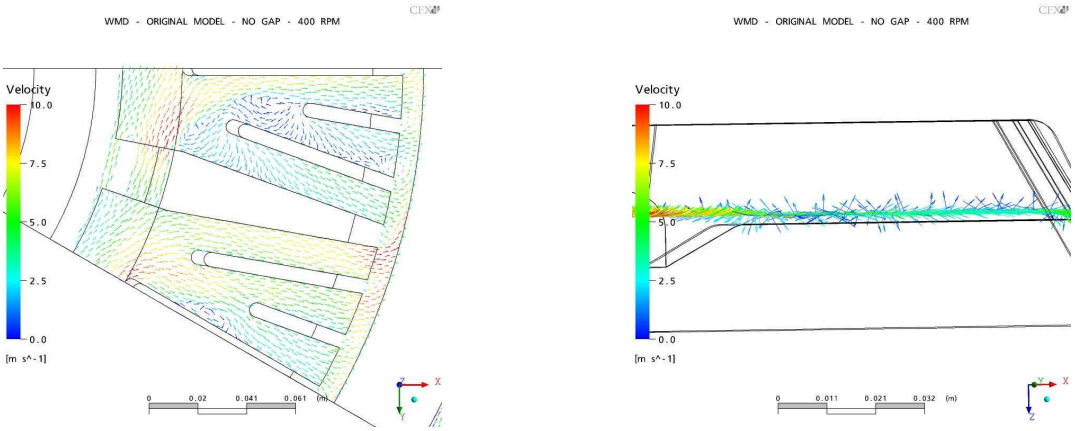

(a) Backface view. (b) Side view.

Figure 7.21: Relative velocity vectors on nearwall plane, WMD Gap 0 at n=400 rpm.

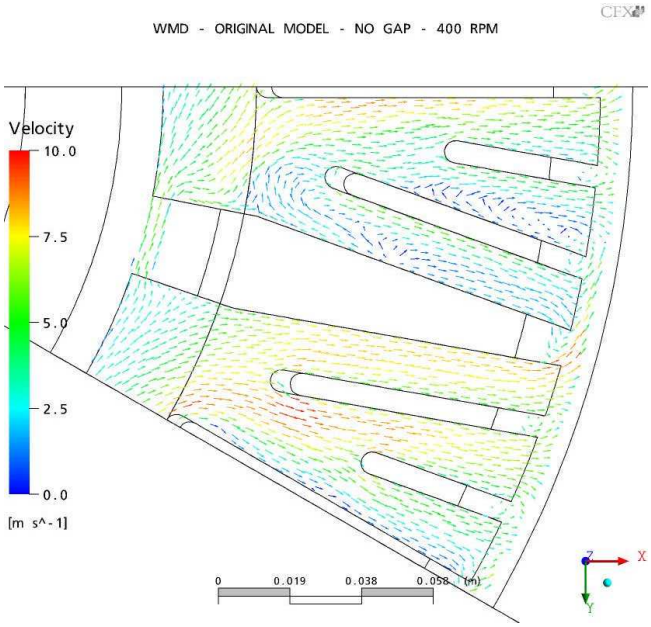

Figure 7.22: Relative velocity vectors in midplane, WMD Gap 0 at 400 rpm.

temperature differences mean poor convection transfer (low temperature gradients). On the other side, the channel on the leading side of the thick vane has the lowest air temperature near the backface, and this promotes convection heat transfer.

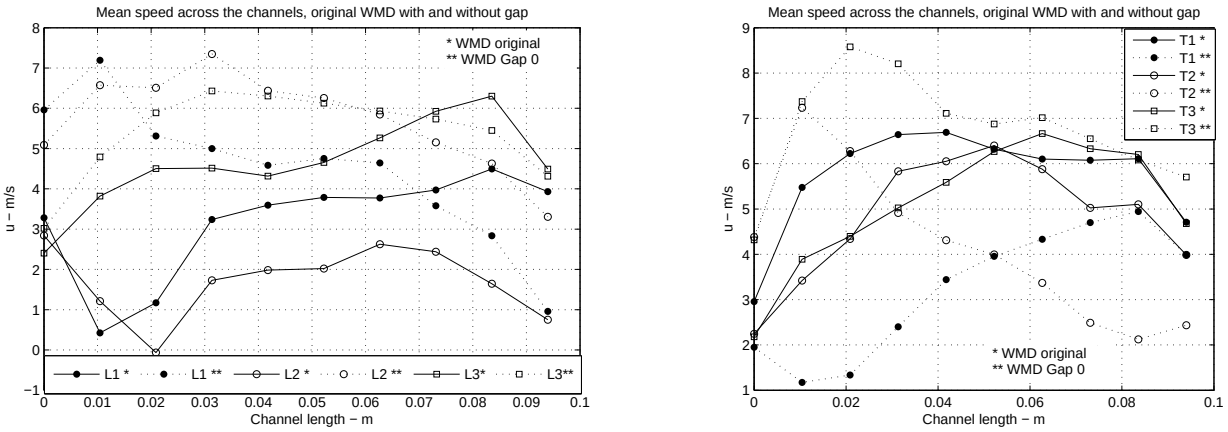

(a) Leading side channels.

(b) Trailing side channels.

Figure 7.23: Absolute speed along channels of WMD and WMD Gap 0 designs, n=400rpm.

Air temperature contours extracted on the mid plane, Figure 7.25, show cooler air near the leading side of the thick vane. On the opposite side channels, air temperature increases significantly. Figure 7.26 shows the contours of heat transfer coefficients on the vaned side of the WMD Gap 0 design. The distribution is uneven, however the leading side of the vanes have improved heat transfer coefficients as results of better interaction with flow stream. The regions with low convection heat transfer are mostly the backface and the channels on the trailing side of the thick vane. High values appearing at the attack edges of the vanes are result of air impingement.

Vectors of relative velocity on the near wall and mid planes of the WMD1 design are shown in Figure 7.27. On the near wall plane, recirculating flows regions appear at the inlet of three channels and on the trailing side of the thick vane. In general, at this plane level, flow recirculation appear in the trailing sides of the larger vanes. The other channels have streamlined air intake. The recirculation regions are likely result of a combination of the backface surface depression and flow misalignment at the inlet of the channels. When the relative velocity vectors are observed on the midplane, the air flow through the channels is much improved by this vane configuration, since most of the recirculation regions vanish. However, the behaviour is similar to the former discs, in the sense that low speed flow develops within the channels on the trailing side of the thick vane (except the latest), and high speed flow develops in at least two channels on its leading side.

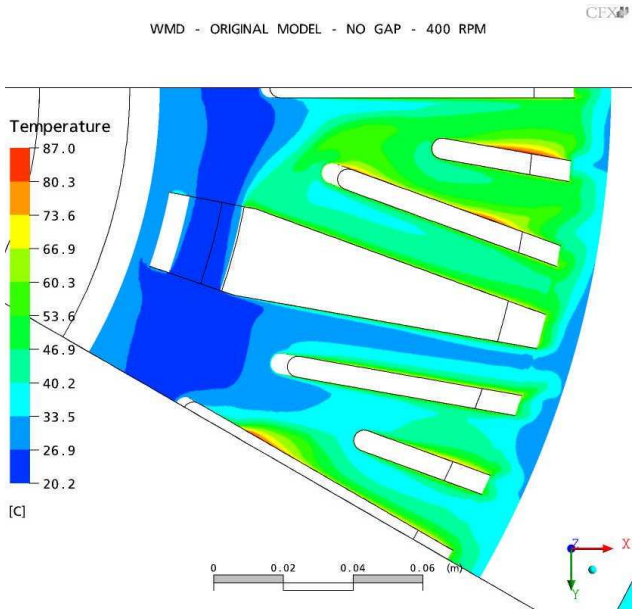

Figure 7.24: Air temperature contours at the near wall plane, WMD Gap 0, n=400 rpm.

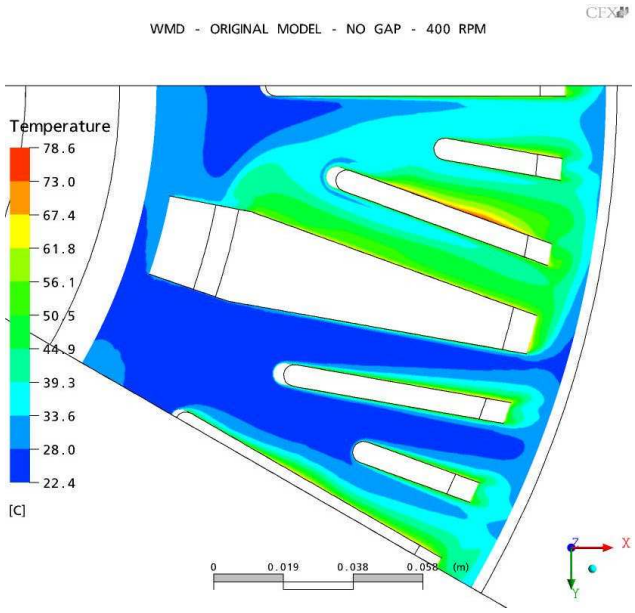

Figure 7.25: Air temperature contours at the midplane, WMD Gap 0, n=400 rpm.

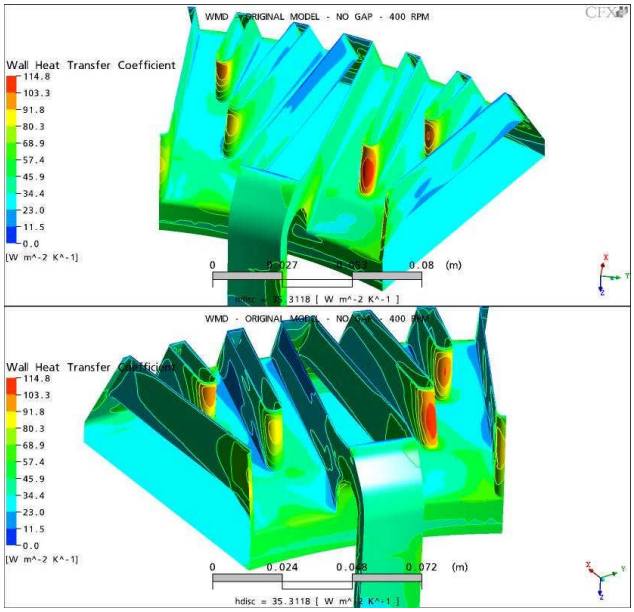

Figure 7.26: Convection heat transfer coefficient contours, WMD Gap 0 at 400 rpm.

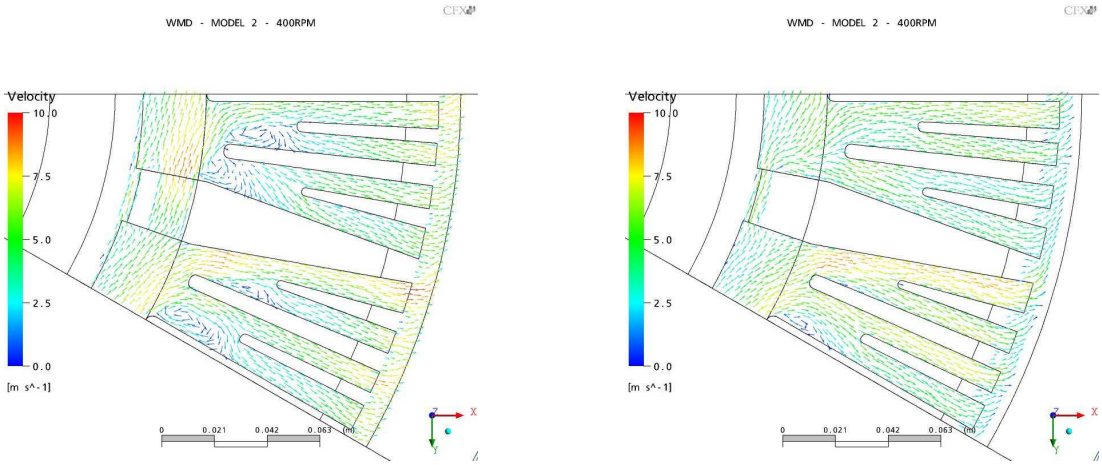

(a) Near wall plane. (b) Mid plane.

Figure 7.27: Relative velocity vectors across the channel of the WMD1 design, n=400 rpm.

The narrowness of the channels improve the air speed across them, but also gives path to quicker heating of the air stream near the disc backface, since now the vanes wall are closer each other and the temperature profile develops faster. Therefore, most of the air (on the near wall plane) toward the exit of the channels show a significant increment in temperature (from 21.2^{o}C at the inlet to 50.9^{o}C at the outlet). The temperature increase is detrimental for heat transfer by convection since reduces the temperature potential. On the midplane, the air stream is much faster and therefore its ability to carry heat is larger, the air mean temperature is almost 28.6^{o}C, this indicates that the heat transfer from the vanes surface is better on the upper side of the vane (toward the wheel web) than near its root. The above can be observed in Figure 7.28.

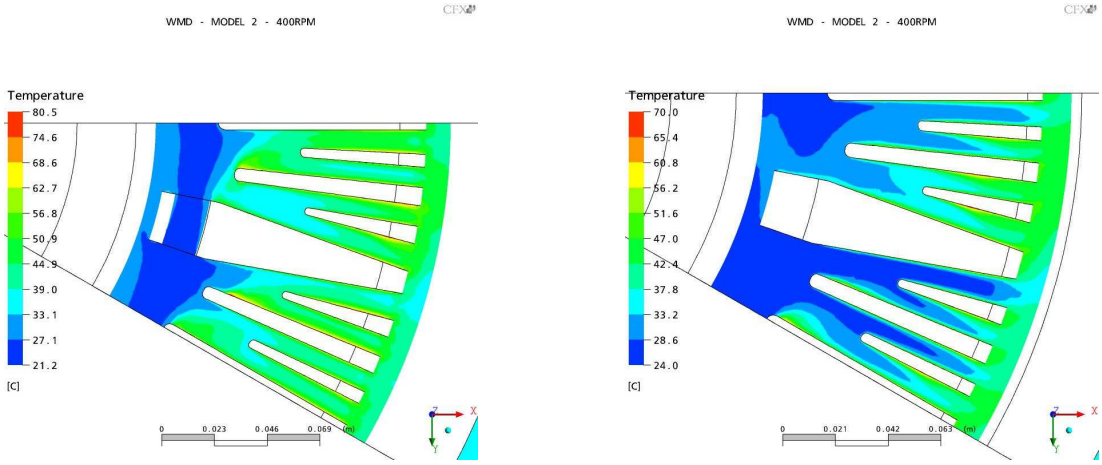

(a) Near wall plane.

(b) Mid plane.

Figure 7.28: Air temperature contours across the channel of the WMD1, n=400 rpm.

Finally, the contours of convective heat transfer coefficient are shown for n=400rpm and n=1100rpm, (Figures 7.29 and 7.30). As pointed out before, higher heat transfer rates by convection are visible in the upper side of the vanes, while the convection heat transfer coefficient drops toward the vanes root. The values of convective heat transfer coefficient on the disc backface are very low, confirming the above described.

The comparison of the performance of average convective heat transfer coefficients per disc as function of rotational speed is shown in Figure 7.31a, where it is seen that little difference exist amongst designs. At n=1100 rpm, the WMD Gap 0 design has 1.25% higher average heat transfer coefficient than the original WMD design. At the same rotational speed, the WMD1 (with a gap of 4 mm) has 3.6% lower average heat transfer coefficient than the original design. However, when cooling rates are compared (Figure 7.31b), the influence of the convection area of the discs becomes significant, and the WMD1 design has 6.8% higher

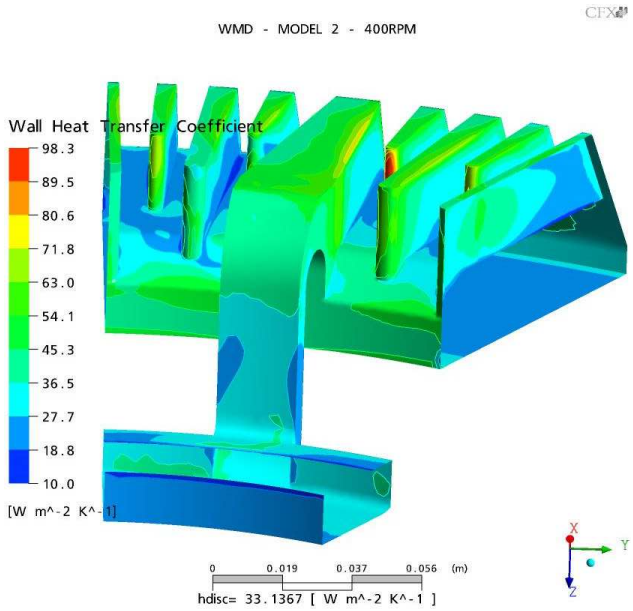

Figure 7.29: Convective heat transfer coefficients, WMD1 design, n=400 rpm.

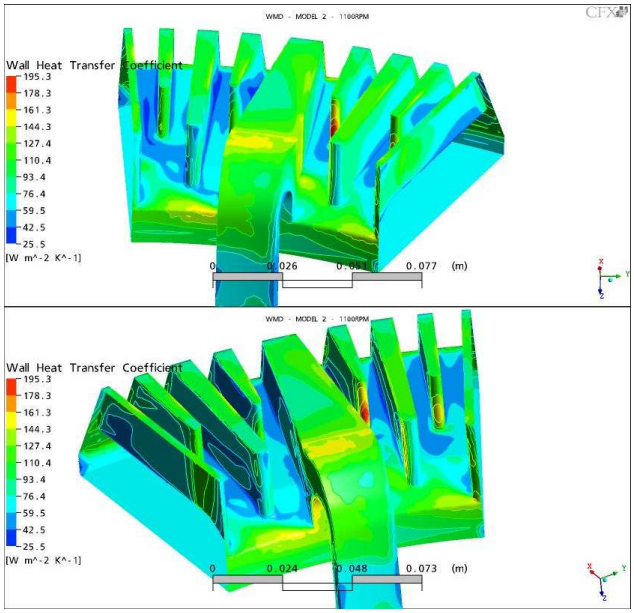

Figure 7.30: Convective heat transfer coefficient contours, WMD1 design, n=1100 rpm.

cooling rate than the original design, at 1100 rpm. At the same speed the WMD Gap 0 design has 3.3% less coling rate than the original design. This indicate that the optimisation of such brake disc designs is more driven by convection area and mass optimisation than by aerothermal optimisation, since little differences are observed in absolute heat transfer coefficient, but larger differences are obtained in cooling rates.

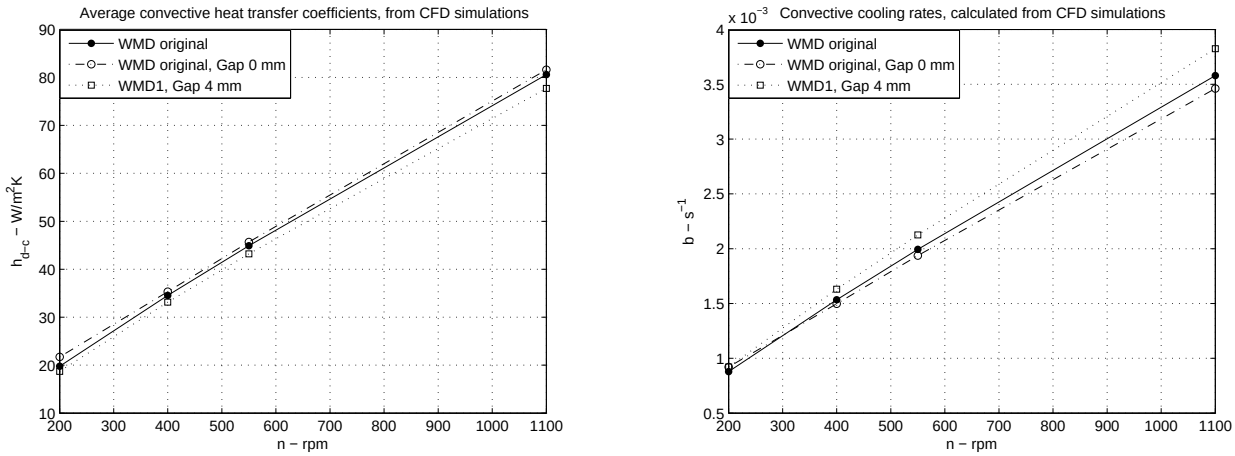

(a) $\overline{h_{d_c}}$ vs n.

(b) b vs n

Figure 7.31: Convective heat transfer coefficients and cooling rates.

Chapter 8

Ventilation System Optimisation

Further insight of convective heat dissipation in brake disc channels concerns to this Chapter, in which a particular analysis approach was developed aiming to providing design selection (or modification) tools. Graphical envelopes of convective heat transfer behaviour within the passage were produced and used to suggest optimal ventilation designs. Also, duct heat convection theory (developed and entry regions) was used to map and investigate the response of convective heat transfer in brake disc channels.

8.1 Convection in Duct Entry Regions

Most of the correlations for internal fluid and heat transfer behaviour in ducts (e.g. equations 2.22 and 3.68), have been calculated for developed flow in ducts of circular section. Developed flow exist when a generalised behaviour of speed and temperature is observed to be invariant with the duct length. In laminar flow this is characterised by well known velocity or temperature profiles while in turbulent flow average values should be considered for these variables since mean profiles may vary from case to case.

Laminar flow in (non-rotating) circular ducts hydro-dynamically develops when the boundary layers have grown enough to meet each other at the duct center. The flow enters with a uniform profile, but since the boundary layer retards its advance near the walls, the speed at the duct centre must increase in order to keep mass continuity. After this point the speed profile is axisymmetric (equation 8.1), invariant with duct length and dependent only in duct radius [1]. Also the wall friction resistance is constant (equation 8.2), (Kays *et al* 2005).

[1] This means: $u_r = 0$, $\frac{\partial u_x}{\partial x} = 0$, $u_x = f(r)$, duct coordinates, (Kays *et al* 2005)

$$u_x = 2U_\infty \left[1 - \left(\frac{r}{R_{duct}}\right)\right] \tag{8.1}$$

$$c_f = \frac{16}{Re_D} \tag{8.2}$$

Hydrodynamic developed conditions exist at a x_l duct length. Then, once known the mass flow a mean speed and Re_D can be calculated to predict the position of x_l for an specific duct geometry.

$$x_l \approx \frac{Re_D D}{20} \tag{8.3}$$

Correspondingly, when a temperature difference exist between the duct wall and fluid, convective heat transfer occurs and the flow is thermally developed when the fluid temperature profile is invariant with duct length and only dependent on its radius. Under this theoretical conditions equation 8.4 is met and therefore the heat transfer coefficient is invariant[2],(Kays *et al* 2005).

$$\frac{q_c/k}{q_c/h_c} = \frac{h_c}{k} = const \tag{8.4}$$

The duct Nusselt number, defined as in equation 5.5 (with D and h_c substituting D_h and h_{ch} respectively), takes a limiting value when wall Constant Surface Temperature and thermal and hydrodynamic developed conditions exist, Nu_{CST}=3.657; when the duct has rectangular cross section, then the ratio of its horizontal and vertical dimensions (P_{cr}/h) plays a role in determining its limiting Nusselt number as seen in Table 8.1.

Table 8.1: Limiting Nusselt numbers in ducts of rectangular shape, (Kays *et al* 2005).

P_{cr}/h	Nu_{CST}	P_{cr}/h	Nu_{CST}
1	2.98	3	3.96
1.43	3.08	4	4.44
2	3.39	8	5.6

The behaviour of convective heat transfer and hydrodynamic variables in the entry length, before the developed state has been reached is variable due to the boundary layer growth toward its maximum thickness. Nusselt number in the entry region may depend on the

[2]This is complex of confirm experimentally.

type of the inlet geometry as shown by Kays *et al* (2005). Theoretical local, mean Nusselt numbers, and mean fluid temperature in the laminar thermal entry region of circular ducts with *hydrodynamically* developed flow have been analytically solved in Kays *et al* (2005) and Bejan (2004) as infinite series. The resulting data are in Table 8.2 where $x^+ = \frac{2(x/D)}{Re_D Pr}$. From this information it can be seen that the series converges to an asymptotic Nusselt number when $x^+ \geq 0.1$, then this is the value of the thermal entry in circular ducts (in x^+ coordinates, see Figure 8.3). Therefore, the laminar thermal entry length for hydrdynamically developed flow is given as mentioned in Kays *et al* (2005) and Bejan (2004):

$$\frac{x_l^{\Theta}}{D} \approx 0.05 Re_D Pr \tag{8.5}$$

Table 8.2: Nusselt numbers in the thermal entry length and hydrodynamic developed conditions, circular duct, CST. From (Kays *et al.* 2005).

x^+	$Nu_{x_{CST}}$	$Nu_{m_{CST}}$
0	∞	∞
0.001	12.80	19.29
0.004	8.03	12.09
0.01	6.00	8.92
0.04	4.17	5.81
0.08	3.77	4.86
0.1	3.71	4.64
0.2	3.66	4.15
∞	3.66	3.66

Comparing between relations 8.3 and 8.5 it is evident that the only difference between them is the Prandtl number in the second one, which means that for the same diameter, laminar conditions and for Prandtl numbers below one, the thermal boundary layers grow faster than the hydrodynamic boundary layers. The corresponding data for ducts of rectangular section is given in Table 8.3. In this case:

$$x^+ = \frac{2(x/D_h)}{Re_D Pr} \tag{8.6}$$

Numerical solutions for convective heat transfer in conditions of hydrodynamic and thermal non-developed flow (entry length) are reported in Kays *et al* (2005) for circular ducts with constant surface temperature. The local Nusselt number ($Nu_{x_{CST}}$) for Pr=0.7 are in Table 8.4. Further information for Pr=2, Pr=5, can be found in the above reference. Comparing

Table 8.3: Nusselt numbers for thermal entry length and hydrodynamic developed conditions, rectangular duct under CST. From (Kays *et al* 2005).

x^+	$Nu_{x_{CST}}$				
	$\frac{P_{cr}}{h}$				
	1	2	4	6	∞
0	∞	∞	∞	∞	∞
0.01	4.55	5.72	6.57	7.02	8.52
0.02	4.12	4.72	5.55	6.07	7.75
0.05	3.46	3.85	4.87	5.48	7.55
0.1	3.1	3.54	4.65	5.34	7.55
0.2	2.99	3.43	4.53	5.24	7.55
∞	2.98	3.39	4.51	5.22	7.55

Table 8.4: Nusselt numbers for combined thermal and hydrodynamic entry lengths, circular duct under CST and Pr=0.7. From (Kays *et al.* 2005).

x^+	$Nu_{x_{CST}}$	$Nu_{m_{CST}}$
0.001	16.80	30.6
0.002	12.60	22.1
0.004	9.60	16.7
0.006	8.25	14.1
0.01	6.80	11.3
0.02	5.30	8.7
0.05	4.20	6.1
∞	3.66	3.66

data between Tables 8.2 and 8.4 is evident the effect of considering thermal and hydrodynamic entries, since the initial Nusselt numbers are around 23% different. However, judging from the information given by Kays *et al* (2005), it would seem that combined hydrodynamic and thermal entry lengths analysis brings earlier the location of thermal development. Information for ducts with annulus cross section or for wall constant heat flux is also reported in Kays *et al* (2005).

The theoretical relations predicting the above Nusselt numbers in ducts are usually infinite series which satisfy the conditions of the energy equation for duct convection heat transfer with developing flow[3]. These are valid for Re_D >400 and Pr >0.1, otherwise they incur into

[3]BC's are different between thermal entry length with hydrodynamic developed flow against combined

non-physical errors (Kays *et al* 2005). However their disadvantage is its low practical use for deducing thermal behaviour, due to the calculation of infinite series for each dimensionless coordinate x^+ where the local or mean Nusselt number is required.

A more approachable solution is given in Kilic's (2004) work on thermal entry length analysis for circular ducts with laminar flow. It has been assumed in this research that Kilic's (2004) results are for thermal entry length in which developed flow occurs from the inlet of the duct, since this is not explicitly confirmed in its report otherwise than by the usage of a mean flow stream velocity. Using *log mean temperature difference* analysis Kreith & Bohn (2001) for energy exchanged from a duct wall to a fluid with different temperature, Kilic (2004) arrives to a relation between the mean fluid temperature and mean Nusselt number in the entry region of the following form:

$$\Theta_m(x^+) = e^{-2Nu_m x^+} \tag{8.7}$$

The expression for Θ_m is assumed in his work as having the form:

$$\Theta_m(x^+) = exp\left[-(f_1 - 2f_2x^+)e^{-f_1} - 2f_2x^+\right] \tag{8.8}$$

Therefore, substituting and solving for Nu_m, a useful expression for the Nusselt number in the entry region of a circular duct results as follows:

$$Nu = \frac{(f_1 - 2f_2x^+)e^{-f_1} + 2f_2x^+}{2x^+} \tag{8.9}$$

Where the functions f_1 and f_2 depend upon x^+ and on experimental constants:

$$f_1 = Ax^{+^{2/3}} + Bx^{+^{5/3}} \tag{8.10}$$

$$f_2 = Nu_\infty + Ce^{-x^+} \tag{8.11}$$

The above Nusselt and mean temperature equations (8.8 and 8.9) work for the two usually considered boundary conditions on the duct wall, provided the appropriate constants are fitted. For Constant Surface Temperature these are provided in Table 8.5 (with Nu_∞=3.66 as per Table 8.4), while those for Constant Heat Flux are available in Kilic (2004). Although the fluid dynamics and local convective heat transfer within rotating channels is different

thermal and hydrodynamic lengths, being the last one the most complex to solve, see (Kays *et al* 2005) or (Bejan 2004)

Table 8.5: Constants for the Nusselt number in the thermal entry length of circular ducts with Constant Surface Temperature. From (Kilic 2004).

	A	B	C
Θ_m	4.04	24.0	0.32
Nu_m			
Nu_x	2.659	6.6	0.08

from that occurring in stationary channels with laminar through-flow, the above information has been selected as theoretical framework for channel Nu analysis aiming to assess:

- The validity of assuming Nusselt numbers for fully developed (thermal and hydrodynamic) conditions for vents of rotating ventilated brake discs.
- The feasibility of using equation 8.9 for predicting heat transfer in channels of ventilated brake discs, or:
- The modifications that should be accomplished in equation 8.9 to mimic the heat transfer coefficient (Nusselt number) found in rotating channels and the angular speed range in which similitudes exist.

8.1.1 Flow Development in Rotating Brake Disc Channels

Solving equations 8.3 and 8.5 for x_l and x_l^{Θ} and using data for brake discs with radial channels revised in Chapter 6 (Table 6.3 and Figure 6.80), required lengths for developed flow conditions are calculated. Results in Tables 8.6 and 8.7 show that all the required lengths are longer than the actual channel length (95 mm), even at the lowest brake rotational speed (100 rpm). The meaning of this analysis is that if effects if rotation in air are disregarded and this is assumed as flow in stationary channels, the physical conditions to get invariant speed and temperature patterns are not met.

Therefore, air temperature patterns observed in plots in Chapter 6 can result from entry length (variable) or semi-constant thermal gradients in the channel wall, but they are not condition to consider flow thermal development unless a rigorous analysis of wall thermal gradients and differences between the wall temperature and the air mean temperature is carried out in order to determine the heat transfer coefficients stability. An analysis of this kind has not been done in this research but a new empirical approach to channel mean heat transfer coefficient is suggested in Section 8.6 on the basis of the theoretical work revised so far.

Table 8.6: Required length in metres for hydrodynamically developed flow (x_l) in brake disc channels as function of angular speed.

n, rpm	20 vanes	30 vanes	45 vanes	60 vanes	90 vanes
100	0.6	0.9	0.6	0.7	0.3
200	1.5	1.9	1.2	1.5	0.5
400	2.8	3.7	2.5	3.1	1.2
600	4.3	5.5	3.7	4.5	1.8
800	5.9	7.3	4.9	6.0	2.5

Table 8.7: Required length in metres for thermally developed flow (x_l^{Θ}) in brake disc channels as function of angular speed.

n, rpm	20 vanes	30 vanes	45 vanes	60 vanes	90 vanes
100	0.5	0.7	0.4	0.5	0.2
200	1.0	1.3	0.9	1.1	0.4
400	2.0	2.6	1.8	2.2	0.8
600	3.0	3.9	2.6	3.2	1.3
800	4.1	5.1	3.5	4.2	1.7

8.2 Flow Index and Convection Analysis of Brake Disc Passages

A quality index was created to understand easier the performance of heat transfer coefficient (or radial speed) as these proceed through the channel. The *Flow Index* has a twofold purpose, to serve as *quality index* and as *design tool* for the early evaluation of vent heat transfer performance.

8.2.1 Flow Index Definition

As a definition, the Flow Index (FI) of the brake disc channel is a characteristic dimensionless number that describes the mean behaviour of a flow variable within the passage as this pass by it. The FI has been conveniently defined as the ratio of a flow variable ϕ values at two locations along the vent length at a specific brake disc angular speed.

$$FI_n = \frac{\phi_n}{\phi_i} \tag{8.12}$$

The locations for the variable ϕ can be arbitrary selected, however for brake disc ventilation geometry optimisation purposes, FI should be referred to ϕ_i value at the inlet of the *baseline* vent geometry. Then, several $FI's$ can be extracted from this channel at prescribed radial locations. The procedure can be repeated for other channel geometries keeping ϕ_i constant for all calculations (if instead ϕ_i is taken from each design, then FI will refer to that design independently of others).

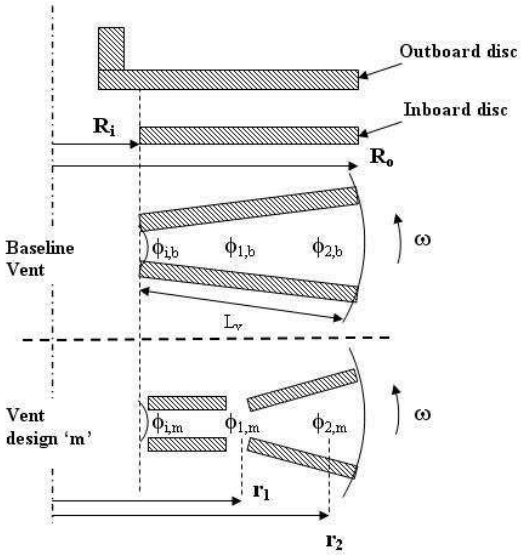

Figure 8.1: Passage Flow Index characterisation.

Figure 8.1 shows schematically the calculation of FI for two brake disc channel geometries, one of which represents the baseline geometry (b) and the other the modified (m) channel geometry. In this case FI can be calculated at three locations: at the inlet and at two radial coordinates defined by radii r_1 and r_2. Then, the FI trend for the baseline geometry is given by $FI_{k,b} = \frac{\phi_{k,b}}{\phi_{i,b}}$ with k as subindex for radial positions. The FI for the modified geometry is therefore given as $FI_{k,m} = \frac{\phi_{k,m}}{\phi_{i,b}}$. Note that $\phi_{i,b}$ remains as a performance datum level.

Upon comparing both FI trends ($FI_{k,b}$ against $FI_{k,m}$) a difference may result as a consequence of the geometry performance, however they both are normalised to only one variable and therefore the trends can be referenced each other, giving a practical way of measure the performance of ϕ along the channel.

8.2.2 Channel Geometry Characterisation

For the purpose of describing the change of FI linked to passage geometry variation, and at the same time having the channel basic characteristics under one frame of study, two channel geometric relations have been obtained from most of the brake disc designs analysed in this research. These are:

1. *Vane pitch ratio*, $\frac{P_{cr}}{R_i}$, is the ratio of the circumferential pitch between vane walls divided by the radius of the innermost vane attack edge.
2. *Channel taper rate*, (TR) equals to local channel circumferential width divided by its width at the inlet minus one. The result is a measure of the channel width increment (positive) or reduction (when negative) from its inlet value.

Figure 8.2 shows a schematic representation of the dimensions involved in the calculation of the above geometric parameters. Also, since equation 8.9 was used at a second stage of this analysis, the dimensionless channel coordinate x^+ was reformulated using the expression:

$$x^+_{rot} = \frac{2r_{loc}/D_{h_{loc}}}{Re_{D_{loc}}Pr} \tag{8.13}$$

Note the difference in the new definition of x^+_{rot} used in this thesis, since now it accounts for the radius corresponding to the channel location where its value is sought, and not just the *local channel* radial length (see Figure 8.3). The above geometry relations are expected to be used as means of comparison between different vent geometries and they could be used for scaling purposes. Having defined these parameters, useful plots can be constructed with the variables selected for ϕ, referencing this to $\frac{P_{cr}}{R_i}$.

8.3 Variables for Flow Index

The Flow Index concept is used in this and the next Sections primarily to investigate the behaviour of the heat transfer coefficient (h_c) through the channels and the flow absolute mean speed (in the core of the stream and in radial direction, u_r). The two Flow Indexes are calculated substituting h_c, u_r in equation 8.12:

$$FI_{k,b}h_c = \frac{h_{c_{k,b}}}{h_{c_{i,b}}} \quad \rightarrow \quad \text{Baseline trend, } h_c \tag{8.14}$$

$$FI_{k,m}h_c = \frac{h_{c_{k,m}}}{h_{c_{i,b}}} \quad \rightarrow \quad \text{Referenced trend, } h_c \tag{8.15}$$

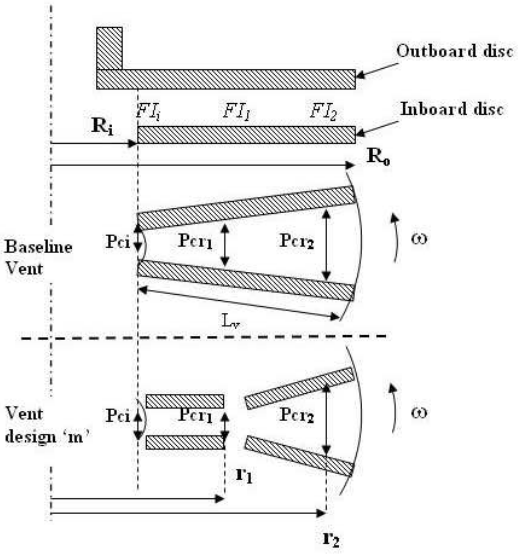

Figure 8.2: Brake disc ventilation geometry characterisation.

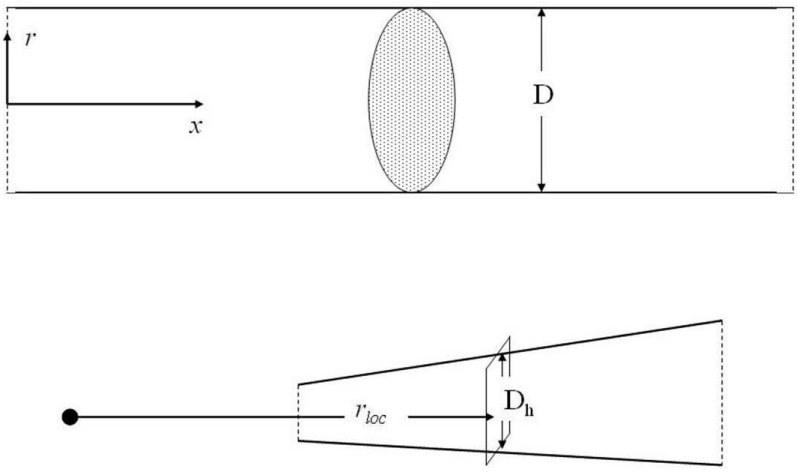

Figure 8.3: Geometry for x^+ (top) and x^+_{rot} (bottom).

$$FI_{k,b}u_r = \frac{u_{r_{k,b}}}{u_{r_{i,b}}} \quad \rightarrow \quad \text{Baseline trend, } u_r \tag{8.16}$$

$$FI_{k,m}u_r = \frac{u_{r_{k,m}}}{u_{r_{i,b}}} \quad \rightarrow \quad \text{Referenced trend, } u_r \tag{8.17}$$

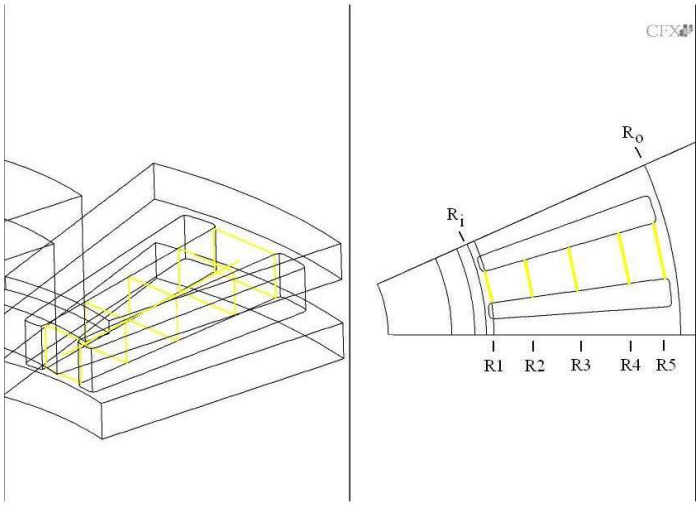

Figure 8.4: Stations where FI was calculated.

Five radial coordinates were selected for the $k-th$ values of $FI's$ along the available channel length (which is $R_o - R_i$=0.101m). These were R1=0.12m, R2=0.141m, R3=0.165m, R4=0.192m and R5=0.211m, shown schematically in Figure 8.4. Therefore, discrete readings of local heat transfer coefficients were taken over the channel walls (vanes and endwalls) at the above specified locations and their arithmetic mean calculated for each radial position. This value was then used to calculate $FI\,h_c$. In the simplest vent geometry (radial channel), 40 h_c samples were taken for each position, ten per wall; therefore to calculate one full $FI\,h_c$ trend (composed by 5 radial points), 200 h_c samples were used. In the case of $FI\,u_r$ the procedure was simpler, since only the local values of radial absolute mean speed corresponding to the five radial positions were used. An independent Flow Index ($FI\,hc^*$) per channel was used to isolate its decay rate per channel design using the expression 8.18 and FI values calculated with equation 8.14 *only* per disc.

$$\Delta FI = FI_{R_i} - FI_{R_{i+1}} \tag{8.18}$$

8.3.1 Flow Index in Radial Channels

The $FI\,h_c$ of brake discs with radial channels (Figure 8.5) is plotted for three angular speeds (100, 400 and 800 rpm). Horizontal arrows are aligned with the inlet value and point toward the outlets. The baseline $FI\,h_c$ (solid black lines) correspond to the baseline disc (30 vanes). Any $FI\,h_c$ trend starting above 1 represents an initial improvement on heat transfer coefficient, and any trend decaying less than the others means better retention of heat transfer coefficient in the channel. An analysis of the performance shown in Figure 8.5 follows:

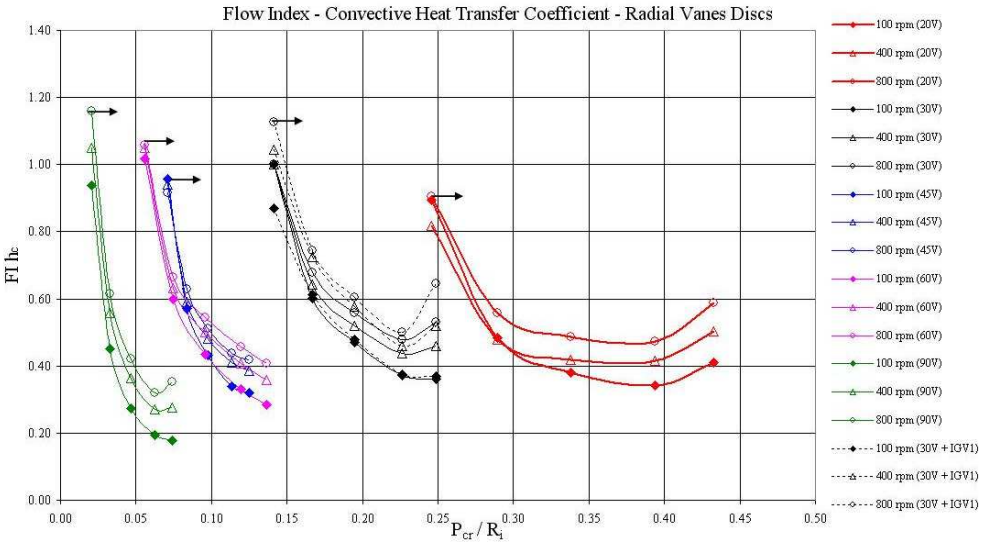

Figure 8.5: Flow Index for radial vents in ventilated brake discs.

1. Channel geometry. Channels with narrow inlet are shifted to the left of the chart and those with wide inlet in the right. The variations of the channel width along the radius may look larger for the disc with 20 vanes than for the others, however this may be a misleading effect of the plot, since the radii are the same for all discs, narrow channels may appear to vary less radially. It is more effective to observe the channels taper ratio (TR), Table 8.8. This shows that TR is the same for 20-, 30- and 45-vane designs has the same channel opening rate, with outlets 1.76 times wider than their inlets; while designs with narrower channels (60 and 90 vanes) have larger opening rate. The 60-vane design has outlets 2.44 times wider than the inlets and the 90-vane design has outlets 3.63 times wider than the inlet.

2. Flow Index. Although the TR for 20-, 30- and 45-vane design is the same, their initial $FI\,h_c$ is different. The baseline $FI\,h_c$ (30 vanes) has higher starting value than the

Table 8.8: Taper ratio (TR) of channels in brake discs with radial vanes.

Layout	TR
20 Vanes	0.76
30 Vanes	
45 Vanes	
60 Vanes	1.44
90 Vanes	2.63

20- and 45-vane designs. However the relative decay of $FI\,h_c$ with channel distance is less for the 20-vane design than for the other two (see also Figure 8.6). The $FI\,h_c$ behaviour for 60- and 90-vane designs is different. The 90-vane gives a very high $FI\,h_c$ at channel inlet but its decay is also the largest. The initial $FI\,h_c$ of the 60-vane design is under that of the 90-vane but is above of designs with 20, 30 and 45 vanes, and its decay is however comparable to these.

3. Inlet Guide Vane. When the IGV1 (see page 207) is added in the baseline channel, its $FI\,h_c$ behaviour depends upon angular speed: At the lowest angular speed the initial $FI\,h_c$ is 13% smaller than the baseline, but it is followed by a quick gain such that it matches the baseline performance later. At 400 and 800 rpm the IGV1 increases the starting $FI\,h_c$ by 4% and 13% (above the baseline) respectively. This gain drops quicker for 400 rpm than for 800 rpm. However, *none of the trapezoidal channel designs holds $FI\,h_c$ enough to avoid a continuous decay.*

4. Variability of $FI\,h_c$ at inlet[4]. The largest variations with angular speed of $FI\,h_c$ at the inlet occur for discs with 20 and 90 vanes, and the 30V+IGV1.

5. Air effects at outlet. A sudden $FI\,h_c$ increment in the channel outlet is observed for the 20-, 30- and 90-vane and IGV1+30V designs. Opposite to this, the $FI\,h_c$ for discs with 45 and 60 vanes show steady drop of $FI\,h_c$ toward the outlet.

6. Summarising, the 60-vane design has the better $FI\,h_c$ behaviour at the inlet, since this is steadily higher than the baseline for all the angular speeds. This means that an optimum channel inlet width is about 5.6% of the channel inlet radius. The 20-vane design, with a channel inlet width of $0.25R_i$ and outlet 1.76 times lager than inlet holds better the value of $FI\,h_c$ in the channel. The addition of a curved IGV improves $FI\,h_c$ only for high angular speeds.

[4]A channel inlet mesh sensitivity analysis was not performed

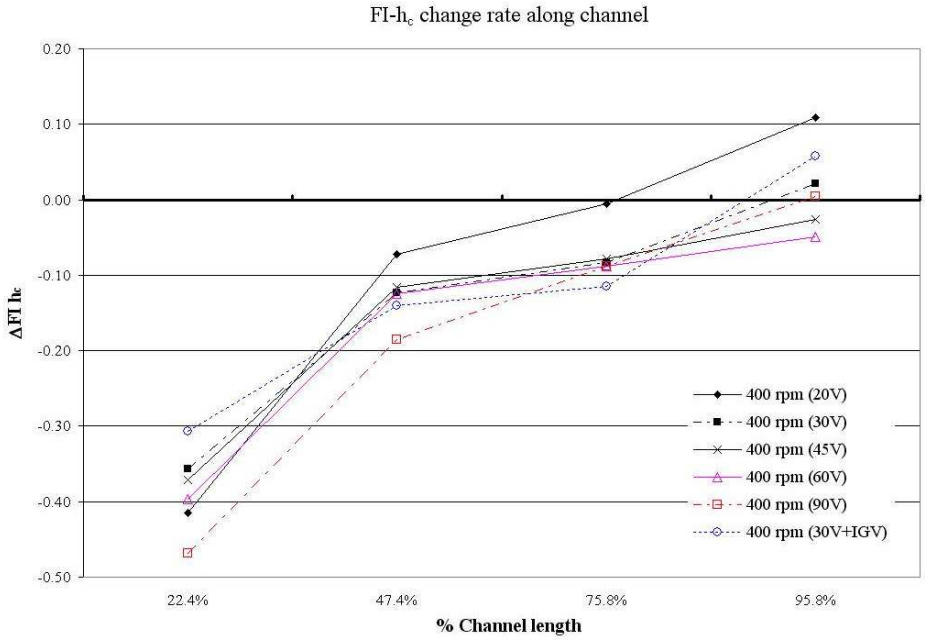

Figure 8.6: Rate of change of $FI\,h_c^*$ for brake discs with radial channels.

Complementing the above, Figure 8.6 shows the rate of change of $FI\,h_c^*$ along the channel (calculated with CFD data). The more negative a ΔFI is, the larger the negative gradient on the Flow Index. ΔFI is shown in four locations since two values are needed to calculate it. The results for ΔFI show that $FI\,h_c^*$ sustains better in the 20-vane design, although after a high initial decay. Interestingly, the 30-, 45- and 60-vane designs give similar h_c decays in the channel. Therefore, similarities in the near wall flow characteristics must exist for these designs. On the other hand, the effect of the curved inlet guide vane (IGV1) on the rate of change of $FI\,h_c^*$ is evident since this design has the smallest initial drop, which means that it provides a high potential level of h_c at the inlet of the channel; however the gradient following and up to one third of the channel is more negative than those from the 30-, 45- and 60-vane designs, which means that the design IGV1+30V does not have capacity to preserve the high potential of heat transfer coefficient in the inlet.

The behaviour of the velocity Flow Index ($FI\,u_r$) is shown in Figure 8.7 where it is seen that:

1. The starting points of $FI\,u_r$ and $FI\,h_c$ for designs with 20 and 45 vanes are very similar [5]. This is not the case for the 60- and 90-vane designs where the starting $FI\,u_r$ is much

[5]The first points of $FI\,u_r$ and $FI\,h_c$ for the 30-vane design must be the same due since this is the baseline reference in both cases

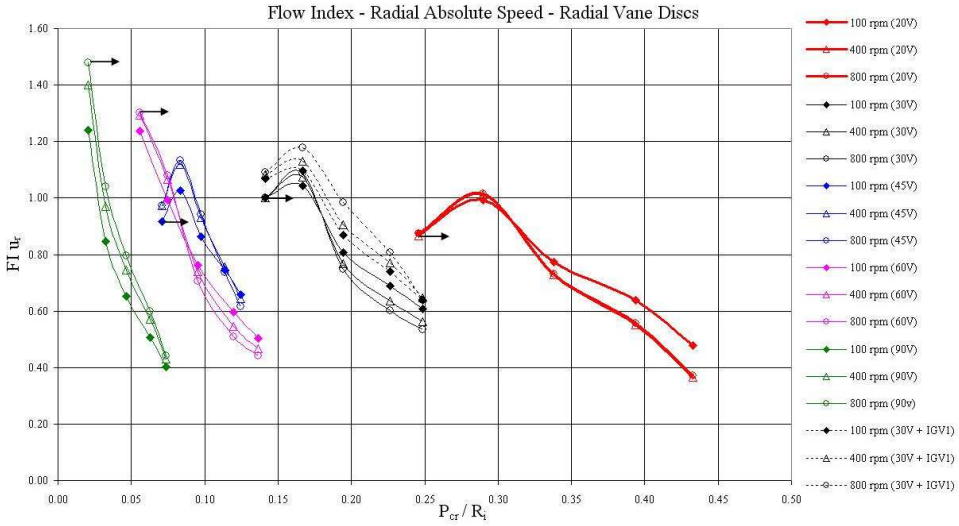

Figure 8.7: Flow Index for absolute radial velocity in brake discs with radial channels.

higher than the corresponding $FI\,h_c$ (e.g.: 1.29 against 1.05 for 60-vane design at 400 rpm).

2. However, what is similar for the 60- and 90-vane designs between $FI\,u_r$ and $FI\,h_c$ is the total decay length, e.g.: 0.70 units for 60-vane design at 400 rpm. The largest $FI\,u_r$ decay of the 45-vane is smaller than that in the 20-vane design (0.48 against 0.65 units. This as expected, a narrow channel promotes high speed. However, the corresponding decays in $FI\,h_c$ are opposite (0.56 against 0.31 units, respectively)[6]. Then, where the energy transport force is brought from for the 20-vane design in order to have better heat transfer coefficient retention in the channel? The answer could possibly reside in the turbulent characteristics of the flow between channels, being locally higher toward the outlet of the channel with 20 vanes than in the 45 vanes design.

8.3.2 Flow Index Analysis of Modified Passages

The $FI\,h_c$ of others designs were also revised (for n=400rpm and 800rpm), all of them were normalised to the baseline $FI\,h_c$ as before. The designs analysed are: SV1-outlet, SV1-middle (page 181) and IGV2+SV1 (page 215). As explained before, values of local heat transfer coefficient were extracted in five stations along the radial direction of the vents (see Figure 8.4). The particular regions of data retrieval are shown in Figure 8.8 for designs with

[6]This does not implies that the average channel heat transfer coefficient in the 20 vanes design is better than in the 45 vanes design, it just means that it drops less

SV1 at middle (a) and at outlet (b) of passage (also used for IGV2+SV1 design).

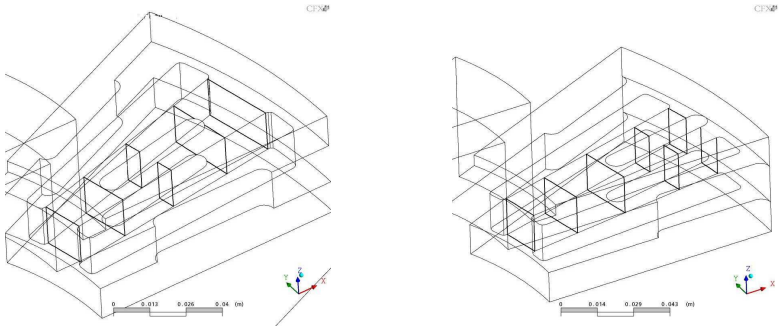

(a) SV1-middle. (b) SV1-outlet.

Figure 8.8: Lines where local h_c was retrieved for $FI\,h_c$.

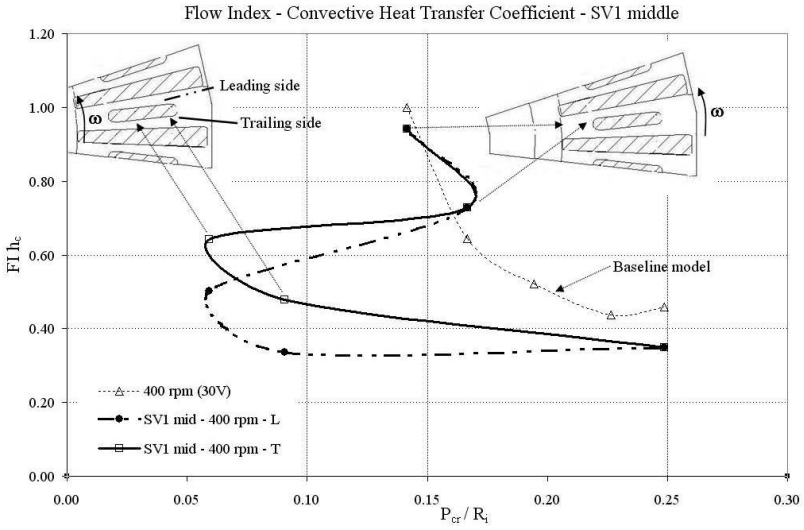

Figure 8.9: Flow Index, $FI\,h_c$, for SV1-middle channel design, n=400rpm.

The trend behaviour of $FI\,h_c$ for the SV1-middle passage design is shown compared versus the baseline trend at n=400rpm in Figure 8.9. Approximate locations of the channel where $FI\,h_c$ corresponds to are shown. The trend shows that the average heat transfer coefficient in the inlet region of the SV1-middle design is 6% below that from the baseline 30-vane design. At $R2$=0.1413m is 10 % higher for the SV1-middle passage design. As of this point, two trends are accounted for the SV1-middle design. The solid line follows $FI\,h_c$ along the trailing side of the vent, while the line-dot curve does the same for the leading side. In the trailing side, $FI\,h_c$ continues higher than the baseline, for 12 and 4% respectively

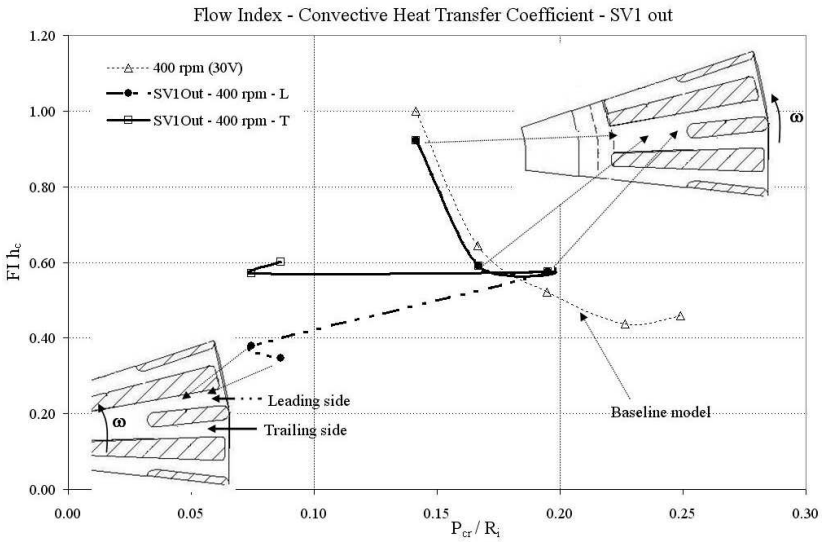

Figure 8.10: $FI\,h_c$ for SV1-outlet channel design at n=400rpm.

(third and fourth points). The corresponding points in the leading side however, are 2 and 10% below the baseline. The final point of the SV1-middle design is under the corresponding baseline by 10% (0.10 FI units) approximately. This means that the convective heat transfer performance of this passage design is only partially better than that given in a simple channel.

The results for the SV1-outlet design at n=400rpm (Figure 8.10) show that the initial magnitude of $FI\,h_c$ is below one by 0.08 $FI\,h_c$ units, and in the second station is still 6% smaller than the corresponding baseline point. However, $FI\,h_c$ for the third location (before the attack edge of the SV1) indicates a positive change in heat transfer coefficient, coming from 0.06 below the baseline 0.06 above it, before the channel partition. Similarly to the behaviour of the SV1-middle design, the $FI\,h_c$ trend depends upon the constricted side. The $FI\,h_c$ in the trailing side of the passage follows a very stable behaviour between stations R3 and R4 (Figure 8.4) and a latter increment of 4% at the exit, this gives $FI\,h_c$ higher than the baseline by 0.13 and 0.14 respectively. Nevertheless, in the leading side, the corresponding $FI\,h_c$ is 0.06 units lower, and the final $FI\,h_c$ is 0.11 units below the baseline. At n=800rpm a relative better behaviour exist, see Figure 8.11. The first two $FI\,h_c$ are smaller than the corresponding in the baseline by the same rate. $FI\,h_c$ at the middle (R3) is again higher than the baseline in the same rate as at $n = 400rpm$. Following the trailing side, the fourth $FI\,h_c$ remains constant however the last one is 0.19 $FI\,h_c$ units higher than the baseline, this is 0.05 units higher than when n=400rpm. These two last points in the leading side are 0.08 and 0.11 units than the baseline trend. It could be said, that the difference in $FI\,h_c$ between these two designs is independent of angular speed.

As for the IGV2+SV1 passage design rotating at n=800rpm, the behaviour of the heat

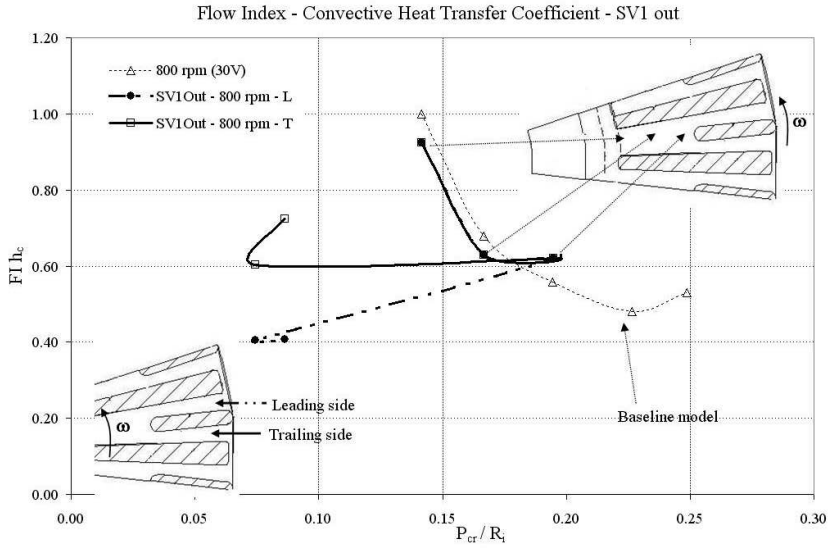

Figure 8.11: $FI\,h_c$ for SV1-outlet channel design at n=800rpm.

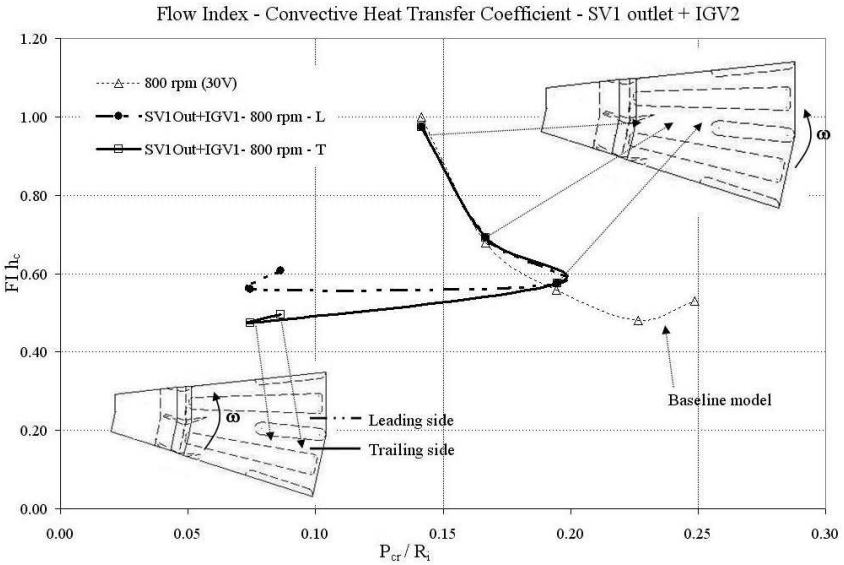

Figure 8.12: $FI\,h_c$ for IGV2+SV1 passage design at n=800rpm.

transfer coefficient Flow Index is the best from the start (Figure 8.12), since it yields a similar potential entry heat transfer coefficient level as in the baseline, and it develops the $FI\,h_c$ to slightly higher figures before entering the channel partition. This is likely due to the swirl and higher inlet speed given by the IGV. Once in the channel partition, due to the curvature of the IGV, the *leading side* has higher $FI\,h_c$ than the trailing side (contrary to other designs). The final two magnitudes of the $FI\,h_c$ in the leading side of the IGV2+SV1 design are 0.56 and 0.61 against 0.48 and 0.53 in the baseline. In the trailing side of the

IGV2+SV1, these are 0.47 and 0.50. This means that this particular configuration enhances $FI\,h_c$ throughout the passage, when compared with the baseline.

From the $FI\,h_c$ behaviour for the two designs discussed at the end, a $FI\,h_c$ characteristic can be raised as function of the ventilation geometry: if the ratio $\frac{P_{cr}}{R_i}$ has magnitudes between 0.07 and 0.10 after the second radial half of the vent, a definite change on the convective heat transfer coefficient behaviour is given. This is observed by noting that the steady falling trend of $FI\,h_c$ in the baseline and in general, in *all* radial channel designs disregarding vane number, changes to a semi-horizontal line just before and along the section where $\frac{P_{cr}}{R_i} = 0.07 \rightarrow 0.10$. Whether the change given in $FI\,h_c$ is positive (above the baseline) or equal to the baseline is seen to depend on the upstream conditions of the airflow (either influenced by an inlet guide vane or by longer vanes toward the inner radius). However, this could be wrongly interpreted as if having a continuously narrow channel would give the best $FI\,h_c$ trend. This is not true, since the air stream would be retarded and core speed degraded with the final consequence of producing steeply decaying $FI\,h_c$ trends, as for example the corresponding to the 90 vanes design in Figure 8.5.

However, is clear that keeping a stable value of heat transfer coefficient, implies narrowing the channel cross section at a certain distance down its inlet. This can be combined with radially dividing the vane length and allocating partial constrictions of cross section along the flow path in order to combine reduction of drag and airflow velocity self-feeding inside the vent. Pursuing this, a new vent layout was conceptualised and modelled. The design is named Staggered Vane Vent and is shown in Figure 8.13. The design is a three-vane layout, all of them radially oriented. The long vane from designs so far was replaced by two vanes aligned one behind the other plus a separate vane lying in between and toward the outer radius. The attack edge of the inner vane locates in the same place where inlet guide vanes have been positioned, this vane reaches half of the available channel length and its surface has been featured with wavy shape in order to promote turbulence in the incoming air. The vane behind this is the SV1 vane and the vane in between is a longer and wider version of the SV1. The position of this intermediate vane radially meets the rear edge of the inner vane and is near the front edge of the SV1, this narrows locally the vent cross section in two places along the flow path. These are expected to *re-build* the air stream velocity at those locations. Finally, except the initial passage, which diverges radially, the partitioned passages do not diverge but keep a constant cross section in the outer half of the disc radius.

CFD simulations were performed with staggered vane design following the same methodology as before. Contour plot results are only shown for heat transfer coefficient distribution and streamlines of relative speed through the vent (disc rotates about $+z$). Figure 8.14 shows the distribution of heat transfer coefficients in the vanes, upper and lower endwalls for a rotational speed of n=400rpm. Peaks (91.7 W/m^{2}K) are in the attack edge of the longer vane, near the outboard endwall. The heat transfer coefficient is also improved in the wavy

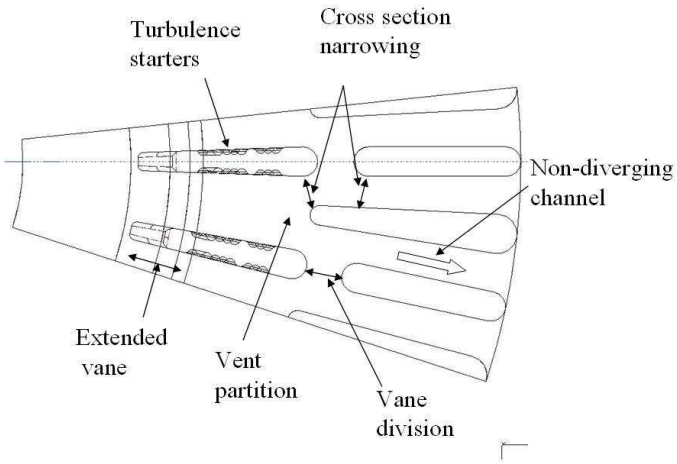

Figure 8.13: Staggered vane design.

wall of the inner vanes, but only in the half oriented toward outboard side (h_c varies from 30 to 75 W/m^{2}K axially). Also the outboard side endwall shows higher and better distributed heat transfer coefficient than the inboard side endwall.

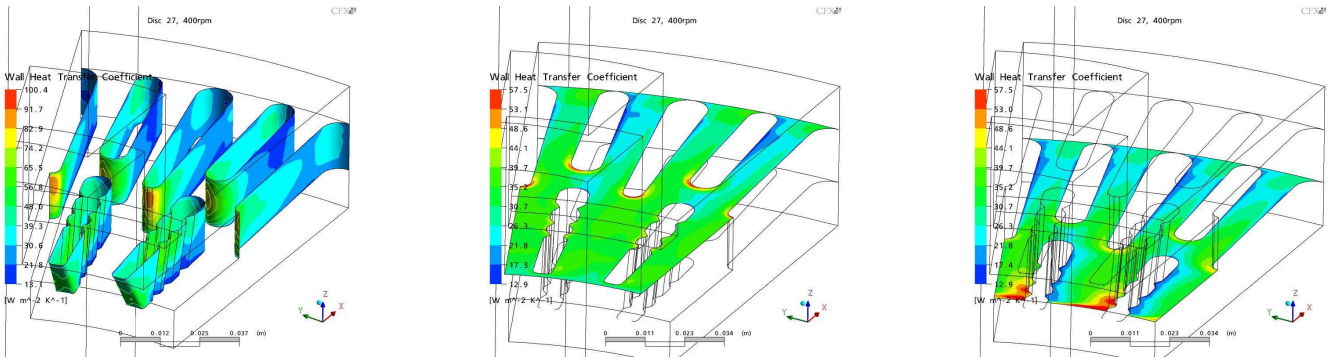

(a) Vanes. (b) Outboard endwall. (c) Inboard endwall.

Figure 8.14: Staggered vane design, heat transfer coefficient distributions, n=400rpm.

The streamlines of relative speed in Figure 8.15 are shown from two perspectives, plot in the left depicts them as seen from the outboard side while streamlines in the right are seen from the opposite side. The effect of the turbulence starters is modest since they do not promote mixing behaviour to a large extend as intended. The instability appearing near to the inboard side endwall occurs in the leading side of the inlet port, therefore it may be due to misalignment between the entry air and innermost vane. Nevertheless, the turbulence

starters seems to propagate the initial flow instability toward the vent partition in the leading side, where this vanishes by effect of vent constriction and vane partition. The air stream in the second half of the vent follows the vent radial direction.

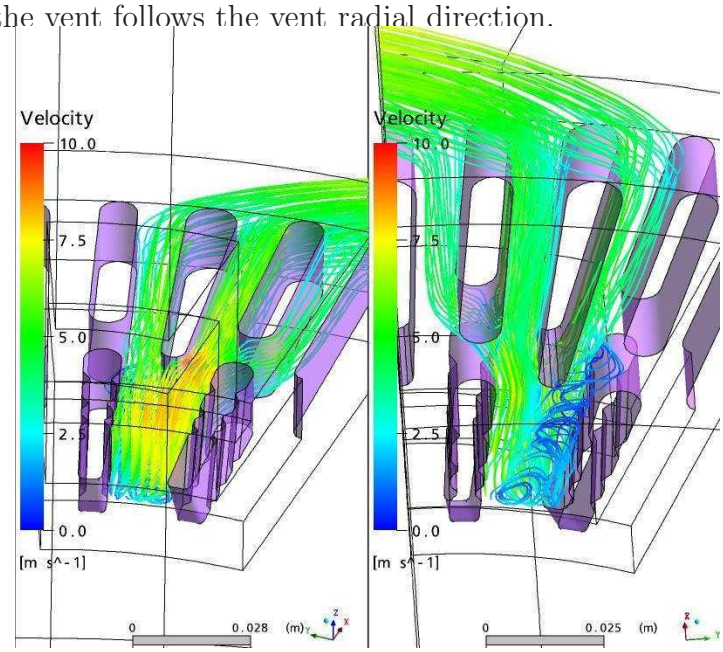

Figure 8.15: Streamlines of relative flow in the staggered vane design at n=400rpm.

Heat transfer coefficients were retrieved from vent walls in locations coinciding with the radii used for $FI\,h_c$ calculations (see Figure 8.16). The convective heat transfer Flow Index calculated for n=400rpm is shown in Figure 8.17. The result is magnitude-wise worse than the baseline model trend, since it starts with $FI\,h_c$=0.58. However, the behaviour along the radius is significantly more stable, since rather than immediately falling, the $FI\,h_c$ increases by 0.01 units in the second point and in the third one, just before the second stage of vanes, it falls to 0.54, which means that the heat transfer coefficient performance looses only 4% from the inlet to the middle of vent radial length (instead of >50% in the baseline). $FI\,h_c$ in the partitioned regions falls and then increases. In the trailing side partition it falls to 0.42 and ends with 0.47. In the leading side channel it falls to 0.38 and raises finally to 0.42. Overall, the largest decay is 0.20 $FI\,h_c$ units, which is the smallest given in any disc revised so far. Therefore the design meets the condition of holding the inlet averaged h_c potential, allowing a small decay of $FI\,h_c$, but it does not provide a competitive $FI\,h_c$ magnitude in the inlet of the vent[7]. Nevertheless, although the initial magnitude of $FI\,h_c$ is 0.42 units below the baseline, the lowest ending $FI\,h_c$ magnitude is just 0.06 below the baseline.

A common behaviour among Figures 8.11, 8.12 and 8.17 is that vent partition (or partial reduction of vent cross section) indicated by $\frac{P_{cr}}{R_i}$ ranging from 0.07 to 0.10, is beneficial for

[7]Scooping air would benefit this

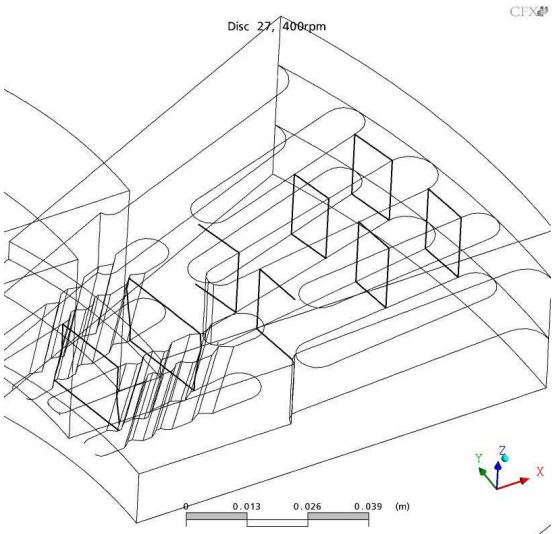

Figure 8.16: Places where h_c was retrieved for $FI\,h_c$ calculations.

the control of the heat transfer coefficient performance in radial direction within the vent. Then, attention must be given to having the highest potential level of $FI\,h_c$ in the inlet and keeping this as much as possible throughout the vent.

From the Flow Index for convective heat transfer coefficient analyses performed above, and with the results obtained in Chapter 6, the following summary concerning convective heat transfer coefficient behaviour in brake disc vents can be drawn:

1. The characteristics of h_c in the inlet of the vent sets the potential level of convection transfer of the full vent. That is, higher h_c near the inlet are likely to promote better vent averaged heat transfer coefficient. An example are the results for brake discs with 60 and 30 vanes in Figure 8.5. The vents of these designs are those having the highest convective performance in Figure 6.23.

2. The convective heat transfer coefficient magnitude in the inlet of the vent is affected by the angle between the vane longitudinal axis (mid-camber) and the core air velocity. Use of inlet swirl promoters such as the IGVs, Section 6.5, or working with the vane incidence angle, as seen later, improve h_c in the inlet region.

3. A concerning behaviour of the heat transfer coefficient through the vent is its deficiency to hold stable magnitudes and its tendency for steeping decays. The method of promoting homogeneity of h_c through the vent drives attention to the local constriction of vent cross section at specific radial locations. This has been revised with the use of the SV1 vane, Section 6.3, and with the staggered vane design, the results indicated that $FI\,h_c$ responds to changes in $\frac{P_{cr}}{R_i}$ in the vent.

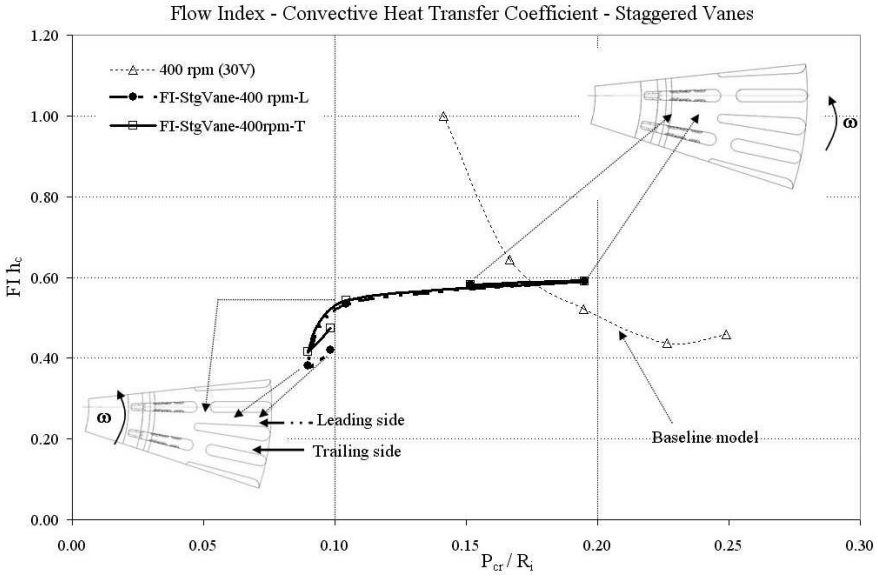

Figure 8.17: $FI\,h_c$ of the staggered vane design, n=400rpm.

4. It has been also seen that purely geometric characteristics of the brake disc design change markedly the *cooling rate*, since this is inverse function of the heat storage capacity ($m_d \cdot C_p$) of the brake disc and direct function of its convective transfer potential ($h_c \cdot A_w$). Therefore maximising the convection area for a brake disc design is an important variable, which is independent of fluid dynamics response (e.g. brake discs designs with 90 and 60 vanes and with pillars).

5. Finally, although not mentioned yet, working towards an appropriate length of channelled vents would be an additional objective, since it has been seen that the available *radial* length in the brake disc provides scope for maximising heat transfer coefficient. This opens space for curved channels.

8.4 Synthesis of New Disc Designs

This Section deals with the optimisation of heat transfer coefficients and their distribution by using results from Chapter 6, Flow Index analysis and above conclusions. The thermal performance of the new designs will be evaluated in terms of their averaged markers (heat transfer coefficients and cooling rates), and in terms of $FI\,h_c$. The development of designs followed curved vent patterns with a twofold aim, reducing the misalignment angle between the incoming air at the inlet and the attack edge of the vane and enlarging the vent convection

passage. Therefore, the new curved vanes designed are longer than the radial straight vanes revised before.

It was suggested at the end of Section 8.3, that magnitudes from 0.06 to 0.10 for $\frac{P_{cr}}{R_i}$ give efficient control of $FI\,h_c$ avoiding steeping decays in the second radial half of the vent. This magnitude however, is not appropriate for the inlet region of the vent, since as seen in Section 6.3, narrowing the air intake cross section is detrimental for the overall convective performance of the vent (a narrow channel in the inlet restricts air admission and, it can only further be divided or widened, the first giving higher resistance to air flow due to narrowness and the second providing expansions which deteriorate the downstream speed).

Table 8.9: Channel width characteristics for design D30.

R, [m]	$\frac{P_{cr}}{R_i}$		
0.12	0.16		
0.141	0.18		
0.165	0.09^L	0.07^T	
0.192	0.13^L	0.06^T	
0.211	0.06^L	0.06^M	0.06^T

8.4.1 Three Curved Vane Designs

The first design as result of the above analysis is identified in this Thesis as D30. The design has three vanes, two of which are curved and the third is straight. The innermost vane incidence angle is 14^o. However, rather than designing the vane itself, attention is given to the channel width management, and the vane thickness followed as result.

The vent width was forced to satisfy the magnitudes $\frac{P_{cr}}{R_i}$ in Table 8.9, while the vent height was kept as in the baseline model. The superscript letters L, M and T stand for leading, middle and trailing sides of the vent attending to direction of rotation. Leading being the side of the *vent* preceding the other ones. The $\frac{P_{cr}}{R_i}$ fractions are referred to an inlet radius of R_i=0.118m, therefore the vent local widths are straightforward to calculate. The passages width and vanes thickness of the resulting vent design is shown in Figures 8.18 and 8.19. As observed, the vent inlet follows a 14 degrees orientation with respect to a radial line. The maximum width of the inlet was set to 24.7 mm at R=0.118m (between attack edges of the largest vanes), however the circumferential pitch at R=0.120m, is 19.6 mm. An expansion widens this to 21.5 mm at R=0.141m and after the expanded vent is partitioned near the middle of the radial length (R=0.165m). The inlet of the leading side partition (Figure 8.20) is wider than the trailing side partition one (10.8mm versus 8.5 mm). The intention behind

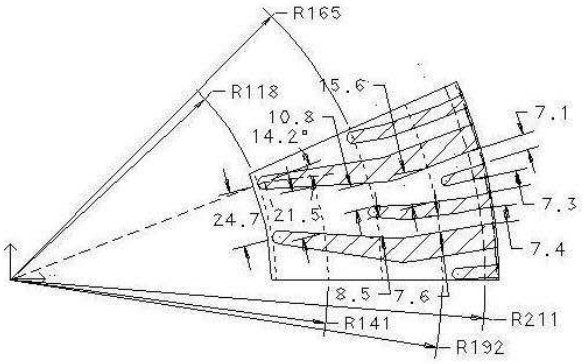

Figure 8.18: Curved vane vent design D30, passages dimensions (mm).

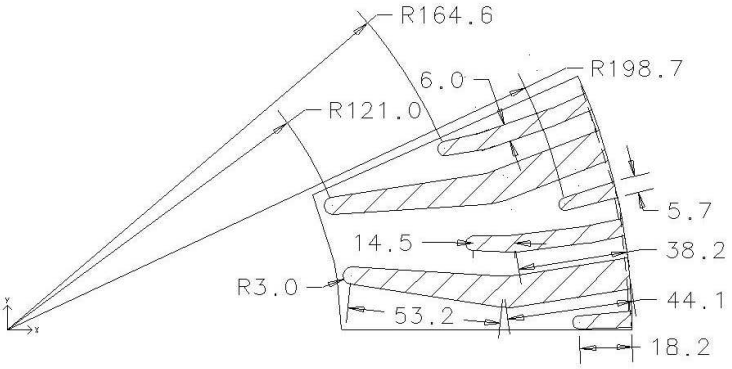

Figure 8.19: Curved vane vent design D30, vanes dimensions (mm).

this is providing wider entrance for low speed air in this side of the channel, while the narrow entrance in the trailing side uses directly high speed flow for enhancement of heat transfer coefficient distribution in this region. Then, while the trailing side partition focused into air speed effect, the leading side focused in collecting air mass flow.

Furthermore, the partitioned passage in the trailing side was designed with a semi-constant cross section throughout the rest of the vent. In the leading side passage, the partition opens wider in order to allow a second sub-partition toward the last 25% of the radial length of the vent. An additional option for this side could have been thickening the largest vane in its outlet region, but this would increase disc mass without providing substantial increment in convection area. In total, the design D30 has 90 vanes, of which 30 occupy the total available vent length, 30 run from the middle radius to the end of the vent and the final 30 were positioned in the last quarter of the radial vent length. A twin design was also

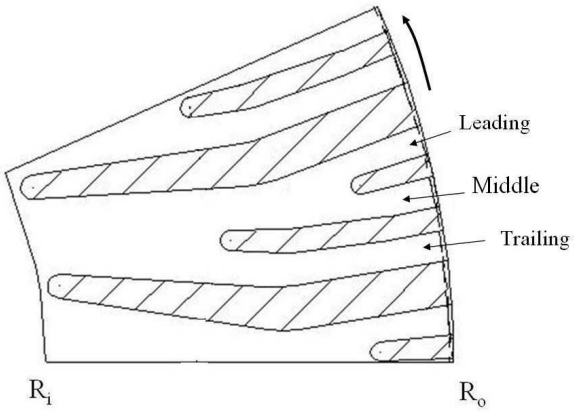

Figure 8.20: Curved vane design D30 description.

constructed to investigate the effect of straight inlet guide vanes in this type of vent layout, this design is named D30+IGV3. The IGV follows the same shape as that shown in Figure 6.69, although it has been oriented at an angle of 30 degrees with a radial line. Finally, the vents height is the same as in other designs (17 mm). CFD models were constructed for the above vent designs and a set of simulations were performed in order to investigate its convective heat transfer behaviour. The physical boundary conditions used were the same as in cases of Chapter 6.

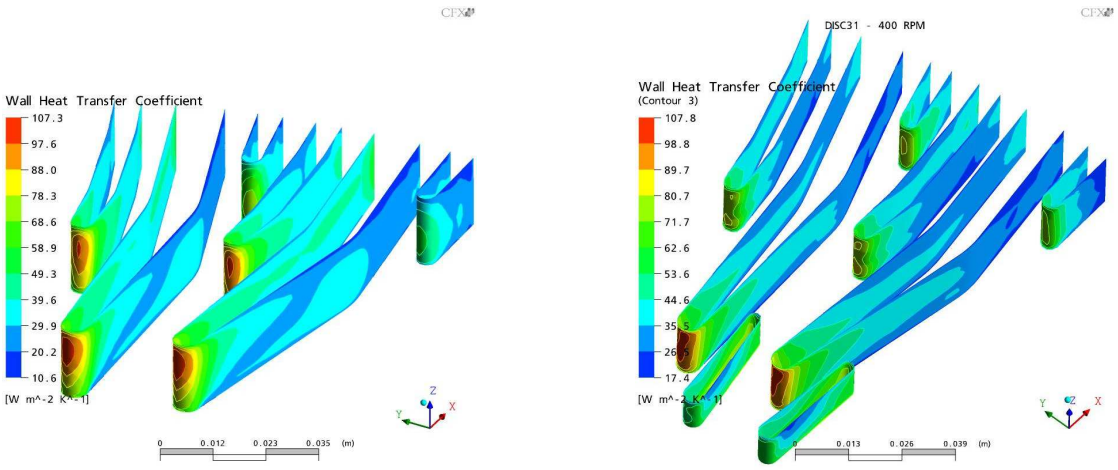

(a) D30 Vent. (b) D30+IGV3 Vent.

Figure 8.21: Convective heat transfer coefficients in vanes, n=400rpm.

Contour plots results for n=400rpm are shown. The heat transfer coefficient distributions

in the vanes of the D30 vent design show peaks of h_c in the attack edges of the largest and intermediate vane (Figure 8.21(a)), while when the IGV3 is attached (b), these only appear in the attack edge of the largest vane. Magnitudes of 29.9 to 49.3 W/m^{2}K are observed in the trailing side channel of the D30 vent, this range falls to 26.5 to 44.6 W/m^{2}K in the same channel when the IGV3 is used. However, in the leading and middle side passages, the heat transfer coefficient distribution is positively influenced by about 10% when the IGV3 is used. The influence of the IGV3 is evident in the heat transfer coefficient distribution of the endwalls, Figure 8.22, since h_c in leading side partition, outboard endwall of D30 (about 14 W/m^{2}K) increases to 30.6 W/m^{2}K in the same location for D30+IGV3 design. However, the h_c in the middle channel of D30, 40.0 W/m^{2}K, falls to 27 in D30+IGV3 design.

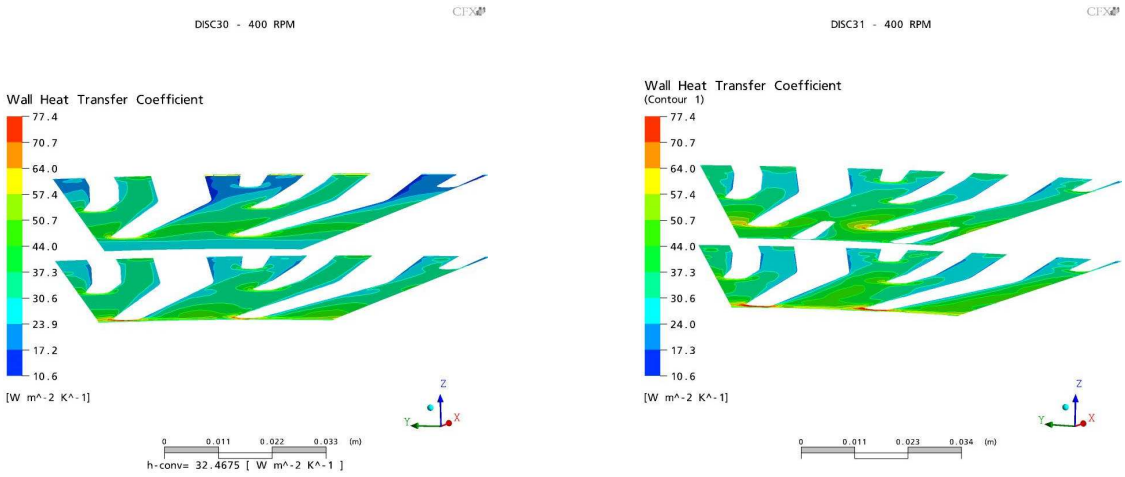

(a) D30 Vent. (b) D30+IGV3 Vent.

Figure 8.22: Convective heat transfer coefficients in endwalls, n=400rpm.

Relative velocity streamlines in Figure 8.23, show that in the D30 design vent inlet air flow separates and recirculates in the leading side. This pattern disappears when the IGV3 is used. The highest relative airspeed in the D30 vent is reached in the exit of the trailing side partition. This behaviour changes when the IGV3 is included, since air is locally accelerated near the leading side *wall* of the IGV3. The consequence of this is no separated flow in the leading side of the inlet and the redistribution of air stream inside the vent, which replaces the high relative speed region in the trailing side partition in D30 by homogenising the flow stream after the second radial half. It is seen in both designs that the relative direction of air exiting the channels is radial.

Averages vent heat transfer coefficients retrieved from the simulations were plotted as function of angular speed for the designs D30 and D30+IGV3. Equivalent results for the baseline

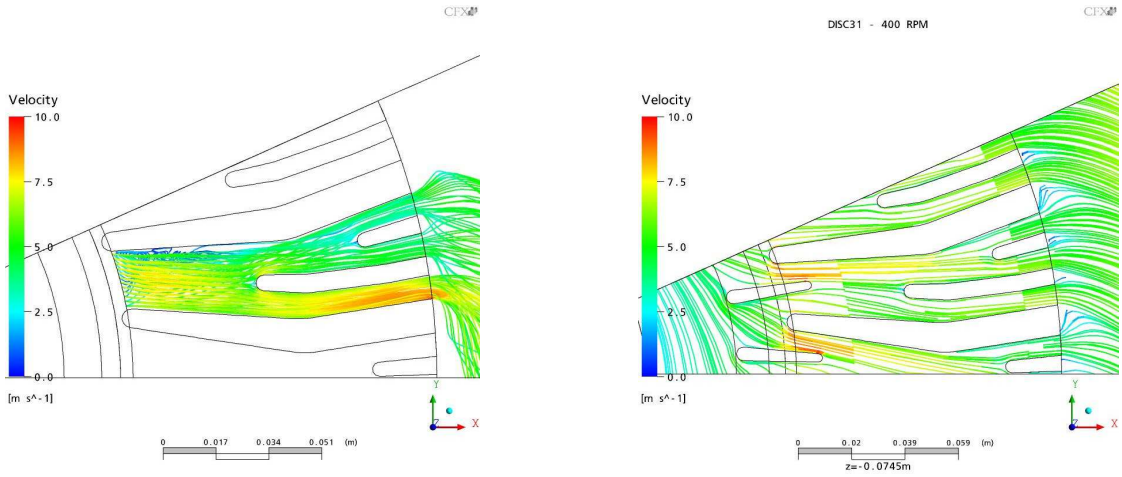

(a) D30 Vent. (b) D30+IGV3 Vent.

Figure 8.23: Relative velocity streamlines at n=400rpm.

design were also included. Figure 8.24 shows that the vent averaged heat transfer coefficient of the D30 vent design is lower than the baseline by 7% approximately (mean for all the speeds). The corresponding difference for the D30+IGV3 is positive by a mean percentage of 1%. This could seem dissapointing from the new designs, however comparing against the baseline (Table 8.11), the channel *convection surface* is 23% and 31% higher in the D30 and D30+IGV designs respectively. Therefore the convective performance of the vent surface has been enhanced, since in the first case a surface 23% larger gives average heat transfer coefficients 7% lower, a net gain of 16% in the product $h_c \cdot A_w$. In the best case (D30+IGV3), the surface is 31% bigger and produces in average slightly larger heat transfer coefficient than the baseline, which means that channel convection performance has been enhanced, not only by increasing the convection area but by maintaining flow performance in longer channels.

The inevitable result of this is higher required torque in the new designs when compared with the baseline (Figure 8.25(a)). The torque difference widens with angular speed and for the vent design D30, this is 11% larger than the baseline, while the torque required by the D30+IGV3 vent design is 13% larger; both are mean values over speed range. The air mass flow propelled by the vents of the D30 vent design is 5% *lower* than baseline across the angular speed range. This makes the design behaviour more interesting since less volume of air requires more mechanical energy and ends producing higher net gain in convective performance, $h_c \cdot A_w$. Following the Euler turbomachine equation (8.19) for energy consumed by a centrifugal pump (Munson *et al* 2006), the above means that, given constant angular speed (ω), less air mass flow will require higher pumping energy if its circumferential speed

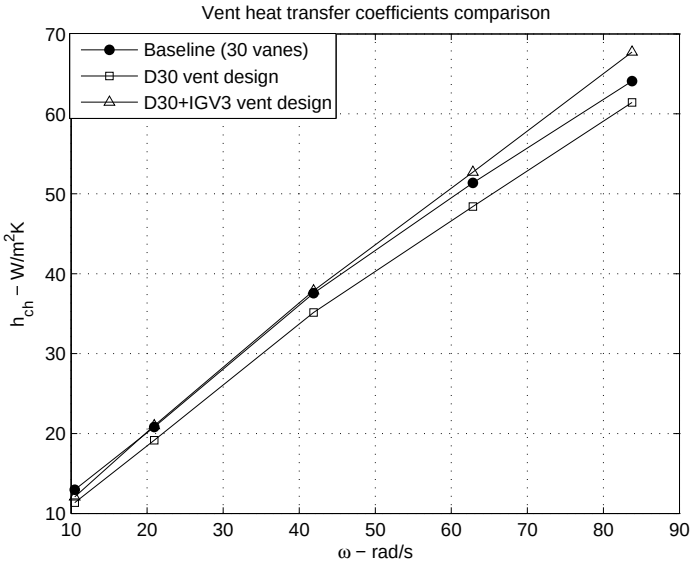

Figure 8.24: Channels average convective heat transfer coefficients, D30, D30+IGV3 and baseline designs.

difference is larger, that is, higher angular momentum. It is assumed that this difference in mechanical energy is what results in higher ability of heat transfer by convection in the vent.

$$W = \dot{m}\omega \left(R_o u_{\theta_o} - R_i u_{\theta_i} \right) \tag{8.19}$$

The $FI\,h_c$ of the D30 and D30+IGV3 vent designs were calculated in the same *radial* positions as in past cases (Figure 8.26, these are plotted together with those from the baseline vent design (see Figure 8.27). The initial $FI\,h_c$ magnitudes for D30 and D30+IGV3 are both below the baseline by 6 and 2% respectively. By the second station (R2) the magnitude of $FI\,h_c$ for both designs continues to be lower than the baseline (0.53 and 0.59 against 0.64). After the partition, at R3, the magnitudes of $FI\,h_c$ increase significantly above the baseline data (which is 0.52). This is due to the constriction itself, in fact $FI\,h_c$ for the D30 vent design increases in both trailing and leading partitions by the same magnitude, increasing from 0.53 to 0.63, which indicates an increase of 10% due to the constriction only (no IGV effect). At the fourth station, $FI\,h_c$ in the trailing side drops to 0.52, and ends with $FI\,h_c$=0.54. In the leading side the behavior is less efficient, since $FI\,h_c$ drops from 0.63 to 0.39 to end in 0.42 for the D30 vent design.

Using a straight IGV gives better $FI\,h_c$ than the D30 vent design in the first and second stations, but both are still under baseline corresponding points. As of the third station, $FI\,h_c$ in the leading side is better for design with the IGV than for that without it (in

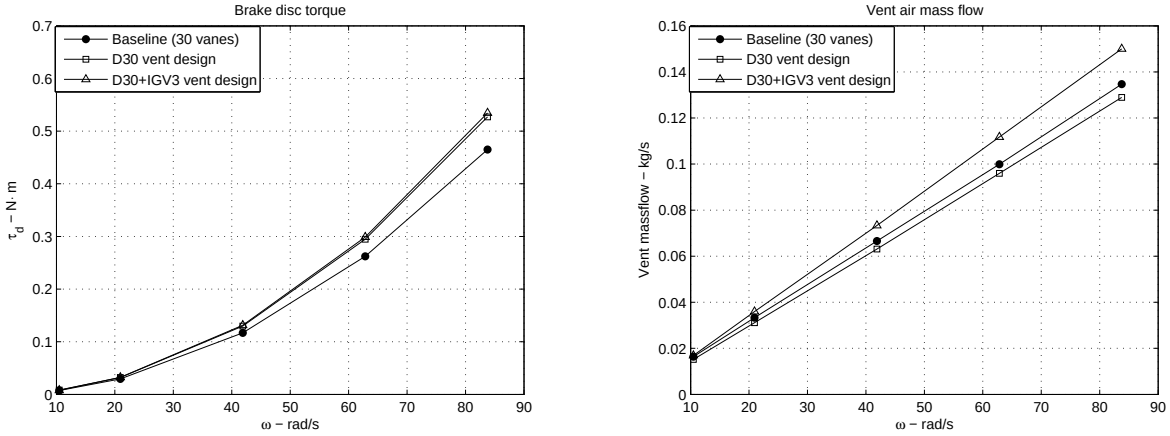

(a) Torque.

(b) Air mass flow.

Figure 8.25: Brake discs pumping torque and air mass flow.

average by 4%). However, in the trailing side of the vent, the $FI\,h_c$ actually falls below that of D30 by 4% and 7% in R3 and R4, to finally end with a magnitude of 0.54, 2% below the corresponding to the trailing side of the vent design D30.

The important characteristic to look at the $FI\,h_c$ diagram is that in the trailing side partition, the average heat transfer coefficient increases locally at the partition inlet and then falls. However, toward the final station (from R=0.192→0.211), it bounces up by 4% *only* as result of channel flow since because of the narrowness of the channel, it is very unlikely that is due to recirculation from outside. In the leading side, is also noticeable that local increments of $FI\,h_c$ correspond with each partition, which means that air speed is self-fed from these and as result brings up the local heat transfer coefficient. Equally important is the low effect that the IGV has on gaining high $FI\,h_c$. This is possible due to quick diffusion of any swirl into main flow as result of air speed enhancement.

8.4.2 Two Curved Vane Designs

A second version of the D30 design was created with the purpose of enhancing the thermal performance in the vents. The design, D32, was developed having only two different vanes which improves its manufacturing features due to its reduced variability; the vanes are referenced as main (larger) and secondary vanes. The shape of the vanes was smoothed and new $\frac{P_{cr}}{R_i}$ ratios were chosen aiming to having equal width channels along the radial direction.

The characteristics of the passages are given in Table 8.10. While the initial separation of

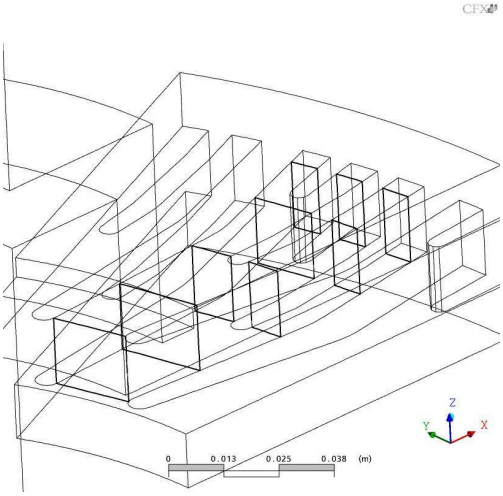

Figure 8.26: Locations where h_c was retrieved to calculate $FI\,h_c$.

the vanes (in R1 and R2) is kept the same as in design D30, only one partition is carried out at R3=0.165, giving way to two channels with similar width. Another important difference is the attack angle of the largest vane, this is 22^o, seven degrees more than in vent D30. This obeyed to air flow separation given in D30 vent design (Figure 8.23). The D32 design is shown in Figure 8.28, where the radii are for positions where channel width was determined previously (Table 8.10. The actual widths at these locations can be calculated knowing that R_i=0.118 m. The height of the vent is kept as 17 mm.

Table 8.10: Channel width characteristics for design D32.

R, [m]	$\frac{P_{cr}}{R_i}$	
0.12	0.16	
0.141	0.17	
0.165	0.07^L	0.077^T
0.192	0.086^L	0.08^T
0.211	0.11^L	0.10^T

In the same form as with D30+IGV3 design, a twin version was drawn from the D32 design, this includes a *curved* IGV located at vent inlet at an angle. The aim was investigating whether a curved IGV and its orientation is beneficial for this type of design. This design is referred as D32+IGV2.

The CFD simulations of the above designs were performed following the same methodology described in previous chapters. The discs are designed to rotate in *forward* direction, about $+z$. Contour plots results are shown for n=400rpm for both designs, following the same

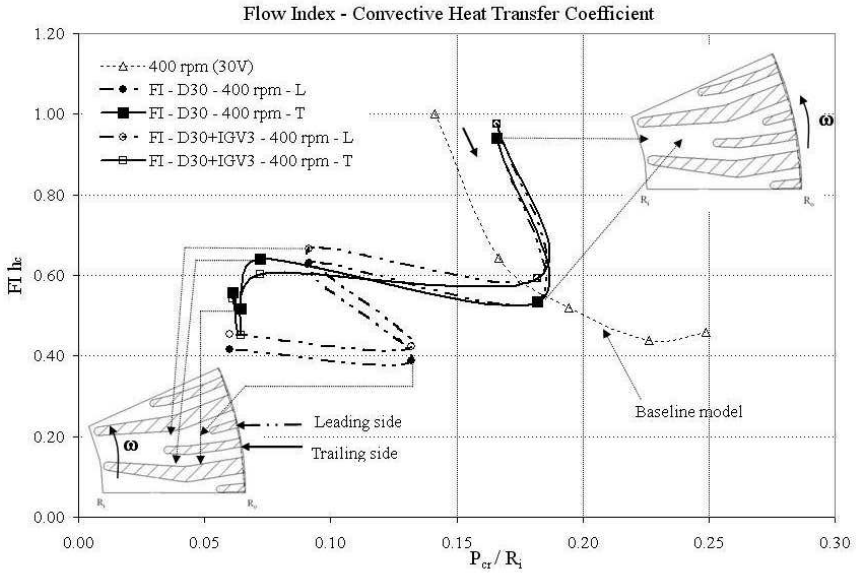

Figure 8.27: Convection heat transfer coefficient Flow Index for designs D30 and D30+IGV3.

analysis approach as for D30 and D30+IGV3 designs.

The distributions of heat transfer coefficients in vane walls of both vent designs, Figure 8.29, display a similarity with those in Figure 8.21 in the sense that peak heat transfer coefficients in the attack edges of the D32 vanes are removed when the IGV2 is included. As result, the maximum heat transfer coefficient is larger in the D32 than in the D32+IGV2 vanes (118.4 versus 111.4 W/m^{2}K). The distribution itself in the main vane is worse in the D32+IGV2 vent than in the D32, e.g.: a h_c=55.2 W/m^{2}K extending along the leading wall of the main vane in D32 is replaced by a lower 43.1 W/m^{2}K in the D32+IGV2. In the same manner, the heat transfer coefficient distribution in the secondary vane is negatively affected by the presence of the IGV2. In the endwalls, Figure 8.30, a similar difference occurs between both designs, with heat transfer coefficients ranging from 41.0 to 55.0 W/m^{2}K the distribution in the D32 vent endwalls is better than in the D32+IGV2.

The relative (to vent) air streams shown in Figure 8.31 depicts that in the D32 vent design air accelerates along the trailing side partition, where relative speed increases for at least 4 m/s. The interesting effect of the partition design, is that unlike the trailing side partitioned vent in D30 vent, the air relative speed is accelerated in most of the vent, which in the D30 case occurs when it approaches the exit. This speed raise must be linked to the continued h_c=55.2 W/m^{2}K distribution mentioned before. In the leading side partition the relative speed is lower but close to 5 m/s.

The relative airflow in design D32+IGV2 is different. Local speed increases in the leading

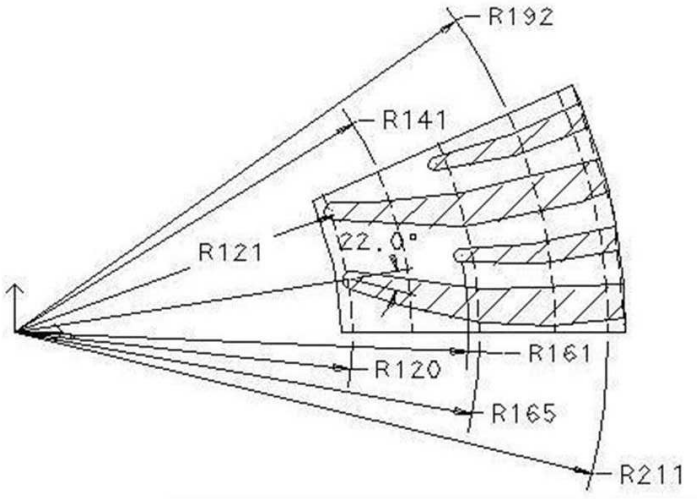

Figure 8.28: D32 brake channels design. Widths as per Table 8.10.

side of the vent inlet and redistributes down the vent to finally allocate similar ranges of speed in both partitions, however although the speed in the leading side partition is increased respect to the D32 vent design, the speed in the trailing side decreases significantly.

The averaged results are plotted versus the angular speed in the same way as before. The results in Figure 8.32 exhibit that vent design D32 improves by 10% the heat transfer coefficient while D32+IGV2 yields similar results to baseline. Nevertheless, the same as above can be argumented if it is considered that the convection areas of D32 and D32+IGV2 vents are 13% and 20% larger than the baseline vent design.

Regarding the aerodynamic torque required by the discs and the air mass flow pumped by the vents of these, both are larger than the baseline (Figure 8.33). However, while the mass flow pumped D32 vent design is 4% in average larger than the baseline, that pumped from the D32+IGV2 is 12% larger. The corresponding torque resistances show opposite behaviours, the mean torque required by the D32 disc is 21% larger than the baseline while that required by the D32+IGV2 disc is 15% in average larger. This means that the aerodynamic design of the D32+IGV2 vent is more efficient than that of the D32 despite representing apparently higher drag. The D32+IGV2 vent design pumps more air with less required rotational energy than the D32 vent design. But also the above indicates that aerodynamic efficiency in the vent is not necessarily linked to pure convective thermal performance efficiency (h_c), unless the magnitudes of the convection areas play otherwise (that is, the product $h_c \cdot A_w$). This is the case when convective cooling rates are calculated for the four recently presented disc designs and compared against the baseline cooling rate.

Convective cooling rates for disc designs D30, D32 and their variants are compared against

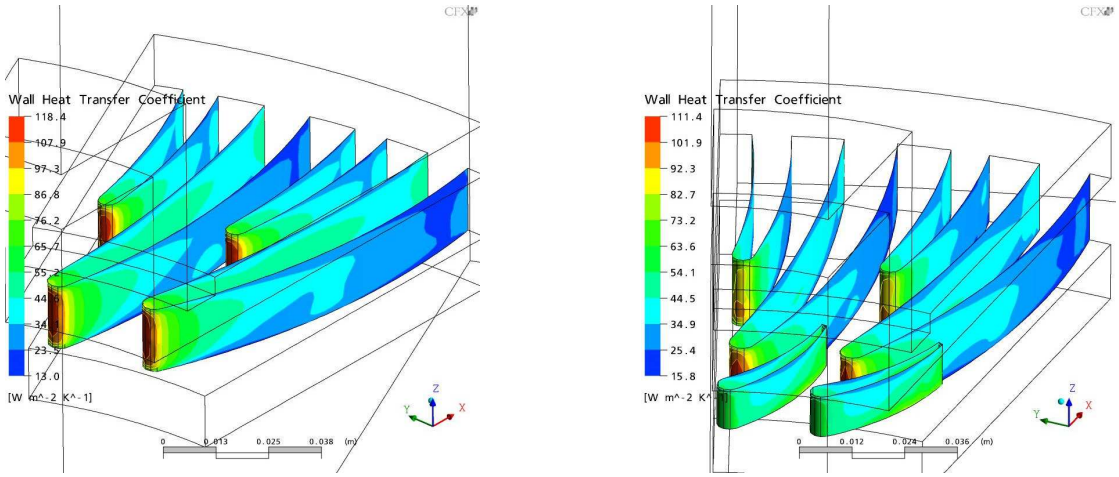

(a) D32 Vent. (b) D32+IGV2 Vent.

Figure 8.29: Convective heat transfer coefficient distributions in vanes, n=400rpm.

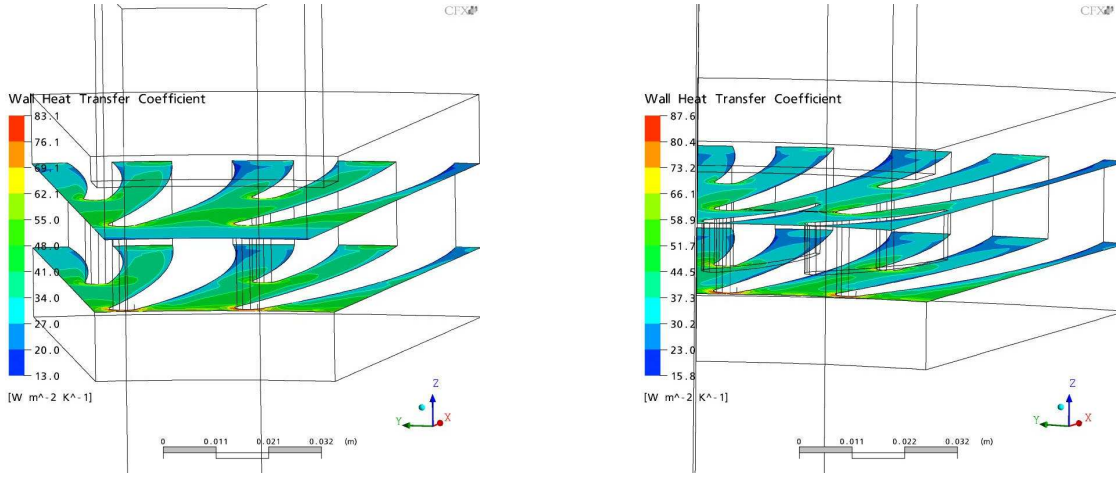

(a) D32 Vent. (b) D32+IGV2 Vent.

Figure 8.30: Convective heat transfer coefficient distributions in endwalls, n=400rpm.

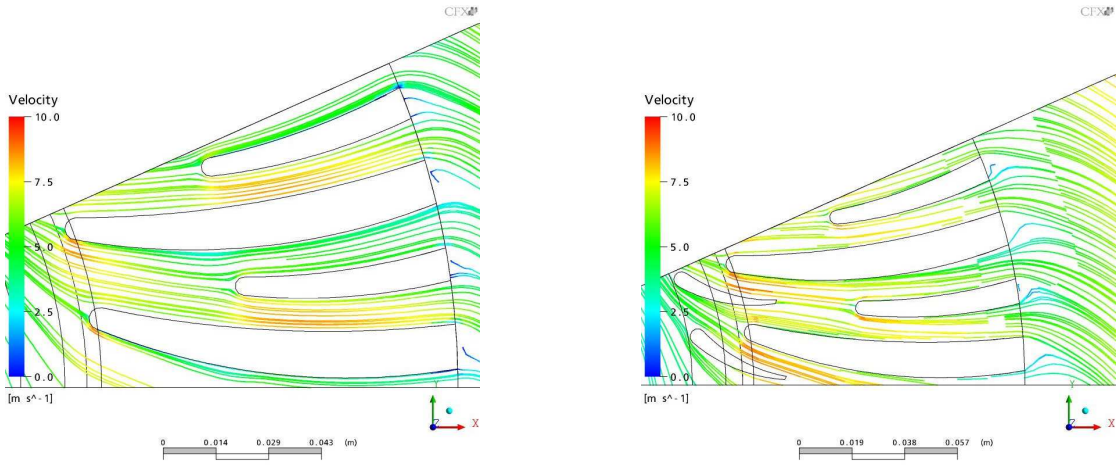

(a) D32 Vent. (b) D32+IGV2 Vent.

Figure 8.31: Relative speed streamlines in vent midplane, n=400rpm.

the baseline in Figure 8.34. The results indicate that all of them have better cooling rate than the baseline brake disc. The shortest difference is for designs D30 and D32 which have 10% higher cooling rate than the baseline brake disc. When the inlet guide vanes are included in the designs, the cooling rates improve in both cases. The cooling rates from D30+IGV3 and D32+IGV2 are 19% and 13% better than those from the baseline design. The above means that a marginal difference exist between disc averaged heat transfer coefficients of designs D32 and D32+IGV2, since the last one improves by only 3% the cooling rate in regards to the former, this difference is due to IGV convection area and mass.

The analysis of the $FI\,h_c$ through the vents in D32 and D32+IGV2 is shown in Figure 8.36. The radial locations where discrete readings of h_c were retrieved are the same as in others designs (Figure 8.35). When compared against the baseline $FI\,h_c$ trend, it is clear that the D32 vent gives higher $FI\,h_c$ starting level (+6%). The corresponding to D32+IGV2 is lower than the baseline by 5%. The results for the second location, R2, gives lower $FI\,h_c$ magnitudes than the baseline in the new designs (about 0.06 $FI\,h_c$ units smaller in both cases). However, the vent partition is important, since $FI\,h_c$ in the trailing and leading sides of D32 vent are higher than the respective baseline magnitude (0.71 and 0.66 against 0.52 respectively).

The magnitudes of $FI\,h_c$ for the third location (after partition) in the D32+IGV2 vent follows from flow equalization described for flow streamlines: both $FI\,h_c$=0.64 disregarding partition side (12% higher than the baseline but 4% lower than the D32). The flow index drop that follows in the fourth location is equal in the trailing sides of both designs and slightly

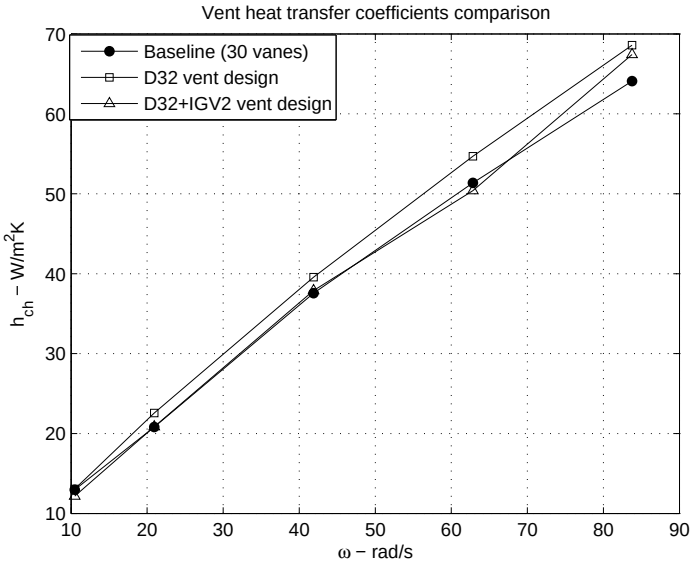

Figure 8.32: Channel average convective heat transfer coefficients; D32, D32+IGV2 and baseline designs.

higher in the leading side of D32 than in D32+IGV2. The final $FI\,h_c$ magnitudes, increase for all except for the leading side of the D32 vent design. In the worst case, the leading side of the D32 vent design reaches the same $FI\,h_c$ final magnitude as the baseline, while its trailing side magnitude is 13% larger. The corresponding magnitudes for the D32+IGV2 design are both higher than the baseline in the final station but lower than the trailing side of the D32 vent.

In summary, D32 vent design have better h_c performance than D32+IGV2 vent design, as noted in Figure 8.29. The obvious advantage of this against the former is its larger convection surface and its capability to pump more air at lower torque cost.

It is also evident that constricting the vent width in R3 with a ratio $\frac{P_{cr}}{R_i}$ ≈0.07 is beneficial for the response of local h_c, since in all cases revised (e.g. staggered vane, D30, D32 and its variations) the magnitude of $FI\,h_c$ in R3 has been always above the baseline design. The lowest increment was given for the staggered vane design, which is 2% higher than the baseline design; recalling that its starting $FI\,h_c$ was much lower than that of the baseline. Finally, it was proved that for the range of angular speeds analysed, an incidence angle of 22^o of the innermost attack edge gives better convective heat transfer coefficient in the vent, while the presence of an IGV increases slightly the vent averaged heat transfer coefficients.

The characteristics of the brake disc designed following the Flow Index results are given in Table 8.11. The heaviest design is the latest revised with 32.2 kg and the lightest design

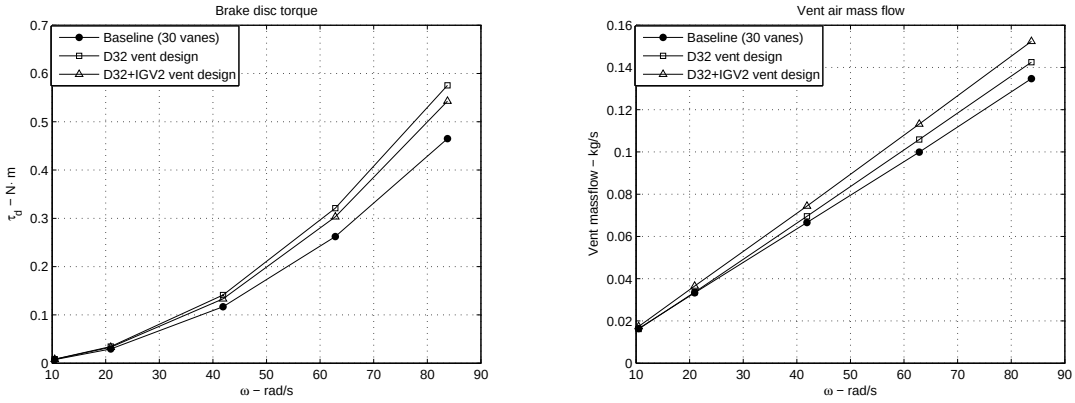

(a) Torque. (b) Air mass flow.

Figure 8.33: Required torque and pumped air mass flow.

is the brake disc with staggered vanes (31.3 kg). The maximum mass difference between the designs is 0.9 kg. Finally, it is important to bring attention to the direction of rotation shown for brake discs designed in this Section. All of them (D30 and D32 vent designs and their variants) should rotate as forward curved vanes, in order for the shape and incidence angle of the vanes to work accordingly with what has been expected.

Table 8.11: Convection area and mass of brake disc vent designs.

Brake	Channel Area, m^2		Disc Area	Disc Area	m_d
Disc	Vanes (plus IGV)	Endwalls	without channels, [m^2]	[m^2]	[kg]
Stagd vanes	0.1884	0.1433	0.3802	0.7119	31.3
D30	0.1842	0.1417	0.3918	0.7177	31.4
D30+IGV3	0.2053	0.1417	0.3918	0.7388	31.6
D32	0.1662	0.1332	0.3909	0.6904	31.9
D32+IGV2	0.1948	0.1292	0.3909	0.7150	32.2

8.4.3 The Effect of Rotational Direction

The effects of rotating the D32 design in backward direction were investigated using CFD. The disc was rotated about $-z$ axis. All the remaining boundary conditions, solution settings and turbulence model remained the same. At n=400rpm, airflow relative streamlines shown

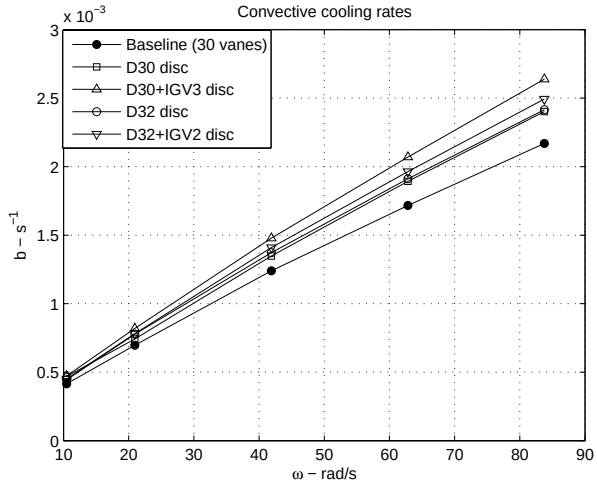

Figure 8.34: Convective cooling rates comparison.

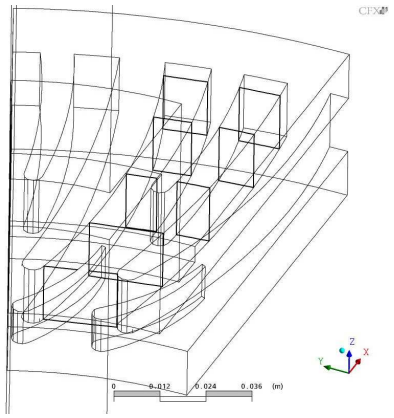

Figure 8.35: Locations where $FI\,h_c$ was calculated (D32+IGV2 design shown).

in Figure 8.37 demonstrate that only one partition of the vent pumps high speed air, this had been referenced as leading side partition before, however it is evident now is the *trailing* side partition due to change in rotation direction. The relative speed in the *leading* side vent partition is very low and this side of the vent could be considered 'stalling' the disc. Unlike results from the disc rotating in forward direction, the relative air in this case is seen to leave the channels following the curvature of the vanes (while in the forward direction rotation the relative air left the disc radially). The above indicates that rotating in this direction will reduce pumping ability of the disc.

The heat transfer coefficient distributions in Figure 8.38 show very good and continued heat transfer coefficient in the trailing side of the vent (on the leading wall of the main vane),

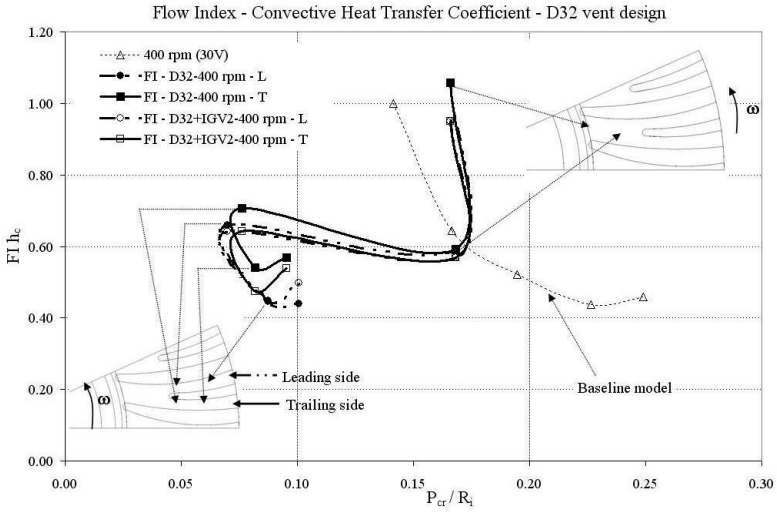

Figure 8.36: Convective heat transfer coefficient Flow Index, designs D32 and D32+IGV2.

since this is the vane wall where contact with air is better. In general the distribution is much better in the trailing side partition than in the opposite vent partition, where very low heat transfer coefficients are observed. The behaviour in the vent endwalls is similar, heat transfer coefficients get better magnitudes in the inlet section and in the trailing side partition, while the leading side partition shows poor performance.

A h_c Flow Index chart (Figure 8.40) shows the differences in behavior in the vent partitions due to change in rotational direction. The potential level of h_c at the inlet of the vent is lower when the disc rotates in backward direction (0.97 against 1.07, approximately 10%). Afterward, what had been called leading side partition shows a good recovery of $FI\,h_c$ (in the third station), and toward the fourth and last station of the vent it only drops to a minimum of $FI\,h_c$=0.50. In the leading side of the vent (formerly called trailing side), the $FI\,h_c$ behaviour is worse since as of the third station drops drastically to end in the last station at $FI\,h_c$=0.25.

Figure 8.39 compares the vent averaged heat transfer coefficients and the mass flow pumped as function of rotational direction. The maximum difference between heat transfer coefficients occurs at the lowest speed, backward rotation produces 20% less heat transfer coefficient than forward rotation at n=200rpm. The difference reduces for higher speeds to 10%. Regarding the amount of mass flow pumped, a constant difference of 30% is observed throughout all the speeds. Although not shown, required torque is 34% less for backward rotation and convective cooling rates are reduced 9% in average for all the speeds.

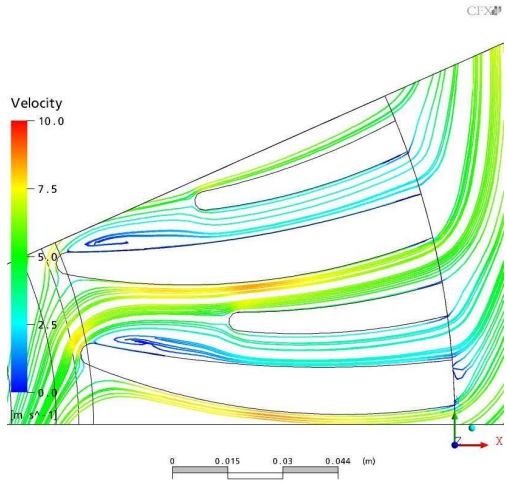

Figure 8.37: D32 design rotating in backward direction, relative speed streamlines at mid-plane, n=400rpm.

8.5 Experimental Modelling

Experimental work was conducted with one of the brake disc vent types designed following the Flow Index methodology. The brake disc vent design selected was D32 (see Figure 8.28). This design was chosen after taking into consideration manufacturing easiness among designs. The design D32 is the simplest to construct since, as described in the attached manufacturing drawings, the vanes shape are profiled by basically four radii which meet at specific locations determined by their origins. The procedure manufacturing philosophy is similar to that described in Section 4.1. A gray cast iron brake disc was sliced into two parts through the vanes and their inner surfaces (vent endwalls) skimmed. Care was asked to the manufacturing shop in order to unnecessary removing material from the disc plates.

The *main* and *secondary* vanes were manufactured of aluminum alloy 6082 T651(HE30) to BS1470,1987. Two M6 DIN7991 countersunk screws were used to secure each vane to the disc plates, while the secondary vane was fastened to one face only using two M3 DIN912 cap metric cap screws. Additionally, as safety measure, three blind studs were included passing approximately through the middle (radially) of three equally circumferentially spaced main vanes. Figure 8.41 shows the main and secondary vanes positioned ready for final assembly between the disc plates, and Figure 8.42 shows the manufactured version of the standard brake disc with the D32 vent layout designed in this Section ready for tests. The prototype was tested and experimental results compared against other brake discs.

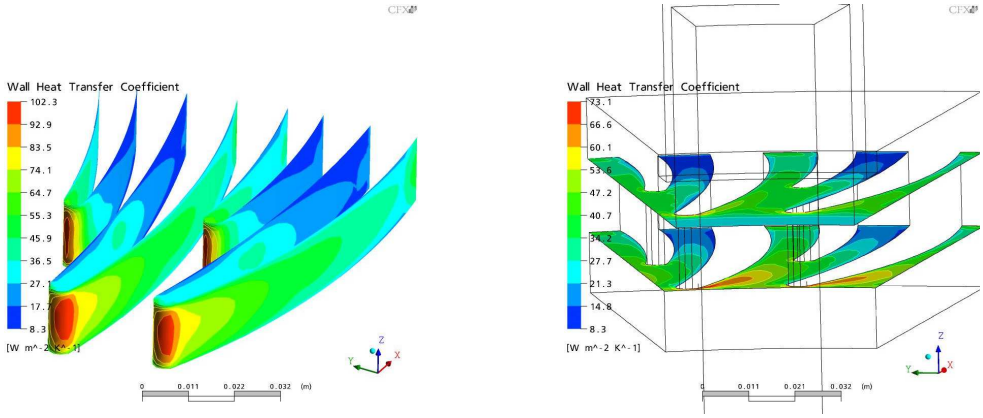

(a) h_c in vanes. (b) h_c in endwalls.

Figure 8.38: Heat transfer coefficient distribution, D32 at n=400rpm in backward direction.

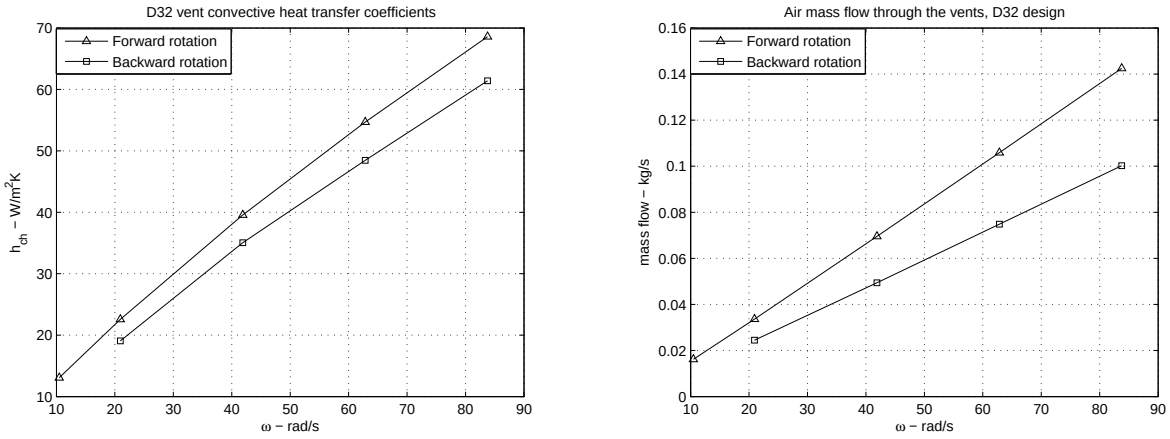

(a) h_{ch} vs ω. (b) Air mass flow.

Figure 8.39: Channel average heat transfer coefficients and mass flow for different modes of rotation in D32 design.

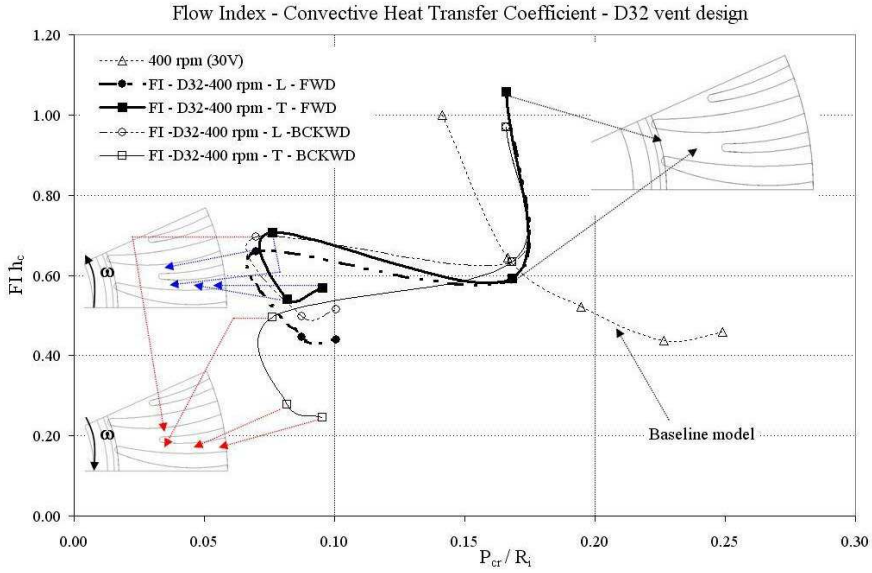

Figure 8.40: Convection heat transfer coefficient Flow Index for design D32 rotating in backward direction at n=400rpm.

8.5.1 Brake Discs Prototypes

The experimental results of four more discs were obtained and used as mean of comparison for results of experimental prototype D32. The additional prototypes were:

1. Brake disc with design *SV1 outlet*
2. A 36 curved vanes brake disc with channel design similar to that developed by Porsche used in the 2007 Carrera S vehicle (see Patent # US 7,100,748 B2).
3. A 30 curved vanes gray cast iron brake disc with venturi type channel cross section, and
4. The baseline detachable brake disc with aluminum vanes (Chapter 5).

The *Porsche JP* brake disc (Figure 8.43) is a modified version of the Porsche 2007 S Carrera model brake disc. The disc constituted the experimental prototype of Zammit's (2007) MSc Thesis, which was a work conducted under the frame of the current research. As mentioned before and in Zammit (2007), the Porsche JP vent layout was constructed following the design philosophy in Patent # US 7,100,748 B2. The patented design claims it has been optimised for maximum static pressure recovery through the vents, which as described therein, brings increased air mass flow.

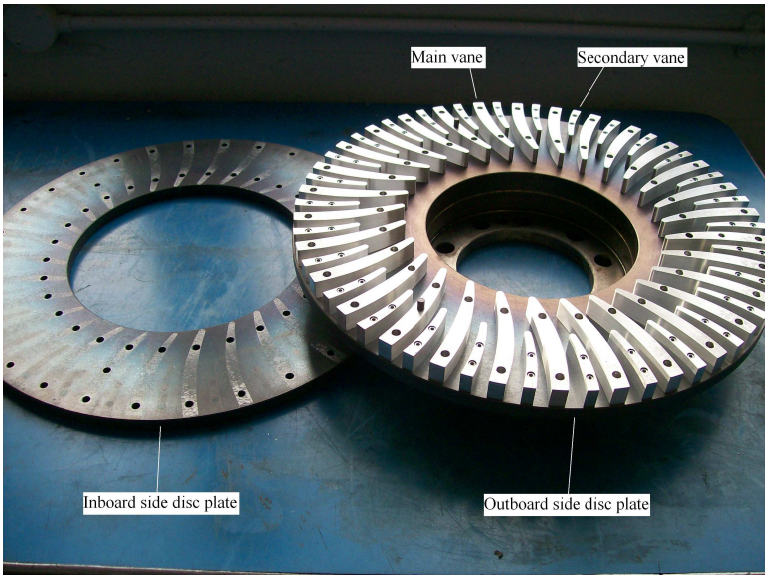

Figure 8.41: Experimental prototype of *D32* brake disc design during assembly.

The curved vane brake disc is the unique disc from the above manufactured exclusively of gray cast iron, and it was researched by Voller (2003). However, this disc was experimentally tested again and the results presented are based on current raw data. The rest of the brake disc prototypes were manufactured following the philosophy of the baseline detachable baseline vane brake disc: vanes manufactured of aluminum alloy, steel bolts and separate gray cast iron discs, all assembled together. The characteristics of the experimental prototypes are provided in Table 8.12.

Table 8.12: Experimental brake discs prototypes data.

Design	Mass, kg		
	Cast Iron	Aluminum	A_w
D32	25.92	1.91	0.6528
SV1-outlet	25.92	1.99	0.6488
Porsche JP	28.00		0.6130
Curved Vane	31.30	0.00	0.6845
Baseline DVB	25.92	1.44	0.6181

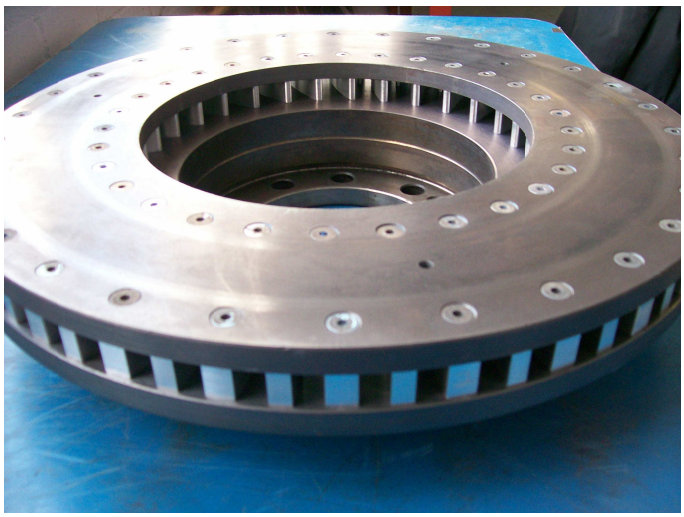

Figure 8.42: Experimental prototype of the *D32* brake disc design fully assembled.

8.5.2 Cooling History

The experimental cooling histories from the above mentioned discs are shown for two angular speeds (400 and 800 rpm). The temperatures shown were arithmetically averaged from thermocouples. At n=400rpm, Figure 8.44(a), different cooling capabilities are evident for each disc. Cooling from 120^{o}C to 60 ^{o}C in the baseline detachable vane brake disc (aluminum alloy vanes) takes 662 seconds. The curved cast iron brake disc takes 27 seconds less while the disc with detachable vane design SV1 outlet takes 77.5 seconds less. The shortest time is taken by the experimental D32 vent disc design, with 145.7 second less. The response at n=800rpm, Figure 8.44(b), is similar in regards to cooling times, the baseline detachable vane brake disc takes the longest time (401 seconds), and the other discs take 376, 365.5 and 323.5 seconds, following the same order for comparison as above.

However, besides being dependent on the vent design and brake disc rotational speed, the cooling times in Figures 8.44(a), (b) are also function of the ambient temperature, which varied among tests. Therefore, rather than comparing average temperatures from thermocouples to find out whether any of them performs better, it is necessary to compare the total cooling rates of the discs. Figure 8.45 shows the total cooling rates from the discs as function of the angular speed[8]. The highest cooling rates are from the D32 vent brake design. In average, these are 5% larger than those from the Porsche JP brake disc, with a maximum difference at 800 rpm, where the D32 prototype is 13% more efficient in cooling respect to the Porsche JP design. However, at n=200rpm the D32 brake disc is less efficient by 3.7%.

[8]D32 and curved vane gray iron brake discs rotated in forward direction, Porsche JP brake prototype as indicated in Patent # US 7,100,748 B2, see Figure 8.43(b)

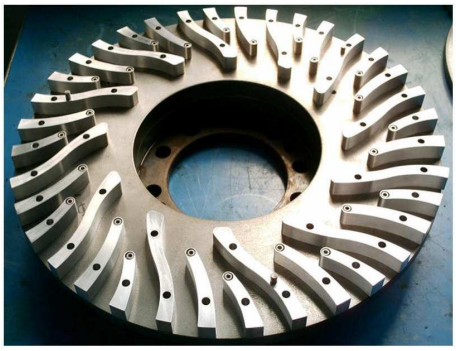

(a) Porsche JP prototype.

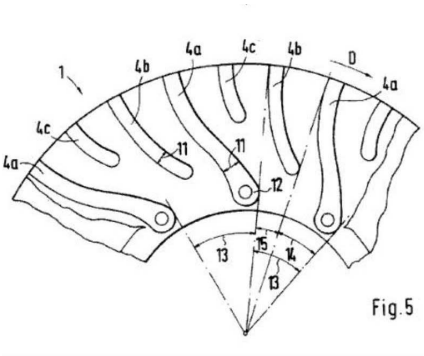

(b) Patent # 7,100,748 B2.

Figure 8.43: Porsche 'JP' brake disc prototype and patent source.

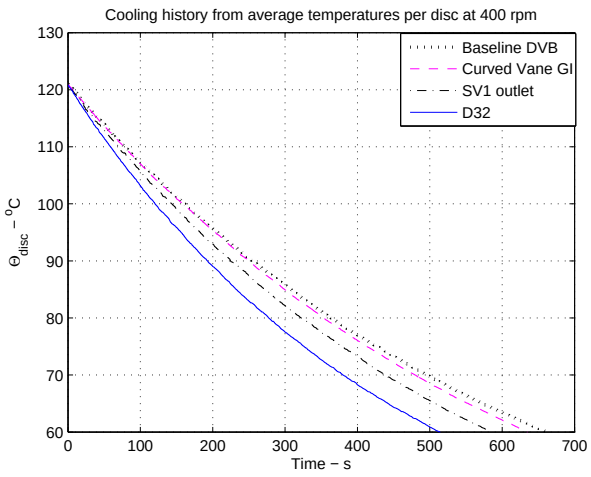

(a) n=400rpm.

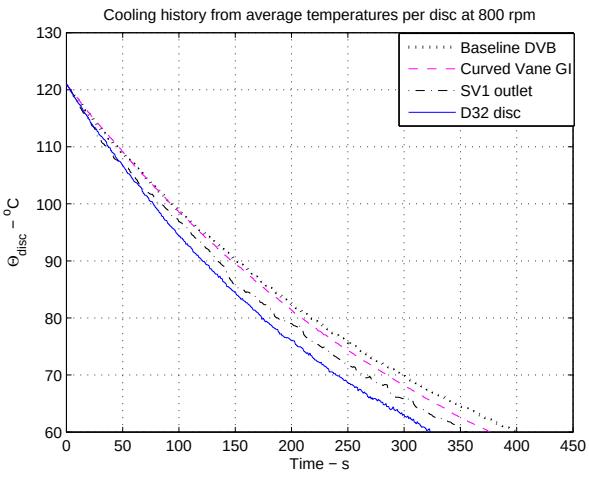

(b) n=800rpm.

Figure 8.44: Cooling histories from experimental brake disc prototypes, $\delta_\Theta = \pm 0.8^oC$.

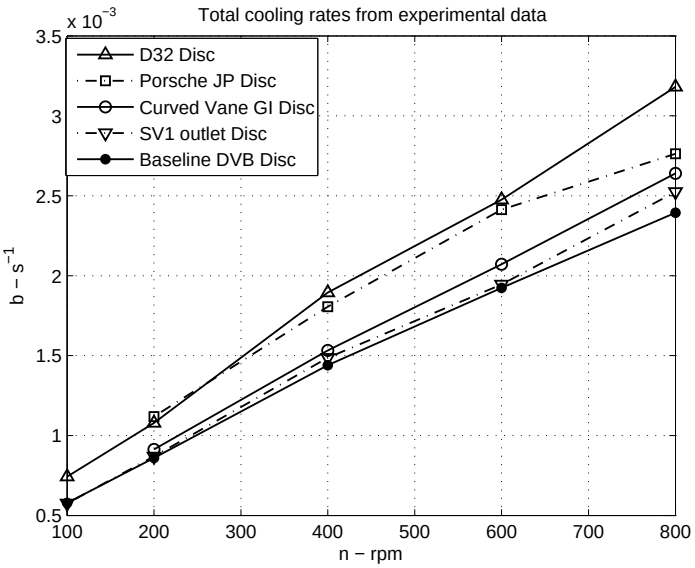

Figure 8.45: Experimental total cooling rates from brake disc prototypes.

A marked difference exist between the cooling rates from these two discs and the others. The cooling rate trend of the curved vane gray iron brake disc is in general 17% smaller than that of the D32 vent disc, while the disc with SV1 outlet design and the baseline brake disc (with aluminum vanes) are 21 and 22% smaller than the D32 disc prototype, respectively.

The above clearly indicates to the D32 vent design as the best, and therefore give confidence in the methodology and assumptions made during its design.

The calculation of experimental convective heat transfer coefficients for the D32 brake disc design follows, using averaged temperatures recorded by thermocouples in its friction surface. The results are shown for both rotational directions and compared against the corresponding data for the baseline brake disc with detachable vanes.

As observed in figure 8.46, the convective heat transfer coefficients of the D32 brake disc vary with rotational direction. The differences depends mainly upon speed range. Between 100 and 800 rpm, the heat transfer coefficient of the D32 disc rotating in forward direction (e.g.: as forward curved vanes) is about 9% larger than the corresponding rotating in backward direction[9]. However at 1200 rpm, the difference increases to 16.6%. The experimental heat transfer coefficients of the baseline brake disc with detachable vanes is substantially smaller than any of the above, which means that for the speed range shown, the D32 is better independently of rotational direction. In average, the heat transfer coefficients from

[9]Except at 200 rpm where the difference reduces to 3%

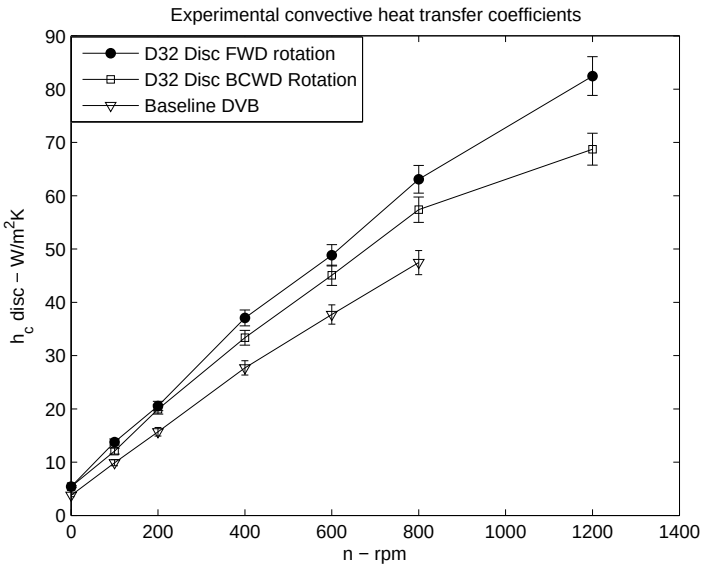

Figure 8.46: Experimental (disc) convective heat transfer coefficients for D32 and baseline detachable vane brake disc prototypes.

the baseline are 18% smaller than those from the D32 brake disc prototype rotating in bacward direction and 25% smaller when D32 disc rotates in forward direction. The difference increases to 30% when bouyant convection heat transfer coefficients are calculated.

The percentage differences among experimental heat transfer coefficients calculated for forward and backward rotations in brake disc D32 agrees with that predicted by CFD results for angular speeds between 200 and 800 rpm (CFD predicted 10% difference, while experiments give 9% difference). However, the actual magnitudes of the experimental (convective) heat transfer coefficients are underpredicted by the CFD model as described in Table 8.13. When the disc is considered rotating in forward direction the maximum discrepancy between experimental and numerical is 24%. The uncertainty range for this speed is 4% about the experimentally calculated value, therefore still exist a considerable difference.

Two reasons may be the cause of this: *a*) the models used in the simulations ($\kappa - \epsilon$ and Kader's (1981) for Θ^+) may not be sufficiently accurate to predict the heat transfer coefficient in disc D32 geometry, or *b*)high experimental heat transfer coefficients may be result from vibration induced cooling, as observed in the results for the prototype with radial vanes and SV1 vane at inlet. Nevertheless, disregarding this both (CFD and experiments) set of results predict substantial improvement of the disc D32 cooling performance against others, and therefore there is confidence in the improvement reached.

Table 8.13: CFD vs Experiments for h_{d_c} of brake disc design D32.

n	Forward Rot.		%	Backward Rot.		%
rpm	Exp.	CFD	Diff.	Exp.	CFD	Diff.
100	13.8	9.1	33.8	12.1	NA	-
200	20.5	16.0	22.3	19.9	14.3	28.5
400	37.1	28.2	24.0	33.4	25.8	22.7
600	48.8	39.3	19.6	45.1	35.8	20.6
800	63.1	49.6	21.3	57.4	45.9	20.0

8.6 Local Convection Analysis of Radial Vents

As mentioned before, Kilic's (2004) paper deals with an analytical equation for predicting the local behaviour of the Nusselt number in the thermal entry length of circular section ducts with hydrodynamic developed flow in stationary (non rotating) conditions. The equation 8.9 depends basically in the value of the dimensionless coordinate x^+ (equation 8.6)[10]. It is assumed that x^+ varies only with x for an specific channel, since the group $\frac{2}{D_h Re_{D_h} Pr}$ remains constant along the duct of circular cross section. However, in a brake disc trapezoidal channel this group would not be constant.

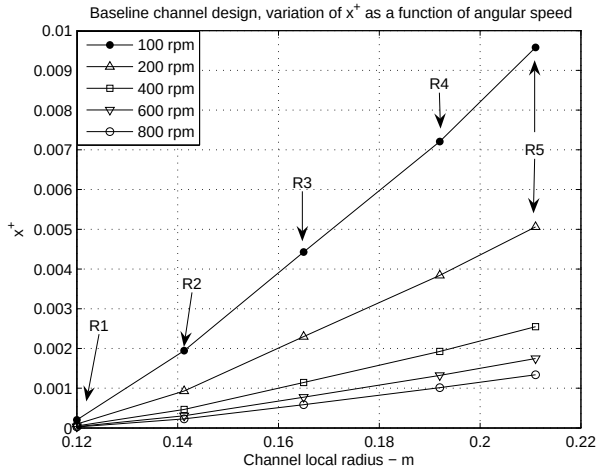

Figure 8.47: x^+ versus channel radial length for baseline channel design (30 vanes), using equation 8.6.

[10] $(x^+/2)^{-1}$ is known as the Graetz number

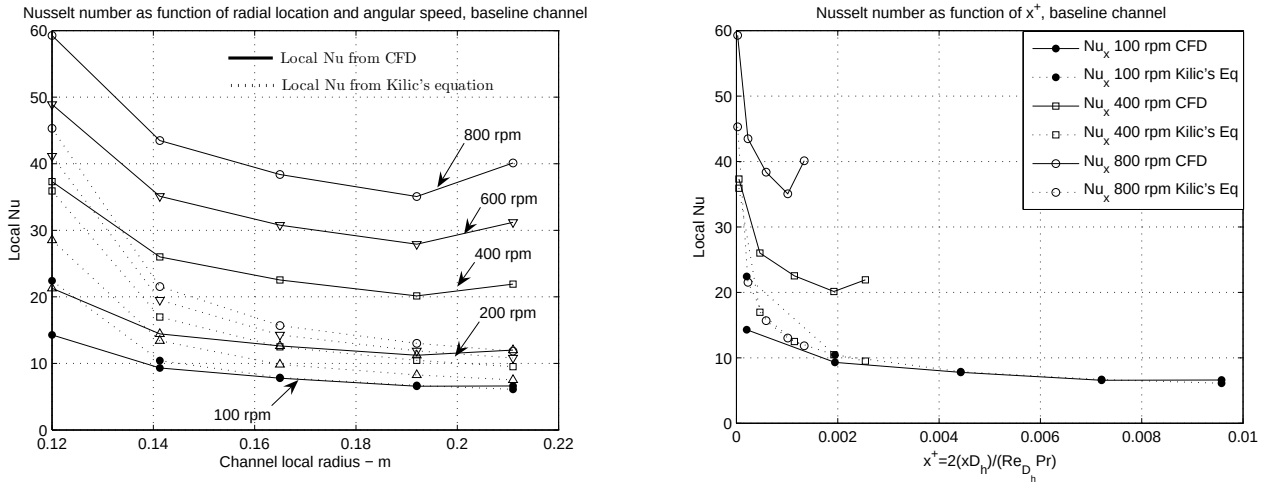

(a) Nu_x vs radius. (b) Nu_x vs x^+.

Figure 8.48: Local channel Nusselt numbers calculated from CFD and with equation 8.9.

Using absolute radial speed along the channel centre from CFD simulations of baseline design (30 vanes), the value of x^+ is calculated and seen that it takes low order magnitudes (Figure 8.47), similar to those in Table 8.4. Then, using equation 8.9 and data for constant surface temperature in Table 8.5, the channel local Nusselt number (Nu_x) is predicted. Also, Nu_x can be calculated from the CFD results, taking the heat transfer coefficients used for Flow Index. Therefore a comparison between the analytically predicted and the numerically computed Nusselt numbers can be carried out for the same channel locations where $FI\,h_c$ was calculated. Equation 5.5 has been used for the local Nusselt number from CFD by substituting local averages of heat transfer coefficient in place of h_{ch}. The results for the baseline channel design, shown in Figure 8.48, indicate that although the behaviours are monotonic in both cases, there is only good correlation for the lowest angular speed (100 rpm), while for higher n the correlation given by equation 8.9 is poor since Kilic's (2004) equation underpredicts the convective heat transfer behaviour in the channel.

Besides, if the arithmetic mean of the Nusselt numbers is calculated per angular speed from both cases (CFD and equation 8.9), and compared it is also evident that Kilic's (2004) equation (8.9) underpredicts the *average channel Nusselt number* for the baseline channel design along all the angular speed range (see Figure 8.49). It is worth mentioning that the channel average Nusselt number calculated with data used for $FI\,h_c$ is very similar (less than 2% difference) to the average Nusselt number calculated using the averaged channel heat transfer coefficient directly postprocessed from ANSYS-CFX (see Figure 6.80).

The above is a theoretical way to confirm what was described in Section 5.2, Chapter 5: convective heat transfer behaviour of rotating channels is not properly replicated by assuming the behaviour of the flow as that of a simple stream within a stationary channel.

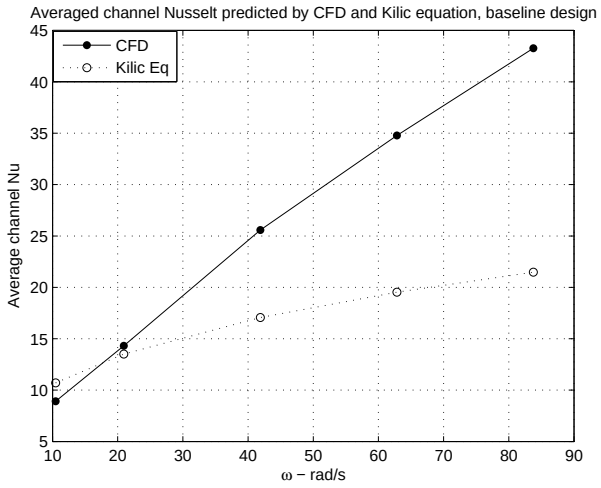

Figure 8.49: Average Nusselt numbers calculated using data for $FI\,h_c$ and equation 8.9.

8.6.1 A Correlation for Nu in Trapezoidal Channels

Following the results above mentioned, a simple analysis of Kilic's (2004) equation is performed in order to identify routes of modification for improving correlations between equation 8.9 and the Nusselt number in the thermal entry length of rotating radial channels in brake discs.

An analysis of the equation 8.9 response to modifications in the constants A, B and C was conducted. While modifying the magnitude of one of them, the remaining were kept constant. Also, to simplify the analysis a constant cross section duct was assumed and therefore a monotonically increasing x^+ taken.

It was seen that Nu_x given by equation 8.9 scales up/down proportionally to constant A. A different response occurs for changes in B and C. These must be significantly modified for a change be observed in Nu_x, and this is only evident for *high* numbers of x^+, that is, for low x^+ the response is similar to the original equation. Figure 8.50 shows the results for Nu_x for four scenarios: using the original constants (Table 8.5), doubling the magnitude of A and increasing the magnitudes of B and C by 10 and 100 factors respectively. All these modifications were implemented independently, as mentioned before.

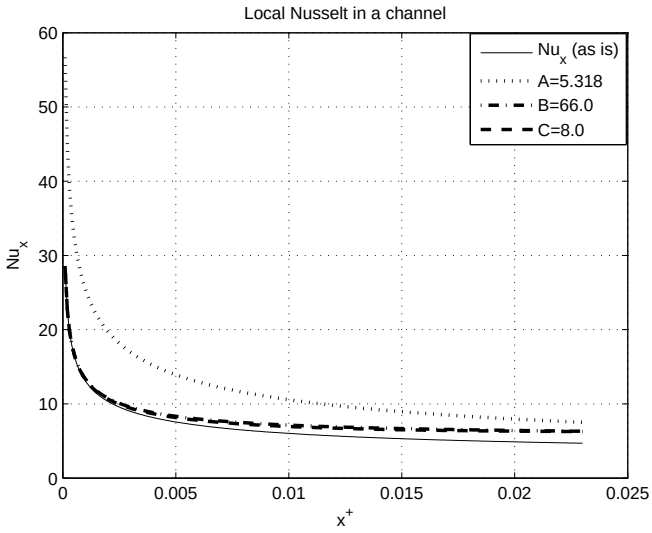

Figure 8.50: Nu_x response under changes in constants A, B and C (see equation 8.9).

Foreseeing the magnitudes of x^+ to fall within orders $10^{-3} \rightarrow 10^{-4}$ for brake disc channels, a new form to this variable was set by assuming it proportional to the *radius* of the place of interest inside the channel. The new x^+ is redefined as x^+_{rot}, see equation 8.13 and Figure 8.3. This induces a change of one order up and therefore the x^+ range where constants B and C have influence is reached. Modifying A was disregarded because of its large impact on Nu_x. Finally, attention was focused on constant C only. The constant status was modified to air speed dependent variable[11].

$$C\ f(u_r)$$

Also, important to raise is that the group $\frac{2}{D_h Re_{D_h} Pr}$ is not longer constant (except Pr), since local changes of channel cross section and radial speeds were considered. Two options for resetting C were revised and only the results of the most appropriate are shown.

1. Including the Rossby number calculated with absolute radial speed in the following way:

$$f_2 = Nu_\infty + \mathbf{R}_o C e^{-x^+}$$

   Where the Rossby number is redefined as

[11] Nu_∞ can not be modified

$$\mathbf{R}_o = \frac{u_r}{\omega r_{loc}}$$

This approach did not produce accurate results, and therefore results obtained were not included in this thesis.

2. Using a power expression of the local channel Reynolds number, and including the redefined dimensionless coordinate x^+_{rot} given in equation 8.13:

$$f_2^* = Nu_\infty + C_1 e^{-x^+_{rot}} \tag{8.20}$$

C_1 is not a constant anymore but a variable dependent upon the behaviour of the *local channel Reynolds number* $(Re_D)_{loc}$ calculated in the station where the Nusselt number is investigated, employing the *local* absolute radial speed at the channel centre and *local* hydraulic diameter at that station:

$$C_1 = 0.08 e^{\lambda_\omega} \tag{8.21}$$

$$\lambda_\omega = (Re_D)^{0.235}_{loc} \tag{8.22}$$

Also, as a result of using x^+_{rot}, the group f_1 (equation 8.10) is redefined as:

$$f_1^* = A x^{+2/3}_{rot} + B x^{+5/3}_{rot} \tag{8.23}$$

Therefore, the *new modified* equation for the Nusselt number in the thermal entry of *rotating* trapezoidal channels is established as:

$$Nu_x^* = \frac{(f_1 - 2f_2^* x^+_{rot}) e^{-f_1} + 2f_2^* x^+_{rot}}{2x^+_{rot}} \tag{8.24}$$

Observing equation 8.24, the elements without modifications are constants A, B and Nu_∞ (used as in Table 8.5), constant C is replaced by a variable named C_1 (equation 8.21), which incorporates into the new equation the effect of absolute air speed in the channel given by rotation of the brake disc and by channel geometry. The equation should hold independently of the units system used, since is dimensionless. The above equation has been referred as *MGL* equation in graphic results.

Revising equation 8.24, the inputs required are:

1. Radii (r_{loc}) inside the channel where Nu_x^* is sought (used in x_{rot}^+, equation 8.13).
2. Local channel Reynolds number calculated using:
   (a) Local channel hydraulic diameter, D_h at r_{loc}.
   (b) Local absolute *radial* air speed, u_r.
   (c) Averaged kinematic viscosity of air (Table 3.2).
3. Prandtl number (Table 3.2).

Therefore, it is evident that changes in brake disc rotational speed and channel width (e.g.: vanes number or thickness) will be directly felt by the equation in the value of $\lambda_\omega = (Re_{D_h})_{loc}^{0.235}$. This value is transcendental for f_2^*, since $x_{rot}^+ << 1$ which makes $e^{x_{rot}^+} \rightarrow 1$, leaving to λ_ω the work of determining the value of f_2^*.

Finally, equation 8.24 responds safely to the case where the brake disc angular speed is zero, that is, $(Re_{D_h})_{loc} = 0$ if $\omega = 0$, which brings $f_2^* = f_2$ provided x_{rot}^+ is replaced by x^+. Then, $Nu_x^* = Nu_x$, that is, the solution for a stationary channel. Using equation (8.24), results for local channel Nusselt numbers (Nu_x^*) are plotted as function of disc radius and angular speed, and compared against the those calculated from CFD simulations of the baseline brake disc.

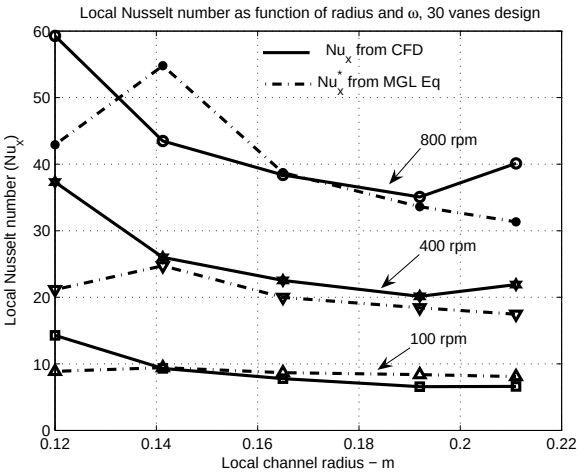

(a) Nu_x^* vs radius.

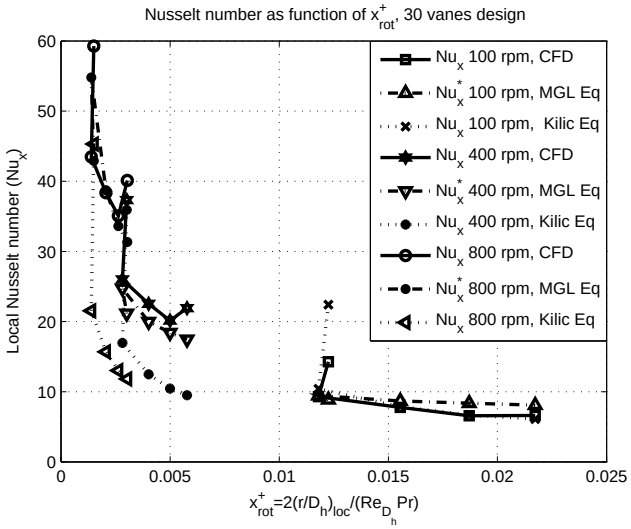

(b) Nu_x^* vs x_{rot}^+.

Figure 8.51: Local channel Nusselt numbers from CFD and with equation 8.24.

The results show an appropriate response of the MGL equation as the angular speed increases (Figure 8.51, baseline disc). The analytically predicted local Nusselt number through the channel is in their best points within 15% error for n=100rpm, 5% for n=200rpm, 15% for n=400rpm and 7% for 600 and 800 rpm (results are plotted only for 100, 400 and 800 rpm). The MGL equation fails to predict the initial peak of heat tranfer coefficient in the inlet of the channel and also, at large angular speeds (n >400rpm) it fails to replicate the heat transfer coefficient peak behaviour in the outlet of the channel. Note that the ordinate in graph (b) of Figure 8.51 is x^+_{rot}.

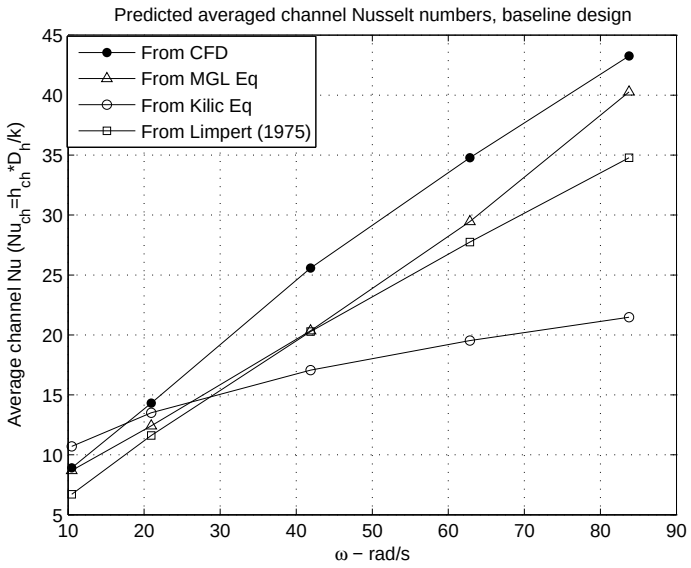

Figure 8.52: Average Nusselt numbers calculated along the channel for the baseline design (30 vanes), using equations 8.24, 2.21 and 8.9

.

Using the above values, averages are calculated for each brake disc angular speed and these compared against those averages calculated from Kilic's (2004) equation and against those predicted by Limpert's (1975) correlation (equation 2.21). This comparison is shown in Figure 8.52, and the discrepancies relative to the channel average Nusselt number calculated from CFD results are shown in Table 8.14.

The above comparison demonstrate that the best approach to averages obtained numerically is given by equation 8.24, with a maximum difference error of 20.5% at n=400rpm. Equation suggested in (Limpert 1975) gives a more stable but larger error, while Kilic's (2004) equation gives the worst fit, which is justified recalling that it was developed for stationary ducts.

This encouraged using equation 8.24 for predicting the channel local Nusselt and channel

Table 8.14: Prediction errors using the MGL equation for Nu_{ch}, baseline design (30 vanes).

n	Nu_{ch} CFD	$\frac{Nu_{CFD}-Nu_{Eqs}}{Nu_{CFD}}\%$		
		vs Kilic Eq	vs MGL Eq	vs Limpert (1975) Eq
100	8.9	-20.1	2.5	24.7
200	14.3	5.6	13.2	18.9
400	25.6	33.3	20.5	20.7
600	34.8	43.9	15.3	20.2
800	43.3	50.4	6.9	19.6

average Nusselt numbers for brake discs designs in which the number of vanes was varied (Section 6.2). Therefore, the Nusselt number in five stations whose radii coincided with those in Figure 8.4 were calculated using the heat transfer coefficients for $FI\,h_c$ (Figure 8.5). The radial absolute airspeed was also required and this was the same used for $FI\,u_r$ (Figure 8.7). Average predictions per channel are shown for brake discs designs with 20 and 60 vanes in tabular form and graphically for brake discs with 45 and 90 vanes.

Table 8.15: Errors in the approaches to channel Nusselt number, brake disc design with 20 vanes.

n	Nu_{ch} CFD	$\frac{Nu_{CFD}-Nu_{Eq}}{Nu_{CFD}}\%$		
		vs Kilic Eq	vs MGL Eq	vs Limpert (1975) Eq
100	9.9	-20.9	8.5	55.7
200	15.1	1.3	16.4	44.5
400	27.3	31.0	24.8	47.6
600	38.0	43.5	22.1	47.6
800	49.6	51.9	15.5	48.4

The average predictions indicate that MGL equation (8.24) correlates acceptably well and better than correlation 2.21 in brake discs designs with 20 and 60 vanes. A maximum error of 24.8% exists for the average Nu_{ch} prediction to the 20 vanes design at n=400rpm, while the error reduces at lower and higher rotational speeds (Table 8.15). Similarly, the approximation to Nu_{ch} of the 60 vanes brake disc is very good for rotational speeds between 200 and 800 rpm, but poor for n=100rpm when equation 8.24 is used, as seen in Table 8.16.

However, equation 8.24 is weak for predictions of local and average channel Nusselt numbers of brake discs with 45 and 90 vanes, as seen in Figures 8.53 and 8.54. The same flawed behaviour is produced with Limpert's (1975) equation in these brake disc channels. Both equations overpredict the average Nusselt number of the channel as function of the rotational

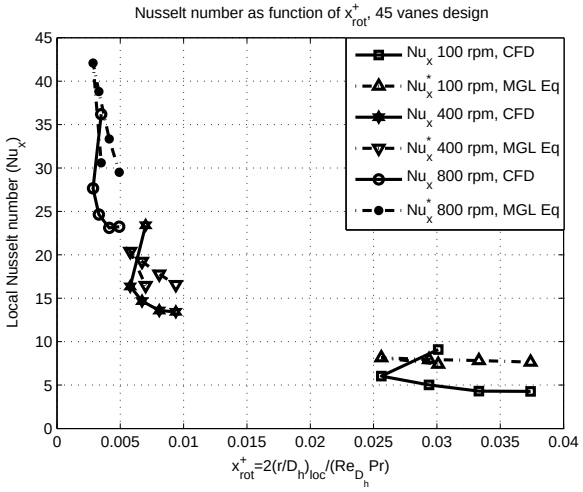

(a) Nu_x^* vs x_{rot}^+.

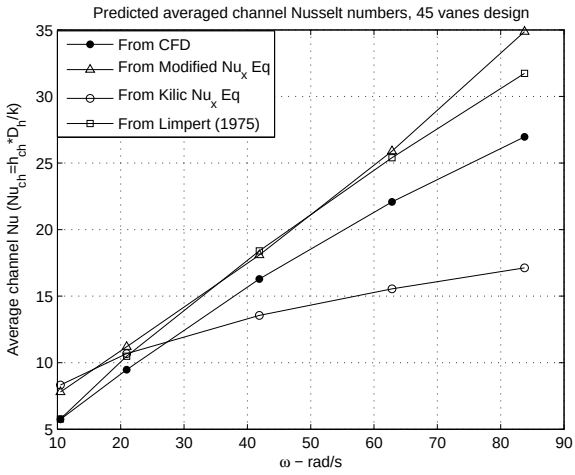

(b) Nu_{ch} vs ω.

Figure 8.53: Local and average predictions of channel Nusselt numbers for brake disc with 45 vanes.

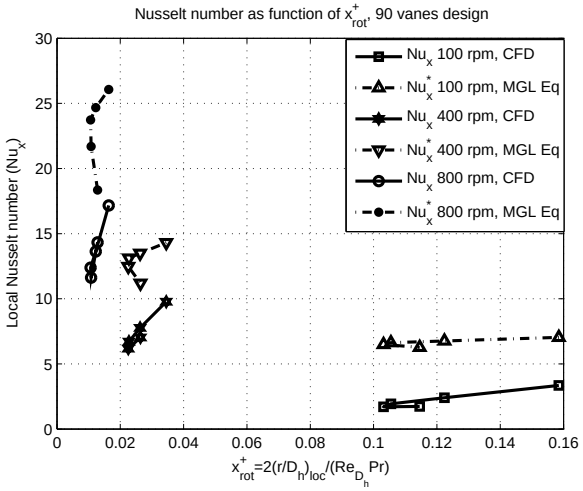

(a) Nu_x^* vs x_{rot}^+.

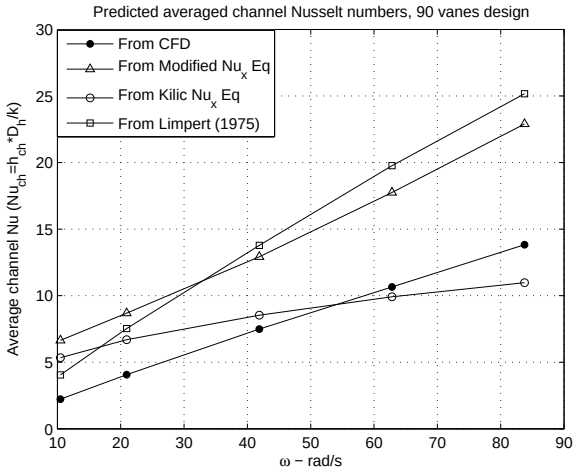

(b) Nu_{ch} vs ω.

Figure 8.54: Local and average predictions of channel Nusselt numbers for brake disc with 90 vanes.

Table 8.16: Errors in the approaches to channel Nusselt number, brake disc design with 60 vanes.

n	Nu_{ch} CFD	$\frac{Nu_{CFD}-Nu_{Eq}}{Nu_{CFD}}\%$		
		vs Kilic Eq	vs MGL Eq	vs Limpert (1975) Eq
100	5.5	-46.5	-37.2	-28.1
200	9.5	-7.1	-9.8	-30.7
400	16.1	20.1	-1.1	-37.1
600	22.0	33.2	-2.9	-35.4
800	27.4	41.0	-8.6	-35.9

speed. It can be seen however, that Kilic's (2004) equation gives a better approximation to Nu_{ch} in these cases, with particular agreement in the 90 vanes brake disc design. The latter could represent that although rotating, fluid behavior in the narrowest channel behaves in similar manner as it were stationary (that is, with symmetric distribution of velocity, temperature and heat transfer coefficient around the centreline of the channel). This can be observed in Figures 6.20 and 6.21 as well.

Summarising, MGL equation (8.24) predicts reasonably the behaviour of the local and average Nusselt number within trapezoidal channels of brake discs designs with 20, 30 and 60 vanes. For narrow channels (45 and 90 vanes) fails. This new expression was developed from that cited in (Kilic 2004) for heat transfer prediction of brake disc channels. Up to date, no equation of this type has been reported for similar purposes in brake disc convective heat transfer research.

8.7 Summary

The topics covered in this Chapter are as the main product of this research effort. The Chapter reviewed available data to classify the heat transfer behaviour of brake disc trapezoidal channels. It was concluded that because of the vent radial length, convective heat dissipation does not follow the behaviour as in fully thermally developed flows within ducts. A new method (Flow Index) for describing the convective heat transfer coefficient evolution within vents has been suggested. The Flow Index links the convective heat transfer ability to the ratio of the local channel width and radial location. Therefore, a fluid based property is related to channel geometry characteristics and the combination of results from various ventilation geometries has allowed to use $FI\,h_c$ charts as design tool. It is found that to hold or increase the channel convective heat transfer coefficient, the ratio $\frac{P_{cr}}{R_i}$=0.07→0.10 must be satisfied at or after the middle radius of the channel. Also, a ratio $\frac{P_{cr}}{R_i}$ ≈0.17 for the

channel inlet brings better results for the average initial heat transfer coefficient and allows management of channel cross section in radial direction.

Four new brake disc channel designs with improved convective heat transfer ability have been achieved. Two of these are design variants and complement the engineering produce of this research in ventilated brake discs convective cooling optimisation. Computational fluid dynamics simulations of the designs confirmed their cooling ability potential. One of these disc was manufactured and its cooling performance tested. The experimental heat transfer results versus those from the baseline brake disc prototype were substantially enhanced, and when the newly designed prototype (brake disc with D32 design) was compared against a high performance brake disc design similar to that in patent # US 7,100,748 B2, experimental data suggest that this research's design is better in terms of convective cooling ability.

Finally, a new theoretical expression has been suggested for Nusselt number prediction inside brake discs channel. Good predictions were obtained for 20-, 30- and 60-vane designs.

Chapter 9

Discussion

The discussion on brake disc convective heat dissipation follows from a summary of CFD based results at two angular speeds, 400 rpm and 800 rpm. Figure 9.1 shows a master chart of *disc convective* cooling rate (s^{-1}) versus torque required (pumping losses, τ_d in equation 5.11) at n=400rpm. Changes in convective cooling rate are represented in the horizontal axis and changes in required torque in the vertical axis. The changes are shown in percentages relative to the baseline brake disc (with 30 radial vanes). Discs located in the upper quadrants have better cooling rates than the baseline, those in the lower quadrants have poorer cooling rates. Discs in the left quadrants offer less resistance to rotation (and may pump less air) than those in the right side quadrants.

At n=400rpm the obvious winner is the 60-vane design with radial channels, with 21% higher cooling rate and about 6% higher rotational resistance, the disc is just 1% heavier than the baseline. Designs produced with the Flow Index technique (D30 and D32 and their variants) produce between 9% and 19% higher cooling rates at a cost of higher resistance (between 10% and 20%) and also higher disc mass (about 4.5%), D32 in backward rotation still produces 2% better cooling rate with 20% less torque. Pillared discs are the most efficient aerodynamically (32% and 41% less torque required than baseline), their cooling rates are about 6.5% higher with the same weight as the baseline. The behaviour of discs with the SV1 vane is linear with SV1 position, coming from low cooling rates to high cooling rates, all of them with less aerodynamic resistance. Discs with 20 and 45 vanes have poorer cooling rates and require less torque, while the 90-vane design on a wetted area basis has a higher cooling rate. None of the discs require higher torque to produce smaller cooling rates (lower right quadrant), this could be physically inconsistent.

Figure 9.2 shows the same scenario for n=800rpm. Significant differences exist for the group of discs designed following the Flow Index, they all have moved upward and slightly rightward increasing their convective cooling rate. The cooling rate of the 60-vane radial

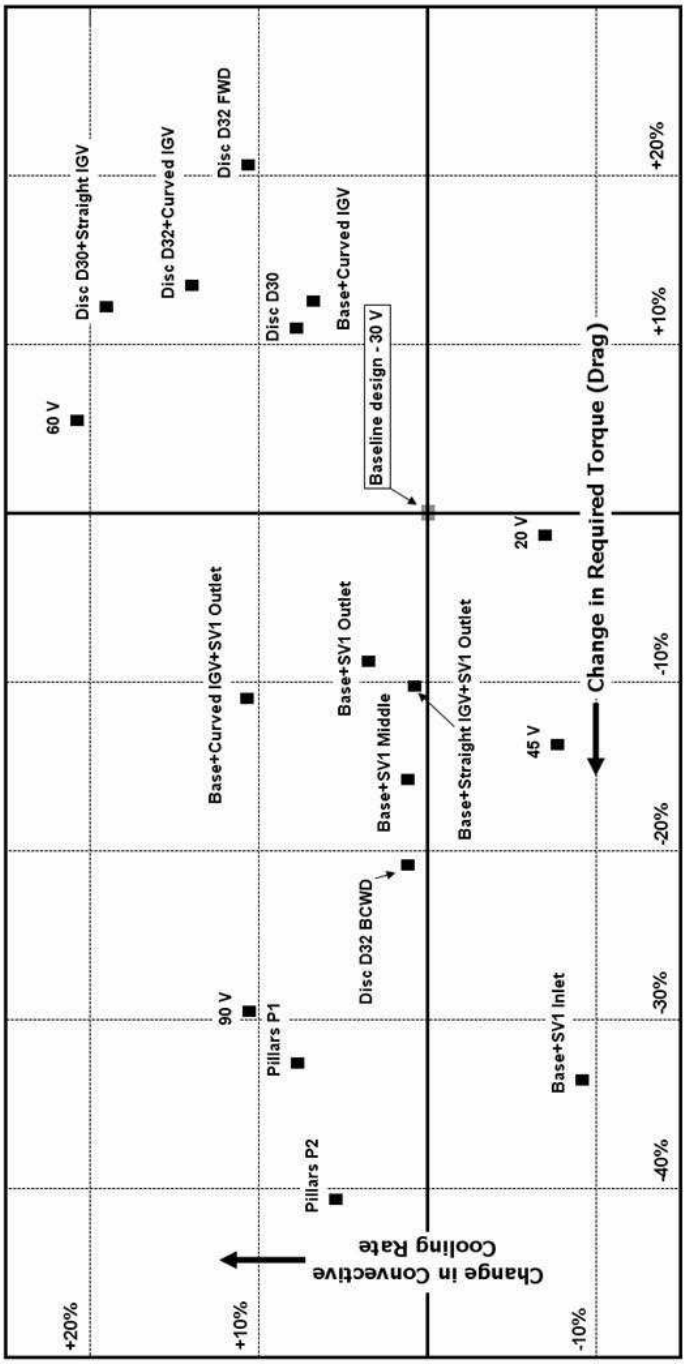

Figure 9.1: Ventilated brake disc master chart at 400 rpm.

channel design (60 V) has been overtaken by the D30+StraightIGV (drop shape IGV). It could be said that cooling ability of D30 and D32 discs increases with speed, while that from the 60-vane design decreases. The 20-vane design behaves similar to the baseline, however is lighter (5%) and although requires the same torque it pumps 7% less air, which can point to higher turbulence inside its channels. Heat dissipation rate from the 45-vane design does not change significantly and that of 90-vane design improves slightly. At n=800rpm the staggered pillar (P2) design retains its performance while the aligned pillar design (P1) losses cooling ability; they both remain with the lowest torque required due to poor air pumping. As for the baseline designs with SV1 vanes, the distance in cooling performance widens since the cooling rate of SV1-inlet design drops and that of SV1-outlet design enhances, approaching to the cooling rate of the SV1-outlet+curvedIGV. This can be understood as a loss of performance in the last one with speed.

It must be emphasised that the above results consider the ventilated brake disc rotating in free air, and as observed in Figure 9.2, designs developed using the Flow Index technique (D30, D32 and their variants) offer good suitability for scooping devices since their convective heat dissipation improves with increasing rotational speed and they have much better retention of h_c through the radius (see Figures 8.27 and 8.36). Another disc worth of mentioning and not included in the above charts is the Staggered Vane design which also has remarkable retention of h_c. In general, the master charts (with heat dissipation rates) are a complement for the Flow Index charts; the effects of vent design changes suggested by Flow Index charts can be evaluated in these.

Finally, a formal assessment of the production costs of the brake designs presented in this Thesis was not performed, (nor this subject was found in the technical literature). However, it is clear that brake discs are mass produced devices, and any design change must be carefully analysed. This research suggests that in the the evolution of a brake design, some of the parameters to be appropriately balanced with the market needs are: Technical Novelty, Power Dissipation vs Torque, Strength, NVH, Weight (unsprung, related to gyroscopic inertia), Manufacturing Cost and Product Demand. It is left to the interested reader or brake development leader to evaluate these parameters and conceal them with others required at the time, to make a final decision.

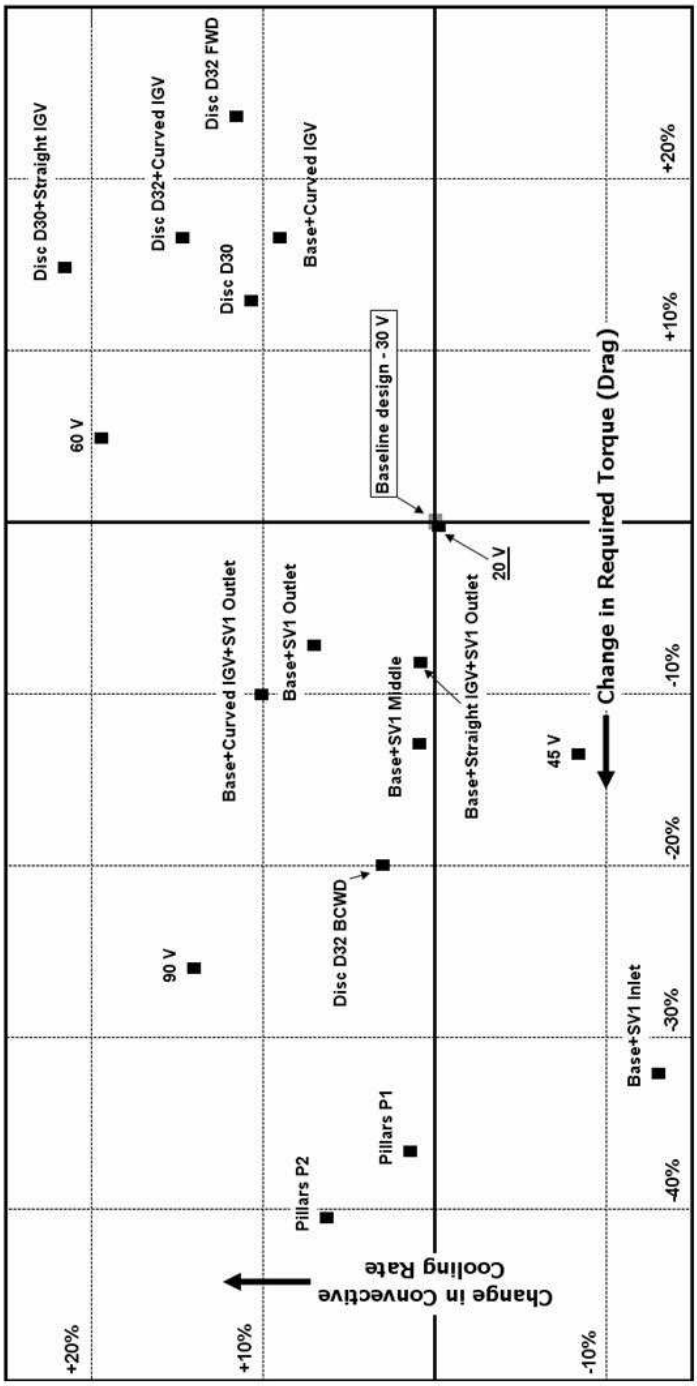

Figure 9.2: Ventilated brake disc master chart at 800 rpm.

Chapter 10

Conclusions and Future Work

The conclusions from the research in optimisation of convective heat dissipation from ventilated brake discs are as follows:

The modelling of the steady CFD and forced convective heat transfer in rotating ventilated brake discs with a stationary channel model is not appropriate since rotational effects are not accounted for. The best way is to use periodic (symmetric) boundary conditions in CFD models within a Rotating Frame of Reference.

The relevance of rotation (Rossby number) in channel airflow patterns is proportional to disc outer radius and angular speed. Also low angular speed in small brake discs will set natural convection (Buoyancy Index near to one), particularly at high disc-air temperature difference.

Remarkable correlation between experimental and numerical convective heat transfer coefficients was found using the lumped mass model with test data; and, the undisturbed (bulk) air temperature as reference value together with the $\kappa - \epsilon$ and Kader's (1981) model in the CFD simulations (mesh convergence checks are required to meet this degree of accuracy). Similarly, results from cooling tests using the original -one piece- brake (gray iron) and the DVB disc (aluminum vanes) correlated acceptably, therefore the DVB was ratified as an effective and affordable testing method for brake discs. Uncertainty ranges calculated serve to confirm these comparisons.

Regarding heat transfer coefficient experimental uncertainty, this is not only sensible to instrumentation accuracy, but rises with disc rotational speed.

Convective heat dissipation rates of discs with radial trapezoidal vanes or pillars are strongly driven by wetted area, with the product $h_c * A_w$ optimised because of this and not due to h_c. The optimum vane number is 60.

Typical heat transfer correlations for cylinder arrays fail to predict the behaviour of pillared designs. The highest heat transfer coefficients are located in the second row of pillars.

Brake discs with radial and cylindrical channels were found to have the lowest heat dissipation rates.

Channels designs with controlled airflow and heat transfer coefficient patterns were achieved, e.g. the SV1-mid, SV1-outlet and curved IGV1 and IGV2 designs. Swirled airflow and enhanced h_c in the suction region with the curved IGVs, and more homogeneous h_c distributions with the SV1-mid and SV1-outlet. This increased $h_c * A_w$. Besides designs with the SV1 vane have reduced torque requirements, i.e. less mass flow, than the baseline design. The best combination was IGV2+SV1-outlet.

Turbulent correlations for rotating solid discs in free air, e.g.: Dorfman (1963), need to be factored to correlate experimental and CFD results from ventilated brake discs, since they underpredict heat transfer coefficients.

Typically channel heat transfer coefficients tend to fall with increasing disc radius, and this is more pronounced for diverging sections (thermal entry effects). Also, heat transfer coefficients are very low in the suction region. The above, caused by local airspeed reduction and flow misalignment, was studied and integrated into a single number, the Flow Index, measuring flow behaviour (h_c or u) versus channel geometry and radial location (P_{cr}/R_i).

For trapezoidal channels FI drops constantly through the radius, nevertheless for staggered vanes or SV1 configurations this shows higher degree of stabilization through the radius. Two brake disc designs having curved (longer) channels with reduced entrance misalignment and P_{cr}/R_i=0.07 at mid swept radius, and ending with P_{cr}/R_i=0.07 to 0.10, promoted stable and high FI in the channel second half. The dissipation rates were (numerically and experimentally) higher than other discs.

Therefore, the FI constitutes an efficient way to analyse and optimise heat transfer coefficients in ventilated brake discs.

The gap wheel-brake in railway WMD enhance air mixing between channels, promoted by secondary recirculation. Gap closure deteriorates heat dissipation and this is mainly improved by wetted area.

A new correlation to predict Nusselt numbers from rotating brake disc channels was developed following Kilic's (2004) work for stationary circular ducts. The results obtained with this new correlation predicted acceptably Nu_{ch} in brake discs with 20, 30 and 60 vanes, while those from 45 and 90 vanes were overpredicted.

10.1 Future Work

Following the research described in this thesis, future activities are envisaged to reinforcing the frame of turbulence models used in brake disc convective cooling prediction. The $\kappa - \epsilon$ model used here is a eddy viscosity technique, in which turbulent kinetic energy and dissipation rate are used to predict the former. However flow recirculation and high rotational effects pose a degree of numerical uncertainty in the results. An option to explore using nonlinear eddy viscosity models (algebraic Reynold stress models) is open from this work. Heat transfer coefficient distributions in the leading side of the channel must be observed and the results from this work can be used to validate these.

Extension of domain physics to include natural convection at low angular speeds (e.g.:100 rpm) is a complementary task to undertake under the frame of this thesis. A bigger CFD model and Boussinesq density approximation are necessary to model.

Alternative CFD activities may look into scooping devices design. It is suggested that rather than modelling complex and costly geometries representing the scoop and the brake disc, an additional *massflow* boundary condition is added to the CFD models created in this research. This new BC would be located *near* the vent inlets. The parameters to investigate would be: *a*)massflow and its direction, *b*)axial distance of the new BC to the channel inlet and, c)effect of *a*) and *b*) on convective heat transfer coefficients with angular speed. Developing new correlations for changes in average heat transfer coefficient will definitively serve as useful tool in automotive underframe design. A second stage of the research would look into scooping devices design to ensure the required massflow and direction.

The CFD models developed in this research can be altered by adding a *solid* disc geometry mesh and in this way attempt to simulate brake disc transient cooling (conjugate heat transfer). The CFD model will be formed of two domains (solid and fluid). This would help to correlate disc surface temperature distributions as result of cooling (using thermal imaging), and would improve experimental procedures.

Casting of the novel brake disc designs developed in this thesis can be commissioned and the prototypes used for a more complete experimental investigation, followed with industrial application.

Advanced experimental techniques are still required to correlate channel heat transfer coefficient distributions given by CFD and by empirical equations as that developed in this research.

Appendix A

Brake Disc Test Program

Table A.1: Testing Summary.

Brake disc cooling	Speed [rpm]
Baseline cast iron brake	100 - 1200
Curved vane cast iron brake	0 - 800
Baseline detachable vane brake	200 - 800
SV1 at inlet, detachable vane brake	0 - 1200
SV1 at outlet, detachable vane brake	100 - 800
Baseline detachable vane brake, blocked channels	200 - 800
Outboard side disc plate	200 - 800
D32 final vent design, detachable vane brake (Forward and Backward rotations)	100 - 800
Torque measurement	Speed [rpm]
Shaft- no disc	100 - 800
Baseline detachable vane brake	100 - 800
Curved vane cast iron brake	100 - 800
D32 final vent design, detachable vane brake (Forward and Backward rotations)	100 - 800
Hot Wire Anemometry	Speed [rpm]
Baseline detachable vane brake	200

Table A.2: Coefficients for K-thermocouple function behavior

Temperature Range [^{o}C]	-200< Θ <0	0< θ <500	500< Θ <1372
Voltage [mV]	-5.891< E <0	0< E <20.644	20.644< E <54.886
c_0	0.0000000	0.0000000	-1.318058e2
c_1	25.173462	25.08355	48.30222
c_2	-1.1662878	7.860106e-2	-1.646031
c_3	-1.0833638	-2.503131e-1	5.464731e-2
c_4	-8.977354e-1	8.31527e-2	-9.650715e-4
c_5	-3.7342377e-1	-1.228034e-2	8.802193e-6
c_6	-8.6632643e-2	9.804036e-4	-3.11081e-8
c_7	-1.0450598e-2	-4.41303e-5	0.0000000
c_8	-5.1920577e-4	1.057734e-6	0.0000000
c_9	0.0000000	-1.0527555e-8	0.0000000

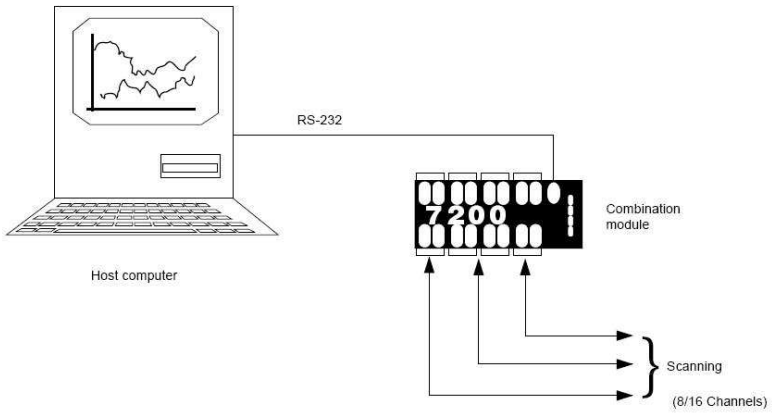

Figure A.1: 7220 RS A/D 16 channel single module connection.

Appendix B

Experimental heat transfer coefficients and uncertainties

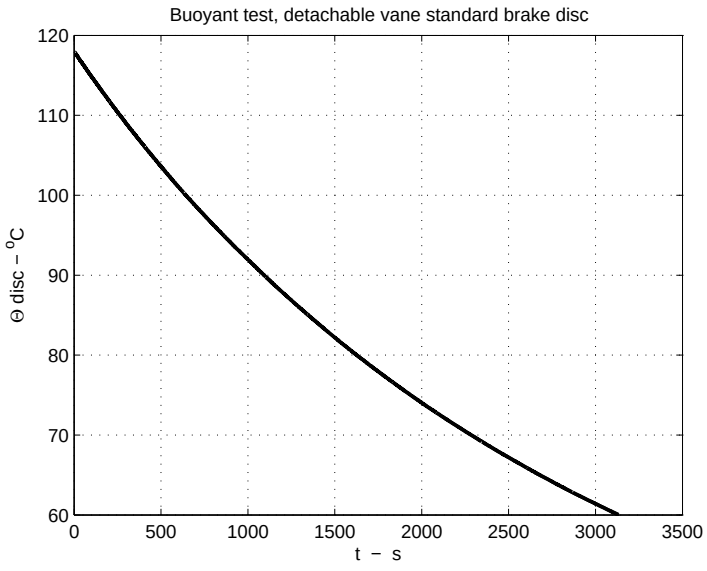

Figure B.1: Cooling temperatures from natural convection test, DVB, $\delta_\Theta \approx \pm 0.8^o C$.

Table B.1: Experimental heat transfer coefficients from tests performed with cast iron brake disc (baseline model). Temperature range: 120^{o}C to 60^{o}C.

n	$\overline{\Theta_1}$	$\overline{\Theta_2}$	$\overline{\Theta_\infty}$	Δt	b_t	$\overline{h_{d_t}}$	$\overline{h_{d_r}}$	$\overline{h_{d_c}}$
$[rpm]$	$[^o\text{C}]$			$[s]$	$[s^{-1}]$	$[W/m^2K]$		
100	120.9	60.0	19.2	1735.5	5.257x10^{-04}	11.5	2.1	9.4
200	120.9	60.0	20.8	1185.0	7.906x10^{-04}	17.3	2.1	15.2
400	120.9	60.0	22.6	776.0	1.245x10^{-03}	27.2	2.1	25.1
600	120.9	60.0	21.1	536.5	1.753x10^{-03}	38.4	2.1	36.3
800	120.8	60.1	21.5	441.5	2.141x10^{-03}	46.8	2.1	44.7
1200	120.7	60.1	20.3	335.5	2.764x10^{-03}	60.5	2.1	58.4

Table B.2: Experimental heat transfer coefficients from tests performed with cast iron brake disc (baseline model), disregarding mass from brake disc hub. Temperature range: 120^{o}C to 60^{o}C.

n	$\overline{h_{d_t}}$	$\overline{h_{d_r}}$	$\overline{h_{d_c}}$
$[rpm]$	$[W/m^2K]$		
100	11.3	1.9	9.4
200	16.9	1.9	15.0
400	26.7	2.0	24.8
600	37.7	1.9	35.7
800	45.9	1.9	44.0
1200	59.4	1.9	57.4

Table B.3: Experimental heat transfer coefficients from tests performed with cast iron brake disc (baseline model). Temperature range:100^{o}C to 60^{o}C.

n	$\overline{\Theta_1}$	$\overline{\Theta_2}$	$\overline{\Theta_\infty}$	Δt	b_t	$\overline{h_{d_t}}$	$\overline{h_{d_r}}$	$\overline{h_{d_c}}$
$[rpm]$	$[^o\text{C}]$			$[s]$	$[s^{-1}]$	$[W/m^2K]$		
100	100.0	60.0	19.2	1342	$5.0832\text{x}10^{-04}$	11.1	2.4	8.7
200	100.1	60.0	20.8	882.5	$7.9662\text{x}10^{-04}$	17.4	2.4	15.0
400	100.1	60.0	22.6	592.5	$1.2285\text{x}10^{-03}$	26.9	2.4	24.5
600	100.1	60.0	21.1	404.0	$1.7506\text{x}10^{-03}$	38.3	2.4	35.9
800	100.0	60.1	21.5	333.5	$2.1301\text{x}10^{-03}$	46.6	2.4	44.2
1200	100.0	60.1	20.3	261.5	$2.6640\text{x}10^{-03}$	58.3	2.4	55.9

Table B.4: Experimental heat transfer coefficients from tests performed with cast iron brake disc (baseline model), disregarding mass from brake disc hub. Temperature range:100^{o}C to 60^{o}C.

n	$\overline{h_{d_t}}$	$\overline{h_{d_r}}$	$\overline{h_{d_c}}$
$[rpm]$	$[W/m^2K]$		
100	10.9	2.2	8.5
200	17.1	2.2	14.7
400	26.4	2.2	24.0
600	37.6	2.2	35.2
800	45.7	2.2	43.3
1200	57.2	2.2	54.8

Table B.5: Experimental heat transfer coefficients from tests performed with detachable vane brake disc (baseline model). Temperature range: 120^{o}C to 60^{o}C.

n	$\overline{\Theta_1}$	$\overline{\Theta_2}$	$\overline{\Theta_\infty}$	Δt	b_t	$\overline{h_{d_t}}$	$\overline{h_{d_r}}$	$\overline{h_{d_c}}$
$[rpm]$	$[^o$C$]$			$[s]$	$[s^{-1}]$	$[W/m^2K]$		
100	115.9	60.0	21.6	1552.7	5.7843x10^{-04}	12.0	2.1	9.9
200	120.7	60.0	21.7	1104.0	8.6000x10^{-04}	17.8	2.1	15.7
400	120.9	60.0	21.8	662.0	1.4394x10^{-03}	29.8	2.1	27.7
600	120.9	60.0	22.8	503.5	1.9238x10^{-03}	39.8	2.1	37.7
800	120.7	60.0	22.4	401.0	2.3941x10^{-03}	49.6	2.1	47.5
-	117.9	60.0	19.2	3134.0	2.8187x10^{-04}	5.8	2.1	3.8

Table B.6: Experimental heat transfer coefficients from tests performed with detachable vane brake disc (baseline model), disregarding mass from brake disc hub. Temperature range: 120^{o}C to 60^{o}C.

n	$\overline{h_{d_t}}$	$\overline{h_{d_r}}$	$\overline{h_{d_c}}$
$[rpm]$	$[W/m^2K]$		
100	11.6	1.9	9.7
200	17.3	1.9	15.3
400	28.9	1.9	27.0
600	38.7	1.9	36.7
800	48.1	1.9	46.1
-	5.7	1.9	3.8

Table B.7: Experimental heat transfer coefficients from tests performed with detachable vane brake disc. Temperature range:100^{o}C to 60^{o}C.

n	$\overline{\Theta_1}$	$\overline{\Theta_2}$	$\overline{\Theta_\infty}$	Δt	b_t	$\overline{h_{d_t}}$	$\overline{h_{d_r}}$	$\overline{h_{d_c}}$
$[rpm]$	$[^o$C$]$			$[s]$	$[s^{-1}]$	$[W/m^2K]$		
100	100.9	60.0	21.6	1257.5	5.7679x10^{-04}	11.9	2.0	9.9
200	100.9	60.0	21.7	856.0	8.4806x10^{-04}	17.6	2.0	15.5
400	100.9	60.0	21.7	509.5	1.4278x10^{-03}	29.6	2.0	27.6
600	100.9	60.0	22.7	392.5	1.8901x10^{-03}	39.1	2.0	37.1
800	100.9	60.0	22.4	312.0	2.3566x10^{-03}	48.8	2.0	46.8
-	100.9	60.0	19.2	2530.8	2.7445x10^{-04}	5.7	2.0	3.7

Table B.8: Experimental heat transfer coefficients from tests performed with detachable vane brake disc (baseline model), disregarding mass from brake disc hub. Temperature range:100^{o}C to 60^{o}C.

n	$\overline{h_{d_t}}$	$\overline{h_{d_r}}$	$\overline{h_{d_c}}$
$[rpm]$	$[W/m^2K]$		
100	10.9	1.8	8.5
200	17.1	1.9	14.7
400	26.4	1.9	24.0
600	37.6	1.9	35.2
800	45.7	1.9	43.3
-	5.8	1.9	3.9

Table B.9: Uncertainties of raw data.

δ_Θ	$\delta_{\Delta t}$	δ_{m_d}	$\delta_{C_{p_d}}$	δ_ς
$[^o$C$]$	$[s]$	$[kg]$	$[J/kg^oK]$	$[m^2]$
$\pm$ 0.8	$\pm$ 0.5	$\pm$ 0.5	$\pm$ 20.0	$\pm$ 10.0

Table B.10: Uncertainty of heat transfer coefficient (derivatives evaluation).

n [rpm]	ς	$\frac{\partial \overline{h_{d_t}}}{\partial \overline{\Theta_2}}$	$\frac{\partial \overline{h_{d_t}}}{\partial \overline{\Theta_1}}$	$\frac{\partial \overline{h_{d_t}}}{\partial \overline{\Theta_\infty}}$	$\frac{\partial \overline{h_{d_t}}}{\partial \Delta t}$	$\frac{\partial \overline{h_{d_t}}}{\partial \varsigma}$
100	21881.6	-0.309	0.124	0.185	0.007	0.001
200	21881.6	-0.471	0.184	0.286	0.015	0.001
400	21881.6	-0.753	0.287	0.467	0.035	0.001
600	21881.6	-1.047	0.409	0.638	0.072	0.002
800	21881.6	-1.284	0.499	0.785	0.106	0.002
1200	21881.6	-1.642	0.650	0.992	0.180	0.003

Table B.11: Calculation of uncertainty on heat transfer coefficient: Squared contributions and final uncertainty of heat transfer coefficient.

n [rpm]	$\left(\frac{\partial \overline{h_{d_t}}}{\partial \overline{\Theta_2}}\delta_\Theta\right)^2$	$\left(\frac{\partial \overline{h_{d_t}}}{\partial \overline{\Theta_1}}\delta_\Theta\right)^2$	$\left(\frac{\partial \overline{h_{d_t}}}{\partial \overline{\Theta_\infty}}\delta_\Theta\right)^2$	$\left(\frac{\partial \overline{h_{d_t}}}{\partial \Delta t}\delta_t\right)^2$	$\left(\frac{\partial \overline{h_{d_t}}}{\partial \varsigma}\delta_\varsigma\right)^2$	$\pm\delta\overline{h_{d_t}}$
100	0.061	0.010	0.022	0.0	0.0	0.30
200	0.142	0.022	0.052	0.0	0.0	0.46
400	0.363	0.053	0.139	0.0	0.0	0.75
600	0.702	0.107	0.261	0.001	0.0	1.04
800	1.055	0.159	0.394	0.003	0.0	1.27
1200	1.726	0.270	0.630	0.008	0.001	1.62

Table B.12: Uncertainty of convection heat transfer coefficients using the cast iron brake disc.

n [rpm]	$\pm\delta\overline{h_{d_c}}$ $\Uparrow$Hub, W/m^2K		$\pm\delta\overline{h_{d_c}}$ $\Downarrow$Hub, W/m^2K	
	Range 1	Range 2	Range 1	Range 2
100	0.30	0.39	0.30	0.38
200	0.46	0.62	0.46	0.61
400	0.75	0.97	0.73	0.95
600	1.04	1.36	1.02	1.34
800	1.27	1.67	1.25	1.64
1200	1.62	2.07	1.59	2.03

*Range 1: 120^{o}C to 60^{o}C; Range 2: 100^{o}C to 60^{o}C

Table B.13: Uncertainty of convection heat transfer coefficients using the detachable vane brake disc.

n [rpm]	$\pm\delta\overline{h_{d_c}}$ $\Uparrow$Hub, W/m^2K		$\pm\delta\overline{h_{d_c}}$ $\Downarrow$Hub, W/m^2K	
	Range 1	Range 2	Range 1	Range 2
100	0.57	0.70	0.50	0.61
200	0.8	1.03	0.71	0.91
400	1.34	1.73	1.18	1.52
600	1.81	2.31	1.60	2.03
800	2.26	2.87	1.99	2.53
Bouyant	0.26	0.33	0.23	0.29

*Range 1: 120^{o}C to 60^{o}C; Range 2: 100^{o}C to 60^{o}C

Appendix C

Vents Researched: Complementary Results

Complementary postprocessing for Chapter 6. The brake disc geometries rotate about $+z$.

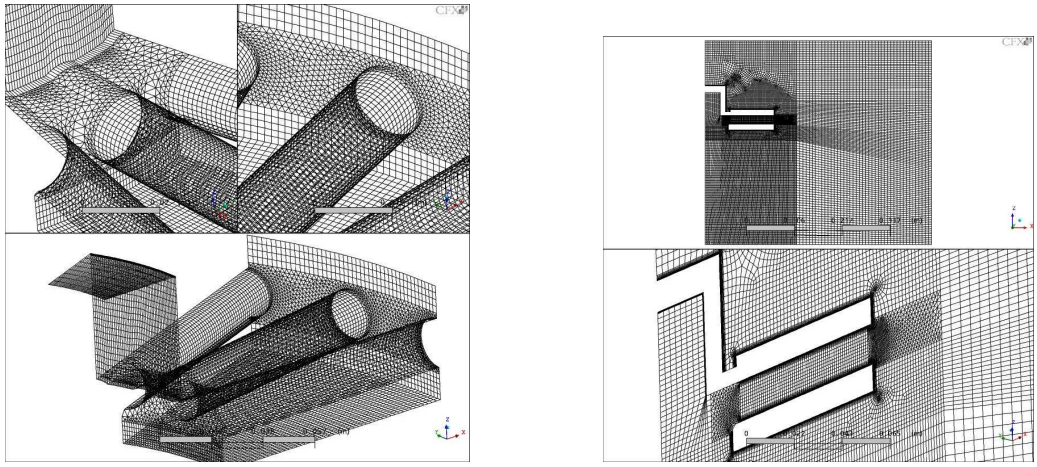

Figure C.1: CFD model of brake disc with cylindrical channels.

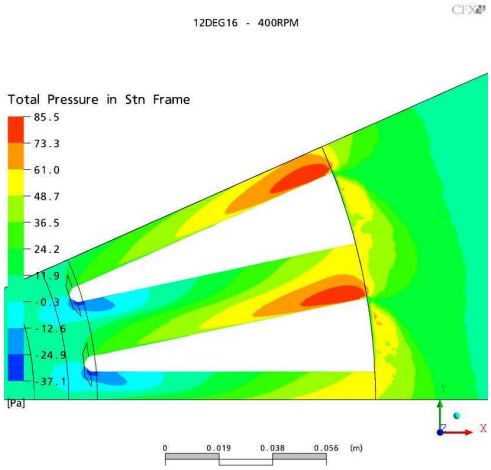

Figure C.2: Cylindrical channels. Contours of total pressure, n=400rpm.

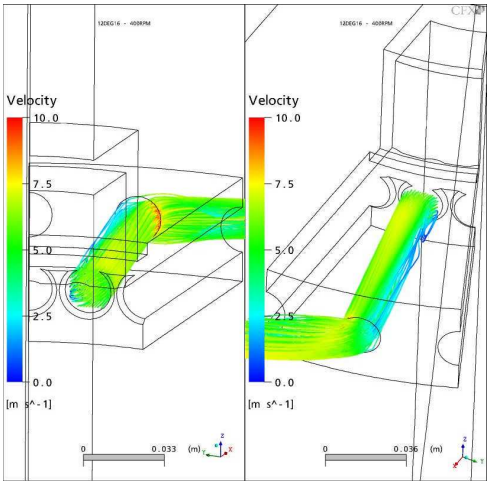

Figure C.3: Brake disc with 30 cylindrical channels, n=400rpm.

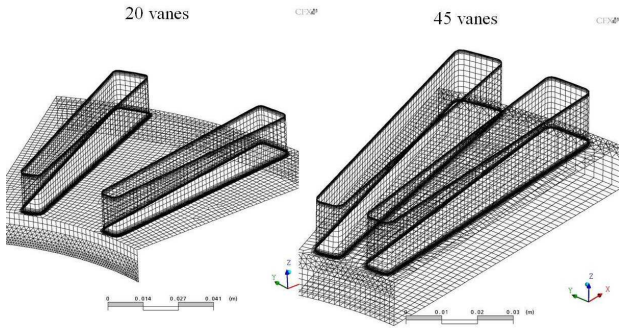

Figure C.4: Mesh details of 20 and 45-vane designs.

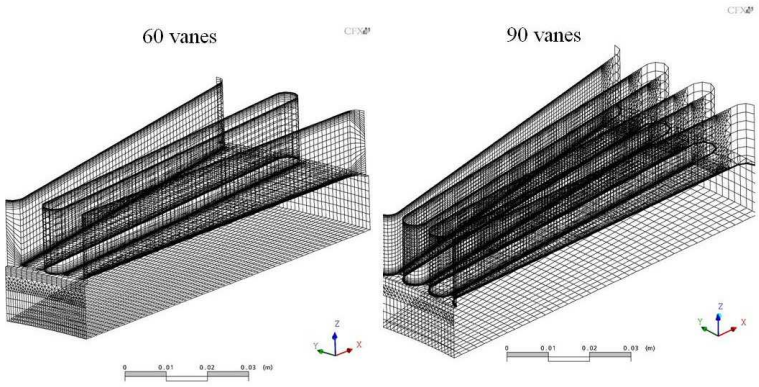

Figure C.5: Mesh details of 60 and 90-vane designs.

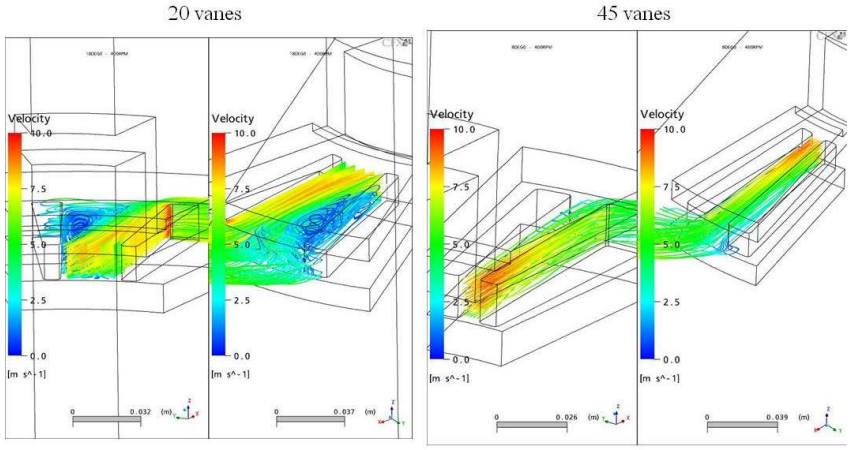

Figure C.6: Streamlines, 20 and 45-vane designs at n=400rpm.

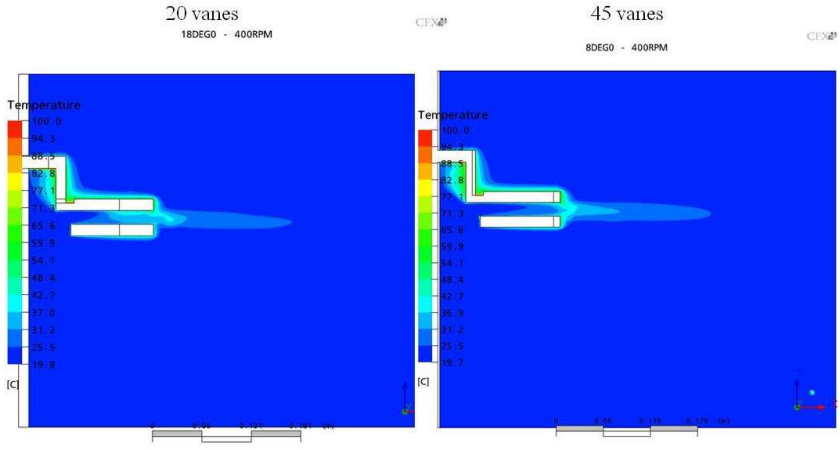

Figure C.7: Air temperature contours across channels, 20 and 45-vane designs, n=400rpm.

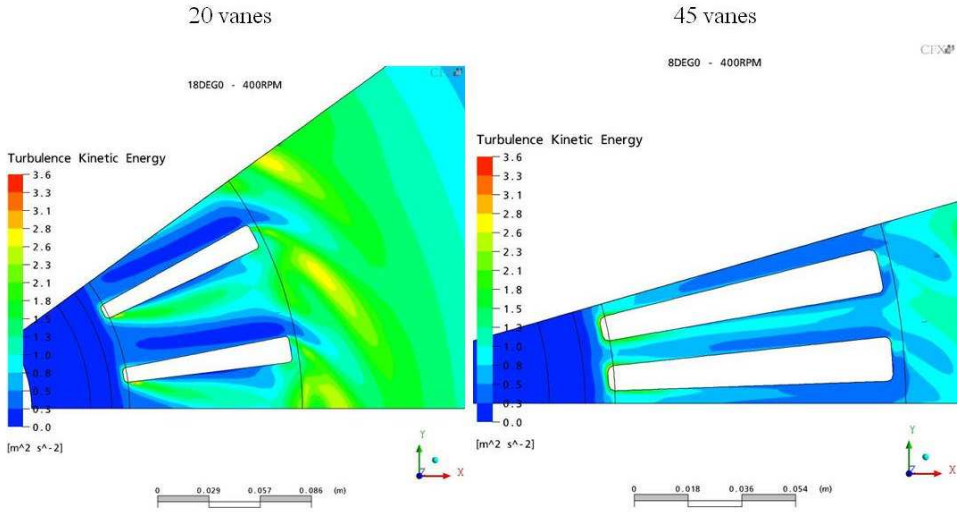

Figure C.8: Turbulent kinetic energy, 20 and 45-vane designs, n=400rpm.

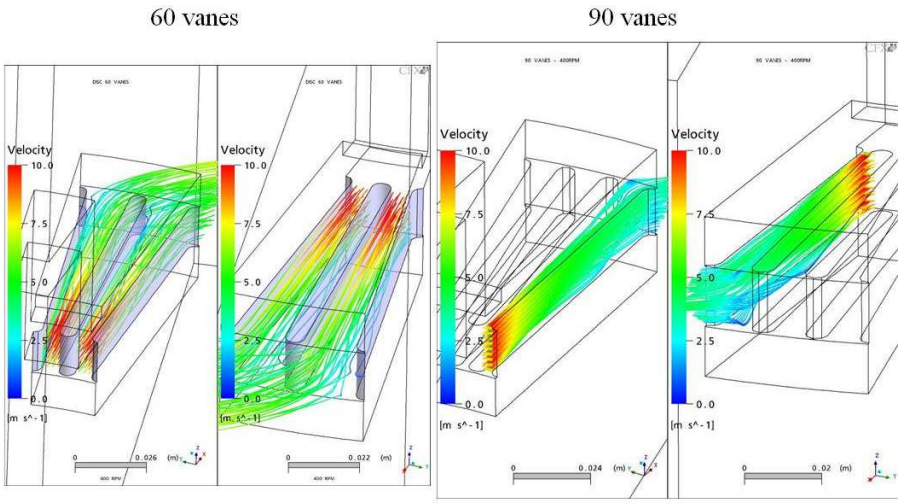

Figure C.9: Streamlines in channels, 60 and 90-vane designs, n=400rpm.

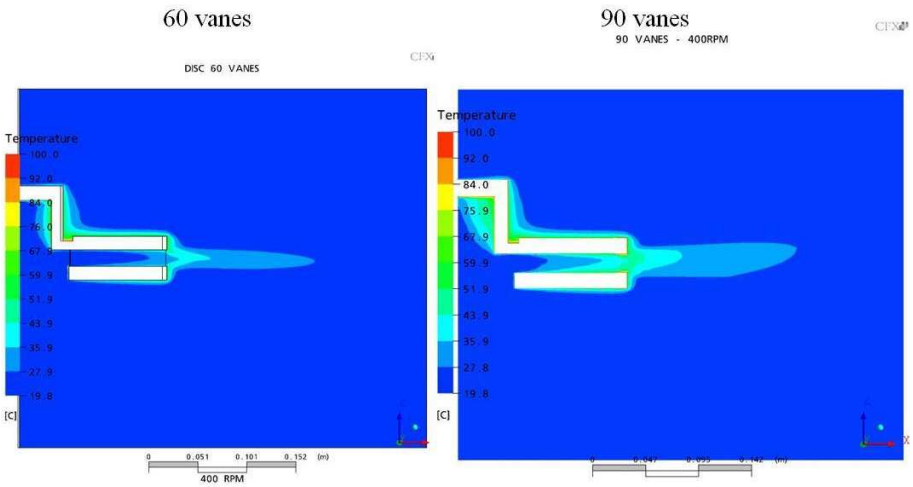

Figure C.10: Air temperature contours across channels, 60 and 90-vane designs, n=400rpm.

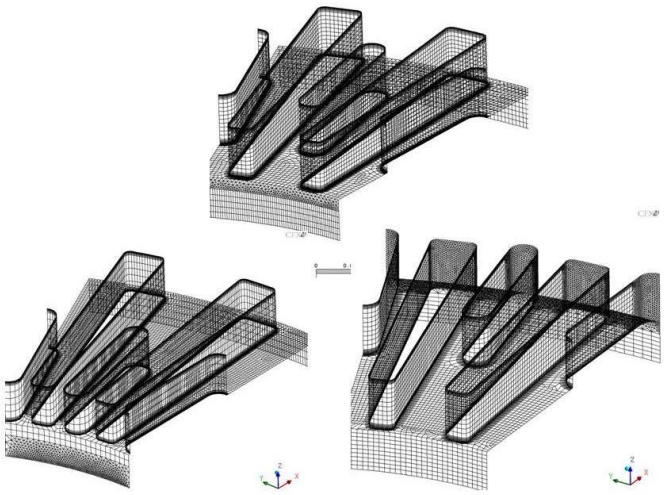

Figure C.11: Mesh details, designs with the SV1 vane in the channel.

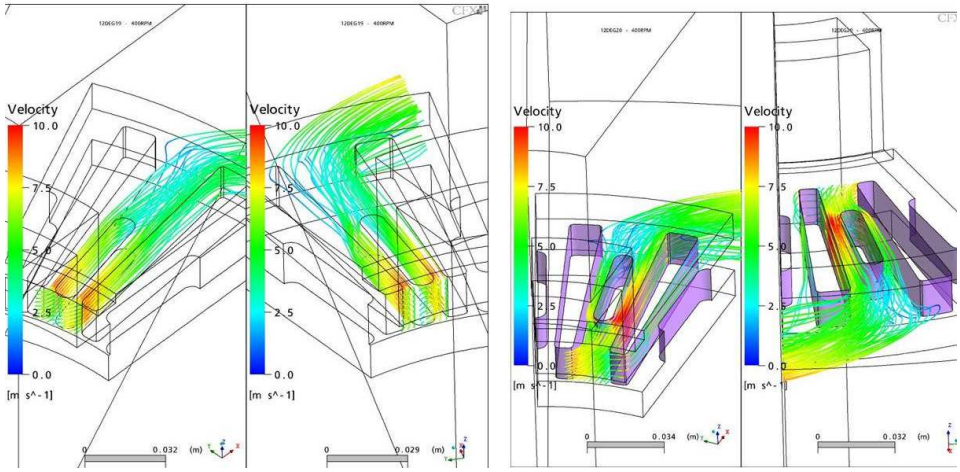

Figure C.12: Streamlines, SV1 vane at the inlet (left) and at the middle (right), n=400rpm.

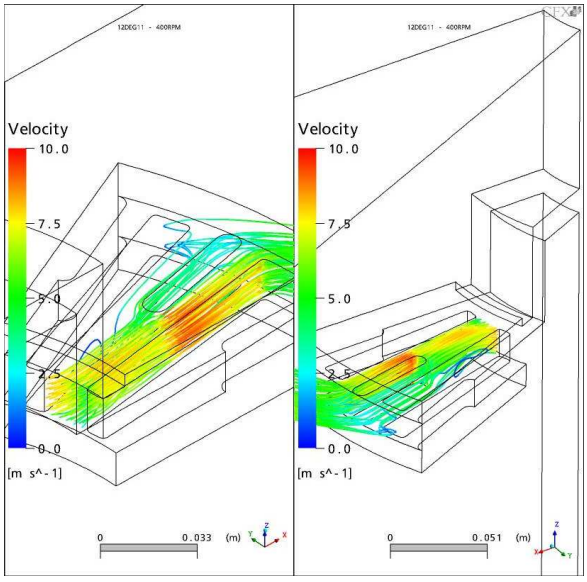

Figure C.13: Streamlines, SV1 vane at the outlet, n=400rpm.

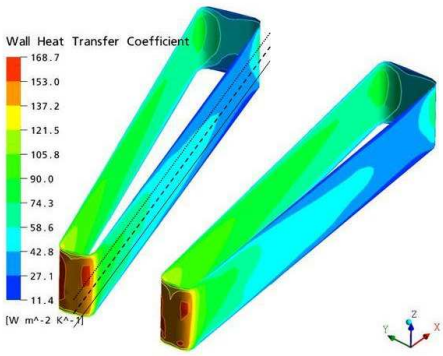

Figure C.14: Lines chosen for near wall airflow analysis, n=800rpm.

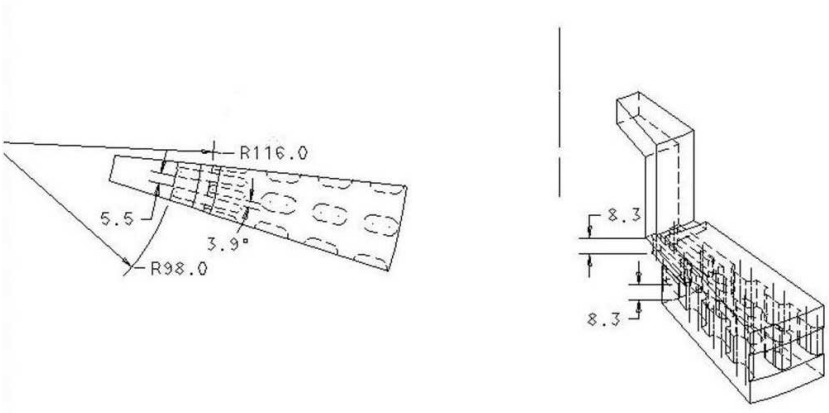

Figure C.15: Pillared disc in configuration 3.

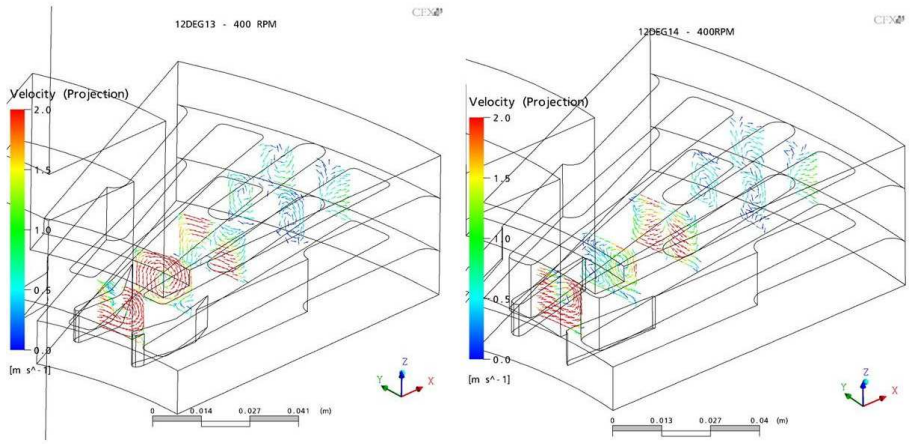

Figure C.16: Secondary flow vectors: IGV2+SV1 in the left and IGV3+SV1 in the right.

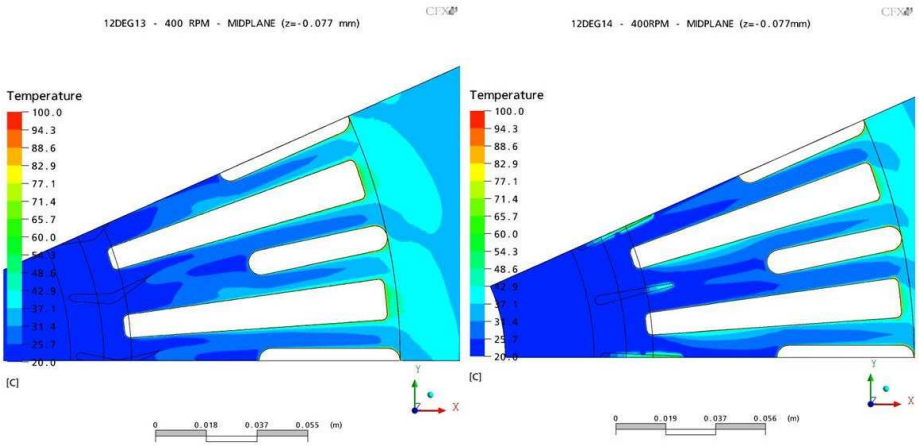

Figure C.17: Air temperature patterns in planes beneath IGVs, IGV2+SV1 (left) and IGV3+SV1 (right), n=400rpm.

Appendix D

Wheel Mounted Brakes, Complementary Results

Complementary postprocess of CFD simulations performed with railway brake wheel mounted designs, Chapter 7. The results should be considered for geometries rotating about $+z$.

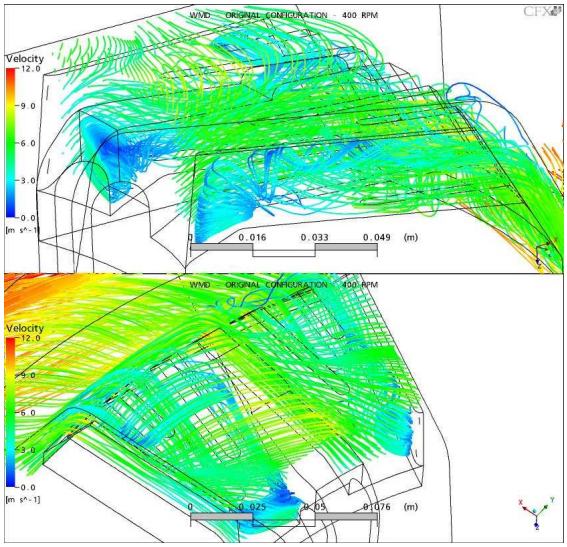

Figure D.1: Streamlines (velocity) in rotating frame around the WMD rotating at 400 rpm.

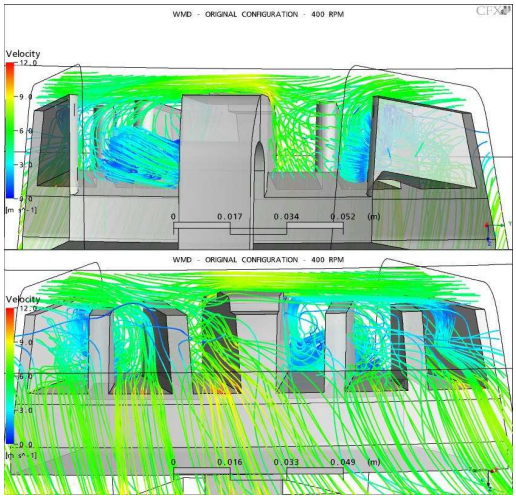

Figure D.2: Streamlines (velocity) in rotating frame around the WMD rotating at 400 rpm.

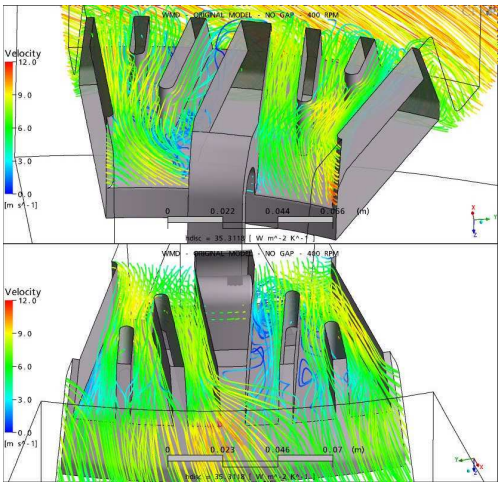

Figure D.3: Streamlines (velocity) in rotating frame in the WMD without gap rotating at 400 rpm.

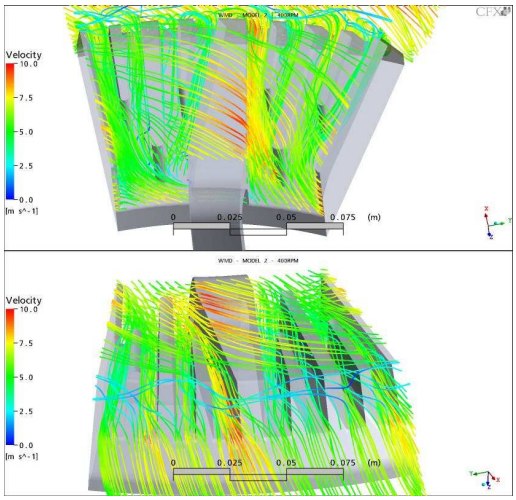

Figure D.4: Streamlines in rotating frame in the new design of WMD (gap=4mm) rotating at 400 rpm.

Appendix E

Glossary of Terms

A/D	Analogue to Digital
CAD	Computer Aided Design
CFD	Computer Fluid Dynamics
CTA, CCA	Constant Temperature (Current) Anemometer
CV	Commercial Vehicle
DVB	Detachable Vane Brake
DoE	Design of Experiments
FEA	Finite Element Analysis
HRS	High Resolution Scheme
IGV	Inlet Guide Vane
NVH	Noise, Vibration and Harshness
PIV	Particle Image Velocimetry
RANS	Reynolds Averaged Navier Stokes
RFR	Rotating Frame of Reference
SV	Small Vane
TCR	Thermal Contact Resistance
TGV	Train à Grande Vitesse
UDS	Upwind Differencing Scheme
WMD	Wheel Mounted Disc

Bibliography

Abbas S. A., Cubitt N. J., Hooke, C. J. (1969). Temperature distributions in disc brakes. *Proc. Inst. Mech. Engrs.*. 184, 2A, p. 1–6.

ANSYS-CFX Solver Theory (July 2005)

Antanaitis D., Rifici A. (2006). The effect of rotor crossdrilling on brake performance SAE Technical Papers 2006-01-0691.

Aron W. & Colombo G.(163). Controlling factors of thermal contact conductance across bolterd joints in a vacuum environment. *ASME* Paper No. 63-WA-196. Cited in

Fletcher L. S., Peterson G. P., Madhusudana C. V. Groll E.(1990). Constriction resistance through bolted and riveted joints. *Journal of Heat Transfer, Trans. ASME.* 112 (4), p. 857–863.

Aus der Wiesche S. (2002). Heat transfer and thermal behavior of a rotating disk passed by a planar air stream. *Forschung im Ingenieurwesen.* 67, Springer-Verlag 2002 DOI 10.1007/s10010-002-0091-2, p. 161–174.

Balakin V. A., Sergienko V. P., Lysenok Y. V.(2004). Design optimisation of car ventilated brakes. *Journal of Friction and Wear.* 25 (5), p. 19–25.

Barigozzi G., Cossali G. E., Perdichizzi A., Lorenzo S., Pacchiana P. (2003). Experimental investigation of the aero-thermal characteristics at the exit of an automotive vented brake disc SAE Technical Papers 2003-01-3338.

Bejan A. (2004). *Convection Heat Transfer.* John Wiley & Sons, Inc. ISBN 0471271500

Bendat J. S., Piersol A. G. (1993). *Engineering Applications of Correlation and Spectral Analysis.* 2nd Edition. John Wiley & Sons, Inc. ISBN 0471570559

Bernard P. S., Wallace J. M. (2004). *Turbulent Flow, Analysis, Measurement and Prediction.* John Wiley & Sons, Inc. ISBN 0471332194

Bruun H. H. (2004). *Hot-wire anemometry: principles and signal analysis* . Oxford University Press, 1995. ISBN 0198563426

Cobb E. C., Saunders O. A. (1956). Heat transfer from a rotating disc *Proc. R. Soc. Part A*. 236, p. 343–351.

Daily J. W., Harleman D. R. F. (1966). *Fluid Dynamics*. Addison-Wesley Publishing Company Inc.

Davidson P. A. (2004). *Turbulence, an Introduction for Scientist and Engineers*. Oxford University Press. ISBN 019852948

Davies, T. W. (1985). Static and dynamic response of a hot-wire anemometer. *International Journal of Heat and Fluid Flow*. 6 3, p. 226.

Davies, T. W. (1986). Modelling the response of a hot-wire anemometer. *Applied Mathematical Modelling*. 10 4, p. 256–261.

Dhaubhadel M. N. (1996). Review: CFD applications in the automotive industry. *Journal of Fluids Engineering*. 118, p. 647–653.

Dorfman L. A. (1963). *Hydrodynamic resistance and the heat loss of rotating solids*. Oliver & Boyd, Edinburgh.

Dunn P. F. (2005). *Measurement andData Analysis for Engineering and Science*. McGraw-Hill Series in Mechanical Engineering. ISBN 0072825383.

Dutta S., Andrews M. J., Han J. C. (1996). Prediction of turbulent heat transfer in rotating smooth square ducts. *International Journal of Heat and Mass Transfer*. 39 12, p. 2505–2514.

Eisengräber R., Grochowicz J., Schuster M., Augsburg K., Koch L.(1999). Comparison of different methods for the determination of the friction temperature of disc brakes. *SAE International Congress and Exposition, Detroit Michigan*. March1–4, 1995. SAE Technical Papers 1999-01-0138.

Eck B. (1973). *Fans, Design and Configuration of Centrifugal, Axial-Flow and Cross-Flow Fans*. Pergamon Press. ISBN 0080158722.

Eriksson M. (2000). *Friction and Contact Phenomena of Disc Brakes Related to Squeal*. PhD Dissertation, 2000. Uppsala University.

Fletcher L. S., Peterson G. P., Madhusudana C. V. Groll E.(1990). Constriction resistance through bolted and riveted joints. *Journal of Heat Transfer, Trans. ASME.* 112 (4), p. 857–863.

Galindo-López C. H. & Tirović M. (2007). Airflow and heat dissipation of commercial vehicle brake discs In EAEC2007 11th European Automotive Congress. Budapest, Hungary.

Gmelin E., Asen-Palmer M., Reuther M., Villar R.(1999). Thermal boundary resistance of mechanical contacts between solids at sub-ambient temperatures. *Journal of Physics (Appl. Phys.)* 32, p. R19–R43.

Greitzer E.M., Tan C.S., Graf M.B. (2003). *Internal flow: Concepts and applications*. (1^{st} ed), Cambridge University Press. ISBN 0521343933

Johnson D. A., Sperandei B. A, Gilbert R.(2003). Analysis of the flow through a vented automotive brake rotor. *Journal of Fluids Engineering* 215, p. 979–985.

Incropera F. P., DeWitt D.P. (2002). *Introduction to Heat Transfer*. (4^{th} ed), Wiley. ISBN 0471386499

Industrial Measurements Ltd (*www.indmeas.co.uk*)

Ito Y., Toyoda J., Negata S.(1979). Interface pressure distribution in a bolt-flange assembly. *ASME Journal of Mechanical Design* 101)2), p. 330–337. Cited in

Fletcher L. S., Peterson G. P., Madhusudana C. V. Groll E.(1990). Constriction resistance through bolted and riveted joints. *Journal of Heat Transfer, Trans. ASME.* 112 (4), p. 857–863.

Kader B. A. (1979). Temperature and concentration profiles in fully turbulent boundary layers. *Int. Journal of Heat and Mass Transfer.* 41 (9), p. 1541–1544.

Kays W. M., Crawford M. E., Weigand B. (2005). *Convective Heat and Mass Transfer.* McGraw Hill. New York. ISBN 0071238298

Kilic M. (2004). Determination of heat transfer rate and Nusselt number on the thermal-entry region in ducts. *Int. Comm. Heat and Mass Transfer.* 31 (2), p. 181–190.

Kreith F., Bohn M. S. (2001). *Principles of Heat Transfer*. (6^{th} ed), Brooks/Cole, Inc. ISBN 0534375960

Krüseman R., Schmidt G. (1995). Analysis and optimization of disc brake cooling via computational fluid dynamics In *Advancements in ABS/TCS and Brake Technology, SAE International Congress and Exposition, Detroit Michigan.* February 27–March 2, 1995. SAE Technical Papers 950791, p. 61–67.

Limpert R. (1975). The thermal performance of automotive disc brakes In *Automobile Engineering Meeting, Detroit Michigan.* October 13–17, 1975. SAE Technical Papers 750873.

Limpert R. (1975). Cooling analysis of disc brake rotors In *Truck Meeting, Philadelphia, Pa.* SAE Technical Papers 751014.

Limpert R. (1999). *Brake Design and Safety.* (2^{nd} ed), SAE, Inc. ISBN 1560919159

Mackin T. J. *et al* (2002). Thermal cracking in disc brakes. *Engineering Failure Analysis.* 9, p. 63–76.

Moffat, Robert J. (1988). Using uncertainty analysis in the planning of an experiment. *Journal of Fluids Engineering.* 107, p. 173–182.

Moffat, Robert J. (1985). Describing the uncertainties in experimental results. *Experimental Thermal and Fluid Science.* 1, p. 249–266.

Morgan S. & Dennis R. W. (1972). A theoretical prediction of disc brake temperatures and a comparison with experimental data SAE Technical Papers 720090.

Munson B. R., Young D. F., Theodore H. O. (2006). *Fundamentals of Fluid Mechanics.* (5^{th} ed), John Wiley & Sons. ISBN 0471675822

Newcomb T. P. (1958). The flow of heat in a parallel-faced infinite solid *British Journal of Applied Physics.* 9, p. 370–372.

Newcomb T. P., Millner N. (1965). Cooling rates of brake drums discs *Proc. Auto. Div. inst. Mech. Engrs.* 195.

Nicoletti G. (1996). Heat and momentum transfer in flows adjacent to vibrating wall surfaces. *Heat and Mass Transfer* Springer Verlag. 31 1, p. 145–151.

Noyes R. N., Vickers P. T. (1969). Prediction of surface temperatures in passenger car disc brakes SAE Technical Papers 690457.

Palmer E., Fieldhouse J., Mishra R. (2006). Optimisation of pin shape and its configuration for a pin type vente brake disc using CFD In *FISITA 2006.* Yokohama, Japan.

Parish D., MacManus D.G. (2005). Aerodynamic investigations of ventilated brake discs *Proc. IMechE, Part D, Journal of Automobile Engineering.* 219, p. 471–486.

Qian C. (2002). Aerodynamic shape optimisation using CFD parametric model with brake cooling application. SAE Technical Papers 2002-01-0599.

Roca R. T., Mikic B. B.(1972). Thermal conductance in a bolted joint. *AIAA* Paper No. 72-282. Cited in

Fletcher L. S., Peterson G. P., Madhusudana C. V. Groll E.(1990). Constriction resistance through bolted and riveted joints. *Journal of Heat Transfer, Trans. ASME.* 112 (4), p. 857–863.

RS Components (1997), RS Datascan data acquisition system March 1997

Sakamoto H. (2004). Heat convection and design of brake discs. *Proc. Instn. Mech. Engr. Part F.* 212, p. 203–212.

Sheridan D. C., Kutchey J. A., Samie F (1988). Approches to the thermal modelling of disc brakes In *SAE International Congress and Exposition, Detroit Michigan.* February 29–March 4, 1988. SAE Technical Papers 880256, p. 1–16.

Siddall R.G., Davies, T. W. (1971). An improved response equation for hot-wire anemometry. *International Journal of Heat and Mass Transfer.* 15 , p. 367–368.

Sisson A. E. (1978). Thermal analysis of vented brake rotors. SAE Technical Papers 780352.

Sun H. (2006). Sensitivity study on brake cooling performance SAE Technical Papers 2006-01-0694.

Tanvir M. A. (1988). On the cooling of disc brakes on a train. *Rail International.* 19 (3), p. 37–32.

Tirović M. (1998). Development of a wheel mounted disc brake for a high-speed train *Proc. Instn. Mech. Engr. Part F.* 212, p. 113–121.

Tirović M. (2005). Investigation into Temperatures, Thermal Stresses and Deflections of Different Brake Disc Designs for Commercial Vehicles In EAEC 2005. Belgrade.

Tirović M., Ali G. (2001). Design synthesis of non-symmetrically loaded high-performance disc brakes *Proc. Instn. Mech. Engr. Part F.* 215, p. 101–109.

Tirović M., & Galindo-López C. H.[a] (2006). Analysis of air flow and heat dissipation from wheel mounted railway brake discs In *Braking 2006 Conference.* York, UK. p. 125–134.

Tirović M., & Galindo-López C. H.[b] (2006). Improvement of heat dissipation from wheel mounted railway brake discs In *Journées Européennes du Freinage 2006.* Lille, France.

Tirovic M., Voller G. P. (2005). Interface pressure distributions and thermal contact resistance of a bolted joint. *Proc. R. Soc. Part A.* 461, p. 2339–2359.

Ventsislav Z. (2004). Predictions of frictions factors and heat transfer coefficients in corrugated tubes combined with twisted tape inserts. Part 1: Friction factors. *International Journal of Heat and Mass Transfer.* 47 , p. 589–599.

Ventsislav Z. (2004). Predictions of frictions factors and heat transfer coefficients in corrugated tubes combined with twisted tape inserts. Part 1: Heat transfer coefficients. *International Journal of Heat and Mass Transfer*. 47 , p. 385–393.

Versteeg H.K., Malalasekera W. (1995). *An Introduction to Computational Fluid Dynamics, The Finite Volume Method*. Pearson Prentice Hall. ISBN 0582218845.

Voller G. P. (2003). *Analysis of heat dissipation from railway and automotive brake discs*. PhD Thesis. Brunel University, UK.

Voller, G. P., Tirović M., Morris R., Gibbens P. (2003). Analysis of automotive disc brake cooling characteristics. *Proc. IMechE, Part D, Journal of Automobile Engineering*. 217, p. 657–666.

Voller G. P., Tirović M. (2007). Conductive heat transfer across a bolted automotive joint and the influence of interface conditioning. *To be published in International Journal of Heat and Mass Transfer*.

Wagner C. (1948). Heat transfer from a rotating disc to ambient air *Journal of Applied Physics*. 19, p. 837–839.

Wan Q, Kuznetsov A. V. (2003). Numerical study of the efficiency of acoustic streaming for enhancing heat transfer between two parallel beams. *Flow:Turbulence and Combustion.* 70, p. 89–114.

Wahid S. M. S., Madhusudana C. V.(2003). Thermal contact conductance: effect of overloading and load cycling. *International Journal of Heat Transfer and Mass Transfer* 46, p. 4139–4143.

Wallis L., Leonardi E., Milton B., Joseph P. (2002). Air flow and heat transfer in ventilated disc brake with diamond and tear-drop pillars *Numerical Heat Transfer*. Part A 41, p. 643–655.

Watkins S., Stephens A., Dixon C. (2005). The aerodynamics of vented disc brakes In EAEC 2005. Belgrade.

Wendt J. F. (editor) (1995). *Computational Fluid Dynamics: An Introduction*. Springer-Verlag, Berlin. ISBN 354059471X.

Yamabe J., Takagi M., Matsui T., Kimura T., Sasaki M.(2002). Development of disc brake rotors for trucks with high thermal fatigue strength. *JSAE*. 23, p. 105–112.

Yan W. M., Soong C.Y.(1995). Simultaneously developing mixed convection in radially rotating rectangular ducts. *International Journal of Heat and Mass Transfer* 38 4, p. 665–677.

Yan W. M., Li H. Y., Lin D.(1999). Mixed convection heat transfer in a radially rotating square duct with radiation effects. *International Journal of Heat and Mass Transfer* 42, p. 35–47.

Yeh C. L., Wen C. Y., Chen Y. F., Yeh S. H., Wu C. H.(2001). An experimental investigation of thermal contact conductance across bolted joints. *Experimental Thermal and Fluid Science* 25, p. 349–357.

Yip F. C.(1972). Theory of thermal contact resistance in vacuum with an application to bolted joints. *AIAA* Paper No. 72-281. Cited in

Fletcher L. S., Peterson G. P., Madhusudana C. V. Groll E.(1990). Constriction resistance through bolted and riveted joints. *Journal of Heat Transfer, Trans. ASME.* 112 (4), p. 857–863.

Zammit J.P. (2007). *Ventilated Discs Design: Optimisation of Heat Dissipation.* MSc Thesis, 2007. Cranfield University.

Zhang J.J. (1997). A high aerodynamic performance brake rotor design method for improved brake cooling SAE Technical Papers 973016.

NIST ITS-90 Thermocouple Database (1999),
http://srdata.nist.gov/its90/main/its90_main_page.html

Cheltenham Induction Heating (2007). *4-20kW ISM Range Instruction Manual.* Version 9.09.

SC 2040 User Manual, PN 371191A-01 (1994),
National Instruments Corporation.